Chapter 9
Synthesis of TRIP Matrix Composites by Field Assisted Sintering Technology—Challenges and Results

Sabine Decker, Markus Radajewski and Lutz Krüger

Abstract This chapter analyses options to synthesis TRIP matrix composites (reinforced with Mg-PSZ), which stand out due to a high strength and the possibility to undergo a stress- and strain-induced phase transformation. These composites are processed using Field Assisted Sintering Technology (FAST). Both, the influence of the powder treatment before sintering and the impact of parameter setting during sintering by FAST are discussed. Due to a careful alignment of these factors, a TRIP matrix composite (reinforced with 5 vol% Mg-PSZ) with an 1% compressive yield strength of 700 MPa was generated. Furthermore, both composite components exhibited a phase transformation during compressive deformation. The fundamental investigations are the basis for the development of Functionally Graded Materials (FGM) with a varying Mg-PSZ content along the sample height. To synthesize these FGMs by FAST, a temperature gradient has to be generated during sintering, which allows to sinter the pure ceramic layer without melting the steel phase. Several possibilities to generate a temperature gradient are discussed.

9.1 Introduction

With the aim to develop a composite material with a high strength while keeping a sufficient ductility and toughness, a Transformation Induced Plasticity (TRIP) steel was combined with MgO Partially Stabilized Zirconia (Mg-PSZ). Both materials have the ability to undergo a phase transformation, if a certain stress or deformation is applied, which improves strength and toughness. TRIP steels have the possibility to transform from austenite into α'-martensite, if a certain trigger stress is reached.

S. Decker (Emeritus)
Institute of Materials Engineering, Technische Universität Bergakademie Freiberg, Gustav-Zeuner-Straße 5, 09599 Freiberg, Germany

M. Radajewski · L. Krüger (✉)
Institute of Materials Engineering, Technische Universität Bergakademie Freiberg, Gustav-Zeuner-Straße 5, 09599 Freiberg, Germany
e-mail: krueger@ww.tu-freiberg.de

H. Biermann and C. G. Aneziris (eds.), *Austenitic TRIP/TWIP Steels and Steel-Zirconia Composites*, Springer Series in Materials Science 298,
https://doi.org/10.1007/978-3-030-42603-3_9

Under this requirement, the α′-martensite content increases with ongoing deformation. The α′-martensite nuclei form mainly in deformation bands and restrict the dislocation movement. This leads to an increase in material strength similar to grain refinement [1–3].

Due to the partial stabilization with MgO, the high temperature phases (cubic and tetragonal) of zirconia are stable at room temperature in Mg-PSZ [4]. If a certain stress is applied, the tetragonal phase transforms into the monoclinic phase. This phase transformation comes along with a volume expansion, which is able to close cracks and introduces compressive stresses to the surrounding area [5]. This effect is used to improve the toughness of ceramic materials. The combination of both materials, the TRIP steel and the Mg-PSZ, holds the possibility to get a composite with a high strength and still a high ductility and toughness. Furthermore, it is assumed, that both phase transformations trigger each other [6].

A promising technique to process high-strength materials on a powder metallurgical route is the Field Assisted Sintering Technology (FAST), known as Spark Plasma Sintering, as well. This sintering technique is similar to hot pressing. That means, the powder is uniaxially compressed inside a die during sintering. However, heat is generated directly in the powder and/or in the sintering tool by an electric current, running through the electrically conductive powder and/or the electrically conductive die. Depending on the producer of the FAST device, the electric current is an alternating current or a direct current, which can be pulsed or continuous. The current passes merely through the electrically conductive die, if the powder is electrically nonconductive [7]. If the current runs through the powder, especially powder particle contacts are areas with a high electrical resistivity, which cause an extreme rise in temperature. Hence, the heat is generated at locations where it is most needed. Due to the heat generation directly within the powder or close to the powder, very fast heating rates can be attained and dwell times can be kept short [7, 8]. Caused by the short sintering process, diffusion driven mechanisms like grain growth and formation of precipitations or solid solutions occur in a reduced manner [7, 8]. Hence, extraordinary microstructures can be achieved and the sintered material exhibits a high strength due to its small grains.

Composites consisting of stainless steel and yttria stabilized zirconia were already sintered by FAST [9–11]. However, none of these studies addressed the effect of FAST parameters on microstructure and in none of these studies phase transformations under mechanical loading in both, in metastable stainless steel and in PSZ, were tried to achieve. However, to develop a high strength material it is important to understand how steel and ceramic influence each other and how the process parameters control the microstructural evolution and the achieved mechanical properties. Since 2008, researchers at TU Bergakademie Freiberg/Germany comprehensively investigate Mg-PSZ reinforced TRIP matrix composites in a collaborative research center (CRC 799). Among other topics, the influence of sintering parameters during FAST, chemical composition of the steel matrix and homogeneity of the composite powder on microstructural evolution and mechanical properties were studied. Based on the results, it was possible to develop a composite material with a high strength and sufficient ductility, where both composite constituents experienced a phase transformation under mechanical loading. Furthermore, the results are the basic principles for

the processing of functionally graded materials (FGMs). To sinter FGMs by FAST, several possibilities to adjust temperature gradients during FAST were investigated. The achieved results are presented in the next paragraphs.

9.2 Experimental Methods

For FAST experiments, different steel (Table 9.1) and Mg-PSZ powders (Table 9.2) were used. The distribution of powder particle size of different powders is shown in Table 9.3. Due to the complexity of nomenclature, the steel and the Mg-PSZ powders are abbreviated with S1–6 and Z1–3, respectively (see Tables 9.1 and 9.2).

The powders Z1, Z2 and Z3 are commercial powders from Saint-Gobian. While the steel powders S1, S5 and S6 were gas atomized by TLS Technik GmbH & Co. Spezialpulver KG (Bitterfeld/Germany), the powders S2, S3 and S4 were gas atomized at the Institute of Iron and Steel Technology at TU Bergakademie Freiberg (Germany). The steel powders consisted of austenite and α′-martensite. As the α′-martensite completely transforms to austenite during sintering, an exact indication of α′-martensite within the steel powder is not required.

Table 9.1 Chemical composition of the steel powders

[wt%]	Cr	Mn	Ni	Si	N	C	S	Fe
PM X3CrMnNi16-6-6								
S1	16.40	6.30	6.30	1.00	0.06	0.03	0.01	Bal.
PM X5CrMnNi14-6-5								
S2	14.37	5.98	5.46	0.97	0.05	0.05	0.02	Bal.
PM X3CrMnNi14-7-8								
S3	14.20	7.98	8.40	0.94	0.03	0.03	0.02	Bal.
S4	14.08	6.68	8.99	0.94	0.04	0.04	0.10	Bal.
PM X4CrMnNi16-6-6								
S5	16.10	5.96	5.97	0.89	0.04	0.04	0.01	Bal.
PM X4CrMnNi16-7-3								
S6	15.60	7.10	3.03	0.01	0.05	0.04	0.01	Bal.
PM X2CrMnNi16-7-6								
S7	16.40	7.10	6.30	0.11	0.06	0.02	0.00	Bal.

Table 9.2 Chemical analysis of the Mg-PSZ powders

[wt%]	SiO_2	MgO	Al_2O_3	CaO	TiO_2	Na_2O	Fe_2O_3	ZrO_2
Z1	4.23	3.37	0.63	0.21	0.14	0.09	0.1	Bal.
Z2	0.41	2.82	0.38	0.15	0.13	0.10	0.13	Bal.
Z3	0.10	3.25	1.58	0.06	0.13	–	0.02	Bal.

Table 9.3 Powder particle size distribution

Powder	d_{10} [μm]	d_{50} [μm]	d_{90} [μm]
TRIP steel			
S1	7.4	20.7	41.3
S2 < 25 μm	6.1	12.3	21.4
S2 25–45 μm	11.7	24.1	36.9
S2 45–63 μm	13.1	38.4	56.2
S3	10.8	37.3	124.2
S4	5.5	17.1	103.6
S5	10.3	28.1	44.4
S6	7.8	19.9	33.0
S7	12.4	25.9	46.6
Mg-PSZ			
Z1	0.1	1.3	10.8
Z2	0.2	3.1	22.4
Z3	13.4	21.1	32.9

The powder Z1 exhibited 10 vol% monoclinic, 37 vol% tetragonal and 53 vol% cubic phase, while the powder Z2 contained 35 vol% monoclinic, 32 vol% tetragonal and 33 vol% cubic phase. Only 1 vol% monoclinic phase was present in powder Z3 while 38 vol% were in the tetragonal and 68 vol% were in the cubic phase.

Composite powders with varying Mg-PSZ contents were mixed in a planetary ball mill PULVERISETTE 6 classic line (FRITSCH GmbH, Germany). For mixing, steel balls with a diameter of 10 mm were used and a ball mass to powder mass ratio of 5:1 was applied. Mixing was carried out for four hours. To achieve a sufficient swirling of the powder, the rotation speed was calculated by using (9.1) [12] depending on used milling vessel size to be 100 or 110 rpm for simply homogenization. A rotation speed of 250 rpm was utilized for high energy milling. Merely, the composite powders that are based upon S6 and Z2 were mixed in a PET vessel for one hour, using yttria stabilized zirconia balls.

$$N_0 = \frac{32}{\sqrt{d}} \tag{9.1}$$

N_0 rotation speed in rpm
d diameter of milling vessel in meter.

Afterwards, pure steel samples, pure Mg-PSZ samples, composites with constant Mg-PSZ volume content (5%, 10% or 40%) and FGMs with varying Mg-PSZ content were sintered. FGMs were prepared by layering composite powders with decreasing Mg-PSZ content on top of each other inside a graphite die. Unless specified otherwise, all sintering experiments were carried out using a FAST device HP D 25 (FCT Systeme GmbH, Germany). To start the sintering process, it is necessary to apply at

least a uniaxial load of 5 kN. Thus, a complete pressureless sintering is not possible in this device. All performed sintering cycles were carried out under fine vacuum and the cooling process after sintering was unregulated by simply switching off the power supply. The used dies and punches consisted of graphite (type 2333 from Mersen, Germany). After sintering, the relative density of the sintered samples was determined by Archimedes density measurements. Considering thermal expansion and elastic deformation of powder and punches during sintering, the evolution of the relative density during sintering was calculated in accordance to [13] by using (9.2).

$$\rho_i = \rho_0 \cdot e^{\varepsilon_{zi}} \tag{9.2}$$

ρ_i density at time i
ε_{zi} shrinkage in z-direction at time i
ρ_0 initial density before sintering.

To investigate the mechanical properties under compressive loading conditions, cylindrical samples with a diameter to height ratio of 1:1 were machined and quasi-static compression tests (10^{-3} s^{-1}, MTS 810) were carried out to a maximum of 60% compressive deformation. Furthermore, hardness measurements were conducted in the layers of FGMs, using Vickers hardness at a load of 9.807 N (HV1). The microstructure of the as sintered samples and of the compressed samples was characterised by XRD measurements, light optical microscopy and scanning electron microscopy in combination with electron backscatter diffraction (EBSD).

9.3 Results and Discussion

9.3.1 Influence of the Composite Powder on the Microstructural Evolution and Mechanical Properties of the Sintered Composite

If the results of a sintering experiment are evaluated, they are not only a consequence of sintering parameters, set on the sintering device. They are a product of chemical composition and the earlier treatment of the material (e.g. mixing). Some aspects of such treatments and chemical variations, which could be used to set the powder into a good initial position to achieve a high-strength material, are discussed in this chapter.

First of all and very important, the **chemical composition** of the steel powder influences the phase composition of the composite. During sintering, the Mg-ions diffuse from the Mg-PSZ into the steel matrix [14]. Thus, the Mg-PSZ destabilizes and the monoclinic phase content increases. However, the alloying elements of the

steel influence the Mg-PSZ as well. For example, Mn from the steel stabilizes Mg-PSZ [14, 15]. Accordingly, it is possible that the Mg-PSZ is destabilized during sintering by FAST depending on the steel matrix. If an PM X5CrNi18-10 was used as matrix material, which contains 0.96 wt% Mn, approximately 45 vol% of the Mg-PSZ were destabilized during sintering [16]. However, if the steel matrix was similar to an PM X3CrMnNi16-6-6, only a few percent of the Mg-PSZ transformed to the monoclinic phase during sintering by FAST [17], as a consequence of the increased Mn content.

Less percentage of Mg-PSZ destabilized, if the **Mg-PSZ content** within the composite increased. Hence, no destabilization was measured, if pure Mg-PSZ was sintered [18]. Furthermore, the Mg-PSZ content influences the material properties, which the composite exhibits after sintering by FAST in general. Not only hardness and strength increase with increasing Mg-PSZ content (Fig. 9.1). Mg-PSZ particles have a pinning effect on the grain boundaries of the steel matrix. Thus, the grain growth within the steel phase is impeded with increasing Mg-PSZ fraction [16, 18]. Accordingly, the strength of the composite is not only a function of the Mg-PSZ content, but also of the grain size of the steel matrix as well. With decreasing steel grain size, the strength of the steel increases, which was already shown by the Hall-Petch relation [19].

In addition, the remaining porosity after sintering by FAST influences the material strength and the ductility [18]. However, the effect of porosity depends on the Mg-PSZ content, as well. Due to more steel-to-steel contacts, composites with a lower Mg-PSZ content exhibit a sufficient ductility, for example 80% true compressive strain for a composite reinforced with 5 vol% Mg-PSZ and only 8% true compressive strain for a composite reinforced with 40 vol% Mg-PSZ (composites containing powders Z1 and S1, see Fig. 9.1) [18].

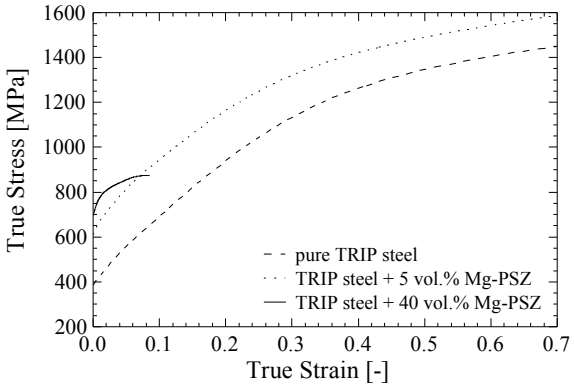

Fig. 9.1 Increase in compression strength with Mg-PSZ content (10^{-3} s^{-1})

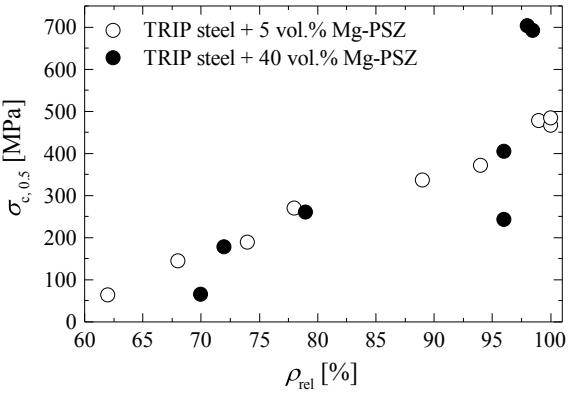

Fig. 9.2 Influence of relative density ρ_{rel} on 0.5% compressive yield strength $\sigma_{c,0.5}$ of composites consisting of Mg-PSZ (Z1) and a TRIP steel (S1), sintered using various parameters

The same effect applies for porosity. Composites with a low Mg-PSZ content can be deformed up to 80% true compressive strain even with a porosity of 22 vol% [18]. However, strength drastically decreases with increasing porosity (Fig. 9.2) [18]. While the 0.5% compressive yield strength increases linearly with relative density for a composite with 5 vol% Mg-PSZ, composites with 40 vol% Mg-PSZ (composites containing powders Z1 and S1) exhibit a strong increase in 0.5% compressive yield strength for a relative density >96%. Besides, for the composites with 40 vol% Mg-PSZ, values for 0.5% compressive yield strength deviate more (Fig. 9.2).

This deviation is caused by weakly sintered Mg-PSZ clusters. For a large relative density the strong increase in 0.5% compressive yield strength is a result of an increase in interfacial strength of Mg-PSZ/steel interfaces. However, the present weakly sintered Mg-PSZ clusters are the initiation areas for failure and they appear more frequently in composites with a higher Mg-PSZ content [18].

Since the α′-martensite formation is strain-induced, α′-martensite content increased with ductility of the composite. Hence, maximum 10 vol% α′-martensite was formed in composite material containing 40 vol% Mg-PSZ (containing S1 and Z1), due to its brittle material performance [18]. With decreasing Mg-PSZ content, ductility increases and more α′-martensite is formed [20]. Besides, the content of strain-induced α′-martensite depends on the chemical composition of the steel matrix, as well [16, 17]. However, a decrease in Mg-PSZ content does not lead necessarily to an increase in strain-induced α′-martensite [16]. As Martin et al. [6] proved, α′-martensite is formed preferential at poles of hard reinforcing particles under compressive deformation. Hence, a certain content of reinforcing phase triggers the α′-martensite formation.

In contrast, pores diminish the α′-martensite formation. If a porous material is compressed, a large content of deformation is engaged with closing pores, which does not involve extensive formation of deformation bands. Deformation bands are the sites for α′-martensite nucleation [2, 21]. For a composite containing 5 vol% Mg-PSZ (consisting of S1 and Z1), a porosity < 10 vol% is necessary to form the maximum possible strain-induced α′-martensite content [18]. With increasing Mg-PSZ content, more Mg-PSZ clusters are formed, which are the origin of damage. Cracks run preferentially through Mg-PSZ clusters and along steel/Mg-PSZ interfaces [16–18]. Hence, the failure behavior becomes more brittle and less α′-martensite is generated.

Thus, to optimize ductility and strength, it is important to achieve a **homogeneous distribution** of the reinforcing phase within the matrix and to avoid clustering of the ceramic particles. This is possible by adjusting the **particle sizes** of matrix powder and reinforcing powder. That means, coarse Mg-PSZ powder is needed and the steel powder has to be refined. To get fine steel powder, it could be sieved to receive the fine fraction of gas atomized powder, or it could chemically be changed in a way to reduce the surface tension. This would lead to smaller particles during gas atomization [22].

However, the used powder particle size distribution influences the densification rate and grain size distribution of the compacted samples [1]. As demonstrated, using steel powder S2, which was sieved to fractions < 25 μm, 25 μm–45 μm and 45 μm–63 μm, the densification rate slightly increased with decreasing particle size. Hence, it is possible to reduce dwell time during sintering by FAST with decreasing particle size [1]. While the steel powder (S2) with a particle size of 45–63 μm needed a dwell time of 4.3 min, dwell time could be reduced to 3 min for the steel powder (S2) with a particle size <25 μm [1]. Furthermore, the maximum in shrinkage is shifted to slightly lower temperatures with decreasing particle size. Thus, the maximum sintering temperature can be reduced, as well [1]. With increasing particle size, it is most likely to get large grains, which can exceed the initial particle size, due to the strong overheating at the few particle contacts of the coarse powder particles [1]. Therefore, the powder mixture should contain a variety of particle sizes to facilitate a large number of powder particle contacts. Furthermore, small particles have small grains, which lead to an increased compressive yield strength due to the Hall-Petch-effect. However, the work hardening rate is higher in large grains due to a higher α′-martensite formation rate. In small grains, α′-martensite formation sets in at larger strain values compared to coarse grains. More energy is needed in small grains in comparison to larger grains to expand deformation bands, which are the locations for α′-martensite formation [1]. But after 60% compression, steel samples sintered from powder particles <25 μm exhibited a similar compressive strength like samples sintered from powder particles in the range of 45–63 μm [1].

Another possibility to reduce the steel particle size as a result of gas atomization is the reduction of the surface tension of liquid steel melt. Thus, smaller steel drops and thereby smaller steel particles are generated during gas atomization [22]. A possibility to reduce this surface tension is the addition of sulfur to the steel melt. Using the steels S3 (0.02 wt% sulfur) and S4 (0.1 wt% sulfur), the influence of sulfur content on microstructure and mechanical properties was investigated. The sulfur content

did not influence the grain size of the steel matrix after sintering of unreinforced steel, due to the high driving force for grain growth in fine grained material [22]. In contrast, the grain size of the steel matrix varied with sulfur content in the composite material due to pinning of the grain boundaries by Mg-PSZ (reinforced with 10 vol% Mg-PSZ of Z1). A smaller grain size was measured, if the sulfur content within the composite material was high. The reinforcing Mg-PSZ particles impeded the grain growth and almost kept the grain size of the initial steel particles [23]. The sulfur formed precipitations during sintering by FAST. According to EBSD measurements, these precipitations were CrS, Cr_2S_3 and MnS [22]. The amount of precipitations increased with sulfur content and resulted in an increase of 40 MPa in compressive yield strength and a rise in work hardening [22]. If the TRIP steel (S4) was reinforced with 10 vol% Mg-PSZ (Z1), more than 50% of the precipitations consisted of MnS and they were formed mainly at the steel/Mg-PSZ interfaces [23]. Due to the binding of Mn in precipitations, less Mn was on hand to stabilize the Mg-PSZ. Thus, more Mg-PSZ destabilized in steel matrix S4 during sintering [23]. Independent of the presence of reinforcement by Mg-PSZ, the compressive yield strength increased 40 MPa due to the increase of the sulfur content from 0.02 to 0.1 wt% and the combined forming of precipitations. Furthermore, the compressive yield strength of the steel increased by 140 MPa due to the addition of 10 vol% Mg-PSZ [23].

In addition to the adjustment of particle sizes of matrix and reinforcing powder, a possibility to avoid clustering of the ceramic is high energy ball milling. By this intensive milling, the Mg-PSZ is knead into the steel matrix and distributed more homogeneously (Fig. 9.3). Furthermore, the steel matrix is strongly deformed. Thus, the steel recrystallizes during sintering and becomes very fine grained [24]. The steel matrix exhibits an average grain diameter of approximately 1.4 µm (determined by EBSD) after ball milling at 250 rpm and sintering at 1100 °C and 5 min dwell time (composite contains 5 vol% Mg-PSZ Z1 and TRIP steel S1) [18]. If the composite powder was mixed at 100 rpm and sintered under the same conditions, the average grain diameter was 2.4 µm [18]. Furthermore, shrinkage rate is drastically increased due to the higher number of dislocations and vacancies within the steel matrix as

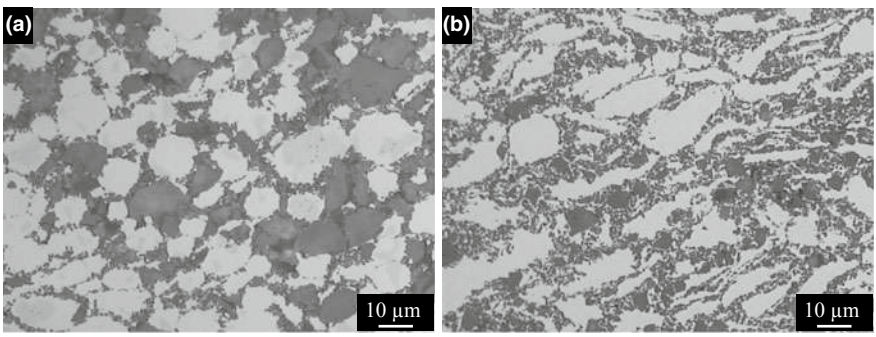

Fig. 9.3 Microstructure of a TRIP matrix composite, reinforced with 40 vol% Mg-PSZ (S1, Z1) after sintering by FAST, powder milled with **a** 100 rpm and **b** 250 rpm

a result of the milling process. Therefore, the necessary temperature for sintering decreases about 75 K, if the powder was milled at 250 rpm [18, 24]. However, due to the homogeneous distribution of the Mg-PSZ within the steel matrix, more Mg-PSZ/steel interfaces exist. Hence, the area where the Mg-ions have the possibility to diffuse into the steel matrix is larger and more Mg-PSZ destabilizes during sintering. Depending on the used powder batch and sintering parameters, approximately 35–45 vol% of the Mg-PSZ are in the monoclinic phase after sintering [18, 24]. Due to the better clamping of the Mg-PSZ with the steel matrix, the interfacial strength is increased and results in an improved transmission of loading from the steel matrix to the Mg-PSZ. Thus, the content of stress-induced phase transformation increases and 40–55 vol% of the Mg-PSZ transform stress-induced into the monoclinic phase under compressive loading [18, 24]. All in all, the compressive strength was drastically affected by the used TRIP steel and the Mg-PSZ content. For a composite (consisting of S1 and Z2) reinforced with 40 vol% Mg-PSZ, the 1% compressive yield strength increased from 776 to 1328 MPa, if the rotation speed was increased from 100 to 250 rpm. The effect of powder processing was further illustrated by the shift of 1% compressive yield strength of a composite with 5 vol% Mg-PSZ (S1 and Z1) from 540 MPa (100 rpm) to 625 MPa (250 rpm) [18]. Even further improvement to 700 MPa was possible by adjusting sintering parameters [18].

9.3.2 Influence of Sintering Parameters on the Microstructure and the Mechanical Properties of the Sintered Composite

Besides the requirements of the initial powders to achieve a high-strength material, which has the ability to undergo phase transformations under mechanical loading, the coordination of the sintering process is decisive for the microstructural evolution and the mechanical properties of the sintered material. In the case of FAST, sintering temperature, heating rate, cooling rate, dwell time, pressure and setting of die and punches influence the result of the sintering process.

If the **pulsing** of the current exhibits an explicit effect on densification behavior and the material properties, is discussed controversially in literature. Chakraborty et al. for example found a decreased relative density for ZrB_2 after sintering by FAST, if the off time of the pulse profile exceeded the on time [25]. Shen et al. reported a slight increase of the temperature which is needed for densification of alumina with increasing on:off pulse ratio [26]. Belmonte et al. found an increase in peak voltage and a shift of the maximum shrinkage rate to lower temperature with decreasing number of pulses and increasing off time during sintering of silicon nitride [27]. Moreover, an influence of the on:off ratio on the presence of an alumina layer on the surface of aluminum powder particles, and on the reactivity of aluminum with carbon was determined by Lalet et al. [28]. As well, they found melting of aluminum already at 500 °C, which is 150 K below the actual melting point of

aluminum, if the dc on:off ratio was < 1 [28]. Furthermore, Jiang et al. reported an improved interfacial reaction between aluminum and Si_3N_4 in an aluminum matrix composite with decreasing pulse ratio. However, the mechanical properties of this composite were best at a short pulse time and an dc on:off ratio > 1 [29]. In contrast, Xie et al. investigated the influence of the frequency of pulsed electric current during sintering on the mechanical and electrical properties of aluminum and found no effect [30]. Furthermore, Chen et al. proved, that the pulse pattern of the current does not influence the formation and growth of an reaction layer between Mo and Si [31].

Using a composite powder (mixed at 100 rpm), consisting of 40 vol% Mg-PSZ (Z1) and 60% of TRIP steel (S1), for sintering by FAST, several pulse pattern were tested (3:1 ms; 12:2 ms; 27:9 ms, 30:2 ms) during heating up to 1020 °C and a dwell time of 5 min (51 MPa uniaxial compression, 20 mm sample diameter) using a FAST device Dr. Sinter 2050 (Sumitomo Coal Mining Co., Ltd., Japan). However, no obvious effect of pulse pattern on densification, grain size and phase fraction was detected. Only temperature measurements during heating to 950 °C in a drill hole to the center of a densified steel sample (S1) and at the surface of the surrounding graphite die indicated a slight increase in temperature deviation with increasing off time. In this case, the sample center was hotter than the die, whereas the die temperature was the control variable. Hence, a temperature deviation of 33 ± 7 K was indicated for a pulse pattern of 27 ms: 9 ms while all remaining pulse pattern lead to a deviation of approximately 21 ± 5 K.

To create a composite material by FAST, it is advisable to understand the sintering behavior of the composite constituents first. Especially for such different composite partners like steel and ceramic, it is necessary to find a parameter range, where both constituents sinter.

Independent of the **heating rate**, the TRIP steel (S1) begins to shrink between 550 and 600 °C (Fig. 9.4) [1, 18]. Above 1100 °C, the TRIP steel starts to melt

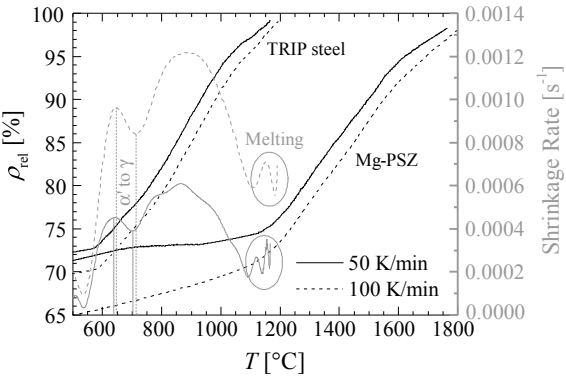

Fig. 9.4 Increase of relative density ρ_{rel} and evolution of shrinkage rate with temperature T of TRIP steel (S1) and Mg-PSZ (Z1) at a constant pressure of 51 MPa

[18] while the actual melting point of this steel is at 1416 °C [32]. The melting of the steel at lower temperatures during FAST is a result of graphite diffusion from the die into the sample during sintering. Due to the increase of carbon content, the melting point is drastically reduced. Furthermore, the temperature is measured by a pyrometer inside a hole in the graphite punch, 5 mm away from the sample surface. Thus, the actual temperature inside the sample is going to be higher than the measured temperature. Hence, the maximum temperature to sinter TRIP steel in this sintering setup is 1100 °C. Mg-PSZ, however, begins to shrink at a temperature slightly above 1100 °C (Fig. 9.4) and its optimum sintering temperature is between 1400 and 1600 °C [18]. With increasing heating rate, shrinkage rate increased [18]. Thus, a higher heating rate of 100 K/min is beneficial. However, caused by the melting of the TRIP steel, the maximum sintering temperature to densify the composite has to be 1100 °C. Higher temperatures are possible for the sintering of composites. However, the graphite die and the graphite punches are destroyed by the occurring steel melt. Besides, the steel melt partly flows out of the die. Furthermore, clustering of Mg-PSZ has to be avoided due to the poor sintering of Mg-PSZ at 1100 °C.

With increasing **temperature**, not only shrinkage occurs, but phase transformation as well. For example, α′-martensite was generated during milling due to deformation by the milling balls. During sintering, the α′-martensite transforms into austenite while heating. For the steel S1, the temperature range for transformation is between 650 and 730 °C (Fig. 9.4) [1, 18]. This effect is marked by a flattened region in the relative density-temperature-curve and a decrease in shrinkage rate (Fig. 9.4). To prove this fact, bulk samples, where first 70 vol% α′-martensite were formed by compressive deformation at −196 °C, were afterwards heated to 700 and 850 °C in a FAST device. While only 10 vol% α′-martensite remained within the sample heated to 700 °C, 99% austenite were measured after heating to 850 °C [1, 18].

The Mg-PSZ undergoes a phase transformation during sintering, as well. While the composite powder with 40 vol% Mg-PSZ (consisting of S1 and Z1) exhibited 18 vol% monoclinic phase, no monoclinic phase was indicated by XRD after heating to 1100 °C without applying a dwell time. Even after sintering at 1100 °C of pure Mg-PSZ (Z1) powder with initially 10 vol% monoclinic phase, no monoclinic phase remained [18]. This is in accordance with Berek et al., who found a phase transformation from monoclinic to tetragonal phase of Mg-PSZ within the temperature range of 700–1200 °C [33]. However, as already mentioned, if Mg-PSZ is in contact with steel, the Mg-ions diffuse into the steel matrix and Mg-PSZ destabilizes. This effect is intensified with increasing temperature due to the rise in diffusion rate. Thus, 28 vol% monoclinic Mg-PSZ were determined within the Mg-PSZ of the composite reinforced with 5 vol% Mg-PSZ (consisting of S1 and Z1) after sintering by FAST at 1200 °C and only 11 vol% monoclinic phase after sintering at 1100 °C. In both cases, no dwell time was used and a pressure of 16 MPa was applied [18]. An equal trend was indicated for a composite reinforced with 40 vol% Mg-PSZ (consisting of S1 and Z1) using the same FAST conditions. While no monoclinic phase was detected after sintering at 1100 °C, 7 vol% of the Mg-PSZ exhibited the monoclinic phase after densification at 1200 °C [18].

An increase of **dwell time** from 5 to 10 min had no influence on grain size distribution within the steel matrix of a composite with 5 vol% Mg-PSZ (consisting of S1 and Z1) [24]. However, during the first five minutes, the grains of the steel matrix grew approximately 2 µm and 4 µm inside composites with 5 and 40 vol% Mg-PSZ (consisting of S1 and Z1), respectively [18]. An exponential reduction of grain growth during dwell time was already reported by Shen et al. [26]. Even though steel grains grow during dwell time and a decrease in composite strength is expected, the compressive yield strength of the composite slightly increased with dwell time. While it was only a slight increase in compressive yield strength and it was within standard deviation, statements concerning correlations between increase in compressive yield strength and dwell time have to be handled with care. However, due to the absence of a decline in compressive yield strength, it is to assume that an increase in dwell time causes an improved interfacial strength by diffusion processes, which counteracts a decline in compressive strength caused by grain growth [18]. This assumption can be confirmed by micrographs (Fig. 9.5) of compressed composites, which exhibit a large number of cracks at steel/Mg-PSZ interfaces, if they were sintered without a dwell time, and, which show particle cracking and only a few locations of delamination, if a dwell time of five minutes was applied.

As already mentioned, the monoclinic phase of the Mg-PSZ transforms during sintering into the tetragonal phase. However, due to the loss of Mg-ions to the steel matrix, the Mg-PSZ destabilizes and more monoclinic phase is formed. These two processes are in the opposite direction. Thus, after sintering at 1100 °C without dwell time no monoclinic phase was indicated in the composite with TRIP steel matrix type S1 [18]. However, destabilization dominates during dwell time. Depending on the used steel matrix and the pre-treatment of the powder, 15–40 vol% of the Mg-PSZ are in the monoclinic phase after sintering at 1100 °C and five minutes dwell time [16–18, 24].

The applied **pressure** during sintering by FAST has an extreme influence on densification. If a composite with 5 vol% Mg-PSZ (consisting of S1 and Z1) is

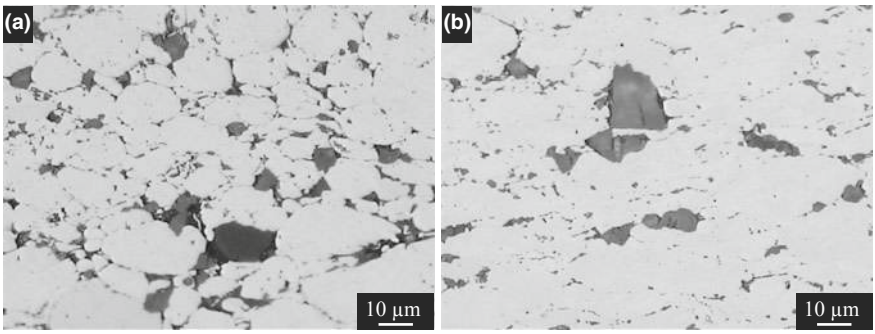

Fig. 9.5 Delamination and cracks after compressive deformation to 60% in a composite reinforced with 5 vol% Mg-PSZ (consisting of S1 and Z1), sintered using FAST at 1100 °C under an uniaxial pressure of 16 MPa and **a** no dwell time, **b** 5 min dwell time

sintered at 1100 °C without dwell time and 16 MPa applied pressure, the composite exhibits a relative density of 78%. A relative density of 99% is realized, if a pressure of 51 MPa is used. The relative density of a composite with 40 vol% Mg-PSZ (consisting of S1 and Z1) rises from 72 to 96% under the same FAST conditions, if the pressure is increased from 16 to 51 MPa [18]. Due to an increased pressure, the particle contacts deform at elevated temperatures. Thus, porosity is reduced by creep of the material [18]. By increasing the pressure, it is possible to reduce the necessary maximum temperature for sintering and shrinkage starts at lower temperatures. This temperature difference increases with increasing Mg-PSZ content. If the pressure is increased from 16 to 51 MPa, onset temperature of shrinkage is reduced 45 K for a composite with 5 vol% Mg-PSZ (consisting of S1 and Z1) and 250 K for a composite with 40 vol% Mg-PSZ (consisting of S1 and Z1) [18]. The grain size of the steel matrix varies only for small Mg-PSZ contents with pressure. If a low pressure is applied during heating up and dwell time, the grain size becomes more heterogeneous. In this case, the porosity is quite high at the beginning of dwell time and only a few steel to steel contacts exist where the current passes through. Inside these preferred paths of the current, very large and elongated grains form, while the grains within electrically isolated areas remain small [18]. For higher Mg-PSZ contents, the influence of the pressure on grain growth decreases.

Due to the overheating at current paths during sintering at low pressure, Mg-PSZ particles, which are close to these current paths, destabilize. Thus, the monoclinic content within the Mg-PSZ of composites with a low Mg-PSZ content increases, if a low pressure is applied during sintering [18].

The interfacial strength between Mg-PSZ and steel of the composite is improved by applying a high pressure during sintering. Hence, composites (reinforced with 40 vol% Mg-PSZ, consisting of S1 and Z1, 4% porosity), which were sintered using a pressure of 16 and 51 MPa exhibited a 0.5% compressive yield strength of 242 and 404 MPa, respectively. Furthermore, a maximum compressive deformation of 3% was reached, if a pressure of 51 MPa was applied. In contrast, the composite sintered using a pressure of 16 MPa fractured after 1% compressive deformation [18]. Certainly, both composites were indeed sintered at the same temperature of 1100 °C but with different dwell times to achieve the same porosity. While no dwell time was needed, if a pressure of 51 MPa was applied, 5 min dwell time were necessary to achieve the same density at a pressure of 16 MPa. An increase in interfacial strength with prolongation of dwell time would be expected. However, the effect is not as strong as an increase in uniaxial pressure. Due to the improvement of interfacial strength by increasing the uniaxial pressure during sintering, slightly more strain-induced α'-martensite is formed during compressive deformation. However, this effect is characteristic for composites with a large Mg-PSZ content [18].

The stress-induced phase transformation of the Mg-PSZ is independent of Mg-PSZ content of the composite, dwell time and applied pressure. After compressive deformation, a constant monoclinic content within the Mg-PSZ (Z1) of approximately 40 vol% was measured within composites with a steel phase type S1 [18]. The initial monoclinic content after sintering depends on the used FAST parameters and the Mg-PSZ content. Thus, different amounts of stress-induced monoclinic phase

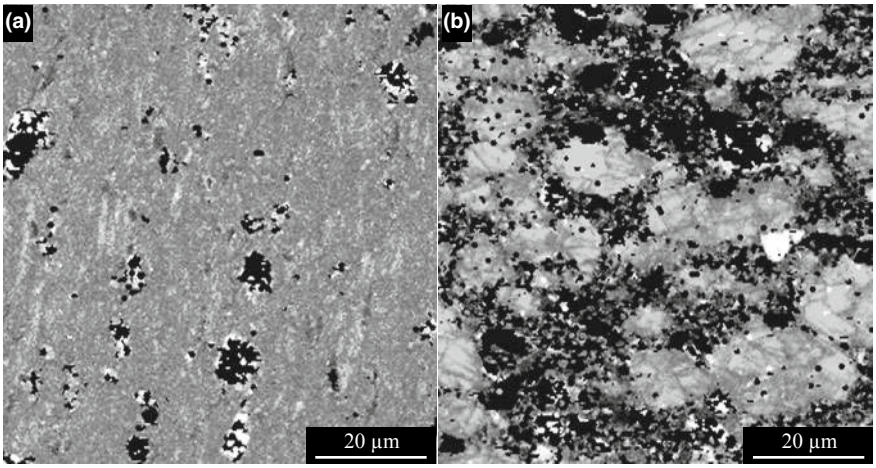

Fig. 9.6 EBSD analysis of the composite with **a** 5 vol% Mg-PSZ after 60% compression and **b** 40 vol% Mg-PSZ after compression to fracture (10^{-3} s^{-1}, grey: steel, white: monoclinic phase, black: tetragonal and cubic phase of the Mg-PSZ)

were formed during compressive deformation due to the chosen sintering parameters. However, it seems, that in this composites only 40 vol% of the Mg-PSZ were able to transform into the monoclinic phase (Fig. 9.6) [18].

If the stress-induced phase transformation of the Mg-PSZ influences positively the compressive flow behavior of the composite is questionable. Martin et al. [6] compared the compressive flow behavior of a composite reinforced with 5 vol% Mg-PSZ to a composite reinforced with 5 vol% alumina. They explained the higher compressive strength of the composite, reinforced with Mg-PSZ, with the stress-induced phase transformation of Mg-PSZ. However, the interfacial strength between matrix and reinforcing phase is not the same in these composites. Furthermore, the median particle size of alumina was 1 µm larger than that of the Mg-PSZ. Thus, the benefit by the stress-induced phase transformation is not entirely proven.

A simplified semiempirical model [see (9.3)] was developed on the basis of the rule of mixture [34], which considers the Mg-PSZ content, the Hall-Petch equation [19] for the influence of steel grain size, the equation of Haynes [35] taking into account the influence of the porosity, the equation of Olson and Cohen [36], which describes the α′-martensite evolution and the equation of Ludwik [37] for the reproduction of the flow behavior of the austenite. With this model, the compressive flow curve under quasi-static loading is well described for TRIP steel (S1) and composites (consisting of S1 and Z1) [18].

$$\sigma_d(\varepsilon_w) = (1 - V_{\mathrm{PSZ}})\left(\left(\sigma_{0\,0.5\%,\mathrm{St}} + \frac{k}{\sqrt{d}} + A \cdot \varepsilon_w^n\right) \cdot (1 - V_\alpha) + V_\alpha \cdot \sigma_\alpha\right) + V_{\mathrm{PSZ}} \cdot \sigma_{0\,\mathrm{PSZ}} \tag{9.3}$$

$\sigma_d(\varepsilon_w)$	true compressive flow stress
V_{PSZ}	volume content of Mg-PSZ
$\sigma_{0\,0.5\%,St}$	0.5% compressive yield strength of the steel phase
V_α	volume content of α′-martensite
σ_α	compressive flow stress of α′-martensite
d	grain size of steel phase
$\sigma_{0\,PSZ}$	critical compressive strength of Mg-PSZ
k, A, n	constants
ε_w	true compressive deformation.

However, the stress-induced phase transformation was not taken into account in this model. Thus, the stress-induced phase transformation obviously does not increase the compressive flow strength, if the compressive flow curve is well described without a considered contribution by the stress-induced phase transformation.

Next to FAST parameters like temperature, dwell time and uniaxial pressure, the used **die geometry** influences the sintering result, as well. The influence of a varying die wall thickness on temperature distribution is well known [38]. But, if for example, the die wall thickness is constant and the sample diameter is increased, the relation between cross-sectional area of the die and cross-sectional area of the sample decreases. Hence, more electrical current is going to run through the electrical conductive sample instead through the die. Thus, the sample is more intensively heated up and onset of densification is shifted to lower temperature.

For example, intensive shrinkage of a composite, reinforced with 5 vol% Mg-PSZ (consisting of S1 and Z1) and sintered in a die with 10 mm wall thickness, begins at 650 °C, if the sample had a diameter of 20 mm, and at 530 °C, if the sample had a diameter of 40 mm [18]. Furthermore, using the same FAST parameters results in different relative densities. Due to the high energy input in larger samples, grain boundaries break away from pores and the pores get inside the grains, which makes it very difficult to close these [12]. However, the porosity increased only 2%. The grain size of the steel phase was not influenced by the sample diameter [18]. Though, the destabilization of the Mg-PSZ was intensified by using a larger sample diameter and the combined increase in energy input inside the sample. The monoclinic content of the Mg-PSZ was doubled in composite samples with 5 vol% Mg-PSZ (consisting of S1 and Z1) sintered with a diameter of 40 mm in comparison to those samples sintered with a diameter of 20 mm [18]. Due to no changes in steel grain size and only a slight difference in porosity, the compressive flow behavior was independent form the sample diameter [18]. However, it is advised to keep the relation between cross-sectional area of the die and cross-sectional area of the sample constant for upscaling, to receive a similar microstructure after sintering by FAST.

It is of great interest in research to determine the acting processes, which lead to densification during sintering by FAST. Kieback and Trapp evaluated several processes suggested in literature critically [39]. They summarized the acting processes to be local heating and melting of powder particle contacts, breaking of oxide layers by electrical breakdown, prevention of grain growth, plastic deformation, diffusion

creep, grain boundary sliding, electron wind and thermodiffusion due to temperature gradients [39]. These processes are supported by a high heating rate and a high pressure [39].

Li et al. developed a way to determine shrinkage mechanisms during FAST. They adapted the load increasing test, which is used to calculate the strain rate exponent m for creep tests [40]. Using this approach for pure steel and composites with 5 and 40 vol% Mg-PSZ (consisting of S1 and Z1) at a test temperature of 1000 °C, strain rate exponents of 0.48 ± 0.22 and 0.47 ± 0.05 were identified for pure steel and composite with 5 vol% Mg-PSZ, respectively. The composite with 40 vol% Mg-PSZ had a strain rate exponent of 0.32 ± 0.10. In this temperature range, mainly the steel is shrinking and the strain rate exponent describes the behavior of the steel phase. According to the calculated strain rate exponents, grain boundary sliding ($m = 0.5$) and potentially dislocation creep ($m = 0.3, \ldots, 0.5$) are the main occurring mechanisms [40].

The load increase test using pure Mg-PSZ was carried out at 1400 °C and a strain rate exponent of 0.37 ± 0.25 was calculated. In this range of the strain rate exponent, sliding and climbing of dislocation dominates [41]. Taking into account the standard deviation, grain boundary sliding is possible as well [40]. At first, deformability of a ceramic seems unlikely, but for example Chen et al. proved that a deformation to 30% of zirconia at 1300 °C is possible [42].

9.3.3 *Sintering of Functionally Graded Materials (FGM) by FAST*

Based on the presented results, FGMs with varying Mg-PSZ contents were developed. Therefore, several layer arrangements were tested using TRIP steel powder S5. For this purpose, composite powders with different amounts of Mg-PSZ (Z1) and TRIP steel were mixed and layered on top of each other to receive a gradation of Mg-PSZ along the height of the sample (diameter: 40 mm). This gradation reached from 0 vol% Mg-PSZ to 40 vol% Mg-PSZ, while every layer should have a thickness of 1 mm after complete densification. Samples with layer arrangements of 0 vol%–20 vol%–40 vol% Mg-PSZ, of 0 vol%–10 vol%–20 vol%–40 vol% Mg-PSZ and of 0 vol%–10 vol%–20 vol%–30 vol%–40 vol% Mg-PSZ were generated (Fig. 9.7). To densify these layer systems, they were heated up with a heating rate of 100 K/min

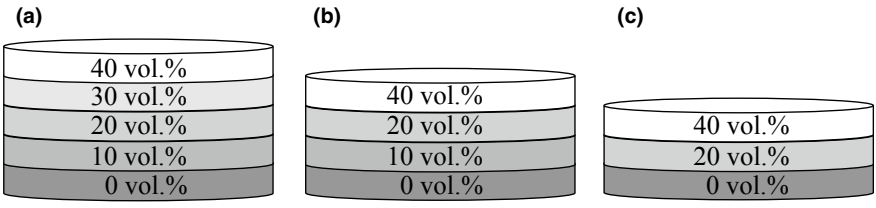

Fig. 9.7 Tested layering systems for the FGM with an Mg-PSZ content from 0 to 40 vol%

to 1100 °C within a FAST device. During heating, the powder was uniaxially compressed while the pressure increased up to 100 MPa and was kept constant during the dwell time of 10 min.

Radwan et al. found a significant influence of layering system of FGMs consisting of stainless steel and alumina on densification behavior and residual stresses [43]. However, no distinct influence on mechanical properties and microstructure was indicated for the FGMs consisting of TRIP steel and Mg-PSZ. Independent of the layer system, the FGMs had a similar hardness, bending strength and grain size of the steel matrix. Except, the four layer system (0 vol%–10 vol%–20 vol%–40 vol% Mg-PSZ) was crack free after sintering, while cracks were found within the FGM with three and five layers. Thus, much higher thermal stresses were present in the three and five layer systems compared to the four layer system. These high thermal stresses caused these cracks. The reduction of thermal stresses is a function of Mg-PSZ layer system. While the tested three layer and five layer systems exhibit a linear increase in Mg-PSZ content, the Mg-PSZ content of the four layer system follows an exponential function. These results confirm the assumption of Radwan et al., that an exponential increase in ceramic content leads to a reduction of thermal stresses [43].

As to be expected, the grain size of the steel matrix decreased with increasing ceramic content of the layer due to the pinning effect of the Mg-PSZ particles. Likewise hardness increased with Mg-PSZ content.

The FGMs exhibited a bending strength of 511 MPa (steel layer on tensile stress). This is 100 MPa larger than the bending strength of a steel matrix composite reinforced with 40 vol% Y_2O_3-PSZ [44]. However, the FGMs were not completely dense. The porosity increased with Mg-PSZ content. Furthermore, the graphite dies do not withstand the high mechanical pressure of 100 MPa during sintering by FAST at all times. Therefore, the pressure had to be decreased.

To completely densify the whole FGM especially applying a pressure < 100 MPa, the temperature distribution within the sintering setup has to be understood and systematically adapted. A vertical temperature gradient has to be expected by sintering of steel/ceramic FGMs using FAST due to the changing electrical conductivity along the sample height with changing ceramic content (Fig. 9.8). However,

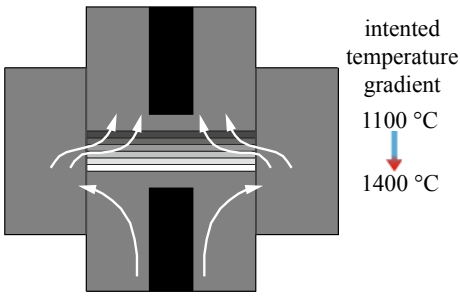

Fig. 9.8 Current path (marked by white arrows) through the sintering tool and the FGM and necessary sintering temperatures

zirconia-rich regions need a temperature of 1200–1300 °C [45] for nano sized powder and 1400–1600 °C for coarser powder [18] to be compacted. Furthermore, steel melts at those temperatures. To densify steel using FAST, temperatures of 1000–1100 °C are required [1]. Thus, a temperature gradient is needed, where the ceramic-rich regions are hotter than the steel-rich regions.

To investigate the vertical temperature gradient caused by the changing ceramic content, an FGM with the layer arrangement 0 vol%–5 vol%–10 vol%–30 vol%–60 vol%–100 vol% Mg-PSZ (from top to bottom, powders S6 and Z2) was sintered (maximum temperature 1100 °C measured in top punch, maximum pressure 51 MPa, dwell time 13 min, heating rate 100 K/min). During densification, the temperature was measured by pyrometer and thermocouples (TCs) within drill holes inside the die 3 mm away from the inner die surface, on the level of the middle of the sample in vertical direction and 2 mm above and below the centric hole. These temperature measurements indicated a much higher temperature at the top, which was close to the steel-rich regions compared to the Mg-PSZ-rich regions at the bottom of the sample [46]. During dwell time, the top and bottom temperatures slightly converged and differed ≈20 K at the end of dwell time. Hence, the steel-rich regions are ≈20 K warmer than the ceramic-rich regions, while it has to be the other way around to densify the FGM properly.

Some researchers introduced vertical temperature gradients by using tapered dies [9, 47] and found a vertical temperature gradient of 220 K. To obtain the required die geometry, extensive simulations and tests are necessary. Other researchers did not change the die geometry. They moved the sample from the die center to the bottom and placed the die directly on the lower larger punch to create a vertical temperature gradient within the sample [48, 49]. However, the temperature gradient varies strongly with the sintering material and the die geometry [50]. Vanmeensel et al. reported a strong increase in electrical resistivity with increasing number of surfaces [51] and therefore, with increasing number of graphite foils at the front surface of the sample. Hence, graphite foil can be used as heating element. To generate heat close to the ceramic-rich regions of the FGM in this study [46], two additional graphite foils were placed between graphite punch and 100% Mg-PSZ layer. Thus, the temperature within the ceramic-rich region converged to the temperature of the steel-rich regions, as indicated by temperature measurements inside the die [46]. During dwell time, the temperature of the ceramic-rich region even exceeded the temperature of the steel-rich region to 10 K [46]. Already, these slight temperature changes led to a lower porosity, improved bending strength and hardness (Fig. 9.9) [46]. However, a higher temperature is needed in the ceramic-rich region.

Since the ceramic-rich regions sinter during dwell time, the temperature gradient has to be existent during dwell time, as well. Furthermore, temperature measurements directly inside the sample are necessary to understand the temperature evolution inside the sample. Only a few studies dealt with direct temperature measurement using homogeneous materials, especially at process temperatures at or above 1000 °C. Temperature measurements utilizing TCs (at least one TC directly within the sample) were performed in the studies of Matsugi et al. [52] or Wang et al. [53].

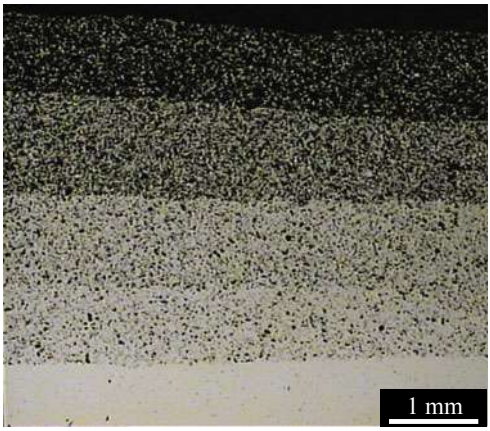

Fig. 9.9 FGM, sintered with additional graphite foils

Furthermore, the thermal insulation around the sintering tool influences the temperature distribution inside the sample. The application of thermal insulation by graphite felt as well as heating elements manufactured by CFRC and its influence on the temperature homogeneity within a conductive (austenitic steel) or non-conductive (8 mol% Y_2O_3 fully stabilized zirconia) sample was studied by Laptev et al. [54]. Particularly for large sample diameter ($\leq$50 mm), the fully thermal insulation of the die was not sufficient to achieve an acceptable horizontal temperature gradient (< 20 K) from the center to the edge of the (conductive) sample. Thus, further thermal insulation by the utilization of CFRC heating elements is required. In the case of non-conductive materials, an optimization (e.g. modification of the die thickness) of the sintering tool, in addition to the application of graphite felt and carbon fiber reinforced carbon (CFRC) heating elements, is often required to obtain an almost homogenous temperature distribution within the sample.

Thus, a further study concerning the temperature distribution within an FGM (consisting of S7 and Z3) during the FAST process dealt with the direct temperature measurement of the vertical temperature gradient of pre-sintered FGMs (at 1050 °C for 15 min) during the dwell time at 1000 °C (duration: 8 min). In reference [43] an equation for the calculation of the steel volume content of each layer within a steel/ceramic FGM is given. A total number of six layers, including the pure Mg-PSZ and steel layer, was selected for the FMG sample (layer thickness: 1.5 mm). For $P = 2$ (material concentration exponent), a steel-rich concentration profile was received, leading to an ceramic volume content of the interlayers of 4, 16, 36 and 64 vol% between the layers of pure steel and Mg-PSZ.

The direct temperature measurement using type S TCs took place within cylindrical bore holes (diameter: 3.5 mm), which had an offset to each other of 90°. The TC-measured temperature T_{TC} was determined in the center of the sintering tool, above (M1), centered (M2) and below (M3) the FGM sample, which is shown in Fig. 9.10. Alumina tubes were used to protect the TCs from high electrical currents,

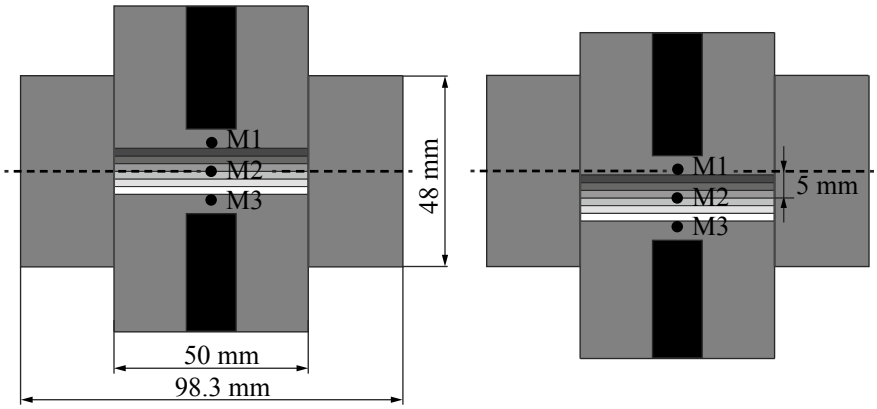

Fig. 9.10 Sintering tool setup, **a** symmetrical tool setup, **b** asymmetrical tool setup—FGM sample shifted by 5 mm downwards

carbonization or sintering to the sample surface. In addition to the experiments with a symmetrical sintering tool setup, asymmetrical sintering tool setups were investigated. For this purpose, the FGM sample was shifted by 5 mm upwards or downwards for both options—with the pure ceramic or steel layer on top.

For all temperature measurement experiments, the outside surface and the top and bottom side of the die were covered with graphite felt (SGL Group: Sigratherm GFA10) to reduce thermal radiation losses. Furthermore, the influence of CFRC discs on the temperature distribution during the SPS/FAST process was investigated.

In general, an 80–90 K higher T_{TC} in comparison to the pyrometer-measured process temperature T_{Pyro} was determined for the symmetrical sintering tool setup at M1 independent of the sample arrangement (pure ceramic layer at the top or at the bottom) and the application of CFRC discs. Furthermore, the highest vertical temperature gradient of approximately 80 K existed for the symmetrical sintering tool setup using an FGM sample with the fully ceramic layer at the top without utilizing CFRC discs for this FAST process. For the same sintering tool, the vertical temperature gradient decreased to approximately 15 K by the application of CFRC discs for the sintering process. Generally, in consequence of the utilization of CFRC discs for the FAST process, the heat was retained in the sintering tool and the electrical power required for the FAST process decreased. Both, the symmetrical or asymmetrical sintering tool setups exhibited vertical temperature gradients < 40 K while using CFRC discs for the sintering process. Despite the application of an asymmetrical sintering tool setup without using CFRC discs for the SPS/FAST process, the vertical temperature gradient never exceeded 80 K. Although, this temperature gradient is still not sufficient to sinter void free FGM, it is an improvement.

9.4 Conclusions

The combination of TRIP steel with Mg-PSZ in a composite and additionally processing this composite by applying FAST resulted in a material with a high strength and a sufficient ductility. By carefully adapting sintering parameters, the material had the ability to undergo strain-induced (TRIP steel) and stress-induced (Mg-PSZ) phase transformations under compressive loading. How the condition of the composite powder and the setting of FAST parameters influence the microstructure and the mechanical properties of the composite is schematically shown in Figs. 9.11 and 9.12. Due to the very short sintering time, only a small amount of the Mg-PSZ transformed into the monoclinic phase during sintering and the steel matrix exhibited very fine grains. Thus, the composites had a high strength. The amount of strength, however, depends on many factors concerning the used parameters, powder characteristics and powder treatment in preparation of FAST. Thus, parameters have to be carefully aligned for every powder condition. However, porosity can remain in the material even after tuning of the sintering parameters, as recently shown on a PM X15CrNiMnN19-4-3 [55]. This steel has a high nitrogen content of 0.17 wt%, which evaporates during sintering and remains partly as porosity (≈5 vol% pores).

Even though the Mg-PSZ has the ability to transform stress-induced after processing by FAST, this stress-induced phase transformation seems to have no influence on flow behavior under compressive deformation. On the one hand, the transforming amount of the Mg-PSZ is very low. On the other hand, the very ductile steel matrix does not transfer all loading to the Mg-PSZ. Thus, composites with a steel matrix, which has a higher strength (e.g. PM X16CrNiMnSiN 15-3-3), are investigated currently in order to increase the strength due to the stress-induced phase transformation of the Mg-PSZ. However, even without an effect of the stress-induced phase transformation, already an addition of 5 vol% Mg-PSZ to a TRIP steel matrix (S1, Z1) increases the specific energy absorption at dynamic deformation at room temperature by 5% [56].

So far, the introduced composites were carefully mechanically characterized by cyclic deformation [57] and by compression tests in a wide range of strain rates and temperatures [16, 17, 56]. Their corrosion behavior was investigated as well [58–60]. A detailed analysis of these results would go beyond the scope of the presented work. So far, weakly sintered ceramic clusters and a low interfacial strength between steel and Mg-PSZ are obstacles for a further improvement of the materials. Especially, the improved sintering of Mg-PSZ-rich layers for the development of FGM requires further research effort.

Acknowledgements The Authors would like to thank Prof. Zhijian James Shen from Stockholm University for his helpful advice and the possibility to carry out experiments using the FAST device (Dr. Sinter 2050, Sumitomo Coal Mining Co., Ltd., Japan) from his group. Furthermore, the authors would like to thank Dr. Tobias Dubberstein (subproject A2) for providing the steel powders with varying sulfur content and Michael Hötzel (subproject A3) for making steel powder, sieved to different particle fractions, available. The authors would like to thank the German Research Foundation (DFG) for supporting the investigations, which were part of the Collaborative Research Center TRIP-Matrix Composites (project number 54473466—SFB 799, subproject A6).

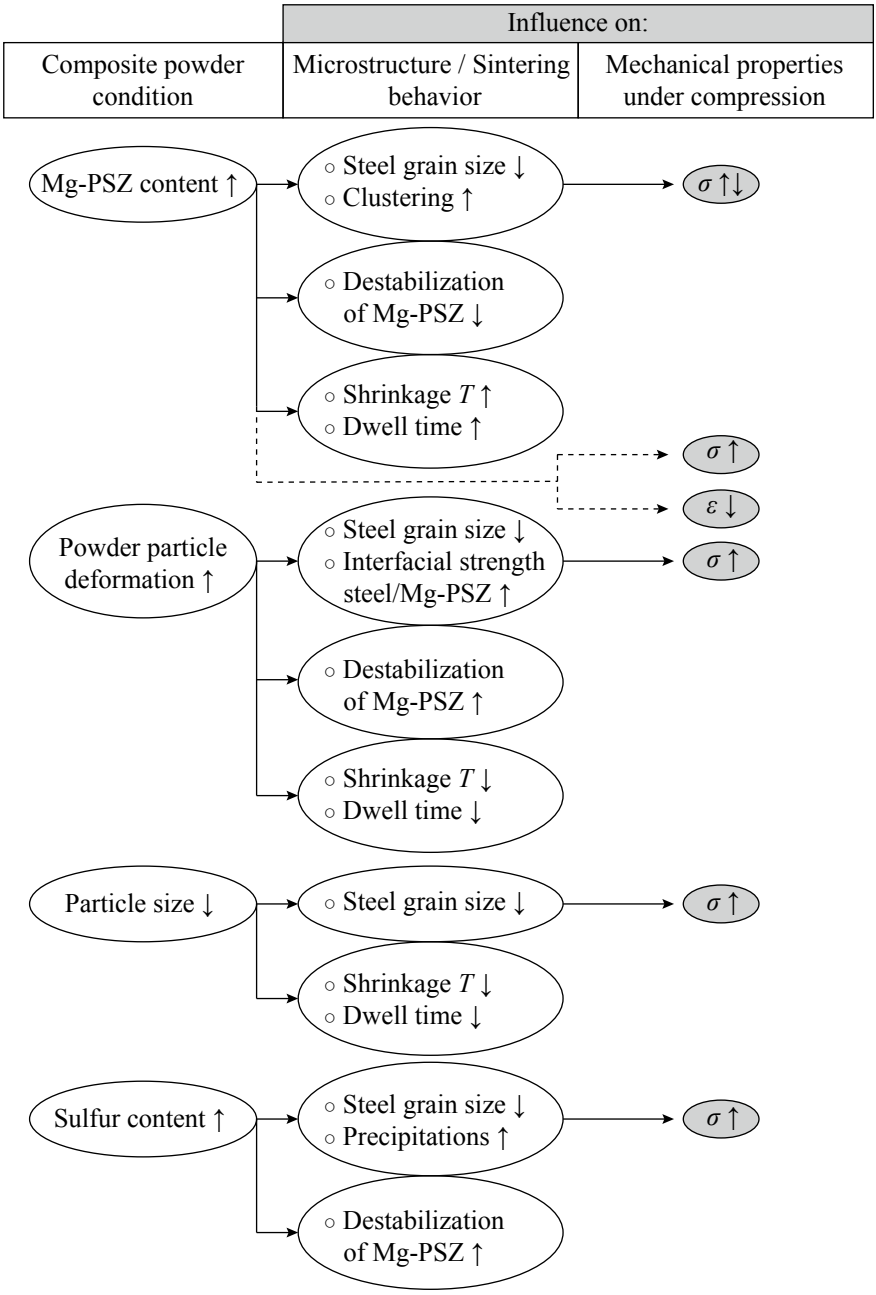

Fig. 9.11 Influence of composite powder condition on sintering behavior, microstructure and mechanical properties (T: temperature, ε: ductility, σ: compressive yield strength)

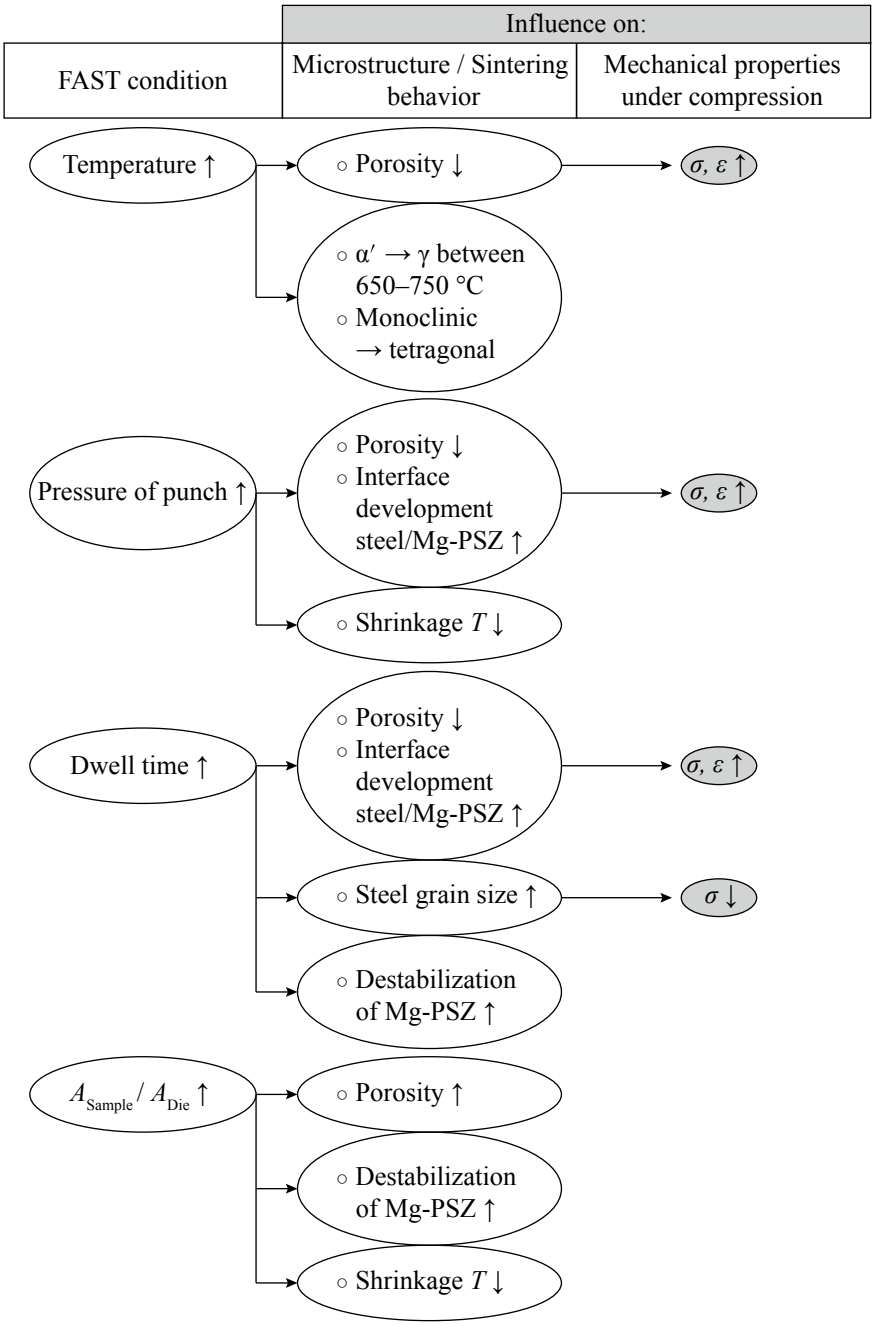

Fig. 9.12 Influence of FAST condition on sintering behavior, microstructure and mechanical properties (A_{Sample}: cross section of sample, A_{Die}: cross section of die, α′: α′-martensite content, γ: austenite content, T: temperature, ε: ductility, σ: compressive yield strength)

References

1. S. Decker, S. Martin, L. Krüger, Metall. Mater. Trans. A **47**, 1 (2016)
2. J.A. Venables, Philos. Mag.: J. Theor. Exp. Appl. Phys. **7**, 73 (2006)
3. O. Grässel, L. Krüger, G. Frommeyer, L. Meyer, Int. J. Plast **16**, 10–11 (2000)
4. H. Salmang, H. Scholze, *Keramik* (Springer, Berlin, 2007)
5. J.R. Kelly, I. Denry, Dent. Mater. **24**, 3 (2008)
6. S. Martin, S. Richter, S. Decker, U. Martin, L. Krüger, D. Rafaja, Steel Res. Int. **82**, 9 (2011)
7. O. Guillon, J. Gonzalez-Julian, B. Dargatz, T. Kessel, G. Schierning, J. Räthel, M. Herrmann, Adv. Eng. Mater. **16**, 7 (2014)
8. Z.A. Munir, U. Anselmi-Tamburini, M. Ohyanagi, J. Mater. Sci. **41**, 3 (2006)
9. M. Tokita, Mater. Sci. Forum 308–311 (1999)
10. L. Hälldahl, M. Nygren, Mater. Sci. Forum 492–493 (2005)
11. K. Ichikawa, S. Murakami, S. Miyamoto, Y. Nakayama, M. Tokita, Mater. Sci. Forum 423–425 (2003)
12. R.M. German, *Powder Metallurgy and Particulate Materials Processing* (Metal Powder Industries Fed, Princeton, NJ, 2005)
13. M.N. Rahaman, *Ceramic Processing and Sintering*, 2nd edn. (CRC Press (Taylor & Francis), Boca Raton, 2003)
14. H. Berek, A. Yanina, C. Weigelt, C.G. Aneziris, Steel Res. Int. **82**, 9 (2011)
15. C. Weigelt, S. Giersberg, C. Wenzel, C.G. Aneziris, Adv. Eng. Mater. **12**, 6 (2010)
16. L. Krüger, S. Decker, R. Ohser-Wiedemann, D. Ehinger, S. Martin, U. Martin, H.J. Seifert, Steel Res. Int. **82**, 9 (2011)
17. S. Decker, L. Krüger, S. Richter, S. Martin, U. Martin, Steel Res. Int. **83**, 6 (2012)
18. S. Decker, Entwicklung der Mikrostruktur und der mechanischen Eigenschaften eines Mg-PSZ-partikelverstärkten TRIP-Matrix-Composits während Spark Plasma Sintering, Dissertation, TU Bergakademie Freiberg (Logos Berlin, Berlin, 2015)
19. E.O. Hall, Proc. Phys. Society. Sect. B **64**, 9 (1951)
20. S. Decker, L. Krüger, Mater. Sci. Eng. A **761** (2019)
21. S. Martin, Deformationsmechanismen bei verschiedenen Verformungstemperaturen in austenitischem TRIP/TWIP-Stahl, Dissertation, TU Bergakademie Freiberg (Freiberger Forschungshefte TU Bergakademie Freiberg, Freiberg, 2014)
22. S. Decker, K. Lange, L. Krüger, T. Dubberstein, Steel Res. Int. **86**, 5 (2015)
23. S. Decker, K. Lange, T. Dubberstein, L. Krüger, Adv. Eng. Mater. **17**, 9 (2015)
24. S. Decker, L. Krüger, J. Compos. Mater. **50**, 13 (2015)
25. S. Chakraborty, A.R. Mallick, D. Debnath, P.K. Das, Int. J. Refract. Metals Hard Mater. **48** (2015)
26. Z. Shen, M. Johnsson, Z. Zhao, M. Nygren, J. Am. Ceram. Soc. **85**, 8 (2002)
27. M. Belmonte, M.I. Osendi, P. Miranzo, Scripta Mater. **65**, 3 (2011)
28. G. Lalet, H. Kurita, T. Miyazaki, A. Kawasaki, J.-F. Silvain, J. Mater. Sci. **49**, 8 (2014)
29. H. Jiang, Z. Xu, Z. Xiu, L. Jiang, H. Gou, C. Zhou, G. Wu, J. Alloy. Compd. **763** (2018)
30. G. Xie, O. Ohashi, K. Chiba, N. Yamaguchi, M. Song, K. Furuya, T. Noda, Mater. Sci. Eng., A **359**, 1–2 (2003)
31. W. Chen, U. Anselmi-Tamburini, J.E. Garay, J.R. Groza, Z.A. Munir, Mater. Sci. Eng., A **394**, 1–2 (2005)
32. T. Dubberstein, M. Hötzel, R. Hagemann, P. Heller, P.R. Scheller, Steel Res. Int. **82**, 9 (2011)
33. H. Berek, C.G. Aneziris, C. Wenzel, T. Westphal, W. Schärfl, Refractories Worldforum **3**, 3 (2011)
34. N. Chawla, K.K. Chawla, *Metal Matrix Composites*, 2nd edn. (Springer, New York, 2013)
35. R. Haynes, Met. Powder Rep. **46**, 2 (1991)
36. G.B. Olson, M. Cohen, Metall. Trans. A **6**, 4 (1975)
37. P. Ludwik, *Elemente der technologischen Mechanik* (Springer, Berlin, 1909)
38. J. Räthel, M. Herrmann, W. Beckert, J. Eur. Ceram. Soc. **29**, 8 (2009)

39. B. Kieback, J. Trapp, in *Sintern - der zentrale Prozess der Pulvermetallurgie*, ed. by H. Kolaska (Heimdall, Hagen, 2011), p. 47
40. W. Li, E.A. Olevsky, J. McKittrick, A.L. Maximenko, R.M. German, J. Mater. Sci. **47**, 20 (2012)
41. J. Weertman, Trans. ASM **61** (1968)
42. I.-W. Chen, L.A. Xue, J. Am. Ceram. Soc. **73**, 9 (1990)
43. M. Radwan, M. Nygren, K. Flodström, S. Esmaelzadeh, J. Mater. Sci. **46** (2011)
44. K. Tohgo, T. Kawaguchi, Key Eng. Mater. 297–300 (2005)
45. J. Langer, M.J. Hoffmann, O. Guillon, J. Am. Ceram. Soc. **94**, 1 (2011)
46. S. Decker, L. Krüger, Mater. Des. **115** (2017)
47. Z. Zhang, X. Shen, C. Zhang, S. Wei, S. Lee, F. Wang, Mater. Sci. Eng. A **565** (2013)
48. Y. Zhang, Z. Li, C. Li, Z. Yu, Ceram. Int. **41**, 10 (2015)
49. M. Belmonte, J. Gonzalez-Julian, P. Miranzo, M.I. Osendi, Acta Mater. **57**, 9 (2009)
50. C. Morin, S. Le Gallet, M. Ariane, F. Bernard, Ceram. Int. **42**, 2 (2016)
51. K. Vanmeensel, A. Laptev, J. Hennicke, J. Vleugels, O. Van der Biest, Acta Mater. **53**, 16 (2005)
52. K. Matsugi, H. Kuramoto, T. Hatayama, O. Yanagisawa, J. Mater. Process. Technol. **134**, 2 (2003)
53. Y.C. Wang, Z.Y. Fu, Q.J. Zhang, Key Eng. Mater. 224–226 (2002)
54. A.M. Laptev, M. Bram, K. Vanmeensel, J. Gonzalez-Julian, O. Guillon, J. Mater. Process. Technol. **262** (2018)
55. M. Radajewski, R. Eckner, S. Decker, M. Wendler, L. Krüger, Adv. Eng. Mater. **21**, 5 (2019)
56. S. Decker, L. Krüger, Mater. Des. **114** (2017)
57. A. Glage, S. Martin, S. Decker, C. Weigelt, M. Junghanns, C.G. Aneziris, U. Martin, L. Krüger, H. Biermann, Steel Res. Int. **83**, 6 (2012)
58. M. Mandel, L. Krüger, S. Decker, Corros. Sci. **90** (2015)
59. M. Mandel, L. Krüger, S. Decker, Mater. Corros. **66**, 12 (2015)
60. M. Mandel, L. Krüger, S. Decker, Mater. Werkst. **46**, 10 (2015)

Chapter 10
Electron Beam Technologies for the Joining of High Alloy TRIP/TWIP Steels and Steel-Matrix Composites

Lars Halbauer, Anja Buchwalder and Horst Biermann

Abstract The use of new, high-alloy TRIP/TWIP steels and the corresponding composite materials requires innovative joining processes. Due to the high power density, the inert working atmosphere and the software-based control, the electron beam is predestined to study different joining strategies. This paper shows how the electron beam can be used as a tool to join high-alloy TRIP/TWIP materials with and without particle reinforcement. Microstructure-property relationships based on the microstructure and tensile tests are established and correlated to the material used. From this, a corresponding joining strategy is derived for each material, which is presented on the basis of various evaluation criteria.

10.1 Introduction

Modern lightweight constructions are subjected to the conflicting demands for lower weight and higher load-bearing capacity. To overcome these challenges, a composite material was developed which combines good ductility, high strength and high specific energy absorption potential [3, 4, 6, 54]. This is achieved by reinforcing a metastable austenitic steel matrix (γ) with MgO partially stabilized zirconia (Mg-PSZ) particles. During deformation between the martensite start M_s- and the M_d-temperature (temperature where 1% strain induced martensite is formed), the matrix of the composites is able to transform into α'-martensite. The associated TRIP effect (TRansformation Induced Plasticity) involves an exceptional strain-hardening capac-

L. Halbauer (✉) · A. Buchwalder · H. Biermann
Institute of Materials Engineering, Technische Universität Bergakademie Freiberg,
Gustav-Zeuner-Str. 5,
09599 Freiberg, Germany
e-mail: lars.halbauer@iwt.tu-freiberg.de

A. Buchwalder
e-mail: anja.buchwalder@ww.tu-freiberg.de

H. Biermann
e-mail: biermann@ww.tu-freiberg.de

H. Biermann and C. G. Aneziris (eds.), *Austenitic TRIP/TWIP Steels and Steel-Zirconia Composites*, Springer Series in Materials Science 298,
https://doi.org/10.1007/978-3-030-42603-3_10

ity with still high ductility under tensile loading [36, 37]. However, the deformation behavior of the matrix material depends strongly on the stacking fault energy (SFE) [29, 41, 50]. At relatively high stacking fault energies ($> 40\,mJ/m^2$), the preferred deformation mechanism is movement of dislocations (wavy glide). Stacking fault energies in the range of 20–40 mJ/m^2 favor the formation of deformation twins (TWinning Induced Plasticity, TWIP effect) [29] which is accompanied by a significant increase in ductility. In steels with a stacking fault energy lower than 15–20 mJ/m^2, the TRIP effect occurs [29, 43, 45, 55]. With applied stress, the Mg-PSZ particles can undergo a phase transformation as well, where the tetragonal phase transforms into monoclinic particles [12]. Consequently, a stress field within the matrix is counteracted by the resulting volume expansion of the particle and thus the fracture resistance of the component is further increased [28].

For the evaluation of a potential application, the weldability of the material has to be investigated. According to DIN ISO/TR 581:2007 [11], the term weldability is referred to as the interdependence of three component properties (cf. Fig. 10.1):

Material	The weldability depends on the material properties such as their chemical composition (e.g. hardening) and their microstructure (e.g. elimination of precipitation hardening, coarsening of grains). The material properties have a strong dependence on the necessary constructional properties and only a weak dependence on the welding process.
Construction	As a generic term, the constructional properties describe the possibility to weld. They are defined by the joint geometry and the type of stress that is applied during or after welding. Constructional properties are strongly dependent on the welding process (which process for which joint geometry) and slightly dependent on the material properties (e.g. metallurgical notches).
Process	Finally, the weldability is defined by the process parameters, which are determined by the type of welding process and the inherent welding parameters. The choice of parameters strongly depends on the material properties and weakly depend on the constructional properties.

Comparable to the laser beam (LB), the electron beam (EB) can be applied for a high energy fusion process. The difference to conventional joining approaches is the use of highly accelerated electrons as energy source which allows the application of very high energy densities. The EB as a joining tool allows essential process parameters such as beam power, feed rate or focal point to be set freely and reproducibly. This also makes comprehensive monitoring of the process possible. At the same time, due to the adjustable power density, both deep welding and heat conduction welding can be established to investigate the influence of the welding process. Due to the high positioning accuracy, the dilution can also be precisely controlled in dissimilar weld joints to set the materials properties. In addition, solid state joining processes, such as soldering, can be carried out via the freely programmable, almost inertia-free

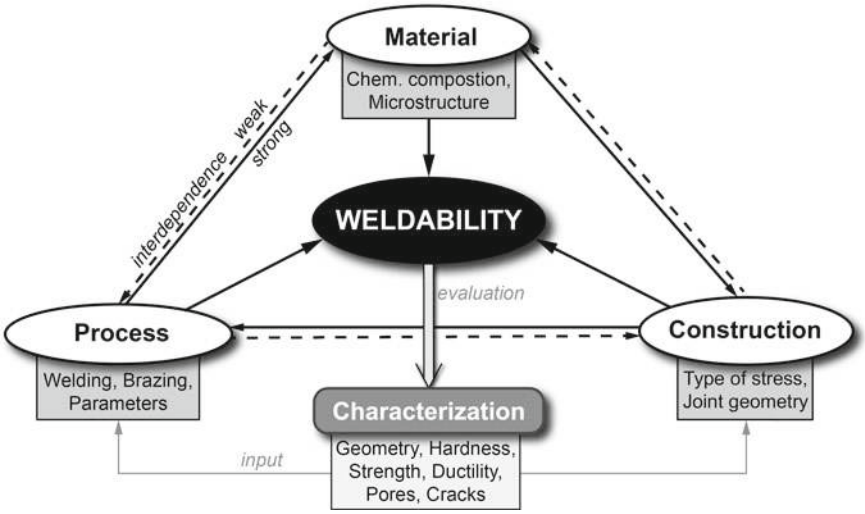

Fig. 10.1 Weldability of TRIP-matrix composites dependent on the the material, the construction and the process (according to DIN ISO/TR 581:2007 [11])

deflection of the EB. Oxide and pore formation is significantly inhibited due to the process inherent vacuum atmosphere. However, it should be noted that elements with a high vapor pressure (such as Mn) may be able to degas.

For high-alloy (HA) TRIP/TWIP-matrix composites the weldability has not been studied yet. First experiments from Buchwalder et al. show a good weldability of the HA base material but no experiments were carried out on the composite [8]. Thus, only partial information on the weldability of similar steels or composites can be obtained from the literature. Reference materials for the base material are low-alloy (LA) TRIP steels and HA TWIP steels. LA TRIP steels, which mainly consist of ferrite, bainite, martensite and retained austenite, show a significant TRIP effect during deformation and are therefore comparable in terms of mechanical behavior to the HA TRIP steels with low SFE. The welding of LA TRIP steels was carried out with a broad variety of welding processes, such as gas metal arc (GMA) [21, 26], resistance spot [22, 34], friction stir [30], and LB welding [7, 25, 42]. Failure takes place within the heat affected zone of the material [22, 26]. The welding seam shows a significant increase in hardness (up to 510 HV) which decreases with decreasing cooling rate [42].

HA TWIP steels can also be welded with various welding processes [33]. During welding, however, the main alloying element manganese has an increasing tendency to evaporate with higher temperatures and lower atmospheric pressure [46]. Mujica et al. showed that the evaporation rate for continuous processes decreases with increasing power density [32]. Typically, up to 2 wt% Mn is evaporating during LB welding [27]. Pulsed welding leads to an above-average evaporation rate of manganese. Due to their fully austenitic microstructure and the strong tendency for

segregation of manganese, HA TWIP steels have a high susceptibility for hot-crack formation [56]. For the hot-rolled alloy Fe–25Mn–3Al–3Si an hardness increase from the base material to the fusion zone from ≈1700 to 2400 HM is reported and explained by the grain refinement after welding [27, 31]. High cooling rates, such as those generated by laser beam welding, can also lead to a significantly increased hardness within the fusion zone (up to 300 HV) [32]. Due to the evaporation and the lower grain size, the stacking fault energy of the welded seam is locally lower than in the base material. Therefore, the welding seam of HA TWIP steels is not capable to deform as much as the TWIP base material. Accordingly, rupture occurs within the base material where the deformation is concentrated [31, 39, 40, 44].

To the current state of the art, there is no suitable process for joining steel-ceramic composites though. Weigelt et al. proposed a method for the joining of Mg-PSZ reinforced steel matrix composites in the green-body state [53]. While the mechanical properties are outstanding, the process is not applicable for components which are not produced by powder metallurgical processing and rely on welding or brazing. Experiments carried out by Tseng et al. [52] showed a strong negative influence of zirconia during fusion welding. The addition of ZrO_2 particles with a diameter ≥0.3 µm leads to the deterioration of weld seam quality due to crack formation and concave root surface.

With respect to the weldability Al-SiC systems can be regarded as alternative composite materials and have already been successfully joined by fusion welding processes, using tungsten inert gas (TIG), LB or EB welding [18, 38]. The melting temperature (T_M) of the ceramic particles of Al-SiC and TWIP-matrix composites are very close to each other ($T_{M,\,SiC} = 2730\,°C$, $T_{M,\,ZrO_2} = 2715\,°C$). The melting point difference ΔT_M between matrix and reinforcement phase of Al-SiC composites ($\Delta T_M = 2070\,°C$) is about 775 K higher than in the case of TRIP-matrix composites with Mg-PSZ ($\Delta T_M = 1295\,°C$). However, this is negligible as the temperatures within the keyhole during deep penetration welding can reach temperatures greater than 10^4 K [51] during electron beam welding (EBW) and 8×10^3 K during laser beam welding (LBW). It was found, that during laser beam welding, the SiC particles are partially melted, move within the melt pool and form clusters [9]. In contrast, welding with electron beam leads to the ejection of molten material due to the evaporation of SiC [18]. For amounts higher than 1% SiC, the ejected volume strongly increased. If the Al matrix is precipitation hardened, softening occurs in the joining zone. In contrast, the formation of Al_3C_4-carbides leads to an increase of hardness. The particle clusters in the weld seam act as locations for stress concentration under external load and cause brittle material failure. This drastically reduces both the strength of the welded joints and the ductility. Rupture occurs within the fusion zone [18, 35]. It can be derived from past investigations that the joining result for metal-matrix composites strongly depends on the material and the joining process selected.

Consequently, the weldability of TRIP/TWIP-matrix composites with the use of the electron beam is examined in this work. First, the influence of the chemical composition is investigated with similar joints of non-reinforced as-cast steels. Second, the effect of added Mg-PSZ is studied in dissimilar joints with TWIP-matrix compos-

ites, which was already published in [13–15]. Furthermore, it is investigated how the electron beam can be used to establish a brazing process to join similar TWIP-matrix composites (see [16]). Finally, the loadability is studied under different loading conditions for similar joints.

10.2 Materials and Methodology

This section gives an overview about the key parameters used for the experiments. To maintain readability, the parameters that were altered for specific experiments are repeatedly given in the particular sections.

10.2.1 Electron Beam Facility and Temperature Measurements

All joining experiments were carried out within an K26-80/15 universal electron beam chamber facility (PRO-BEAM, Neukirchen, Germany) at an ambient pressure of 2×10^{-2} mbar. In general, three different processes were applied, i.e. similar electron beam welding (S-EBW), dissimiliar electron beam welding (DS-EBW) and electron beam brazing (EBB). The corresponding parameters are given in Table 10.1 and the sample geometry in Fig. 10.2a.

During S-EBW and DS-EBW the samples were fixed within an clamping device to prevent unwanted movement. It should be noted, that all similar joining experiments were carried out without welding gap (zero gap) to neglect the influence of the joint faces on the welding results. The dissimilar welding experiments were carried out on butt joints. If a beam offset Δx was applied, the offset in x-direction was referred to as the distance between the EB and the dissimilar weld joint face. To increase the accuracy of the electron beam position, a notch ($0.3\,\text{mm} \times 45°$) was applied to the joint edge.

For the brazing experiments, a temperature-controlled power regulation system was used to control the temperature within the energy transfer field (ETF). This

Table 10.1 EB parameters used: acceleration voltage U_A, beam current I_B, offset to beam current ΔI_B, welding speed v_s, holding time t_H, beam shift relative to the joint gap Δx, offset to lens current ΔI_L, oscillation figure OF, diameter of oscillation figure d_{OF}

Process	U_A (kV)	I_B (mA)	ΔI_B (mA)	v_s (mm/s)	t_H (s)	Δx (mm)	ΔI_L (mA)	OF	d_{OF} (mm)
S-EBW	80	5 …180	0	1 …80	–	0	−5 …+75	Circle	0.5
DS-EBW		30 …110	0	5 …45	–	0 …0.8	−5 …+30		
EBB	60	0	70	–	43 …600	0	+10	Field	–

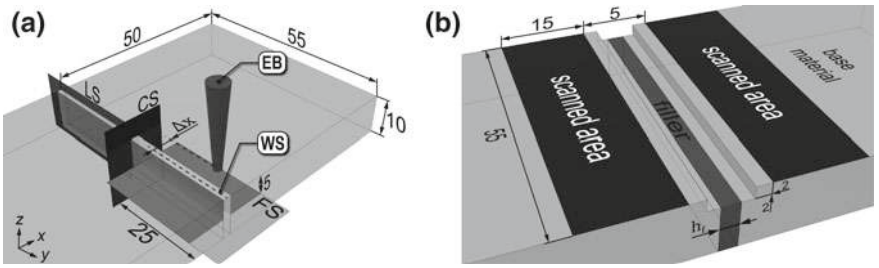

Fig. 10.2 Sample geometry and positioning of EB for **a** all joining methods with beam offset (if applied) and information about cross-sections (CS), longitudinal-sections (LS) and flat-sections (FS) with respect to the welding seam (WS); **b** electron beam brazing with material setup and dimensions of the beam interaction field used. All dimensions in (mm)

system consisted of a temperature sensor (two-color pyrometer, regulation time = 3 ms) and a software that calculated the power output. It was necessary to assign an initial beam current (I_B) and a beam current offset (ΔI_B) for the brazing process. The temperature sensor was placed at the edge between the joint gap and the ETF. Figure 10.2b shows the dimensions of the field. During the experiments, the filler gap (h_f) was increased in the range of 200–1500 µm. To ensure constant temperatures alongside the filler gap, an polynomial energy distribution P_y according to (10.1) was used with $-27.5 < y < 27.5$. It was found, that the energy in the center of the scanning area had to be lowered to a minimum of $P_{min} = 0.8$.

$$P(y) = (1 - P_{min}) \left(\frac{y}{27.5}\right)^2 + P_{min} \tag{10.1}$$

An infrared camera was used to evaluate the temperature distribution across the sample width and depth. For a detailed explanation regarding the temperature measurements, please refer to [16].

10.2.2 Base Materials

Different types of base materials with the chemical compositions given in Table 10.2 were used for the three joining approaches (S-EBW, DS-EBW, EBB). It should be mentioned, that the amount of alloying elements for the composite material (TWIP+Mg-PSZ) refers to the steel matrix. Accordingly, the chemical composition of the zirconia particles is given in Table 10.3. The base materials were available in three different states:

AC cast-material which was produced by AC-TECH GMBH (Freiberg, Germany) by means of sand casting with a grain size of ≈2 mm

HR commercial grade AISI 304 in hot-rolled condition (grain size ≈130 µm)

Table 10.2 Chemical composition (in wt%) of the basic materials used sorted according to the joining process used. The materials were available in as-cast (AC), hot-rolled (HR) and powder metallurgically produced (PM) (containing 10 vol% ZrO_2) conditions

Process	Steel name	Short	State	Fe	C	Cr	Mn	Ni	Si
S-EBW	16Cr-7Mn-3Ni	16-7-3	Cast	*Bal.*	0.055	15.9	6.7	3.1	0.75
	16Cr-7Mn-6Ni	16-7-6		*Bal.*	0.048	16.3	6.6	6.3	0.85
	16Cr-6Mn-9Ni	16-6-9		*Bal.*	0.074	15.9	6.2	9.1	0.82
DS-EBW	AISI 304	A304	HR	*Bal.*	0.022	16.8	1.93	7.8	0.23
	TWIP+Mg-PSZ	MMC	PM	*Bal.*	0.03	13.4	7.4	8.7	0.64
EBB	AISI 304	A304-B	HR	*Bal.*	0.01	19.19	1.84	8.23	0.28
	TWIP+Mg-PSZ	MMC	PM	*Bal.*	0.031	14.77	6.97	10.03	1.01

Table 10.3 Chemical composition of the Mg-PSZ powder used for producing the MMC

(wt%)							
ZrO_2	HfO_2	MgO	SiO_2	Al_2O_3	CaO	TiO_2	Fe_2O_3
Bal.	1.73	3.37	2.43	0.63	0.21	0.14	0.01

Table 10.4 Chemical composition and nomenclature of the filler material used

		(wt%)					(°C)
Filler	DIN EN 1044	Ni	Cu	Si	Cr	B	T_f
HTL 5	NI 105	*Bal.*	–	10.1	19	< 0.03	1190

PM composite which was produced by mixing steel and Mg-PSZ powders (SAINT-GOBAIN, USA, see Table 10.3) by ball milling (100 rpm, 30 min) and subsequent hot pressing (1050 °C, 30 min) at FRAUNHOFER IKTS (Dresden, Germany).

Table 10.4 shows both the chemical composition and working temperature T_f of the filler paste (BOEHLER WELDING, Hamm, Germany) used. The composite was produced with a d_{50} of 55 µm for the matrix material. Due to local agglomeration of the Mg-PSZ powder, clusters of particles with sizes of up to 20 µm were formed during hot pressing.

Before joining, the samples were demagnetized and cleaned with ethanol without additional grinding of the joint faces. For the brazing experiments, the joint faces were ground in direction of gravity.

10.2.3 Microstructural Characterization

After joining, the samples were cut, ground and polished with diamond paste up to 1 µm. For light optical investigations, the materials were etched either with V2A reagent at a temperature of 60 °C or with LICHTENEGGER solution. The Electron Backscattered Diffraction (EBSD) investigations were carried out with a LEO 1530 (TESCAN, Czech Republic), an acceleration voltage of 20 kV, 120 µm aperture, 70° tilting and 17 mm working distance. Channel 5 (Oxford, HKL) was used as analysis software. Detailed investigations of the connection quality for dissimilar welded materials were carried out on focussed ion beam (FIB) prepared samples at the transmission electron microscope (TEM) JEM 200 FS from JEOL (Japan) at U_A = 200 kV with varying apertures. The investigations were carried out using the analysis software DIGITAL MICROGRAPH from GATAN and ANALYSIS STATION from JEOL.

10.2.4 Mechanical Characterization

The microhardness (HV0.3) of the welding seams was determined with an semi-automatic tester (LECO, Mönchengladbach, Germany). Therefore, hardness indentations with an indentation distance of 0.08 mm were linearly distributed across the welding seam (WS). After brazing the hardness of the different microstructural constituents within the filler was evaluated using a nanohardness tester Fischerscope (HELMUT FISCHER, Sindelfingen, Germany) with increasing load conditions and a maximum indentation force of 50 mN. For all joining processes, the mechanical properties of the material were evaluated in quasistatic tensile tests under displacement control on standard testing machines from HEGEWALD & PESCHKE (Nossen, Germany) and ZWICK ROELL (Ulm, Germany). Figure 10.5 gives a summary of the geometries of the tensile specimens used.

Table 10.5 Specimen dimensions and the location of the joining zone (JZ) for the quasistatic tensile tests for different joining processes. All dimensions in (mm)

Process	a	b	c	d	e	f	R
S-EBW	30	97	27	5	-	M8	10
DS-EBW	16	71	18	4	2	8	12
EBB	30	97	27	5	2	9	12

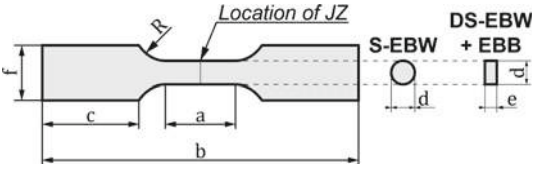

10.2.5 Non-destructive Testing

In order to determine the volume defects within the WS, such as pores or shrinkage, X-ray examinations were carried out with an acceleration voltage of 120 kV at a working distance of 90 cm on parts of the longitudinal sections (see LS, Fig. 10.2a). The samples were placed on an X-ray storage foil and irradiated for an exposure time of 4–8 min (depending on the thickness) with an ERESCO (UK) 200/8 X-ray inspection system.

For the non-destructive ultrasonic immersion tests, a high-frequency USPC 3060 UHF ultrasonic imaging system (INGENIEURBÜRO DR. HILLGER, Braunschweig, Germany) was used (Fig. 10.3). During the test procedure, the test specimen and the immersion probe were located within a liquid coupling medium (deionized water with 1.25% Echokor LF anti-corrosion reagent), which ensured uniform coupling. The specimens (height: approx. 10 mm, cf. Fig. 10.2a) were scanned parallel to the yz plane, while the shortest increment size in the y and z directions was 13 µm. A focused broadband transducer (6–12MHz) STS 6 PB 6 12 P 15 (KARL DEUTSCH, Wuppertal, Germany) with an active diameter of 6 mm and a focal length of 15 mm in water was applied.

The focal depth inside the TWIP matrix composite was ≈3.1 mm and the one-way water path between the transducer and the front surface of the specimen was set to 3 mm, respectively. For the acoustic parameters, densities of 7.883 g/cm^3 (AISI 304) and 7.594 g/cm^3 (MMC) and impedances of 45.4 kg/m^{2}s (AISI 304) and 44.3 kg/m^{2}s (MMC) were used. The wave velocity was measured using a Panametrics V109 transducer (5 MHz). The Archimedes method was applied for the density measurements of both welded materials.

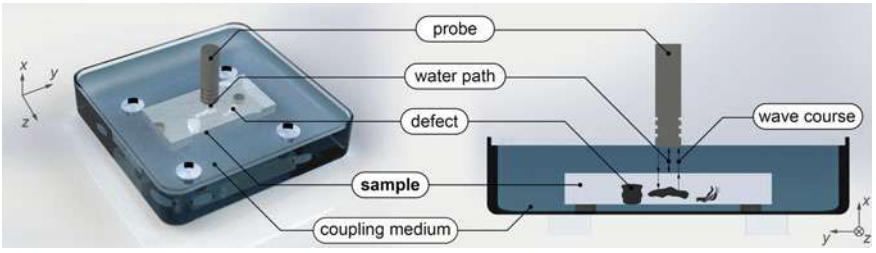

Fig. 10.3 Schematic illustration of the ultrasonic immersion testing method [15]

10.2.6 *Electron Beam Welding of Similar Joints Without Reinforcement*

10.2.6.1 Influence of the Welding Parameters on the Seam Geometry

In order to investigate the welding behavior of the base material without the influence of the ceramic particles, welding was carried out on cast steels with different nickel contents (cf. Table 10.2). Figure 10.4a shows the evolution of the geometric parameters weld seam depth (t_{WS}), weld seam width (b_{WS}), nail head width (b_{NH}) and face reinforcement (h) as a function of the beam current for a constant welding speed of 10 mm/s.

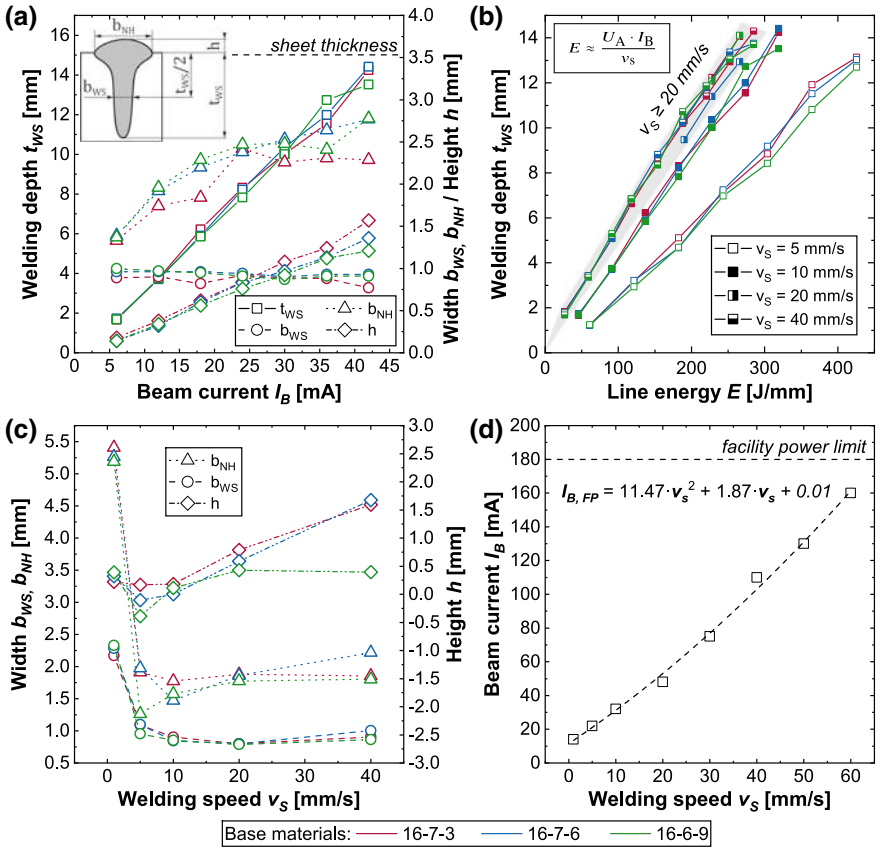

Fig. 10.4 Influence of the welding power on the weld seam geometry depending on **a** the beam current I_B for $v_s = 10$ mm/s; **b** the line energy E and the welding speed v_s; **c** the welding speed during full penetration welding; **d** the beam current required for full penetration ($I_{B,FP}$; $t_{WS} = 10$ mm) at different welding speeds

In the examined beam current range the welding depth is directly proportional to the beam current. Since the welds were placed in 15 mm thick sheets, the selected test parameters did not result in full penetration welding. As a result, the welding depth exhibits fluctuations which depend on the welding speed. At 5 mm/s the standard deviation of the welding depth and the maximum depth difference were determined to 0.49 mm and 1.59 mm, respectively. For higher welding speeds, the fluctuation of the welding depth decreases to an average of 0.11 mm and a maximum of 0.44 mm. According to Huang et al. [17], this is caused by protuberances formed by the recoil pressure within the keyhole, leading to irregular temperature distributions within the capillary. Based on these results, no clear tendency could be derived with regard to the differences in welding depth between the individual test materials. With regard to the welding depth, all three investigated materials showed the same tendency and almost identical welding depths could be achieved. The width of the weld seam of all materials exhibited only a slight decrease with increasing beam current. This was attributed to the formation of the keyhole even at low power inputs.

To evaluate the influence of the welding speed and the beam current on the welding depth, the line energy (cf. Fig. 10.4b) was calculated after (10.2) with an efficiency $k \approx 1$.

$$E = k \cdot \frac{U_A \cdot I_B}{v_s} \tag{10.2}$$

For welding speeds lower than 20 mm/s, the welding depth depends on both the welding speed and the line energy. With increasing welding speed, the welding depth becomes independent on the welding speed used. Again, this behavior can be attributed to the deep penetration effect. Lower welding speeds require lower beam currents to achieve the same line energy as with higher welding speeds. Thus, the lower the welding speed, the lower the power density for equal line energies. Since the deep penetration effect depends primarily on the power density, it is only incompletely formed at low welding speeds. In order to produce deep penetration welds at a given energy input per line length, the welding speed has to be increased to compensate the higher required power density. Accordingly, a stable formation of the keyhole occurred above a certain welding speed threshold of 20 mm/s. At higher welding speeds only the welding depth is increased proportional to the beam power, while the other geometrical parameters remain nearly constant.

In most application-relevant processes, it is necessary to produce a weld seam over the entire sheet thickness with a single pass (full penetration welding). For this purpose, tests were carried out in which the beam current was increased for various welding speeds until the root was completely formed. The beam current needed for full penetration ($I_{B,FP}$) is shown in Fig. 10.4d as a function of the welding speed. The fitting function was a parabola and proved to be valid for all three investigated materials. Experimental practice has also shown that the fit was suitable for both interpolation and extrapolation of beam currents.

In full penetration welds the welding depth is constant for all welding speeds (cf. Fig. 10.4c). With increasing welding speed from 1 to 10 mm/s, both the seam and

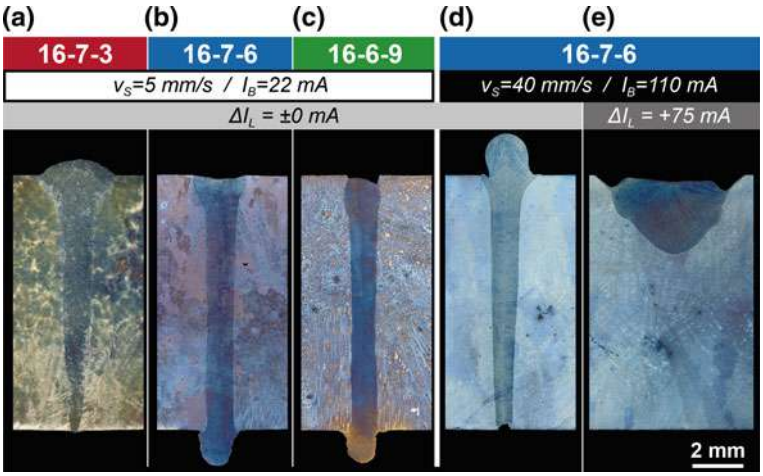

Fig. 10.5 Macroscopic appearance of the welding seam dependent on the welding speed, the base material and the focal plane

the nail head width decreased independent of the base material used. A reason for this was the limited sample volume used in the experiments. At low welding speeds a significant heat build-up occurred which contributed to the widening of the weld seam in the keyhole area. Although an influence on the welding seam width could have been expected due to differences in the thermal conductivity of the samples (due to the varying nickel content), no clear correlation could be found between the weld width and the material used. This was attributed to the fact that the seam width varies over the seam length due to the keyhole oscillation. Consequently, the seam widths fall within a scatter band. At a welding speed of 10 mm/s, a beam current of 32 mA was necessary to achieve full penetration. This was very similar to the threshold of the beam current ($I_{\mathrm{Th}} = 25$ mA), that was found for a stable keyhole welding in the experiments with increasing beam current (cf. Fig. 10.4a). Due to the limitation of t_{WS}, welding speeds >10 mm/s led to a slight increase of b_{WS}, while b_{NH} remained nearly constant.

10.2.6.2 Macroscopic Appearance of the Welding Joints

Figure 10.5 shows representative cross sections of the three materials welded with different welding speeds and focal offsets. It is shown that the steel 16-7-3 was barely fully penetrated at a beam current of 22 mA (Fig. 10.5a). An increasing nickel content leads to a stronger formation of the root face and an increasing root convexity (Fig. 10.5a–c). Steel 16-6-9 already shows undercuts (cf. Fig. 10.5c). At the same time, the V-shape of the seams decreases with increasing nickel content. While steel 16-7-3 still has a pronounced nail head due to its higher thermal conductivity, steel

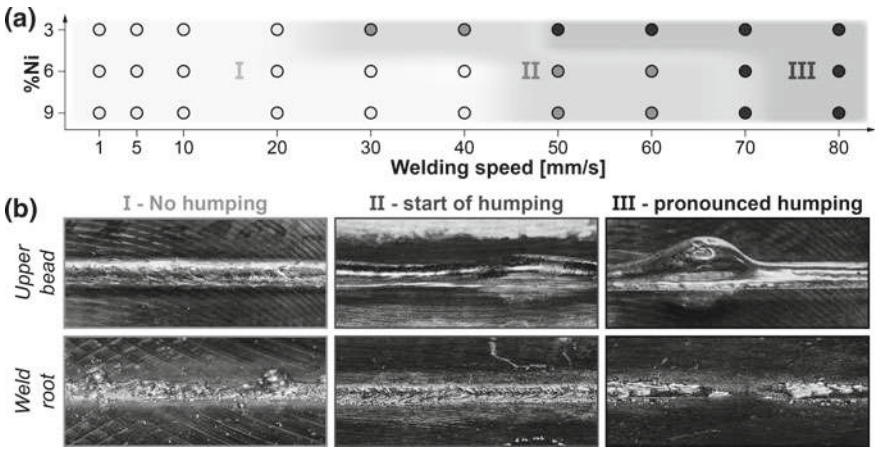

Fig. 10.6 **a** Representative appearance of upper bead and weld root for different humping tendencies; **b** humping tendency dependent on the welding speed for the three high alloy steels

16-6-9 shows almost completely parallel fusion faces. This is attributed to the fact that $I_{B,FP}$ for the formation of the keyhole has been reached and slightly exceeded for steels 16-7-6 and 16-6-9 respectively. On the other hand, higher beam currents would have been necessary for 16-7-3 steel to increase the deep penetration effect.

This effect disappears at higher welding speeds, so that all welds look as in Fig. 10.5d at 40 mm/s. They exhibit nearly parallel fusion faces and a pronounced nail head formation. The reason for this is the increasing power density, which produces a keyhole at higher welding speeds independent of the material selected. To prove the assumption of the correlation between power density and the deep penetration effect, welds were carried out with a strong defocus (cf. Fig. 10.5e, $\Delta I_L = +75$ mA). It was observed that a reduction of the power density resulted in a significant decrease of the welding depth and an increase of the seam width (cf. Fig. 10.5d, e). The typical seam shape is present, as it is created by heat conduction during GMA or TIG welding. Due to the circular beam oscillation, undercuts are formed on the weld face. Apart from undercuts at individual welding speeds, which were caused by too high beam currents or beam oscillation, no macroscopic defects such as cracks, pores or non-metallic inclusions were detected within the welds.

During the experiments, it was noticed that depending on the welding speed, the formation of humping occurred. Thereby the appearance of the weld face and root could in principle be divided into three stages (I–III), which are illustrated in Fig. 10.6b. In stage I the weld face showed no differences in height except for the typical scaling. Only in the lower bead single material elevations were detected which were caused by the oscillation of the keyhole described above. This represented the humping-free state and the predominant portion of the samples. Stage II was characterized by height differences in the upper caterpillar. The seam scaling was not visible at the weld face and could only be found in the root layer, which in addition

showed no significant height differences. In stage III typical humping features were observed. For example, the weld seam showed periodic protuberances, an incomplete root face and a considerable proportion of ejected weld metal.

The stages described occurred as a function of welding speed and material (Fig. 10.6a). As expected, the humping started at high welding speed ($v_s \geq 50$ mm/s). In addition, steel 16-7-3 had a much stronger tendency to hump and already showed signs of humping at a welding speed of 30 mm/s. Above a welding speed of 50 mm/s the material could not be considered weldable due to strong humping effects. The steels 16-7-6 and 16-6-9 showed signs of humping only at 50 mm/s. The weldability limit for the selected parameter set was found at 60 mm/s. Above this speed the weldability could no longer be guaranteed.

It is known from the literature [5] that humping starts at a certain welding speed and strongly depends on the welding depth and the alloying elements of the base materials. Therefore, it is pointed out that these results are only valid for the investigated sheet thickness of 10 mm and have to be re-evaluated for other chemical compositions and/or thicknesses of the base material used.

10.2.6.3 Influence of the Welding Parameters on Evaporation

During DPW, the material is locally molten and vaporized to form a keyhole of plasma surrounded by a molten pool. Elements with low vapor pressure, such as manganese, tend to evaporate during welding which is intensified by the low ambient pressure within the vacuum chamber. It was investigated how the process parameters effect the chemical composition of the welding seam with respect to the base material. Independent of the welding speed, no change of the main alloying elements chromium and nickel was detected. In contrast, manganese exhibited a strong evaporation tendency which was dependent on the welding speed (cf. Fig. 10.7a).

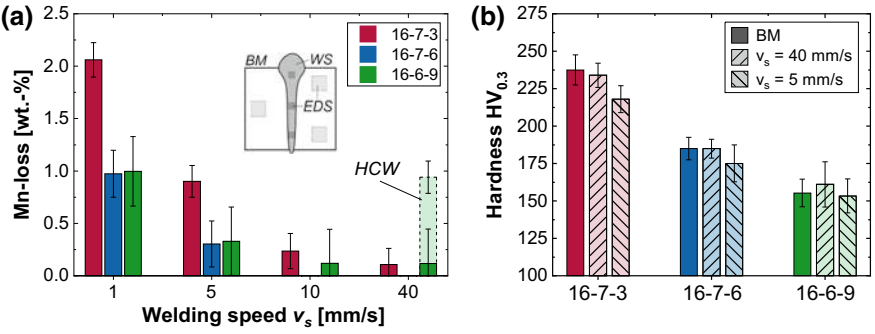

Fig. 10.7 **a** Manganese loss within the welding seam produced by DPW compared to the base material dependent on the welding speed. HCW: welds produced by HCW; **b** mean hardness within the base material and the welding seam for two different welding speeds

At a welding speed of 1 mm/s, DPW led to a loss of 1–2 wt% manganese. This corresponded to a reduction of the Mn content within the base material by about 17–33%. However, it should be noted that such welding speeds are rather unusual in practice and have been investigated as extreme values. As the welding speed increased, the manganese loss decreased sharply. For welding speeds of 5 mm/s the weld seam exhibited about 0.3–0.9 wt% manganese loss. At 10 mm/s a slight manganese loss of 0.24 wt% could be detected for the 16-7-3 steel. The manganese loss of the other two steels was in the range of scatter. For welding speeds >10 mm/s no measurable manganese loss could be detected during DPW. Regardless of the welding speed, the 16-7-3 steel always showed the maximum loss of manganese. This was attributed to the increased thermal conductivity and the associated enlargement of the nail head. A proof for this assumption were welding seams, which were produced without keyhole welding (Fig. 10.7a, HCW). With HCW welding, a loss of almost 1 wt% manganese was measured, which increased with a lower welding speed following the described tendency (up to 2.5 wt% Mn-loss). It was therefore assumed that the deep welding effect at reasonable welding speeds had no measurable effect on Mn evaporation. Rather, the Mn evaporation was mainly determined by the liquid fraction of the weld seam. There are two effects to be considered:

1. the reduction of the welding speed increases the interaction time of the melt with the environment and more manganese can evaporate.
2. lower welding speeds increase the seam width and, thus, also increasing the area of interaction with the environment.

In order to minimize evaporation, therefore, the lowest possible proportion of HCW like increasing the welding speed or the power density as given in Fig. 10.4 should be set during welding.

To characterize the influence of manganese loss, hardness measurements were performed in both the weld seam and the base material (see Fig. 10.7b). With increasing nickel content the hardness of the base materials was reduced from 240 HV0.3 (3% Ni) to 155 HV0.3 (9% Ni). At a welding speed $v_s = 40$ mm/s no significant influence on the hardness was found, which correlates to the low manganese loss. In contrast, welds with a lower feed rate (5 mm/s) showed a slight loss of hardness in the weld seam. The decrease in hardness decreased with increasing nickel content. For steel 16-7-3 there was a decrease in hardness of about 20 HV0.3. Steel 16-7-6 showed only a slight decrease in hardness of about 10 HV0.3. The difference in hardness between the weld and the base material was in the range of scatter for steel 16-6-9. These results are in good agreement with the manganese losses which also implies, that low welding speeds should be avoided to minimize the loss of hardness.

10.2.6.4 Microstructure of the Welding Joints

For the investigation of the microstructure, the coloring of the Lichtenegger etching allowed conclusions to be drawn about the primary solidification behaviour of the samples. Typically ferrite (δ) remains **white**, austenite solidified primarily from

the melt (γ_P) becomes **blue** and austenite, formed by solid phase transformation (secondary austenite, γ_S) is colored **brown** [48].

According to FACTSAGE calculations, a primary ferritic solidification should be present for all three materials studied [20]. For steel **16-7-3**, the primary solidification mode was not clearly recognizable for both the base material and the weld seam (cf. Fig. 10.8a, d). Typical segregation zones around the ferrite were missing. Both the austenite and ferrite were etched by the reagent. Weld seam and base material showed a comparable plate-shaped morphology of the ferrite. In the weld seam, whose appearance was almost independent of the welding speed, dark etched areas were also visible (Fig. 10.8d). These consisted of stress induced martensite which had been formed unavoidably during the preparation routine. It was assumed that the etching process favored the martensitic areas and therefore falsified the typical Lichtenegger etching reaction. However, measurements of the element distribution over the ferrite regions (Fig. 10.9a) showed an opposed distribution of Cr and Ni, which typically occurs during primary ferritic solidification [49].

For steel **16-7-6** this primary ferritic solidification was very well recognizable in both the base material and the weld seam (cf. Fig. 10.8b, e). Although the ferrite had a dark coloration, it was expectedly located within the dendrite core (DC) surrounded by typical bright segregation zones of the austenitic interdendritic region (IDR). The ferrite possessed a skeletal morphology (or 'vermicular' in American terminology), which was randomly distributed within the former dendrites (Fig. 10.8e). Measurements of the element distribution over single dendrites showed atypical element distributions. As can be seen in Fig. 10.9b, both the DC and the IDR were enriched with Cr. However, areas were found in which there was both an equal and an opposite elemental distribution. According to the authors, this could result from the peritectic

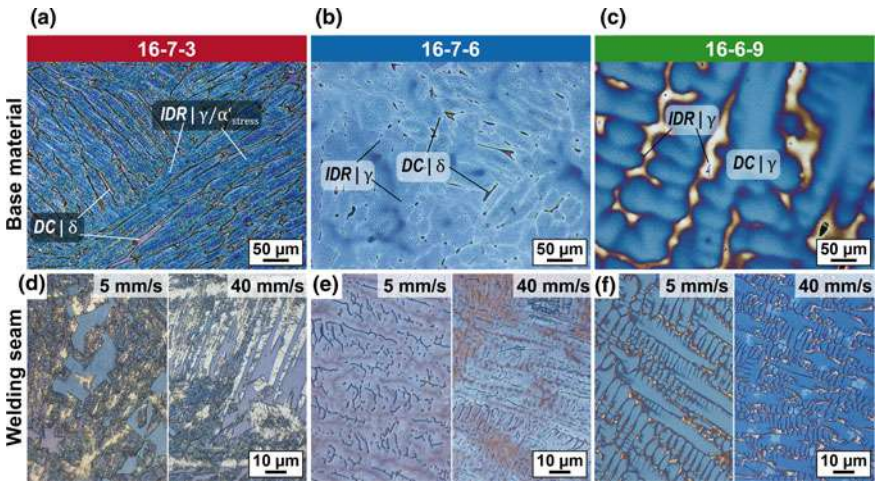

Fig. 10.8 Light optical appearance of the base material and the welding seam ($v_s = 5$–40 mm/s) for different steels after etching

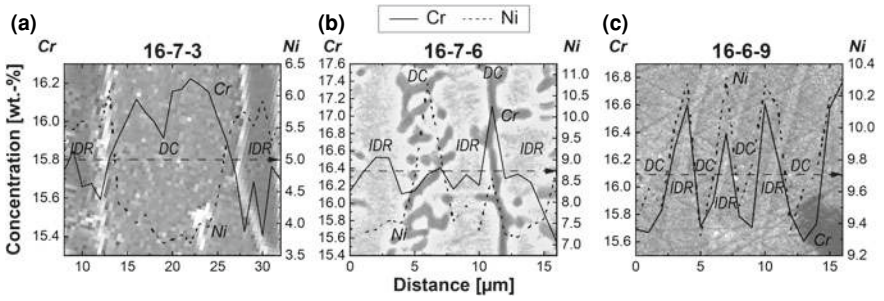

Fig. 10.9 Influence of the base material on the element distribution of Cr and Ni regarding the dendrite core (DC) and interdendritic regions (IDR) measured by EDS line scans

reaction calculated for both steel 16-7-6 and 16-6-9. It is known from literature [19] that simultaneous crystallization of the δ and γ phases does not occur during technical solidification. Accordingly it is assumed for the 16-7-6 steel that first a ferritic solidification took place which subsequently was followed by a peritectic reaction. In this reaction, the austenite phase was preferred and segregation of Cr and Ni took place in opposite as well as in the same direction.

The steel 16-6-9 showed a fully austenitic structure in the base material as well as in the weld seam with clearly recognizable primary austenitic components (cf. Fig. 10.8c, f). The solidification structures were completely dendritic and the IDR had a light coloration without a clearly recognizable phase boundary. During welding the dendritic arm spaceing (DAS) became smaller, otherwise the behavior did not change. In addition, an equidistant distribution of Cr and Ni could be detected (Fig. 10.9c), which supported the assumption of the primary austenitic solidification mode (cf. [23]).

In conclusion, the solidification of the steels 16-7-3 and 16-7-6 was classified as ferritic-austenitic (FA) mode, whereas the steel 16-6-9 solidified according to the austenitic-ferritic (AF) mode.

10.2.6.5 Mechanical Behavior of the Welding Joints

The quasi-static behavior of the investigated materials is summarized in Fig. 10.10. A δ ferrite content of 7.4% was detected in the base material of the **16-7-3** steel. In the milled samples, about 20–24% grinding martensite was determined. With increasing strain (up to 12% engineering strain), the martensite content increased to about 50–65%. This indicated that a TRIP effect was occurring with corresponding martensite formation. For all samples of the steel 16-7-3 less martensite was detected in the base material than in the weld seam. At a welding speed of 5 mm/s, about 5–10% less martensite was detected compared to the weld seams welded with 40 mm/s.

This behavior was attributed to the reduction of the grain size in the weld seam. With increasing welding speed a reduction of the sub-grain size and thus an intrinsic

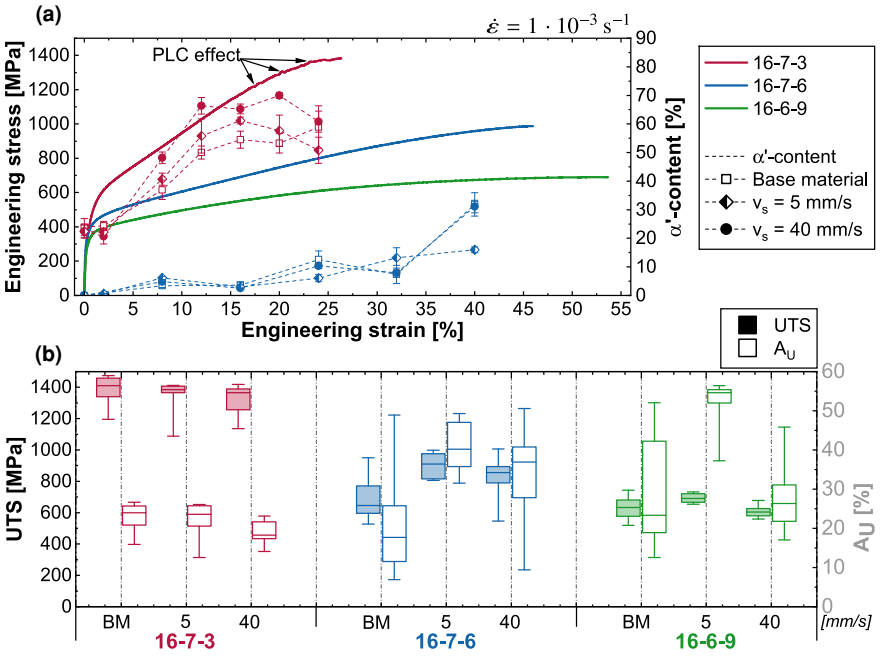

Fig. 10.10 **a** Representative stress/strain-curves with martensite evolution for the tested materials; **b** mechanical properties with ultimate tensile strength (UTS) and elongation at UTS (A_U) dependent on the welding parameters and the base material (BM) used

increase of the SFE could be proven. This shifts martensite formation to higher temperatures, leading to increased martensite formation at room temperature. The typical inflection points of the stress-strain curve were not visible and the Portevin-Le Châtelier effect (visible as serrations in the stress-strain curve, Fig. 10.10a) occurred at higher stress levels.

A slight increase in martensite content was also observed in the **16-7-6** steel (Fig. 10.10a), which contained approximately 1.2% δ ferrite in the initial state. However, this was significantly lower than for steel 16-7-3 and no clear influence of the welding parameters on the martensite evolution was observed. Between 32 and 40% technical strain, samples welded with 40 mm/s showed a sharp increase in martensite content to about 30%. Since the base material exhibited the same values, it is assumed that this was an influence of the chemical composition (due to segregation within the as-cast material).

Steel **16-6-9** showed the lowest strain hardening behavior and the highest elongation of all investigated materials (Fig. 10.10a). Neither δ ferrite nor α' martensite could be detected in the base material or in the weld seam.

Independent on the base material and the welding parameters used, all specimens broke outside the welding seam. The steel **16-7-3** exhibited a UTS of about 1400 MPa regardless of the welding condition (cf. Fig. 10.10b). The ductility of the specimens

decreased slightly at higher welding speed, which could be attributed to the higher amount of martensite. Nevertheless, the data were equivalent within scatter. Steels **16-7-6** and **16-6-9** showed a slight increase in strength after welding of the samples which, however, was also within scatter (cf. Fig. 10.10b). In addition, a strong scatter of elongation values was observed (Fig. 10.10b). After further examination of the broken specimens, it was found that a large number of pores was present in the cross-section of the specimens. They were responsible for the sharp decrease in elongation values and reduced strength in both materials. Accordingly, the maximum strength was achieved in the welded condition. At a lower welding speed ($v_s = 5\,\text{mm/s}$), the strength and elongation of the welding joint was higher than for high welding speed ($v_s = 40\,\text{mm/s}$). This was attributed to the slightly increased seam width and the higher degassing at low welding speeds. Thus, steel **16-7-6** achieved strengths of about 950 MPa at a maximum elongation of 36–47%. The steel **16-6-9** exhibited tensile strengths of about 720 MPa at an elongation at rupture of 52–56%.

10.2.7 Electron Beam Welding of Similar Joints with Reinforcement

The preliminary investigations showed that the welding process has no negative influence on the mechanical behavior of the AC material. Therefore, the welding result of the composite material with added Mg-PSZ particles was investigated. A hot-pressed composite based on steel 16-6-9 with 10% Mg-PSZ was used. Figure 10.11 shows the cross section of a typical weld.

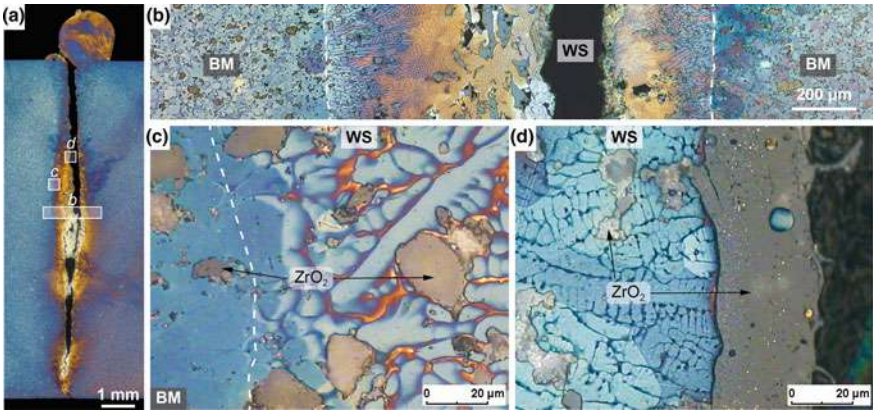

Fig. 10.11 Light optical micrographs of a respresentative welding seam ($I_B = 15\,\text{mA}$, $v_s = 5\,\text{mm/s}$). **a** Macroscopic view; **b** enlarged section of the joint; **c** transition zone between BM and WS; **d** transition zone between WS and the cavity. Dashed lines mark the melting line

Irrespective of the parameter set selected, the formation of a cavity occurred in the centerline of the weld which extended across the entire weld depth. During the welding process, strong spatter formation occurred, resulting from the explosive evaporation of the ceramic particles. As can be seen in Fig. 10.11c, individual Mg-PSZ particles appeared to remain unchanged in the weld. Other ceramic particles were partially melted and deposited at the edge of the cavity (cf. Fig. 10.11d).

Parameter studies showed that the cavity could not be avoided. Its size could be minimized by the following measures:

1. reduction of welding speed (down to 5 mm/s)
2. increase of oscillation width up to 1.5 mm
3. shift of the beam focus below the sheet surface.

Investigations on welds without keyhole showed that the ceramic particles only tend to evaporate when the deep welding effect occurs. With wide melting baths and low penetration depths, it was possible to produce defect-free remelting paths. The ceramic particles floated on top of the melt and formed a firmly adhering, cracked top layer during cooling. The residual melt was almost free of Mg-PSZ. Other process specific optimizations, such as a pulsed beam current and the use of several concurrent welding spots (Multi-Spot-technique) had no significant influence on the formation of cavities.

Concludingly, deep penetration welding of the similar joints with particle-reinforced composite materials was not feasible. In the following, two alternative joining processes are presented: On the one hand, a welding partner of the joint was replaced by a conventional steel (Sect. 10.3). On the other hand, a soldering process with the electron beam was implemented in order to dispense with the deep welding effect (Sect. 10.4).

10.3 Electron Beam Welding of Dissimilar Joints with TWIP-Matrix Composites

10.3.1 Typical Microstructure of the Welded Zone

To investigate the influence of the ceramic particles on the welding behavior of the MMC, dissimilar joints between a TWIP matrix composite and a particle-free stainless steel (AISI 304) were produced. In order to minimize the influence of the chemical composition, a stainless steel was selected which is chemically very similar to the matrix of the composite material due to its C, Cr, Mn and Ni content. In order to describe the quality of the welding seams, a catalog of criteria was used based on DIN EN ISO 13919-1. The main defects observed were porosity, underfill and lack of fusion. Based on the criteria shown in Table 10.6, the welds were classified into evaluation groups (EG) ranging from ‘B’ (best weld quality) to ‘D’ (worst weld quality).

Table 10.6 Criteria for categorization of welding seams into evaluation groups (EG) according to DIN EN ISO 13919-1. f_P: area of cavities, h*: underfill, LoF: dimension of lack of fusion, t: sheet thickness

EG	f_P	h*	LoF
B	≤0.7	≤0.1 t	n.p.
C	≤2	≤0.2 t	n.p.
D	≤6	≤0.3 t	≤0.25 t

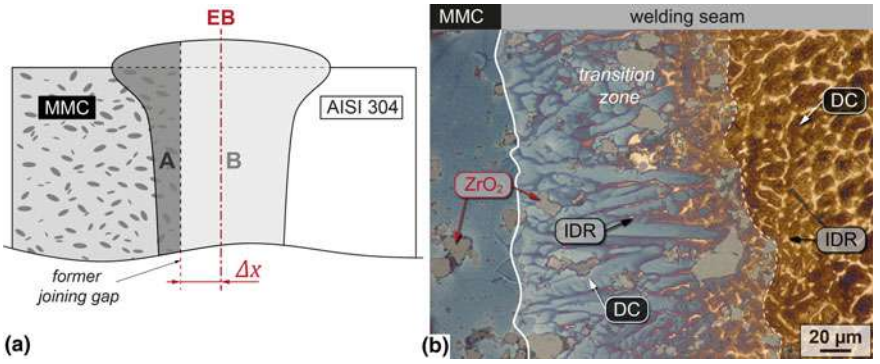

Fig. 10.12 **a** Schematic illustration for measuring the beam displacement and calculating the level of dilution (D). **b** Representative section of the transition zone (TZ) between the TWIP MMC base material and the welding seam [15]. $I_B = 45$ mA, $v_s = 15$ mm/s, $\Delta x = 0.4$ mm

To obtain a defect-free weld, the beam offset Δx had to be shifted relative to the particle-reinforced material (Fig. 10.12a). The level of dilution (D) was used as a measure of the amount of Mg-PSZ introduced into the weld pool (Fig. 10.12a).

Figure 10.12b shows the typical microstructure of the welded samples with a beam offset $\Delta x = 0.4$ mm. The fusion zone consisted of the two base materials (TWIP Mg-PSZ and steel AISI 304) and the welding seam, which could further be divided into two separate regions. Firstly, on the right of Fig. 10.12b, typical dendritic structures were present with brown-colored dendrite cores (DC) (cf. Suutala et al. [48]). This was the area where the steel AISI 304 was molten. Due to the primary ferritic solidification of the steel AISI 304, the ferrite was transformed into secondary austenite during cooling. Secondly, a TZ was present between the MMC material and the welding seam. In this TZ, Mg-PSZ particles were embedded within dendritic structures with a blue etching color. This coloring was due to the primary austenitic solidification of the TWIP matrix material [14]. Previous investigations have shown that the Mg-PSZ is introduced into the welding seam by the electron beam welding process, where it is agglomerated, melted and partially evaporated. This evaporation process leads to the formation of a mixture of oxides of zirconium and magnesium, which can accumulate during welding in cavities or during braze-welding in the joining gap [14]. As Fig. 10.12b shows, the particles in the welding seam and in the base

metal possessed approximately the same dimensions. It was therefore assumed that some Mg-PSZ particles could have been introduced into the melt pool. A current field of interest is the manner in which the Mg-PSZ particles interact with the melt, the electron beam and the keyhole.

10.3.2 Influence of Beam Parameters on the Weld Quality

During the welding experiments without beam displacement ($\Delta x = 0$ mm), the molten metal was periodically ejected (similar to the humping effect). This led to material loss and the formation of cavities (Fig. 10.13a) in the welding seam, which is known from the similar welding joints (Sect. 10.2.7).

With increasing beam displacement (up to 0.3 mm), material separations along the entire weld length, even reaching the weld face were observed. Moreover, pronounced cavity formation was visible (Fig. 10.13b). From a beam offset of 0.4 mm (Fig. 10.13c), the typical smoothly scaled upper bead and a microscopically flawless welding seam were obtained. Occasionally, the welding seam was widened, though material separation did not occur. In summary, the welding quality improved with decreasing amounts of Mg-PSZ within the weld pool.

An underfill was evident at a beam offset of 0.4 mm. Despite having the same bevel geometries, higher beam offsets (0.5–0.6 mm) did not result in underfill, but produced joints with the same scaling of upper beads (Fig. 10.13d). In order to counteract the underfill, tests were carried out without machining a bevel on the samples, with these samples exhibiting a general reduction and, partly, a complete prevention of seam

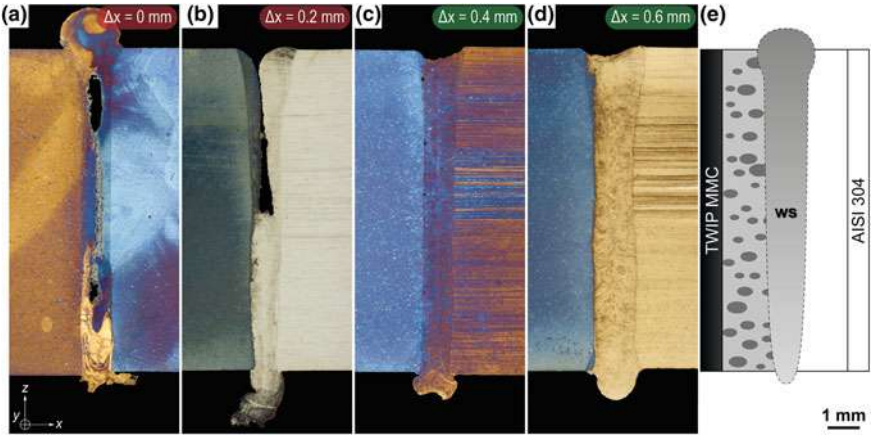

Fig. 10.13 Influence of the beam offset Δx on the weld quality (red: EG < 'D', green: EG better than 'D'); **a**–**d** light optical cross sections, **e** schematic position of the welded materials. Beam parameters: $I_B = 45$ mA, $v_s = 15$ mm/s [15]

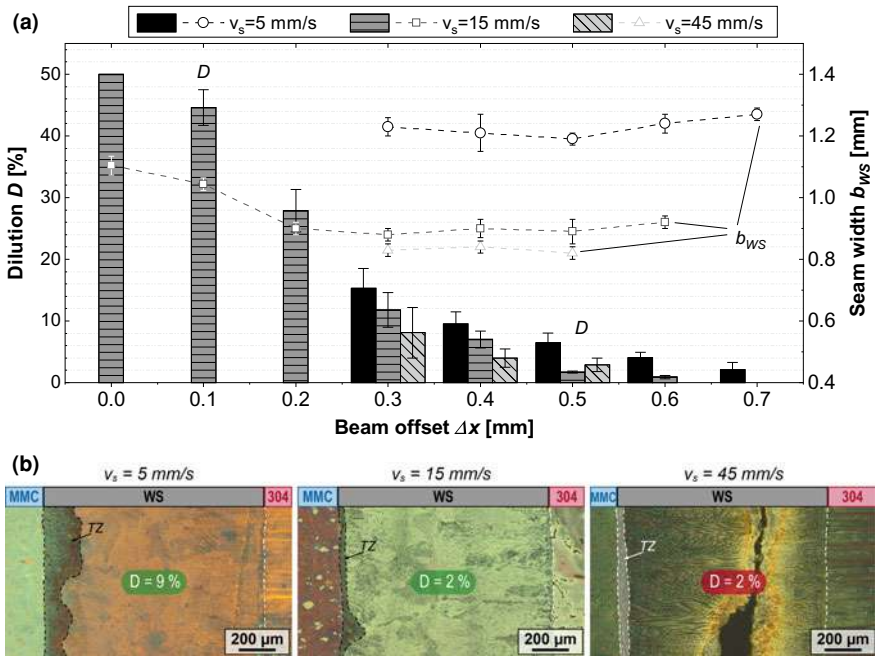

Fig. 10.14 **a** Resulting level of dilution (shown in bars, left axis) for different welding speeds as a function of the beam offset used. Datapoints mark the corresponding seam width (right axis). **b** Influence of the welding speed v_s and the level of dilution D on the weld quality with respect to the area of the transition zone (TZ) for $\Delta x = 0.5$ mm. $v_s = 5$ mm/s: $I_B = 30$ mA, EG = 'C', $v_s = 15$ mm/s: $I_B = 45$ mA, EG = 'D', $v_s = 45$ mm/s: $I_B = 110$ mA, EG < 'D' [15]

concavity. Further examinations were then carried out with a beam offset of 0.4 mm, and did not exhibit any underfill. For all tests without bevels, an upper bead was produced that was free of macroscopic faults. Even without a bevel, the welding gap could be located easily with the monitoring system of the EB facility.

The experiments had shown that the beam displacement was associated with characteristic defects in the welding seam. With the level of dilution (D), there was an additional characteristic value which acted as a measure for the ingress of the Mg-PSZ particles and the corresponding width of the mixing zone. In Fig. 10.14a, the degrees of mixing for different welding speeds (5–45 mm/s) are plotted with the corresponding welding seam widths as a function of the beam offset used. As expected, the level of dilution decreased with increasing beam offset regardless of the welding speed. The defect-free welds with a beam offset of 0.4–0.6 mm corresponded to an ingress of <10% (Fig. 10.14a). All samples with higher dilution exhibited pores, underfills or other significant defects. The standard deviations determined were also the smallest in the offset range for samples without defects (0.4–0.6 mm) and increased with decreasing beam offset. Consequently, the process stability increased with increasing beam displacement.

Based on the results of welding experiments at 15 mm/s, it could be deduced that starting from $\Delta x = 0$ mm, the welding seam width decreased with increasing beam offset up to a beam offset of 0.2 mm. This was due to the significantly lower thermal conductivity of the TWIP MMC compared to the austenitic AISI304 steel, which led to heat accumulation and, thus, to seam broadening. Above a beam offset of 0.3 mm and with less than 28% dilution, the welding seam width remained approximately constant, which was due to the decreasing influence of TWIP MMC material. In addition, it was shown that there was no significant change in welding seam width for welding speeds of 15–45 mm/s. On the other hand, welds with 5 mm/s exhibited an increase in welding seam width of ≈35% compared to welds produced at 15 mm/s. The reason for this was the limited sample volume, which was discussed in Sect. 10.2.6.1. Regardless of the set level of dilution, all welds carried out with a welding speed of 45 mm/s had significant defects. The micrographs in Fig. 10.14b show that despite similar levels of dilution, there were significant differences in welding quality. The ingress of the Mg-PSZ particles was therefore not the only factor that impaired the weldability of TWIP Mg-PSZ. It became clear that despite similar energy inputs per unit length, pore-containing seams were produced at welding speeds of 45 mm/s, while pore-free joints could be welded at 15 mm/s. At the same time, a higher energy input per unit length also led to an improvement in the quality of the welding seam. Therefore, it was not possible to identify any clear tendencies for the evaluation of the welding seam quality from the selected value of E. However, the influence of the welding speed on the quality of the welding seam was proven in this work. In contrast to the work of Chen et al. [10], improvement of the weld quality with increasing welding speed could not be found for the TWIP MMC used.

Thus, in the case of a very large beam offset ($\Delta x = 0.6$ mm), it was possible to change the seam geometry by lowering the welding speed to $v_s = 5$ mm/s in such a way that almost parallel edges of the seam were created. This prevented connection faults in the root position area. Tests were carried out to select the optimum welding beam current at small beam offsets ($\Delta x = 0.4$ mm) and correspondingly high entries of Mg-PSZ ($D \approx 12\%$) into the weld pool. It was observed that the minimal beam currents necessary for full-penetration welding often led to pore formation and connection errors in the root position. Raising the beam current by ≈20% led to better melt degassing, on the one hand, and to more parallel weld edges on the other hand, which positively influenced both the connection quality and the melt degassing. However, the welding seam could only be classified as EG = 'D' due to the presence of underfill.

Further tests on the influence of the focal plane position on the seam quality showed that a sharp surface focus–(ΔI_F) = 0 mA–led to strong shrinkage, underfill, and a scaled seam surface (cf. Fig. 10.15b). It should be noted that all experiments were carried out with a beam offset of 0.4 mm, i.e. the TWIP MMC was molten and cavity formation occured, which is associated with the ingress of Mg-PSZ to the weld pool. The formation of cavities could be prevented with a shift of the focal plane over the top of the sheet metal ($\Delta I_F = 5$ mA), but the underfill increased drastically (Fig. 10.15a). A defocus of $\Delta I_F = -5$ mA below the sheet surface, on the other hand,

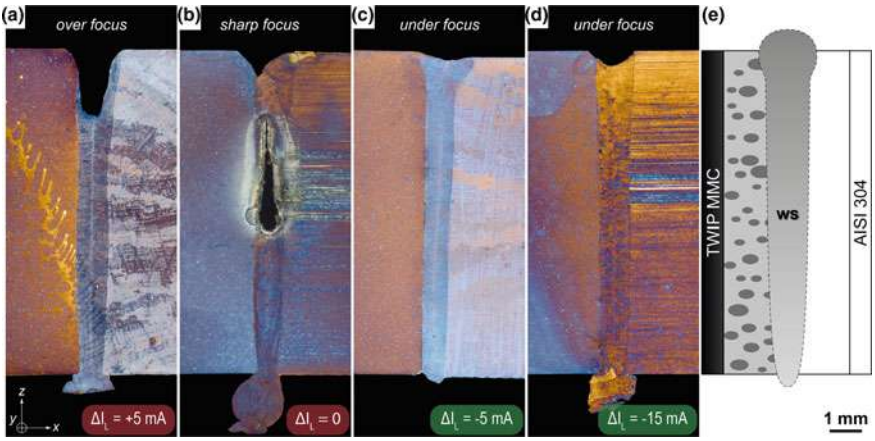

Fig. 10.15 Influence of the focal position of the EB on the weld quality (red: EG < 'D', green: EG better than 'D'), according to the lens current used; **a**–**d** light optical cross sections; **e** schematic position of the welded materials. Beam parameters: $I_B = 45\,\text{mA}$, $v_s = 15\,\text{mm/s}$, $\Delta x = 0.4\,\text{mm}$ [15]

produced a pore-free welding seam with a finely scaled bead surface and without underfill (Fig. 10.15c). With further defocusing of the beam, however, the porosity was unaffected (pore size <80 µm), but the underfill was increased (see Fig. 10.15d). This was attributed to the dependence of process stability on the stability of the keyhole. With a sharp focus on the surface, the capillary was not opened wide enough, and was quite susceptible to the ingress of ceramic particles. A larger opening of the steam channel resulted in better degassing and, therefore, better welding results. Tests on welded aluminum joints by Ahn et al. showed similar tendencies [2].

10.3.3 Verification of Welding Defects

For the ultrasonic immersion tests, the entire welding seam was scanned in the longitudinal direction (see Fig. 10.3). The aim of the non-destructive testing was to detect welding defects, such as a lack of fusion or cavities. In addition to the determination of the defect position in the y-z direction, the flaw depth was determined while taking into consideration the longitudinal wave velocity of the AISI 304 steel. The size of the Mg-PSZ particles was below the resolution limit, which meant that no negative influence could be detected using either the ultrasonic immersion test or X-ray inspection.

Figure 10.16a1 shows the D-scan of a welding seam with pores and lack of fusion for a sample with EG < 'D'. With respect to the D-scan, it was assumed that a connection was only present at the edge of the sample. This was confirmed by the light optical micrographs in Fig. 10.16a3, a4. The flaw depth information indicated a planar defect (lack of fusion) at a depth of ≈5.5–6.5 mm (indicated by the light

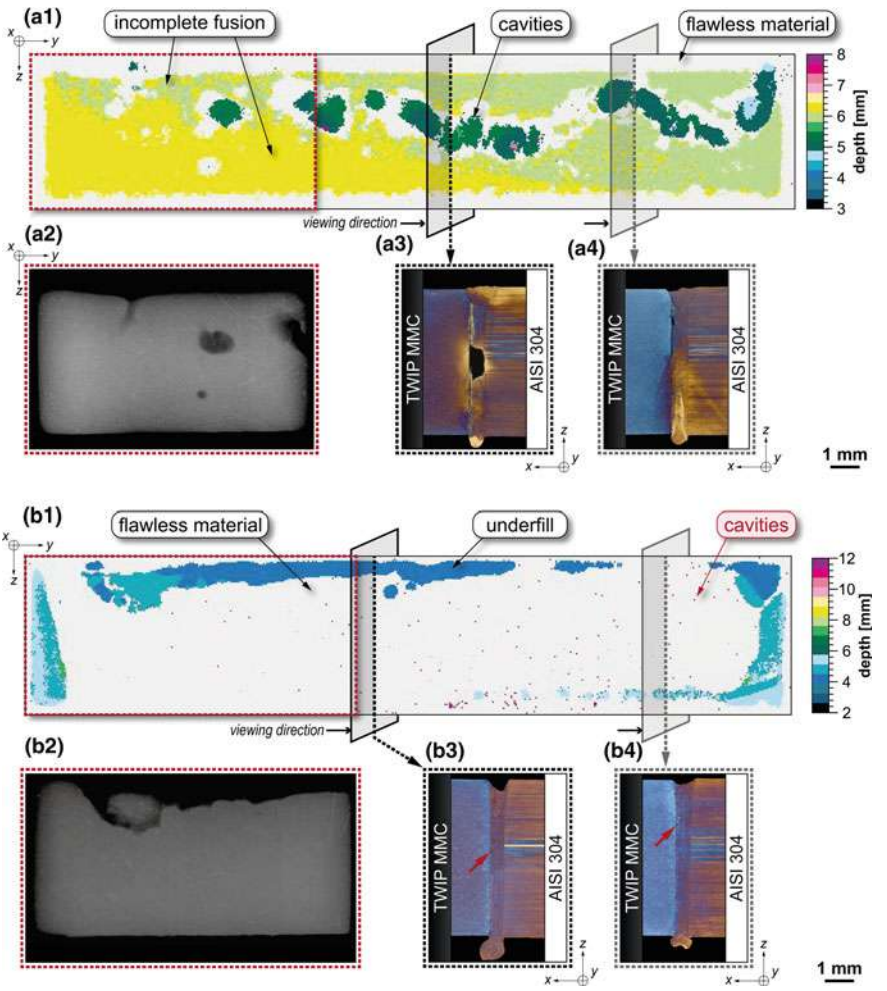

Fig. 10.16 **a** Testing results of sample with EG = 'C', beam parameters: $I_B = 46\,mA$, $v_s = 15\,mm/s$, $\Delta x = 0.6\,mm$; **b** testing results of sample with EG < 'D', beam parameters: $I_B = 45\,mA$, $v_s = 15\,mm/s$, $\Delta x = 0.4\,mm$. 1 Ultrasonic immersion results with the depth information of the signal (testing axis: x). 2 X-ray image of the marked section (red dashes, testing axis: x). 3, 4 Cross sections at positions marked in 1 (dashed arrows) [15]

green to yellow color), which was assigned to the TWIP MMC. Small deviations in the measured depths of planar defects resulted from deviations in plane-parallelism in the processing of samples for the ultrasonic immersion testing. The areas with the dark green color in Fig. 10.16a1 indicated weld defects—where ultrasonic waves are reflected earlier than from planar defects. Taking into account the shape of the defect, which extended into the welding seam, the occurrence of pores in the sample was assumed. The light optical micrograph in Fig. 10.16a3 supports this assumption.

Indeed, the formation of worm-holes was assumed due to the irregular arrangement of the pores in the longitudinal direction of the welding seam. Worm-holes are formed by rising gases that remain in the welding seam. In addition to the verification of the investigation via ultrasonic immersion testing, X-ray inspection was applied for a selected area of the sample (see Fig. 10.16a2). Volume defects such as pores were located within the X-ray image, which concurred with the D-scan carried out by means of ultrasonic immersion testing and the light optical micrographs. However, no information was available about the flaw depth. Furthermore, a lack of fusion was not detected via X-ray inspection.

Figure 10.16b1 shows the D-scan of a welding seam for a sample with EG = 'C'. The welding seam exhibited an almost flawless connection between the joining partners. However, an underfill and pores at the micrometer scale were derived from the D-scan. Furthermore, due to slope-in and slope-out effects, a defective connection was observed at the edge of the sample. The existence of pores at the micrometer scale was verified by light optical micrographs (see red arrows in Fig. 10.16b3 and Fig. 10.16b4). Thus, the detection limit for the pore diameter was 90–100 µm. According to DIN EN ISO 13919-1, individual pores with this dimension can be tolerated within welding seams if no special type of load is defined. Hence, an adequate resolution limit existed to detect all significant defects via ultrasonic immersion testing. By X-ray inspection, both the underfill and the microporosity were determined to a resolution limit of 25 µm (see Fig. 10.16b2).

10.3.4 Mechanical Characterization

Investigations were carried out to determine whether the welding process was associated with a change in hardness from the base material (TWIP) to the welding seam and, in particular, to the transition zone (cf. Fig. 10.17). In the transition zone, a drop in Martens hardness of about 300 MPa was detected compared to the remaining welding seam (Fig. 10.17). These differences were due to the different solidification modes from the transition zone (AF mode) as well as the welding seam (FA mode) and the associated δ-ferrite contents.

Furthermore, the presence of Mg-PSZ particles within the base material led to higher measured hardness values. On the other hand, the absence of those particles within the transition zone again led to lower measured hardness values. Due to the very similar chemical composition of both joining partners, however, no significant change in hardness was found within the measured profile. Individual areas that had a very high degree of hardness (≈2600 MPa) in the TWIP base material were interpreted as Mg-PSZ particles.

Figure 10.18 shows the mechanical properties of the tensile test for a comparative characterization of the welded joints with different levels of dilution. With respect to the experiments at $v_s = 15$ mm/s, it became clear that the highest ultimate tensile strengths were present at D of 12% ($\Delta x = 0.3$ mm). The median tensile strengths achieved were at 545 MPa with an uniform strain of 8.2%. However, these welding

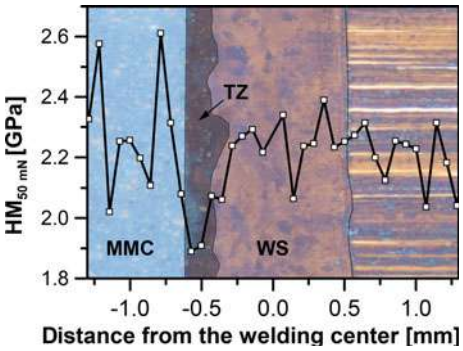

Fig. 10.17 Microhardness profile across the welded materials and the fusion zone. Beam parameters: $I_B = 30\,\text{mA}$, $v_s = 5\,\text{mm/s}$, $\Delta x = 0.5\,\text{mm}$, $D \approx 9\%$ [15]

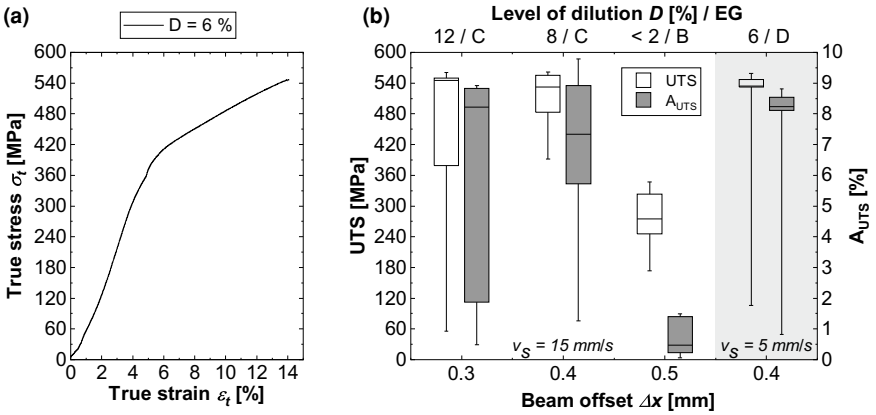

Fig. 10.18 Influence of the level of dilution and the beam offset on the mechanical properties. **a** Representative stress-strain curve for $D = 6\%$; **b** boxplot of the ultimate tensile strength and the uniform strain (A_U) as a function of Δx and D [15]

seams were categorized as EG = 'C' due to the very high porosity. Therefore, failure took place within the welding seam with a very high amount of scatter. At lower degrees of mixing ($D = 8\%$, $\Delta x = 0.4\,\text{mm}$), the joints could also be evaluated as EG = 'C', but exhibited slightly lower strength and strain values (UTS = 532 MPa, $A_{UTS} = 7.3\%$, both medians). Individual large pores within the welding seam led to failure of the samples. Joints that exhibited hardly any melting of the base metal ($D < 2\%$, $\Delta x = 0.5\,\text{mm}$) exhibited the worst mechanical properties. Failure took place alongside the fusion line even at low stress levels ($UTS_{med.} = 275\,\text{MPa}$). The samples broke in an almost brittle manner with hardly any measurable elongation ($A_{UTS,\,med.} = 0.5\%$).

Contrary to these findings, the joints were free of pores, exhibited neither underfill nor lack of fusion and were evaluated as EG = 'B' according to DIN EN ISO 13919-1.

Halbauer et al. [13] attribute the low mechanical properties at very high beam offsets to the formation of an oxide-containing layer at the fusion line, which prevents complete joining of the two welding materials. Since the occurrence of planar defects and, in particular, non-wettable oxide layers are not covered by DIN EN ISO 13919-1, the mechanical properties of the welding joints could not be derived solely from the evaluation group. Instead, further investigations were required to determine, in particular, the quality of connectivity. The investigation of this bonding strength on the microscopic scale will be discussed in detail in a future publication. Improvement of the mechanical properties was achieved by using a lower welding speed ($v_s = 5\,\mathrm{mm/s}$) and setting a low dilution level of the TWIP MMC ($D = 6\%$, $\Delta x = 0.4\,\mathrm{mm}$). In this way, tensile strengths of 535 MPa (med.) were achieved with a uniform elongation of 8.2% and with minimum scatter of the tensile strength. Since no significant porosity was found, rupture of the samples took place within the base material of the TWIP MMC. This was made possible by the significantly longer interaction time between the EB and the melt, which led to better degassing and calming of the melt. According to DIN EN ISO 13919-1, these welds had to be categorized as EG = 'D' due to the presence of underfill. However, these defects were not relevant for the mechanical properties due to the high ductility of the steel AISI 304 within the welding seam.

10.4 Electron Beam Brazing of TWIP-Matrix Composites

10.4.1 Macroscopic Phenomena

It was investigated, how the energy distribution $P(y)$ of the electron beam as a function of the position can influence the temperature distribution at the sample surface (Fig. 10.19) during the brazing process. First, heating experiments without filler material were carried out with a constant energy across the EB field width (Fig. 10.19a). As expected, the temperature exhibited a maximum at the center of the separate energy transfer fields and a sharp temperature gradient towards the edges was present (Fig. 10.19c). Accordingly, this temperature distribution led to partial melting in the middle of the EB interaction field and high distortion in x-direction.

Second, $P(y)$ was adjusted according to (10.1) with $P_{\min} = 0.8$ (Fig. 10.19b). Due to the variation of energy input, the resulting temperature distribution was homogeneous in y-direction, which allowed the filler to melt more homogeneous, prevented partial surface melting and reduced the distortion of the samples significantly (Fig. 10.19d). If $P_{\min}$ was further decreased, more energy was introduced to the edges of the samples, which again led to inhomogeneous temperature distributions and partial melting of the sample surface. All samples discussed in the following were brazed with this adjustment of the energy distribution.

Figure 10.20a illustrates the evolution of the filler gap (h_f) after brazing and is representative for the investigated samples in the longitudinal section (y-direction). The gap width after brazing was much smaller than the initial gap width ($h_{f,init}$) (i.e.

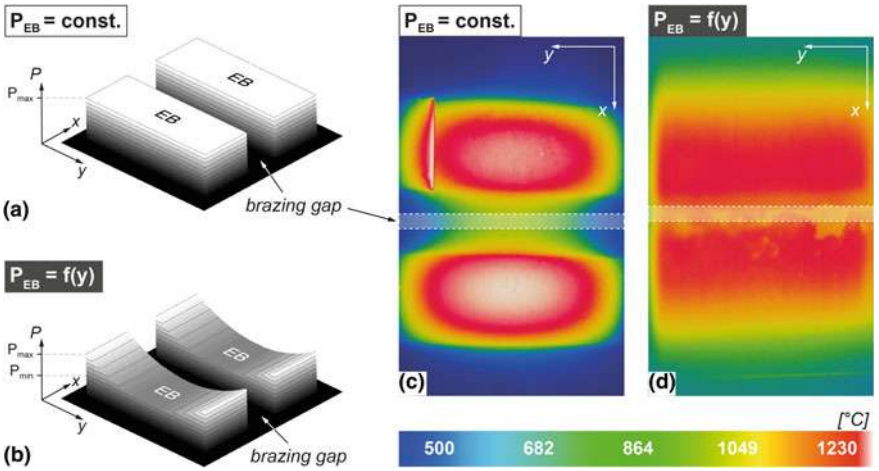

Fig. 10.19 Influence of the energy distribution on the temperature distribution at the sample surface during brazing. **a**, **b** Schematic illustrations of the set beam interaction field; **c**, **d** resulting temperature distribution measured with a thermographic camera (adapted from [16])

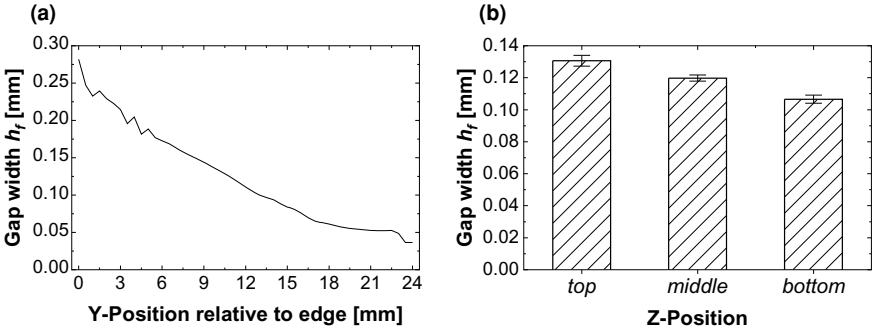

Fig. 10.20 Evolution of the filler gap width (h_f) after brazing **a** depending on the distance from the sample edge (longitudinal section); **b** depending on the z-position of the measurement (cross-section). Initial gap = 800 µm, t_H = 67 s (adapted from [16])

$h_{f,init} = 1200\,\mu m$, $h_{f,max} = 300\,\mu m$). During heating, the width of the gap decreases according to thermal expansion, since the samples are fixed within the clamping device. If the gap is too small, the clamping device is able to compensate the contact stress with an internal suspension. However, during cooling, the solidified filler material prevented the base material from retaining its original shape which clearly led to internal stresses. After brazing the resulting gap width decreased sightly from the top ($130 \pm 3\,\mu m$) to the bottom ($106 \pm 2\,\mu m$) of the samples (cf. Fig. 10.20b). Due to the high sheet thickness, the unilateral heating of the samples and the short holding time a temperature gradient of $\approx 100\ K$ from the top to the bottom of the samples (z-direction) developed. However, in the authors' opinion the resulting gra-

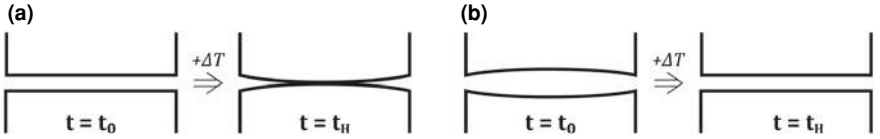

Fig. 10.21 Evolution of the filler gap geometry before ($t = t_0$) and during brazing ($t = t_H$) due to distortion **a** without uniform gap, **b** with crowned gap geometry. $t_0 = 0$ s (after [16])

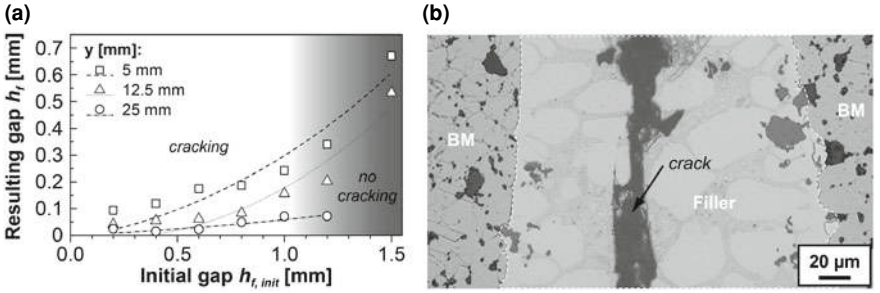

Fig. 10.22 **a** Gap width after brazing (resulting gap) 2 mm below the sheet surface as a function of the initial gap at different distances from the sample edge ($t_H = 52$ s); **b** Typical crack within the center of the brazing gap (modified from [16])

dient in thermal expansion from the top to the bottom was negligible and was not the reason for the gradient of the gap width. It was more likely, that diffusion controlled mechanisms such as erosion, caused the gap to widen at the top, which is explained in detail in Sect. 10.4.2.

Though the energy field was optimized to ensure uniform temperatures across the sample, the thermal expansion exhibited a gradient from the center (high) to the edge (low) (Fig. 10.21a). This gradient could be compensated by the addition of a crowned gap geometry (Fig. 10.21b).

The gap width h_f was also influenced by the initial gap width before brazing, cf. Fig. 10.22a. As expected, the resulting gap width decreased with the decreasing initial gap. For $h_{f,init}$ <1 mm the two joining partners had direct contact in the center of the gap and therefore h_f was mainly influenced by the solidification of the surrounding filler material and exhibited cracks due to insufficient feeding (cf. Fig. 10.22b). With increasing $h_{f,init}$ (>1.2 mm) the gap width was mainly influenced by the thermal expansion across the sample and no cracks were observed. Concludingly, a gap width ≥1.2 mm should be used for potential application.

10.4.2 Microscopic Characterization

Figure 10.23 shows an exemplary cross section of the joint between the particle reinforced TWIP steel (TWIP matrix composite (TMC)) with Ni-filler and $h_{f,init}$ = 1.2 mm. From the edge to a distance of $y \approx 10$ mm neither pores nor cracks were found. Due to the strong distortion during heating, the center of the gap exhibited solidification cracks across the whole sample height. A dendritic microstructure consisting of dendrite cores (DC) (Fig. 10.23b, light grey) and an interdendritic region (IDR) (Fig. 10.23b, dark grey) were present. Following the temperature gradient in z-direction, a transition zone was detected (Fig. 10.23c, d), which decreased in width from the top (≈ 85 µm) to the bottom (≈18 µm) of the samples. In this transition zone, particles from the base material were visible. The chemical composition of the matrix between the particles was similar to that of the filler material. Based on the investigations made, the transition zone formed as a result of a diffusion induced erosion and the formation of phases between the filler and the base material. The IDR consisted of low melting phases, exhibited a fine, lathy internal structure (Fig. 10.23b) and is believed to be an eutectic phase.

The distribution of the low melting phases was investigated by the binarization of the light optical micrographs. Independent on the base material used, the joined area consisted of ≈ 50% eutectic phases and the phases were distributed heterogeneously across the sheet thickness. If a very long holding time was applied (t_H = 600 s), the

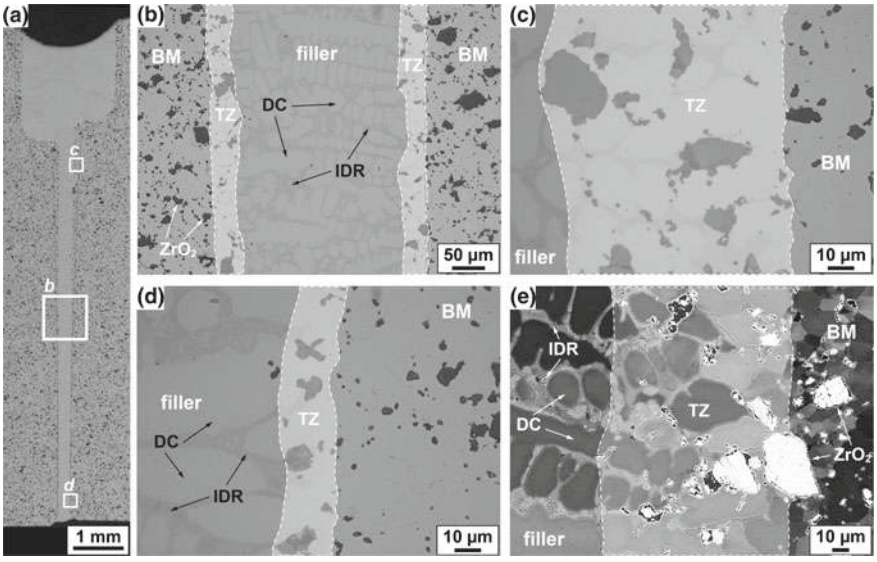

Fig. 10.23 Microstructure of the brazed samples (cross sections at 5 mm from the sample edge), **a**–**d** light optical investigations at different positions, **e** SEM image of the gap center (detail). BM: base material, TZ: transition zone, IDR: interdendritic region [16]

content of eutectic phases could be reduced to at least 35% with a minimum of 20% at the middle of the sample height. However, due to the high amount of energy input, such long holding times have to be considered critically in terms of efficiency and economics. To minimize the content of brittle phases, either the dendritic solidification has to be enhanced drastically by applying significantly higher solidification rates or a change of the alloying system has to be considered.

The evolution of the transition zone was further analyzed by a combination of EBSD investigation with parallel energy-dispersive X-ray spectroscopy (EDS) (Fig. 10.24). The transition zone between the base material and the filler consisted of FCC dendrite cores (Fig. 10.24b) and Cr-Ni-Si intermetallic compounds with varying stoichiometry within the IDR. According to literature, these compounds are likely to occur as eutectic phases within the Cr-Ni-Si system. They are characterized by a good oxidation resistance but are also very brittle [1, 24, 47]. Also the tetragonal phase of zirconia was present, which implies, that zirconia particles would still be able to undergo a phase transformation during deformation. At the fusion line, a strong orientation relationship between the filler and the base material was present (Fig. 10.24c). Furthermore, a preferred orientation in [001]-direction was found within the dendrites, which is common for materials with a cubic microstructure.

Though the filler material was initially free of iron, significant iron contents were found within the filler after brazing. Concludingly, a diffusion of Fe from the BM into the filler had happened. As expected, the dendrite cores were also enriched with Cr and Ni, since these were the main constituents of the filler material. The IDRs were enriched with Si due to the formation of the intermetallic phases. Zr was primarily found within the Mg-PSZ particles of the base material and the transition zone within the filler (Fig. 10.24e–h). It should be noted, that a strict separation between Zr and Si is not possible due to the EDS analysis method. The Kα peak of silicon and the Lα peak of zirconium have a very similar energy level. As a result the analysis software tends to detect Si in regions enriched with zirconium and vice versa. Accordingly, the very high amounts of silicon within the ceramic particles (Fig. 10.24g) should not be considered as realistic. The Mg-PSZ particles were only found at a distance of 18–85 µm from the fusion line and were distributed as homogeneously as in the base material. It was concluded, that the particles penetrated into the filler with a significant melt flow. This rather suggested, that an erosion process had taken place during the brazing process, which was incorporated with a chemical dissolution of the matrix and without movement of the particles. Since the erosion ensures the wettability of the base material it is a desired phenomenon and should not be avoided. Altogether, the formation of the brazing zone can be described as followed:

1. erosion of the BM by the filler and formation of a Fe–Cr–Ni–Si system
2. epitactic growth of the filler onto the BM with primary FCC-solidification
3. formation of a preferred orientation in growth direction
4. enrichment of the remaining melt with Si and Ni
5. formation of low melting phases/eutectics within the IDR
6. contraction of the dendrite cores during further cooling.

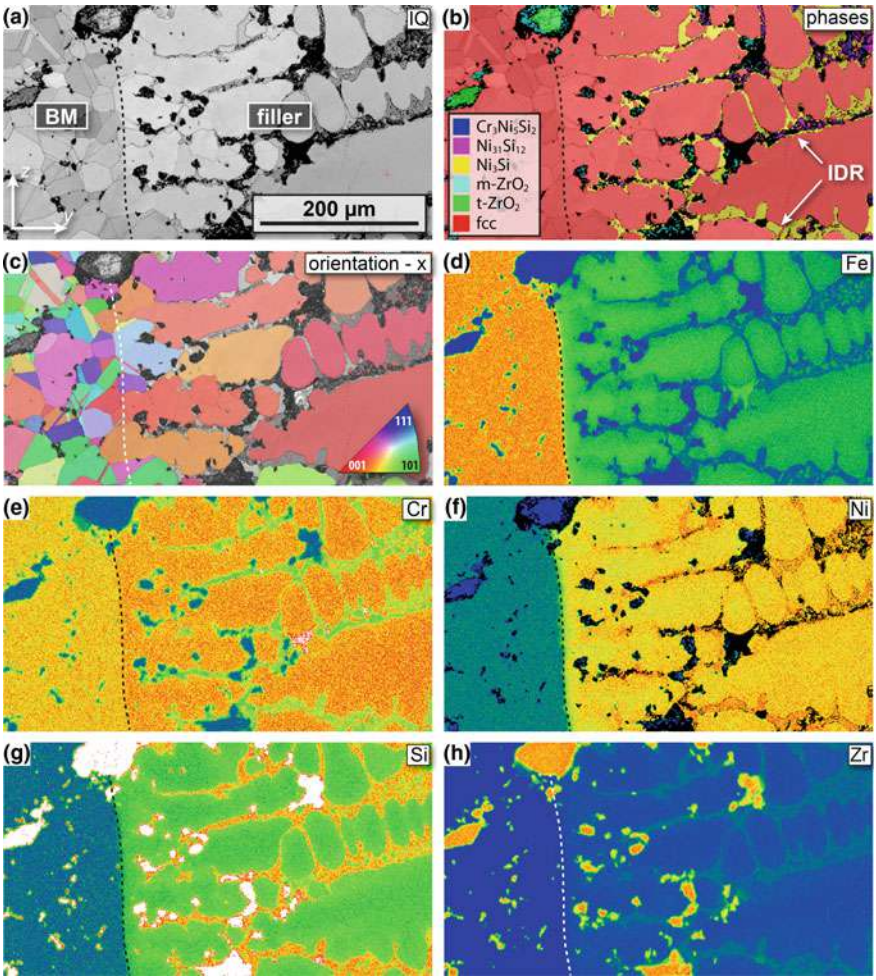

Fig. 10.24 EBSD investigation of the transition zone between BM and filler. **a** Image quality (IQ) map, **b** phase distribution map + IQ, **c** grain orientation in x-direction. **d**–**h** EDS mapping of different alloying elements as heat maps (the warmer the color, the higher the local content; black/white areas indicate data below/above the scale). Dashed lines represent the fusion line [16]

10.4.3 Tensile Tests

Figure 10.25 shows the results of the tensile tests with the mechanical properties UTS and elongation at rupture (A_R). Brazing joints with TMC reached up to 358 MPa and 3.3% elongation (Fig. 10.25a). The mechanical properties can be compared to the base material only to a limited degree since the production process and chemical composition have a huge impact. When compared to braze welded flat tensile specimen (TWIP + as-cast TRIP), the UTS dropped to ≈ 62% of the base material (BM:

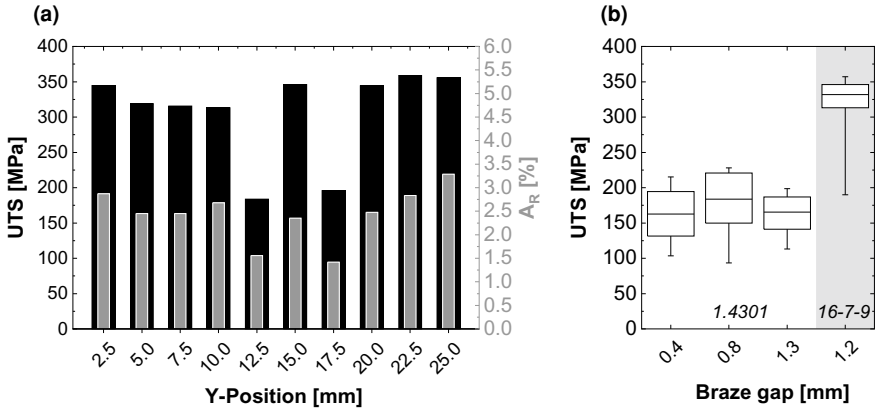

Fig. 10.25 Results of tensile tests with Ni-based filler. **a** UTS and A_R depending on the position of preparation (TMC, t_H = 67 s, h_f = 1200 µm), **b** UTS dependent on the brazed material and the width of the initial braze gap [16]

UTS = 558 MPa) and only 12% of the elongation was left (BM: A_R = 26%). These values are in good agreement with the investigations on round tensile specimen [14] (UTS = 573 MPa, A_R = 29%). Eckner et al. investigated a TRIP/TWIP steel with 6.6% Ni and found a true tensile strength of 686 MPa and 21% true strain for a SPS sintered base material. Though the samples exhibited high differences in the gap width, the mechanical properties remained nearly constant within all tested samples (Fig. 10.25a). At some positions, a sudden drop in strength and ductility was detected, which correlated with an incomplete filling of the gap due to pores or material separation.

Moreover, the gap width had an influence on the UTS of joints with steel 1.4301 and Ni-filler (Fig. 10.25b). Though the scatter decreased slightly with increasing $h_{f,init}$, the strength of the braze joint was independent of the initial gap width. As a result of the higher amount of eutectic phases, joints with steel 1.4301 exhibited a significantly lower tensile strength compared to the TWIP matrix composite. The samples exhibited mostly elastic deformation and always broke within the filler material. Investigations with nano hardness measurements confirmed the existence of brittle phases within the IDR (cf. Fig. 10.26). These phases could not be avoided by the variation of the holding time and had a Martens hardness of HM 50 mN = 6.8–7.4 GPa. Due to the limitation of the minimum force and the positioning system, the separate phases within the IDR could not be investigated separately. Accordingly, the hardness is averaged across all phases of the IDR. Neither the hardness values of the IDR nor of the dendrite core were dependent on the holding time applied. With higher holding time the content of eutectica as well as the scatter of hardness decreased, due to the more homogeneous distribution of the formed phases. Since the formation of brittle phases is intensified by the formation of large dendrites within the Ni-filler, they could be minimized by decreasing the DAS value either with even shorter holding times or smaller gaps. Since shorter holding times would lead to higher heating rates, the temperature differences between the sheet surface

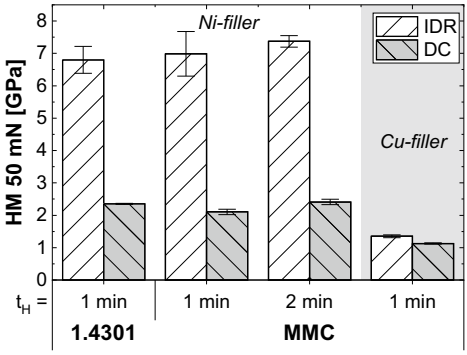

Fig. 10.26 Nano hardness investigation of the filler components depending on both the holding time and filler material. DC: dendrite core, IDR: interdendritic region (adapted from [16])

and bottom would also increase, which is not desirable for thick sheets. Smaller gaps would imply, that the joint geometry had to be changed. Two possible ways are the overlap joint, which would be beneficial for thin sheets, or the production of crowned geometries for butt joints for thick sheets. For future work, a Cu-based filler material was pre-investigated, which has the advantage of a single phased solidification and a very low overall hardness (1.13 ± 0.02 GPa). Individual phases formed within the IDR were on a comparable hardness level (1.35 ± 0.04 GPa) which could result in significantly higher deformation of the brazing joints.

10.5 Summary

The contribution deals with the investigation regarding the weldability of high-alloy TRIP/TWIP materials (sheet thickness 10 mm) with and without particle reinforcement. A very good weldability was found for the as-cast material without particle reinforcement. The influence of the nickel content on the welding seam geometry was only marginal. Independent of the nickel content the welding seams were free of pores and cracks and had almost parallel seam flanks.

During the welding process manganese evaporated from the base material. For welding speeds $\leq$5 mm/s, Mn loss up to 0.9 wt% was detected by EDS measurements. The evaporation correlated with the expansion of the molten zone at the upper bead. With both decreasing welding speed and power density the manganese evaporation increased. No significant change in the chemical composition was observed with a fully pronounced deep penetration welding effect.

The weldability of the base materials was essentially limited by humping. Similar to conventional stainless steels, increasing welding speed is accompanied by an increased tendency to hump, as shown in the literature. Steel 16-7-3 showed the highest tendency of humping. This steel was fully weldable up to a welding speed of 20 mm/s and showed first signs of humping up to 40 mm/s. The beginning of humping for the 16-7-6 and 16-6-9 steels was at 50–60 mm/s. For welding speeds $\geq$80 mm/s, all materials were not weldable due to pronounced humping.

The mechanical characteristics of the joints were not negatively affected by the welding process. As the nickel content increased, a decrease in strength and an increase in elongation were observed. It could be proven that the deformation mechanisms of the base material also remain effective in the weld seam. Accordingly, the weld seam also showed a very good ductility.

The particle-reinforced composite material could not be welded with keyhole. A strong melt ejection occurred and a cavity was formed in the middle of the welding zone. This cavity could be minimized, but could not be avoided by any welding parameter.

If the amount of Mg-PSZ introduced into the weld pool of dissimilar welding joints was lower than a threshold of ≈10% the welding seam was free of pores and cracks. The tolerable proportion of Mg-PSZ increased with decreasing welding speed. At welding speeds of 5 and 15 mm/s, 9 and 2% Mg-PSZ were tolerable, respectively. The resulting welds were free of pores and cracks and showed mechanical properties at the level of the base material. Higher levels of dilution and velocities caused the formation of the center cavity. Furthermore, it could be shown that an underfocus of about −5 mA had to be set to produce a flawless weld seam. It was assumed that this had a positive influence on the degassing behavior of the samples and was therefore necessary. Basically, it was observed that all parameters which favor degassing of the melt led to an improvement of the welding result. However, the decisive parameter for weldability was always the level of dilution. Therefore, when changing individual parameters, it may be necessary to check to what extent the weld width and thus the degree of dilution will change.

It was found that the Mg-PSZ that enters the welding zone is partially melted and tends to form clusters. Particles detected in the dendritically solidified weld metal showed no morphological changes. Therefore it was concluded that only a part of the particles interacted with the keyhole and only this part contributed to the deterioration of the material behavior. Thus, current investigations focus on the interaction of the Mg-PSZ with the electron beam.

A soldering process was carried out on butt joints consisting of a TWIP matrix composite (MMC) and a nickel-base filler material with a sheet thickness of 10 mm. In order to keep the temperature within the soldering field as constant as possible, a polynomial energy distribution of the electron beam was used. The control of this process was realized by a temperature controlled power regulation system. Due to the geometry-related strain obstruction at the edge of the specimen, the center of the joints exhibited a lack of fusion. A complete filler connection was therefore only possible at the edge of the specimen.

Chemical erosion created a transition zone from the filler to the MMC with metallic bonding character. Thus, the nickel-base filler formed an excellent connection with the base material and a high mechanical loadability of joints was expected. Due to the high silicon content of the filler material, silicon-rich intermetallic phases were formed in the solidified solder. Due to their brittleness, the samples broke within the IDR of the filler outside of the transition zone. This lowered both the strength and the ductility of the samples.

Acknowledgements This work was supported financially by the German Research Foundation (DFG) within the framework of the Collaborative Research Center "TRIP matrix composites" (CRC 799, project number 54473466, subproject A7). Special thanks of the authors go to Prof. Rolf Zenker for his commitment to project management in the second funding period. Our thanks also go to his helpful suggestions and professional input. The authors gratefully acknowledge Dr. Karsten Rüthrich for his helpful discussions, his initial work and commitment regarding the electron beam facility. Furthermore, the authors like to thank Prof. P. Hübner for the realization of the X-ray analysis, Dipl.-Ing. G. Schade for the many tensile tests as well as G. Bittner for the hardness measurements.

References

1. R. Ahmad, R.F. Cochrane, A.M. Mullis, The formation of regular αNi-γ(Ni31Si12) eutectic structures from undercooled Ni–25 at.% Si melts. Intermetallics **22**, 55–61 (2012). https://doi.org/10.1016/j.intermet.2011.10.021
2. J. Ahn, E. He, L. Chen, J. Dear, C. Davies, The effect of Ar and He shielding gas on fibre laser weld shape and microstructure in AA 2024–T3. J. Manuf. Process. **29**, 62–73 (2017). https://doi.org/10.1016/j.jmapro.2017.07.011
3. C.G. Aneziris, W. Schärfl, H. Biermann, U. Martin, Energy-absorbing TRIP-steel/Mg-PSZ composite honeycomb structures based on ceramic extrusion at room temperature. Int. J. Appl. Ceram. Technol. **6**(6), 727–735 (2009). https://doi.org/10.1111/j.1744-7402.2008.02321.x
4. C. Baumgart, D. Ehinger, C. Weigelt, L. Krüger, C.G. Aneziris, Comparative study of TRIP/TWIP assisted high density composite honeycomb structures under compressive load. Compos. Struct. **136**, 297–304 (2016). https://doi.org/10.1016/j.compstruct.2015.09.053
5. P. Berger, H. Hügel, A. Hess, R. Weber, T. Graf, Understanding of humping based on conservation of volume flow. Phys. Proc. **12**, 232–240 (2011). https://doi.org/10.1016/j.phpro.2011.03.030
6. H. Biermann, U. Martin, C.G. Aneziris, A. Kolbe, A. Müller, W. Schärfl, M. Herrmann, Microstructure and compression strength of novel TRIP-steel/Mg-PSZ composites. Adv. Eng. Mater. **11**(12), 1000–1006 (2009). https://doi.org/10.1002/adem.200900210
7. V. Braga, R.A.d.F. Mansur, R.H.M.d. Siqueira, M.S.F.d. Lima, Formability of in-situ Austempered transformation-induced plasticity steels after laser beam welding. Soldagem & Inspeção **23**(3), 402–412 (2018). https://doi.org/10.1590/0104-9224/si2303.09
8. A. Buchwalder, K. Rüthrich, R. Zenker, H. Biermann, Electron Beam welding of high alloy CrMnNi cast steels with TRIP/TWIP effect. Adv. Eng. Mater. **15**(7), 566–570 (2013). https://doi.org/10.1002/adem.201200355
9. I. Calliari, M. Dabalà, M. Penasa, Pulsed Nd-YAG laser welding of MMCs. Adv. Eng. Mater. **2**(10), 653–656 (2000). https://doi.org/10.1002/1527-2648(200010)2:10<653::AID-ADEM653>3.0.CO;2-Q
10. H.C. Chen, A.J. Pinkerton, L. Li, Fibre laser welding of dissimilar alloys of Ti-6Al-4V and Inconel 718 for aerospace applications. Int. J. Adv. Manuf. Technol. **52**(9–12), 977–987 (2011). https://doi.org/10.1007/s00170-010-2791-3
11. Deutsches Institut für Normung e.V.: Schweißbarkeit—Metallische Werkstoffe—Allgemeine Grundlagen (2007-04-01)
12. T.K. Gupta, F.F. Lange, J.H. Bechtold, Effect of stress-induced phase transformation on the properties of polycrystalline zirconia containing metastable tetragonal phase. J. Mater. Sci. **13**(7), 1464–1470 (1978). https://doi.org/10.1007/BF00553200
13. L. Halbauer, A. Buchwalder, R. Zenker, H. Biermann, Influence of EB parameters on the microstructure and mechanical properties of dissimilar welded joints in high alloy TRIP/TWIP steels, in *JOM18 Conference Proceedings* (JOM Institute for the Joining of Materials, 2015)

14. L. Halbauer, A. Buchwalder, R. Zenker, H. Biermann, The influence of dilution on dissimilar weld joints with high-alloy TRIP/TWIP steels. Weld. World **60**(4), 645–652 (2016). https://doi.org/10.1007/s40194-016-0324-x
15. L. Halbauer, R. Laubstein, M. Radajewski, A. Buchwalder, L. Krüger, H. Biermann, Electron beam welding and characterization of dissimilar joints with TWIP matrix composites. Adv. Eng. Mater. **114**, 1800586 (2018). https://doi.org/10.1002/adem.201800586
16. L. Halbauer, P. Proksch, A. Buchwalder, R. Zenker, H. Biermann, Joining of TWIP-matrix composites by electron beam brazing. Weld. World **62**(1), 19–27 (2018). https://doi.org/10.1007/s40194-017-0519-9
17. B. Huang, X. Chen, S. Pang, R. Hu, A three-dimensional model of coupling dynamics of keyhole and weld pool during electron beam welding. Int. J. Heat Mass Transf. **115**, 159–173 (2017). https://doi.org/10.1016/j.ijheatmasstransfer.2017.08.010
18. R. Hunag, S. Chen, J.C. Huang, Electron and laser beam welding of high strain rate superplastic Al-6061/SiC composites. Metall. Mater. Trans. A **32A**, 2575–2584 (2001)
19. H. Inoue, T. Koseki, Clarification of solidification behaviors in austenitic stainless steels based on welding process. Nippon Steel Tech. Rep. **95**, 62–70 (2007)
20. A. Jahn, Einfluss der Martensitbildung auf die mechanischen Eigenschaften von ein- und mehrphasigen gegossenen und warm gewalzten Cr-Mn-Ni Stählen. Doctoral thesis, Technische Universität Bergakdemie Freierg, Freiberg, Germany, 2012
21. N. Kapustka, C. Conrardy, S. Babu, C. Albright, Effect of GMAW process and material conditions on DP 780 and TRIP 780 welds. Weld. Res. Suppl. **87**(6), 135–148 (2008)
22. M.I. Khan, M.L. Kuntz, Y. Zhou, Effects of weld microstructure on static and impact performance of resistance spot welded joints in advanced high strength steels. Sci. Technol. Weld. Join. **13**(3), 294–304 (2008). https://doi.org/10.1179/174329308X271733
23. C.J. Lippold, W.F. Savage, Solidification of austenitic stainless steel weldments: part 2—the effect of alloy composition on ferrite morphology. Weld. Res. Suppl. **2**, 48–58 (1980)
24. X. Liu, M. Lin, S. Yang, J. Ruan, C. Wang, Experimental investigation of phase equilibria in the Ni-Cr-Si ternary system. J. Phase Equilib. Diffus. **35**(3), 334–342 (2014). https://doi.org/10.1007/s11669-014-0279-9
25. V. Lopez, A. Reyes, P. Zambrano, Effect of the Heat input in the transformation of retained austenite in advanced steels of transformation induced plasticity (TRIP) welded with gas metal arc welding. Appl. Mech. Mater. **339**, 700–705 (2013). https://doi.org/10.4028/www.scientific.net/AMM.339.700
26. V.H. López Cortéz, G.Y. Pérez Medina, F.A. Reyes Valdéz, H.F. López, Effects of the heat input in the mechanical integrity of the welding joints welded by GMAW and LBW process in transformation induced plasticity steel (TRIP) used in the automotive industry. Soldagem & Inspeção **15**(3), 234–241 (2010). https://doi.org/10.1590/S0104-92242010000300010
27. L.l. Ma, Y.H. Wei, L.F. Hou, C.l. Guo, Evaluation on fatigue performance and fracture mechanism of laser welded TWIP steel joint based on evolution of microstructure and micromechanical properties. J. Iron Steel Res. Int. **23**(7), 677–684 (2016). https://doi.org/10.1016/S1006-706X(16)30105-4
28. S. Martin, S. Richter, S. Decker, U. Martin, L. Krüger, D. Rafaja, Reinforcing mechanism of Mg-PSZ particles in highly-alloyed TRIP steel. Steel Res. Int. **82**(9), 1133–1140 (2011). https://doi.org/10.1002/srin.201100099
29. S. Martin, S. Wolf, U. Martin, L. Krüger, D. Rafaja, Deformation mechanisms in austenitic TRIP/TWIP steel as a function of temperature. Metall. Mater. Trans. A **47**(1), 49–58 (2016). https://doi.org/10.1007/s11661-014-2684-4
30. G.P. Medina, H.L. Ferreira, P.Z. Robledo, A.M. Pérez, F.A.R. Valdés, Microstructural development in a TRIP-780 Steel joined by friction stir welding (FSW): quantitative evaluations and comparisons with EBSD predictions. Soldagem & Inspeção **21**(2), 146–155 (2016). https://doi.org/10.1590/0104-9224/SI2102.04
31. L. Mujica, S. Weber, C. Thomy, F. Vollertsen, Microstructure and mechanical properties of laser welded austenitic high manganese steels. Sci. Technol. Weld. Join. **14**(6), 517–522 (2009). https://doi.org/10.1179/136217109X434243

32. L. Mújica Roncery, Development of high-strength corrosion-resistant austenitic TWIP steels with C+N. Doctoral thesis, Ruhr–Universität Bochum, Bochum, Germany, 2010
33. L. Mújica Roncery, S. Weber, W. Theisen, Welding of twinning-induced plasticity steels. Scripta Mater. **66**(12), 997–1001 (2012). https://doi.org/10.1016/j.scriptamat.2011.11.041
34. S. Nayak, V. Baltazar Hernandez, Y. Okita, Y. Zhou, Microstructure-hardness relationship in the fusion zone of TRIP steel welds. Mater. Sci. Eng. A **551**, 73–81 (2012). https://doi.org/10.1016/j.msea.2012.04.096
35. J. Niu, L. Pan, M. Wang, C. Fu, X. Meng, Research on laser welding of aluminum matrix composite SiCw/6061. Vacuum **80**(11–12), 1396–1399 (2006). https://doi.org/10.1016/j.vacuum.2006.01.023
36. G.B. Olson, M. Cohen, A mechanism for the strain-induced nucleation of martensitic transformations. J. Less Common Metals **28**, 107–118 (1972)
37. M. Onyuna, H. Oettel, U. Martin, A. Weiß, On the deformation behavior and martensitic transformations of metastable austenitic steels. Adv. Eng. Mater. **6**, 529–535 (2004)
38. S. Pichumani, R. Srinivasan, V. Ramamoorthi, Mechanical properties, thermal profiles, and microstructural characteristics of Al-8 %SiC composite welded using pulsed current TIG welding. J. Mech. Sci. Technol. **32**(4), 1713–1723 (2018). https://doi.org/10.1007/s12206-018-0130-4
39. P. Podany, M. Koukolikova, T. Kubina, R. Prochazka, A. Franc, Fe-Mn(Al, Si) TWIP steel—strengthening characteristics and weldability. IOP Conf. Ser. Mater. Sci. Eng. **179**, 012057 (2017). https://doi.org/10.1088/1757-899X/179/1/012057
40. P. Podany, C. Reardon, M. Koukolikova, R. Prochazka, A. Franc, Microstructure, mechanical properties and welding of low carbon. Medium manganese TWIP/TRIP steel. Metals **8**(4), 263 (2018). https://doi.org/10.3390/met8040263
41. D. Rafaja, C. Krbetschek, C. Ullrich, S. Martin, Stacking fault energy in austenitic steels determined by using in situ X-ray diffraction during bending. J. Appl. Crystallogr. **47**(3), 936–947 (2014). https://doi.org/10.1107/S1600576714007109
42. U. Reisgen, M. Schleser, O. Mokrov, E. Ahmed, Numerical and experimental investigation of tensile behavior of laser beam welded TRIP700 steel. ISIJ Int. **51**(3), 429–434 (2011). https://doi.org/10.2355/isijinternational.51.429
43. L. Remy, A. Pineau, Twinning and strain-induced F.C.C. → H.C.P. transformation in the Fe-Mn-Cr-C system. Mater. Sci. Eng. **28**(1), 99–107 (1977)
44. D.C. Saha, Y. Cho, Y.D. Park, Metallographic and fracture characteristics of resistance spot welded TWIP steels. Sci. Technol. Weld. Join. **18**(8), 711–720 (2013). https://doi.org/10.1179/1362171813Y.0000000151
45. K. Sato, M. Ichinose, Y. Hirotsu, Y. Inoue, Effects of deformation induced phase transformation and twinning on the mechanical properties of austenitic Fe-Mn-Al alloys. ISIJ Int. **29**(10), 868–877 (1989)
46. P.J. Spencer, J.N. Pratt, A study of the vapour pressure of manganese using a new high-temperature torsion—effusion apparatus. Brit. J. Appl. Phys. **18**(10), 1473–1478 (1967). https://doi.org/10.1088/0508-3443/18/10/314
47. S. Subramanian, D.A. Muller, J. Silcox, S.L. Sass, Chemistry, bonding and fracture of grain boundaries in Ni3Si. Acta Metall. **45**(9), 3565–3571 (1997)
48. N. Suutala, T. Takalo, T. Moisio, Ferritic-austenitic solidification mode in austenitic stainless steel welds. Metall. Mater. Trans. A **11A**, 717–725 (1980)
49. N. Suutala, T. Takalo, T. Moisio, Ferritic-austenitic solidification mode in austenitic stainless steel welds. Metall. Trans. A **11**(5), 717–725 (1980). https://doi.org/10.1007/BF02661201
50. J. Talonen, Effect of strain-induced α'-martensite transformation on mechanical properties of metastable austenitic stainless steels. Ph.D. thesis, Helsinki University of Technology, Helsinki, Finland, 2007
51. D.N. Trushnikov, G.M. Mladenov, V.Y. Belenkiy, E.G. Koleva, S.V. Varushkin, Current-driven ion-acoustic and potential-relaxation instabilities excited in plasma plume during electron beam welding. AIP Adv. **4**(4), 047105 (2014). https://doi.org/10.1063/1.4870944

52. K.H. Tseng, Study on surface appearance, geometry size, and delta-ferrite content of ZrO2-aided TIG welding of AISI 316LN stainless steel. Int. J. Adv. Manuf. Technol. **89**(5–8), 2355–2362 (2017). https://doi.org/10.1007/s00170-016-9280-2
53. C. Weigelt, H. Berek, C.G. Aneziris, R. Eckner, L. Krüger, Joining of Zirconia reinforced metal-matrix composites. Mater. Sci. Forum **825–826**, 498–505 (2015). https://doi.org/10.4028/www.scientific.net/MSF.825-826.498
54. C. Weigelt, G. Schmidt, C.G. Aneziris, R. Eckner, D. Ehinger, L. Krüger, C. Ullrich, D. Rafaja, Compressive and tensile deformation behaviour of TRIP steel-matrix composite materials with reinforcing additions of zirconia and/or aluminium titanate. J. Alloys Compd. **695**, 9–20 (2017). https://doi.org/10.1016/j.jallcom.2016.10.176
55. M. Wendler, A. Weiß, L. Krüger, J. Mola, A. Franke, A. Kovalev, S. Wolf, Effect of manganese on microstructure and mechanical properties of cast high alloyed CrMnNi-N steels. Adv. Eng. Mater. **15**(7), 558–565 (2013). https://doi.org/10.1002/adem.201200318
56. J. Yoo, K. Han, Y. Park, J. Choi, C. Lee, Evaluation of solidification cracking susceptibility of Fe-18Mn-0.6C steel welds. Sci. Technol. Weld. Join. **19**(6), 514–520 (2014). https://doi.org/10.1179/1362171814Y.0000000216

Chapter 11
Microstructure Aspects of the Deformation Mechanisms in Metastable Austenitic Steels

David Rafaja, Christiane Ullrich, Mykhaylo Motylenko and Stefan Martin

Abstract This chapter presents microstructure features, which are responsible for transformation-induced and twinning-induced plasticity in austenitic steels, gives an overview of relevant microstructure defects and shows how the microstructure defects and their interactions affect the deformation behaviour of these steels. Numerous examples illustrate the capability of scanning and transmission electron microscopy and X-ray and electron diffraction to detect, to identify and to quantify dislocations, stacking faults, twins and their clusters. In this context, the benefits of the in situ techniques of microstructure analysis are emphasized. As the presence and arrangement of stacking faults in austenite play a central role in the plasticity of the austenitic steels, a large part of this chapter is devoted to the characterization and description of their formation, widening and ordering. A novel method for determination of the stacking fault energy is presented that utilizes in situ X-ray or synchrotron diffraction under deformation. Finally, the dependence of the stacking fault energy on the chemical composition of the steel and on the deformation temperature is addressed, and considered as an effective tool for design of steels with desirable mechanical properties.

11.1 Introduction

The highly tunable properties of metastable austenitic steels are typically based on polymorphic phase transformations that allow a desired phase composition and microstructure of the steels to be adjusted. Moreover, the phase transformations and the twinning in metastable austenite are the most important mechanisms behind the transformation-induced plasticity (TRIP) and for the twinning-induced plasticity (TWIP) of these steels.

D. Rafaja (✉) · C. Ullrich · M. Motylenko · S. Martin
Institute of Materials Science, Technische Universität Bergakademie Freiberg,
Gustav-Zeuner-Straße 5, 09599 Freiberg, Germany
e-mail: rafaja@ww.tu-freiberg.de

H. Biermann and C. G. Aneziris (eds.), *Austenitic TRIP/TWIP Steels and Steel-Zirconia Composites*, Springer Series in Materials Science 298,
https://doi.org/10.1007/978-3-030-42603-3_11

At room temperature and ambient pressure, pure iron possesses *bcc* lattice that is stabilized by the ferromagnetic ordering of magnetic moments [1]. When the ferromagnetism is deactivated, e.g., through a high hydrostatic pressure (> 13 GPa), a hexagonal close packed modification of iron with a smaller specific volume becomes stable [2, 3]. Above 911 °C the *fcc* modification and above 1392 °C up to the melting point at 1536 °C the *bcc* structure are thermodynamically stable. By alloying iron with substitutional elements like chromium, nickel and manganese or with interstitial elements like carbon or nitrogen, the high temperature *fcc* phase can be stabilized down to room temperature. Such steels are known as *austenitic stainless steels*, as a high chromium content (> 12 wt%) impedes corrosion.

The *fcc* metals and alloys are usually ductile and show an excellent formability. Their stress-strain curves are characterized by the occurrence of high elongation and modest strain hardening that typically depend on the deformation temperature. In Fig. 11.1a, b, the temperature dependence of the mechanical behavior is illustrated on the true stress-strain curves measured under tensile load and on the strain hardening calculated from these stress-strain curves, respectively. The different characteristics of oxygen-free high conductive (OFHC) copper and a metastable austenitic stainless steel of the type X3CrMnNi16-6-6[1] illustrate the effect of the alloying elements. The yield stress and the applied stress needed to maintain plastic deformation are much higher for the alloyed steel than for the OFHC copper. Consequently, the alloyed steel shows a higher strain hardening than the OFHC copper.

Further differences are visible in the temperature dependence of the mechanical properties. Whereas the strain hardening of the OFHC copper increases only slightly

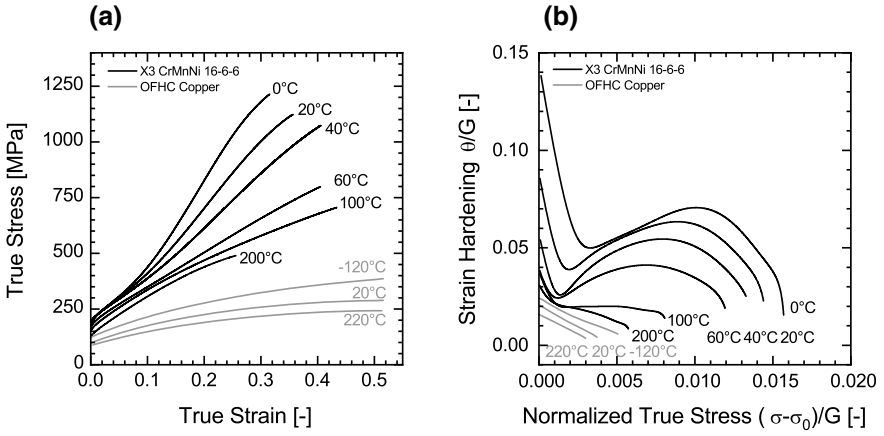

Fig. 11.1 Mechanical properties of X3 CrMnNi16-6-6 TRIP/TWIP steel [4] and pure (OFHC) copper [5] obtained from tensile testing at different temperatures: **a** stress-strain behavior and **b** corresponding strain hardening depicted in form of the Kocks-Mecking plot

[1]Chemical composition 16 wt% Cr, 6 wt% Mn, 6 wt% Ni, 1 wt% Si, 0.03 wt% C of the reference stainless steel in this Chapter, deviating chemical compositions from this one are given.

with decreasing deformation temperature, the increase of the strain hardening in the metastable austenitic steel plastically deformed at low temperatures is much more pronounced. Below 100 °C, the steel shows a tremendous increase of the strength and an additional hardening in the strain range between approx. 0.05 and 0.25. This difference in the temperature dependence of the mechanical properties can be explained by different deformation mechanisms in the OFHC copper and in the TRIP/TWIP steels, and by different activities of underlying microstructure defects and microstructure phenomena like dislocations, stacking faults and deformation-induced martensitic phase transformations.

In this Chapter, the role of dislocation slip, dissociation of dislocations, formation of partial dislocations, expansion of stacking faults and martensitic transformations in the plastic deformation of the TRIP/TWIP steels is discussed in order to explain the specific stress-strain behavior of these materials. Particular attention is paid to the effect of the stacking fault energy on the dislocation glide, nucleation of the martensites and to the interaction of microstructure defects and features among each other.

11.2 Fundamental Microstructure Defects, Their Activity and Configurations in Austenitic Steels

11.2.1 Dislocations and Stacking Faults in fcc *Materials*

Plastic deformation of metals is typically based on dislocation slip. Perfect dislocations in *fcc* austenite have the Burgers vectors ⟨110⟩ and glide on the close-packed planes {111}. In austenitic steels, the perfect dislocations tend to split into Shockley partial dislocations, which can be described by the following reaction:

$$\frac{a}{2}\left[10\bar{1}\right] \rightarrow \frac{a}{6}\left[11\bar{2}\right] + \frac{a}{6}\left[2\bar{1}\bar{1}\right] \tag{11.1}$$

In (11.1), a is the lattice parameter of the *fcc* structure and $\frac{a}{2}\left[10\bar{1}\right]$ the Burgers vector of the original perfect dislocation. The Burgers vectors of the Shockley partials are $\frac{a}{6}\left[11\bar{2}\right]$ and $\frac{a}{6}\left[2\bar{1}\bar{1}\right]$. This dissociation reaction is a consequence of the line energy reduction upon dissociation. As the line energies of dislocations are proportional to the square of their Burgers vectors [6], the sum of the line energies of the partials is lower than the line energy of the perfect dislocation. The equilibrium dissociation width x_0 is reciprocally proportional to the stacking fault energy (SFE) γ_{SF}. For screw dislocations, the following relationship holds [6]:

$$x_0 = \frac{Gb_p^2}{8\pi\gamma_{\mathrm{SF}}}\frac{2-3\nu}{1-\nu} \tag{11.2}$$

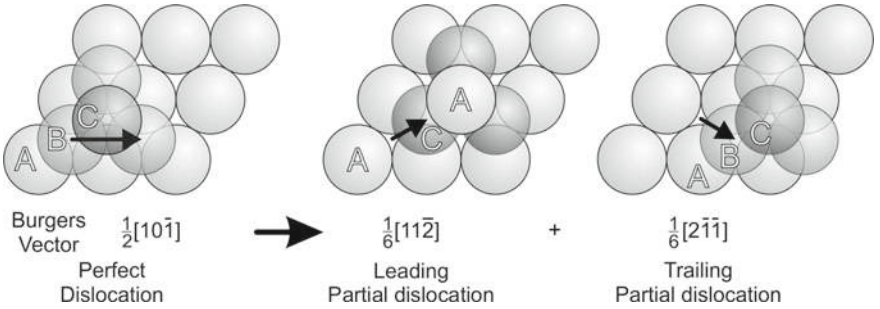

Fig. 11.2 Schematic arrangement of the atoms in the close-packed layers in an unfaulted *fcc* crystal (left), after the passage of the leading partial dislocation (middle) and beyond the stacking fault terminated by the trailing partial (right). Adopted from [8]

In (11.2), G is the shear modulus, b_p the magnitude of the Burgers vector of the partial dislocations and ν the Poisson ratio. The reciprocity of the equilibrium dissociation width and SFE means that the dissociation width is small for metals with a high SFE like Al (~200 mJ/m^2 [7]), where it is comparable with the length of the Burgers vector, and large for *fcc* materials with a low SFE, e.g. Ag (~25 mJ/m^2 [7]).

The occurrence of partial dislocations modifies the stacking order of the adjacent atomic planes {111}. In unfaulted *fcc* crystals, the stacking sequence of the close-packed planes {111} along the respective perpendicular direction ⟨111⟩ is *ABCABC* (Fig. 11.2, left). After the passage of the leading partial having the Burgers vector $\frac{a}{6}[11\bar{2}]$, it is modified to *ABCACA* (Fig. 11.2, middle). The passing of the trailing partial with the Burgers vector $\frac{a}{6}[2\bar{1}\bar{1}]$ reconstitutes the original stacking sequence (Fig. 11.2, right). The stacking fault is spanned between the partial dislocations.

Upon loading, the Burgers vectors of the partials interact with the external load, which modifies the movement of the partial dislocations and the widening of the stacking faults. This interaction was described by Copley [9] and Byun [10] as

$$\left[\hat{l}\times\left(\overleftrightarrow{\tau}\cdot\overrightarrow{b_1}\right)\right]\cdot\hat{x}=\gamma_{SF}-\frac{G}{2\pi x_0}\left[\left(\overrightarrow{b_1}\cdot\hat{l}\right)\left(\overrightarrow{b_2}\cdot\hat{l}\right)+\frac{\left(\overrightarrow{b_1}\times\hat{l}\right)\left(\overrightarrow{b_2}\times\hat{l}\right)}{1+\nu}\right]+f_0 \tag{11.3}$$

$$\left[\hat{l}\times\left(\overleftrightarrow{\tau}\cdot\overrightarrow{b_2}\right)\right]\cdot\hat{x}=-\gamma_{SF}+\frac{G}{2\pi x_0}\left[\left(\overrightarrow{b_1}\cdot\hat{l}\right)\left(\overrightarrow{b_2}\cdot\hat{l}\right)+\frac{\left(\overrightarrow{b_1}\times\hat{l}\right)\left(\overrightarrow{b_2}\times\hat{l}\right)}{1+\nu}\right]+f_0 \tag{11.4}$$

In (11.3) and (11.4), $\overrightarrow{b_1}$ and $\overrightarrow{b_2}$ are the Burgers vectors of the partial dislocations, $\overleftrightarrow{\tau}$ is the stress tensor, $\hat{l}$ corresponds to the line vector of the dislocation,

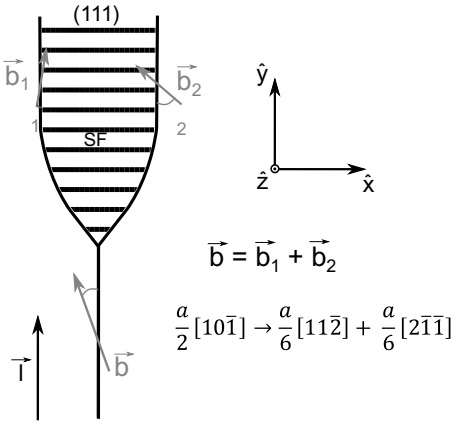

Fig. 11.3 Dissociation of a perfect dislocation with the Burgers vector $\vec{b}$ to partial dislocations with the Burgers vectors $\vec{b}_1$ and $\vec{b}_2$ spanning a stacking fault [10]

$\hat{x}$ is the unit direction according to the setup in Fig. 11.3, x_0 the separation distance of the partials and f_0 the lattice friction force. The different forces acting on the leading and trailing partial that are induced by the external stress are represented by the left-hand sides of (11.3) and (11.4) [11]. The SFE (γ_{SF}) pulls the partials together, whereas the repulsive interaction force due to their stress fields, i.e., $\pm\frac{G}{2\pi x_0}\left[\left(\vec{b_1}\cdot\hat{l}\right)\left(\vec{b_2}\cdot\hat{l}\right)+\frac{\left(\vec{b_1}\times\hat{l}\right)\left(\vec{b_2}\times\hat{l}\right)}{1+\nu}\right]$, pushes the partials apart. The lattice friction against the dislocation movement (f_0) is equal for leading and trailing partial dislocation. Using these equations, the equilibrium of the dynamic force under an applied stress can be calculated. The maximum stress effect on the dissociation width is found for screw dislocations. For such dislocations, the separation distance x_0 can be calculated as [10]:

$$x_0 = \frac{(2-3\nu)Gb_p^2}{8\pi(1-\nu)\left[\gamma_{SF} - \tau_{zx}b_p/2\right]} \tag{11.5}$$

Consequently, the dissociation distance between the partial dislocations is strongly affected by the SFE (γ_{SF}) and external stress (τ_{zx}). Both effects are illustrated in Fig. 11.4, where the dependence of x_0 on τ_{zx} is plotted for several SFE values. The separation distance increases drastically above a critical stress level [10],

$$\tau_{zx}^{crit} = 2\gamma_{SF}/b_p, \tag{11.6}$$

at which the separation distance in (11.5) approaches infinity. In reality, the stacking fault extends through the entire grain. In materials with lower SFE, wide stacking faults are formed and the critical stress for quasi-infinite dissociation is lower than in materials with higher SFEs. Wide stacking faults are found in the microstructure of deformed austenitic CrMnNi steels and are the reason for their special mechanical behavior. As the SFEs of the austenitic CrMnNi steels with TWIP and TRIP

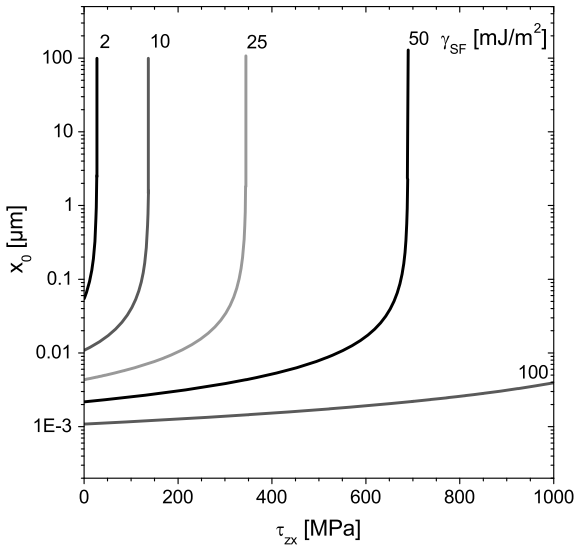

Fig. 11.4 The dissociation width as a function of the applied stress, plotted for several SFE values according to [10]

effect range between 2 and 40 mJ/m^2 [12, 13], wide stacking faults form in their microstructure already at low deformations and affect the deformation behavior seriously.

11.2.2 Dislocations and Stacking Faults in Austenitic Steels, Their Configurations and Interactions

The most important microstructure defects in metastable austenite are dislocations with the Burgers vectors $\frac{a}{2}\langle 110\rangle$ and the stacking faults on the lattice planes {111}. Their configurations and interactions are depicted in the transmission electron microscopy (TEM) micrographs in Fig. 11.5, which were taken in an austenitic steel containing 16 wt% Cr, 7 wt% Mn, 9 wt% Ni, 1 wt% Si, 0.02 wt% C and 0.02 wt% N that was subjected to 2% deformation.

Nearly perfect dislocations (SFs with a very short dissociation width) are visible in area I of Fig. 11.5a, b. They stem from the Frank-Read-like dislocation sources [14]. One example of the Frank-Read source can be seen in the area II of Fig. 11.5a. Larger dissociation is observed for dislocations that are suitably oriented with respect to the applied force. The largely dissociated Shockley partial dislocations form stacking faults that are highlighted by red arrows in Fig. 11.5a. As the partial dislocations can only move on their slip planes, their cross slip to other planes is impeded and only possible, if the partials constrict and recombine. Furthermore, both perfect and partial dislocations are piling up at obstacles during plastic deformation (see, e.g., area I in Fig. 11.5b). These obstacles might be the stress fields produced by immobile dislocations or dislocation clusters as well as the grain boundaries. The pile-ups

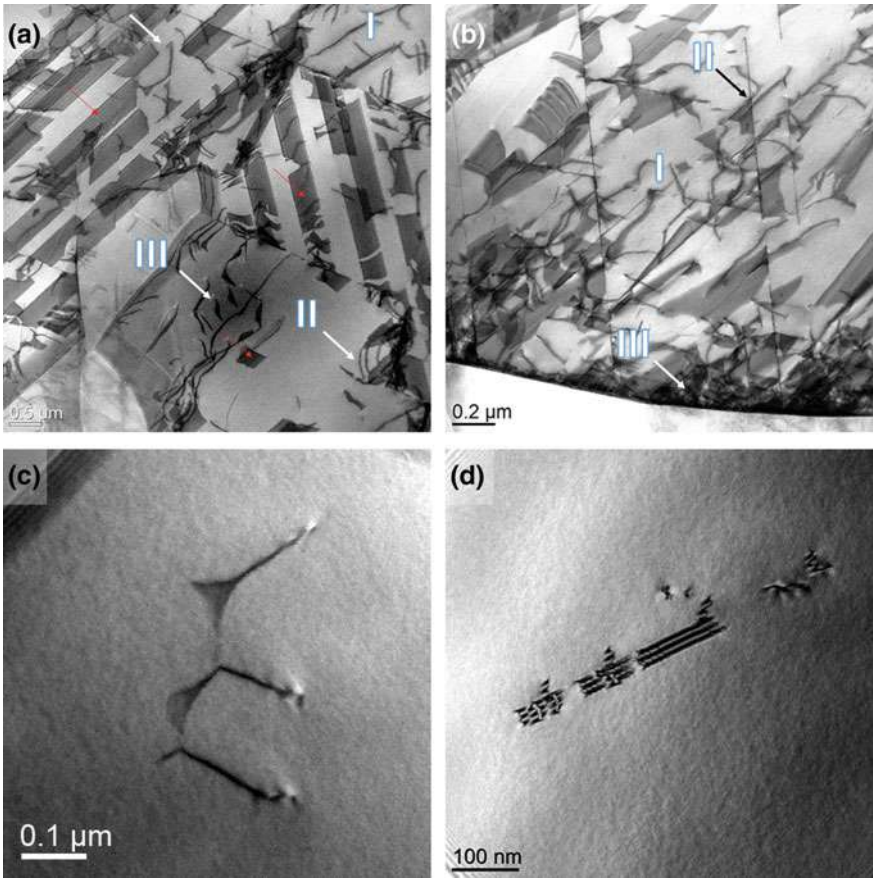

Fig. 11.5 Characteristic dislocation configurations in X2CrMnNi16-7-9 stainless steel having a low stacking fault energy after 2% straining. **a** Depending on the resolved shear stress on individual glide planes, dissociated dislocations form short or wide stacking faults (area III). **b** Beginning of the SF interaction, the deformation band formation, dislocation pile up and Lomer-Cottrell lock formation. **c** Dislocation nodes spanning stacking faults in between. **d** Overlapping stacking faults indicating the SF band formation. Micrographs (**a**) and (**b**) were taken in the scanning TEM mode, micrographs (**c**) and (**d**) in the TEM mode

generate long-range stress fields, which enable further dislocation reactions like the cross-slip of screw dislocations [15].

If multiple slip systems are activated, which is generally the case for plastic deformation of polycrystalline metals, the dislocations can interact with SFs and specific dislocation reactions occur. Dissociated dislocations on intersecting slip planes form Lomer-Cottrell locks [16, 17] as seen in Fig. 11.5b, area II. These locks are generated, when stacking faults on different slip planes encounter. This can be illustrated by the edge-on stacking faults, which seem to stop the SFs on the other slip planes. The normal directions of the edge-on stacking faults lie in

the plane of the TEM sample, thus they are visible just as thin lines in the TEM micrograph. Such locks immobilize SFs on both slip planes, which are now in a sessile configuration, and can cause further dislocation reactions or pile-ups, as the locks are obstacles for following dislocation slip. In Fig. 11.5b, area III, an intense interaction between dislocations and SFs near the grain boundary is obvious. The generation and slip of perfect dislocations, their dissociation, the formation of stacking faults and their widening are the microstructure phenomena that dominate the behavior of the metastable austenitic steels upon plastic deformation [18].

If three dislocations with different Burgers vectors meet on the same slip plane, then they form dislocation nodes [19], as shown in Fig. 11.5c. In the center of such a node, a small stacking fault is produced. This dislocation node behaves like a Lomer-Cottrell lock and persists, therefore, in a stable configuration, which can affect the slip or the formation of following dislocations and SFs [18, 19].

In contrast, the overlap of multiple SFs located on the same slip plane initiates the formation of deformation bands that are depicted in Fig. 11.5d. In this micrograph, the overlap of the parallel stacking faults and the presence of the bordering partial dislocations cause a change in the fringe contrast. The stacking faults accumulated within a deformation band are highly correlated. The deformation bands form first on a primary slip system that possesses the maximum Schmid factor and that experiences the highest shear stress. With increasing applied stress, the deformation bands widen, until they extend over the entire grain size. Concurrently, the increasing applied stress triggers the formation of deformation bands on secondary slip systems. In low-SFE austenitic steels, the formation of deformation bands is the most important deformation mechanism [20].

11.2.3 Arrangement of the Stacking Faults in Austenite: Formation of ε-Martensite and Twinned Austenite

11.2.3.1 Crystallographic and Thermodynamic Aspects of the Stacking Fault Arrangement in *Fcc* Materials

In *fcc* materials, the stacking faults form on the {111} lattice planes via dissociation of perfect dislocations and repulsion of the Shockley partials. As explained in Sect. 11.2.1, the separation distance of partial dislocations and the width of the stacking faults are controlled by the stacking fault energy and by the magnitude of the local shear stress on the glide plane. These two parameters influence, furthermore, the number and/or the density and the arrangement of the stacking faults. At low SF densities, the stacking faults are typically randomly distributed. At (locally) high SF densities, the distances between next stacking faults become much smaller. Consequently, the stacking faults start to arrange.

Two stacking fault configurations deserve a special attention—the arrangement of the stacking faults on ***every second*** {111} plane and the arrangement of the stacking

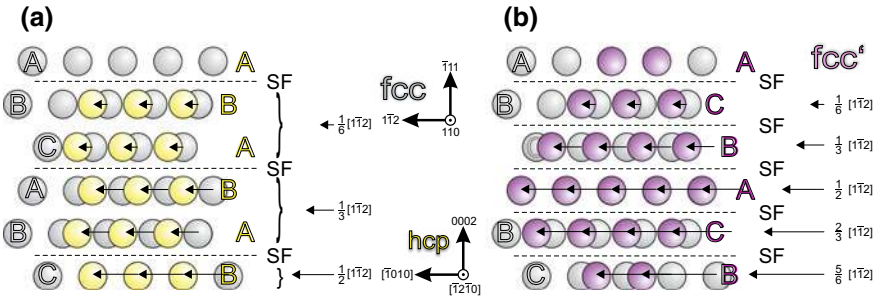

Fig. 11.6 Schemes of special local arrangements of stacking faults (SF) in austenite. **a** The stacking faults are located on every second {111} lattice plane, which leads to the *hcp* stacking. **b** The stacking faults are located on every {111} lattice plane, which leads to the formation of twins (fcc') according to [4]

faults on ***every*** {111} plane. The arrangement of stacking faults in an *fcc* structure on every second {111} glide plane (Fig. 11.6a) introduces regular *hcp ABABAB* stacking sequence, which is called ε-martensite for the originally austenitic steels. The arrangement of stacking faults on every {111} lattice plane (Fig. 11.6b) reverses the original stacking order *ABCABC* to *CBACBA*, which is denoted as twinning.

From the thermodynamic point of view, the tendency of the stacking faults in austenite to arrange on each second lattice plane {111} is quantified by the Gibbs free energy of the phase transformation of *fcc* γ-austenite to *hcp* ε-martensite ($\Delta G^{\gamma\to\varepsilon}$) [21, 22]. The relationship between $\Delta G^{\gamma\to\varepsilon}$ and the stacking fault energy (γ_{SF}) was described by Olson [21] and Ferreira [23] as

$$\gamma_{\mathrm{SF}} = n\rho_A\left(\Delta G^{\gamma\to\varepsilon} + E^{\mathrm{str}}\right) + 2\sigma(n) + \sigma_p \tag{11.7}$$

In (11.7), n is the number of the lattice planes {111} that form ε-martensite, ρ_A the molar area density within the close packed lattice planes (mol per area), E^{str} the strain energy resulting from the faulting and $2\sigma(n)$ the interface energy between the faulted structure and the undistorted austenitic matrix (along the $\{111\}_{fcc}$ planes), and σ_p the strain energy of the partial dislocations. The meaning of this formula was discussed in detail by Geissler et al. [22] and De Cooman et al. [12]. The strain energy term (E^{str}) originates from the formation of ε-martensite that is embedded in the austenite matrix. E^{str} is widely accepted to be negligible, because the relative change in the molar volume during the $\gamma \to \varepsilon$ transformation is very small (1.2% in the present case). The dependence of $\sigma(n)$ on n is hardly assessable by experiment, but it can be estimated from the results of ab initio calculations [24]. The contribution of the strain fields of partials (σ_p) can be neglected, in particular if the stacking faults are wide [21].

For isolated stacking faults affecting just two neighboring lattice planes ($n = 2$), (11.7) can be rewritten into the following form that is used for estimation of the SFE from the Gibbs energy of the $\gamma \to \varepsilon$ phase transformation

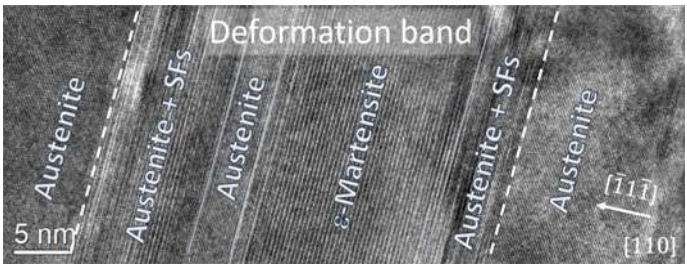

Fig. 11.7 HRTEM image of a 5% strained tensile sample of an X2CrMnNi16-7-6 steel showing various clusters of stacking faults within a deformation band

$$\gamma_{\mathrm{SF}}\left[\mathrm{mJ/m^2}\right] = 2(\rho_A \Delta G^{\gamma\to\varepsilon} + \sigma) \tag{11.8}$$

Both parameters $\Delta G^{\gamma\to\varepsilon}$ and σ are strongly dependent on the chemical composition of the steel and on temperature. Still, according to Geissler [22] the term $\rho_A \Delta G^{\gamma\to\varepsilon}$ is approximately one order of magnitude larger than the contribution of the interface energy, $\rho_A \Delta G^{\gamma\to\varepsilon} \cong 5-50\ \mathrm{mJ/m^2}$ versus $\sigma \cong 0.1-27\ \mathrm{mJ/m^2}$, despite the huge span of values available in literature for austenitic steels [22, 25, 26]. It is worth noting that the highest interface energies reported in literature for austenitic steels are not necessarily physically reasonable, because the interfaces between ε-martensite and austenite are almost perfectly heteroepitaxial. Thus, the term $\rho_A \Delta G^{\gamma\to\varepsilon}$ is the most important parameter influencing the stacking fault energy.

It is known from experiments that the distribution of SFs is not homogeneous, as the SFs are typically arranged in deformation bands in plastically deformed samples (Fig. 11.7). This local clustering of SFs has manifold reasons, but most of them are related to a localized nucleation of SFs at stress concentrations, which occurs through the dislocation interactions, local chemical inhomogeneities, or at crystallite boundaries [12].

The stress relaxation through the formation of SFs in austenite is connected with a lattice shear deformation (γ), which is proportional to the magnitude of the Burgers vector of the partial dislocations, $\left|\vec{b}_p\right| = a\left|\left[1\bar{1}2\right]\right|/6$, and which scales with the distance between the next SFs as $\gamma = \left|\vec{b}_p\right|/(n_d d_{111})$. a is the lattice parameter of austenite, $d_{111} = a/\sqrt{3}$ the distance of the close packed lattice planes (neglecting a change of d_{111} near the partials) and n_d the SF distance expressed in the units of d_{111}. The largest shear deformations are achieved in ε-martensite and in twinned austenite. For ε-martensite, where the SFs appear after each second lattice plane {111}, the lattice shear deformation is about $\gamma_{hcp} = \frac{a}{6}\left|\left[1\bar{1}2\right]\right|/(2d_{111}) = \sqrt{2}/4$. For twins, the lattice shear is twice as large, $\gamma_{\mathrm{twin}} = \frac{a}{6}\left|\left[1\bar{1}2\right]\right|/d_{111} = \sqrt{2}/2$, because the SFs are present on each close packed lattice plane. Consequently, the formation of domains, which contain either hexagonally ordered close packed planes of austenite (basal planes of ε-martensite) or twinned austenite, is the most effective way to reduce the local stress concentrations. These domains, which are typically located within

the deformation bands, are fully crystallographically coherent with the austenitic matrix along the respective $\langle 111 \rangle_{fcc}$ or $\langle 0001 \rangle_{hcp}$ direction but incoherent in the perpendicular directions, where the SFs are confined by partial dislocations.

The occurrence of the local stress concentrations in austenitic steels is expected to rise with increasing SFE. According to the stacking fault model from Sect. 11.2.1, the shear stress needed to separate the partials in SFs increases with increasing SFE [10]. Assuming that the amplitude of the local stress concentrations increases if the overall stress level increases, more intense stress concentrations and strongly clustered SFs will appear in austenite with a higher SFE. Very low SFE, in contrast, will facilitate the widening of SFs already at a low overall stress level. This mechanism will prevent strong stress concentrations and local arrangement of the SFs.

11.2.3.2 Detection of the Stacking Faults and Their Arrangements by Diffraction Methods

The impact of stacking faults (SFs) on the diffraction patterns of *fcc* metals was described by Wilson [27], Paterson [28], Warren and Warekois [29] and Warren [30]. This description comprises an anisotropic (i.e., *hkl*-dependent) shift of the diffraction lines, their anisotropic broadening and asymmetry. In the approaches above, the faulting of an *fcc* structure is described as a change in the regular sequence of the lattice planes {111} along the respective normal direction ⟨111⟩. The translation vectors of the regular and faulted *fcc* stacking, $\vec{t} = \left(\frac{1}{3}a_h, \frac{2}{3}a_h, \frac{1}{3}c_h\right)$ and $\vec{t_|} = \left(\frac{2}{3}a_h, \frac{1}{3}a_h, \frac{1}{3}c_h\right)$, respectively, are typically defined in the hexagonal coordinate system obeying the orientation relationship $\left[11\bar{2}0\right]_{hcp} \parallel \left[1\bar{1}0\right]_{fcc}$ and $(0001)_{hcp} \parallel (111)_{fcc}$ with respect to the cubic system (Fig. 11.8). The hexagonal lattice parameters a_{hcp} and c_{hcp} are related to the cubic one (a_{fcc}) as

$$a_{hcp} = a_{fcc}/\sqrt{2} \text{ and } c_{hcp} = 2a_{fcc}/\sqrt{3} \tag{11.9}$$

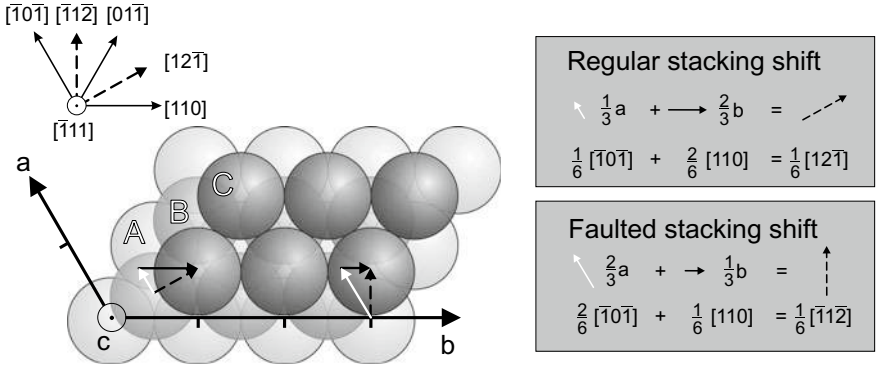

Fig. 11.8 Description of the in-plane shift in the *fcc* lattice in a hexagonal coordinate system as stacking sequence of {111} austenite lattice planes. Adopted from [31]

Martin et al. [31] simulated the effect of the layer stacking on the powder X-ray diffraction (PXRD) patterns using the DIFFaX routine [32] for different stacking fault configurations. The relevant stacking faults configurations are summarized in Table 11.1, the corresponding diffraction patterns are plotted in Fig. 11.9.

As long as the regular *fcc* stacking is maintained ($P_{\text{regular}} = 1$), only the diffraction lines corresponding to the *fcc* structure appear (black curve in Fig. 11.9a). The

Table 11.1 Overview of the SF sequences that were used for the DIFFaX simulation (Fig. 11.9) of the PXRD patterns

Sequence of the lattice planes	Probability	Microstructural interpretation
…ABC…	P_{regular}	Relative amount of undistorted *fcc* phase
…CAB$_{\perp}$ABC…	P_{intr}	Relative amount of isolated intrinsic (single) SFs
…CAB$_{\perp}$A$_{\perp}$CAB…	P_{extr}	Relative amount of isolated extrinsic (double) SFs
…CAB$_{\perp}$AB$_{\perp}$ABC…	P_{hcp}	Relative amount of narrowly spaced SFs appearing repetitively after two lattice planes $\{111\}_{fcc}$
…CAB$_{\perp}$A$_{\perp}$C$_{\perp}$B$_{\perp}$…	P_{twin}	Relative amount of twins (SFs appearing repetitively after each lattice plane $\{111\}_{fcc}$)
…CAB$_{\perp}$A$_{\perp}$C$_{\perp}$B$_{\perp}$…	P_{tl}	Extent of the twins (tl—twin length)

The sequence of lattice planes is related to the *fcc* lattice planes {111}. The appearance of a SF is depicted by the symbol ⊥. The DIFFaX probability is denoted by the respective symbol *P*

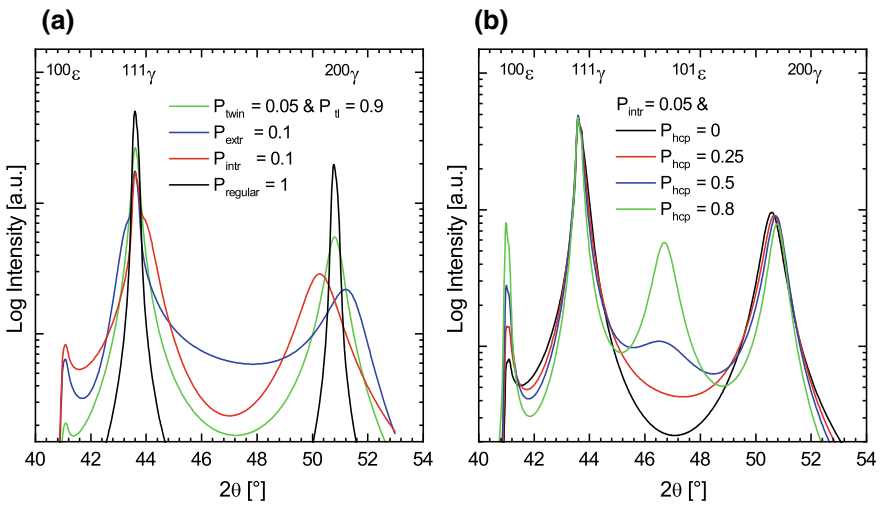

Fig. 11.9 Influence of the stacking fault arrangements on the diffraction pattern: **a** Effect of the isolated SFs and specific SF arrangements on the diffraction pattern, **b** influence of increasing probability (P_{hcp}) for SF arrangements on every second {111} glide plane forming hexagonal intensities

presence of isolated intrinsic and extrinsic SFs leads to the line shift and to the line broadening (Fig. 11.9a). Extrinsic SFs and twins make the diffraction profiles strongly asymmetric. According to the Warren theory [30], the line shift caused by the isolated intrinsic stacking faults depends on the diffraction indices (*hkl*) like

$$\Delta 2\theta(^\circ) = 2 \cdot \frac{180^\circ}{\pi} \cdot \frac{\sqrt{3}\alpha}{4\pi} \cdot \frac{\sum_{(\text{affected})} \pm(h+k+l)}{\left(h^2+k^2+l^2\right)m_{hkl}}, \tag{11.10}$$

where α is the probability of the occurrence of the isolated intrinsic SFs and m_{hkl} the multiplicity of the lattice planes $\{hkl\}$. Concurrently, the occurrence of isolated (intrinsic and extrinsic) SFs breaks the coherence of the parts of the crystal structure, which are mutually separated by the stacking faults. This loss of the coherence leads to a line broadening, which can be written in the reciprocal space units as

$$\Delta d^*_{hkl} = \frac{1}{D} + \frac{1.5\alpha+\beta}{a} \sum_{(\text{affected})} \frac{|h+k+l|}{m_{hkl}\sqrt{h^2+k^2+l^2}} \tag{11.11}$$

In (11.11), D is the average crystallite size, β the density of extrinsic SFs and a the cubic lattice parameter. The meaning of other symbols is the same like in (11.10). In both equations, the summations are performed over the indices of the diffraction lines, which are affected by the stacking faults, i.e., for $(h+k+l) \bmod 3 \neq 0$. In (11.10), the positive sign applies for $(h+k+l) \bmod 3 = 1$, the negative one for $(h+k+l) \bmod 3 = 2$.

In contrast to the isolated SFs and twins, SFs appearing repetitively after two lattice planes cause a marginal shift and broadening of the diffraction lines (Fig. 11.9b), but they imitate a hexagonal crystal structure, which is known as ε-martensite in the transformed austenite. Thus, these correlated SFs are not recognized by the diffraction methods as SFs in austenite but as a new phase. The DIFFaX model was tested on the diffraction pattern of a fine-grained sample of an X2CrMnNi16-6-6 TRIP steel that was compressed to 15%. The best agreement between the measured and simulated diffraction patterns was achieved with the probabilities $P_{\text{intr}} = 0.018$, $P_{hcp} = 0.9$, $P_{\text{twin}} = 0.04$ and $P_{\text{tl}} = 0.96$. The successful modelling of the measured XRD pattern using the SF model shows that faulted austenite and ε-martensite present in the microstructure of plastically deformed TRIP steels can be described using specific SF configurations.

Alternatively, the microstructure of deformed steel samples can be described in terms of microstructure components (austenite, ε-martensite and α'-martensite) and microstructure features (dislocation densities and SF probabilities in relevant phases) that are available in most microstructure models used for the whole pattern refinement, i.e., for the Rietveld-like refinement of the XRD patterns. The individual phases (*fcc* austenite, *hcp* ε-martensite and *bcc* α'-martensite) are described using their intrinsic (non-disturbed) crystal structures. The effect of SFs in austenite on the line positions is quantified using (11.10), the effect of SFs in austenite on the line broadening using (11.11) and the effect of SFs in ε-martensite on the line broadening using

(11.14), see Sect. 11.4. The effect of perfect dislocations on the line broadening is described for all phases using (11.15).

The Rietveld refinement of the diffraction pattern of the fine-grained sample X2CrMnNi16-6-6 compressed to 15%, cf. previous simulation using the DIFFaX model, revealed an intrinsic stacking fault probability in ε-martensite of about 10%, which agrees well with the value of $1 - P_{hcp}$ obtained from the DIFFaX model. The volume faction of ε-martensite correlates directly with P_{hcp}. In the austenite, the intrinsic and extrinsic SF probabilities calculated using the DIFFaX model and the Warren model can be compared directly as well. The parameter P_{twin} can hardly be compared with the microstructure parameters obtained from the Warren model, because the twinning does not cause any shift of the diffraction lines but only a line broadening, see (11.11). However, as it can be seen from (11.11), the densities of intrinsic (isolated) SFs (α) and extrinsic SFs (β) terminating the twins cannot be determined simultaneously solely from the line broadening, but only in conjunction with the analysis of the line shift, or from the line asymmetry [30]. However, as the density of the twin boundaries in the steels under study is much lower than the density of intrinsic SFs, it cannot be determined reliably using the combined analysis of the line shift and line broadening. The analysis of the line asymmetry fails as well, as the asymmetry of the diffraction lines is not very pronounced [33].

Another result of the Rietveld refinement was that the distance between the adjacent $\{111\}_{fcc}$ lattice planes within the faulted stacking sequences was smaller than the interplanar spacing within the regular stacking sequences. Consequently, the ε-martensite had the c/a ratio of 1.62, which is slightly below the value of $c/a = 2\sqrt{2/3} = 1.633$ that corresponds to a pseudo-cubic *hcp* crystal structure with $a = a^{fcc}/\sqrt{2}$ and $c = 2d_{111}^{fcc} = 2a^{fcc}/\sqrt{3}$.

11.2.3.3 Coexistence of Different Stacking Fault Arrangements: Continuous Transition Between ε-Martensite and Twinning

The coexistence of different stacking fault arrangements in highly alloyed metastable austenitic steels with a SFE of approx. 20 mJ/m^2 was confirmed by X-ray diffraction (see previous Section) that found isolated stacking faults together with hexagonal faulted sequences and twins in the samples under study. The local nature of the stacking fault clusters was revealed by electron backscatter diffraction in a scanning electron microscope (EBSD/SEM) and by transmission electron microscopy with high resolution (HRTEM). On a mesoscopic scale, EBSD disclosed that the crystal structure defects are concentrated in the deformation bands, which contain typically ε-martensite slabs and deformation twins (Fig. 11.10). The character of the deformation bands (predominantly ε-martensite or mainly deformation twins) depends generally on the SFE and deformation state. The occurrence of these deformation bands varies with the crystallographic orientation of the originally austenitic grains with respect to the deformation direction.

On the atomic scale, the coexistence of the different stacking fault arrangements was proven by HRTEM that was complemented by the fast Fourier transform (FFT) of

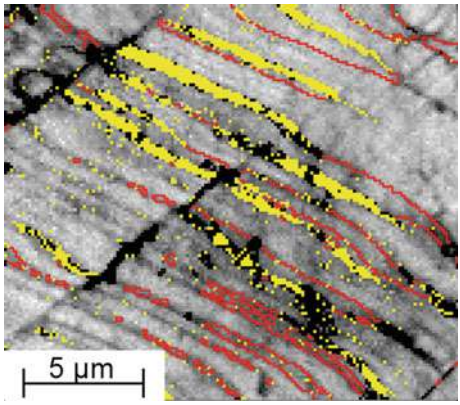

Fig. 11.10 EBSD mapping of deformation bands in compressed X5CrMnNi16-6-9 steel, austenite in grey, ε-martensite in yellow, twin boundaries in red, unindexed pixels in black. Adopted from [34]

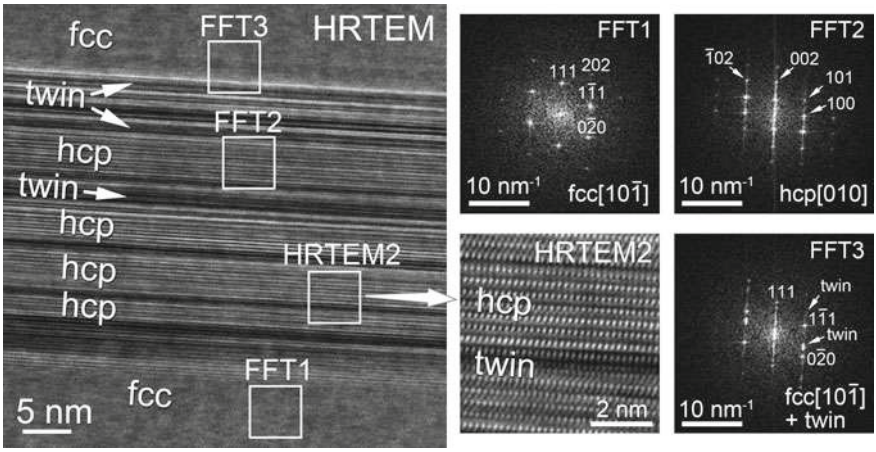

Fig. 11.11 HRTEM image of a deformation band, where atomic arrangements of both twins and ε-martensite are found coexisting in close vicinity

the HRTEM micrographs. Figure 11.11 illustrates the different stacking sequences of the former $\{111\}_{fcc}$ lattice planes, which can be described as an irregular ordering of stacking faults. Extended sequences $AB_{\perp}AB_{\perp}AB_{\perp}AB$ of the lattice planes $\{111\}_{fcc}$ are interpreted as *hcp* ε-martensite, extended sequences $ABCAB_{\perp}A_{\perp}C_{\perp}B_{\perp}\ A_{\perp}C_{\perp}$ as twins. The irregular sequences of SFs produce streaks in the reciprocal lattice of austenite along the faulted $\langle 111\rangle_{fcc}$ direction, which include the reciprocal lattice points of ε-martensite (see FFT2 in Figs. 11.11 and 11.12b). The streaks stem from superimposed truncation rods produced by thin slabs of faulted austenite [28, 35, 36]. The presence of extended slabs of ε-martensite or extended twins leads to the

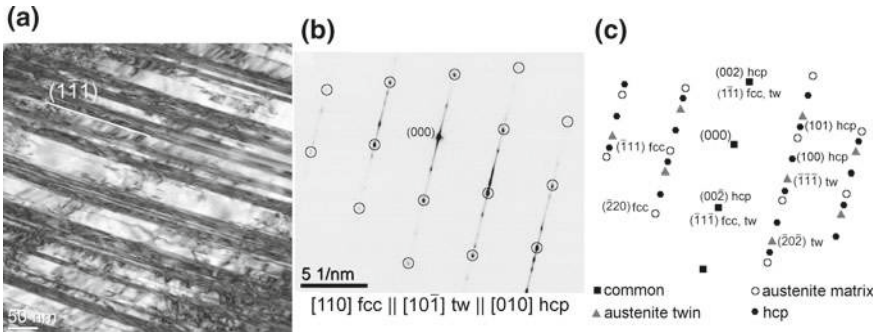

Fig. 11.12 TEM characterization of deformation bands in PM X5CrMnNi16-6-9 steel. **a** Bright-field image of parallel deformation bands, **b** corresponding SAED, recorded with a 200 nm aperture, **c** indexing of spots assigned to austenite matrix, twin and ε-martensite. Adopted from [34]

fragmentation of the streaks and to the formation of separated diffraction spots that correspond to ε-martensite or to twins in austenite (see FFT2 and FFT3 in Fig. 11.11). These microstructure features are interpreted in a very similar way by all diffraction methods, i.e., EBSD (Fig. 11.10), selected area electron diffraction (SAED) in TEM (Fig. 11.12) and XRD (Fig. 11.9).

The crystallographic explanation of these diffraction phenomena is based on the stacking fault models from Figs. 11.6 and 11.7, and on the orientation relationships between austenite, ε-martensite and twinned austenite that can be described as $(0001)_{hcp} \parallel \left(1\bar{1}1\right)_{fcc} \parallel \left(1\bar{1}1\right)_{\text{twin}}$ and $\left[01\bar{1}0\right]_{hcp} \parallel [110]_{fcc} \parallel \left[10\bar{1}\right]_{\text{twin}}$, cf. Fig. 11.12b, c. The deformation bands visible in the TEM micrograph (Fig. 11.12a) contain remainders of the austenite matrix, uncorrelated SFs and areas, which are interpreted as ε-martensite or as twins in austenite. In the SAED pattern (Fig. 11.12b), the remainders of the austenite matrix, the ε-martensite areas and the twinned austenite produce intense diffraction spots, the uncorrelated SFs streaks along the $\left(1\bar{1}1\right)_{fcc}$ reciprocal space direction.

From the thermodynamic point of view, the simultaneous occurrence of twinned austenite and ε-martensite can be discussed in terms of SFE and interface energy [22]. In the case of a low thermodynamic driving force ($\Delta G^{\gamma\to\varepsilon} \cong 0$, cf. Sect. 11.2.3.1), all arrangements of stacking faults corresponding to isolated intrinsic and extrinsic SFs, ε-martensite and twins result in the same overall energy. Therefore, the transition between the transformation-induced plasticity (TRIP) and the twinning-induced plasticity (TWIP) is continuous. Assuming that there are no other obstacles for the phase transition, the TRIP effect and the generation of a local hexagonal stacking sequence are preferred for $\Delta G^{\gamma\to\varepsilon} < 0$, while for $\Delta G^{\gamma\to\varepsilon} > 0$, the twinning dominates.

An important consequence of this microstructure model is an improved atomistic description of the ε-martensite formation. Although SFs were always regarded as nucleation precursor [21] of the ε-martensite formation, the ε-martensite has been treated as a metastable martensitic phase occurring along the $\gamma \to \varepsilon \to \alpha'$ transformation path [37, 38] and as a product of bulk martensitic transformation of austenite

[39]. The current understanding of ε-martensite, which evolves during plastic deformation of austenite, is that it is rather a heavily faulted austenite than a distinct phase.

Using electron microscopy, the ε-martensite was found to appear within deformation bands [31, 40], where a high density of stacking faults is present. Consequently, the deformations bands and hence the ε-martensite form during the plastic deformation of austenite, when a low SFE facilitates the SF formation as a competing mechanism to the dislocation mobility. On the other hand, the deformation bands and the ε-martensite act as repositories of dissociated dislocations, which are bound to their slip planes. Hence, the dynamic recovery is inhibited, as the annihilation would be possible only for perfect dislocations, which are not stable, as their dissociation is facilitated by the low SFE.

11.2.3.4 Thermal Stability of the Deformation-Induced ε-Martensite

The defective character of ε-martensite was confirmed by the thermal behavior of the X2CrMnNi16-7-6 TRIP steel, which was deformed to 25% true compressive deformation at room temperature. In this deformation state, the originally austenitic steel contained 51 vol% *fcc* austenite, 30 vol% *bcc* α'-martensite and 19 vol% *hcp* ε-martensite. The in situ high-temperature XRD measurement carried out upon heating revealed that the ε-martensite disappears between 250 and 350 °C, while the α'-martensite vanishes at approximately 600 °C (Fig. 11.13a). The transformation of α'-martensite to γ-austenite was confirmed by differential scanning calorimetry (DSC), which showed a distinct maximum of the heat flux between 500 and 600 °C (Fig. 11.13b), that is in agreement with the existence range of the *bcc* phase from Fig. 11.13c. The σ-phase from the phase diagram was not observed, because its formation was kinetically inhibited through the rapid quenching.

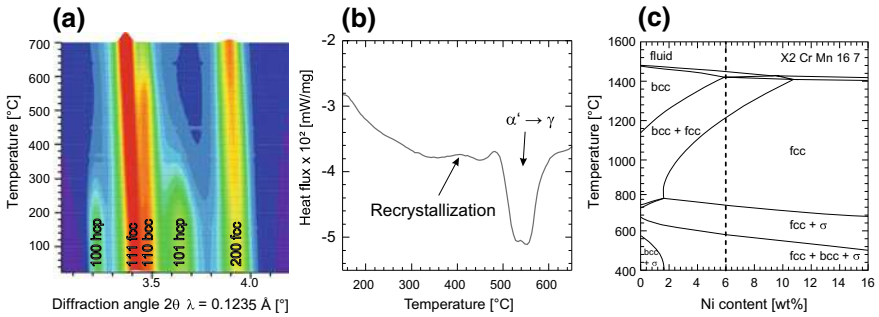

Fig. 11.13 Thermal behavior of an X2CrMnNi16-7-6 TRIP steel deformed to 25%. **a** X-ray synchrotron diffraction patterns recorded during continuous heating. The intensities are plotted in logarithmic scale. **b** The DSC heat flux signal during continuous heating at 10 K/min. **c** Isopleth section of the X2CrMnNi16-7-x steel for Ni concentrations between 0 and 15%

The ε-martensite is no thermodynamically stable phase, thus its existence cannot be proven by the phase diagram. Also in the DSC measurement, no pronounced signal related to the back transformation of ε-martensite was detected. The small differences in the heat flux measured between 250 and 350 °C are comparable with the DSC signal that originates from recrystallization, i.e., from the annihilation of the crystal structure defects in austenite [41, 42]. The absence of a pronounced DSC signal stemming from the dissolution of ε-martensite confirms that the reverse transformation of ε-martensite to austenite happens via 'unfaulting' [43], for which no pronounced diffusion activity of the lattice atoms is needed.

The recovery of austenite and the disappearance of SFs upon heating are supported by the increase of the SFE with increasing temperature ($\delta SFE/\delta T$), which is between 0.05 and 0.1 mJ/(m^2K) [7, 44]. Thus, the energy stored in the existing stacking faults increases with increasing temperature. The increase of SFE produces a significant constriction force that acts on partial dislocations and reduces the width of the stacking faults. Large stacking faults collapse and the SFs arrangement in deformation bands disappears in favor of the recovery of original austenite.

11.2.3.5 Phase Transformations in Austenitic Steels Under High Pressure

Pure iron is known to undergo a *bcc* → *hcp* transformation during hydrostatic compression between 8 and 13 GPa and room temperature [45–48]. This transition was explained theoretically by a change of the magnetic state of iron from a ferromagnetic one to a non-magnetic or antiferromagnetic one, when hydrostatic pressure is applied [49–51]. In order to find out possible analogies between the formation of ε-martensite in austenitic steels and the *hcp* high-pressure phase in ferrite under hydrostatic pressure, in situ high-pressure synchrotron diffraction experiments up to 18 GPa were carried out on a *fcc* TRIP steel using a multi-anvil apparatus [52].

For this purpose, small cylinders of the austenitic X2 CrMnNi16-7-6 TRIP steel were encapsulated in an MgO container together with indium that served as a pressure standard, and compressed by WC anvils. The XRD patterns were collected in the energy-dispersive mode at the diffraction angle $2\theta = 3.1557°$ (calibrated by a LaB_6 standard). An excerpt of the analyzed raw data is displayed in Fig. 11.14a. The effective applied pressure was calculated from the change of the specific volume of the reference material.

In contrast to ferrite (pure iron), where the phase transition occurs between 8 and 13 GPa, the *hcp* phase in the TRIP steel appeared already at approx. 0.5 GPa [52]. Its amount was about 20 vol%. This earlier phase transformation may be facilitated by shear stress components, which result from the strong crystallographic anisotropy of the elastic constants of austenite and from the polycrystalline nature of the investigated sample. The local shear stress components and the stress concentrations at the grain boundaries are released by local plastic deformation involving dislocation slip and formation of stacking faults and deformation bands, which support the martensitic transformation of *fcc* austenite to *hcp* ε-martensite. For these reasons, the

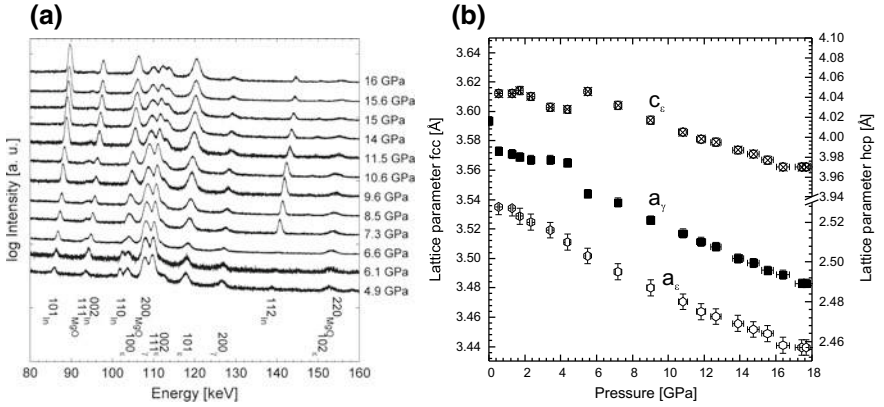

Fig. 11.14 Evolution of the ε-martensite formation at increasing hydrostatic compression. **a** Raw data of the compression experiments show a clear increase of the *hcp* phase fraction with increasing hydrostatic pressure. **b** Evolution of the lattice parameters. Adopted from [52]

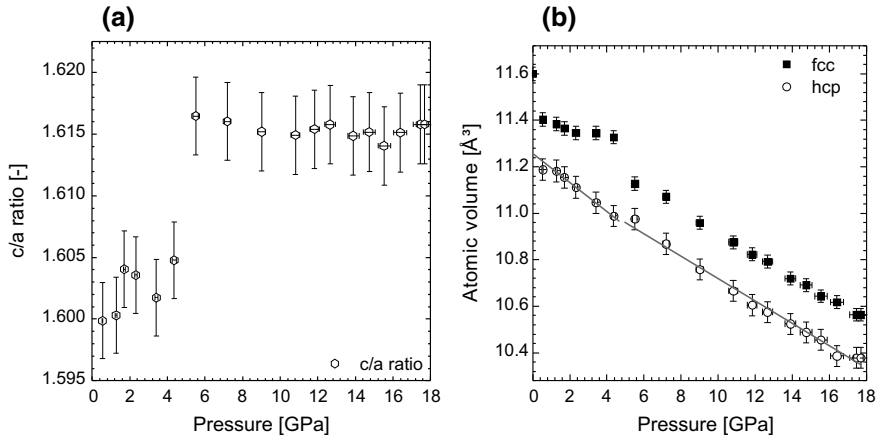

Fig. 11.15 Structural changes in *fcc* austenite and *hcp* ε-martensite during hydrostatic compression. **a** Evolution of the *c*/*a* ratio in *hcp* ε-martensite during compression. **b** Change of the atomic volume (volume per Fe atom in the unit cell) in both phases. According to [52]

hcp phase found in austenite subjected to high hydrostatic pressures above 5 GPa is inherently of the same nature as the deformation-induced ε-martensite, which is produced by uniaxial loading. Still, up to the hydrostatic pressure of 5 GPa the *c*/*a* ratio calculated from the lattice parameters of the *hcp* phase (Fig. 11.14b) was between 1.600 and 1.605 (Fig. 11.15a) [52], which agrees well with the $c/a = 1.602 - 1.603$ reported for the high-pressure phase of iron by Mao et al. [46], Takahashi et al. [47] and Giles et al. [48].

Above the hydrostatic pressure of ~6 GPa, more than 50 vol% of the sample transformed to ε-martensite. This phase transformation was accompanied by an apparently higher compressibility of the austenite and by an abrupt increase of the *c*/*a* ratio from ~1.605 to 1.617, which was caused mainly by the expansion of the hexagonal lattice parameter *c* (Fig. 11.14b). A generally smaller specific volume of the *hcp* phase hexagonal structure in comparison with the *fcc* phase together with the higher compressibility of austenite and a faster reduction of its volume at the pressures above 6 GPa (Fig. 11.15b) can be, according to Le Chatelier's principle [53, 54], a significant driving force for the phase transformation. The value of $c/a = 1.617$ approaches the *c*/*a* ratio in ε-martensite produced by plastic deformation. The change of the *c*/*a* ratio from 1.605 to 1.617 is possibly related to the change in the ordering of magnetic moments. As the change of the *c*/*a* ratio is accompanied by a slight expansion of the elementary cell of the *hcp* ε-martensite at ~6 GPa, a transition from the paramagnetic to the antiferromagnetic state is expected.

11.3 Formation of α'-Martensite

The formation of *bcc* α'-martensite is a characteristic feature of metastable austenitic steels with a low SFE that has a prominent effect on their mechanical properties. The α'-martensite formation is triggered by cooling the metastable austenite below a critical temperature and enhanced by mechanical load [55]. The driving force of the $\gamma \rightarrow \alpha'$ transformation is proportional to the difference in the Gibbs energies of the *fcc* and the *bcc* phase, $\Delta G^{\gamma \rightarrow \alpha'}$, which, in turn, depends on temperature and on the chemical composition of the steel [56]. In metastable austenite, $\Delta G^{\gamma \rightarrow \alpha'}$ is negative below the thermodynamic equilibrium temperature T_0, which is about 600 °C (see Fig. 11.13c) for the austenitic TRIP steel X3CrMnNi16-7-6.

However, as the transformation temperature, which is observed experimentally, e.g., by dilatometry, is affected by several factors, the martensite start temperature (M_S) is introduced that describes the real onset of the phase transformation in terms of a characteristic amount of undercooling. The difference between T_0 and M_S is caused by the obstruction of the $\gamma \rightarrow \alpha'$ transformation—mainly through the formation of the γ/α' interfaces and through the lattice strain resulting from the approx. 2% volume expansion during the $\gamma \rightarrow \alpha'$ transformation. The formation energy of the γ/α' interface and the lattice strain produced by the phase transformation must be compensated by a sufficiently negative value of $\Delta G^{\gamma \rightarrow \alpha'}$. The plastic deformation of austenite caused by external force may aid the martensitic transformation by imposing shear stress that acts as mechanical driving force [55] and by providing favorable nucleation sites for α'-martensite. Thus, a threshold temperature (M_D), below which the deformation-induced martensitic transformation occurs, is located between M_S and T_0.

In high alloy metastable austenitic steels, which possess a low SFE (< 20 mJ/m^2 [12]) and which show the TRIP effect [57], the transformation path follows mostly the $\gamma \rightarrow \varepsilon \rightarrow \alpha'$ sequence [21, 58, 59]. This sequence implies that α'-martensite is

formed predominantly by shearing the previously formed ε-martensite. This particular conclusion is confirmed by the SEM/EBSD micrographs of plastically deformed TRIP steels, which show that α'-martensite arises mainly at the intersections of deformation bands containing ε-martensite (see left-hand side of Fig. 11.16). The stages of the phase transformation are schematically depicted in the middle column and on the left-hand side of Fig. 11.16. The phase transformation starts with a simple arrangement of stacking faults on parallel {111} lattice planes and the formation of deformation bands (panel (1) in Fig. 11.16). When at a higher strain such deformation bands form on crystallographically equivalent {111} planes and intersect, then the intersections provide, according to the Olson-Cohen model [21, 60], favorable nucleation conditions for α'-martensite (panel (2) in Fig. 11.16). The phase transformation within a deformation band can even be triggered by a single stacking fault appearing on a secondary slip plane that crosses the deformation band (Fig. 11.16 panel (2)) [61–63].

According to the Bogers-Burgers mechanism [64], the *fcc* → *bcc* transformation can be realized by two shears on different slip planes, which are equal to $a/18[211]$ on

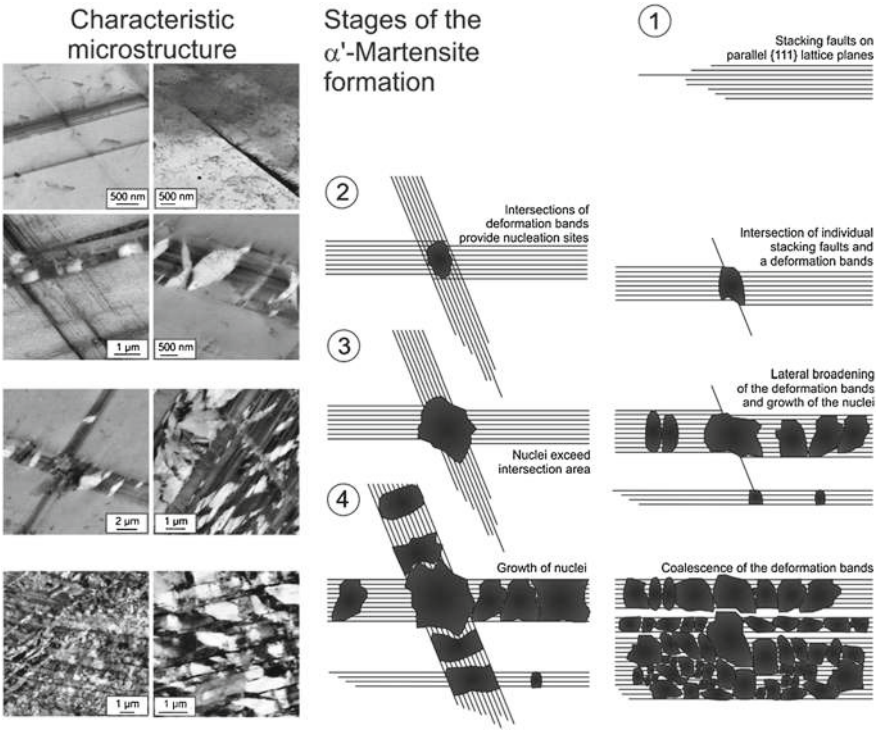

Fig. 11.16 Stages of the deformation-induced α'-martensite transformation in an X2 CrMnNi16-7-6 steel as seen by ECCI (left-hand side), and depicted schematically for nucleation at deformation band intersections (centre) and inside deformation bands (right), respectively

the $(\bar{1}11)$ plane and to $a/12[21\bar{1}]$ on the $(1\bar{1}1)$ plane [60]. The first shear corresponds to one third of the twinning shear; the second shear is equivalent to the shear of partial dislocations passing on every second {111} plane, or within the ε-martensite slab [65]. The resulting local atomic arrangement resembles the *bcc* structure of α'-martensite, and can be described by a hypothetic intersection of a perfect and a faulted ε-martensite bands. The formation of ε-martensite comprises already a shearing (leading to the development of the *hcp* stacking sequences), which reduces significantly the energetic barrier for the α'-martensite nucleation.

Upon further straining, the α'-martensite nuclei grow and eventually outrun the original deformation band at the intersection points (panel (3) in Fig. 11.16). Finally, the α'-martensite nuclei grow together, thus the former deformation bands containing the ε-martensite slabs gradually transform into α'-martensite (panel (4) in Fig. 11.16). Due to the thickening of the α'-martensite regions, the distances between individual deformation bands become smaller and the originally separated α'-martensite regions merge partially, so that entire grains of original austenite transform to α'-martensite.

The mechanism of the α'-martensite formation was confirmed by TEM and FFT/HRTEM (Fig. 11.17). Inside of a deformation band (labelled as (2)), which intersects with few individual SFs but not with a pronounced deformation band, several α'-martensite nuclei (labelled as (3)) were identified. This case was discussed in Fig. 11.16, panel (2), above. In addition to the local phase identification, the FFT/HRTEM patterns from the adjacent regions A, B and C in Fig. 11.17, were used for the analysis of the orientation relationships (ORs) between original austenite (phase 1), faulted ε-martensite (phase 2) and α'-martensite (phase 3). The faulting of austenite and ε-martensite produces diffraction contrasts in the TEM micrograph and perpendicular streaks in the FFT pattern. From the coincidence of the distinct reciprocal lattice points in the FFT/HRTEM patterns, the following parallelisms of

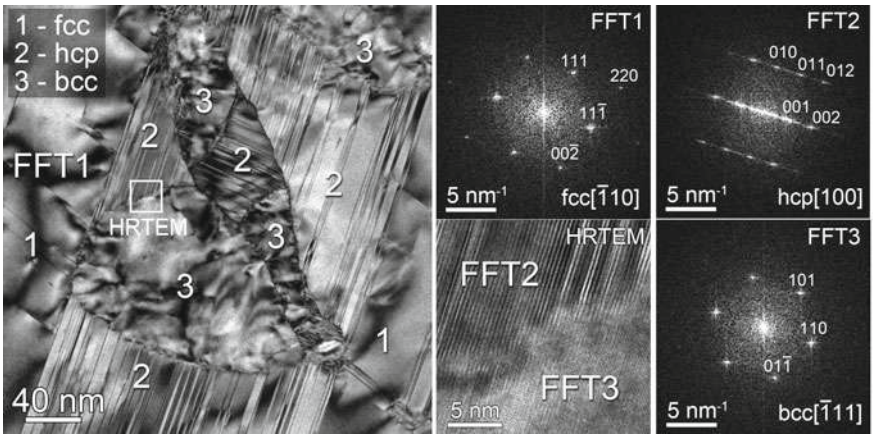

Fig. 11.17 TEM micrograph of the martensitic transformation in a deformation band, FFTs of high-resolution TEM images revealing the local crystal structure and orientation in the marked areas. The crystal structure identified in different regions is indicated by numbers

the close-packed planes and directions were concluded:

$$\{11\bar{1}\}_{fcc} \| \{001\}_{hcp} \| \{110\}_{bcc} \tag{11.12}$$

$$\langle \bar{1}10 \rangle_{fcc} \| \langle 100 \rangle_{hcp} \| \langle \bar{1}11 \rangle_{bcc} \tag{11.13}$$

In literature, these relations are known as Kurdjumow-Sachs OR [66] (for the *fcc*/*bcc* interface) and as Shoji-Nishiyama OR (for the *fcc*/*hcp* interface) [67]. In particular, the OR between *fcc* austenite and *hcp* ε-martensite corroborates the concept of the formation of ε-martensite by stacking faults.

11.4 Quantification of Microstructure Features and Microstructure Defects in TRIP/TWIP Steels, Determination of the Stacking Fault Energy in Austenite

11.4.1 Experimental Methods for Quantitative Microstructure Analysis

The characteristic microstructure features of the TRIP/TWIP steels are the amounts of original metastable γ-austenite and twinned austenite, ε-martensite and α'-martensite, the size of the grains or crystallites of the respective phase, the densities of microstructure defects (mainly dislocations and stacking faults), the preferred orientations of crystallites and the macroscopic or mesoscopic lattice deformations. The mechanisms of the microstructure defect formation and phase transformations were described in Sects. 11.2 and 11.3. Preferred orientation of crystallites is a result of local lattice rotations occurring during the plastic deformation. Macroscopic (elastic) lattice deformations stem from the external load, which is not relieved by the crystal plasticity. Mesoscopic elastic lattice deformations are induced by the interaction of neighboring grains or phases at their interfaces.

From the historical point of view, the first microstructure feature of interest in the TRIP steels was the amount of α'-martensite, as the progress of the martensitic phase transformation was related to the strength and the strain hardening of these steels [68]. For the quantification of the α'-martensite phase fraction, several methods were established. One of them utilizes the measurement of the magnetic permeability by a magnetic balance (ferritescope). The physical background of this method is that α'-martensite is a ferromagnetic phase, while austenite and ε-martensite are not ferromagnetic. The main drawbacks of the permeability measurement are that it cannot distinguish between α'-martensite and δ-ferrite,[2] and that the magnetization of

[2]The δ-ferrite is another ferromagnetic phase that can be retained in austenitic steels as a high-temperature *bcc* phase during the dendritic solidification.

α'-martensite depends on the strain. Hence, the ferritescope must be calibrated using a fully martensitic standard [69]. The advantage of the magnetic measurement is that it covers a large sample volume and provides a good statistics even for coarse-grained cast steels.

As ε-martensite and residual austenite are non-ferromagnetic phases, their amounts are typically quantified using diffraction methods like XRD and EBSD. For the phase identification, γ-austenite is described as an *fcc* phase (structure type Cu) with the lattice parameter about 3.59 Å, ε-martensite as a *hcp* phase (structure type Mg) with the lattice parameters $a \approx 2.54$ Å and $c \approx 4.11$ Å, and α'-martensite as a *bcc* phase (structure type W) with the lattice parameter about 2.87 Å. For the phase quantification, XRD uses the intensity ratios [70]. Nowadays, the phase quantification using XRD is usually carried out by employing the Rietveld analysis of the diffraction pattern [71, 72]. Phase quantification using EBSD is based on the comparison of the respective phase areas.

In comparison to the magnetic measurement, XRD and EBSD probe a significantly smaller sample volume. The penetration depth of X-rays (Cu Kα radiation) in TRIP/TWIP steels is about 8 μm, the irradiated area usually several mm^2. Typical information depth of the backscattered electrons in steels is about 70 nm (at the acceleration voltage of 20 kV), the analyzed area below 1 mm^2. Still, in most cases the amount of α'-martensite determined using XRD agrees very well with the values obtained from the magnetic measurement, as it is illustrated in Fig. 11.18 for several compression steps.

The quantification of the phase fractions using EBSD is generally biased by a low quality of the Kikuchi patterns in the regions that experienced a high local deformation, e.g., within the deformation bands. In such regions, the indexing of the Kikuchi patterns is frequently not possible, thus heavily deformed austenite and ε-martensite are not be considered for the quantitative phase analysis. For this reason, EBSD

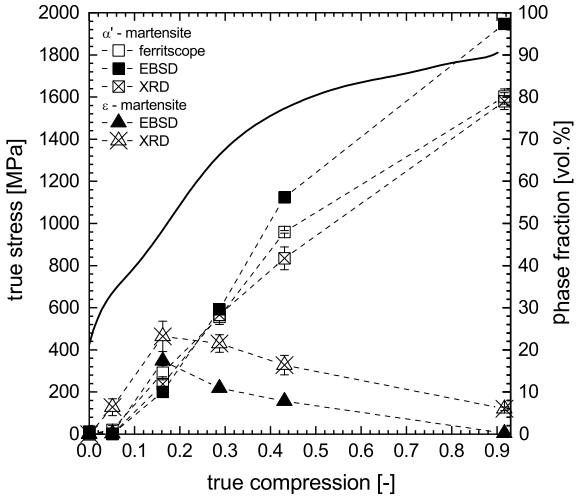

Fig. 11.18 Comparison of the results of the ε- and α'-martensite quantification using magnetic measurement, EBSD and XRD. The stress-strain curve (solid line) shows the deformation state of the PM X3CrMnNi16-7-6 steel

systematically underestimates the amount of ε-martensite, which contains a considerable amount of SFs. Furthermore, thin ε-martensite lamellae having a thickness below 100 nm cannot be resolved by EBSD, because the Kikuchi patterns from the ε-martensite lamellae are superimposed by the Kikuchi pattern from the surrounding (faulted) austenite. Finally, the α'-martensite fraction determined using EBSD in highly strained samples is overestimated at the expense of the deformed austenite, which is not recognized (because not indexed) due to a high defect density. Consequently, XRD provides a better accuracy in determining the ε-martensite fraction than EBSD. The influence of this effect is perceptible in Fig. 11.18, where the results of the quantitative phase analysis using EBSD and XRD are compared.

Another microstructure component, which is important for explanation and modelling of the mechanical behavior of the TWIP steels, is the twinned austenite [12, 73–76]. However, as the strength of the steels is governed rather by the density of the twin boundaries restraining the dislocation slip [75] than by the volume fraction of the twins, the density of the twin boundaries is the relevant quantity, which has to be determined experimentally. However, due to the usually very fine morphology of the twins (thickness ~50 nm), neither SEM nor XRD can quantify the density of the twin boundaries accurately. The typically practiced EBSD orientation mapping [73, 77, 78] cannot account for the very fine twin structure, as its lateral resolution is limited. The twins can be more easily identified by electron channeling contrast (ECC). However, the ECC images are not commonly used as additional information for automated EBSD phase analysis.

The effect of the limited lateral resolution of EBSD on the result of the quantitative microstructure analysis is illustrated in Fig. 11.19. The ECC image reveals twin bundles, which are only partly recognized as twins in the corresponding EBSD mapping. In case of the not recognized twins, the measured Kikuchi pattern is a superposition of the Kikuchi patterns from the matrix and from twins that is indexed according to the dominant diffraction volume, which is the matrix. The only technique, which is capable of resolving the nanoscopic twin structures, is HRTEM (see, e.g., Figure 11.11). However, it is limited to small sampling sizes and therefore it suffers from the statistical unreliability.

The quantification of the twin density in austenite by XRD is difficult, as the twinning causes mainly an *hkl*-dependent asymmetry of the diffraction lines [30]. For low twin densities, the line asymmetry is relatively weak, because the shape of the diffraction lines from the *fcc* phase is dominated by the undisturbed austenite regions, while the contribution of the twins is negligible. Furthermore, the influence of the twinning on the line broadening and shift is small as compared to isolated stacking faults [33].

Still, XRD is capable of quantifying the density of isolated stacking faults in austenite and ε-martensite. In austenite, the isolated stacking faults affect both the positions and the broadening of diffraction lines as described in Sect. 11.2.3.2. In ε-martensite, the presence of isolated stacking faults leads to the broadening of diffraction lines $\beta_{hkl}^{\mathrm{SF}}$ with $h - k = 3n \pm 1$ that is equal to [30, 79]

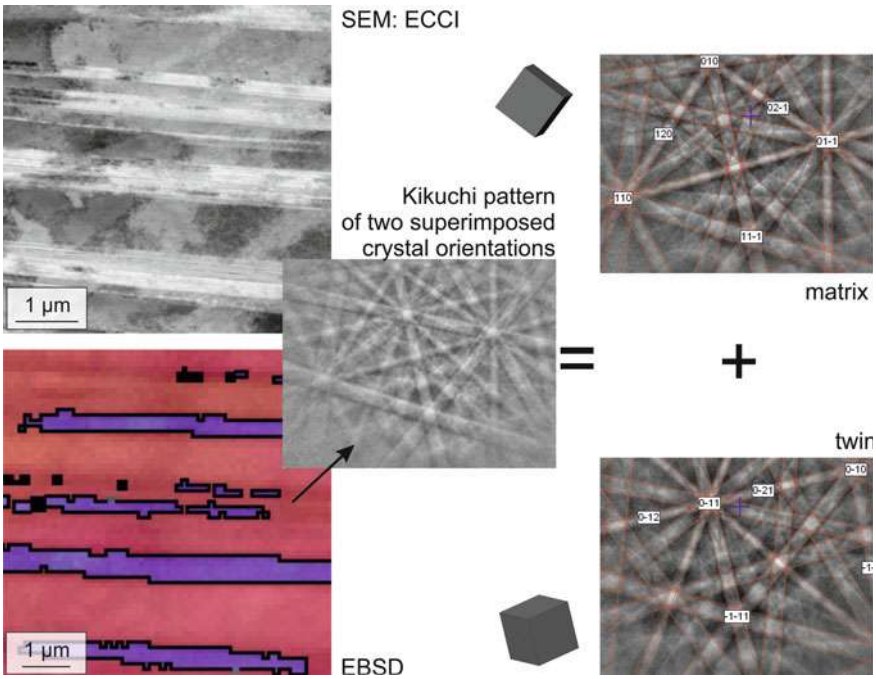

Fig. 11.19 Difficulty of indexing twin bundles by EBSD due to the limited resolution and the superposition of Kikuchi patterns in the fine-scale microstructure

$$\beta_{hkl}^{\mathrm{SF}} = \frac{3l\alpha}{c^2 d_{hkl}^*}, \tag{11.14}$$

where l is the diffraction index, c the hexagonal lattice parameter and d_{hkl}^* the interplanar spacing in the reciprocal space. The densities of dislocations are determined from the *hkl*-dependent line broadening as well. The line broadening caused by dislocations is proportional to the square root of the dislocation density (ρ) and to the square root of the contrast factor of dislocations ($\bar{C}_{hkl}$) [80–85]:

$$\beta_{hkl}^{disl} = \sqrt{\frac{\pi}{2}} M \sqrt{\rho} b \sqrt{\bar{C}_{hkl}} d_{hkl}^* \tag{11.15}$$

Further parameters affecting the magnitude of the line broadening in (11.15) are the Wilkens factor M, the Burgers vector b and the length of the reciprocal space vector (d_{hkl}^*). As the contrast factors describe the elastic response of the material on the presence of dislocations, they are basically calculated from the elastic constants of the material under study [82, 83, 86]. Nevertheless, Ungár et al. showed that for cubic and hexagonal materials, the *hkl*-dependence of the contrast factors must comply with the crystallographic anisotropy of the elastic constants [84, 87]. Therefore, it can be described by the respective crystallographic invariant:

$$\bar{C}_{hkl}^{\text{cub}} = \bar{C}_{100}\left[1 - A\frac{h^2k^2 + k^2l^2 + l^2k^2}{\left(h^2 + k^2 + l^2\right)^2}\right] \tag{11.16}$$

$$\bar{C}_{hkl}^{\text{hex}} = \bar{C}_{hk0} + \frac{\left[2A\left(h^2 + hk + k^2\right) + Bl^2\right]l^2}{\frac{9}{4}\left(ad_{hkl}^*\right)^4} \tag{11.17}$$

The factors A and B characterize the degree of the crystallographic anisotropy. In the computer routines employed for the Rietveld refinement of the XRD patterns, the dependence of the dislocation-induced line broadening on the diffraction indices is calculated using the Popa model [88].

11.4.2 Methods for Determination of the Stacking Fault Energy (SFE) in fcc *Crystals*

As discussed above, the knowledge of the SFE is crucial for the prediction of the deformation behavior of *fcc* metals and alloys, because it determines the occurring deformation mechanisms and consequently the strain hardening. In literature, various attempts to measure the SFE are reported that are mostly based on TEM or XRD methods. The most common TEM technique is the measurement of the separation distance of the partial dislocations [89–92]. Usually, weak beam imaging is utilized to identify the dissociation distance between the partials, which amounts several nanometers and depends on the dislocation character (edge or screw). Indeed, detectable dissociation widths are found in materials with a relatively low SFE only. Another TEM approach examines extended dislocation nodes, in particular the curvature radius, from which the SFE is concluded [93–96]. Some problems might arise from the delicate preparation of thin TEM foils, which can produce undefined strains in the area close to the investigated triangle dislocation node. Another source of systematic errors is a high sensitivity of the width of the dislocation nodes to the local concentration of the alloying atoms [90]. A general drawback of TEM is its limited statistical relevance.

The first technique for the SFE determination using XRD was developed by Dillamore [97, 98], who proposed obtaining SFE from the degree of the preferred orientation of crystallites, and directly from the ratio of two different texture components extracted from the pole figures. The idea behind this approach is that the formation of a crystallographic texture requires cross slip of perfect dislocations, which is a competing mechanism to the dislocation dissociation driven by a low SFE. This method can be applied for a wide range of SFEs, but is purely empirical and offers only a rough estimation of the SFE.

A more reliable XRD technique for the SFE determination is based on the analysis of the broadening and shift of the diffraction lines in XRD patterns of plastically deformed samples [99, 100]. Within this approach, the SFE (γ_{SF}) is proportional to the ratio of the squared dislocation-induced microstrain measured in the ⟨111⟩

direction $\left(\left\langle\varepsilon_{111}^2\right\rangle\right)$ and the SF probability (α):

$$\gamma_{\mathrm{SF}} = \frac{K_{111}\omega_0 G_{111} a_0}{\pi\sqrt{3}} \cdot \frac{\left\langle\varepsilon_{111}^2\right\rangle}{\alpha} \tag{11.18}$$

The microstrain and the SF probability are determined from the line broadening and from the line shift, respectively, using the Warren model [30]. Further quantities in (11.18) are the shear modulus of austenite in the fault plane (G_{111}) and the lattice parameter (a_0). $K_{111}\omega_0$ is a proportionality factor describing the relationship between the microstrain and the dislocation density, the dislocation character and the dislocation interaction [99]. This approach is commonly employed [101–103] despite the problems with the determination of the proportionality factor $K_{111}\omega_0$.

An alternative method for the SFE determination using XRD [104] is based on the proportionality between the SFE and the critical shear stress component (τ_{zx}),

$$\gamma_{\mathrm{SF}} = \frac{\tau_{zx} b_p}{2}, \tag{11.19}$$

that is valid for the formation of very wide stacking faults, [cf. (11.6)]. $b_p = a_0|\langle 211\rangle|/6$ is the magnitude of the Burgers vector of the partial dislocations. According to Copley and Byun [9, 10], the separation distance between partial dislocations follows from the balance of the forces that act on the partial dislocations terminating a stacking fault, and is given by:

$$d_s = \frac{1}{8\pi} \cdot \frac{2-3\nu}{1-\nu} \cdot \frac{G b_p^2}{\gamma_{\mathrm{SF}} - \frac{\tau_{zx} b_p}{2}}, \tag{11.20}$$

see also (11.5). In (11.20), ν is the Poisson ratio and G the shear modulus. If the distance between the partials becomes 'infinite', the work resulting from the impact of the shear stress component τ_{zx} on the partials must be in equilibrium with the stacking fault energy as described by (11.19). In the XRD approach from [104], the shear stress τ_{zx} is calculated from a (uniaxial) internal stress σ_x, which is needed to produce 'infinitely' wide SFs, and from the mean Schmid factor (M) that corresponds to the respective deformation state

$$\tau_{zx} = M\sigma_x. \tag{11.21}$$

The stress σ_x is proportional to the 'residual' elastic lattice deformation, which remains in the austenite after the plastic deformation. If the applied load is uniaxial and if the lattice deformation is measured in a direction perpendicular to this load [105], then the proportionality between stress and deformation is described by

$$\varepsilon_z^{hkl} \equiv \frac{d_z^{hkl} - d_0}{d_0} = s_1^{hkl}\sigma_x, \tag{11.22}$$

where $s_1^{hkl} = -\nu^{hkl}/E^{hkl}$ is the X-ray elastic constant (XEC) of austenite. The indices *hkl* emphasize the crystallographic anisotropy of the elastic constants. As for cubic materials, the interplanar distances can be converted directly to the lattice parameters,

$$\varepsilon^{hkl} \equiv \left\langle \frac{d^{hkl} - d_0}{d_0} \right\rangle = \left\langle \frac{a^{hkl} - a_0}{a_0} \right\rangle, \tag{11.23}$$

the internal stress in *fcc* austenite can be determined from the measured lattice parameters a^{hkl}. However, as the presence of the stacking faults leads to additional shift of the diffraction lines, [cf. (11.10)], the lattice parameter affected by the internal stress and stacking faults has the form of [104, 105]

$$\begin{aligned} a^{hkl} &= a_0\left(1 + \sigma_x s_1^{100}\right) + 3a_0\left(s_1^{111} - s_1^{100}\right)\sigma_x \Gamma_{hkl} \\ &+ \frac{\sqrt{3}}{4\pi} a_0 \alpha G_{hkl}^{\mathrm{SF}} - a_0 \cot\theta \, \Delta\theta \end{aligned} \tag{11.24}$$

a_0 is the intrinsic lattice parameter of austenite (unaffected by internal stress and SFs), α the SF probability and $G_{hkl}^{\mathrm{SF}} = \sum_{af} \pm(h + k + l)/\left[\left(h^2 + k^2 + l^2\right)m_{hkl}\right]$ the contrast factor of SFs from (11.10). In (11.24), the XEC s_1^{hkl} was replaced by

$$s_1^{hkl} = s_1^{100} + 3\Gamma_{hkl}\left(s_1^{111} - s_1^{100}\right), \tag{11.25}$$

where

$$\Gamma_{hkl} = \frac{h^2k^2 + k^2l^2 + l^2h^2}{\left(h^2 + k^2 + l^2\right)^2} \tag{11.26}$$

is the cubic invariant describing the crystallographic anisotropy of XECs. The last term in (11.24) describes the correction of the measured lattice parameters for instrumental aberrations, which cause a line shift $\Delta\theta$. The fitting of measured lattice parameters with the function from (11.24) yields the intrinsic lattice parameter of austenite (a_0), the internal stress (σ_x) and the SF probability (α). Finally, the internal stress is used for calculation of the SFE:

$$\gamma_{\mathrm{SF}} = \frac{\tau_{zx} b_p}{2} = \frac{1}{2} M \sigma_x \frac{a_0}{6} |\langle 211 \rangle| = \frac{\sqrt{6}}{12} M \sigma_x a_0 \tag{11.27}$$

Another important method is the SFE calculation. Within the thermodynamic approach [23, 25, 106, 107], the SFE is calculated from the difference in the Gibbs energies of austenite and ε-martensite and from the strain and interface energies resulting from the faulting, see Sect. 11.2.3.1. The thermodynamic calculations are applied mainly to estimate the influence of certain alloying elements on the SFE. Nowadays, they are increasingly complemented by first-principles studies [24, 108].

However, if not based on experimental data, the modelled predictions often fail in giving reasonable trends, and show a systematic offset [107]. Therefore, the SFE calculations must be combined with experimental studies [92] or supported by other approaches like multivariate linear regression [109] or data driven machine-learning [110] in order to be verified.

11.4.3 In Situ Diffraction Studies on TRIP/TWIP Steels During Plastic Deformation

The capability of XRD methods to track the microstructure changes in TRIP/TWIP steels during their plastic deformation was tested on samples containing 3, 6 and 9 wt% Ni (PM X4CrMnNi16-7-3, X3CrMnNi16-7-6, PM X2CrMnNi16-7-9) that possess different SFEs and consequently different stabilities of metastable austenite. One part of the in situ XRD experiments was performed with a laboratory source under bending the samples in a four-point bending apparatus (Fig. 11.20). Advanced synchrotron XRD experiments were carried out at the PETRA III/DESY beamline P07 in Hamburg (Germany) in a deformation dilatometer.

During the XRD measurement in the four-point bending apparatus from Fig. 11.20, the total deformation force and the amount of the bending are measured in addition to the XRD patterns. These quantities are converted into the mechanical tensile stress σ_x^{mech} and into the strain in the outer fiber $\varepsilon_x^{\text{mech}}$ [105], respectively. The lattice parameters obtained from the line positions are plotted for selected deformation states as function of $3\Gamma_{hkl}$, cf. Fig. 11.21 and (11.24). In Fig. 11.21, the slope of the diagram is proportional to the internal stress σ_x, the departure of the lattice parameters from the linear dependence scales with the SF probability. As the measured line positions were corrected using an internal standard, the line shift in (11.24) was set to zero for fitting ($\Delta\theta = 0$).

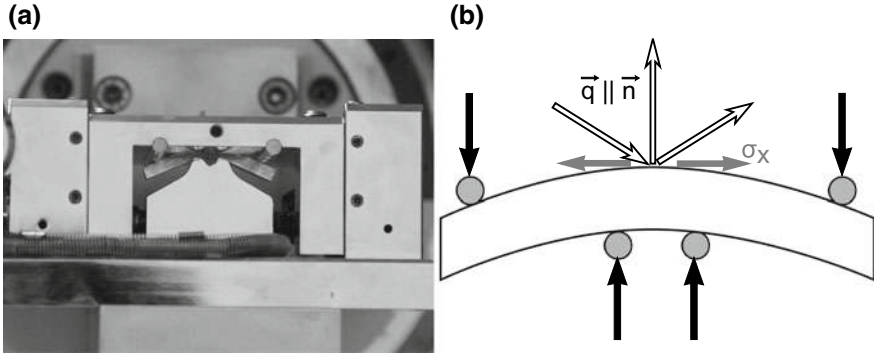

Fig. 11.20 Bending table used for the in situ XRD experiments (**a**). The beam path is shown schematically by the hollow arrows in (**b**)

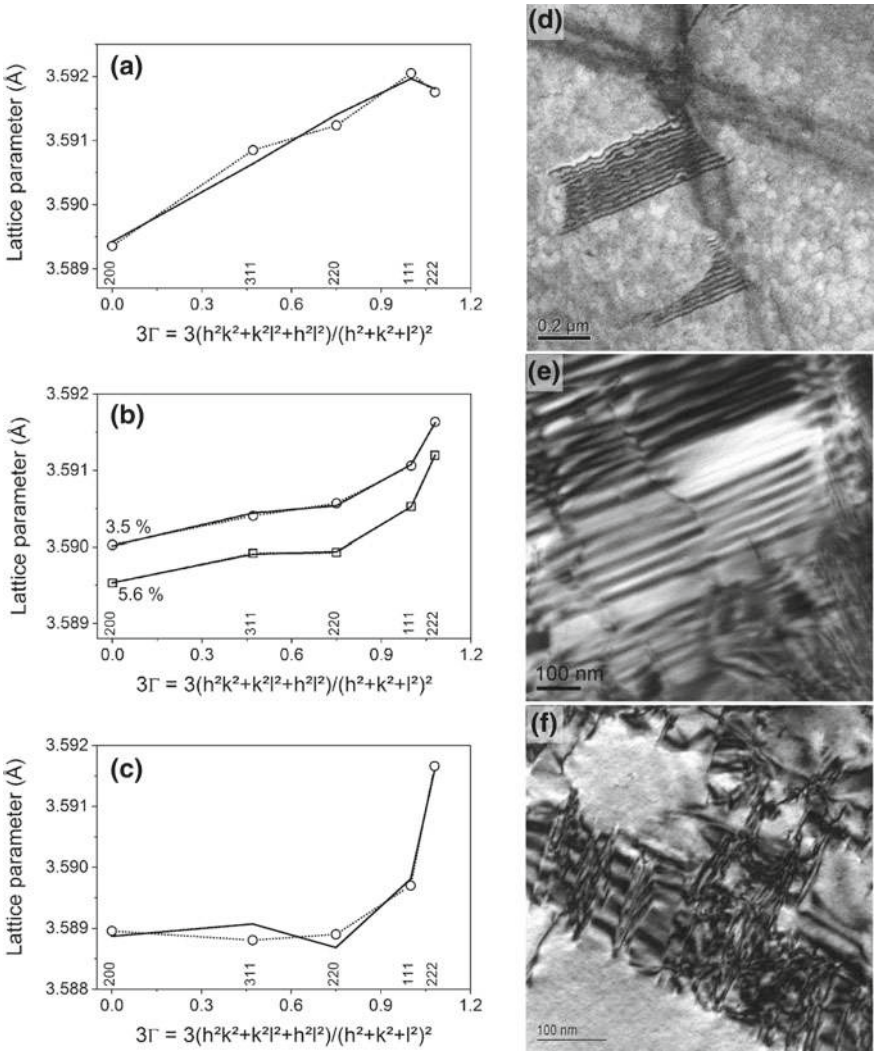

Fig. 11.21 Left-hand side: Lattice parameters of austenite deformed at the strains in the outer fiber of 1% (**a**), 3.5% and 5.6% (**b**), and 8.3% (**c**). Measured lattice parameters are plotted by interconnected open symbols, the lattice parameters fitted using (11.24) by solid lines. Corresponding TEM micrographs (d–f) at the right-hand side of the figure were taken in samples deformed to 0.5, 5 and 9%. Adopted from [104, 105]

The comparison of the measured lattice parameters with the lattice parameters fitted using (11.24) shows that the applied microstructure model is not valid for all deformation states (Fig. 11.21). While an excellent agreement between the measured and the calculated (fitted) lattice parameters was achieved for medium deformation states (Fig. 11.21b), the microstructure model cannot explain the anisotropy of the

lattice parameters observed at the lowest and highest deformations (Fig. 11.21a, c). The reason for the observed discrepancies is the invalidity of the Warren model for short (Fig. 11.21d) and crossing (Fig. 11.21f) stacking faults. Consequently, the application of this microstructure model to the measured lattice parameters can be used for verification of the presence of wide but non-intersecting SFs.

In Fig. 11.22, the lattice parameters a_0, the SF probabilities and the in-plane stresses (σ_x) are plotted against the strain in the outer fiber, and compared with the changes in the phase composition of the steel. As the intrinsic lattice parameter a_0 is supposed to stay constant during the deformation, its increase observed for $\varepsilon_x^{\text{mech}} < 2\%$ and $\varepsilon_x^{\text{mech}} > 6\%$ is another indicator of the invalidity of the Warren SF model. Analogously, the apparently negative SF probability observed for $\varepsilon_x^{\text{mech}} < 2\%$ is related to the early stage of the SF formation (cf. Fig. 11.21d). From the difference of the stress values σ_x, $\sigma_{\parallel}(311)$ and $\sigma_{\parallel}(222)$ in Fig. 11.22d, it can be supposed that the interaction of the local strain fields produced by partial dislocations in narrow SFs changes the crystallographic anisotropy of the SFs contrast factors. The SF crossing at larger deformations ($\varepsilon_x^{\text{mech}} > 6\%$, cf. Fig. 11.21f) leads to an apparent change of the crystallographic anisotropy of XECs, which can be seen on the difference

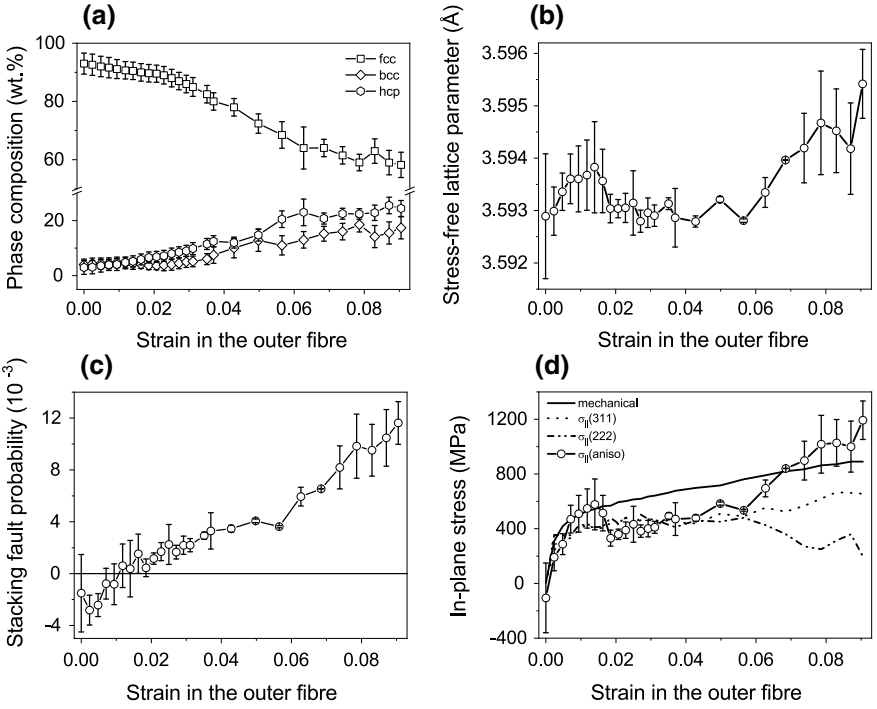

Fig. 11.22 Changes in the phase composition (**a**) and microstructure characteristics of the TRIP steel during plastic deformation. The lattice parameter a_0 (**b**), SF probability (**c**) and the internal stress in austenite σ_x (**d**) were obtained by fitting the measured lattice parameters according to (11.24)

between $\sigma_{\parallel}(311)$ and $\sigma_{\parallel}(222)$. These stresses were calculated directly from the lattice deformations measured in the respective crystallographic direction:

$$\sigma_{\parallel}(hkl) = \left(s_1^{hkl}\right)^{-1} \frac{d^{hkl} - d_0}{d_0} = \left(s_1^{hkl}\right)^{-1} \frac{a^{hkl} - a_0}{a_0} \tag{11.28}$$

The XECs, $s_1^{311} = -1.60 \times 10^{-12}\,\mathrm{Pa}^{-1}$, $s_1^{222} = s_1^{111} = -9.52 \times 10^{-13}\,\mathrm{Pa}^{-1}$ and $s_1^{100} = s_1^{200} = -2.17 \times 10^{-12}\ \mathrm{Pa}^{-1}$, were calculated using the Kröner approach [111] from the single-crystalline elastic constants of austenite, i.e., $C_{11} = 1.975 \times 10^{11}$, $C_{12} = 1.245 \times 10^{11}$ and $C_{44} = 1.220 \times 10^{11}$ Pa that were taken from the Landolt-Börnstein database [112].

The comparison of the SF densities (Fig. 11.22c) with the phase compositions (Fig. 11.22a) and the corresponding TEM micrographs (Fig. 11.21d–f) confirmed that up to $\varepsilon_x^{\mathrm{mech}} \cong 2\%$, the deformation behavior of austenite is dominated by the formation and widening of SFs. For $\varepsilon_x^{\mathrm{mech}}$ above 2%, the SF density increases, which leads to the local ordering of SFs that is recognized by XRD as the ε-martensite formation. At the deformations above 6%, the SFs form also on crystallographically equivalent lattice planes {111} and interact, which facilitates the formation of α'-martensite as explained in Sect. 11.3.

The validity range of the Warren model that was identified by the above routine was used for calculation of the SFE from the internal stress (σ_x, $\sigma_{\parallel}(311)$ or $\sigma_{\parallel}(222)$) and from the lattice parameter a_0 measured by XRD. For the SFE calculation, (11.27) was employed. As the change in the preferential orientation of crystallites was negligible in this deformation range, the Schmid factors were assumed constant (independent of the deformation state) and obtained from the EBSD measurements that were carried out on non-deformed samples. The SFEs determined using this method were 17.5 $\pm$ 1.4 mJ m^{-2} for the TRIP steel X3CrMnNi16-7-6 and 8.1 $\pm$ 0.9 mJ m^{-2} for the TRIP steel X4CrMnNi16-7-3 [104], and 24.1 $\pm$ 2.5 mJ m^{-2} for the TRIP steel X2CrMnNi16-7-9.

For a comprehensive description of the microstructure development during plastic deformation, the TRIP/TWIP steels PM X4CrMnNi16-7-3, X3CrMnNi16-7-6 and PM X2CrMnNi16-7-9 containing 3, 6 and 9 wt% Ni, respectively, were investigated using in situ synchrotron diffraction during compression [113]. In the non-deformed state, the samples had cylindrical shape ($\varnothing$ 4 mm $\times$ 8 mm), and were fully austenitic and fine-grained. The synchrotron diffraction experiments were carried out at beamline P07 of PETRA III at DESY (Hamburg, Germany). The high energy and the short wavelength of the synchrotron radiation (100 keV, $\lambda = 0.1235$ Å) enabled measurements in transmission diffraction geometry, which is more appropriate for explanation of the bulk materials properties than the surface-sensitive laboratory XRD studies [114]. Furthermore, the short wavelength of the synchrotron radiation provided a broad coverage of the reciprocal space up to

$$q = \frac{2\pi}{d} = \frac{4\pi \sin\theta}{\lambda} = 8.87\,\text{Å}^{-1}, \tag{11.29}$$

which is beneficial for measurements in a broad range of the diffraction indices *hkl*, especially in materials with relatively small elementary cell. For austenite, nine diffraction peaks were recorded (up to 422). In (11.29), q is the maximum magnitude of the diffraction vector and d the minimum interplanar spacing that are accessible at the maximum diffraction angle $2\theta = 10°$ and at the wavelength of 0.1235 Å. High flux of the synchrotron beam enables real in situ measurements. Relaxation effects in the sample during the acquisition of the individual diffraction patterns (measuring time about 1 s) are almost eliminated.

The samples were deformed in a deformation dilatometer (BÄHR DIL 850) until the maximum force, corresponding to a technical stress of 1590 MPa. The in situ compression was carried out in 35 quasi-static discrete load steps. The holding time between the deformation steps (approx. 1 s) resulted from the time that was needed for recording the diffraction patterns. The load direction was perpendicular to the direction of the primary synchrotron beam (Fig. 11.23). In this diffraction geometry, the angle Ψ between the load direction and the diffraction vector varies between $2\theta/2$ and 90° along the Debye rings. The continuous change of the angle Ψ allows the determination of internal stresses and preferred orientations of crystallites in all present phases from a single 2D diffraction pattern.

For the analysis of the 2D diffraction patterns, the recorded images were integrated in 5° wide sections along the Debye rings in order to conserve the Ψ-dependent information. The 72 diffraction patterns (diffracted intensities versus diffraction angles for individual Ψ sections, see Fig. 11.24) were subjected to a coupled Rietveld refinement using MAUD [115, 116]. The microstructure models employed for the Rietveld refinement of individual diffraction patterns included: (i) anisotropic line broadening from perfect dislocations according to the Popa model [88], (ii) anisotropic line

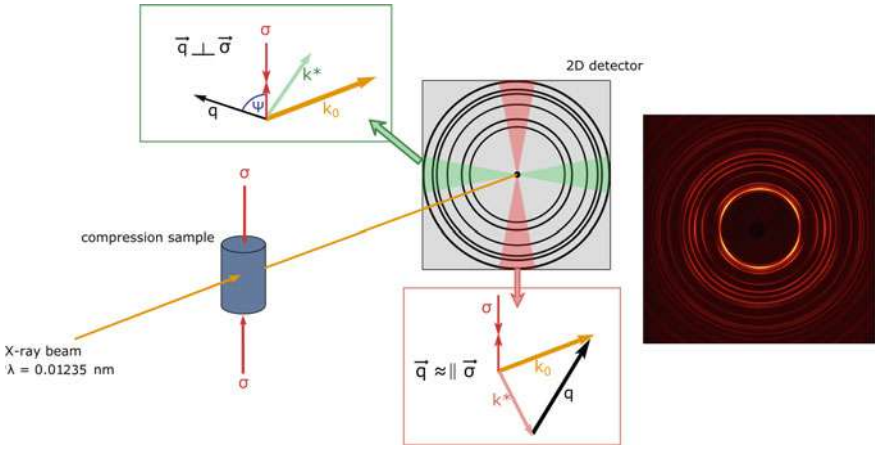

Fig. 11.23 Setup of the in situ compression tests in transmission geometry. The sketches in the green and red boxes show the alignment of the diffraction vector that is perpendicular and nearly parallel to the load direction in the correspondingly colored segments of the 2D diffraction pattern. On the right-hand side of the panel, a single 2D diffraction pattern is shown

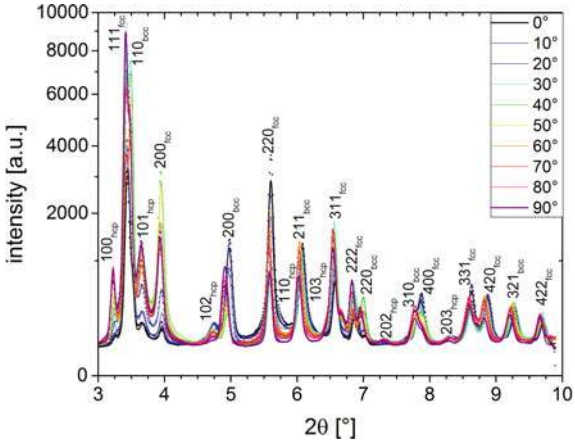

Fig. 11.24 The 1D diffraction patterns integrated over 5° wide segments of the 2D diffraction pattern from Fig. 11.23

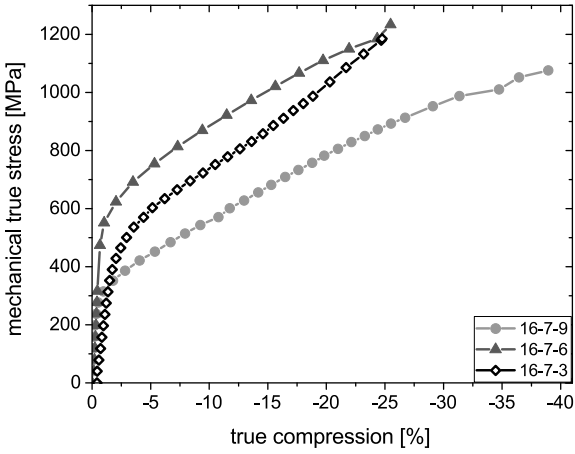

Fig. 11.25 True stress—true strain curves measured during the compressive deformation of the 16Cr-7Mn-xNi steels. Adopted from [113]

broadening and anisotropic line shift caused by SFs according to the Warren model [30] and (iii) anisotropic line shift caused by anisotropic elastic lattice deformation according to the Moment Pole Stress model [117]. In the Moment Pole Stress model, only the stress component σ_{33} was considered. The same elastic constants of the austenite were used like for the in situ XRD experiments during bending. Fractions of individual phases were determined after the diffracted intensities have been corrected for preferred orientations of crystallites using the Ψ dependence of the diffracted intensities [115, 118], because the texture correction improves significantly the reliability of the quantitative phase analysis [119].

Mechanical behavior of the Cr–Mn–Ni 16-7-x TRIP/TWIP steel samples during the compressive load is depicted in Fig. 11.25. The deformation and the applied force were measured by the dilatometer and converted to true stress and true strain. The material with the highest SFE (24.1 mJ/m^2) and with the highest Ni content

(9%) exhibits the lowest stress level and a nearly constant strain hardening. This kind of strain hardening is commonly associated with the TWIP effect [120]. The sample with the lowest SFE (8.5 mJ/m^2) and lowest Ni content (3%) possesses the most pronounced strain hardening, which results in a sigmoidal flow curve that is characteristic for intense martensitic transformation [121]. In the sample containing 3 wt% Ni, the formation of ε-martensite begins at ca. 1% compression.

The maximum amount of ε-martensite (about 19 vol%) is reached at 20% deformation (Fig. 11.26). The α'-martensite forms at relatively low deformations. At the deformation of 15%, it becomes the dominant martensitic phase, which grows at the expense of austenite and ε-martensite at deformations exceeding 20%. In sample X2CrMnNi16-7-9, the formation of ε-martensite is delayed and the α'-martensite does not form up to a 40% compression. This dependence of the martensites formation on the Ni content is a result of a lower driving force for the martensitic transformation in materials with higher SFE that was discussed in Sects. 11.2.3 and 11.3. The sample containing 6% Ni (SFE = 17.5 mJ/m^2) shows almost constant strain hardening like the steel X2CrMnNi16-7-9, while the development of the phase composition resembles the TRIP steel with 3 wt% Ni. However, the stress level in sample X3CrMnNi16-7-6 measured beyond the onset of the plastic deformation is clearly too high. The results of the diffraction analysis (see below) support the assumption that the high stress level is related to an incompletely recrystallized initial microstructure.

The σ_{33} component of the internal stress in austenite, which is parallel to the applied compression, increases during the sample compression (Fig. 11.27a), but is constantly lower than applied mechanical stress (cf. Fig. 11.25). The increase of σ_{33} indicates the strain hardening that is caused by the increase of dislocation density and thus by the increase of dislocation-induced microstrain (Fig. 11.28), and by the interaction of dislocations in austenite with the newly formed martensites [113].

The interplay of these effects can be illustrated on the lowest internal stress (Figs. 11.24 and 11.27a), lowest microstrain (Fig. 11.28) and delayed martensite

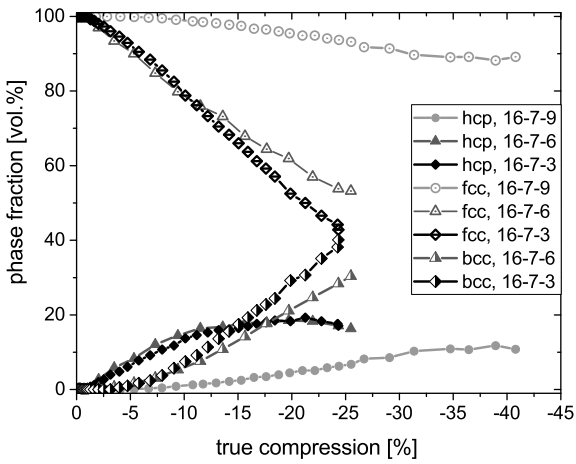

Fig. 11.26 Phase fractions of *fcc* austenite, *hcp* ε-martensite and *bcc* α'-martensite during the deformation of the samples. Adopted from [113]

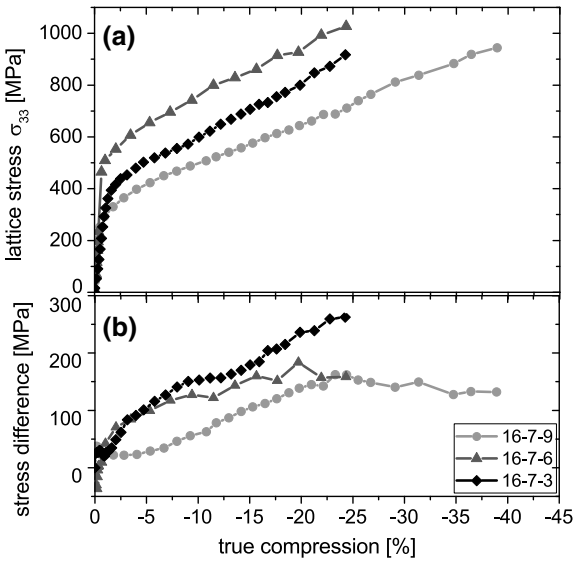

Fig. 11.27 **a** Internal elastic lattice stress in austenite in the compression direction, obtained from the in situ synchrotron diffraction. **b** Difference between the (total) mechanical true stress from Fig. 11.25 and the lattice stress, adopted from [113]

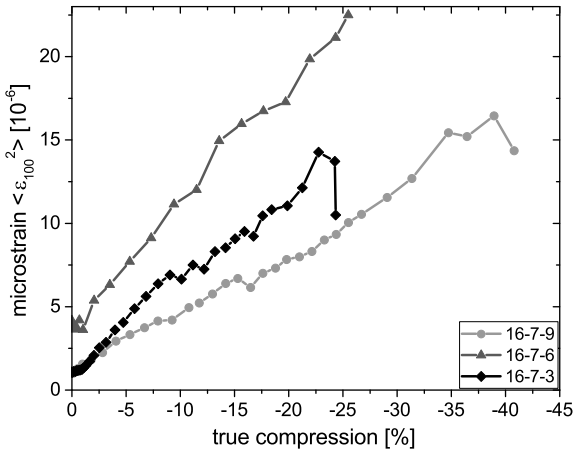

Fig. 11.28 Squared microstrain—a quantity proportional to the dislocation density

formation (Fig. 11.26) in sample X2CrMnNi16-7-9. Weaker defect formation and retarded martensitic phase transformation are also the reasons for the smallest difference between the applied mechanical stress and internal (elastic) lattice stress in sample X2CrMnNi16-7-9 (Fig. 11.27b).

The largest difference between the mechanical stress and σ_{33} observed in sample X4CrMnNi16-7-3 for deformations beyond 7.5% suggests that newly formed martensites carry a significant part of the external load. In this deformation range, the amount of α'-martensite increases most quickly in the steel with lowest Ni content (sample X4CrMnNi16-7-3 in Fig. 11.26).

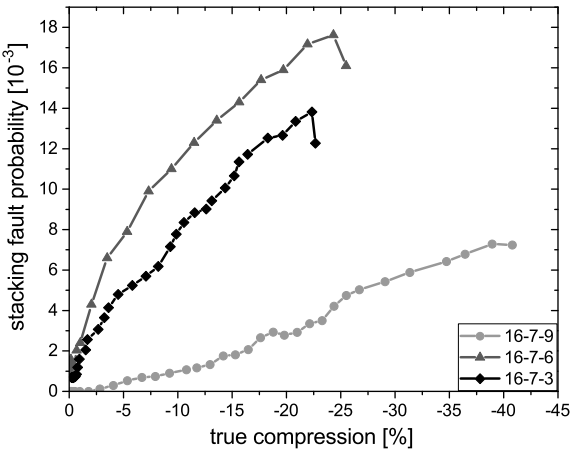

Fig. 11.29 Evolution of the probability of isolated intrinsic stacking faults in austenite under compression

The stacking fault probabilities (SFPs, Fig. 11.29) correlate generally with the amount of ε-martensite (Fig. 11.26), because the ε-martensite is formed by the ordering of dense stacking faults, see Sect. 11.2. For this reason, both quantities are expected to increase with decreasing SFE. Still, at the lowest deformations, the SFs must be created before ε-martensite can form, thus the initial increase of SFP occurs always earlier, i.e., at lower strains than the onset of the ε-martensite formation. The steep increase of the SFP in samples X4CrMnNi16-7-3 and X3CrMnNi16-7-6 and the early onset of the ε-martensite formation indicate the dominant role of stacking faults as deformation mechanism. The unexpectedly high SFP in the deformed steel X3CrMnNi16-7-6 as compared with the SFP in the steel X3CrMnNi16-7-3 (Fig. 11.29) is caused by a higher density of dislocations in incompletely recrystallized initial sample X3CrMnNi16-7-6 (Fig. 11.28). The lowest SFPs were measured for the 9% Ni steel, because this steel possesses the highest SFE. Especially in this steel, the onset of the SF formation is slightly delayed (shifted to higher strains), because the initial deformation is realized by dislocation slip. Because of its higher SFE, the formation of twins is expected in this steel, but the presence of the twins cannot be evidenced easily from the diffraction data.

Although the formation of SFs and the martensitic transformations are the dominant deformation mechanisms in the TRIP steels, the role of perfect dislocations is not neglectable, because the perfect dislocations are the precursors of partial dislocations, SFs and ε-martensite (or twins in TWIP steels). In order to visualize the development of the dislocation density in the TRIP/TWIP steels during their plastic deformation, the squared microstrain $\langle\varepsilon^2_{100}\rangle$ was plotted as a function of the true compression in Fig. 11.28. According to Wilkens [122], the squared microstrain is proportional to the dislocation density [cf. (11.15)]

$$\left\langle \varepsilon^2_{hkl} \right\rangle = \frac{\pi}{8} M^2 \rho b^2 \bar{C}_{hkl}, \tag{11.30}$$

and can be determined directly from the dependence of the diffraction line broadening on the magnitude of the diffraction vector ($|\vec{q}| = 2\pi d^*_{hkl}$):

$$\beta_{hkl} = \frac{K}{D} + \beta^{\mathrm{SF}}_{hkl} + 2\sqrt{\langle \varepsilon^2_{hkl} \rangle} \cdot d^*_{hkl}. \tag{11.31}$$

Additional contributions to the measured line broadening stem from the (small) crystallite size (K/D) and from stacking faults ($\beta^{\mathrm{SF}}_{hkl}$), [cf. (11.14)].

In the steels containing 3 and 6% Ni, the dislocation-induced microstrain increases steeply during initial straining (Fig. 11.28). The offset of both curves is caused by the incompletely recrystallized initial microstructure of sample X3CrMnNi16-7-6 that contained a higher dislocation density. The higher dislocation density persists throughout the whole deformation process, and accounts for the higher SFP, higher lattice stress level and more intense ε-martensite formation in this sample. While the squared microstrain in steel X3CrMnNi16-7-6 increases almost linearly with increasing deformation, in the steel with a lower Ni concentration (X4CrMnNi16-7-3) the increase of the squared microstrain is reduced after ca. 9% compression, due to an intense stacking fault formation and martensitic transformation. The squared microstrain in the steel X2CrMnNi16-7-9 increases also almost linearly, but its increase is slower than in the steel X3CrMnNi16-7-6.

The comparison of the evolution of the dislocation-induced microstrain in the three steels under study suggests that the dislocation density and consequently the expected contribution of the dislocation slip to the plastic deformation decreases with decreasing SFE. Other deformation mechanisms such as the formation of stacking faults and phase transformations become dominant [113]. This change in the dominant deformation mechanism goes along with the transition from the TWIP to the TRIP behavior, and can be substantiated by microscopic studies using, e.g., ECCI and EBSD.

The ECCI and EBSD micrographs of the TRIP/TWIP steels deformed up to the maximum compression depicted in Fig. 11.30 show dislocation arrangements, stacking faults, deformation bands and α'-martensite nuclei. The characteristic microstructure features of the 3% Ni steel are pronounced deformation bands existing on several slip planes, single stacking faults and regions transformed to α'-martensite (Fig. 11.30a). The 6% Ni steel (Fig. 11.30b) exhibits similar features, which are finer scaled because of the incompletely recrystallized initial microstructure. Distinct dislocation structures and their mutual interactions can be seen in deformed steel X2CrMnNi16-7-9 (Fig. 11.30c), where some deformation bands become curved due to their intense interaction with the dislocation arrangements. As twins in austenite are hardly to be distinguished from ε-martensite using ECCI (see Sect. 11.4.1), the nature of the deformation bands and the relative density of the stacking faults within the bands were investigated by EBSD in the 9% Ni steel (Fig. 11.30d).

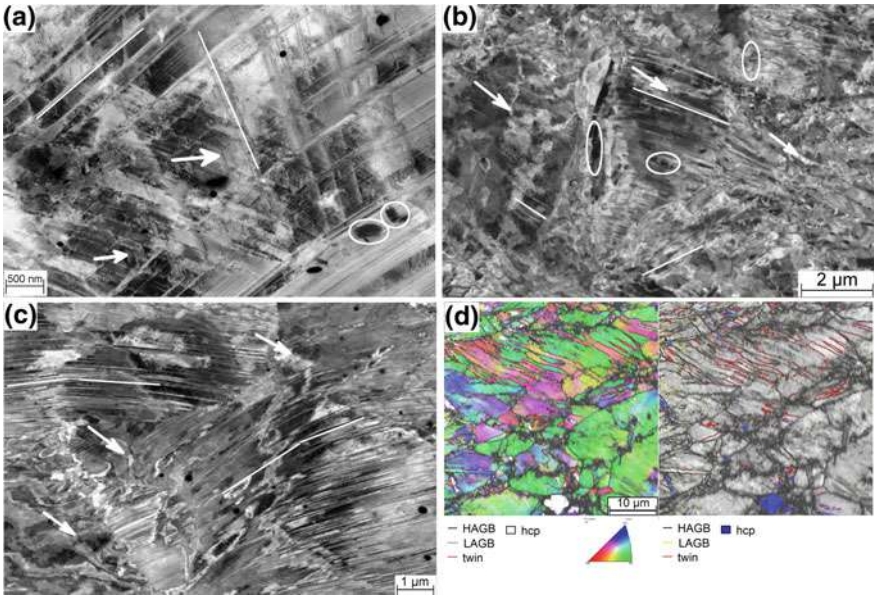

Fig. 11.30 SEM microstructure characterization of deformed samples after the respective maximum compression. **a** ECC image of the 3% Ni steel showing deformation bands (lines), single stacking faults (arrows) and α'-martensite nuclei (circles). **b** ECC image of the highly defective microstructure in the 6% Ni steel showing deformation bands (lines), dislocation arrangements (arrows) and α'-martensite nuclei (circles). **c** Curved deformation bands (lines) and dislocation structures (arrows) in the 9% Ni sample. **d** EBSD maps of this sample, at the left: grain orientation and grain boundaries, especially twins (red lines), as well as local occurrence of *hcp* ε-martensite (white); at the right: mapping of the same area, grain and twin boundaries are plotted together with the band contrast (gray)

11.5 Interplay of Deformation Mechanisms, Development of Deformation Microstructure

11.5.1 Interaction of Microstructure Defects in Deformation Bands

The formation of deformation bands plays a central role in the strain hardening of austenitic steels. As discussed above, the deformation bands accommodate dense SFs that serve as precursors of martensitic phase transformations and twinning in austenite. From the micromechanical point of view, the deformation bands produce strain fields, which interact with the microstructure defects existing outside of the deformation bands. This interaction is illustrated by the TEM image shown in Fig. 11.31, where a deformation band formed on the primary slip system acts as an obstacle for the motion of SFs and for the dislocation slip on the secondary slip systems. The interaction between the primary deformation band and the dislocations gliding on the

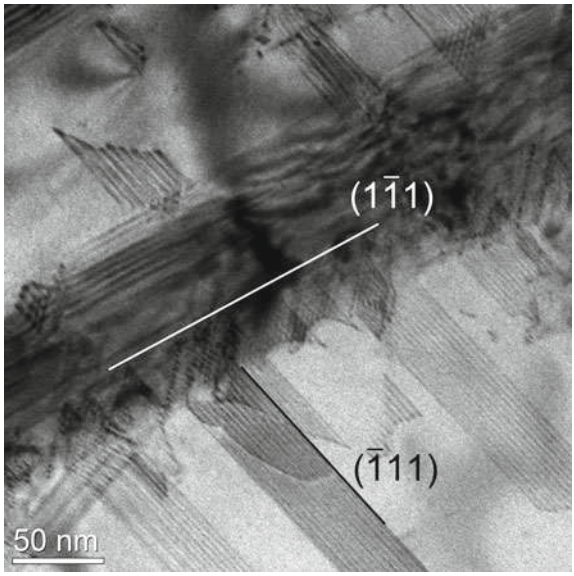

Fig. 11.31 TEM micrograph evidencing the obstacle effect of a deformation band for the dislocation motion on secondary slip systems. Adopted from [34]

secondary slip systems reduces the mean free path length of the dislocations [120, 123, 124], which is a phenomenon that is known as dynamic Hall-Petch effect.

A secondary stacking fault impinging a twin or deformation band must constrict, which means that the partial dislocations of the SF must recombine in order to be able to react with the stacking fault arrangement. Such a dislocation reaction is energetically unfavorable, and can only occur under a local stress concentration [125]. The interactions between deformation bands and other microstructure defects are illustrated exemplarily in Fig. 11.31, where the secondary stacking faults ($\bar{1}$11) that are stopped at the deformation band on the (1$\bar{1}$1) plane seem to constrict partially, but a straight intersection of SFs located on the primary slip system by the SFs located on the secondary slip system is not observed.

Furthermore, the presence of the deformation bands inhibits the annihilation of nearly perfect dislocations having opposite Burgers vectors, as these dislocations are simply separated from each other. The annihilation of dislocations is additionally obstructed by their reduced cross-slip. The deformation bands also impede an arrangement of the dislocations in lower-energetic cell structures. Hence, the presence of deformation bands suppresses the dynamic recovery and enhances the dislocation storage capacity of the material. Dislocations accumulate in the interspace between the deformation bands much more than in materials without planar defects. This finding is confirmed by the continuous increase of the dislocation-induced microstrain measured by XRD in compressed steel PM X5CrMnNi16-6-9 (Fig. 11.32). The simultaneously increasing SF probability indicates that the stacking faults form during the whole deformation process, also on secondary slip systems, contribute continuously to a refinement of the microstructure, and thus maintain a high strain-hardening rate by reducing the mean free paths of gliding dislocations.

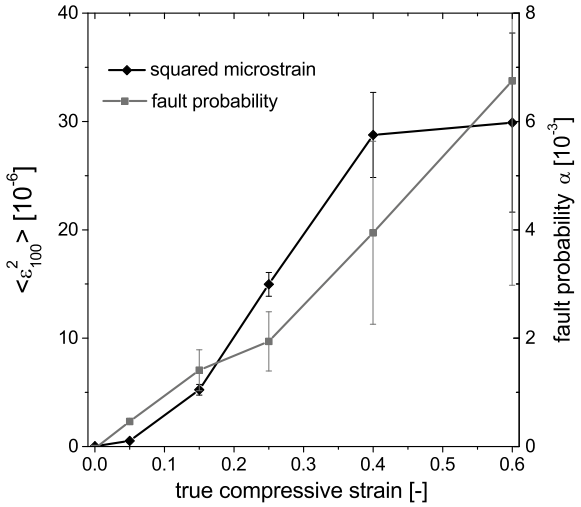

Fig. 11.32 Trends of squared microstrain and SF probability for a deformed PM X5CrMnNi16-6-9 steel evidencing the reduced recovery and resulting high dislocation density [34]

The interactions of microstructure defects discussed above can be found in deformation bands containing isolated SFs and concentrated SFs in form of ε-martensite and twins in austenite. Nevertheless, the extent of the interaction increases with the SF density, thus it is superior for imperfect twins. Correspondingly, enhanced strain hardening was reported for the TWIP steels showing no martensitic transformation [12, 120, 126].

If α'-martensite forms within the deformation bands, even enhanced strengthening is observed. The dislocation glide within the deformation bands is additionally obstructed by the newly formed phase boundaries. The mechanisms of the deformation band formation and the strengthening by the α'-martensite nucleation are summarized in Fig. 11.33.

During plastic deformation, the equilibrium dissociation width of beneficially oriented partial dislocations in austenite (1) is increased by external applied shear stress (2). New dislocations are generated and the deformation band forms (3), which is accompanied by conventional cold work strengthening. Formation of SFs and deformation bands on the secondary slip systems produces local strain fields that facilitate the nucleation of α'-martensite (4) having a specific volume of about 2.5% larger than austenite. The α'-martensite boundaries and the lattice strains resulting from the volume expansion are hard obstacles for the dislocation motion. They pin existing SFs, thus the further plastic deformation produces new (perfect) dislocations alongside the existing deformation band and leads to their dissociation (5). This explains the observed lateral growth of the deformation bands [40] and the high volume fraction of the ε-martensite of ≤ 25 vol% (Figs. 11.18 and 11.26) at moderate stages of straining.

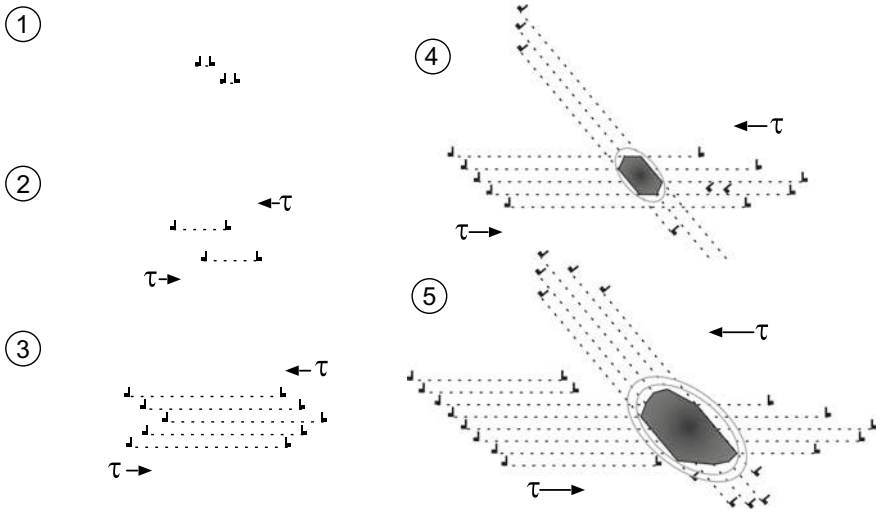

Fig. 11.33 The interplay of the deformation band formation and the α'-martensite nucleation contributes additionally to the strain hardening in austenite. Adopted from [61]

11.5.2 Orientation Dependence of the Stacking Fault and Deformation Band Formation

A complex, heterogeneous microstructure is observed in deformed austenitic steels, even if they consist of equiaxed grains with unimodal grain-size distribution. As shown in the ECCI micrograph in Fig. 11.34, in some grains the stacking faults and deformation bands dominate, whereas other grains are free of planar defects and exhibit dislocation structures instead.

These differences in the deformation behavior can be explained by the orientation dependence of the stacking fault and deformation band formation, which follows from the dependence of the difference between the Schmid factors of the leading and trailing partials on the individual grain orientation (Fig. 11.35a). These partial dislocations experience different shear stresses, which depends on the orientation of their Burgers vector with respect to the direction of the external load [9]. From Fig. 11.35a, it can be concluded that the grains oriented with their ⟨001⟩ direction nearly parallel to the applied compression should have the highest tendency to the stacking fault formation. In these grains, the leading partial dislocation has a clearly higher Schmid factor than the trailing one, thus the SFs are widened upon compression. For the grain orientations with a negative Schmid factor difference (Fig. 11.35a), the trailing partial dislocations move faster than the leading ones, thus the stacking fault is closed.

For the grains with negative difference of the Schmid factors of leading and trailing partial dislocation, this trend was confirmed by EBSD measurements, which revealed

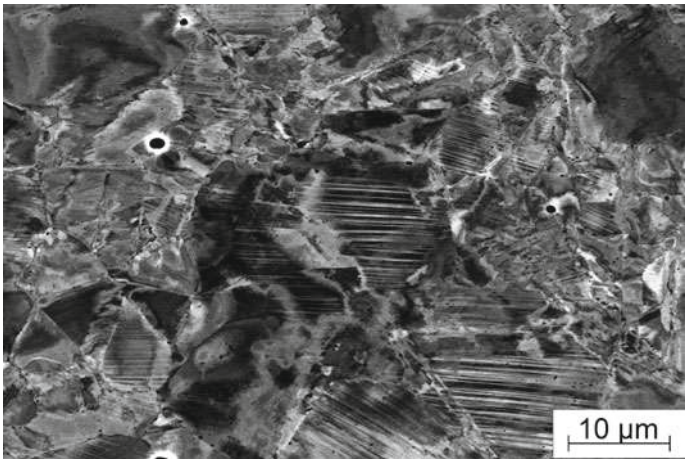

Fig. 11.34 Electron channeling contrast (ECC) image of the heterogeneous microstructure in a 15% strained PM X5CrMnNi16-6-9 steel. Adopted from [34]

that grains with the orientations between ⟨101⟩ and ⟨111⟩ along the deformation direction were almost free of deformation bands (Fig. 11.35c, e). In Fig. 11.35c, these grains are highlighted. Figure 11.35e shows their orientation density distribution. The highest density of SFs and deformation bands should be observed for grain orientations with positive Schmid factor difference (Fig. 11.35a). However, this expectation was not confirmed experimentally, as the ECCI/EBSD measurement (Fig. 11.35d, f) revealed that the grains with the highest density of SFs and deformation bands have orientations between ⟨102⟩ and ⟨113⟩ with respect to the compression direction. The reason for this apparent discrepancy is that the dissociation of perfect dislocations must be preceded by their formation that is activated according to the Schmid factor from Fig. 11.35b. After the initiation of faulting, the grain orientation can still be rotated by dislocation slip (on secondary slip systems), producing the typical formation of a ⟨101⟩ compression texture in *fcc* materials. This results in the observation of Fig. 11.35f that faulted grains are not sharply clustered around ⟨001⟩, but rather found between ⟨102⟩ and ⟨113⟩ orientations. The grains without stacking faults are oriented according to the ⟨101⟩ fiber texture in compressive load direction.

Consequently, the orientation dependence of the stacking fault and deformation band formation in austenite is controlled by the Schmid factors of perfect dislocations and SFs, because the plastic deformation of austenite is activated by the formation of perfect dislocation and their dissociation. For compression, the interplay of these mechanisms favors the SF formation on the primary slip system for orientations between ⟨102⟩, ⟨113⟩ and ⟨001⟩, while the formation of the deformation bands is delayed in grains having the orientations between ⟨101⟩, ⟨111⟩, ⟨113⟩ and ⟨102⟩. For tensile deformation, the favorable and unfavorable grain orientations are exchanged, because the sign of the Schmid factors of the partials switches with the inversion of the load direction.

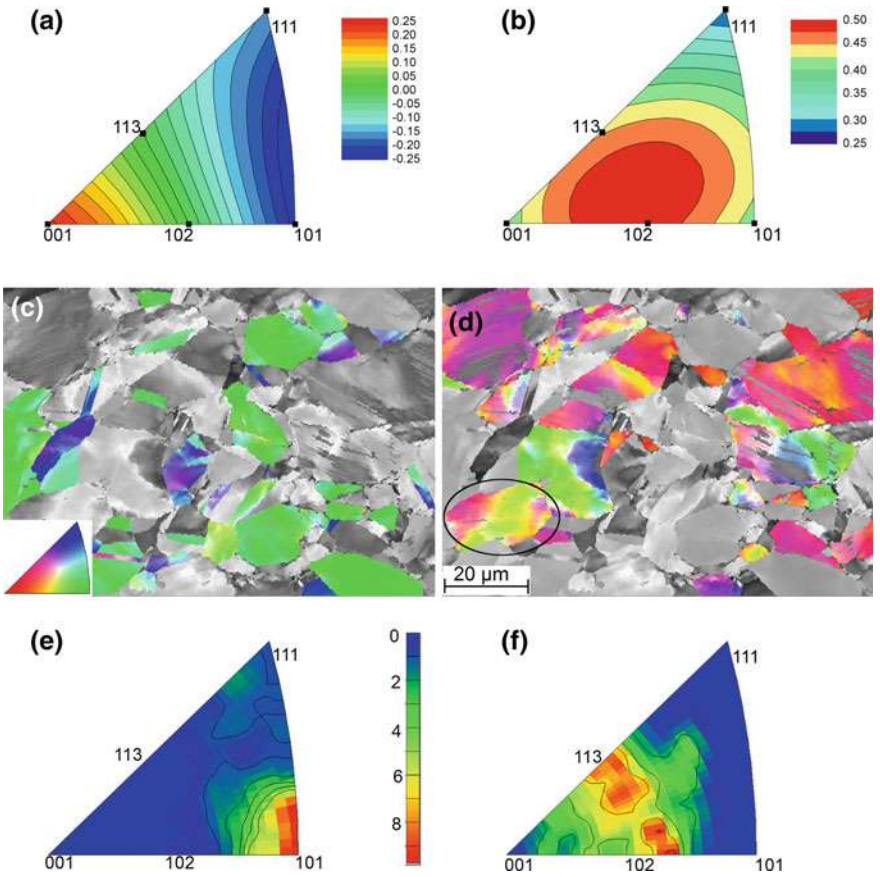

Fig. 11.35 Orientation dependence of the stacking fault and deformation band formation after 15% compression. In panel (**a**), the difference between the Schmid factors of leading and trailing partial for compression is presented. In panel (**b**), the orientation dependence of the Schmid factor for perfect dislocations on the primary slip system is plotted. EBSD maps show the orientation of grains that are almost free of deformation bands (**c**) and that accommodate pronounced deformation bands (**d**). The grey scale values in panels (**c**) and (**d**) are related to the EBSD band contrast. The corresponding inverse pole figures shown in panels (**e**) and (**f**) depict the orientation density distribution of the respective grains. Adopted from [34]

11.5.3 Dependence of the Deformation Mechanisms on Local Chemical Composition and Temperature

The dependence of the stacking fault and deformation band formation on the local orientation of the austenite grains is no exclusive reason for the existence of complex heterogeneous microstructures that are typically observed in deformed austenitic steels. In general, the prevailing deformation mechanism in these steels depends on the SFE of austenite, which is, from the thermodynamic point of view, a function

of the difference between the Gibbs energy of austenite and the Gibbs energy of ε-martensite (Sect. 11.2.3.1). As the difference of the Gibbs energies depends on the chemical composition of the steel, the deformation mechanisms are strongly influenced by the concentrations of the alloying elements. This is not only true on the macroscopic scale, where the SFE is generally affected by the overall chemical composition of the TRIP/TWIP steels (Sect. 11.4.3), but also on the microscopic scale, where local concentration fluctuations lead to a coexistence of deformation mechanisms even within individual grains [127].

Another result of the thermodynamic consideration of SFE is that the stacking fault energy increases with increasing temperature (through the temperature dependence of the Gibbs energies). The corresponding dependence of the deformation mechanisms on the temperature is illustrated in Fig. 11.36 for the steel composition X3CrMnNi16-6-6. From the XRD patterns, it can be seen that at the end of the uniform elongation the amount of the martensitic transformation decreases with increasing deformation temperature. As discussed in Sects. 11.2 and 11.3, both martensites (ε and α') occur in deformation bands, which accommodate a high density of (ordered) SFs. With decreasing deformation temperature, the SFE decreases, which facilitates the formation of extended SFs and the transformation of austenite to ε- and α'-martensites. The sample deformed at −60 °C contains mainly α'-martensite. At higher temperatures (above room temperature), the increase of SFE with increasing deformation temperature hinders the SF formation. Above approx. 60 °C, the deformed steel X3CrMnNi16-6-6 consists predominantly of austenite. The diffraction peaks corresponding to the *bcc* phase that were observed above 100 °C stem from initial δ-ferrite,

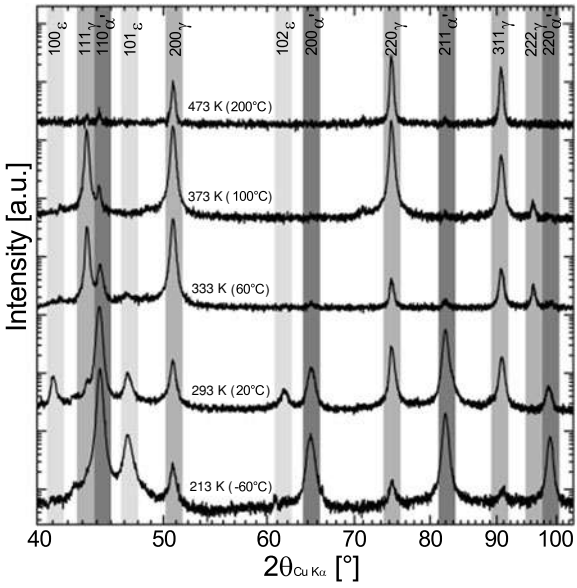

Fig. 11.36 XRD patterns after mechanical straining of cast TRIP steel samples at different testing temperatures until the end of uniform elongation (see right column of Fig. 11.37), indicating different amounts of martensitic transformation and remaining austenite [4]

which is also present in small fractions from the primary ferritic solidification of the cast material.

The results of XRD phase analysis were complemented by the SEM/EBSD experiments (Fig. 11.37), which helped in visualization of the microstructure defects and their arrangement that are related to the change in the phase composition of the deformed samples.

It was confirmed that the martensites, which form at the deformation temperatures below 60 °C, grow first inside and later out of the (former) deformation bands (Fig. 11.37a, b, f and g). At deformation temperatures above 60 °C, the martensite formation is reduced, while the twinning of austenite and the formation and slip of perfect dislocations become the most important mechanisms of the plastic deformation (Fig. 11.37c, d, e, h, i and j). At the deformation temperature of 60 °C, all microstructure features, i.e., α'-martensite, SFs, ε-martensite and twins in austenite are present (Fig. 11.37c, h), which means that the deformation mechanisms facilitated by the formation of the respective microstructure feature coexist. At the deformation temperatures above 60 °C, the density of twins in austenite increases rapidly (Fig. 11.37d, i). As the twins act as obstacles for dislocation glide, the perfect dislocations are concentrated in the areas between the deformation bands consisting of twins (Fig. 11.37d, e). At 200 °C, twins are only scarcely observed and dislocation configurations indicate that the deformation was essentially carried by perfect dislocation slip (Fig. 11.37e, j).

The temperature dependence of the deformation mechanisms discussed above is depicted schematically in Fig. 11.38. The link between the deformation temperature and SFE (γ_{SF}) emphasizes that the deformation mechanisms are essentially controlled by the stacking fault energy. The SFE at room temperature was determined experimentally (Sect. 11.4.3). The increase of SFE with increasing temperature was calculated from the change of $\Delta G^{\gamma\rightarrow\varepsilon}$ with temperature (Sect. 11.2.3.1).

The dislocation-induced plasticity is the fundamental deformation mechanism, thus its occurrence is highlighted by a grey hachure in the entire temperature range. At room temperature, the perfect dislocations dissociate quickly upon deformation, and form stacking faults. The stacking faults concentrate in deformation bands and form ε-martensite, below the critical temperature (M_D) also α'-martensite. Below the martensite start temperature (M_s), the formation of α'-martensite is further accelerated even without deformation. A high volume of α'-martensite at low (deformation) temperatures is one of the reasons for a high ultimate tensile stress (UTS in Fig. 11.38). Another reason for the increase of UTS with decreasing deformation temperature is the reduction of the mean free path of dislocations in the deformation bands by the successive nucleation of α'-martensite crystallites (cf. Sect. 11.5.1).

In contrast to UTS, which decreases monotonously with increasing deformation temperature, the uniform elongation (UE) shows pronounced maximum between room temperature and 150 °C, which corresponds to the SFE range between 15 and 34 mJ/m^2. In this temperature/SFE range, an intensified formation of ε-martensite and twins was observed that was already reported for various austenitic stainless steels in literature [59, 128]. The high amount of local shear approaching $0.35\left(\cong \sqrt{2}/4\right)$ and

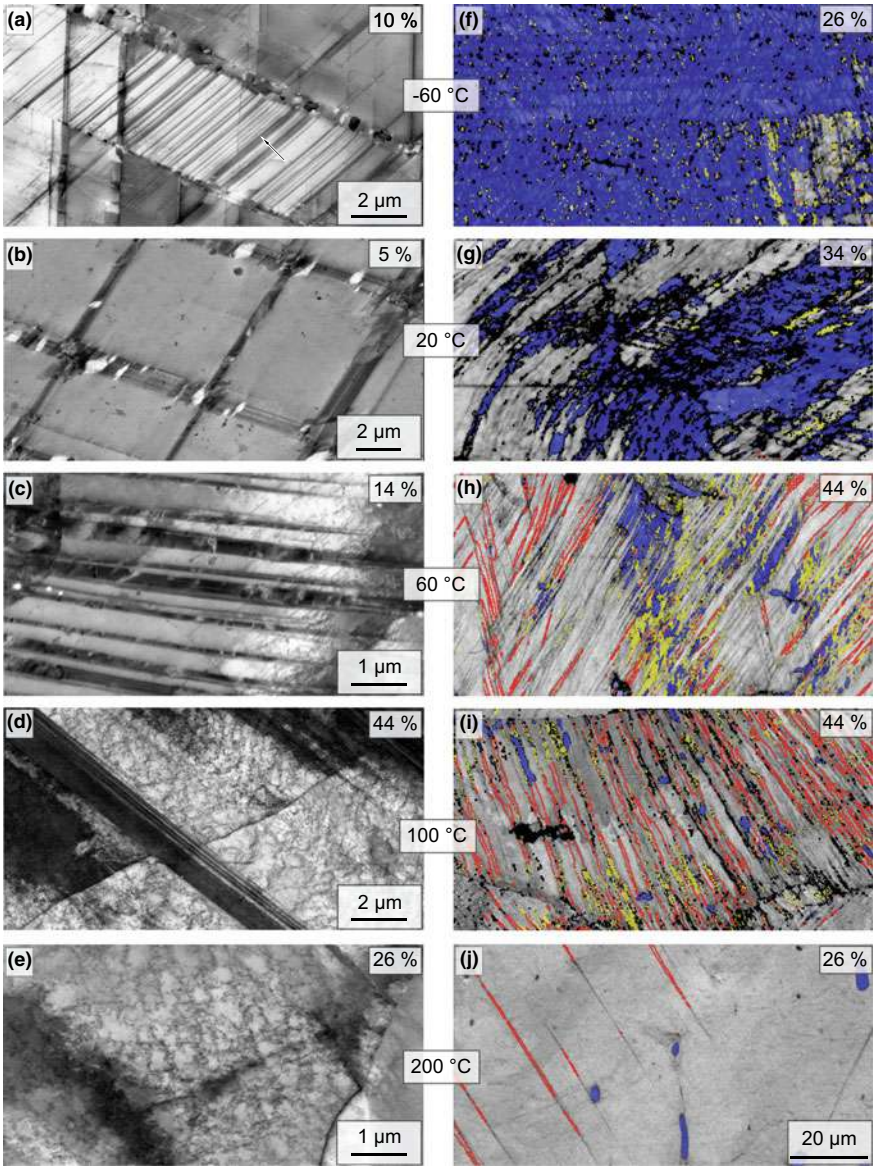

Fig. 11.37 Micrographs of coarse-grained TRIP/TWIP steel samples deformed at different strains at various testing temperatures. Left column: inverted ECCI images showing the deformation microstructures. Right column: EBSD phase maps highlighting austenite (the grey scale corresponds to the band contrast), ε-martensite (in yellow), α'-martensite (in blue) and not indexed regions (in black). The red lines mark the $\Sigma 3$ boundaries between deformation twins. All EBSD maps share the same scale bar. According to [4]

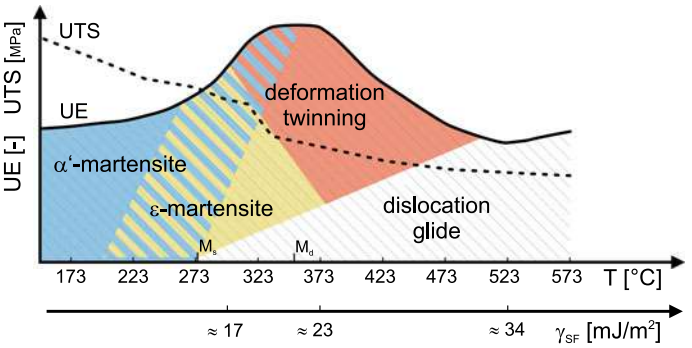

Fig. 11.38 Schematic representation of temperature dependence of the active deformation mechanisms in the X3 CrMnNi16-6-6 steel and their influence on ultimate elongation (UE) and ultimate tensile strength (UTS) [4]. The relationship between temperature and SFE (γ_{SF}) is shown in order to make clear that the dominant deformation mechanisms in austenitic steels are controlled by the stacking fault energy

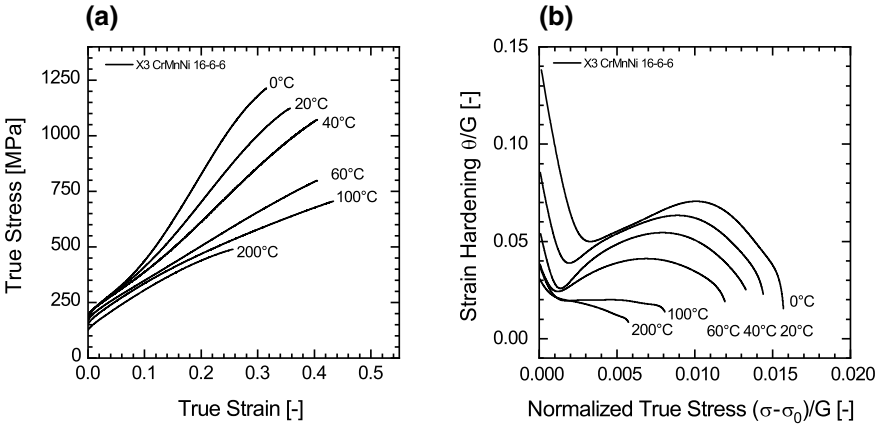

Fig. 11.39 Stress-strain curve (**a**) and strain hardening (**b**) of the X3CrMnNi16-6-6 TRIP/TWIP steel deformed at temperatures between 0 and 200 °C [4]

$0.71(\cong \sqrt{2}/2)$ for ε-martensite and twins, respectively, which is stored within the deformation bands because of the high SF density (see Sect. 11.2.3.1), contributes significantly to the overall dislocation based plasticity.

The alteration of deformation mechanisms with the temperature is also responsible for the change of the shape of the stress-strain curve and for the magnitude of the strain hardening (Fig. 11.39). The correlation between Figs. 11.38 and 11.39 confirms that the α'-martensite formation is a very effective hardening mechanism.

11.6 Conclusions

In this Chapter, the microstructure aspects of the deformation mechanisms in metastable austenitic steels were discussed. It was shown that the presence and form of the deformation bands play a crucial role in understanding the mechanical properties of the steels. It was demonstrated, that the deformation bands are composed of wide and tightly arranged stacking faults and, in some cases, of crossing deformation bands. The formation and widening of the stacking faults are the consequences of a low stacking fault energy of austenite, which facilitates the dissociation of perfect dislocations and the separation of partial dislocation under applied mechanical load. A high density of stacking faults within the deformation bands is recognized by diffraction methods (XRD, EBSD, SAED, FFT/HRTEM) either as an *hcp* stacking sequence, i.e., as ε-martensite, or as twinned austenite—depending on the SF density. A continuous transition between ε-martensite and twinned austenite is possible.

As the stacking fault energy of austenite depends strongly on its chemical composition and on temperature, already small variations in the kind and concentrations of the alloying elements and/or in the deformation temperature of the steel lead to serious changes in the dominant deformation mechanism. In many cases, perfect dislocations, isolated SFs, SF clusters, ε-martensite, twins and/or α'-martensite occur concurrently, but their fractions depend always on the stacking fault energy, and therefore on the steel composition, on the deformation temperature and on the deformation degree. Based on these results, the mechanical behavior of the TRIP/TWIP steels (mainly the ultimate tensile stress and the ultimate elongation) were related to the present microstructure defects and to their complex interplay. Formation of α'-martensite was found to contribute considerably to the strain hardening.

Finally, the potential of the in situ diffraction methods was illustrated. It was shown, how the stacking fault energy can be determined from the internal stresses measured during the deformation process and how the development of the deformation microstructure can be followed during an in situ deformation experiment.

Acknowledgements Former SFB799 project collaborators are highly acknowledged for their contributions: Daria Borisova, Anna Poklad, Benedikt Reichel and Volker Klemm. Further we thank Sabine Decker, Markus Radajewski, Steffen Wolf, Ralf Eckner, Christine Baumgart, Marco Wendler and Andreas Jahn for sample production and deformation experiments. The German Research Foundation (DFG) is acknowledged for funding the Collaborative Research Center SFB 799 (Project number 54473466).

References

1. H. Hasegawa, D.G. Pettifor, Phys. Rev. Lett. **50**, 130 (1983)
2. D. Bancroft, E.L. Peterson, S. Minshall, J. Appl. Phys. **27**, 291 (1956)
3. T. Takahashi, W. Bassett, Science **145**, 483 (1964)

4. S. Martin, S. Wolf, U. Martin, L. Krüger, D. Rafaja, Metall. Mater. Trans. **47**, 49 (2016)
5. W. Bleck, Werkstoffprüfung in Studium und Praxis, 15th edn. (Verlagsgruppe Mainz, 2011)
6. J.P. Hirth, J. Lothe, *Theory of Dislocations*, 2nd edn. (Krieger Publishing, Malabar, 1982)
7. P.C.J. Gallagher, Metall. Trans. **1**, 2429 (1970)
8. E.H. Lee, M.H. Yoo, T.S. Byun, J.D. Hunn, K. Farrell, L.K. Mansur, Acta Mater. **49**, 3277 (2001)
9. S.M. Copley, B.H. Kear, Acta Metall. **16**, 227 (1968)
10. T.S. Byun, Acta Mater. **51**, 3063 (2003)
11. M. Peach, J.S. Koehler, Phys. Rev. **80**, 436 (1950)
12. B.C. De Cooman, Y. Estrin, S.K. Kim, Acta Mater. **142**, 283 (2018)
13. A. Das, Metall. Mater. Trans. A **47**, 748 (2016)
14. F.C. Frank, W.R. Read, Phys. Rev. **79**, 722 (1950)
15. D. Hull, D.J. Bacon, *Introduction to Dislocations*, 5th edn. (Butterworth Heinemann, Oxford, 2011)
16. W.M. Lomer, Phil. Mag. **42**, 1327 (1951)
17. A.H. Cottrell, Phil. Mag. **43**, 645 (1952)
18. D. Borisova, V. Klemm, S. Martin, S. Wolf, D. Rafaja, Adv. Eng. Mater. **15**, 571 (2013)
19. N. Thompson, Proc. Phys. Soc. B **66**, 481 (1953)
20. S. Martin, C. Ullrich, D. Rafaja, Mater. Today: Proc. **2**, 643 (2015)
21. G.B. Olson, M. Cohen, Metall. Trans. A **7**, 1897 (1976)
22. D. Geissler, J. Freudenberger, A. Kauffmann, S. Martin, D. Rafaja, Phil. Mag. **94**, 2967 (2014)
23. P.J. Ferreira, P. Müllner, Acta Mater. **46**, 4479 (1998)
24. L. Vitos, J.-O. Nilsson, B. Johansson, Acta Mater. **54**, 3821 (2006)
25. A. Saeed-Akbari, J. Imlau, U. Prahl, W. Bleck, Metall. Mater. Trans. A **40**, 3076 (2009)
26. J. Nakano, P.J. Jacques, Calphad **34**, 167 (2010)
27. A.J.C. Wilson, Proc. R. Soc. London Ser. A **180**, 277 (1942)
28. M.S. Paterson, J. Appl. Phys. **23**, 805 (1952)
29. B.E. Warren, E.P. Warekois, Acta Metal. **3**, 473 (1955)
30. B.E. Warren, *X-Ray Diffraction*, 2nd edn. (Dover Inc., New York, 1990)
31. S. Martin, C. Ullrich, D. Šimek, U. Martin, D. Rafaja, J. Appl. Cryst. **44**, 779 (2011)
32. M.M.J. Treacy, J.M. Newsam, M.W. Deem, Proc. Roy. Soc. A **433**, 499 (1991)
33. L. Balogh, G. Ribárik, T. Ungár, J. Appl. Phys. **100**, 23512 (2006)
34. C. Ullrich, R. Eckner, L. Krüger, S. Martin, V. Klemm, D. Rafaja, Mater. Sci. Eng. A **649**, 390 (2016)
35. M.J. Whelan, P.B. Hirsch, Phil. Mag. **2**, 1303 (1957)
36. G. Thomas, W.L. Bell, H.M. Otte, Phys. Status Solidi A **12**, 353 (1965)
37. B. Cina, Acta Metall. **6**, 748 (1958)
38. C.W. Sinclair, R.G. Hoagland, Acta Mater. **70**, 4160 (2008)
39. H. Schumann, Krist. Tech. **9**, 1141 (1974)
40. A. Weidner, S. Martin, V. Klemm, U. Martin, H. Biermann, Scr. Mater. **64**, 513 (2011)
41. M. El-Tahawy, Y. Huang, T. Um, H. Choe, J.L. Lábár, T.G. Langdon, J. Gubicza, J. Mater. Res. Technol. **6**, 339 (2017)
42. C. E. Rodriguez Torres, F. H. Sánchez, A. González, F. Actis, R. Herreara, Metall. Mater. Trans. A **33**, 25 (2002)
43. K. Guy, E. Butler, D. Wes, J. de Phys. Colloques. **43**, 575 (1982)
44. L. Rémy, Acta Metall. **25**, 173 (1977)
45. R. Clendenen, H. Drickamer, J. Phys. Chem. Solids **25**, 865 (1964)
46. H.-K. Mao, W.A. Bassett, T. Takahashi, J. Appl. Phys. **38**, 272 (1967)
47. T. Takahashi, W.A. Bassett, M. Hokwang, J. Geophys. Res. B **73**, 4717 (1968)
48. P.M. Giles, M.H. Longenbach, A.R. Marder, J. Appl. Phys. **42**, 4290 (1971)
49. M. Friák, M. Šob, Phys. Rev. B **77**, 174117 (2008)
50. M. Friák, Steel Res. Int. **82**, 86 (2011)
51. N.A. Zarkevich, D.D. Johnson, Phys. Rev. B **91**, 174104 (2015)

52. S. Ackermann, S. Martin, M.R. Schwarz, C. Schimpf, D. Kulawinski, C. Lathe, S. Henkel, D. Rafaja, H. Biermann, A. Weidner, Metall. Mater. Trans. A **47**, 95 (2016)
53. H. Le Chatelier, Comptes Rendus **99**, 786 (1884)
54. M. Hillert, *Phase Equilibria, Phase Diagrams and Phase Transformations*, Chapter 6.9, 2nd edn. (Cambridge University Press, 2008)
55. J.R. Patel, M. Cohen, Acta Metall. **1**, 531 (1953)
56. L. Kaufman, M. Cohen, Prog. in Met. Phys. **7**, 165 (1958)
57. I. Tamura, Met. Sci. **16**, 245 (1982)
58. J.A. Venables, Phil. Mag. **7**, 35 (1962)
59. F. Lecroisey, A. Pineau, Metall. Trans. **3**, 387 (1972)
60. G.B. Olson, M. Cohen, J. Less Comm. Met. **28**, 107 (1972)
61. S. Martin, S. Wolf, S. Decker, L. Krüger, U. Martin, Steel Res. Int. **86**, 1187 (2015)
62. X.-S. Yang, S. Sun, T.-Y. Zhang, Acta Mater. **95**, 264 (2015)
63. Y. Tian, O.I. Gorbatov, A. Borgenstam, A.V. Ruban, P. Hedström, Metall. Mater. Trans. A **48**, 1 (2017)
64. A.J. Bogers, W.G. Burgers, Acta Metall. **12**, 255 (1964)
65. L. Bracke, L. Kestens, J. Penning, Scripta Mater. **57**, 385 (2007)
66. G. Kurdjumow, G. Sachs, Z. Phys. **64**, 325 (1930)
67. Z. Nishiyama, *Martensitic Transformation*, 1st edn. (Academic Press, New York, 1978)
68. G. Olson, M. Azrin, Metall. Mater. Trans. A **9**, 713 (1978)
69. J. Talonen, P. Aspegren, H. Hänninen, Mater. Sci. Technol. **20**, 1506 (2004)
70. L.S. Zevin, G. Kimmel, I. Mureinik, *Quantitative X-Ray Diffractometry* (Springer, New York, 1995)
71. H.M. Rietveld, J. Appl. Cryst. **2**, 65 (1969)
72. R.A. Young, *The Rietveld Method* (Oxford University Press, IUCr, 1993)
73. S. Allain, J.-P. Chateau, D. Dahmoun, O. Bouaziz, Mater. Sci. Eng. A **397–389**, 272 (2004)
74. O. Bouaziz, Scripta Mater. **66**, 982 (2012)
75. D.R. Steinmetz, T. Jäpel, B. Wietbrock, P. Eisenlohr, I. Gutierrez-Urrutia, A. Saeed-Akbari, T. Hickel, F. Roters, D. Raabe, Acta Mater. **61**, 494 (2013)
76. S. Allain, J.-P. Chateau, O. Bouaziz, Steel Res. Int. **79**, 299 (2002)
77. K. Renard, P.J. Jacques, Mater. Sci. Eng. A **542**, 8 (2012)
78. D. Barbier, N. Gey, S. Allain, N. Bozzolo, M. Humbert, Mater. Sci. Eng. A **540**, 212 (2012)
79. C. Schimpf, M. Motylenko, D. Rafaja, Mater. Char. **86**, 190 (2013)
80. M.A. Krivoglaz, *Theory of X-ray and Thermal Neutron Scattering by Real Crystals* (Plenum Press, New York, 1969)
81. M. Wilkens, Phys. Status Solidi A **2**, 359 (1970)
82. P. Klimanek, R. Kužel, J. Appl. Cryst. **21**, 59 (1988)
83. R. Kužel, P. Klimanek, J. Appl. Cryst. **21**, 363 (1988)
84. T. Ungár, G. Tichy, Phys. Status Solidi A **171**, 425 (1999)
85. T. Ungár, I. Dragomir, Á. Révész, A. Borbély, J. Appl. Cryst. **32**, 992 (1999)
86. A. Borbély, J. Dragomir-Cernatescu, G. Ribárik, T. Ungár, J. Appl. Cryst. **36**, 160 (2003)
87. I. Dragomir, T. Ungár, J. Appl. Cryst. **35**, 556 (2002)
88. N.C. Popa, J. Appl. Cryst. **31**, 176 (1998)
89. D.J.H. Cockayne, Phil. Mag. **20**, 1265 (1969)
90. C.C. Bampton, I.P. Jones, M.H. Loretto, Acta Metall. **26**, 39 (1978)
91. M.J. Mills, P. Stadelmann, Phil. Mag. A **60**, 355 (1989)
92. J. Lu, L. Hultman, E. Holmström, K.H. Antonsson, M. Grehk, W. Li, L. Vitos, A. Golpayegani, Acta Mater. **111**, 39 (2016)
93. M.J. Whelan, Proc. Roy. Soc. A **249**, 114 (1959)
94. A. Howie, P.R. Swann, Phil. Mag. **6**, 1215 (1961)
95. A. Ruff, L. Ives, Acta Metall. **15**, 189 (1967)
96. R.M. Latinision, A.W. Ruff, Metall. Trans. **2**, 505 (1971)
97. I.L. Dillamore, Phil. Mag. **9**, 517 (1964)
98. I.L. Dillamore, Metall. Trans. **1**, 2463 (1970)

99. R.P. Reed, R.E. Schramm, J. Appl. Phys. **45**, 4705 (1974)
100. R.E. Schramm, R.P. Reed, Metall. Trans. A **6**, 1345 (1975)
101. J. Talonen, H. Hänninen, Acta Mater. **55**, 6108 (2007)
102. T.-H. Lee, E. Shin, C.-S. Oh, H.-Y. Ha, S.-J. Kim, Acta Mater. **58**, 3173 (2010)
103. J.S. Jeong, W. Woo, K.H. Oh, S.K. Kwon, Y.M. Koo, Acta Mater. **60**, 2290 (2012)
104. D. Rafaja, C. Krbetschek, C. Ullrich, S. Martin, J. Appl. Cryst. **47**, 936 (2014)
105. D. Rafaja, C. Krbetschek, D. Borisova, G. Schreiber, V. Klemm, Thin Solid Films **530**, 103 (2013)
106. S. Allain, J.-P. Chateau, O. Bouaziz, S. Migot, N. Guelton, Mater. Sci. Eng. A **387–389**, 158 (2004)
107. S. Curtze, V.-T. Kuokkala, A. Oikari, J. Talonen, H. Hänninen, Acta Mater. **59**, 1068 (2011)
108. A. Abbasi, A. Dick, T. Hickel, J. Neugebauer, Acta Mater. **59**, 3041 (2011)
109. G.M. de Bellefon, J.C. van Duysen, K. Sridharan, J. Nucl. Mater. **492**, 227 (2017)
110. N. Chaudhary, A. Abu-Odeh, I. Karaman, R. Arróyave, J. Mater. Sci. **52**, 11048 (2017)
111. E. Kröner, Z. Phys. **151**, 504 (1958)
112. A. G. Every, A. K. McCurdy, Fe-Al-Nb-O, in *Springer Materials—The Landolt–Börnstein Database*ed. by D.F. Nelson (2011)
113. C. Ullrich, S. Martin, C. Schimpf, A. Stark, N. Schell, D. Rafaja, Adv. Eng. Mater. **21**, 1801101 (2019)
114. H. Van Swygenhoven, S. Van Petegem, Mater. Charact. **78**, 47 (2013)
115. L. Lutterotti, S. Matthies, H.-R. Wenk, A.S. Schultz, J.W. Richardson, J. Appl. Phys. **81**, 594 (1997)
116. L. Lutterotti, S. Matthies, H.-R. Wenk, IUCr Commission on Powder Diffraction Newsletter **21**, 14 (1999)
117. S. Matthies, G.W. Vinel, Phys. Status Solidi A **112**, K111 (1982)
118. M. Ferrari, L. Lutterotti, J. Appl. Phys. **76**, 7246 (1994)
119. A. Creuziger, C.A. Calhoun, W.A. Poling, T. Gnäupel-Herold, J. Appl. Cryst. **51**, 720 (2018)
120. S. Allain, J.-P. Chateau, O. Bouaziz, Mater. Sci. Eng. A **387–389**, 143 (2004)
121. T. Narutani, Mater. Trans. JIM **30**, 33 (1989)
122. M. Wilkens, Phys. Status Solidi A **104**, K1 (1987)
123. L. Rémy, Acta Metall. **26**, 443 (1978)
124. I. Gutierrez-Urrutia, D. Raabe, Acta Mater. **60**, 5791 (2012)
125. L. Rémy, Metall. Trans. A **12**, 387 (1981)
126. O. Bouaziz, S. Allain, C.P. Scott, P. Cugy, D. Barbier, Curr. Opin. Solid State Mater. Sci. **15**, 141 (2011)
127. S. Martin, O. Fabrichnaya, D. Rafaja, Mater. Lett. **159**, 484 (2015)
128. L. Rémy, A. Pineau, Mater. Sci. Eng. **28**, 99 (1977)

Chapter 12
Investigations on the Influence of Strain Rate, Temperature and Reinforcement on Strength and Deformation Behavior of CrMnNi-Steels

Ralf Eckner, Christine Baumgart, and Lutz Krüger

Abstract This section presents the results of comprehensive investigations into the strength and deformation behavior of CrMnNi-TRIP/TWIP steels and particle-reinforced TRIP-Matrix-Composites. These investigations combined quasi-static and dynamic tensile, compressive, and plate impact tests with ex situ microstructure analysis using electron microscopy and diffraction techniques on representative samples. The aim was the investigation and microstructurally-based description and modeling of the temperature and strain rate dependent strength, deformation and failure behavior of these advanced materials. It could be shown that the behavior of austenitic CrMnNi steels is controlled by different deformation mechanisms. These include mechanical twinning and martensitic phase transformations, whose occurrences or interactions are influenced by the chemical composition or the austenite stability, the stacking fault energy, the deformation temperature and rate as well as by the loading direction. Furthermore, the mechanical properties of honeycomb structures made of CrMnNi steel or TRIP-Matrix-Composites have been investigated. These are intended as lightweight and high strength components to improve the crash performance of constructions in the field of mobility. Since their mechanical properties are influenced by several parameters such as the chemical composition of the material, the structure type or the reinforcement content, detailed analyses are necessary before their application in vehicle components.

R. Eckner (Emeritus)
Institute of Materials Engineering, Technische Universität Bergakademie Freiberg, Gustav-Zeuner-Str. 5, 09599 Freiberg, Germany

C. Baumgart · L. Krüger (✉)
Institute of Materials Engineering, Technische Universität Bergakademie Freiberg, Gustav-Zeuner-Str. 5, 09599 Freiberg, Germany
e-mail: krueger@ww.tu-freiberg.de

H. Biermann and C. G. Aneziris (eds.), *Austenitic TRIP/TWIP Steels and Steel-Zirconia Composites*, Springer Series in Materials Science 298,
https://doi.org/10.1007/978-3-030-42603-3_12

12.1 Introduction

The automotive industry is always looking for ways to increase safety and performance while reducing fuel consumption. These requirements led to the development of so-called *High Strength Steels* (HSS) and *Advanced High Strength Steels* (AHSS). Among these, high-alloy austenitic stainless steels are characterized by extraordinary properties such as excellent formability, high corrosion resistance, and good weldability, and are used for applications ranging from cryogenic up to elevated temperatures. Such steels take advantage of the TRIP- and/or TWIP-effects (TRansformation Induced Plasticity or TWinning Induced Plasticity), which are both triggered by plastic deformation and depend strongly on the stacking fault energy of the steel. At relatively high stacking fault energies (>40 mJ/m^2), the material deforms and hardens substantially due to the motion of dislocations. Stacking fault energies between 20 and 40 mJ/m^2 favor the emergence of stacking faults and deformation twins (TWIP-effect) [1–3]. Such planar defects act as obstacles for further dislocation movement and consequently increase the strain hardening rate of the material, which is known as the "dynamic Hall-Petch effect" [4]. In steel with lower stacking fault energy, the TRIP-effect is evident which is associated with the formation of ε- and α'-martensite and involves the enhancement of strength and ductility below the M_d-temperature [5–7]. The stacking fault energy mainly depends on the chemical composition of the steel and the deformation temperature [8]. The necessary mechanical driving force for the transformation $\gamma \rightarrow \alpha'$ is provided by the mechanical stress applied on the material [7]. Both mechanisms are already being used in the development of modern advanced high strength steels, e.g. for automotive applications [9]. These materials offer great potential for improving occupant safety in the event of a crash as well as for lightweight construction to reduce weight and energy consumption.

Within the Collaborative Research Center 799, two development routes are utilized in order to generate weight efficient energy absorbing materials. On the one hand, the combination of two different material groups. This exploits the beneficial properties of each component, like in the case of mother-of-pearl, and is implemented by reinforcing ductile TRIP-steel with high strength MgO partially stabilized zirconia (Mg-PSZ) [10]. On the other hand, the use of these metal matrix composites (MMC) in cellular networks follows the example of wood or cork which could have a favorable strength to weight ratio [11]. Those cellular materials belong to the honeycomb-like structures. Unlike established materials for cellular structures such as aluminum, titanium or magnesium, TRIP-steel and TRIP-Matrix-Composites do not belong to light metals. However, it has been proven that the deformation induced phase transformation of TRIP-steels is an energy consuming process which helps to balance the influence of a higher density when comparing the specific energy absorption capability of different structures [12].

The intention of the present survey is to highlight the deformation mechanisms which are active under dynamic loading and under shock wave loading by flyer-plate impact in bulk cast high-alloy CrMnNi TRIP/TWIP-steel. Detailed investigations of the developed microstructure were performed in order to explain the experimental results, with special focus on the martensitic transformation. Furthermore, static

compression tests were conducted at room temperature in order to compare the fundamental performance of the different cellular materials made of TRIP-steel and TRIP-Matrix-Composites with focus on the compressive strength, deformation and damage behavior.

12.2 High Strain Rate Deformation of Austenitic High-Alloy TRIP/TWIP Steel

12.2.1 Processing and Experimental Methods

Table 12.1 represents the chemical compositions of the investigated high-alloy austenitic TRIP/TWIP steel. The examined material is based on a patent-protected development [13] and is described as 16-6-6, according to the concentrations of Cr, Mn, and Ni in wt%. The material was cast in plates (dimensions 200 × 200 × 16 mm^3) by ACTech GmbH (Freiberg, Germany) using sand casting technology. The manufactured samples were subsequently solution-heat-treated at 1323 K (1050 °C) for 30 min to retransform any martensite induced by previous machining. A dendritic austenite microstructure with coarse grains in the range of 100–1000 μm was received. Due to the chemical composition of the steel, a certain amount of δ-ferrite (~2 vol%) was formed during solidification. This steel belongs to AHSS of the 1st generation and is characterized by a high strain hardening capacity in combination with high formability, though the yield strength is rather low (YS ~200 MPa, UTS ~800 MPa, total elongation ~50%) [14].

Quasistatic compression tests at 0.0004 1/s were performed in a servohydraulic universal testing machine. For the dynamic impact and high-rate experiments up to 2300 1/s a drop weight tower and a Split-Hopkinson pressure bar system (SHPB) were used [15]. All mechanical tests were carried out on cylindrical samples with 6 mm in diameter and 6 mm in height. The samples were instrumented with strain gauges in order to allow a local deformation measurement even at high deformation speeds. In order to obtain consistent high rate compressive stress/strain data, the SHPB apparatus was modified by a pulse shaping technique using OFHC-copper platelets [16] and numerical dispersion correction [17].

In order to determine the strength properties of the test material, a flyer-plate impact assembly of the Russian Academy of Sciences, Institute of Problems of Chemical Physics, Chernogolovka near Moscow was used, which is shown schematically in Fig. 12.1. The test specimens had a thickness of 5 mm with a square area of 45 ×

Table 12.1 Chemical composition of the investigated high-alloy CrMnNi TRIP/TWIP steel

(wt%)	C	N	Cr	Mn	Ni	Si	Fe + others
Cast X3CrMnNi16-6-6 (abbr.: 16-6-6)	0.03	0.03	15.5	6.1	6.1	0.9	Bal.

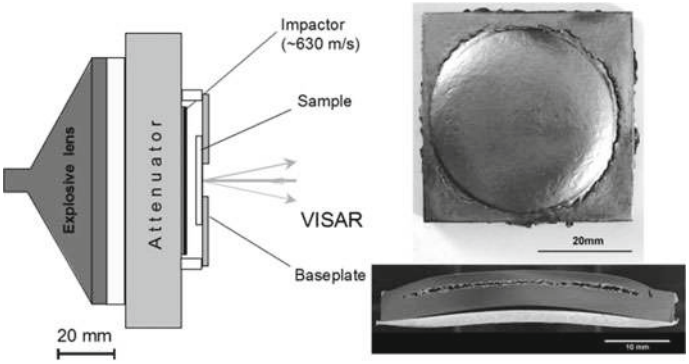

Fig. 12.1 Schematic setup of the plate impact experiments to determine the strength properties under planar shock loading at room temperature [20]

45 mm^2 and were shocked by plates (thickness 2 mm) of technically pure aluminum. The acceleration of the flyer-plates was carried out by means of a blasting lens to speeds of 650 ± 30 m/s. The shock pressure yielded 7–8 GPa and the strain rate behind the wave front and before spallation was 5–6 × 10^4 1/s. The planar impact of the aluminum plate produced a shock wave within the target sample and resulted in a uniaxial state of deformation over a pulse length of less than one microsecond. Therefore, the free surface velocity profiles were recorded using VISAR Laser Doppler Velocimetry [18] with a time resolution of ~1 ns and a space resolution of ~0.1 mm^2, giving a measurement accuracy of ~5 m/s. Evaluation of such plate-impact experiments is described in detail for instance in [19].

For shock wave experiments on large-volume samples at higher pressures, a plate-impact setup of the Freiberg High Pressure Research Center (FHP) was also used, which is shown schematically in Fig. 12.2. This experimental setup was originally developed for the high-pressure synthesis of ultra-hard materials (Diamond, c-BN, γ-Si_3N_4) and builds up on the findings and specifications of the EMI (Ernst Mach-Institute) in Freiburg [21]. The difference to the above-described plate impact structure of the Russian Academy of Sciences consists in the ability to produce reproducible pressures up to 120 GPa or more within the sample and thereby have a much larger sample volume available.

In the experiments, the amount of explosive used was varied, whereby pressures of 30, 60, 90 and 120 GPa (or 0.3–1.2 Mbar) could be set. After ignition, the flyer-plate was accelerated over a distance of 20 mm and then hit flat on the sample surface. Depending on the amount of explosive, the final velocity varied between 1.5 and 4 km/s. The target, the cylindrical material sample, was located in a form-fitting round container with a diameter of 220 mm, which was made of structural steel S355 (St-52). Below the sample a hardened steel plate was positioned, which was supported on a sand bed and acted as a damping plate or impulse trap. This design pursued two goals; on the one hand, the sample container prevented the free adiabatic expansion of the sample. On the other hand, the impedance difference between the

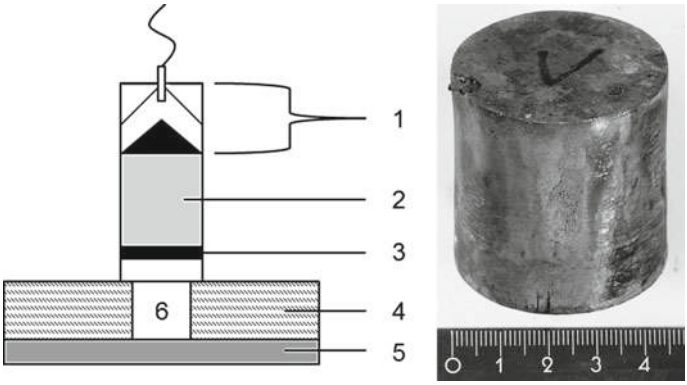

Fig. 12.2 Setup for shock experiments on large-volume samples: (1) plane wave generator with electric detonator (PETN explosive) (2) C-4 explosive (3) CrMnNi steel flyer-plate, (4) structural steel container (S355), (5) QT steel plate, (6) CrMnNi steel sample [22]

sample and the overlay was small, so that the shockwave was not reflected at the interface and the spallation could be prevented. Thus, the sample remained intact during the experiment and could then be mechanically removed from the sample container.

After mechanical testing, the α'-martensite volume fraction was quantified using a Metis MSAT type magnetic saturation device for both, the deformed compression specimens and shock-loaded conditions. For light-optical characterization, the samples were ground, polished, and etched with Beraha II etchant or V2A etchant, in order to contrast the deformation features such as deformation bands or martensite. Subsequently, microstructural investigations were carried out by scanning electron microscopy (SEM), transmission electron microscopy (TEM) in combination with electron backscatter diffraction (EBSD), selected area electron diffraction (SAED) or convergent beam electron diffraction (CBED) techniques.

12.2.2 Approaches to Rate-Dependent Constitutive Modeling

The influence of strain rate on the flow curves and the hardening behavior of metastable austenitic CrMnNi steels is of great importance considering technical application fields. Their plastic deformation is based essentially on the separation of Shockley partial dislocations and the subsequent stacking fault and deformation band formation [23, 24]. The increasing stacking fault density as well as the development of ε- and α'-martensite nuclei leads in consequence to strain hardening or to the dynamic Hall-Petch effect. However, the adiabatic sample heating effect increases with increasing strain rate, whereby much of the plastic deformation work remains in the sample as thermal energy. A nonlinear development of strain and strength characteristics with increasing strain rate is usually caused by this phenomenon. It

was as well shown that the α'-martensite formation rate decreases with increasing strain rate and tends towards zero at high strain values ($\varepsilon \geq 0.3$) [25], caused by an increasing stacking fault energy and a reduction in chemical driving force for the $\gamma \rightarrow \alpha'$ transformation [26, 27]. Previous studies highlighted the influence of a temperature change on the SFE and the separation distance of dislocations in detail [28]. The splitting into partial dislocations and the corresponding stacking fault formation require a critical stress level, which increases with increasing SFE. The SFE in turn increases with increasing temperature. In addition, both an increase in temperature and an increased strain rate increase the threshold stress for martensite formation [28, 29]. However, this effect is partly compensated, since the threshold stress for stacking fault or twin formation can be achieved at even lower strain values due to the rise in yield strength with increasing strain rate [30].

The reduced rate of martensite formation and the consequent decreasing strain hardening with increasing strain rate cause a decrease in flow stress with increasing deformation [25, 31]. On this occasion, the so-called curve crossing phenomenon can occur, whereby the strain softening leads to the intersection of the dynamic flow curves with the quasi-static flow curves [32]. In general, flattening of the flow curves can be observed at high strain rates, which is associated with a reduced maximum strength. The characteristic strain hardening curve is shifted to lower values and lower deformations, and the sigmoidal character changes into a plateau or disappears [33–35]. Furthermore, sample heating in high-speed tests leads to a decrease in the volume fraction of austenite converted into α'-martensite [25, 27, 36, 37]. Depending on the alloy composition and the degree of sample heating, a change in the dominant deformation mechanism is also possible, from stacking fault/ε-martensite formation to twinning or dislocation glide [8]. This transition is associated with decreasing strain hardening capability during deformation. Figure 12.3 shows results of strain-rate-dependent compression tests on the 16-6-6 steel alloy as an example for the effects mentioned. As expected, increasing strain rate led to crossing of the flow curves (Fig. 12.3a) owing to reduced strain hardening due to a lower fraction of α'-martensite formed (Fig. 12.3b).

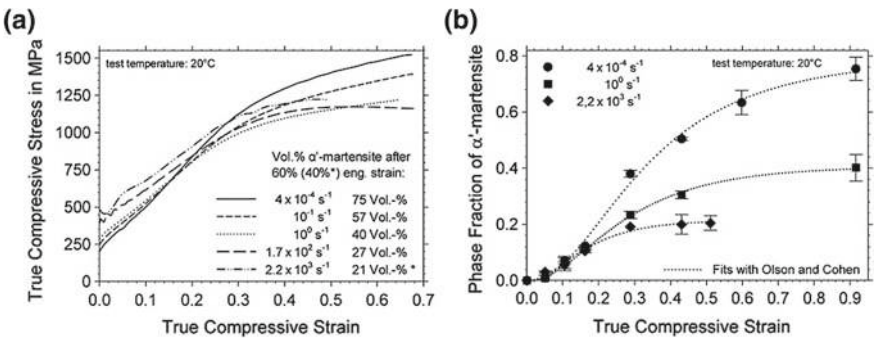

Fig. 12.3 CrMnNi16-6-6 steel: **a** Strain rate dependent mechanical behavior under compressive loading and **b** martensite kinetics at various strain rates (fitted according to [6]) [38]

Within the scope of the investigations, an empirical model of the flow stress on the basis of the rule of mixture (RM) was developed, which includes all important microstructural deformation mechanisms of CrMnNi TRIP steels as a function of temperature and strain rate. Several earlier research works dealt with the problem of modelling a deformation-induced martensitic transformation in austenitic steels. At this point, the publications of Ludwigson and Berger [39] and of Narutani et al. [40] are considered more in detail, representing two of the most significant works.

Ludwigson and Berger pointed out that the flow behavior of austenitic steel differs significantly from that of carbon steel due to the strain-induced martensitic transformation. For this reason, the flow curve cannot be described only by the relationship in (12.1),[1] which is valid for a variety of steels.

$$\sigma = K \cdot [\ln(1+\varepsilon)]^n \tag{12.1}$$

They assumed an autocatalytic formation reaction of the martensite and were therefore able to extend the existing model by a strength contribution of the martensitic phase depending on the actual strain value. Ludwigson and Berger introduced a factor A, which describes the ease with which an austenitic structure can undergo a strain-induced transformation to martensite, and the factors C and Q which characterize the martensite strength contribution. Equation (12.2)[2] shows the corresponding flow-curve equation relating true stress to strain.

$$\sigma = K[\ln(1+\varepsilon)]^n \cdot \left[1 - \left(1 + \frac{\varepsilon^{-B}}{A}\right)^{-1}\right] + C\left(1 + \frac{\varepsilon^{-B}}{A}\right)^{-Q} \tag{12.2}$$

Narutani et al. later recognized that for a more accurate description of the flow curves, it is also necessary to incorporate a softening term into the model. This necessity arises from the operation of the martensitic transformation as an additional deformation mechanism. For this reason, they developed a strain-corrected rule of mixture model (SCRM), based on the data of a metastable austenite, a stable austenite and a martensitic steel variant. Their complete constitutive relation for the plastic flow of metastable austenitic steel shows the following (12.3).[3]

---

[1] K = strength factor
n = strain-hardening index.

[2] A = factor describing the driving force for strain-induced $\gamma \rightarrow \alpha'$ transformation
B = factor describing the autocatalytic effect of transformed martensite
C = factor representing the flow stress of a fully martensitic structure
Q = factor describing stress contribution of the transformed martensite.

[3] $f_{\alpha'}$ = volume fraction of α'-martensite
α, β = material coefficients from the analysis of experimental data
σ_γ = flow stress of stable austenite
$\sigma_{\alpha'}$ = flow stress of martensite.

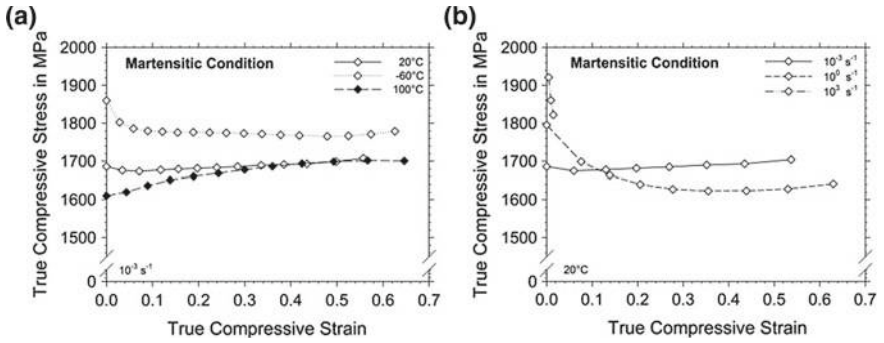

Fig. 12.4 CrMnNi16-6-6 steel: True stress-true strain curves of the α'-martensite phase: **a** influence of temperature and **b** strain rate effects [41]

$$\sigma = \left\{[1 - f_{\alpha'}] \cdot \sigma_{\gamma}(\varepsilon - \alpha \cdot f_{\alpha'}) + f_{\alpha'} \cdot \sigma_{\alpha'}(\varepsilon - \alpha \cdot f_{\alpha'})\right\} \cdot \left[1 - \beta \cdot \frac{df_{\alpha'}}{d\varepsilon}\right] \quad (12.3)$$

Recently, the existing approaches have been extended by Wolf et al. [38, 41, 42] in order to be able to model the behavior of highly metastable CrMnNi steels with low SFE by incorporating their temperature and strain rate dependence. They used the flow stress data of 16-6-6 steel in the strain rate regime 10^{-3} to 10^{3} 1/s and included the effect of thermal softening as a function of strain and strain rate. Of particular note is that the flow behavior of the martensitic phase was characterized at different temperatures and strain rates (see Fig. 12.4). Due to the low carbon content of the 16-6-6 alloy, the martensite phase received excellent ductility under compression loading up to 10^{0} 1/s. This was most likely also promoted by a few volume percent of unavoidable residual austenite. With increasing strain rate the flow stress of the martensite increased, but the influence of thermal softening also increased in significance up to adiabatic shear banding at 10^{3} 1/s.

For the formulation of the model, it was first necessary to represent the strain rate dependence of yield strength and strain hardening of the two phases austenite and martensite. To describe the yield stress, the technical proof stress values at 0.2% compression strain were used whose strain rate dependence for both phases can be described by the following logarithmic relationships[4] [38]:

$$\sigma_{d0.2}(\gamma) = \sigma_{d0.2}(\dot{\varepsilon}_{\text{ref}}) + (0.954 \cdot \ln(\dot{\varepsilon}) + 10.564) \cdot \ln\left(\frac{\dot{\varepsilon}}{\dot{\varepsilon}_{\text{ref}}}\right) \quad (12.4)$$

$$\sigma_{d0.2}(\alpha') = 16.094 \cdot \ln(\dot{\varepsilon}) + 1796.8 \quad (12.5)$$

[4] $\sigma_{d0.2}$ = proof stress value at 0.2% compression strain
$\dot{\varepsilon}_{\text{ref}}$ = reference strain rate (0.0004 1/s).

The strain hardening of a stable austenite phase could be described by (12.4), while no strain hardening was assumed for the martensitic phase based on the quasi-static results. In agreement with Narutani [40], the amount of strain caused by the martensitic phase transformation was also considered by the following correlation $\varepsilon_T = \alpha \cdot f_{\alpha'}$ with $\alpha = 0.12$. The introduction of a correction term was of particular importance in order to account for the dynamic softening caused by adiabatic sample heating.

For this purpose, a term was inserted, which originates from the well-known model of Johnson and Cook [43] [(12.6)[5]]. The amount of temperature increase originates from [44] with the extension by Meyer et al. [45].

$$\sigma_{\text{Mod}} = \sigma_{\text{Cal}} \cdot \left[1 - \left(\frac{\Delta T}{T_S - T_{\text{ref}}}\right)^m\right] \tag{12.6}$$

All the above considerations are included in the constitutive flow curve model of Wolf et al. [38] which is presented in (12.7). An estimation of the transformed volume fraction of α'-martensite $f_{\alpha'}$ can be done by using experimental data from magnetic measurements or on the basis of the model by Olson and Cohen [6], which is given in (12.8).[6]

$$\sigma_{\text{Mod}} = \left[\sigma_{d0.2}(\gamma) \cdot (\varepsilon + \varepsilon_T) \cdot f_\gamma + \sigma_{d0.2}(\alpha') \cdot f_{\alpha'}\right] \cdot \left[1 - \left(\frac{\Delta T}{T_S - T_{\text{ref}}}\right)^m\right] \tag{12.7}$$

$$f_{\alpha'} = 1 - \exp\left\{-\beta \cdot \left[1 - \exp(-\alpha \cdot \varepsilon)\right]^n\right\} \tag{12.8}$$

Figure 12.5 shows the modeled flow curves of 16-6-6 steel for three different strain rates in comparison with experimental data points. The accordance is very good and especially the curve crossing phenomenon at higher strain rates due to thermal softening effect is reproduced in the model. Thus, the goal could be achieved, to include the essential physical mechanisms of deformation in high-alloy CrMnNi TRIP/TWIP steels into a constitutive flow curve model. The underlying microstructural deformation mechanisms during high-speed loading are also of great importance and will be discussed more in detail below.

[5] σ_{Mod} = predicted flow stress with temperature correction
σ_{Cal} = calculated flow stress without temperature correction
T_S = melting temperature
T_{ref} = reference temperature at which the material is tested.

[6] α = parameter which defines the shear band formation with strain
β = parameter which defines the intersection of shear bands with strain
n = fixed exponent, which is fitted to the experimental data.

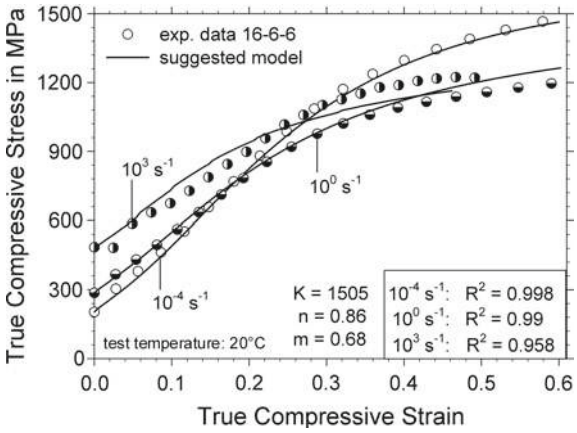

Fig. 12.5 Flow stress prediction of the developed constitutive model and experimentally determined flow stress data of 16-6-6 TRIP steel for three different strain rates [38]

12.2.3 Microstructural Deformation Mechanisms at High Strain Rates

As mentioned above, the primary deformation mechanism of TRIP/TWIP steels is the formation of planar defects such as separated Shockley partial dislocations, stacking faults or twins [8, 23, 24]. These mechanisms cause greater strength and strain hardening in comparison with wavy dislocation glide, which is active in common steel variants. The great particularity is the strong temperature dependence of these special deformation mechanisms, which means that the occurrence of glide planarity and martensite formation depends strongly on the respective environmental conditions during deformation. The investigations of Wolf et al. have shown that the same deformation mechanisms are active also in the high strain rate regime up to 10^3 1/s [25, 41, 42].

Figure 12.6 shows an example of the comparison of the microstructure of steel 16-6-6 after quasi-static compressive loading and dynamic compressive loading. In both cases, the microstructure of the deformed state up to 60% compression loading consisted of fine deformation bands and α'-martensite (cf. Fig. 12.6). Thin deformation bands evolved in the austenitic phase already at low strain values. With further straining, these deformation bands grew larger, crossed each other and α'-martensite nuclei were formed at their intersections. After quasi-static deformation the microstructure contained more and thicker bands, whereas after dynamic loading the bands appeared to be very thin and they were often oriented in one direction only. These findings were confirmed also by magnetic balance measurements, the results of which are already shown in Fig. 12.3b and indicated that an increasing strain rate caused a decreasing martensite formation due to adiabatic sample heating.

Generally, it is of great interest to use the additional deformation mechanisms, such as the TRIP- or the TWIP effect, since these lead to an increase in the energy

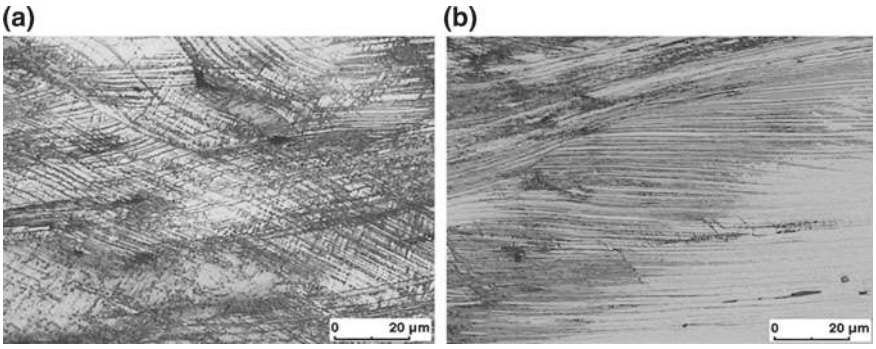

Fig. 12.6 Microstructure of steel 16-6-6 after deformation up to 60% compressive strain at strain rate of **a** 10^{-4} 1/s and **b** 10^{2} 1/s [25]

absorption capability of a material [25, 46] and thus, for example, to improved occupant protection in the event of impact in the automotive sector. Borisova et al. have shown that the high energy absorption results from interactions between individual microstructure defects with complex defect structures in which the formation of stacking faults can absorb approximately 1/30 of the whole deformation energy only [47]. Other essential absorption mechanisms include: (1) transition regions between ε-martensite and twinned austenite, (2) the formation of α'-martensite in deformation bands and (3) the formation of Lomer-Cottrell locks, stacking fault tetrahedra, and dislocation clusters. Nevertheless, the absorption of mechanical energy corresponds to the product of achievable strength level and the maximum ductility. Martin et al. showed that the strain hardening in TRIP/TWIP steels results from a continuous fragmentation of the dislocation mean free path due to deformation bands, stacking faults or the nucleation of α'-martensite [23]. A comparative consideration demonstrated that α'-martensite (G/25)[7] has a higher work hardening capacity than twins (G/50) in the austenite. However, the tensile elongation contribution is much more pronounced when twinning occurs. Huang et al. measured the greatest increase in ductility as soon as a high degree of glide planarity occurred, that means the occurrence of separated dislocations, stacking faults or austenite twins [48]. By contrast, the increase in tensile elongation due to α'-martensite formation was at best only 1/4 of that due to twinning.

As shown above, both the temperature dependence and the strain-rate dependence of the mechanical properties are important factors if the use of TRIP/TWIP steels for dynamically loaded components is considered. When the strain rate is further increased up to 10^{4} 1/s or above, the deformation and stresses are characterized by the propagation of elastic and plastic waves through the material. The deformation over the entire specimen cannot longer be considered as equilibrium, because stresses are transferred between several atomic layers, similar to a pulse with a length of only a few nanoseconds. Iron and steels have been subject to numerous shock wave studies

[7] G = shear modulus.

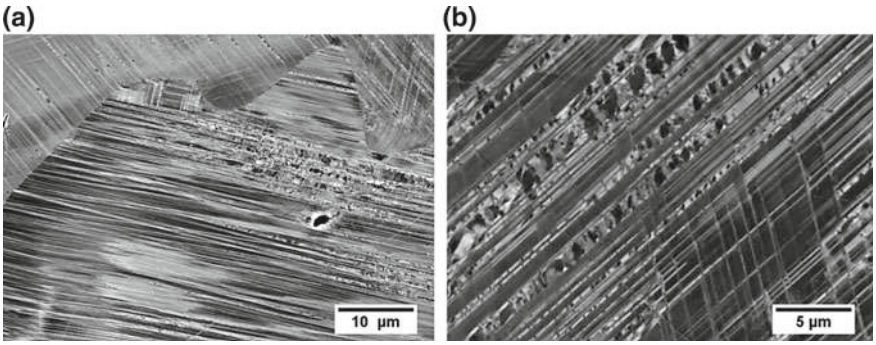

Fig. 12.7 SEM micrographs of the post-shock microstructure: **a** deformation band contrasts from backscattered electrons; **b** lenses within the bands indicate α'-martensite. The loading direction was vertical [20]

in the past. Especially the polymorphic phase transformation in iron from α-Fe to ε-Fe has been investigated extensively [49, 50]. However, in alloys with low stacking fault energy, e.g., in austenitic stainless steels, shock waves can cause additional martensitic transformations. Several studies have been carried out on steels corresponding to the composition of AISI 304 (~18% Cr, 8% Ni) under strain rates up to 10^5 1/s [51, 52]. On this occasion, the results confirmed the presence of the $\gamma \rightarrow \alpha'$ phase transformation up to such high loading rates. The microstructural changes comprised the formation of shear bands with a high concentration of deformation, whose intersections could act as nucleation sites for ε- and α'-martensite. Generally, shock prestraining led to increased microhardness and refined grains, due to high dislocation density and deformation twinning, which are both responsible for a strengthening effect [53].

Using the flyer-plate method, it was possible to identify the deformation mechanisms of CrMnNi TRIP/TWIP steels which are active under shock loading. Eckner et al. showed that an elastic-plastic shock wave produces a microstructure characterized by a high density of deformation bands, stacking faults and deformation-induced α'-martensite [20]. Figure 12.7 shows micrographs of this microstructural features, whereby the bands are clearly visible in BSE contrast. The grains had different deformation band densities and orientations, depending on the orientation to the load axis. Preferentially, their sites of origin were on active {111} slip planes of the face-centered cubic crystal lattice, due to the highest shear stresses under plastic deformation. Within the bands and at their intersections, α'-martensite was recognizable as small lenses. In accordance with results of quasi-static measurements, it could also be demonstrated that the driving force for the martensite formation increased at low temperature shock loading [20].

In order to demonstrate the deformation mechanisms, detailed TEM analyses were subsequently performed on the test samples [54]. It became clear that the austenite retained a high defect density through the plate impact and exhibited fine band structures. Intersection points of the deformation bands preferably showed

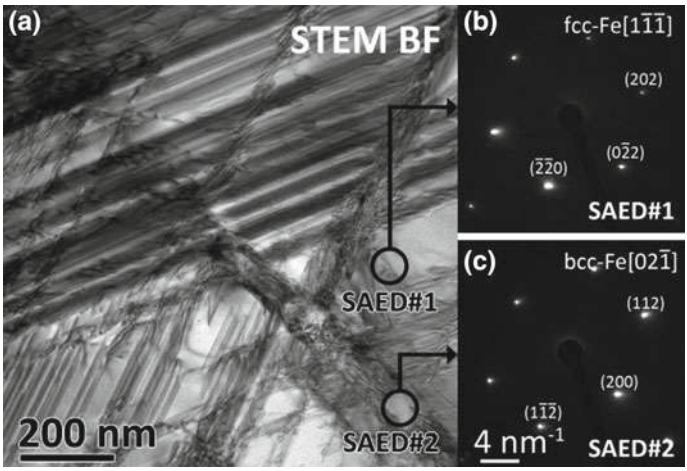

Fig. 12.8 Scanning TEM-micrograph of closely spaced deformation bands (**a**) in three different orientations (slip systems) within the γ-phase (**b**). The band intersections acted as nucleation sites for the formation of bcc α′-martensite (**c**) [54]

α′-martensite islands. At high magnification of the bands, their structure became clear as an arrangement of numerous parallel stacking faults or planar defects. In areas with high stacking fault density, it could be shown that α′-martensite was formed as assumed at the crossing points of the stacking fault bands. Figure 12.8 shows the STEM image of such a region. The enlargement of a nodal point of broader deformation bands shows that areas of the body-centered cubic phase have formed there. Using selected area electron diffraction (SAED), the lattice structure could be detected. In the area of the intersection point, the image contrasts indicated a very high defect density in the material. As reported by Martin et al. [23], the formation of α′-martensite nuclei led to the obstruction of the dislocation movement within the deformation bands and the accumulation of dislocations at the phase boundaries. In addition, the volume increase associated with the phase transformation caused a certain stress field around this area. However, the austenite outside of the bands was less deformed and parallel stacking faults could be detected here occasionally.

In the present case, the signal of the VISAR system was used to determine the characteristic strength values in the plate impact tests. A typical free surface velocity history, acquired during flyer-plate impact testing, is shown in Fig. 12.9a for the metastable austenitic CrMnNi16-6-6 cast steel. The wave form obtained was rather typical for elastic-plastic material behavior, and contained information about the yield point and the fracture strength. Initially, the elastic precursor arrived at the free end, which determined the Hugoniot elastic limit (HEL). Thereafter, the surface velocity increased again, which was associated with plastic deformation and ended in the steady Hugoniot state. The subsequent drop in surface velocity was due to the release wave or rarefaction, which reduced the pressure on the material and led to

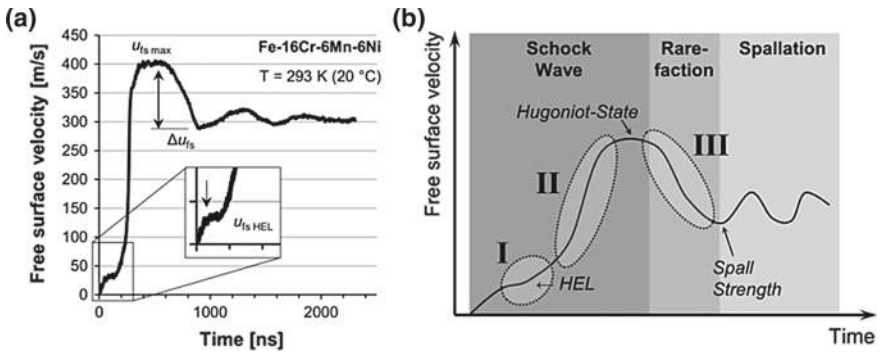

Fig. 12.9 **a** Free surface velocity profile of 16-6-6 cast steel impacted by an aluminum flyer plate at room temperature; **b** Schematic representation of the deformation mechanisms of metastable austenitic TRIP/TWIP steel during different loading states under flyer-plate impact [54]

spall fracture. The velocity pullback (Δu_{fs}) was used to determine the spall fracture strength.

Figure 12.9b presents a scheme of the deformation mechanisms of metastable austenitic TRIP/TWIP steel during shock wave loading, which was developed on the basis of the above shown experimental results of the microstructure analysis [54]. In stage I, at the very beginning of the shock deformation, elastic deformation and localized microplasticity occurred, based on the nucleation of stacking faults and thin deformation bands (planar dislocation glide). Slip occurred on several intersecting and closely-spaced planes, due to the very thin shock front and the uniaxial strain during the compression wave. In the following stage II, progressive strain hardening developed, due to a static and dynamic Hall-Petch effect caused by partial dislocation separation, slip band formation, increasing deformation band density and the formation of ε-martensite and α'-martensite nucleation sites. After the steady state (Hugoniot state), in stage III an expanding wave followed the shock wave, which reduced the materials density. The occurring tensile stresses promoted the $\gamma \rightarrow \varepsilon \rightarrow \alpha'$–transformation through an increase in formation and intersection probability of deformation bands with subsequent martensite nucleation and growth. Internal cavitation occurred, due to stresses generated by the interaction of stress waves which exceeded the local dynamic tensile strength of the steel. The coalescence of the cavities created a fragment (spall) which was finally separated from the free end of the plate.

Generally, this scheme of deformation mechanisms is also applicable to low or high temperature; however, there are various peculiarities that need to be considered here. Under shock conditions below room temperature, the thermodynamic driving force for the $\gamma \rightarrow \alpha'$–transformation increased strongly. This generally led to an increase in the strength characteristics of metastable austenitic steels, while at the same time the deformability was reduced. In addition, when the temperature fell below the M_S temperature (at about 1 °C for the CrMnNi 16-7-6 cast steel [14]), the α'-martensite also formed athermically, i.e. without the contribution of a mechanical

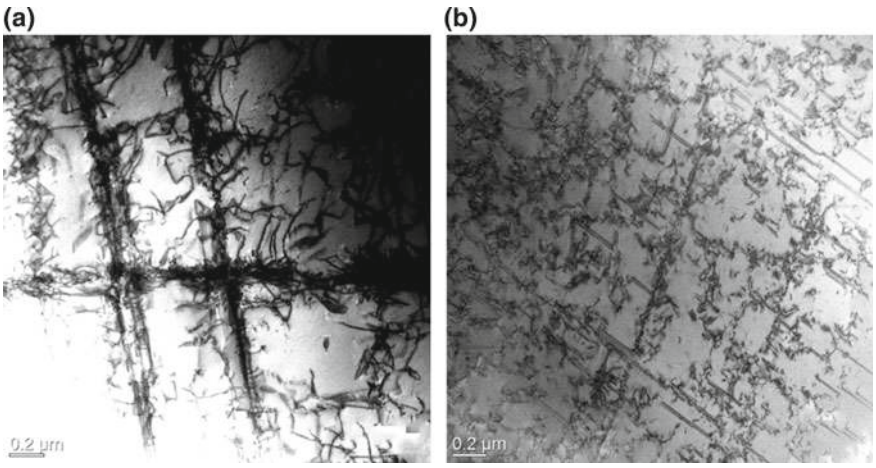

Fig. 12.10 Scanning TEM-micrographs of defect structures in CrMnNi16-6-6 steel after flyer-plate impact at **a** 100 °C and **b** 200 °C

deformation. Here, in addition to the deformation band structures already present at room temperature, coarse laths appeared within the microstructure, which also had a needle-like internal structuring. This was the cooling martensite or lath martensite, which is predominant in steels with <0.4% carbon. Similar martensite blocks can also be easily formed without further deformation in a simple cooling test. In general, the structure of the samples deformed at low temperatures was characterized by a very high density of deformation bands, which were evenly distributed over the entire inner sample area.

Furthermore, the more detailed analysis of samples tested at 100 °C and higher test temperatures showed partly fine deformation bands without significant α'-martensite nuclei at their intersection points. Also signs for wavy glide could be found, which is typical for face-centered cubic steels at high temperatures or materials with high stacking fault energies. Figure 12.10 shows exemplifying TEM images from the generated microstructures after plate impact at high temperatures. From previous investigations it is known that the deformation mechanisms change with increasing test temperature for the TRIP/TWIP steel investigated here [8]. Consequently, at 100 °C, the mechanical twinning or TWIP effect was a primary deformation mechanism also under shock loading. Moreover, there was a simultaneous occurrence of stacking fault bands (see Fig. 12.10a) and twins, which was not uncommon, since the movement of partial dislocations is a prerequisite for the occurrence of the TWIP effect [55]. Still, ε-martensite was identifiable at a low level after 100 °C shock loading, whereas nuclei of α'-martensite were only very rarely recognizable. The shock loading at 200 °C caused only a small degree of the occurrence of planar defects in the microstructure (see Fig. 12.10b). At such a high deformation temperature, it was to be expected that the deformation proceeds primarily due to dislocation glide. The

separation width of partial dislocations can only be small, due to the increased stacking fault energy. As a result, only isolated stacking fault contrasts could be found and twins were also extremely rare in this temperature range.

12.3 Honeycomb-Like Structures Made from TRIP-Steel and TRIP-Matrix-Composites

The introduction of novel cellular materials in crashworthiness-related fields of application requires a characterization of structure response and microstructure evolution in the cell wall material as a function of different parameters. In the following sections, the influence of the loading direction and the cell wall composition on the strength, deformation and damage behavior of honeycomb-like structures will be discussed in detail. Closer information about the effects of an altered test temperature and strain rate can be found in [12, 56–58].

12.3.1 Deformation Behavior of Honeycomb-Like Structures

The periodic 2D arrangement of unit cells in the investigated honeycomb-like structures results in an anisotropic material behavior which makes a distinction into two load modes necessary. The Out-Of-Plane (OOP) mode indicates the application of load parallel to the channel axis, defined as the $X3$-direction in Fig. 12.11, whereas in In-Plane (IP) mode the load is applied parallel to the $X1$–$X2$ plane.

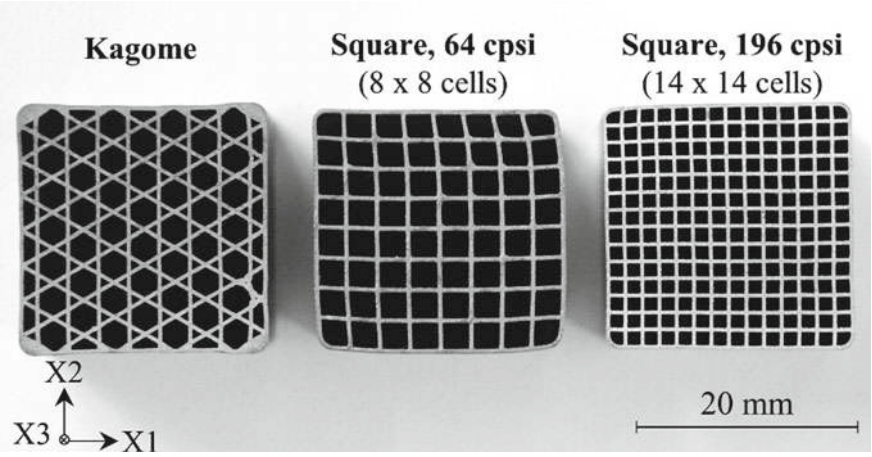

Fig. 12.11 Cross-section of investigated honeycomb-like structures in sintered state

In order to investigate the differences of OOP and IP deformation behavior, compression tests on samples with an approximate aspect ratio of 1:1 were conducted. Mechanical machining on the front sides ($X1$–$X2$ plane) ensured the desired sample dimensions and the orthogonal alignment of the cell walls, especially in OOP mode. The use of servohydraulic universal testing machines with load cells of 250 and 500 kN served for testing at quasi-static strain rates. Subsequent microstructural investigations on the deformed samples, using light optical microscopy and scanning electron microscopy in connection with EDX- and EBSD-measurements, supported the identification of the effective deformation mechanisms in the TRIP-steel matrix and the Mg-PSZ particles. The quantification of ferromagnetic α'-martensite evolution was realized by magnetic balance measurements at the beginning of the project and later continued with a MSAT magnetic saturation device.

Table 12.2 gives an overview on the TRIP-steel batches which were used for comparing the OOP and IP deformation characteristics and analyzing the effect of an altered cell wall composition. In addition, the table contains the calculated chromium and nickel equivalents, the stacking fault energies according to [59] and the additional constituents of the MgO partially stabilized zirconia.

12.3.1.1 Out-of-Plane Direction

The compressive deformation in OOP direction causes a stretch-dominated deformation mechanism in the honeycomb-like structures. Initially, the cell walls are elastically compressed until the yield strength is exceeded. With increasing compression a distinct strain hardening takes place characterized by a continuous rise in stress. In agreement with the observations of Côté et al. [60], the flow curve incline of a cell wall of the honeycomb-like structures and the respective bulk material are similar up to certain strains in this deformation stage called pre-buckling region. However, the offset in the absolute stress value derives from the varying microporosity amounting up to 15% in the struts of the cellular materials [57]. A higher microporosity results in reduced strength and deformation values, as discussed by Bocchini et al. [61].

The point of deviation in flow curve incline of cellular material from bulk material identifies the onset of structure bifurcation and hence the transition from stable to instable plastic deformation. With the onset of this post-buckling stage, progressive damage processes in the cell walls lead to a reduced strain-hardening potential. As a result, a stress maximum is formed. Within the ensuing deformation range, the buckled and fractured cell walls are compressed by an almost constant force until contacts between neighboring cell walls are formed. The densification of the entire structure involves a steep stress increase. Principally, all the investigated honeycomb-like structures display these characteristic deformation stages. However, the relative density $\bar{\rho}$ of the structures has a great influence on the achievable strength level and the strains at which a transition in deformation behavior occurs [12, 62].

Table 12.2 Overview of steel alloying elements and additional constituents of MgO partially stabilized zirconia in wt%

Batch	Abbr.	Cr	Mn	Ni	C	N	Si	Mo	Cr_{eq} [13]	Ni_{eq} [13]	γSFE[a]
X1CrNi 18-9	18-1-9	18.4	1.1	9.3	0.009	0.127	0.67	0.028	19.4	12.4	23
X3CrMnNi 17-8-10	17-8-10	16.6	7.7	10.1	0.025	0.065	1.17	0.002	18.4	15.9	19
X3CrMnNi 16-7-7	16-7-7	16.3	7.2	6.6	0.030	0.088	1.00	0.007	17.8	12.7	14
X3CrMnNi 17-7-6	17-7-6	17.0	6.5	6.1	0.030	0.082	0.30	<0.01	17.5	11.7	16
X5CrMnNi 17-7-3	17-7-3	16.7	7.1	3.4	0.050	0.097	0.91	0.024	18.1	10.2	9

[a] according to Dai et al. [59] $\gamma = 39 + 1.59\%Ni - 1.34\%Mn + 0.06\%Mn^2 - 1.75\%Cr + 0.01\%Cr^2 + 15.21\%Mo - 5.59\%Si + 26.27(\%C + 1.2\%N)(\%Cr + \%Mn + \%Mo)^{0.5} + 0.61(\%Ni(\%Cr + \%Mn))^{0.5} - 60.69(\%C + 1.2\%N)^{0.5}$

	MgO	SiO_2	HfO_2	Al_2O_3	CaO	TiO_2	ZrO_2
Mg-PSZ	3.4	2.4	1.7	0.6	0.2	0.1	Bal.

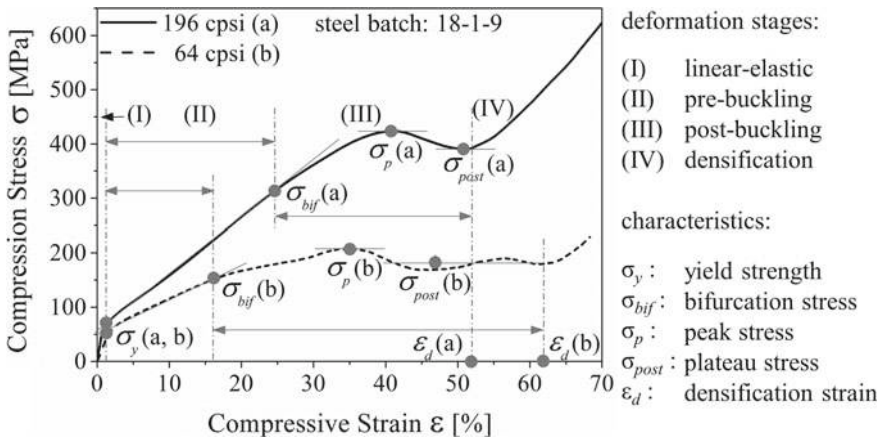

Fig. 12.12 Stress-strain curves of square-celled structures with 64 cpsi and 196 cpsi made from steel batch 18-1-9, compressed at quasi-static strain rates and room temperature [62]

An estimation of $\bar{\rho}$ for the square-celled structures can be made according to (12.9).[8] In addition, the ratio of global structure density ρ^* and density of the cell wall material ρ_s is also suitable to calculate this structure parameter [62, 63].

$$\bar{\rho} = \frac{\rho^*}{\rho_s} \cong (1 - p_m)\left[2\left(\frac{t}{l}\right) - \left(\frac{t}{l}\right)^2\right] \approx 2(1 - p_m)\frac{t}{l} \tag{12.9}$$

Both investigated square-celled structures have a comparable average cell wall thickness of approx. 300 µm (64 cpsi) and 320 µm (196 cpsi) and a residual amount of porosity in the cell walls due to the manufacturing process. However, the cell edge length differs considerably from approx. 2400–1500 µm resulting in relative densities of 0.24 and 0.36 [57]. Differences of these parameters in varying batches of honeycomb-like structures can be traced to an altered amount of microporosity and shrinkage. Figure 12.12 visualizes that minor strength is provided by the low-density structure over the whole deformation range. Besides, structural damages and the ultimate collapse identified by the peak stress are initiated at lower strains. In comparison to the 196 cpsi structure, a distinct stress plateau is developed in the cellular material with 64 cpsi prior to densification which takes place at higher strains. These tendencies conform with findings of other research groups [60, 63] reporting an increase of peak stress and a reduced densification strain with increasing

8 $\bar{\rho}$ = relative density
ρ^* = global structure density
ρ_s = density of the cell wall material
t = cell wall thickness
l = cell edge length
p_m = cell wall microporosity.

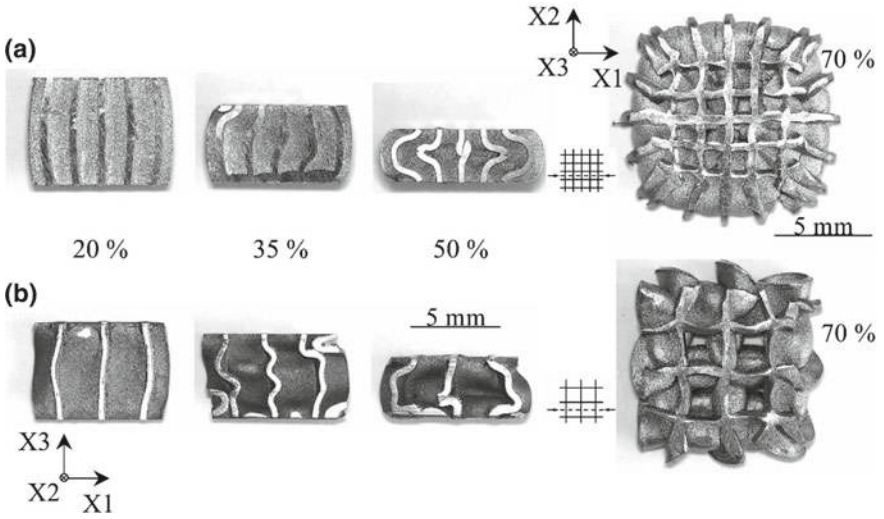

Fig. 12.13 Side view of buckling and failure patterns within the core of down-scaled samples made from steel batch 18-1-9 at different deformation stages and top view of 70% strained state: **a** 196 cpsi and **b** 64 cpsi structure [57]

relative density. However, the formation of a pre-buckling stage seems to be more common for steel matrix structures than for structures composed of aluminum [64]. Object of investigation is further the number of cells required to describe the stress-strain behavior properly. In order to assess this aspect, segments with 4 × 4 and 2 × 2 cells and an equal aspect ratio are cut out of the 196 cpsi and 64 cpsi structure, respectively. Quasi-static compression tests on the down-scaled samples demonstrate that no significant difference is recorded in the linear-elastic and pre-buckling stage. The absence of the stiffened outer skin causes only a slight shift of peak stress to lower strains, cf. [12, 57].

Interrupted compression tests serve to record the different macroscopic deformation mechanisms of the two structures. In the 196 cpsi sample, stable plastic deformation is accompanied by axial crushing and global buckling of cell walls within the $X1$–$X3$ and $X2$–$X3$ plane (cf. Fig. 12.13a). The radius of curvature increases with increasing compressive strain, until plastic kinks are built involving the onset of instable deformation. However, centered cell walls are restricted to deform freely due to the constraining effect of the outer elements. Hence, shear failure and fracture is promoted. In contrast to this global plastic "Euler-type" buckling, the low-density structures deform by local and torsional buckling which leads to folding collapse (cf. Fig. 12.13b) [57].

Sometimes the structures exhibit manufacturing related defects like cracks and inhomogeneities in the undeformed state which can be visualized by computer-tomographic investigations [65]. In order to generate a better comparability of batches

with a varying amount of imperfections the recorded stress is normalized to the relative density of the particular structure in the following sections.

12.3.1.2 In-Plane Direction

At the beginning of deformation, the stress-strain behavior in IP direction is determined by the elastic compression of cell walls similar to OOP mode. However, in case of the square-celled structures, the passing of compressive yield strength is closely linked to the compressive peak strength indicating that no stable plastic deformation within a pre-buckling stage takes place (Fig. 12.14). The subsequent steep stress decrease initiates the plateau stage which is characterized by an almost constant stress signal with only small oscillations and limited by structure densification [62]. By comparing the stress-strain response with the one in OOP mode, it is obvious that less mechanical work is required for IP deformation. An explanation is given by the macroscopic failure mechanism.

Ideally, the sintered honeycomb-like structures with square cells possess exactly aligned cell walls as predetermined by the employed die of the extrusion process. Therefore, the struts oriented parallel to the applied force, will be loaded with primarily axial stresses. As a result of the sintering process, cavities in the green bodies are more and more eliminated leading to a shrinkage of 10–15% [67]. Despite the occurrence of an almost homogenous shrinkage, small deflections of the cell walls cannot be excluded. These structural imperfections in addition to residual pores and cracks have a wider impact on IP deformation, because they are initiation points of instable plastic deformation. The onset is concentrated in the cell row with the highest deviation of structural integrity. Therefore, bending moments are initiated leading to cell wall rotation processes around adjacent cell nodes. In addition, the lattice design of the square-celled structure provides no sufficient transverse rigidity so that asymmetric shearing takes place with increasing strain, cf. Fig. 12.15. In contrast to

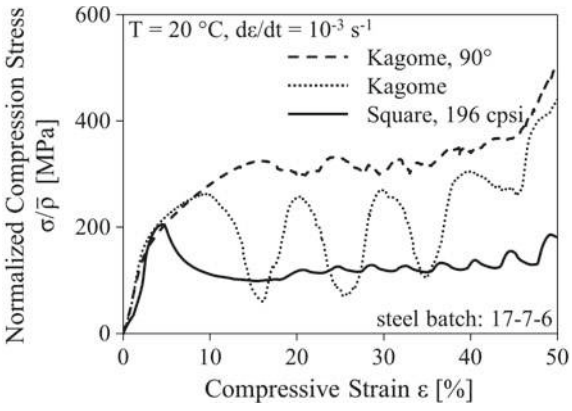

Fig. 12.14 Quasi-static stress-strain curves of Kagome (deformation in $X1$-direction), Kagome 90° (deformation in $X2$-direction) and square-celled structures recorded in IP mode according to [66]

Fig. 12.15 Deformation patterns of Kagome (deformation in $X1$-direction), Kagome 90° (deformation in $X2$-direction) and square-celled structures at engineering strains of 25% for IP mode and quasi-static strain rates according to [66]

OOP mode, where all three spatial directions are affected, IP plastic deformation is limited in the $X1$–$X2$ plane due to the 2D assembling of cells [62, 66].

In order to improve the IP properties of the honeycomb-like structures, altered cell designs are investigated by simulation on the basis of Finite Element Method (FEM) analysis [68]. Computation is conducted by the use of an isotropic, strain rate dependent and isothermal material model, based on true stress-strain curves of steel 18-1-9 and an explicit solver in ABAQUS. Nine main profiles serve as input files. For five of these profiles, a 90°-rotation is necessary to describe the whole mechanical behavior in IP mode due to the axial anisotropy of the lattice. The mass-specific (m) energy absorption capability as a characteristic value and integral information of the force (F)-displacement (s) curve is chosen to compare the performance of the investigated structures. It can be calculated as follows:

$$\mathrm{SEA}_m = \frac{\int_0^{s_i} F(s)\mathrm{d}s}{m} \tag{12.10}$$

As a result of the FEM analysis, the Kagome lattice, which consists of an ordered sequence of hexagons and triangles, provides superior properties compared to the square-celled structure. In OOP direction the relative increase of specific energy absorption capability is moderate whereas in IP mode the increment for both Kagome orientations is immense. The comparative experimental investigations of the Kagome and the square-celled lattice, both manufactured out of steel batch 17-7-6, serve to verify the results of the FEM analysis [66, 68]. In OOP mode the increase of static energy absorption capability of the Kagome configuration is no more than 2 kJ/kg at 40% engineering strain and hence less than 5% of the absolute value. However, in IP direction the static absorption capability of the Kagome structure loaded in $X2$-direction (denoted as Kagome 90°) is more than twice as much as that of the square-celled structure and in $X1$-loading (denoted as Kagome) a raise of approx. 70% is measureable. By considering the progression of the stress-strain curve in Fig. 12.14, a continuous raise of stress takes place after passing the transition point from elastic to plastic deformation for both Kagome alignments in contrast to the square-celled structure. Furthermore, the average stress level in the plateau stage is

higher than compared to the square-celled structure. Fundamental reason for the IP improvement is the change of deformation mechanism. As discussed in literature [69, 70], stretching-dominated cellular materials provide a higher stiffness and a greater strength as compared to bending-dominated structures. The latter mechanism is predominant in the square-celled structure due to the mentioned manufacturing-caused imperfections.

The deformation patterns are also in good agreement with the simulation. For both Kagome orientations, plastic deformation is symmetric with respect to the direction of loading, cf. Fig. 12.15. For $X1$–loading, the deformation pattern is characterized by buckling of angled lattice struts and cell wall rotation processes around adjacent cell nodes with increasing strain. A mainly triangle-shaped deformation pattern, which is formed by buckling of the vertical cell walls, defines the deformation in $X2$-orientation. At high strain levels a combination with upper deformation bands takes place.

12.3.2 Selection of Cell Wall Materials

Apart from the loading direction and the lattice design, the mechanical properties of honeycomb-like structures are significantly influenced by the characteristics of the cell wall material. In the following, the effect of nickel content in the steel matrix and the volume fraction of Mg-PSZ particles have been analyzed to demonstrate how the OOP deformation behavior of the 196 cpsi honeycomb-like structure can change.

12.3.2.1 Influence of Nickel Content

Metastable austenitic steels can respond to plastic deformation with different deformation mechanisms. The transformation from γ austenite into ε- or α'-martensite, called TRIP-effect, represents one possibility in addition to dislocation glide. Another alternative is the occurrence of mechanical twinning, called TWIP-effect. Decisive for the occurring mechanism are several parameters like chemical composition, stacking fault energy (SFE), temperature, stress state and strain rate, which can interact with each other [8, 25, 71–74].

Principally, a spontaneous transformation of austenite into martensite is possible if the difference in Gibbs free energy of both phases exceeds a certain threshold value below the martensite start temperature M_s. However, in plastically deformed TRIP-steels an amount of mechanical work can be added to the chemical driving force causing the start of martensite nucleation to shift to temperatures above M_s. The upper limit for deformation induced martensite formation is determined by the M_d temperature. At this temperature, the applied load is still sufficient to generate the critical shear stress in order to form 1 vol% of α'-martensite [7, 75].

Whether the selected steel is able to show the TRIP-effect and how great the extent will be, strongly depends on the austenite stability which is affected by the

chemical composition. Alloying elements like carbon, nitrogen, nickel and manganese promote the stability. The weighting of their influence is contained in the equation of the nickel-equivalent, cf. (12.11) in wt% [13]. In connection with the chromium equivalent, a classification within the Schaeffler-diagram is possible and hence the estimation of microstructure constitution for a given chemical composition at room temperature in the undeformed state. The closer the alloys are situated at the separation line of the single phase austenite and the two-phase austenite/martensite region in this diagram, the greater the tendency for a deformation induced phase transformation. The nickel-equivalent can also be employed for the estimation of M_s as Jahn et al. [76] demonstrated on the basis of dilatometer measurements on CrMnNi steels with varying chemical composition. According to this, M_s shows a parabolic increase with decreasing Ni_{eq}, which is closely associated with a reduction of austenite stability.

$$Ni_{eq} = \%\ Ni + 30\%\ C + 18\%\ N + 0.5\%\ Mn + 0.3\%\ Co + 0.2\%\ Cu\ - 0.2\%\ Al \quad (12.11)$$

Another parameter with great impact on the occurring deformation mechanism is the SFE which is a function of chemical composition and temperature [8, 59]. Austenitic steels with a low SFE possess Shockley partial dislocations with a great split-up implying that recombination of partial dislocations is not favored. For this reason, plastic deformation is dominated by planar glide and localized in deformation bands. With increasing strain, the amount of stacking faults on every second {111} plane increases and hcp ε-martensite therefore can be measured [77]. Furthermore, more and more nucleation sites for the α'-martensite transformation are built by the intersection of these deformation bands in addition to an increasing stress level which finally exceeds the triggering stress [75]. Austenitic steels with high SFE require a high stress to separate partial dislocations and form large stacking faults. Besides, the energy barrier for the ε-martensite formation increases and thus the formation of an hcp structure becomes unfavorable from the thermodynamic point of view [78]. As a consequence, stacking faults are generated on every successive {111} plane leading to the formation of mechanical twins (TWIP-effect) [79]. Regarding the nature of glide in steels with high SFE, lower stresses have to be applied to cause a recombination of partial dislocations. Therefore, cross-slip is possible resulting in a lower strain hardening potential. At a certain amount of SFE, plastic deformation proceeds by pure dislocation glide since the stress level required for the separation of partial dislocation exceeds the fracture strength of the steel.

Martin et al. [8, 73] conducted microstructural investigations on CrMnNi samples deformed at different temperatures. Since the variation in temperature is accompanied with a change in SFE energy, they extrapolated the SFE under the assumption that the SFE increases by 0.075 $mJK^{-1}\ m^{-2}$. Therefore, SFE ranges with characteristic deformation mechanisms could be proposed. Above 40 $mJ\ m^{-2}$ pure dislocation glide is prevalent whereas between 20 and 40 $mJ\ m^{-2}$ pronounced deformation twinning occurs. For energies below 20 $mJ\ m^{-2}$, a continuous transition to ε- and α'-martensite formation takes place which is always supported by dislocation glide.

In Fig. 12.16 the effect of varying deformation mechanisms within the steel matrix is displayed for the square-celled 196 cpsi honeycomb-like structures. Mayor difference of the investigated samples is the nickel content which influences the nickel equivalent and the stacking fault energy, as Table 12.2 reveals.

The graph shows that the compressive yield strength increases by decreasing the nickel content. Furthermore, plastic deformation in the pre-buckling stage generates the highest flow stress and the greatest strain-hardening in the honeycomb-like structure containing 3 wt% nickel, followed by the 7 wt% nickel sample. However, considering the onset of structure bifurcation and the start of softening due to immense structural damages at the peak stress, a decreasing triggering strain with decreasing nickel content becomes obvious. Nevertheless, the stress level of 3 and 7 wt% nickel containing samples is still higher in comparison to the sample with 10 wt% nickel. Consequently, the area enclosed by the stress-strain curve, which correlates with the energy absorption potential of the structures, decreases with increasing nickel content. Interrupted compression tests in combination with MSAT-measurements served to monitor the evolution of α'-martensite in

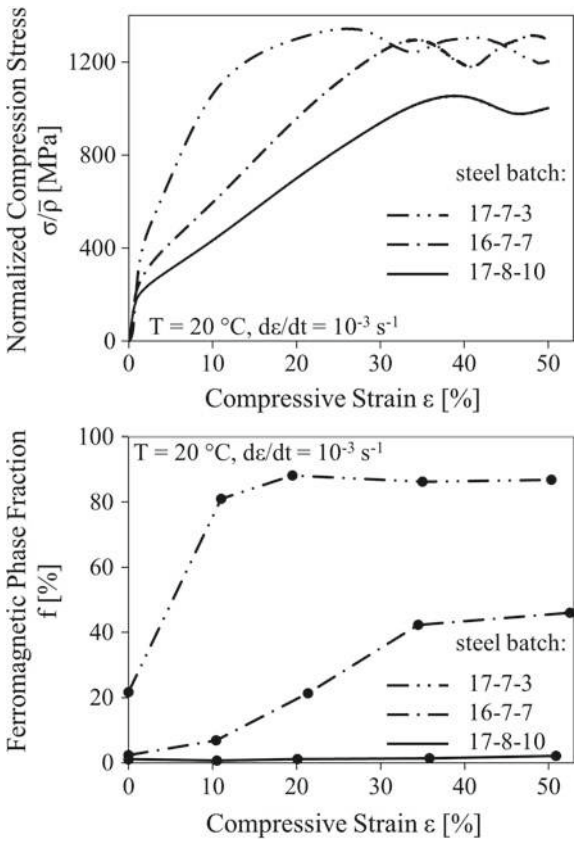

Fig. 12.16 Stress-strain behavior and α'-martensite evolution of CrMnNi square-celled honeycomb-like structures with varying nickel contents deformed in OOP mode, data used from [46]

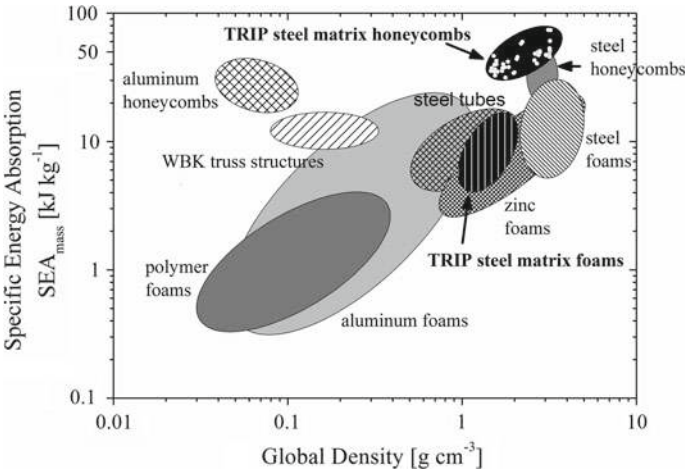

Fig. 12.17 Comparative overview of mass specific energy absorption of TRIP-steel matrix honeycombs and other structures according to [12], additional results of samples made from 17-7-3, 16-7-7 and 17-8-10 steel batches have been added (each single white dot refers to one single measurement result)

the structures, cf. Fig. 12.16. As expected, the highest amount of deformation induced α'-martensite is found in the 3 wt% nickel sample possessing the lowest Ni_{eq} and the lowest SFE. At 20% engineering strain the saturation content of α'-martensite is already reached. Due to the small amount of interstitial alloying elements, the lattice distortion and hence the strength of the α'-martensite islands is comparatively low. Nevertheless, α'-martensite is an effective obstacle regarding dislocation movement which contributes to a distinct strengthening effect [24]. The high driving force for the TRIP-effect in the 3 wt% nickel structure results, however, in the restriction of deformation capacity. Similar observations are made in the related bulk material, cf. uniform/fracture elongation [72].

In the 7 wt% nickel containing sample, the TRIP-effect is less dominant as indicated by the lower absolute ferromagnetic phase fraction. Besides, it becomes obvious that a higher amount of plastic strain is necessary to achieve the saturation content of α'-martensite in these samples. Microstructural investigations visualize that α'-martensite has an oval lense-shaped appearance and forms within deformation bands. Increasing the nickel content up to 10 wt% shifts the deformation mechanism to ε-martensite formation and mechanical twinning (TWIP-effect). Therefore, no significant ferromagnetic content is measureable even at 50% engineering strain. The microstructure images prove that an increased amount of stacking fault arrangements is contained in the samples but no α'-martensite is recognizable [46].

In order to classify the obtained results, the energy absorption performance of the honeycomb-like samples (196/64 cpsi) at 50% engineering strain is compared to several other structures, cf. Figure 12.17. All considered data refer to quasi-static compressive loading and to OOP mode in case of honeycomb(-like) structures and

tubes. The TRIP-steel matrix honeycombs belong to the cellular materials with high global density, but they still provide a great mass specific energy absorption capability. The TRIP-steel matrix honeycombs based on the initial 18-1-9 steel batch already exhibit a maximum absorption capability of 54 kJ/kg, as presented in [12]. With introduction of the 16-7-7 and 17-7-3 steel generation, the energy consumption can be further increased up to 74 kJ/kg, due to the higher driving force for the deformation induced martensitic phase transformation leading to an enhanced strength level. However, the honeycombs made from steels with a lower austenite stability are more prone to structural softening as a result of quasi-adiabatic sample heating even at strain rates of 10^2 1/s. Curve crossing phenomena of statically and dynamically deformed samples are shifted to lower strains which is also valid for the bulk material [33, 46]. Therefore, it has to be considered that the dynamic energy absorption capability can adapt or can fall even below the quasi-static one at elevated strains [25].

12.3.2.2 Effect of Particle Reinforcement

The addition of MgO partially stabilized zirconia particles in the TRIP-/TWIP-steels is intended to increase the strength of the composite which bases on several mechanisms. On the one hand, external applied loads are supposed to be transmitted from the matrix through the interface to the stronger ceramic. Additionally, the different ductility of the components and the misfit due to the varying crystal structures contribute to an increase in strength. On the other hand, an indirect strengthening mechanism results from the different coefficients of thermal expansion. During cooling from processing temperature, the steel contracts stronger in comparison to the ceramic so that dislocations are generated at the interfaces and the material is subjected to strain hardening. In principle, the effectiveness of the mechanisms depends on the volume content, the shape and the orientation with respect to the load direction of the reinforcing phase [80].

Apart from the described mechanisms, which are the basis for all metal matrix composites (MMC) with superior strength properties, the Mg-PSZ particles are supposed to contribute to further strengthening by a martensitic phase transformation. At initial state the particles exhibit a cubic/tetragonal microstructure which transforms into monoclinic state by mechanical loading in connection with exceedance of the triggering stress. The transformation is accompanied by a volume expansion generating an additional amount of compressive strain in the surrounding matrix. Hence, more mechanical work is available for the TRIP-effect in grains with a favorable orientation. Martin et al. [81] proved the occurrence of this interaction and its positive effect on the mechanical properties by comparing MMCs reinforced with 5 vol% Al_2O_3 and Mg-PSZ, respectively. The greatest flow stress in the whole deformation range was provided by the Mg-PSZ sample although the content of α'-martensite was lower as compared to the non-reinforced sample. This fact was explained by the limited deformability in the ceramic which restricts plastic flow in the TRIP-matrix. However, an increase in monoclinic phase fraction with increasing strain

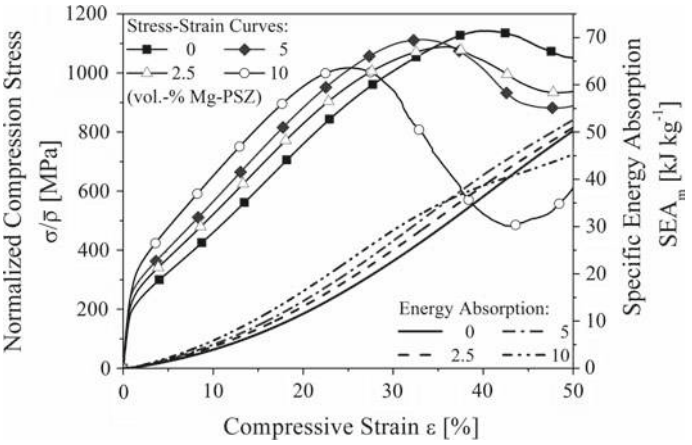

Fig. 12.18 Quasi-static stress-strain response of 196 cpsi honeycomb-like structures composed of 18-1-9 steel batch with 0 to 10 vol% Mg-PSZ particles, data used from [67]

was detected and more α'-martensite was measured in the Mg-PSZ sample than in the one containing Al_2O_3.

In order to exploit the whole potential of these mechanisms, the amount of monoclinic phase has to be reduced at initial state. For bulk material, synthesized by Spark Plasma Sintering, this precondition can be ensured as the results of Krüger et al. [10] demonstrated. However, the honeycomb-like structures are manufactured by conventional sintering which requires high temperatures and long dwell times to receive dense products. The manufacturing parameters permit diffusion processes both in direction of the steel and the other way around, as Berek et al. [82] reported. As a consequence, magnesium reacts to silicates and spinels with alloying elements of the steel and is no longer stabilizing the ceramic in the cubic/tetragonal phase. However, Weigelt et al. [83] observed that exposing pure Mg-PSZ to temperatures of 1300 °C, which is close to the tetragonal → monoclinic phase transformation temperature, resulted also in a significant decrease of stabilized cubic/tetragonal phase even without a steel interaction. At initial state 90% of the Mg-PSZ microstructure was of cubic/tetragonal phase whereas only 30% remained after firing at 1300 °C for 3 h. Elevating the sintering temperatures to 1400 °C was favorable for a greater cubic/tetragonal phase content, but is close to the melting temperature of the steel. Consequently, the strengthening effect of the martensitic phase transformation within the Mg-PSZ is comparatively low in conventionally sintered honeycomb-like structures [84].

The effect of different Mg-PSZ volume contents, varying between 2.5 and 10 vol%, on the OOP deformation behavior of square-celled 196 cpsi honeycomb-like structures is depicted in Fig. 12.18. In accordance with the mechanical response of the related bulk material, the compressive yield strength of the honeycomb-like structures increases with increasing amounts of Mg-PSZ [57]. The enhancement of

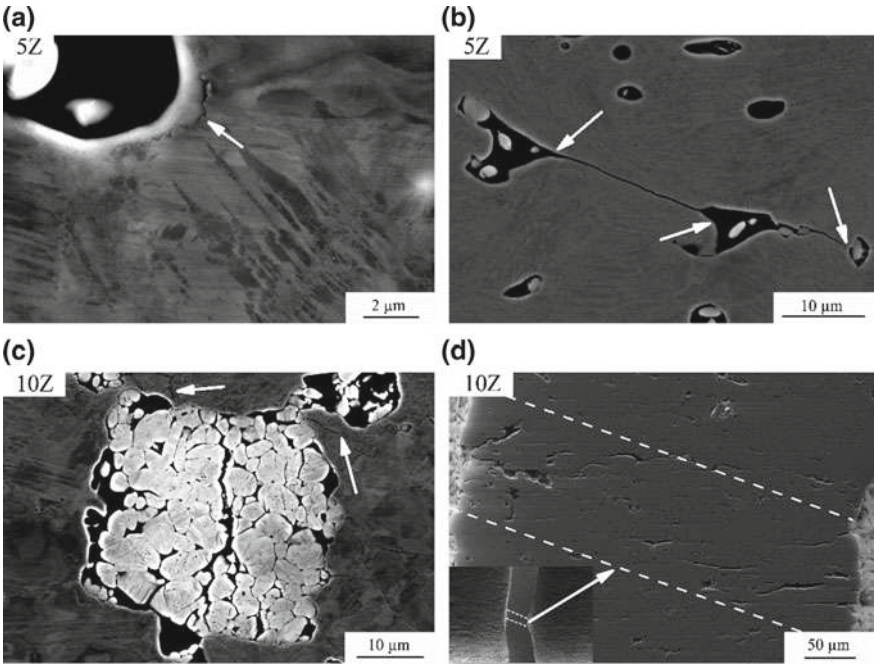

Fig. 12.19 Damage processes of TRIP-Matrix-Composites according to [62] at $\varepsilon = 20\%$ **a** interface debonding, **b** crack bifurcation at particles and pores, **c** failure of Mg-PSZ agglomerate as well as matrix cracks and **d** weakened cell wall cross-section at $\varepsilon = 35\%$; Z denotes vol% Mg-PSZ

plastic compression stress and work hardening rate continue up to certain deformation stages in the pre-buckling stage due to a constrained plastic flow in the matrix arising by the presence of the rigid ceramic particles. In addition, the polygonal shape of the Mg-PSZ leads to stress concentrations at the interfaces between matrix and particle, possessing a perpendicular orientation to the loading direction. Depending on the crystal orientation of the surrounding austenitic grains, more dislocations can form, further glide systems can be activated and an increased ε- and α'-martensite formation is possible [81]. It is obvious that the more particles are contained the greater the impact of these mechanisms on the resulting strength.

However, the increasing inhomogeneous stress distributions can finally exceed the steel/ceramic interfacial strength and the fracture strength of the steel matrix, respectively. Debonding processes and crack initiation are the result, visualized by Fig. 12.19a. Additionally, the fracture of brittle ceramic particles, cracking of Mg-PSZ agglomerates and crack bifurcation contribute to material softening processes, cf. Figure 12.19b, c. Hence, with increasing Mg-PSZ content a lower crush resistance (maximum strength) is provided and failure shifts to lower strains, cf. Figure 12.18. The steeper stress decrease of the composite structures within the post-buckling stage arises by the formation of micro crack networks which can combine to macro cracks. Especially areas with high particle density and great strain localizations are prone to

cracking which is accompanied with particle rearrangement processes. As a result, Mg-PSZ particles are lined up in unattached cluster chains leading to a weakening of the cell wall cross section, cf. Figure 12.19d.

The sum of damage processes is adverse for the α'-martensite evolution as the measurements of ferromagnetic phase content reveal. At low engineering strains (up to approx. 10%), partially higher α'-martensite contents can be identified in the central deformation areas of the composite honeycomb-like structures whereas at 50% engineering strain the highest α'-martensite content within the same area is found in the non-reinforced sample [62, 67]. Nevertheless, the reinforcement of TRIP-steel with Mg-PSZ particles can contribute to an increased energy absorption capability up to 50% engineering strain as the comparison of the non-reinforced and the 5 vol% Mg-PSZ containing sample in Fig. 12.18 shows.

Thus, the main finding—likewise on basis of other employed steel batches—is the increase of energy absorption capability by reinforcing the steel with Mg-PSZ particles being most effective for low strains where material damages are not pronounced [46].

12.4 Conclusions

The material behavior of metastable TRIP-steels was investigated in the form of bulk material and honeycomb-like structures. Strain-rate and temperature dependent compression tests with subsequent microstructural investigations on the bulk samples led to the following findings:

- In dependence of the deformation temperature different deformation mechanisms are dominating: below 100 °C the deformation-induced formation of ε- and α'-martensite, between 100 and 250 °C mechanical twinning and above 250 °C dislocation glide.
- An own model was presented to describe the material behavior under consideration of the strain rate sensitivity of austenite and martensite, adiabatic heating and strain hardening of the austenite. The model, which is based in a modified rule of mixture, provides excellent results.
- The dominant deformation mechanisms of the 16-6-6 CrMnNi steel in the strain rate range of 10^{-3} up to ~5×10^4 1/s were the accumulation of stacking faults in lamellar deformation bands and the strain-induced formation of ε- and α'-martensite. Low temperatures raised the driving force for α'-martensite formation also in shock loading. The particularly high strain rates during flyer-plate impact induced α'-martensite formation even at very low strains. However, the $\gamma \rightarrow \varepsilon$ transformation still occurred as an intermediate step.

Compression tests on honeycomb-like structures in dependence of loading direction, nickel content in the steel and volume content of Mg-PSZ can be summarized as follows:

- In OOP mode the cell walls were exposed to a stretch-dominated deformation mechanism and the occurrence of a plastic pre-buckling stage was identified. The strength level and strain hardening potential, respectively, in this stage were controlled by the relative density of the structure, the deformation mechanisms in the steel and the steel/Mg-PSZ particle interactions.
- IP compression resulted in a lower strength and thus in a reduced energy absorption capability in comparison to OOP loading. However, altering the cell shape from square-celled to Kagome configuration contributed considerably to an enhanced IP performance.
- Decreasing the austenite stability and the stacking fault energy led to an increase of flow stress and strain hardening rate. Even though the failure strain at the peak stress decreased with decreasing nickel content, the low nickel containing samples exhibited the highest TRIP-effect, and thereby possessed the greatest energy absorption capability.
- The reinforcement with Mg-PSZ particles contributed to an increase of flow stress and energy absorption capability. Damage processes like interfacial debonding, particle cracking and crack bifurcation caused a shift of structural collapse to lower stresses and strains.

Acknowledgements This work was funded by the German Research Foundation or Deutsche Forschungsgemeinschaft (DFG), and was created as part of the Collaborative Research Center TRIP-Matrix-Composites (Project number 54473466—CRC 799). The build-up of the Freiberg Shock Wave Laboratory was fully financed by the Dr. Erich Krüger foundation. Special thanks are addressed to Dr. D. Ehinger and Dr. S. Wolf for their outstanding work in this sub-project generating numerous publications and hence significant foundation for this book chapter. Prof. T. Halle of OVGU Magdeburg supported the project with FEM-calculations. Moreover, part of the experimental work was done by Ms. C. Ullrich, Dr. M. Motylenko, Dr. A. S. Savinykh and Prof. S. V. Razorenov (RAS, Chernogolovka, Russia), for which we would like to express our sincere thanks. Additionally, the authors thank all technical employees who were tasked with mechanical processing of samples for mechanical testing and microstructure analysis as well as all students supporting the research project.

References

1. L. Remy, A. Pineau, Mater. Sci. Eng. **28**, 99 (1977)
2. O. Grässel, L. Krüger, G. Frommeyer, L.W. Meyer, Int. J. Plast **16**, 1391 (2000)
3. G. Frommeyer, U. Brüx, P. Neumann, ISIJ Int. **43**, 438 (2003)
4. O. Bouaziz, S. Allain, C. Scott, Scr. Mater. **58**, 484 (2008)
5. V.F. Zackay, E.R. Parker, D. Fahr, R. Busch, Trans. ASM **60**, 252 (1967)
6. G.B. Olson, M. Cohen, Metall. Trans. A **6**, 791 (1975)
7. I. Tamura, Met. Sci. **16**, 245 (1982)
8. S. Martin, S. Wolf, U. Martin, L. Krüger, D. Rafaja, Metall. Mater. Trans. A **47**, 49 (2016)
9. O. Bouaziz, H. Zurob, M. Huang, Steel Res. Int. **12**, 937 (2013)
10. L. Krüger, S. Decker, R. Ohser-Wiedemann, D. Ehinger, S. Martin, U. Martin, H.J. Seifert, Steel Res. Int. **82**, 1017 (2011)
11. C.G. Aneziris, W. Schärfl, H. Biermann, U. Martin, Int. J. Appl. Ceram. Technol. **6**, 727 (2009)

12. D. Ehinger, L. Krüger, S. Krause, U. Martin, C. Weigelt, C.G. Aneziris, EPJ Web Conf. **26**, 1056 (2012). https://doi.org/10.1051/epjconf/20122601056
13. A. Weiß, P.R. Scheller, A. Jahn, Patent WO 2008/009722, 24 Jan 2008
14. A. Jahn, A. Kovalev, A. Weiß, S. Wolf, L. Krüger, P.R. Scheller, Steel Res. Int. **82**, 39 (2011)
15. G.T. Gray III, Mechanical testing and evaluation, in *ASM Handbook,* vol. 8 ed. by H. Kuhn, D. Medlin (ASM International, Materials Park, OhioText, 2000), p. 462
16. D.J. Frew, Exp. Mech. **45**, 186 (2005)
17. J.C. Gong, L.E. Malvern, D.A. Jenkins, J. Eng. Mater. Technol. **112**, 309 (1990)
18. L.M. Barker, R.E. Hollenbach, J. Appl. Phys. **43**, 4669 (1972)
19. G.I. Kanel, S.V. Razorenov, V.E. Fortov (eds.), *Shock-Wave Phenomena and the Properties of Condensed Matter* (Springer, New York, 2004)
20. R. Eckner, B. Reichel, A.S. Savinykh, L. Krüger, S.V. Razorenov, G.V. Garkushin, Metall. Mater. Trans. A **47**, 75 (2016)
21. K. Thoma, U. Hornemann, M. Sauer, E. Schneider, Meteorit. Planet. Sci. **40**, 1283 (2005)
22. R. Eckner, L. Krüger, C. Ullrich, D. Rafaja, T. Schlothauer, G. Heide, Metall. Mater. Trans. A **47**, 4922 (2016)
23. S. Martin, S. Wolf, S. Decker, L. Krüger, U. Martin, Steel Res. Int. **86**, 1187 (2015)
24. A. Weidner, H. Biermann, JOM **67**, 1729 (2015)
25. L. Krüger, S. Wolf, S. Martin, U. Martin, A. Jahn, A. Weiß, P.R. Scheller, Steel Res. Int. **82**, 1087 (2011)
26. L. Krüger, S. Wolf, U. Martin, S. Martin, P.R. Scheller, A. Jahn, A. Weiß, J. Phys: Conf. Ser. **240**, 12098 (2010)
27. J. Talonen, H. Hänninen, P. Nenonen, G. Pape, Metall. Mater. Trans. A **36**, 421 (2005)
28. J. Talonen, H. Hänninen, Acta Mater. **55**, 6108 (2007)
29. M. Isakov, S. Hiermaier, V.-T. Kuokkala, Metall. Mater. Trans. A **46**, 2352 (2015)
30. T.S. Byun, Acta Mater. **51**, 3063 (2003)
31. L. Krüger, S. Wolf, M. Rüssel, U. Martin, A. Jahn, A. Weiß, P.R. Scheller, MP Materials Testing **52**, 588 (2010)
32. A. Andrade-Campos, F. Teixeira-Dias, U. Krupp, F. Barlat, E.F. Rauch, J.J. Grácio, Strain **46**, 283 (2010)
33. R. Eckner, L. Krüger, KEM **742**, 113 (2017)
34. G.L. Huang, D. Matlock, G. Krauss, Metall. Trans. A **20**, 1239 (1989)
35. A. Bäumer, J.A. Jiménez, W. Bleck, Int. J. Mater. Res. **101**, 705 (2010)
36. L. Krüger, S. Wolf, U. Martin, P. Scheller, A. Jahn, A. Weiß, in *Proceedings of the 9th International Conferences on the Mechanical and Physical Behaviour of Materials under Dynamic Loading (DYMAT 2009),* Brussels, Belgium, 7–11 September 2009
37. A.Y. Chen, H.H. Ruan, J. Wang, H.L. Chan, Q. Wang, Q. Li, J. Lu, Acta Mater. **59**, 3697 (2011)
38. S. Wolf, S. Martin, L. Krüger, U. Martin, Mater. Sci. Eng., A **594**, 72 (2014)
39. D.C. Ludwigson, J.A. Berger, J. Iron Steel Inst. **207**, 63 (1969)
40. T. Narutani, G.B. Olson, M. Cohen, J. Phys. **43**, 429 (1982)
41. S. Wolf, S. Martin, L. Krüger, U. Martin, U. Lorenz, Steel Res. Int. **83**, 529 (2012)
42. S. Wolf, Dissertation, TU Bergakademie Freiberg, 2012
43. G.R. Johnson, W.H. Cook, in *Proceedings of the 7th International Symposium on Ballistics,* The Hague, The Netherlands, 19–21 April 1983
44. S. Nemat-Nasser, Mechanical testing and evaluation, in *ASM Handbook,* vol. 8, ed. by H. Kuhn, D. Medlin (ASM International, Materials Park, OhioText, 2000), p. 429
45. L.W. Meyer, N. Herzig, T. Halle, F. Hahn, L. Krüger, K.P. Staudhammer, J. Mater. Process. Technol. **182**, 319 (2007)
46. C. Baumgart, D. Ehinger, C. Weigelt, L. Krüger, C.G. Aneziris, Compos. Struct. **136**, 297 (2016)
47. D. Borisova, V. Klemm, S. Martin, S. Wolf, D. Rafaja, Adv. Eng. Mater. **15**, 571 (2013)
48. Q. Huang, O. Volkova, H. Biermann, J. Mola, Mater. Sci. Technol. **33**, 1224 (2017)
49. D. Bancroft, E.L. Peterson, S. Minshall, J. Appl. Phys. **27**, 291 (1956)
50. L.M. Barker, R.E. Hollenbach, J. Appl. Phys. **45**, 4872 (1974)

51. S.A. Maloy, G.T. Gray, C.M. Cady, R.W. Rutherford, R.S. Hixson, Metall. Mater. Trans. A **35**, 2617 (2004)
52. L.E. Murr, J.A. Korbonski, Metall. Trans. **1**, 3333 (1970)
53. K. Chen, C. Zheng, Z. Yuan, J. Lu, X. Ren, X. Luo, Mater. Sci. Eng., A **587**, 244 (2013)
54. R. Eckner, L. Krüger, M. Motylenko, A.S. Savinykh, S.V. Razorenov, G.V. Garkushin, EPJ Web Conf. **183**, 3007 (2018). https://doi.org/10.1051/epjconf/201818303007
55. C. Ullrich, R. Eckner, L. Krüger, S. Martin, V. Klemm, D. Rafaja, Mater. Sci. Eng., A **649**, 390 (2016)
56. D. Ehinger, L. Krüger, U. Martin, C. Weigelt, C.G. Aneziris, Steel Res. Int. **82**, 1048 (2011)
57. D. Ehinger, L. Krüger, U. Martin, C. Weigelt, C.G. Aneziris, Int. J. Solids Struct. **66**, 207 (2015). https://doi.org/10.1016/j.ijsolstr.2015.02.052
58. D. Ehinger, L. Krüger, U. Martin, C. Weigelt, C.G. Aneziris, Adv. Eng. Mater. **15**, 646 (2013)
59. Q.-X. Dai, A.-D. Wang, X.-N. Cheng, X.-M. Luo, Chin. Phys. **11**, 596 (2002)
60. F. Côté, V.S. Deshpande, N.A. Fleck, A.G. Evans, Mater. Sci. Eng., A **380**, 272 (2004)
61. G.F. Bocchini, Int. J. Powder Metall **22**, 185 (1986)
62. D. Ehinger, Dissertation, TU Bergakademie Freiberg, 2013
63. L.J. Gibson, M.F. Ashby, *Cellular Solids* (Cambridge University Press, Cambridge, 1997)
64. W.E. Baker, T.C. Togami, J.C. Weydert, Int. J. Impact Eng **21**, 149 (1998)
65. U. Ballaschk, H. Berek, D. Ehinger, C.G. Aneziris, L. Krüger, Adv. Eng. Mater. **15**, 590 (2013)
66. C. Baumgart, C. Weigelt, C.G. Aneziris, L. Krüger, EPJ Web Conf. **183**, 3014 (2018). https://doi.org/10.1051/epjconf/201818303014
67. D. Ehinger, L. Krüger, U. Martin, C. Weigelt, C.G. Aneziris, Steel Res. Int. **83**, 565 (2012)
68. C. Baumgart, T. Halle, C. Weigelt, L. Krüger, C.G. Aneziris, Sci. Technol. Mater. **30**, 35 (2018)
69. V.S. Deshpande, M.F. Ashby, N.A. Fleck, Acta Mater. **49**, 1035 (2001)
70. A.-J. Wang, D.L. McDowell, J. Eng. Mater. Technol. **126**, 137 (2004)
71. M. Wendler, A. Weiß, L. Krüger, J. Mola, A. Franke, A. Kovalev, S. Wolf, Adv. Eng. Mater. **15**, 558 (2013)
72. A. Jahn, A. Kovalev, A. Weiβ, P.R. Scheller, S. Wolf, L. Krüger, S. Martin, U. Martin, in *Proceedings of the 8th European Symposium on Martensitic Transformations (ESOMAT 2009),* Prague, Czech Republic, 7–11 September 2009
73. S. Martin, S. Wolf, U. Martin, L. Krüger, Solid State Phenom. **172–174**, 172 (2011)
74. T. Iwamoto, T. Tsuta, Y. Tomita, Int. J. Mech. Sci. **40**, 173 (1998)
75. H. Schumann, Krist. Tech. **10**, 401 (1975)
76. A. Jahn, A. Kovalev, A. Weiß, P.R. Scheller, Steel Res. Int. **82**, 1108 (2011)
77. S. Martin, C. Ullrich, D. Šimek, U. Martin, D. Rafaja, J. Appl. Crystallogr. **44**, 779 (2011)
78. G.B. Olson, M. Cohen, Metall. Trans. A **7**, 1897 (1976)
79. F. Lecroisey, A. Pineau, Metall. Mater. Trans. B **3**, 391 (1972)
80. N. Chawla, Y.-L. Shen, Adv. Eng. Mater. **3**, 357 (2001)
81. S. Martin, S. Richter, S. Decker, U. Martin, L. Krüger, D. Rafaja, Steel Res. Int. **82**, 1133 (2011)
82. H. Berek, A. Yanina, C. Weigelt, C.G. Aneziris, Steel Res. Int. **82**, 1094 (2011)
83. C. Weigelt, S. Giersberg, C. Wenzel, C.G. Aneziris, Adv. Eng. Mater. **12**, 486 (2010)
84. C. Weigelt, C.G. Aneziris, H. Berek, D. Ehinger, U. Martin, Adv. Eng. Mater. **14**, 53 (2012)

Chapter 13
Cyclic Deformation and Fatigue Behavior of Metastable Austenitic Steels and Steel-Matrix-Composites

Horst Biermann and Matthias Droste

Abstract The present contribution highlights the cyclic deformation behavior of metastable austenitic steels focusing on the effects of different (i) chemical compositions, (ii) manufacturing methods and (iii) strengthening methods in terms of a particle reinforcement and a quenching and partitioning treatment. The investigations are based on total strain controlled fatigue tests and the observed mechanical properties are discussed in context with the microstructural processes in the material, in particular the fatigue-induced α'-martensite formation. Overall, a major relevance is ascribed to the stacking fault energy and the grain size of the material. The fatigue behavior of the steels with different chemical compositions and the steels processed via casting, additive manufacturing, reversion annealing and hot pressing, respectively, is dominated by these two factors. In contrast, the most important factor in case of the reinforced steel-matrix-composites are the Mg-PSZ particles. The advantage of increasing stress amplitudes with increasing particle fraction is purchased with particle-related damage mechanisms like debonding and particle rupture causing a shorter fatigue life. The quenching and partitioning steel on the other hand benefits from higher α'-martensite fractions after partitioning increasing both, the strength and the fatigue life of the material.

13.1 Introduction

Metastability of austenitic steels means the tendency of the material for a martensitic phase transformation to reach a state of lower energy. More precisely, the face centered cubic (fcc) austenite exhibits the ability to transform to the body centered cubic (bcc) α'-martensite under mechanical loading [1–3] or due to a temperature decrease below the material-specific martensite start temperature M_s. Under loading the diffusionless phase transformation is the reason for the so-called TRIP (TRansformation

H. Biermann (✉) · M. Droste
Institute of Materials Engineering, Technische Universität Bergakademie Freiberg, Gustav-Zeuner-Straße 5, 09599 Freiberg, Germany
e-mail: biermann@ww.tu-freiberg.de

H. Biermann and C. G. Aneziris (eds.), *Austenitic TRIP/TWIP Steels and Steel-Zirconia Composites*, Springer Series in Materials Science 298,
https://doi.org/10.1007/978-3-030-42603-3_13

Induced Plasticity) effect, i.e. an increase in strength and ductility in comparison to a stable austenitic steel without a phase transformation, e.g. [4, 5]. Thus, these steels are also known as TRIP steels. However, in contrast to the stress-assisted phase transformation occurring during pure elastic loading, the deformation-induced α'-martensite formation requires plasticity to generate potential nucleation sites in terms of intersecting deformation bands and stacking faults, respectively [1].

Besides the austenite stability, an essential factor for activation of particular deformation mechanisms is the stacking fault energy (SFE). Of course, dislocation movement is always present in case of plastic deformation, but the dislocation glide characteristic, i.e. wavy or planar glide, strongly depends on the SFE and the presence of short range order [6]. At low SFE dislocations split up in Shockley partial dislocations forming a stacking fault promoting planar glide and the formation of α'-martensite. With increasing SFE the dominance of α'-martensite formation decreases and a transition to ε-martensite formation (cf. Sect. 13.3.2, [7]) and later on twinning sets in [5, 8, 9]. The latter leads to the TWIP (TWinning Induced Plasticity) effect which in comparison to the TRIP effect is characterized by a reduced increase in strength but an even higher increase in ductility [5]. Finally, at high SFE neither deformation-induced twinning nor a phase transformation occur but wavy dislocation glide is favored. Overall, the SFE has a quite strong influence on the mechanical properties and is itself determined by the temperature and the chemical composition of the material [5, 8–11].

Like in case of other materials, many structural components out of metastable austenitic steels are subjected to cyclic loads during their application. As fatigue cracks initiate and propagate far below characteristic quasi-static values like the yield strength or ultimate tensile strength, the knowledge of the respective fatigue properties is of utmost importance. Accordingly, the present chapter aims to describe the fundamental principles of the cyclic deformation and fatigue behavior of metastable austenitic steels and steel-matrix composites and to highlight the correlation to the observed deformation mechanisms.

At first, the influence of the chemical composition and, thus, of the SFE on the cyclic deformation behavior and in particular on the fatigue life is presented in Sect. 13.3 [12, 13]. Subsequently in Sect. 13.4, the influence of the manufacturing method of austenitic steels is discussed including additively manufactured [14, 15], cast [12] and ultrafine-grained material states [16].

However, like for other materials there are efforts to further improve the mechanical properties of austenitic steels of course. Two approaches, namely particle reinforcement and quenching and partitioning (Q&P) processing are presented in context with their individual benefits and drawbacks.

For aluminum for instance, particle reinforcement is a common and well known way for increasing the strength. In case of the present high alloy austenitic steels (cf. Sect. 13.3) particles of MgO partially-stabilized zirconia (Mg-PSZ) are used for reinforcement [17]. The MgO addition stabilizes the tetragonal phase of ZrO_2 to room temperature and, thereby, enables a stress-assisted phase transformation to the monoclinic phase during loading. This phase transformation is accompanied by a volume expansion of the Mg-PSZ producing compressive stresses in the vicinity.

The influence of the particle reinforcement on the fatigue behavior is presented in Sect. 13.5 [13, 18, 19].

Quenching and partitioning (Q&P) processing [20, 21] has been another intensely investigated topic for many researchers over the last years. Their mutual aim is to design steels which meet the criteria for the 3rd generation of Advanced High Strength Steels (AHSS), i.e. a significant enhancement of the strength compared to common metastable austenitic steels (2nd generation of AHSS) but still at a reasonable ductility better than martensitic steels. So far, most publications focus on developing and investigating the process and the achieved monotonic properties, however, the fatigue behavior is hardly considered. Hence, Sect. 13.6 presents one of the first investigations on the cyclic deformation behavior of an ultra-high strength steel processed via a modified Q&P route including the fatigue life and the microstructure after cyclic deformation [22].

13.2 Methodology

This chapter introduces the experimental details and methodical issues necessary for understanding and interpretation of the results discussed afterwards. Therefore, the chemical composition and manufacturing methods of the different test materials are presented. In addition, the details of fatigue testing as well as the analytical methods used for characterization of the cyclic deformation behavior are pointed out.

13.2.1 Materials

The investigated materials are high alloy austenitic TRIP and TWIP steels and their particle-reinforced counterparts. An overview of the chemical compositions and particle size distributions is given in Table 13.1 for the steels and in Table 13.2 for the Mg-PSZ reinforcement particles. It should be noted, that the last steel of Table 13.1 (Cr14NC11.15) is austenitic at room temperature (RT) after solution annealing, but exhibited a relatively high α'-martensite fraction before cyclic deformation due to a novel quenching and partitioning (Q&P) treatment, cf. Sect. 13.2.2.

The steel powders were gas atomized by TLS (Bitterfeld, Germany) and the Mg-PSZ powder (Table 13.2) was mechanically milled and delivered by Saint-Gobain (USA). However, the steel powders used for hot pressing (HP) and electron beam melting (EBM) differed significantly regarding the particle size distribution. Whereas the HP powders exhibited d_{50} values in the range 26–28 µm and a d_{90} of 44 µm, the equivalent values were 73 µm and 119 µm, respectively, for the EBM powder.

Table 13.1 Chemical compositions of the investigated steel alloys in wt.% and their designations in this chapter. In addition, the last column indicates the average grain sizes in µm

Steel Alloy	Designation in this book	Cr	Mn	Ni	C	N	Si	Fe	$\bar{d}$
X8CrMnNi16-6-4	HP 16-6-4	16.2	6.0	3.5	0.08	0.08	0.9	Bal.	11
X4CrMnNi16-6-6	HP 16-6-6	16.1	6.0	6.0	0.04	0.04	0.9	Bal.	10
X5CrMnNi16-6-9	HP 16-6-9	15.8	5.6	8.9	0.05	0.06	1.0	Bal.	15
X6CrMnNi15-6-6	Cast 15-6-6	15.2	5.5	5.7	0.06	0.06	1.0	Bal.	774
X5CrMnNi16-6-6	EBM 16-6-6	15.8	6.4	5.9	0.05	0.04	0.9	Bal.	38
X4CrMnNi17-7-6	UFG 17-7-6	16.6	7.1	6.4	0.04	0.02	1.0	Bal.	0.7
X15CrNiMnN14-3-3	Cast Cr14NC11.15	14.2	3.0	3.3	0.15	0.11	0.4	Bal.	/

Table 13.2 Chemical composition of the delivered Mg-PSZ powder in wt.% and its designation in this book (5 and 10, respectively, indicate the volume fraction). In addition, the d_{10}, d_{50} and d_{90} values of the particle size distribution in μm and the phase fractions in vol.% are given

	Designation in this book	MgO	HfO_2	ZrO_2	d_{10}	d_{50}	d_{90}	mon.	tetr.	cub.
Mg-PSZ	5Z/10Z	2.82	1.74	Bal.	0.2	3.1	22.4	≈35	≈32	≈33

13.2.2 Manufacturing Methods

Hot pressing (HP) is a powder metallurgical processing route under vacuum atmosphere. The powder was hot pressed by Fraunhofer IKTS (Dresden, Germany) at 1250 °C for 30 min at a pressure of approximately 30 MPa applied via a piston. The heating and cooling rates were set to 10 and 5 K/min, respectively. The HP discs exhibited a diameter of 150 mm at a height of 15–20 mm.

Casting was carried out either by ACTech (Freiberg, Germany) using the sand-casting technique in case of the Cast 15-6-6 steel or by the Institute of Iron and Steel Technology (TU Bergakademie Freiberg, Germany) using die-casting for the Cast Cr14NC11.15 material. The latter was melted in a vacuum induction furnace and cast into a water-cooled copper mold placed in the furnace chamber. After casting, all steels were solution annealed for 30 min at 1050 °C (Cast 15-6-6) and at 1150 °C (Cast Cr14NC11.15), respectively.

Electron beam melting (EBM) is a powder-bed based additive manufacturing technology. The component is built in layers under a controlled atmosphere, i.e. a low helium pressure, enabling the electron beam to melt the powder. For the fatigue tests, cylindrical rods with a diameter of 14 mm and a height of 130 mm were built upright, i.e. parallel to the building direction. An Arcam A2X (Mölndal, Sweden) EBM machine was operated at a helium pressure of 2×10^{-3} mbar with beam parameters set to: acceleration voltage 60 kV, beam current 7.5 mA, scan speed 4.500 mm/s and hatch distance 50 μm. A meander-shape scan strategy in combination with a rotation of the scan direction of 90° after each layer was used. The layer thickness was 50 μm.

Reversion annealing is a heat treatment step within a more comprehensive thermo-mechanically controlled processing (TMCP) [23–30] which is the most common way for metastable austenitic steels to produce an ultrafine-grained (UFG) microstructure. The TMCP always includes a cold deformation step to induce a high amount of α'-martensite in the microstructure.

At first, the present material UFG 17-7-6 was forged at 1200 °C reducing the diameter from an initial 50 mm to 27 mm (Fig. 13.1). Afterwards, the metastable austenite was deformed at RT by rotary swaging further reducing the diameter to 8.3 mm in 11 passes and , thereby, inducing a high α'-martensite fraction of about

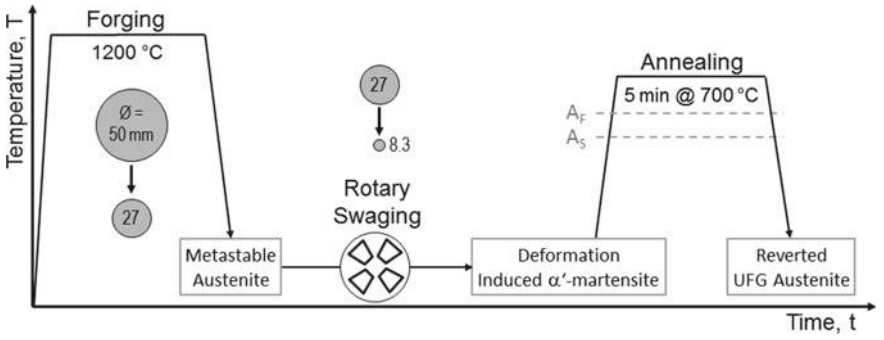

Fig. 13.1 Schematic representation of the thermo-mechanically controlled processing to achieve an UFG microstructure. After [16]

75 vol.%. The final step was an annealing treatment at 700 °C for 5 min to provoke the reversion of this α'-martensite back to austenite, called reversion annealing in literature. As reported by Weidner et al. [31] for a steel of similar chemical composition, the reversion path is based on a shear process without diffusion which is typical for interstitial free steels [32–35]. Thus, this TMCP route led to an UFG microstructure with an average grain size of 0.7 μm (cf. Sect. 13.4.1).

Quenching and partitioning (Q&P) is a thermal processing technology aiming for mechanical properties meeting the demands for the third generation of advanced high-strength steels (AHSS) [36–40], i.e. a very high strength comparable to martensitic steels but at a higher ductility. The key factor for these properties is the microstructure after Q&P consisting of tempered α'-martensite and interstitially-enriched austenite. However, usual Q&P processing includes austenization followed by quenching to a temperature well above RT due to the relatively high martensite start (M_s) temperature of the steels. In addition, a subsequent partitioning treatment is necessary before cooling down to RT. In contrast, the present steel Cr14NC11.15 exhibits a M_s temperature slightly below RT simplifying this temperature-time control. This novel Q&P process designed by Wendler et al. [21] requires a subzero cooling in a second step (Fig. 13.2) to induce athermal α'-martensite whose target fraction can be adjusted by variation of the cooling temperature T_c. Finally, a partitioning treatment has to be performed to provoke a diffusion of interstitials *C* and *N* from the supersaturated α'-martensite to the retained austenite. For the present steel two different cooling temperatures of −120 °C and −20 °C have been used in combination with a partitioning at 450 °C for 3 min (Fig. 13.2).

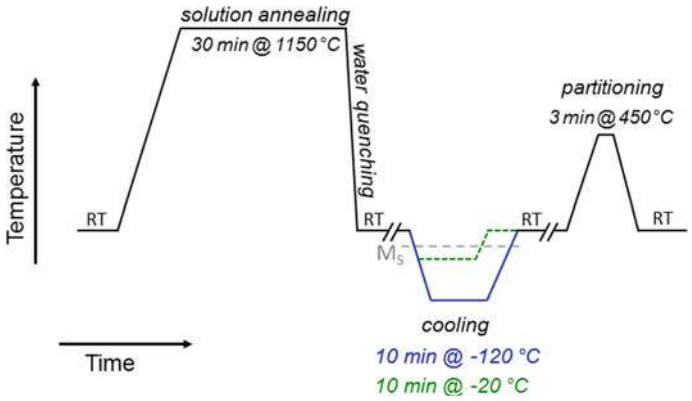

Fig. 13.2 Schematic representation of the Q&P process to achieve an ultra-high strength austenitic-martensitic microstructure. After [22]

13.2.3 Fatigue Testing

All fatigue tests presented in this work are total strain controlled tests performed either on a Landmark 250 or a Landmark 100, both servo-hydraulic testing systems by MTS (Eden Prairie, USA). Constant strain amplitude tests under symmetrical push-pull conditions (strain ratio $R_\varepsilon = -1$) were conducted in the range of $0.25\% \leq \Delta\varepsilon_t/2 \leq 2\%$ following a triangular strain function with a constant strain rate of 4×10^{-3} s^{-1}.

Furthermore, a Feritscope® (Fischerscope® MMS® PC, Sindelfingen, Germany) has been attached to the specimens to record the evolution of α'-martensite in situ during cyclic deformation. As this device is calibrated for measuring the δ-ferrite phase fraction denoted in Fe-%, its readings have to be multiplied by a correction factor of 1.7 to obtain the actual α'-martensite fraction [41]. However, this linear correlation is only valid up to 55 Fe-%, which is exceeded in some of the presented tests. Hence, all α'-martensite evolutions presented in this chapter are the pure Feritscope® readings in Fe-% without any correction factor.

The fatigue specimens exhibited a gauge length of 14 mm at a diameter of 5 mm (UFG 17-7-6) and 6 mm (all other materials), respectively. They were ground and polished mechanically before testing.

13.2.4 Analytical Methods

Scanning electron microscopy (SEM) was used to characterize the microstructure of the different materials before and after cyclic deformation. Therefore, imaging methods like backscattered electron (BSE) imaging, electron channeling contrast imaging (ECCI) and SEM in transmission mode (t-SEM) as well as the analytical method electron backscattered diffraction (EBSD) are employed. The EBSD (EDAX,

New Jersey, USA) scans are used for calculation of the average grain size $\bar{d}$ according to the following relationship

$$\bar{d} = \frac{\sum_{i=1}^{N} A_i \cdot d_i}{\sum_{i=1}^{N} A_i} \tag{13.1}$$

where A_i and d_i are the area and diameter of the i^{th} grain, respectively. All SEM investigations were performed on a field emission gun Mira 3 FE-SEM by Tescan (Brno, Czech Republic) operated at an acceleration voltage between 20 and 30 kV.

Transmission electron microscopy (TEM) was applied for the UFG 17-7-6 material which was thinned by electrolytic etching. The investigations were carried out on a field emission gun JEOL JEM-2200FS operated at 200 kV.

X-ray micro-computed tomography (μ-CT) was used for defect characterization in the additive manufactured EBM 16-6-6 material and the HP 16-6-6 for reference purposes. The analyzed volumes were 45.6 mm^3 (EBM) and 48.2 mm^3 (HP), respectively. The Nikon system was operated at 160 kV with a micro-focus of 3 μm using a tungsten filament for X-ray emission (further details of setup are given in [42]). The data was analyzed by the software VGSTUDIO MAX 3.1 using the algorithm "VGEasyPore".

13.3 Influence of Chemical Composition on the Fatigue Behavior

This chapter investigates the influence of different concentrations of Ni on the fatigue behavior and deformation mechanisms of three hot pressed high alloy austenitic steels[1] (HP 16-6-4, HP 16-6-6, HP 16-6-9, cf. Table 13.1). Ni is an austenite stabilizer and increases the stacking fault energy (SFE) of a material and, thereby, strongly influences the characteristics of plastic deformation.

13.3.1 Cyclic Deformation Behavior

The cyclic deformation curves of Fig. 13.3 indicate a distinct difference between the variants with low and medium Ni content compared to the HP 16-6-9 with 9 wt.% Ni. The latter exhibits a pronounced primary hardening whose intensity decreases with decreasing strain amplitude and finally merges to continuous cyclic softening at $\Delta\varepsilon_t/2 = 0.2\%$. This behavior is typical for high alloy austenitic steels and related to an increase in dislocation density and interactions between the dislocations [43, 44]. For the highest strain amplitude $\Delta\varepsilon_t/2 = 2\%$ cyclic hardening goes on until failure whereas it is replaced by cyclic softening for the other strain amplitudes

[1] The present discussion is based on investigations by Glage and summarizes results of his doctoral thesis [13].

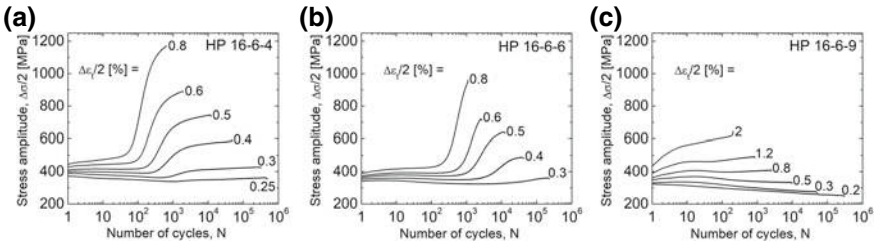

Fig. 13.3 Cyclic deformation curves for different strain amplitudes of the materials HP 16-6-4 (**a**), HP 16-6-6 (**b**) and HP 16-6-9 (**c**). After [13, 18, 19]

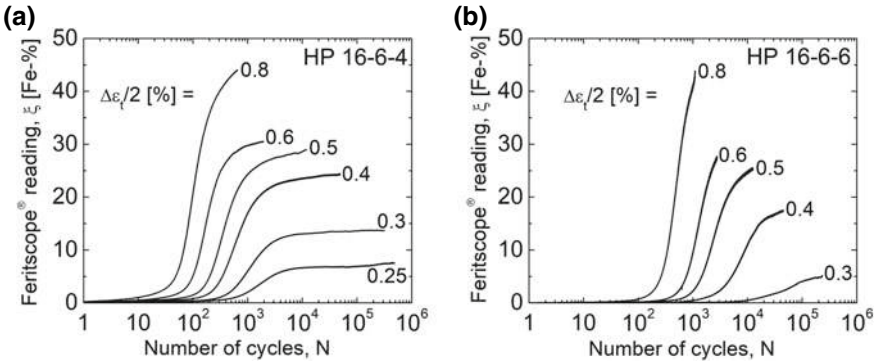

Fig. 13.4 α'-martensite evolution during cyclic deformation at different strain amplitudes for the materials HP 16-6-4 (**a**) and HP 16-6-6 (**b**). After [13, 19]

probably caused by rearrangement of dislocations. However, in case of the high strain amplitudes $\Delta\varepsilon_t/2 \geq 0.8\%$ secondary hardening, mainly attributed to the formation of fatigue-induced twinning (Sect. 13.3.2), sets in after a certain number of cycles. The twin boundaries lead to a reduction of the mean free path of dislocations [45] often called dynamic Hall-Petch effect in literature, e.g. [46], leading to an increase of the stress amplitudes.

In the beginning of cyclic deformation the qualitative courses of the cyclic deformation curves of the other two HP steels (Fig. 13.3a, b) are similar to the described behavior, although the primary hardening slightly decreases with decreasing Ni content. A substantial difference occurs once the secondary hardening sets in. Its magnitude significantly increases with decreasing Ni content and, in addition, the secondary hardening is triggered at a lower number of cycles. Besides the chemical composition, the intensity and onset is of course affected by the applied strain amplitude, i.e. a shorter incubation period and increasing magnitude with increasing strain amplitude. Especially in case of the HP 16-6-4 the cyclic hardening merges to a saturation-like stage at low and medium strain amplitudes continuing until fracture. However, including the α'-martensite evolution (Fig. 13.4) in the investigation

of cyclic deformation behavior shows obviously, that the secondary hardening correlates quite well with the cyclic deformation behavior. In fact, the α'-martensite formation causes the cyclic hardening as it is well-known for metastable austenitic steels, e.g. [9, 44, 47–49]. In the present alloys, this hardening effect is not solely due to the higher hardness of the martensitic phase, but a strong impact is attributed to (i) the lower grain size of the α'-martensite compared to the austenite and (ii) a reduced mean free path for dislocations as the α'-martensite nuclei preferentially form within deformation bands [4, 50].

Based on the finding that the cyclic hardening is due to the martensitic phase transformation, the reasons for the differences between the materials as well as for the different onset times and intensities can be discussed. Figure 13.5 shows the threshold value of the cumulated plastic strain $\lambda_{p,\mathrm{th}}$ which has to be exceeded to trigger the α'-martensite formation [9, 48, 49] plotted against the applied total strain amplitudes. This threshold value stems from the premiss that the deformation-induced α'-martensite formation is triggered by a double shear mechanism of at least two intersecting stacking faults on different slip planes [1, 51]. Thus, the threshold value decreases with increasing strain amplitude (Fig. 13.5) as a consequence of an increase in lattice defects and a higher density of deformation bands, i.e. more sites for α'-martensite nucleation [43, 49, 52]. Consequently, decreasing strain amplitudes lead to increasing incubation periods for the martensitic phase transformation (Fig. 13.4) and the accompanied secondary hardening (Fig. 13.3a, b). Furthermore, the lower threshold values of the HP 16-6-4 steel compared to HP 16-6-6 are due to its lower austenite stability.

The cyclic hardening causes a decrease in the plastic strain amplitude $\Delta\varepsilon_{\mathrm{pl}}/2$, i.e. the plasticity within a cycle decreases. As a consequence of this, the driving force for further α'-martensite formation decreases as well which leads to the described stage of saturation-like behavior, especially in case of medium and small amplitudes. An additional contribution to this behavior is attributed to internal stresses due to the formation of α'-martensite inhibiting a further phase transformation.

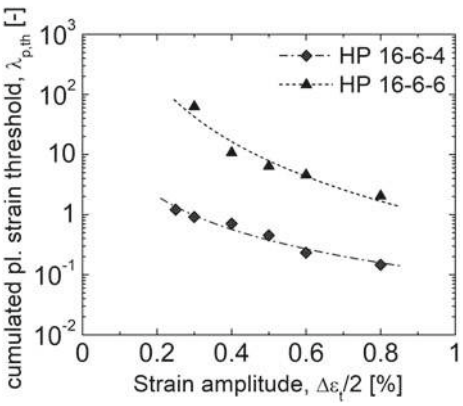

Fig. 13.5 Threshold values of the cumulated plastic strain $\lambda_{p,\mathrm{th}}$ plotted against the applied strain amplitudes. After [13]

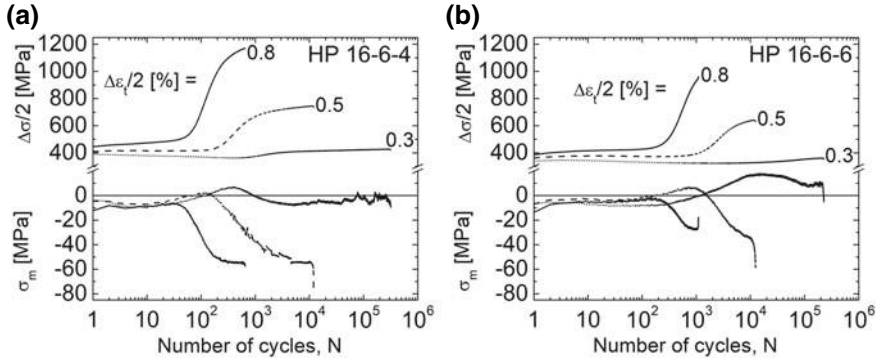

Fig. 13.6 Stress amplitudes and mean stresses of selected strain amplitudes versus number of cycles for the HP 16-6-4 (**a**) and HP 16-6-6 (**b**). After [13]

Figure 13.6 illustrates the connection between stress amplitude and mean stress arising during cyclic deformation. As discussed above, the martensitic phase transformation provokes an increase of the stress amplitude which, in addition, goes along with a decreasing mean stress whose magnitude as well increases with increasing strain amplitude. This behavior was also observed by other authors [47, 53, 54] and is attributed to the volume expansion accompanying the α'-martensite formation. Prior to the described behavior, a stage of increasing mean stress is observed which is more pronounced with decreasing strain amplitude, i.e. with a less pronounced α'-martensite formation. This increase of the mean stress is probably due to highly faulted areas, i.e. regions with a high density of stacking faults called ε-martensite in literature. This ε-martensite causes a volume contraction and, thereby, an increasing mean stress in total strain controlled fatigue tests. However, this effect is overcompensated once the α'-martensite formation and its volume expansion sets in resulting in the described decreasing mean stresses.

13.3.2 Microstructure After Cyclic Deformation

The formation of stacking faults, ε-martensite and α'-martensite is verified by SEM investigations and exemplarily shown in Fig. 13.7 for the HP 16-6-4 steel cyclically deformed at $\Delta\varepsilon_t/2 = 0.25\%$. A high amount of deformation bands is formed inside the grains (Fig. 13.7a, b) and their stacking fault density increases with ongoing plastic deformation. However, after cyclic deformation these bands are often indexed as ε-martensite by EBSD (Fig. 13.7d, yellow coloured) due to the high density of stacking faults changing the stacking sequence of the {1 1 1} planes from ABCABC of the fcc crystal lattice to the hexagonal ABAB [7]. In accordance with other authors, e.g. [55], these highly faulted deformation bands are a preferred nucleation site for

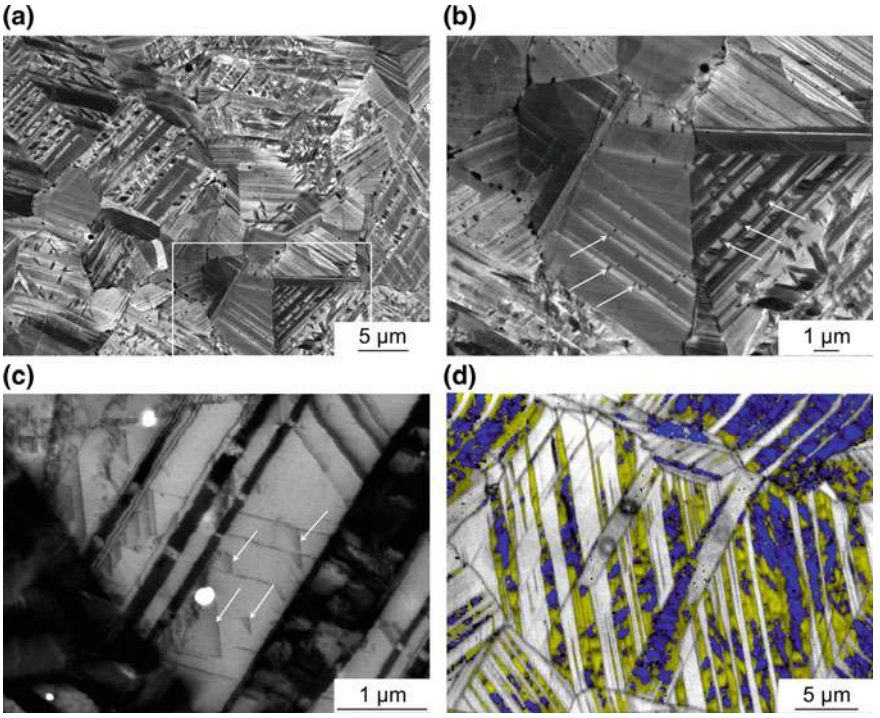

Fig. 13.7 Microstructure of the steel HP 16-6-4 after cyclic deformation at $\Delta\varepsilon_t/2 = 0.25\%$. BSE (**a**, **b**) and ECCI (**c**) images as well as EBSD phase map (**d**, blue—α'-martensite, yellow—ε-martensite, grey—band contrast). After [13, 19]

α'-martensite as revealed by Fig. 13.7b (white arrows) and d indicating a martensitic phase transformation in the order $\gamma \rightarrow \varepsilon \rightarrow \alpha'$.

Some individual stacking faults are also present in between the deformation bands as shown in Fig. 13.7c (white arrows). Furthermore, this micrograph reveals the quite planar glide character of the material due to its low SFE.

The increased SFE of the HP 16-6-9 on the other hand causes a change in the deformation mechanisms, which in addition are depending on the applied strain amplitude. At small strain amplitudes only few grains contain deformation bands which are usually oriented approximately 45° in relation to the loading axis (Fig. 13.8a, b). As already known for the steel HP 16-6-4 the deformation bands consist of stacking faults. In the vicinity of the crack tip a higher deformation band density (Fig. 13.8c) is observed due to the higher local plasticity. Figure 13.8d even reveals Σ3-twin boundaries which are marked in yellow indicating deformation bands of sufficient thickness with respect to the resolution of the EBSD scan thus being fatigue-induced twins.

At a higher strain amplitude of $\Delta\varepsilon_t/2 = 0.8\%$ the density of deformation bands increases. In between the bands dislocation cells are formed (Fig. 13.8e) indicating

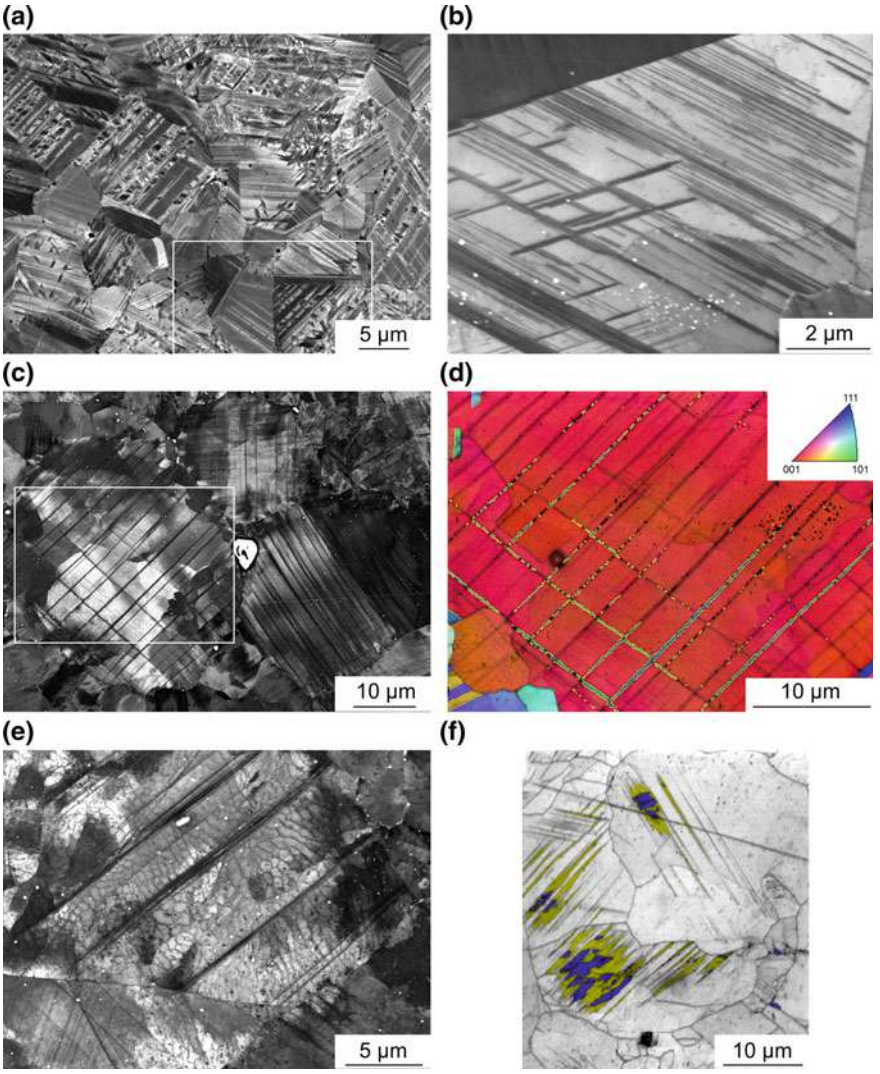

Fig. 13.8 BSE (**a**) and ECCI (**b**, **c**, **e**) images and EBSD orientation (**d**) and phase (**f**) maps of the steel HP 16-6-9 cyclically deformed at $\Delta\varepsilon_t/2 = 0.4\%$ (**a**–**d**) and $\Delta\varepsilon_t/2 = 0.8\%$ (**e**, **f**), respectively. Loading axis is horizontally. After [13, 18, 19]

the beginning transition to a wavy glide character [56]. Nevertheless, a rare formation of α'-martensite via the intermediate ε-martensite is observed as well (Fig. 13.8f) at this high strain amplitude. However, the secondary hardening in the cyclic deformation curve (Fig. 13.3c) is rather due to fatigue-induced twinning as the α'-martensite fraction remains low and the twins are strong obstacles for dislocation movement reducing the mean free path for dislocations on a second slip system [18, 46, 57].

13.3.3 Fatigue Life

The fatigue life estimation for the HP materials according to Basquin-Manson-Coffin is shown in Fig. 13.9a. Obviously, the most metastable steel HP 16-6-4 exhibits a superior lifetime at small strain amplitudes compared to HP 16-6-9 and vice versa. Accordingly, the α'-martensite formation seems to be detrimental at high strain amplitudes due to the decreased ductility of the material which is a determining factor in this lifetime regime [58]. On the other hand, at small strain amplitudes the α'-martensite formation leads to a significant decrease in the plastic strain amplitude and, thereby, to an increase in the fatigue life. This strain amplitude-dependent impact of the martensitic phase transformation on the fatigue life causes a crossover of the lifetime curves for the different austenite stabilities at a total strain amplitude of approximately $\Delta\varepsilon_t/2 = 0.5\%$ (Fig. 13.9a).

For the lifetime description of all HP variants with just one power law, Glage [13] proposed the plastic stress-strain product SSP_{pl}:

$$SSP_{pl} = \sqrt{\frac{\Delta\sigma}{2}\frac{\Delta\varepsilon_{pl}}{2}E} \tag{13.2}$$

As already discussed, the α'-martensite formation provokes an increase of the stress amplitude $\Delta\sigma/2$ which is accompanied by a decrease in the plastic strain amplitude $\Delta\varepsilon_{pl}/2$. The SSP_{pl} considers both parameters resulting in much smaller differences between the material variants (Fig. 13.9b). Despite the fact that variant specific lifetime curves would still exhibit slightly different slopes, it is possible to provide a surprisingly good lifetime description for all materials with just one power law (Fig. 13.9b). In fact, almost all test data is located within a scatter band of factor 3.

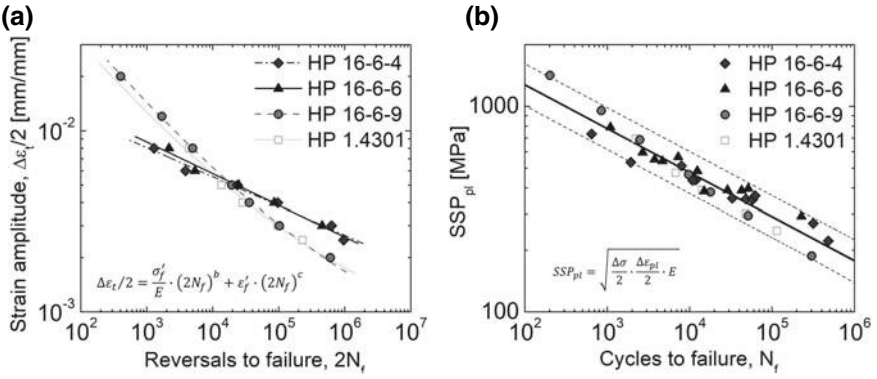

Fig. 13.9 Total strain based fatigue life curves (**a**), and SSP_{pl} parameter for lifetime estimation with one power law and corresponding scatter band of factor 3 (**b**). After [13, 19]

13.4 Influence of the Manufacturing Method on the Fatigue Behavior

This section compares the fatigue properties of the same steel grade (base composition 16-6-6, cf. Table 13.1) manufactured via different processing routes: (i) Casting, (ii) additive manufacturing by EBM and (iii) reversion annealing to achieve an UFG microstructure.[2] In addition, the results will be compared to the HP counterpart which was introduced in Sect. 13.3. The manufacturing methods are described in more detail in Sect. 13.2.2.

13.4.1 Microstructure of the Undeformed State

The microstructures of the different material states before cyclic deformation are shown in Fig. 13.10. The biggest difference is observed regarding the average grain size. The cast material by far exhibits the biggest grain size of 774 μm whereas the smallest one is observed for the UFG state with 0.7 μm. In between these two materials, the EBM and HP states fit in with average grain sizes of 38 μm and 10 μm, respectively. However, for an additive manufactured material the microstructure of the EBM 16-6-6 (Fig. 13.10b) is relatively isotropic which is attributed to multiple phase transformations caused by the process-inherent cyclic heat treatment [14, 15]. Nevertheless, the grains are characterized by a slightly elongated shape oriented along the build direction as indicated by an average aspect ratio of 0.34 and a grain shape orientation of 91°, cf. Fig. 13.10b.

Besides anisotropy, another issue regarding additive manufactured materials are process-induced defects like lack of fusion which have a detrimental effect on the mechanical properties, in particular the fatigue lifetime. The present EBM 16-6-6 exhibited a relative density of 99.4% compared to over 99.99% for the HP 16-6-6 according to μCT-scans. As depicted in Fig. 13.11, the EBM material contains a high number of small pores with a sphericity of more than 0.5, i.e. with a relatively round and spherical shape. The pore density decreases significantly for higher equivalent pore diameters d_P. Accordingly, less than 20 pores with a $d_P > 200$ μm were detected. However, the sphericity decreases with increasing d_P and the two biggest pores with a d_P of almost 1600 μm exhibit a sphericity below 0.2. In contrast, the few defects in the HP state all exhibit a $d_P < 100$ μm and sphericities above 0.5.

[2]For a discussion in detail of the individual material states the reader is referred to [12] (cast), [14] (EBM) and [16] (UFG) which the present discussion is based on.

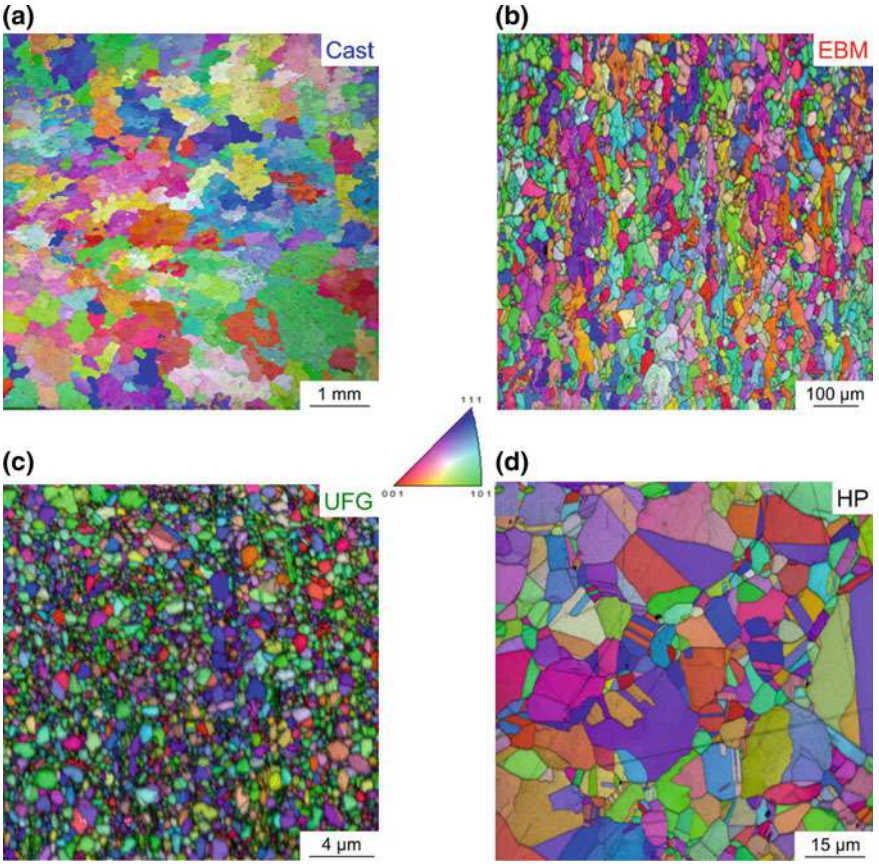

Fig. 13.10 EBSD orientation maps of the microstructures before cyclic deformation of the cast (**a**), EBM (**b**, build direction vertical), UFG (**c**) and HP (**d**) state, respectively. (**d**) After [14]

13.4.2 Cyclic Deformation Behavior and α′-Martensite Formation

The stress amplitudes at the beginning of cyclic deformation strongly depend on the material state and, in particular, on the grain size (Fig. 13.12). The cast 15-6-6 with the biggest grain size exhibits the lowest initial stress amplitudes of 200–300 MPa. With decreasing grain size the stress amplitudes of the first cycles increase to about 290–400 MPa for the EBM state and are once again slightly higher in case of the HP reference material (Fig. 13.3b). By far the highest initial stress amplitudes are observed for the UFG state with about 600–1000 MPa. These differences are supposed to stem from a reduced mean free path for dislocation movement as the number of obstacles in terms of grain boundaries increases with decreasing

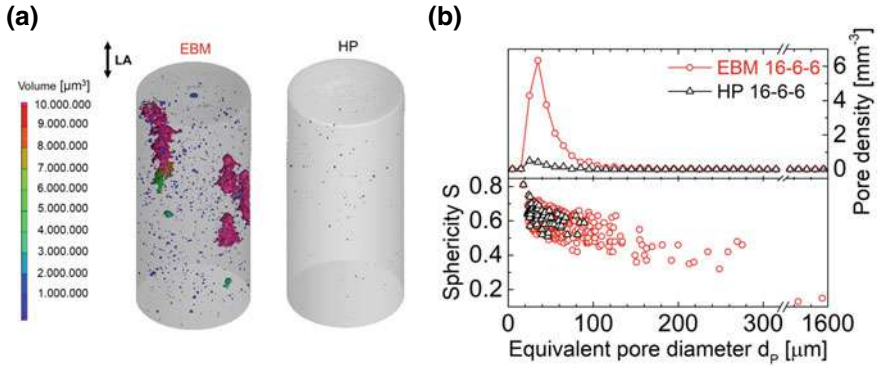

Fig. 13.11 µCT results of the EBM and HP 16-606 materials. **a** 3D-volume defect distribution (LA: loading axis) and **b** pore density and sphericity plotted against the equivalent pore diameter. The diameter of the scanned gauge length was 3 mm. After [14]

grain size of the austenite. In this context it has to be noted, that the materials discussed here all exhibit a mostly planar glide character. Wavy glide materials on the other hand exhibit other dislocation arrangements like bundles or cells whose size is significantly smaller compared to conventional grain sizes, i.e. the grain boundaries have a minor influence on the dislocation movement. Accordingly, in wavy glide a grain size dependence regarding the cyclic stress is only observed for UFG and NC materials [59].

A further difference is observed for the cyclic hardening behavior of the material states. Whereas the cast and the EBM materials exhibit similar behavior compared to the HP state discussed in Sect. 13.3.1, i.e. a strong cyclic hardening especially at high strain amplitudes caused by α'-martensite formation (Fig. 13.13), the cyclic hardening is less pronounced for the UFG material (Fig. 13.12c). Although the α'-martensite fraction after cyclic deformation at high strain amplitudes is the highest for the UFG state, the induced cyclic hardening is the least pronounced. This is attributed to the origins of α'-martensite induced hardening, namely (i) the higher strength of α'-martensite compared to austenite, (ii) the smaller grain size of α'-martensite and

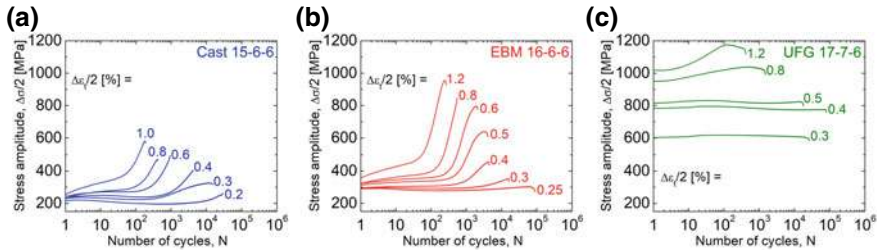

Fig. 13.12 Cyclic deformation curves of the cast (**a**), EBM (**b**) and UFG (**c**) states. After [12] (**a**), [14] (**b**) and [16] (**c**)

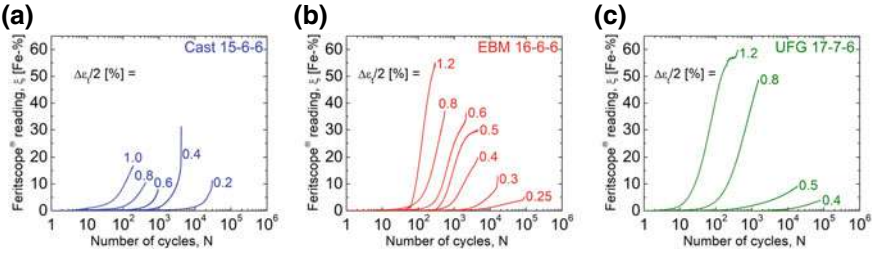

Fig. 13.13 α'-martensite evolution during cyclic deformation at different strain amplitudes for the material states cast (**a**), EBM (**b**) and UFG (**c**). After [12] (**a**), [14] (**b**) and [16] (**c**)

(iii) the reduced mean free path for dislocation movement in the austenite due to the formation of α'-martensite nuclei in the deformation bands [4, 50]. As the average austenitic grain size of 0.7 μm in the UFG material is already quite small, the α'-martensite formation does not lead to a distinct grain refinement. Furthermore, no deformation bands are formed and the influence of the α'-martensite formation on the mean free path is negligible as will be seen in Sect. 13.4.3. However, as only the first out of three hardening mechanisms is relevant in the UFG state, the least pronounced increase of the cyclic stress compared to the other material states where all three mechanisms are active is consistent.

Moreover, a difference in the incubation period for the onset of α′-martensite formation is observed. Figure 13.14 shows the cumulated plastic strain threshold $\lambda_{p,\mathrm{th}}$ which has to be exceeded to trigger the phase transformation plotted against the applied strain amplitude. As expected, the threshold value decreases with increasing strain amplitude (cf. Sect. 13.3.1 for more detailed discussion on this). The only exception is the EBM state cyclically deformed at $\Delta\varepsilon_t/2 = 1.2\%$. As obvious in Fig. 13.13b, the signal of the Feritscope® is quite unusual for the respective specimen probably due to a misalignment or other experimental issues during the test. However,

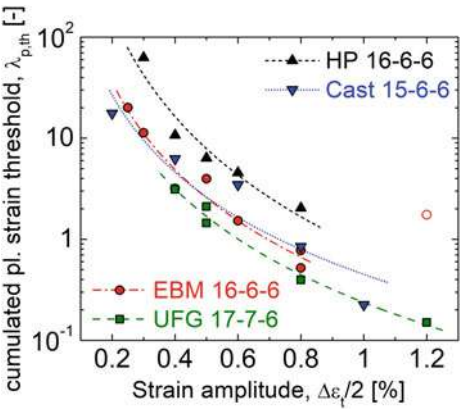

Fig. 13.14 Cumulated plastic strain threshold $\lambda_{p,\mathrm{th}}$ which has to be exceeded to trigger the fatigue-induced α'-martensite formation plotted against the applied total strain amplitude for the different material states

due to this irregularity, this specimen is excluded from the following discussion on the incubation period.

The EBM and cast states exhibit similar threshold values $\lambda_{p,\mathrm{th}}$ (Fig. 13.14) which are reduced in comparison to the already known HP material. This difference most probably stems from differences in the chemical composition. The values given in Table 13.1 are valid for the powders of the EBM and HP states, respectively. However, the bulk EBM material contains 0.5 wt.% less Mn than the HP state due to evaporation during EBM processing [15, 60]. The cast material as well exhibits a lower Mn content and a slightly lower Ni content than the HP state. This reduced content of austenite stabilizers leads to a decrease in austenite stability [61, 62] and a shift of the cumulated plastic strain threshold $\lambda_{p,\mathrm{th}}$ to lower values.

The UFG state on the other hand exhibits a slightly higher Mn and Ni content than the HP material but an even lower threshold $\lambda_{p,\mathrm{th}}$ than the EBM and cast states. Hence, in this case another factor has to be more dominant than the higher austenite stability due to the chemical composition. This is supposed to be the significantly higher stress amplitude at the onset of α'-martensite formation. These high cyclic stresses lead to the formation of small α'-martensite nuclei at an earlier stage of deformation compared to the other material states.

13.4.3 Microstructure After Cyclic Deformation

The microstructural features developing during cyclic deformation are similar in case of the cast, EBM processed and HP states. Figures 13.15a, b exemplarily show a grain of the EBM state cyclically deformed at $\Delta\varepsilon_t/2 = 0.3\%$. Deformation bands containing a high density of stacking faults have developed inside the grain. The stacking fault density increases with ongoing plastic deformation and as already discussed in Sect. 13.3.2 at a high density the deformation bands get indexed as ε-martensite by EBSD indicating a highly faulted microstructure (Fig. 13.15b). Furthermore, α'-martensite nuclei form inside the deformation bands acting as dislocation barriers for the stacking faults. Thus, the martensitic phase transformation occurs via the intermediate ε-martensite, i.e. $\gamma \rightarrow \varepsilon \rightarrow \alpha'$. At higher strain amplitudes several glide systems are activated and intersecting deformation bands provide a preferred nucleation site for α'-martensite [1, 2, 63]. In general, the α'-martensite formation is triggered by a double shear mechanism of at least two intersecting stacking faults on different slip planes.

However, this characteristic deformation band structure is not observed in the UFG material. Instead, individual stacking faults often reach through the entire grain (Fig. 13.15c, d). At this grain size, the stacking faults are supposed not to nucleate within the grains but at the grain boundaries, i.e. single partial dislocations are emitted from grain boundaries and propagate into the grain interior until they reach the grain boundary on the opposite side or some other obstacle. However, the stacking fault density in the grains is supposed to increase in this manner until ε-martensite is indexed by EBSD as well, cf. [16]. Due to the high stresses quite small α'-martensite

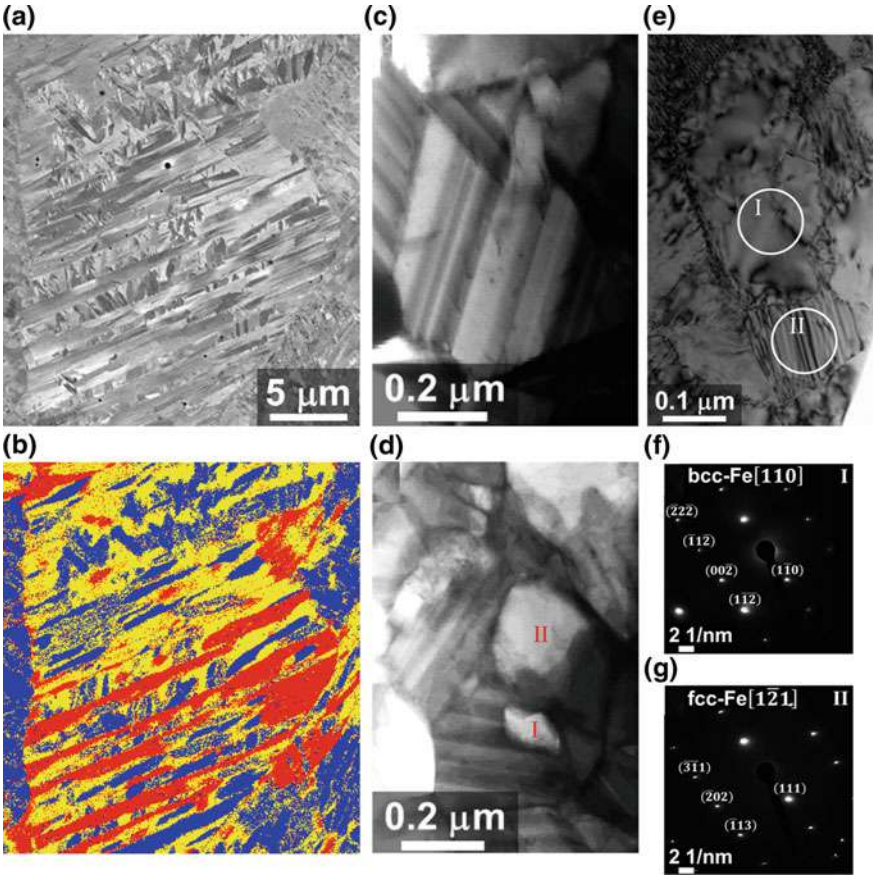

Fig. 13.15 **a**, **b** BSE image and corresponding EBSD phase map of the EBM state cyclically deformed at $\Delta\varepsilon_t/2 = 0.3\%$ (loading axis is vertical; red—austenite, yellow—ε-martensite, blue—α'-martensite). **c**, **d** t-SEM micrographs and **e** TEM bright field image of the UFG state cyclically deformed at $\Delta\varepsilon_t/2 = 0.8\%$. **f**, **g** SAED patterns of the areas marked by I and II in (**e**). After [14] (**a**, **b**) and [16] (**c**–**g**)

nuclei form inside these highly faulted grains (Fig. 13.15d, marked by I and II) and grow until the whole grain is martensitic. SAED patterns verify this assumption. The area marked by I in Fig. 13.15e is already transformed to α'-martensite as indicated by its bcc SAED pattern (Fig. 13.15f). It exhibits a Nishiyama-Wassermann orientation in relation to the adjacent fcc area marked by II (Fig. 13.15e, g). Hence, the α'martensite nucleated inside this grain, i.e. even at this small size the grains do not transform entirely at once.

13.4.4 Fatigue Life

Figure 13.16 shows the fatigue life curves of the discussed material states. In addition, a curve labeled EBM 16-6-6 ann. is plotted which represents a solution annealed (1050 °C, 30 min) state of the EBM material (see [14] for further details). However, the shortest fatigue life with the highest scatter is observed for the cast material. The quite big grain size with just a few grains per cross section may contributes to this inferior behavior. Further factors are supposed to be the inhomogeneous microstructure in terms of segregations and the porosity originating from the casting process.

In contrast, the highest fatigue life is observed for the UFG material. In the high cycle fatigue (HCF) regime where the strength is an important lifetime determining factor this is a quite usual behavior and often reported in literature, e.g. [59, 64, 65]. In the low cycle fatigue (LCF) regime on the other hand, the increased strength does not lead to a significant reduction of the plastic strain amplitude and the ductility of the material becomes an essential factor for fatigue life. Hence, coarse grained (CG) materials usually exhibit an enhanced lifetime in the LCF regime due to their higher ductility [59, 64, 65]. In contrast, the present UFG state exhibits the highest lifetime even in the LCF regime. This behavior is supposed to be related to the different phases, more precisely a more homogenous strain partitioning between the austenitic and martensitic phase in comparison to the other material states. As already discussed above, the grain size of the austenite and α'-martensite is similar in the UFG state (<1 μm). Thus, the difference in strength is due to the different hardness values of the individual phases. As Weidner et al. [50] revealed by nano indentation experiments on the present steel alloy this difference is just about 25% in favor of a higher hardness of the α'-martensite. In the CG materials the smaller grain size of the α'-martensite increases the resistance against plastic deformation significantly due to the Hall-Petch effect. Thus, in CG materials the austenite has to carry a disproportionally high share of the strain in relation to its phase fraction. With increasing α'-martensite fraction, i.e. with increasing strain amplitude, this mismatch increases as well. In the UFG state with similar grain size and, thus, similar

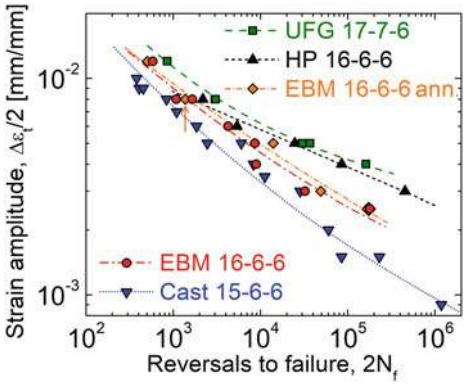

Fig. 13.16 Total strain based fatigue life curves of the different material states. Data from [12] (cast), [14] (EBM), [16] (UFG) and [13] (HP)

resistance against plastic deformation, the α'-martensite has to bear its fair share of the applied strain. Hence, the more homogenous strain distribution overcompensates the decreased ductility in comparison to the CG materials and leads to a higher fatigue life in the LCF regime [16].

The fatigue life of the EBM as-built and annealed states lies in between the cast and HP material. In this context, the relatively high porosity of the material after EBM processing (cf. Sect. 13.4.1) has to be taken into account. Figure 13.17 shows the fracture surface of an annealed EBM specimen ($\Delta\varepsilon_t/2 = 0.8\%$) with severe lack of fusion defects. Some of these defects reach dimensions of up to 500 µm and are located directly underneath the surface. Despite this quite detrimental condition, the cyclic deformation curve does not seem to be affected by these defects. Even the fatigue life almost matches the calculated fatigue life curve (Fig. 13.16, marked

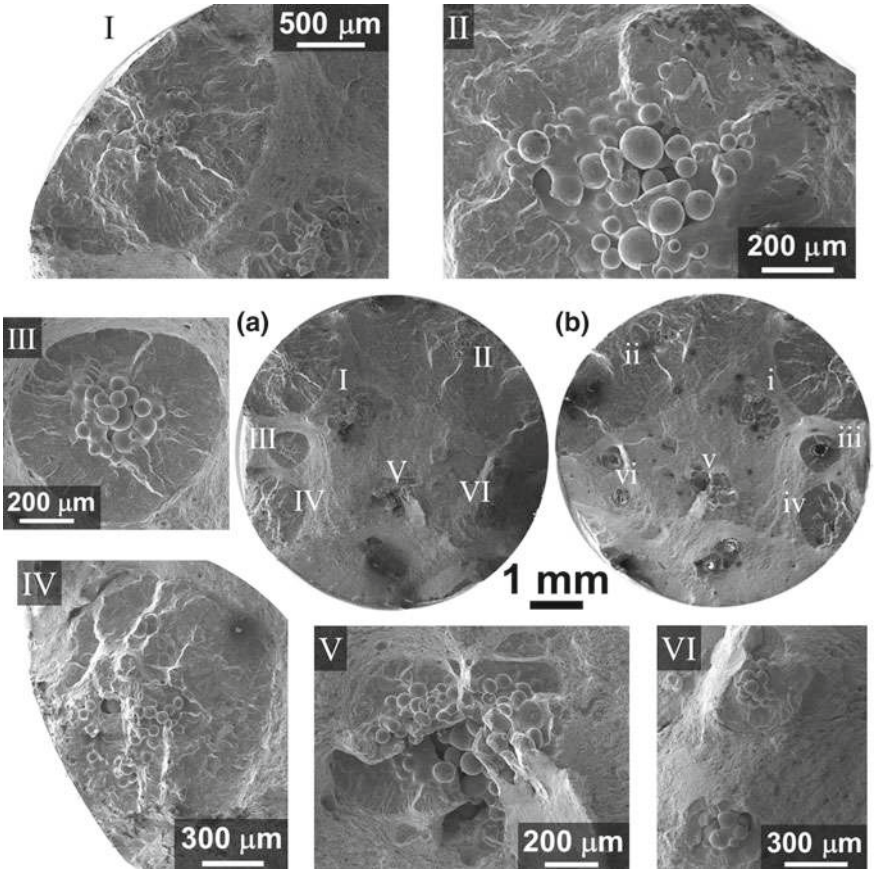

Fig. 13.17 Both sides of the fracture surface (**a**, **b**) of the EBM 16-6-6 ann. specimen cyclically deformed at $\Delta\varepsilon_t/2 = 0.8\%$. (I-VI) Magnified views of selected defects marked by I-VI in (**a**). After [14]

by an arrow). Moreover, the scatter of the EBM states is surprisingly low and the fatigue performance quite good when keeping in mind the severe defects. Of course the detrimental effect of the defects regarding the lifetime increases with decreasing strain amplitude because the crack initiation phase becomes more dominant [58]. Hence, the fatigue life decreases in comparison to the HP state but it is still quite reasonable. This damage tolerant behavior is supposed to stem from the high ductility of the material combined with its outstanding hardening capability. The process-inherent defects act as notches and the highest stresses occur at the roots of the notches. Thus, the deformation in the vicinity of the defects is quite pronounced at the beginning of cyclic deformation. Consequently, these areas exhibit the highest cyclic hardening and, thus, transfer the deformation to other areas of the material. Of course, this "shielding effect" gets the more effective the higher the hardening capability of the material is, which in the present alloy is quite high as revealed by the cyclic deformation curves (Fig. 13.12b). Another beneficial factor is of course the high ductility of the material which reduces the stress concentrations at the defects as also observed for an additive manufactured 316 L austenitic steel by other authors [66].

13.5 Influence of Particle Reinforcement

This section presents the influence of a particle reinforcement on the fatigue properties and cyclic deformation behavior of metastable austenitic steels.[3] Therefore, composites based on the HP 16-6-6 and HP 16-6-9 (cf. Sect. 13.3.1) with 5 and 10 vol.% zirconia, respectively, were processed via HP (cf. Sect. 13.2.2). The zirconia was partially stabilized by MgO (Mg-PSZ) enabling a tetragonal phase fraction of about 32% (cf. Table 13.2).

13.5.1 Cyclic Deformation Behavior of Particle Reinforced Steel-Matrix-Composites

The cyclic deformation curves in Fig. 13.18 reveal the reinforcing effect of the Mg-PSZ particles. Especially at medium and high strain amplitudes the initial stress amplitudes increase with increasing Mg-PSZ fraction. The qualitative courses of the composites based on the HP 16-6-6 steel (Fig. 13.18a–c) are similar to the cyclic deformation curves of the particle-free steel exhibiting an initial cyclic hardening followed by cyclic softening at medium and low strain amplitudes. The subsequent cyclic hardening due to the fatigue-induced α'-martensite formation is observed as

[3]The present discussion is based on investigations by Glage and summarizes results of his doctoral thesis [13] and the publications [18, 19].

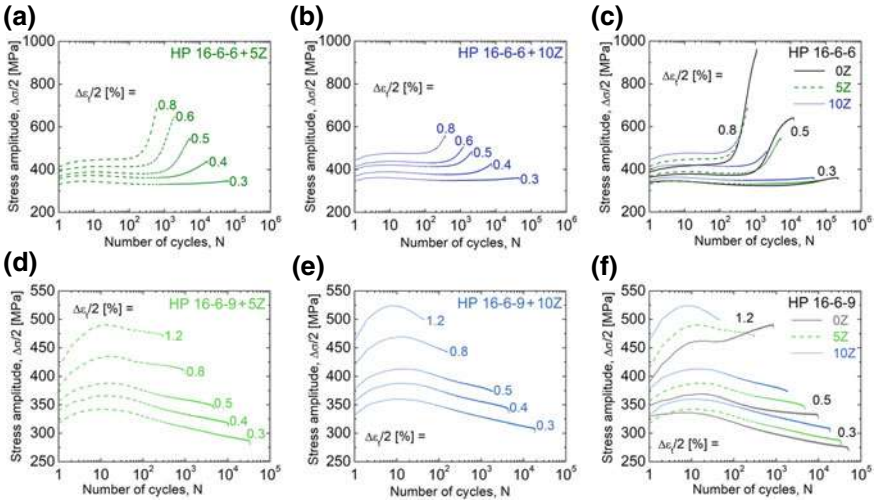

Fig. 13.18 Cyclic deformation curves of the composites reinforced with 5% Mg-PSZ (**a**, **d**) and 10% Mg-PSZ (**b**, **e**) based on the HP 16-6-6 (**a**, **b**) and HP 16-6-9 steels (**d**, **e**), respectively. (**c**, **f**) Comparison of the composite materials with the unreinforced HP 16-6-6 (**c**) and HP 16-6-9 (**f**). After [13] (**c**) and [18, 19] (**d**–**f**)

well but is considerably less pronounced and decreases significantly with increasing Mg-PSZ fraction. This diverging cyclic hardening gets even more obvious with increasing strain amplitudes.

For the variants based on the HP 16-6-9 steel (Fig. 13.18d–f) the secondary hardening due to deformation-induced twinning (cf. Sect. 13.3.1) is even suppressed entirely in case of the composites. A primary hardening similar to the particle-free steel but at higher stress levels is observed followed by cyclic softening until failure. Even the highest strain amplitude of $\Delta\varepsilon_t/2 = 1.2\%$ does not exhibit a secondary hardening regime.

The inhibition of the cyclic hardening due to fatigue-induced α'-martensite formation and twinning, respectively, is attributed to the occurring damage inside the composite materials in terms of rupture and debonding of particles as well as coalescence of cracks. These particle-related damage mechanisms seem to be more dominant than the still active hardening mechanisms in the steel matrices and lead to the observed macroscopic cyclic softening [13, 18, 19]. Thus, the damage evolution will be discussed in more detail in the next section.

13.5.2 Damage Evolution

The damage evolution is investigated by means of the damage parameters D_T (under tension) and D_C (under compression) which are based on the changes of

the specimens' stiffness and are calculated according to Hartmann et al. [67] as follows

$$D_T(N) = \frac{E_{T,0} - E_T(N)}{E_0} \tag{13.3}$$

$$D_C(N) = \frac{E_{C,0} - E_C(N)}{E_0} \tag{13.4}$$

where $E_{T,0}$ and $E_{C,0}$ are the stress dependent stiffnesses of the undamaged material and E_0 is the stiffness at zero stress. A fatigue test accompanied by a Long Distance Microscope (Institute of Physics of Materials, Brno, Czech Republic) revealed the validity of D_T as an indicator for damage by comparing the latter with the evolution of the surface crack length [13]. However, among the present materials the HP 16-6-9 steel and its composites have the best ability for investigations on the damage parameter evolution as the calculations are not influenced by a phase transformation [13].

Both damage parameters generally increase with increasing number of cycles as shown in Fig. 13.19. For small strain amplitudes $\Delta\varepsilon_t/2 \leq 0.3\%$ the evolution is similar for tension (D_T) and compression (D_C) in both material states. Of course, at the end of lifetime, D_T strongly increases due to the formation of a macrocrack which significantly decreases the specimen stiffness under tensile stress. However, up to that point no considerable damage seems to take place at small strain amplitudes and the increase of the damage parameters is mainly attributed to a stiffness reduction in consequence of the plastic deformation. For higher strain amplitudes the magnitude of D_T and D_C start to differ and further diverge with increasing strain amplitude. In case of the particle-free steel, crack initiation and subsequent crack growth lead to a decrease in specimen stiffness. In the composite with 10 vol.% Mg-PSZ particle rupture, particle debonding and crack coalescence additionally contribute to the

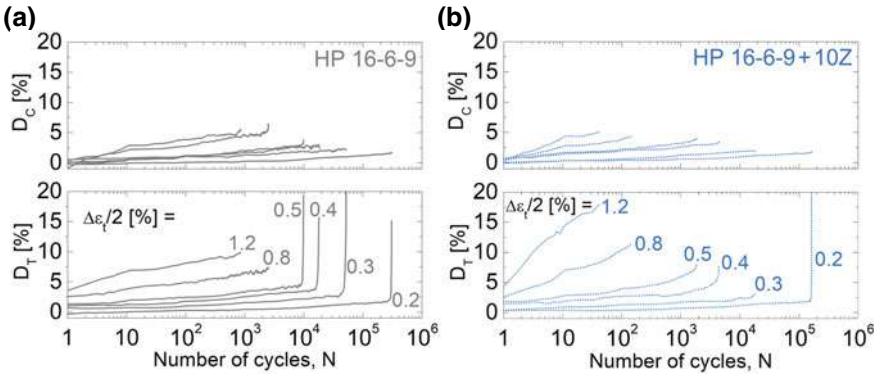

Fig. 13.19 Evolution of the damage parameters D_C and D_T for the particle-free HP 16-6-9 steel (**a**) and its counterpart reinforced with 10 vol.% Mg-PSZ (**b**). After [13]

stiffness reduction under tension causing a stronger increase of D_T (Fig. 13.19b). These particle-related damage mechanisms seem to be rare and negligible at small strain amplitudes but the impact on D_T increases markedly with higher loads. The reduction of the load-bearing cross section is of course less obvious in compression as the cracks and debonded interfaces are mostly closed and, thus, are contributing to the load transfer which explains the diverging evolution of D_T and D_C [13, 67].

13.5.3 Cyclically Deformed Microstructure

This section presents the microstructure of the composite HP 16-6-9+10Z with focus to the Mg-PSZ particles. For description of the deformation mechanisms of the steel matrix the reader is referred to Sect. 13.3.2. The BSE image in Fig. 13.20a gives an overview on the typical damage mechanisms related to the particle reinforcement, i.e. particle rupture, debonding and crack coalescence. Which of the former two mechanisms occurs depends on the particle shape and in particular its size. Particle rupture is mainly observed for large particles which often break perpendicular to the loading axis. Debonding is found for all particle sizes and is the dominant mechanism for small particles which break rarely. Similar size effects have been observed for particle reinforced aluminum matrix composites [68].

Figure 13.20b shows a BSE image of a Mg-PSZ particle embedded in the austenitic matrix after cyclic deformation at a high strain amplitude. Deformation is clearly visible inside the particle and the corresponding EBSD image (Fig. 13.20c) reveals the monoclinic phase for the band-like structures. The remaining particle is most probably in the tetragonal condition of ZrO_2. Hence, it is assumed that a stress-assisted phase transformation from the tetragonal to the monoclinic condition has occurred during cyclic deformation. In contrast, the monoclinic fringe at the interface to the austenitic matrix most probably stems from a depletion of stabilizing elements

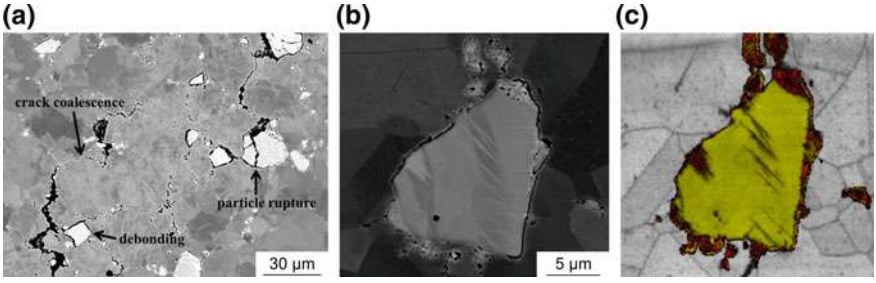

Fig. 13.20 **a** BSE image of HP 16-6-9+10Z showing the particle-related damage mechanisms after cyclic deformation at $\Delta\varepsilon_t/2 = 0.3\%$. **b**, **c** BSE image and EBSD phase map of the same Mg-PSZ particle in a HP 16-6-9+10Z specimen cyclically deformed at $\Delta\varepsilon_t/2 = 0.8\%$ (red—m-ZrO_2, yellow—c/t-ZrO_2; grey—band contrast). Loading axis was horizontal. After [18]

(mainly Mg) due to diffusion to interface phases and/or into the austenite during HP [69].

13.5.4 Fatigue Life

The influence of the particle reinforcement on the fatigue life is shown in Fig. 13.21 for the HP 16-6-6 and HP 16-6-9. The fatigue life decreases with increasing volume fraction of Mg-PSZ particles for both variants. Nevertheless, there are differences in the lifetime in dependence of the applied strain amplitude. For the HP 16-6-9 (Fig. 13.21b) the lifetime reduction due to the particles decreases with decreasing strain amplitude and the lifetime curves converge at high fatigue lifetimes. This is in accordance with the damage behavior discussed in the previous section. As the particle-related damage decreases with decreasing strain amplitude its detrimental influence on the lifetime decreases as well leading to the convergence.

One would expect similar results for the HP 16-6-6 as the particle-related damage should influence the fatigue life in a similar manner. However, a convergence of the fatigue life curves is not observed (Fig. 13.21a). The lifetime reduction due to the particle reinforcement stays constant or even tends to increase with decreasing strain amplitude. This is not attributed to a change in the particle-related damage but to a less pronounced α'-martensite formation in the composites compared to the unreinforced steel, cf. [13, 17, 19]. As discussed in Sect. 13.3.3, the α'-martensite formation is beneficial for the fatigue life in the HCF regime. Thus, the decreased particle-related damage at small strain amplitudes is more or less compensated by a detrimental reduction of the α'-martensite formation. Overall, the fatigue life decreases with increasing particle volume fraction for all strain amplitudes applied.

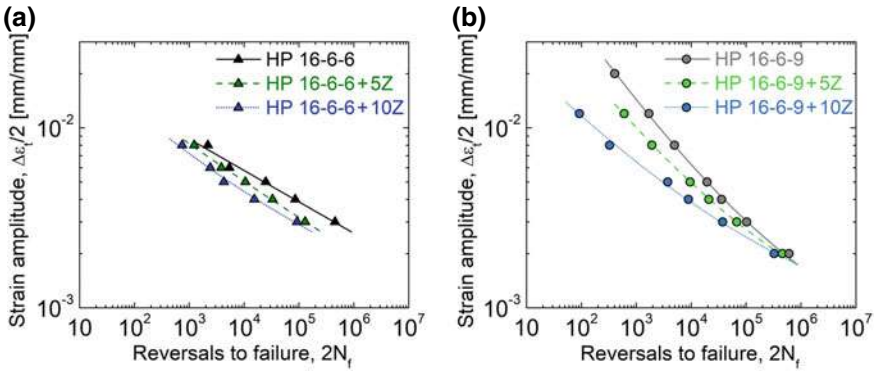

Fig. 13.21 Total strain based fatigue life curves of the composites materials based on the HP 16-6-6 (**a**) and the HP 16-6-9 (**b**) in comparison to its unreinforced counterparts. After [13] (**a**) and [18, 19] (**b**)

13.6 Fatigue Properties of a Q&P Ultra-High Strength Steel

This section presents the fatigue properties of an ultra-high strength austenitic steel alloy which was designed to exceed the strength of the steels discussed in the previous sections at simultaneously reasonable ductility [21]. As this steel is fully austenitic at room temperature, the usual quenching and partitioning (Q&P) process has been modified (cf. Sect. 13.2.2), provoking the formation of α'-martensite during a cooling step. Two material states which differ in the α'-martensite fraction due to different cooling temperatures ($T_{c,1} = -120$ °C, $T_{c,2} = -20$ °C) have been cyclically deformed. Moreover, Q&P and, thus, the fatigue tests were performed in the cast condition of this stainless steel.[4]

13.6.1 Microstructure After Q&P

Magnetic measurements reveal different α'-martensite fractions after Q&P of 45 vol.% for the material state cooled down to $T_c = -120$ °C and of 22 vol.% for $T_c = -20$ °C, respectively. The different phase fractions are also evident in the light optical micrography images of etched specimens in Fig. 13.22. The α'-martensite appears darker and especially for $T_c = -20$ °C (Fig. 13.22b) the dendritic structure of the cast material is still apparent. The dendrite cores solidify first and contain less alloying elements compared to the interdendritic regions. Thus, the martensite start temperature M_s of the former is higher triggering a preferred formation of α'-martensite during the cooling stage.

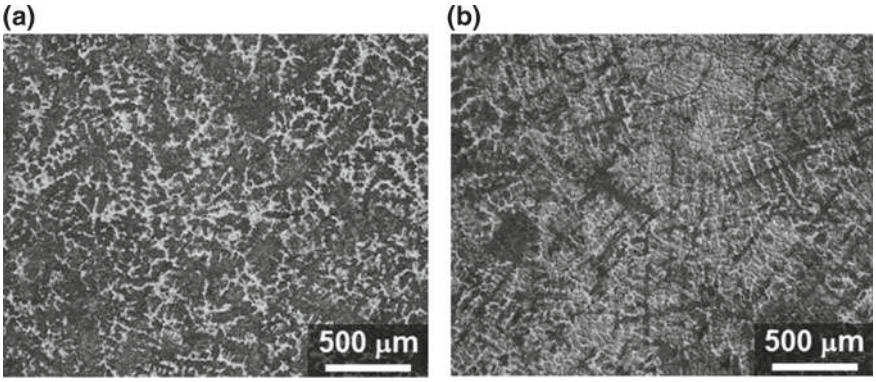

Fig. 13.22 Micrographs taken by light optical micrography of the etched microstructures of the −120 °C (**a**) and −20 °C (**b**) state after Q&P. After [22]

[4]For a discussion in more detail the reader is referred to [22] for the fatigue properties of this steel and to [21] for the modified Q&P processing.

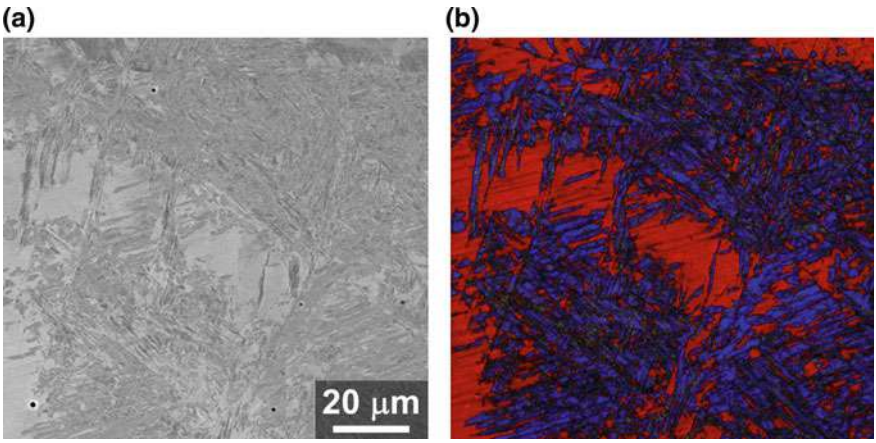

Fig. 13.23 BSE image (**a**) and corresponding EBSD phase map with superimposed band contrast (**b**, red—austenite, yellow—ε-martensite, blue—α'-martensite) of the −120 °C state after Q&P. After [22]

A micrograph at higher magnification is shown in Fig. 13.23a in terms of a BSE image. The corresponding EBSD phase map (Fig. 13.23b) reveals large blocky austenitic areas of about 20 µm in size which are most probably interdentritic regions with higher austenite stability. In addition, fine so-called interlath austenite is observed in areas which are mostly martensitic. Besides mechanical properties, this is important in context with the partitioning treatment and the provoked diffusion of *C* and *N* from the supersaturated α'-martensite into austenite. Due to a limited diffusion length of the interstitial elements *C* and *N* the stabilizing effect will most likely be more pronounced in the interlath austenite [21]. Furthermore, the α'-martensite fraction after the cooling stage is supposed to have an influence on the extent of diffusion and, thus, stabilization, i.e. with increasing α'-martensite fraction the austenite stabilization should increase as well.

13.6.2 Cyclic Deformation Behavior

The cyclic deformation curves of the −120 °C state (partitioned condition) are given in Fig. 13.24a. The stress amplitudes are quite high and even exceed 1400 MPa for $\Delta\varepsilon_t/2 = 1.2\%$. Moreover, the cyclic stress markedly increases with increasing strain amplitude indicating a high amount of obstacles for dislocation glide most probably due to the high amount of α'-martensite. In addition, carbides inside the α'-martensite formed during partitioning may contribute to the high cyclic stress. However, at high strain amplitudes the material exhibits a continuous cyclic hardening until failure.

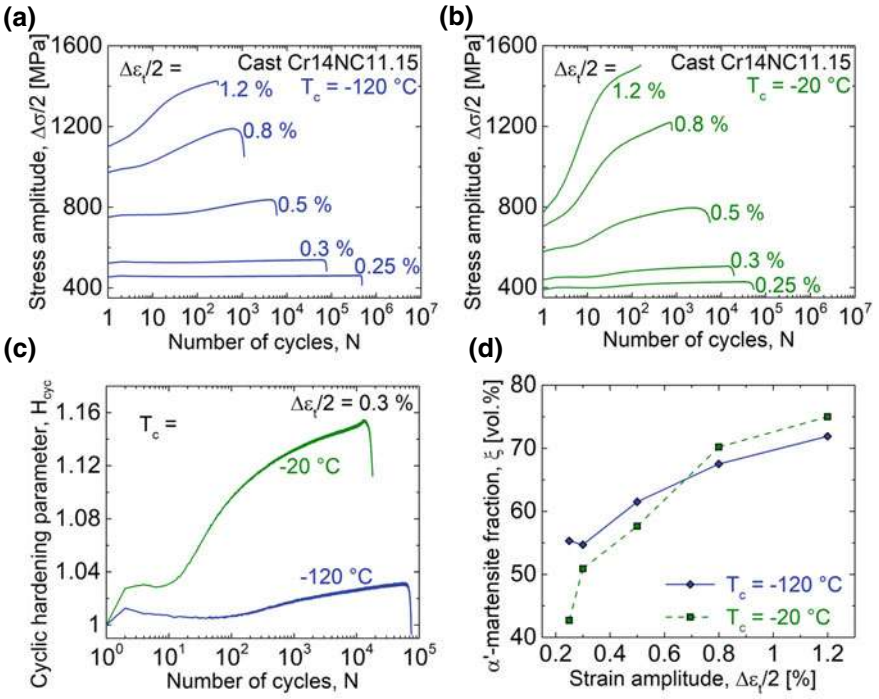

Fig. 13.24 Cyclic deformation curves of the −120 °C (**a**) and −20 °C (**b**) states, cyclic hardening parameter H_{cyc} for a strain amplitude of $\Delta\varepsilon_t/2 = 0.3\%$ (c) and α'-martensite fraction after cyclic deformation (**d**), respectively, of the Q&P ultra-high strength steel. After [22]

After several cycles the hardening gets more pronounced which is attributed to a fatigue-induced formation of α'-martensite, cf. Sect. 13.3.1. In contrast, the course of the cyclic deformation curves for the small strain amplitudes $\Delta\varepsilon_t/2 \leq 0.3\%$ seem to be relatively constant, i.e. without any cyclic softening or hardening. However, this is just a scaling issue due to the wide range of the ordinate. For this reason, a cyclic hardening parameter H_{cyc} is introduced calculated according to

$$H_{\mathrm{cyc}} = \frac{(\Delta\sigma/2)_{N_i}}{(\Delta\sigma/2)_{N=1}} \tag{13.5}$$

where $\Delta\sigma/2_{\,Ni}$ and $\Delta\sigma/2_{N\,=\,1}$ are the stress amplitudes of the current and first cycle, respectively. Figure 13.24c shows the course of H_{cyc} for the strain amplitude of $\Delta\varepsilon_t/2 = 0.3\%$. A similar behavior to the high alloy austenitic steels discussed in the previous sections is observed. At beginning of cyclic deformation a short stage of cyclic hardening is observed followed by cyclic softening. After an incubation period secondary hardening sets in and continues until failure, cf. Sect. 13.3.1. Thus, similar mechanisms in terms of dislocation interaction and martensitic phase transformation are supposed to be active in the Q&P steel as well.

Qualitatively, the −20 °C material state exhibits similar cyclic deformation curves (Fig. 13.24b) but the stress amplitudes at the beginning of cyclic deformation are considerably lower and the cyclic hardening is more pronounced. The reduced initial stress amplitudes are due to the lower initial α'-martensite fraction. In contrast, due to a lower austenite stability the fatigue-induced α'-martensite formation is more pronounced compared to the −120 °C state and this difference significantly increases with increasing strain amplitude. Whereas at medium and small strain amplitudes the overall α'-martensite fraction after failure (Fig. 13.24d) remains lower in case of the −20 °C state, at $\Delta\varepsilon_t/2 \geq 0.8\%$ its phase transformation during cyclic deformation even overcompensates the lower initial fraction leading to higher overall values. This is reflected in the cyclic deformation curves as well. Just in the case of the high strain amplitudes the −20 °C state exceeds its counterpart in terms of the maximum stress amplitude. Hence, the cyclic stresses correlate quite well with the α'-martensite fraction and seem to be relatively independent on the type of α'-martensite, i.e. thermally-induced or fatigue-induced. However, for the strain amplitude $\Delta\varepsilon_t/2 = 1.2\%$ the crossover of stress amplitudes already occurs in an early stage of cyclic deformation (13 cycles) as the fatigue-induced phase transformation is quite strong.

13.6.3 Fatigue Life

As discussed in Sect. 13.3.3 different austenite stabilities cause a crossover of the fatigue life curves in case of high alloy austenitic steels (Fig. 13.9a). As the austenite stability of the present Q&P steels differs as well, a similar behavior could be expected. In contrast, the −120 °C state exhibits a superior fatigue life at all applied strain amplitudes (Fig. 13.25). The lifetime advantage even increases with decreasing strain amplitude. Well known for the high alloy steels, α'-martensite is assumed to have a beneficial effect on the fatigue life in the HCF regime due to the higher strength

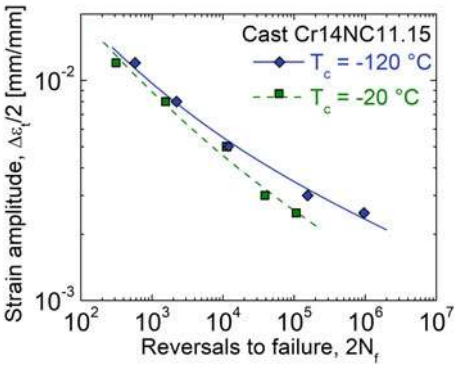

Fig. 13.25 Total strain based fatigue life curves of the −120 °C (blue) and −20 °C (green) states of the Q&P ultra-high strength steel. After [22]

of the material, but a detrimental effect in the LCF regime due to the decrease in ductility. Thus, at high strain amplitudes the pronounced fatigue-induced phase transformation in the −20 °C state which overcompensates its lower initial α'-martensite fraction (cf. Sect. 13.6.2) leads to the inferior fatigue life. At small strain amplitudes on the other hand, the fatigue-induced phase transformation is less pronounced and the overall α'-martensite fraction as well as the cyclic stresses of the −20 °C state never reach the level of its counterpart. In this fatigue regime a higher strength markedly reduces the plastic strain amplitude and, thus, reduces the damage and enhances the lifetime. Accordingly, once again the −120 °C state exhibits a higher fatigue life.

13.6.4 Microstructure After Cyclic Deformation

The BSE, ECCI and EBSD images of Fig. 13.26 give an impression of the microstructure of the Q&P steel after cyclic deformation. As already observed for the qualitative course of the cyclic deformation curves, the micrographs reveal distinct similarities with the other high alloy austenitic steels. Figure 13.26a shows an austenitic area surrounded by α'-martensite. A lot of deformation bands on different slip systems have formed inside the austenite. Within these deformation bands α'-martensite nuclei are found (marked by white arrows in Fig. 13.26a, b) which in part are quite small. According to the EBSD phase maps in Fig. 13.26g, i the deformation bands are often indexed as ε-martensite, i.e. the density of stacking faults is quite high in these areas. Thus, analogue to the other high alloy austenitic steels presented in this work, the α'-martensite is supposed to form in the sequence $\gamma \rightarrow \varepsilon \rightarrow \alpha'$.

However, the plasticity is not limited to the deformation bands but also stacking faults form in between the deformation bands on different slip systems as revealed by ECCI images in Fig. 13.26c, d. Moreover, all micrographs reveal a quite planar glide character as no dislocation arrangements due to wavy glide like dislocation cells have been observed.

Even though the triggered microstructural mechanisms are similar in both Q&P states, there are some indications for their different austenite stabilities as well. The α'-martensite fraction inside the deformation bands appears higher for the −20 °C state (Fig. 13.26e, f) when comparing specimens cyclically deformed at the same strain amplitude. Hence, the martensitic phase transformation occurs more rapidly in the −20 °C state due to its lower austenite stability. These observations support the statements regarding the cyclic hardening behavior discussed in Sect. 13.6.2.

13.7 Conclusions

Several aspects of the cyclic deformation and fatigue behavior of metastable austenitic steels were discussed in the present work including the influence of a

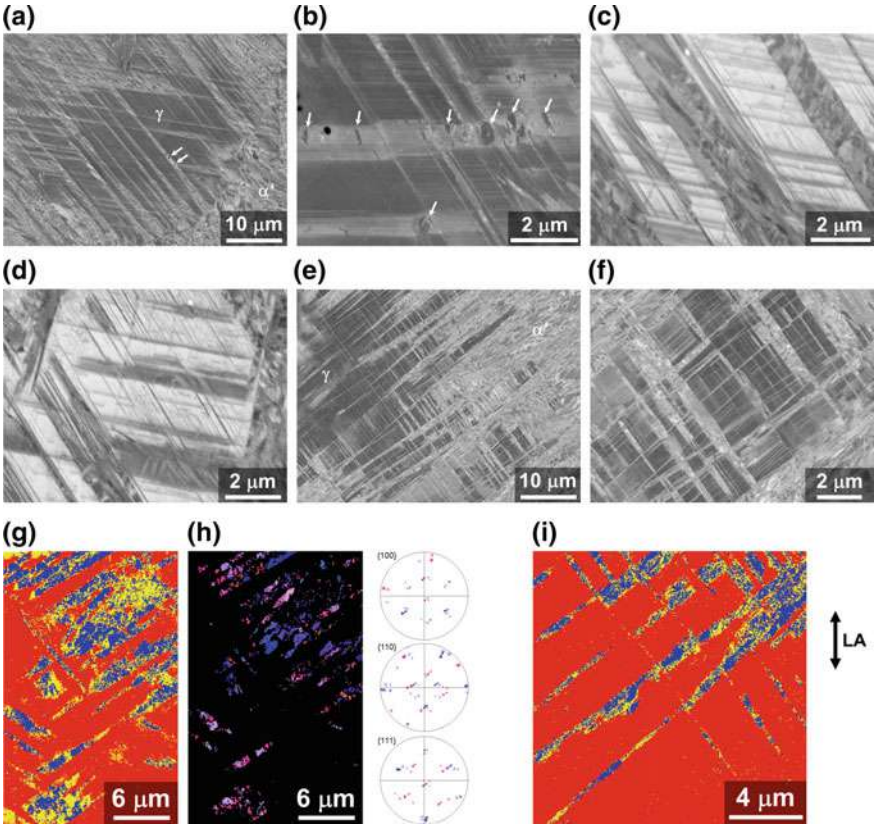

Fig. 13.26 Microstructures of the −120 °C (**a**–**d**, **g**, **h**) and −20 °C (**e**, **f**, **i**) state cyclically deformed at $\Delta\varepsilon_t/2 = 0.3\%$ (**a**, **c**–**f**, **i**), $\Delta\varepsilon_t/2 = 0.5\%$ (**b**) and $\Delta\varepsilon_t/2 = 0.8\%$ (**g**, **h**), respectively. **a**, **b**, **e**, **f** BSE images. **c**, **d** ECCI images. **g**, **i** EBSD phase maps (red—austenite, yellow—ε-martensite, blue—α'-martensite). **h** EBSD orientation map of the α'-martensite phase of (**g**) and corresponding bcc pole figures. Loading axis is vertical for all micrographs. After [22]

particle reinforcement and the chemical composition. Furthermore, different manufacturing methods in terms of casting, additive manufacturing, hot pressing and reversion annealing and their effect on the fatigue properties were investigated. Finally, a newly designed ultra-high strength steel produced via a modified Q&P route was presented. The main conclusions are summarized in the following.

- The SFE of an austenitic steel controls its dislocation glide character (planar or wavy) and the activation of other deformation mechanisms in terms of deformation-induced α'-martensite formation and twinning. With decreasing SFE besides dislocation movement, a fluent transition from twinning to ε-martensite and α'-martensite formation is observed.

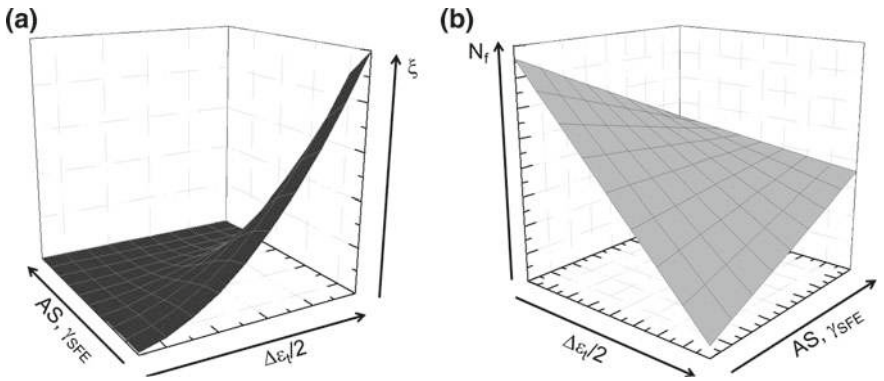

Fig. 13.27 α'-martensite fraction ξ (**a**) and fatigue life N_f (**b**) of high alloy austenitic steels as a function of strain amplitude $\Delta\varepsilon_t/2$, austenite stability (AS) and stacking fault energy γ_{SFE}, respectively. After [13]

- The SFE has a major influence on the mechanical properties and the cyclic deformation behavior as the fatigue-induced twinning and even more the fatigue-induced α'-martensite formation lead to a significant cyclic hardening.
- Besides a decreasing SFE, of course increasing strain amplitudes promote the formation of α'-martensite (Fig. 13.27a).
- The fatigue life is affected by the α'-martensite formation as well. The latter is beneficial in the HCF regime due to its strengthening effect but detrimental in the LCF regime due to the lower ductility. This opposing character leads to different slopes of the fatigue life curves and, thus, to their crossover. More precisely, the slope decreases with decreasing SFE (Fig. 13.9a), i.e. the fatigue life difference between high and small strain amplitudes increases (Fig. 13.27b), and vice versa.
- The martensitic phase transformation of all investigated steels occurs via the sequence $\gamma \rightarrow \varepsilon \rightarrow \alpha'$. The intermediate ε-martensite is assumed to stem from highly faulted areas, i.e. a high stacking fault density.
- The grain size of the steel affects the cyclic deformation behavior and the martensitic phase transformation. In particular ultra-fine grained (UFG) materials with grain sizes below 1 μm exhibit significantly higher initial stress amplitudes but a less pronounced cyclic hardening due to α'-martensite formation. Furthermore, the UFG grains are not characterized by a deformation band structure but their interior is subjected to an increase in stacking fault density as a whole.
- The remarkable hardening capability in combination with the high ductility of the high alloy steels yield an outstanding damage tolerance. A shielding effect due to the high hardening at defects and a transition of the deformation to adjacent areas is assumed to occur. Especially with regard to additive manufactured materials which suffer upon process-inherent defects like lack of fusion this damage tolerance brings advantages in terms of a less affected cyclic deformation behavior and a more than reasonable fatigue life.

- A reinforcement with Mg-PSZ particles causes a strengthening effect in terms of increasing stress amplitudes with increasing Mg-PSZ particle fraction. On the other hand, the detrimental particle-related damage in terms of debonding, particle rupture and crack coalescence increases with increasing strain amplitude. Hence, the fatigue life of the composites is reduced in the total-strain controlled experiments, especially in the LCF regime.
- The cast austenitic steel subjected to a modified Q&P processing exhibited extraordinary high stress amplitudes. Of the two material states which differ in the α'-martensite fraction after Q&P especially the state with the higher fraction achieved quite high cyclic stresses right from the beginning of cyclic deformation.

Acknowledgements The authors gratefully acknowledge the work and research of Dr. -Ing. Alexander Glage providing a major contribution to the present chapter. Furthermore, special thanks go to the Deutsche Forschungsgemeinschaft (DFG, German Research Foundation) for funding the Collaborative Research Centre "TRIP-Matrix-Composite" (project number 54473466—SFB 799, subproject B3). For preparation of SEM and TEM specimens the authors wish to thank R. Prang, K. Zuber, K. Becker and A. Leuteritz (all TU Bergakademie Freiberg).

References

1. G.B. Olson, M. Cohen, J. Less-Common Met. **28**, 107 (1972)
2. G.B. Olson, M. Cohen, Metall. Trans. A **6**, 791 (1975)
3. A. Weidner, H. Biermann, JOM **67**, 1729 (2015)
4. S. Martin, S. Wolf, S. Decker, L. Krüger, U. Martin, Steel Res. Int. *86*, 1187 (2015)
5. S. Martin, S. Wolf, U. Martin, L. Krüger, Solid State Phenom. **172–174**, 172 (2011)
6. H. Mughrabi, Procedia Eng. **2**, 3 (2010)
7. S. Martin, C. Ullrich, D. Šimek, U. Martin, D. Rafaja, J. Appl. Crystallogr. **44**, 779 (2011)
8. A. Weidner, A. Glage, S. Martin, J. Man, V. Klemm, U. Martin, J. Polák, D. Rafaja, H. Biermann, Int. J. Mater. Res. **102**, 1374 (2011)
9. H. Biermann, A. Glage, M. Droste, Metall. Mater. Trans. A **47**, 84 (2016)
10. L. Rémy, A. Pineau, Mater. Sci. Eng. **36**, 47 (1978)
11. A. Jahn, A. Kovalev, A. Weiß, S. Wolf, L. Krüger, P.R. Scheller, Steel Res. Int. *82*, 39 (2011)
12. A. Glage, A. Weidner, H. Biermann, Steel Res. Int. **82**, 1040 (2011)
13. A. Glage, Ph.D. thesis, Technische Universität Bergakademie Freiberg, 2014
14. M. Droste, J. Günther, D. Kotzem, F. Walther, T. Niendorf, H. Biermann, Int. J. Fatigue **114**, 262 (2018)
15. J. Günther, F. Brenne, M. Droste, M. Wendler, O. Volkova, H. Biermann, T. Niendorf, Sci. Reports **8**, 1298 (2018)
16. M. Droste, C. Ullrich, M. Motylenko, M. Fleischer, A. Weidner, J. Freudenberger, D. Rafaja, H. Biermann, Int. J. Fatigue **106**, 143 (2018)
17. S. Martin, S. Richter, S. Decker, U. Martin, L. Krüger, D. Rafaja, Steel Res. Int. **82**, 1133 (2011)
18. A. Glage, C. Weigelt, J. Räthel, H. Biermann, Int. J. Fatigue **65**, 9 (2014)
19. A. Glage, C. Weigelt, J. Räthel, H. Biermann, Adv. Eng. Mater. **15**, 7 (2013)
20. J. Speer, D.K. Matlock, B.C. de Cooman, J.G. Schroth, Acta Mater. **51**, 2611 (2003)
21. M. Wendler, C. Ullrich, M. Hauser, L. Krüger, O. Volkova, A. Weiß, J. Mola, Acta Mater. **133**, 346 (2017)

22. M. Droste, M. Wendler, O. Volkova, H. Biermann, Adv. Eng. Mater. 51 (2018)
23. A. Weidner, A. Müller, A. Weiß, H. Biermann, Mater. Sci. Eng., A **571**, 68 (2013)
24. M. Moallemi, A. Najafizadeh, A. Kermanpur, A. Rezaee, Mater. Sci. Eng., A **530**, 378 (2011)
25. A. Rezaee, A. Kermanpur, A. Najafizadeh, M. Moallemi, Mater. Sci. Eng., A **528**, 5025 (2011)
26. F. Forouzan, A. Najafizadeh, A. Kermanpur, A. Hedayati, R. Surkialiabad, Mater. Sci. Eng., A **527**, 7334 (2010)
27. M. Karimi, A. Najafizadeh, A. Kermanpur, M. Eskandari, Mater. Charact. **60**, 1220 (2009)
28. M. Eskandari, A. Najafizadeh, A. Kermanpur, Mater. Sci. Eng., A **519**, 46 (2009)
29. D.L. Johannsen, A. Kyröläinen, P.J. Ferreira, Metall. Mater. Trans. A **37**, 2325 (2006)
30. R. Song, D. Ponge, D. Raabe, J.G. Speer, D.K. Matlock, Mater. Sci. Eng., A **441**, 1 (2006)
31. A. Weidner et al., in *IOP Conference Series: Materials Science and Engineering, 17th International Conference on Textures of Materials*, vol. 82 (IOP Publishing 2015), article no. 012069
32. R.D.K. Misra, Z. Zhang, P.K.C. Venkatasurya, M.C. Somani, L.P. Karjalainen, Mater. Sci. Eng., A **528**, 1889 (2011)
33. R.D.K. Misra, S. Nayak, S.A. Mali, J.S. Shah, M.C. Somani, L.P. Karjalainen, Metall. Mater. Trans. A **41**, 3 (2010)
34. R.D.K. Misra, S. Nayak, P.K.C. Venkatasurya, V. Ramuni, M.C. Somani, L.P. Karjalainen, Metall. Mater. Trans. A **41**, 2162 (2010)
35. R.D.K. Misra, Z. Zhang, P.K.C. Venkatasurya, M.C. Somani, L.P. Karjalainen, Mater. Sci. Eng., A **527**, 7779 (2010)
36. J. Kähkönen, D.T. Pierce, J.G. Speer, E. de Moor, G.A. Thomas, D. Coughlin, K. Clarke, A. Clarke, JOM **68**, 210 (2016)
37. S. Yan, X. Liu, W.J. Liu, H. Lan, H. Wu, Mater. Sci. Eng., A **620**, 58 (2015)
38. E.J. Seo, L. Cho, B.C. de Cooman, Metall. Mater. Trans. A **46**, 27 (2015)
39. M. de Sanctis, G. Lovicu, R. Valentini, A. Dimatteo, R. Ishak, U. Migliaccio, R. Montanari, E. Pietrangeli, Metall. Mater. Trans. A **46**, 1878 (2015)
40. D.V. Edmonds, J.G. Speer, Mater. Sci. Technol. **26**, 386 (2010)
41. J. Talonen, P. Aspegren, H. Hänninen, Mater. Sci. Technol. **20**, 1506 (2004)
42. S. Siddique, M. Imran, M. Rauer, M. Kaloudis, E. Wycisk, C. Emmelmann, F. Walther, Mater. Des. **83**, 661 (2015)
43. S. Ganesh Sundara Raman, K.A. Padmanabhan, Int. J. Fatigue **17**, 271 (1995)
44. F. Hahnenberger, M. Smaga, D. Eifler, Int. J. Fatigue **69**, 36 (2014)
45. L. Rémy, Acta Metall. **26**, 443 (1978)
46. O. Bouaziz, S. Allain, C. Scott, Scr. Mater. **58**, 484 (2008)
47. M. Bayerlein, H. Mughrabi, M. Kesten, B. Meier, Mater. Sci. Eng., A **159**, 35 (1992)
48. M. Bayerlein, H.-J. Christ, H. Mughrabi, Mater. Sci. Eng., A **114**, L11 (1989)
49. G. Baudry, A. Pineau, Mater. Sci. Eng., A **28**, 229 (1977)
50. A. Weidner, U.D. Hangen, H. Biermann, Philos. Mag. Lett. **94**, 522 (2014)
51. H. Schumann, Krist. Techn. **12**, 363 (1977)
52. S.-G. Hong, S.-B. Lee, T.-S. Byun, Mater. Sci. Eng., A **457**, 139 (2007)
53. G. Franke, C. Altstetter, Metall. Trans. A **7**, 1719 (1976)
54. D. Hennessy, G. Steckel, C. Altstetter, Metall. Trans. A **7**, 415 (1976)
55. D. Borisova, V. Klemm, S. Martin, S. Wolf, D. Rafaja, Adv. Eng. Mater. **15**, 571 (2013)
56. Y. Li, C. Laird, Mater. Sci. Eng., A **186**, 87 (1994)
57. H.-G. Lambers, C.J. Rüsing, T. Niendorf, D. Geissler, J. Freudenberger, H.J. Maier, Int. J. Fatigue **40**, 51 (2012)
58. H. Mughrabi, Philos. Trans. A **373**, 20140132 (2015)
59. H. Mughrabi, H.W. Höppel, Int. J. Fatigue **32**, 1413 (2010)
60. A. Šalak, M. Selecká, *Manganese in Powder Metallurgy Steels* (Cambridge International Science Publishing Ltd, Springer, 2012)
61. M. Wendler, A. Weiß, L. Krüger, J. Mola, A. Franke, A. Kovalev, S. Wolf, Adv. Eng. Mater. **15**, 558 (2013)
62. M. Wendler, J. Mola, L. Krüger, A. Weiß, Steel Res. Int. **85**, 803 (2014)

63. J.A. Venables, Philos. Mag. **7**, 35 (1962)
64. H. Mughrabi, H.W. Höppel, M. Kautz, Scr. Mater. **51**, 807 (2004)
65. H.W. Höppel, M. Kautz, C. Xu, M. Murashkin, T.G. Langdon, R.Z. Valiev, H. Mughrabi, Int. J. Fatigue **28**, 1001 (2006)
66. S. Leuders, T. Lieneke, S. Lammers, T. Tröster, T. Niendorf, J. Mater. Res. **29**, 1911 (2014)
67. O. Hartmann, K. Herrmann, H. Biermann, Adv. Eng. Mater. **6**, 477 (2004)
68. W. Li, Z.H. Chen, D. Chen, J. Teng, L. Changhao, J. Mater. Sci. **46**, 1153 (2011)
69. A. Glage, S. Martin, S. Decker, C. Weigelt, M. Junghanns, C.G. Aneziris, U. Martin, L. Krüger, H. Biermann, Steel Res. Int. **83**, 554 (2012)

Chapter 14
Behaviour of Metastable and Stable Austenitic Stainless Steels Under Planar-Biaxial Load

Carl H. Wolf, Sebastian Henkel and Horst Biermann

Abstract The aim of the present study was to investigate the behaviour of a powder metallurgically produced high alloy X5CrMnNi16-7-6 metastable austenitic stainless steel under planar-biaxial loading. For this purpose, cruciform specimens made of this material were subjected both to quasi-static loading and to cyclic loading for low cycle fatigue and crack growth investigations. In addition to quasi-static shear loading with load axes force ratio $\lambda = -1$ and quasi-static equibiaxial loading with $\lambda = 1$, further specimens were subjected to a load ratio of $\lambda = 0.5$ to determine the yield surface. Quasi-static sequence tests with permanently changing λ were carried out to determine load sequence effects. The characterization of the low cycle fatigue behavior was carried out under equibiaxial tensile loading with load axes strain ratio $\Phi = 1$ and shear loading with $\Phi = -1$. Furthermore, investigations were carried out at different strain ratios. The description of the low cycle fatigue lives was performed using the Basquin-Manson-Coffin relationship. For both quasi-static and LCF experiments, the martensite content was measured in situ, so that the influence of the phase transformation on the material behaviour could be described. The fatigue crack growth investigations were performed on cruciform specimens under uniaxial, equibiaxial and initially equibiaxial and subsequently phase-shifted loading on a stable austenitic steel variant. In order to describe the fatigue crack growth, a finite element (FE) analysis of the specimen geometry was carried out first, so that a correlation between force and resulting stress in the uncracked specimen could be established. A geometry function for straight growing cracks was established by correlation between force and resulting stress in the specimen and K-solution

C. H. Wolf (✉) · S. Henkel · H. Biermann
Institute of Materials Engineering, Technische Universität Bergakademie Freiberg, Gustav-Zeuner-Str. 5, 09599 Freiberg, Germany
e-mail: Carl.Wolf@ww.tu-freiberg.de

S. Henkel
e-mail: henkel@ww.tu-freiberg.de

H. Biermann
e-mail: biermann@ww.tu-freiberg.de

H. Biermann and C. G. Aneziris (eds.), *Austenitic TRIP/TWIP Steels and Steel-Zirconia Composites*, Springer Series in Materials Science 298,
https://doi.org/10.1007/978-3-030-42603-3_14

at different crack lengths. A comparison of the crack growth between uniaxial or equibiaxial and phase-shifted loading with kinking crack paths was made by means of Paris law.

14.1 Introduction

On real components, multiaxial stress states often occur. These are caused, for example, by stress gradients in the area around notches, but also by several simultaneously acting loads in different directions. Even in material testing, an exclusively uniaxial material test is rarely carried out, since necking in the tensile test of plastically deformable materials already represents a multiaxial loading condition [1].

In the present work, a newly developed, high-alloy, metastable austenitic stainless steel is studied under multiaxial quasi-static as well as multiaxial low-cyclic fatigue (LCF) loading. Moreover, multiaxial fatigue crack growth (FCG) was investigated. This steel exhibits the TRIP effect [2, 3] (**TR**ansformation **I**nduced **P**lasticity) caused by a transformation of γ-austenite to α'-martensite via a hexagonal structure called ε-martensite [4–8]. The phase transformations take place with volume effects, i.e. during the phase transformation from γ-austenite to ε-martensite a volume contraction and during the subsequent phase transformation from ε-martensite to α'-martensite a volume expansion occur.

Knowledge of the influence of the TRIP effect on the deformation and strain hardening behavior under multiaxial loading is relevant for the application of this material. With this expertise, forming processes can be simulated and safety reserves of e.g. pipes and pressure vessels can be calculated. Moreover, in the automotive industry, increasingly complex forming processes require knowledge of yield surface and strain hardening behavior [9, 10]. Often only uniaxial material data is available for calculations and component design, so that multiaxial stress cases are usually converted into uniaxial equivalent stress cases [1]. Various transmission hypotheses are usually used for this purpose. For ductile materials, the distortion energy hypothesis according to von Mises, Huber and Hencky is usually utilized, which was initially established as a yield condition. For brittle materials, the maximum normal stress theory according to Rankine is applied. These hypotheses can be utilized to describe most technical applications for isotropic materials under static loading. The better the material behavior is phenomenologically known, the better are the results of e.g. the finite element method calculations. This also includes the knowledge of the yield surface and the elastic-plastic deformation behaviour [11]. For the purpose of generating defined multiaxial stress states under quasi-static loading, planar-biaxial experiments on cruciform specimens are suitable [9, 12, 13].

In addition to the interest in quasi-static multiaxial stress states, there has been an interest in the influence of various multiaxial strain states on crack initiation and crack propagation behavior for more than 40 years [14, 15]. Unfortunately, there are only few data in the literature with different phase shifts φ between the principal strains ε_1 and ε_2 in the range of $0° \leq \varphi \leq 180°$ [16–18]. Some authors determined the

longest fatigue life under shear loading, i.e. with $\lambda = -1$, compared to other loading cases like uniaxial or biaxial tension [16, 19–22]. Pascoe and de Villiers [20] found, that the fatigue life for specimens loaded equibiaxially, i.e. with $\lambda = 1$, had the shortest fatigue life. Ogata and Takahashi [16] stated, that fatigue life for uniaxially loaded specimens is even shorter than for equibiaxially loaded specimens. Many authors [16, 17, 19–23] correlated fatigue life N_f with the von Mises equivalent strain amplitude $\Delta\varepsilon_{\mathrm{vM}}/2$ as a scalar parameter. Furthermore, numerous theories have been established for the calculation of fatigue life under multiaxial loadings in the LCF regime, see e.g. [14, 16, 20, 24–29]. Uniaxial cyclic investigations on metastable high-alloy austenitic steels like AISI 301 and 304 L showed, that the formation of α'-martensite led to an increasing stress amplitude, i.e. the strength increased significantly during cyclic deformation. Consequently, this leads to higher fatigue life in high-cycle fatigue and to a reduction of the fatigue life in the LCF regime in comparison to a stable steel [7, 30–33].

The calculation of fatigue life for fatigue crack growth is also often based on uniaxial data [34–37]. However, components are often multiaxially loaded due to their geometry or loadings in different directions [38, 39], e.g. thin walled structural components as pressure vessels [40] or the outer skin of an aircraft [41, 42] as well as blade integrated disks in aircraft engines [43, 44]. During the service life of the components, both in-phase and out-of-phase loadings can occur. The change from in-phase to out-of-phase loading can lead to crack branching [45–49] as well as kinking of the crack path [49, 50]. To test the influence of such loading conditions on FCG, cruciform specimens serve as a link between uniaxial laboratory tests and complex component tests [40], since they can be used to investigate the material behaviour under well-defined biaxial stress conditions [9, 43].

Up to now, there is no standardized specimen design for cruciform specimens, but there are five commonly used specimen designs. These specimen designs differ in the specimen thickness, i.e. uniform specimen thickness or thinned out measuring area, the radius between the load arms and the design of the load arms. Thin specimens of uniform thickness and with (i) large radii between the load arms were examined e.g. by [51–53], (ii) small radii between the loading arms were examined e.g. by [47, 50, 54–61] and (iii) small radii between the loading arms as well as relief slits within the load introduction arms were examined e.g. by [41, 42, 53, 60, 62]. Specimens with (iv) a thickness-reduced measuring area and small radii between the loading arms were examined e.g. by [16, 43, 44, 53, 63–67]. The specimen design (v), used by many researchers [40, 45, 46, 48, 49, 56, 59, 60, 63, 68–80], was realized by inserting relief slits in the load introduction arms of specimen design (iv). These slits realize a good decoupling of the forces, as it was shown in [81].

A disadvantage of these many specimen geometries is that there is no simple formula or rather solution to calculate the stress intensity factor K or rather its range ΔK, i.e. for both straight and curved crack paths, thus, the K-solution must be determined material-dependently. This calculation can be time-consuming so that it is not always carried out. The consequence is that for planar-biaxial crack growth experiments, the crack growth is described in different dependencies: (i) exclusive consideration of the fatigue crack growth in a–N plots, as done e.g. by [44, 50], (ii) consideration

of the fatigue crack growth in da/dN–N plots, as done by Neerukatti et al. [49], (iii) consideration of the fatigue crack growth in da/dN–a plots, as done by Wang et al. [79], (iv) consideration of the fatigue crack growth in da/dN–ΔG plots, see [47, 55], and (v) consideration of the fatigue crack growth in a–N plots as well as crack growth rate plots (da/dN–ΔK plots), as done by many authors, cf. e.g. [40, 41, 45, 46, 48, 51, 52, 54–56, 58, 61, 66–70, 74–78, 80]. In this article, both a–N plots and da/dN–ΔK plots are used for the study of the fatigue crack growth. Furthermore, a comparison with the Paris law is made.

14.2 Materials and Methods

14.2.1 Material

A newly developed metastable austenitic stainless steel X5CrMnNi16-7-6 called »16-7-6« in the following was studied. A significant characteristic of this material is the **TR**ansformation **I**nduced **P**lasticity, called TRIP effect [2, 3]. It is achieved by a transformation of γ-austenite to α'-martensite via a hexagonal structure called ε-martensite [4–8]. The main alloying elements are chromium (≈16 wt.%), manganese (≈7 wt.%) and nickel (≈6 wt.%). The chemical compositions of the individual batches for the various investigations varied slightly and are given in Table 14.1. However, these variations result in a pronounced martensitic transformation, as with »16-7-6 (Batch 1)« and »16-7-6 (Batch 2)«, or the material is rather stable, as in »16-7-6 (Batch 3)«. The »16-7-6 (Batch 1)« was used for the quasi-static investigations, the »16-7-6 (Batch 2)« was used for the LCF investigations and the »16-7-6 (Batch 3)« was used for the fatigue crack growth investigations. All materials were produced by powder metallurgy (PM).

The powder for the specimens was manufactured by inert gas atomisation (TLS, Bitterfeld, Germany). It was subsequently hot pressed under vacuum at a temperature of 1050 °C at a pressure of 30 MPa to a circular blank (Fraunhofer IKTS, Dresden, Germany). The heating and cooling rate was 10 K/min. The blanks had a thickness of (i) ≈11 mm and a diameter of ≈140 mm for the quasi-static specimens, (ii) a thickness of ≈16 mm and a diameter of ≈140 mm for the LCF specimens and

Table 14.1 Chemical compositions of the investigated steel in wt.%. The composition of the elements marked with * was determined by spark emission. The composition of the elements marked with ** and with *** was determined by combustion method and by melt extraction, respectively

	Fe*	Cr*	Mn*	Ni*	C**	N***	Si*
16-7-6 (Batch 1)	Bal.	15.9	6.2	6.2	0.05	0.04	0.9
16-7-6 (Batch 2)	Bal.	16.1	6.0	6.0	0.04	0.04	0.9
16-7-6 (Batch 3)	Bal.	16.2	7.2	6.7	0.049	0.056	0.94

(iii) a thickness of ≈15 mm and a diameter of ≈150 mm for the fatigue crack growth specimens. However, the cross-shaped biaxial-planar specimens have dimensions of (i), (iii) 332 mm × 332 mm, or (ii) 197 mm × 197 mm, respectively, so that the discs were welded into a commercial AISI304 base material. For this purpose, the following production steps were carried out:

1. A hole with a diameter of (i) and (iii) 140 mm, or (ii) 130 mm was cut by water jet cutting into the square plates made of AISI304 (PRO VA Blechbearbeitung GmbH, Olbernhau, Germany) with a thickness of (i) and (ii) 10 mm or (iii) 15 mm and an edge length of (i) and (iii) 340 mm, or (ii) 200 mm.
2. The hole in the square plate was enlarged to a diameter of (i) and (iii) 144.8 mm, or (ii) 134.8 mm by milling.
3. The circular blanks were milled to a diameter of (i) and (iii) 145 mm, or (ii) 135 mm and a height of (i) and (ii) 10 mm, or (iii) 15 mm.
4. Afterwards the circular blanks were cooled with liquid nitrogen for 30 min and subsequently placed into the squared plates, so that a specimen base plate is formed from one circular blank and one squared plate, which are held together by means of an interference fit.
5. The circular blank and the squared plate of the specimen base plate were welded together using an electron beam.
6. Afterwards, the specimen base plates were solution annealed at 1050 °C for 30 min and then quenched with nitrogen at 9 bar (G+M Vacutherm Härterei-und Oberflächentechnik GmbH, Brand-Erbisdorf, Germany).
7. Then, the specimens base plates were milled into their cruciform specimen shape, cf. Fig. 14.1.
8. The specimens for quasi-static investigations and for fatigue crack growth investigations were further mechanically processed after milling:
   - Quasi-static specimens:
     The slits of the »Triple-slit« and the »Double-slit« specimens were subsequently inserted by water jet cutting, cf. Fig. 14.1a, b.
   - Fatigue crack growth specimens:
     A hole with diameter of $d = 4$ mm was drilled in the middle of the specimens. Afterwards, two notches with a length of $l = 3$ mm each were inserted by electro-discharge machining, cf. Fig 14.1d.
9. Finally, the surfaces were polished mechanically.

14.2.2 Quasi-static Loading

The cruciform specimens for quasi-static tests were designed according to [82–84]. This geometry was developed using FE simulations with the aim of a homogeneous stress and strain distribution in the measuring area. In this work, two different specimen geometries were used, which are based on those proposed by [83, 84]. The

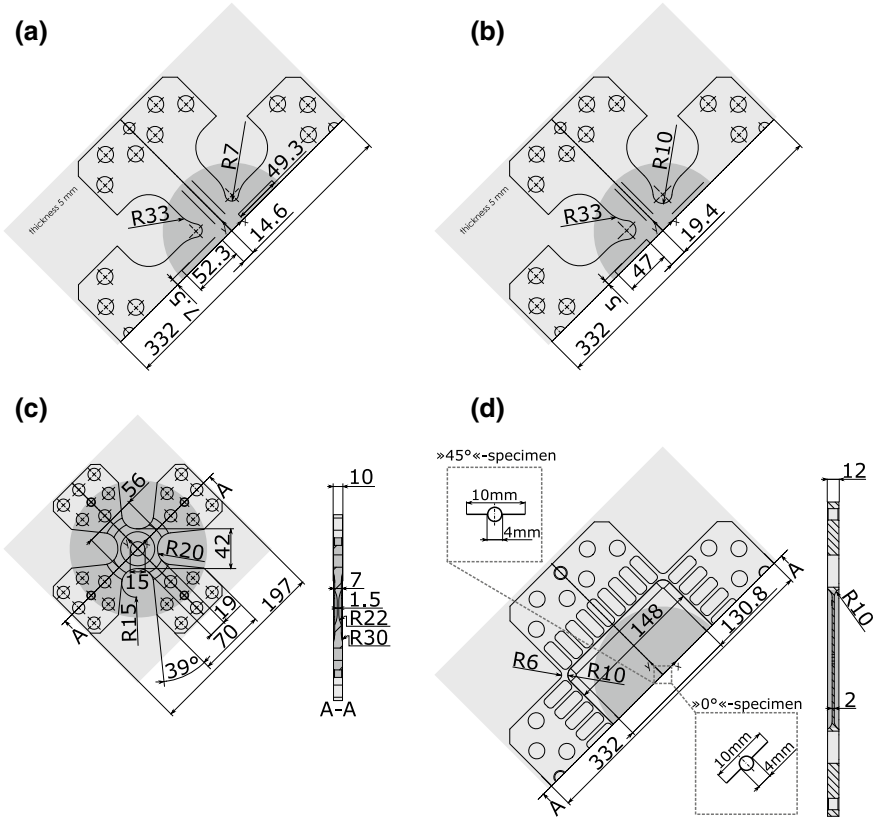

Fig. 14.1 Cruciform specimen geometries for biaxial-planar **a**, **b** quasi-static, **c** low cycle fatigue as well as **d** fatigue crack growth investigations with the essential dimensions in mm and the material illustration: light grey represents AISI304 and dark grey represents PM. Quasi-static specimen with **a** 3 slits (»Triple-slit« specimen) and **b** 2 slits (»Double-slit« specimen). **d** Fatigue crack growth specimen with notches aligned parallel to one loading axis (»0°«-specimen, rectangle bottom right) and at an angle of 45° to both load axes (»45°«-specimen, rectangle top left)

thickness of the specimens was 5 mm. The two specimen shapes used differ on the one hand in the number of slits within the loading arms and on the other hand in the transmission radius. The specimens with three slits called »Triple-slit« specimen had a transmission radius of 7 mm, cf. Fig. 14.1a. The specimens with two slits called »Double-slit« specimen had a transmission radius of 10 mm, cf. Fig. 14.1b. The length of the slits was different for both specimens. On the »Triple-slit« specimen, the middle slit was longer than the slits to the left and right. The two slits of the »Double-slit« specimen had the same length and were shorter than the slits of the »Triple-slit« specimen. Furthermore, the »Triple-slit« specimen had a homogeneous stress and strain distribution in the area of the yield strength at equibiaxial loading with $\lambda = 1$, where λ is the load ratio of the forces of both loading axes according to

(14.1). The »Double-slit« specimen also showed a homogeneous stress and strain distribution without stress and strain concentration areas. In particular, higher strains up to failure were possible in this case. Details of the two specimen designs are given in [85].

$$\lambda = \frac{F_x}{F_y} \tag{14.1}$$

with F_x and F_y the forces in axes x and y, respectively.

In addition to tests with a constant load ratio, i.e. shear loading with $\lambda = -1$, equibiaxial loading with $\lambda = 1$, and tests with $\lambda = 0.5$, sequence tests with alternating λ were also carried out to determine a part of the subsequent yield surface and characterize the hardening behavior as proposed by [86, 87]. The stresses were calculated using the partial unloading method [87]. Hooke's law was then used to calculate the principal stresses for the plane stress state [87].

The load ratios of the sequence tests were given in [85]. In addition to the biaxial tests, uniaxial tests were performed on both flat and cylindrical specimens. The flat specimens were tested on a MTS Landmark 250 (MTS Systems Corporation, Eden Prairie, USA).

14.2.3 Low Cycle Fatigue

The LCF experiments were performed on specimens with a planar thinned measuring area with a diameter of 15 mm and a thickness of 1.5 mm. In the highly loaded measuring area in the middle of the specimens there was a homogeneous stress distribution. The specimen geometry is shown in Fig. 14.1c. The design was similar to that reported repeatedly in the literature, cf. e.g. [16–20, 23, 88].

The LCF tests were performed under total strain-control, whereby the strains ε_x and ε_y were measured by a biaxial extensometer (Sandner Messtechnik GmbH, Biebesheim, Germany). Different strain states Φ, where Φ is the strain ratio of the strains of both axes, cf. (14.2), were investigated with a strain rate of $\dot{\varepsilon} = 0.004/\mathrm{s}$.

$$\Phi = \frac{\varepsilon_x}{\varepsilon_y} \tag{14.2}$$

In addition to equibiaxial tensile strain tests with $\Phi = 1$ and shear tests with $\Phi = -1$, strain ratios of $\Phi = 0.5$, $\Phi = -0.1$ and $\Phi = -0.5$ have also been tested. The schematic course of the triangular strain-time function for $\Phi = 1$ is shown in Fig. 14.2a, for $\Phi = -1$ in Fig. 14.2b and for $\Phi = -0.5$ in Fig. 14.2c. For shear and for equibiaxial strain, the frequencies and amplitudes of the strains had the same values, Fig. 14.2a, b, while the amplitudes differed for $\Phi = -0.5$, cf. Fig. 14.2c.

The von Mises equivalent strain amplitude $\Delta\varepsilon_{\mathrm{vM}}/2$ was calculated according to [89]. The tested von Mises equivalent strain amplitudes $\Delta\varepsilon_{\mathrm{vM}}/2$ were in the range

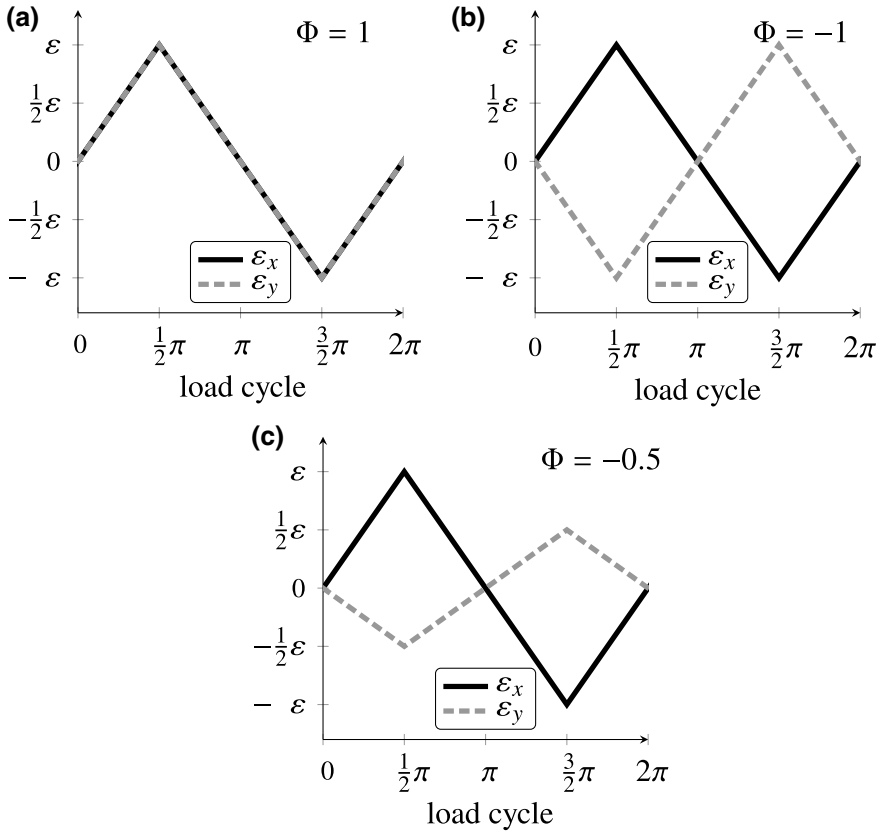

Fig. 14.2 Schematic course of the strains ε_x and ε_y for different strain ratios Φ for in-phase loading

of $0.3 \cdot 10^{-2} \leq \Delta\varepsilon_{vM}/2 \leq 0.6 \cdot 10^{-2}$. In addition, uniaxial reference tests were performed on a MTS Landmark 250 (Eden Prairie, USA).

The characterization of the cyclic deformation behaviour is based on the von Mises force amplitude $\Delta F_{vM}/2$ due to the fact that the cross section could not be determined and numerical calculations as performed by Itoh et al. [19] were not available. The calculation of $\Delta F_{vM}/2$ was carried out according to [18] using the forces F_x and F_y at maximum principal strains in axis x, cf. (14.3). It is assumed that hardening and yielding took place in a defined cross-section and the maximum stresses and strains occur in the thinned measuring area of the specimen with a homogeneous distribution.

$$F_{vM} = \sqrt{(F_x)^2 + \left(F_y\right)^2 - F_x \cdot F_y} \tag{14.3}$$

14.2.4 Fatigue Crack Growth

The fatigue crack growth experiments were performed on cruciform specimens with a thinned measuring area and slitted arms as proposed by Brown and Miller [69] on the base of [81]. The design is widely used [40, 45, 46, 48, 49, 56, 59, 60, 63, 68–80]. It shall simulate the internal crack in a plate of infinite size and small thickness according to [90]. The slitted arms shall ensure a good decoupling of the forces [40, 81, 91]. Furthermore, the stresses in the cross section of the gauge area shall be higher compared to the stresses in the loading arms. The thickness of the measuring area was approximately 2 mm. The exact specimen thickness may vary slightly due to polishing, so that the exact specimen thickness was measured after the tests.

Depending on the investigation, two different configurations of the start notch have been used [40, 76, 77, 91]. On the one hand, uniaxial investigations have been performed at the cruciform specimens with the notches aligned parallel to one loading axis, i.e. at an angle of 0° to one loading axis. This kind of specimen is called »0°«-specimen and shown in Fig. 14.1d. On the other hand, the equibiaxial as well as biaxial investigations with a phase shift have been performed on specimens with notches aligned at an angle of 45° to both loading axes. This kind of specimen is called »45°«-specimen and is also shown in Fig. 14.1d. The hole in the middle of both specimens had a diameter of $d = 4\,\text{mm}$. The total length of both notches was $2 \cdot a = 10\,\text{mm}$, i.e. the notches represented two cracks with a length of $a = 5\,\text{mm}$ each at the beginning of the investigation.

The length of the two cracks was calculated from the center of the cruciform specimen. As long as the crack grew straight, i.e. in the direction of the start notches, the crack length a was measured as the Euclidean distance between starting notch tip and the respective crack tip. Subsequently, the radius of the hole, i.e. $d/2 = 2\,\text{mm}$, and the length of the notch, $l = 3\,\text{mm}$, were added to that Euclidean distance. As soon as the crack path kinked, the Euclidean distance between the currently observed measuring point and the previously observed measuring point was calculated. This distance was added to the crack length of the previously considered measuring point. This means that the crack length is ultimately the sum of the crack length of the straight crack and the individual crack lengths of the kinked crack path. Unfortunately, the measurement errors were added. To minimize measurement errors, the scatter band reduction proposed in [92] in accordance with ASTM E647 [93] was performed. In other words, the given crack length is the arc length of the crack.

The investigations were conducted force controlled with a frequency of 20 Hz and a force ratio of $R = 0.1$. If a force ratio different to $R = 0.1$ was used, it is indicated. The exact forces are given in a recent work [77]. In the case of uniaxial loading, the forces were applied just in y-direction. In the case of biaxial loading, the forces were applied in x- and y-direction. The course of the forces for equibiaxial loading is shown in Fig. 14.3a. Figure 14.3b shows the course for phase-shifted loading with a phase shift of $\varphi = 90°$. The phase shift φ is the time dependent shift of the two forces relative to each other. In the case of in-phase loading, the load ratio λ, cf. (14.1),

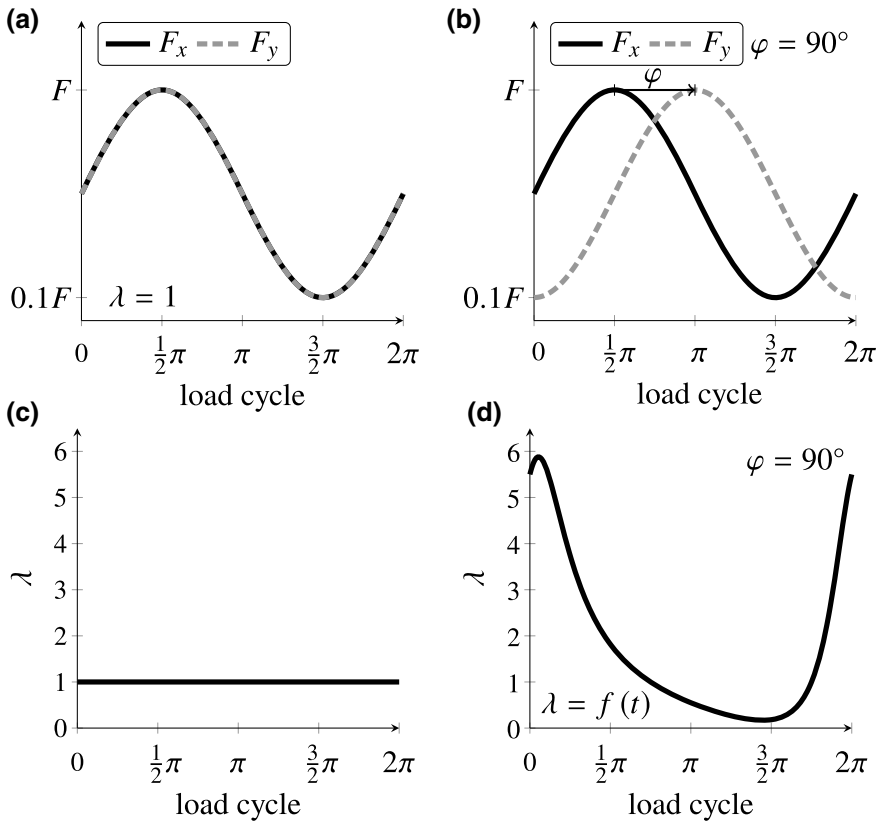

Fig. 14.3 Schematic course of **a**, **b** the applied forces in x- and y-direction and **c**, **d** the resultant biaxial force ratio λ during one load cycle for **a**, **c** in-phase loading as well as **b**, **d** ouf-of-phase loading with a phase shift of $\varphi = 90°$

was $\lambda = 1$ during the entire load cycle, cf. Fig. 14.3c. In the case of out-of-phase loading, the load ratio λ changed permanently during the load cycle, cf. Fig. 14.3d for the example of $\varphi = 90°$.

Four different load cases were investigated: (i) uniaxial loading, (ii) equibiaxial loading, (iii) first equibiaxial loading to start the fatigue crack growth and afterward phase-shifted loading, and (iv) first equibiaxial loading to start the fatigue crack growth and afterward phase-shifted loading with an increase of the phase shift after a change in the crack length a of more than $\Delta a = 1.5$ mm.

For the calculation of the stress intensity factor K and range ΔK, the occurring stresses have to be known. They were calculated using commercial software ABAQUS for 2D finite element analyses with a linear elastic material model and unit forces of $f_x = 1$ kN or $f_y = 1$ kN [91]. The investigations showed, that a material-independent solution for the transmission of force into stress can be given. An applied force of $F_y = 1$ kN in y-direction resulted in a stress of $\sigma_y = 2.94$ MPa in y-direction

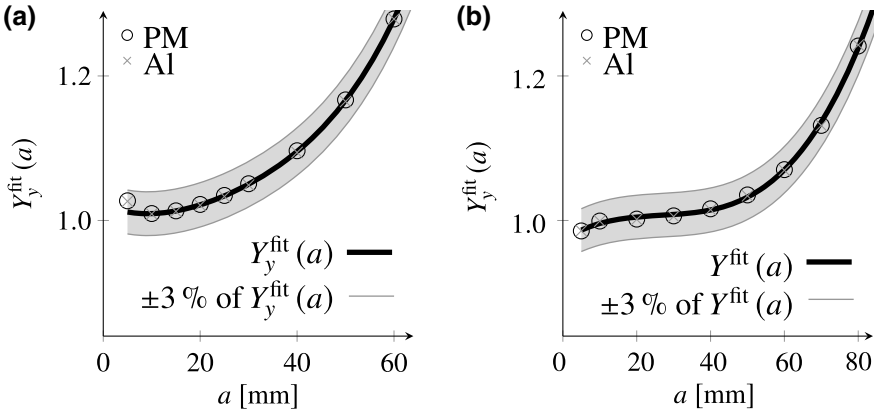

Fig. 14.4 Plot of the geometry functions $Y(a)$ versus the crack length a for the **a** »0°«-specimen and **b** »45°«-specimen. Comparison of the exact solutions for PM and Al with the determined fit function and the ±3% deviation [91]

in the center of the specimen. An applied force of $F_x = 1\,\text{kN}$ in x-direction resulted in a stress of $\sigma_y = -0.05\,\text{MPa}$ in y-direction in the center of the specimen. Due to the principal of superposition and the possibility of scaling, cf. [40, 76, 77, 91], the effective stress can thus be determined at each time of the load cycle. Furthermore, in dependence of the alignment of the start notches, i.e. for the »0°«-specimen as well as for the »45°«-specimen, material-independent and crack length dependent geometry functions $Y(a)$ were determined, cf. [91]. Figure 14.4a, b show the geometry functions $Y_y(a)$ for the »0°«-specimen and $Y(a)$ for the »45°«-specimen, respectively. Both plots in Fig. 14.4 show the exact solution of the geometry factor $Y(a)$ at different crack lengths for the investigated steel, called PM, as well as for an aluminium alloy, called Al. The calculations are based on the material parameters Young's modulus $E = 192\,\text{GPa}$ and Poisson's ratio $\nu = 0.24$ for PM and $E = 72\,\text{GPa}$ and $\nu = 0.34$ for the Al alloy, respectively. It becomes clear, that the geometry functions approximate the calculated geometry factors well for both materials, in each case for the corresponding notch configuration for straight crack paths. Influences on the fatigue crack growth due to differences in the thickness of the measuring area can be corrected using a thickness correction [76]. As soon as the crack paths begin to kink, the calculation of the K-solution has to be done using FE-calculations, cf. [76, 77].

14.2.5 Experimental Details

The planar-biaxial investigations were performed on a servo-hydraulic tension-compression system (Instron 8800, Instron, Norwood, USA), cf. Fig. 14.5. The test rig had four actuators in two perpendicular loading axes. In addition, depending on

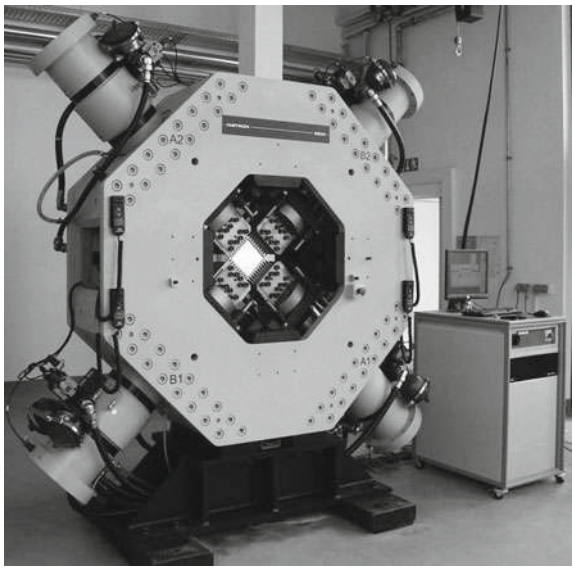

Fig. 14.5 Servo-hydraulic planar-biaxial tension-compression test system [1]

the test, i.e. quasi-static, LCF or FCG tests, various other measuring instruments were attached, cf. Fig. 14.6.

A biaxial orthogonal extensometer (Sandner Messtechnik GmbH, Biebesheim, Germany) was applied for the quasi-static investigations as well as for the LCF investigations, cf. #1 in Fig. 14.6a, c, d. The extensometer had four ceramic arms with a gauge length of 13 mm for strain measurement in the two orthogonal axes. It was mounted in the middle of the measuring area at one side of the specimen, cf. #1 in Fig. 14.6a for quasi-static investigations [85, 87] and #1 in Fig. 14.6c, d for LCF investigations [18, 94]. The measured strains corresponded to principal strains.

The ferrite measuring device Fischerscope MMS PC (Helmut Fischer GmbH, Sindelfingen, Germany), cf. #2 in Fig. 14.6a, c, d, was applied at the quasi-static investigations as well as for the LCF investigations to measure the martensite content opposite to the extensometer. The martensite content was calculated according to [95] by multiplying the measured ferrite content calibrated for δ-ferrite by a factor of 1.7.

Support plates were mounted on the specimen during quasi-static tests with compressive loading, cf. #3 in Fig. 14.6b to prevent buckling.

Fatigue crack growth tests were carried out by applying crack gages (Krak Gage B20, Russenberger Prüfmaschinen AG, Neuhausen, Switzerland) to the front of specimen, cf. #4 in Fig. 14.6e. The crack length for cracks that extend the two start notches was measured using the indirect potential method using Fractomat (Russenberger Prüfmaschinen AG, Neuhausen, Switzerland).

Furthermore, a high speed camera (mvBlueCOUGAR-XD 104 bG, Matrix Vision GmbH, Oppenweiler, Germany), cf. #5 in Fig. 14.6f, with optics was located at the back of the specimen to document the crack opening. For this purpose a speckle pattern was sprayed onto the specimen surface to evaluate the movement of the

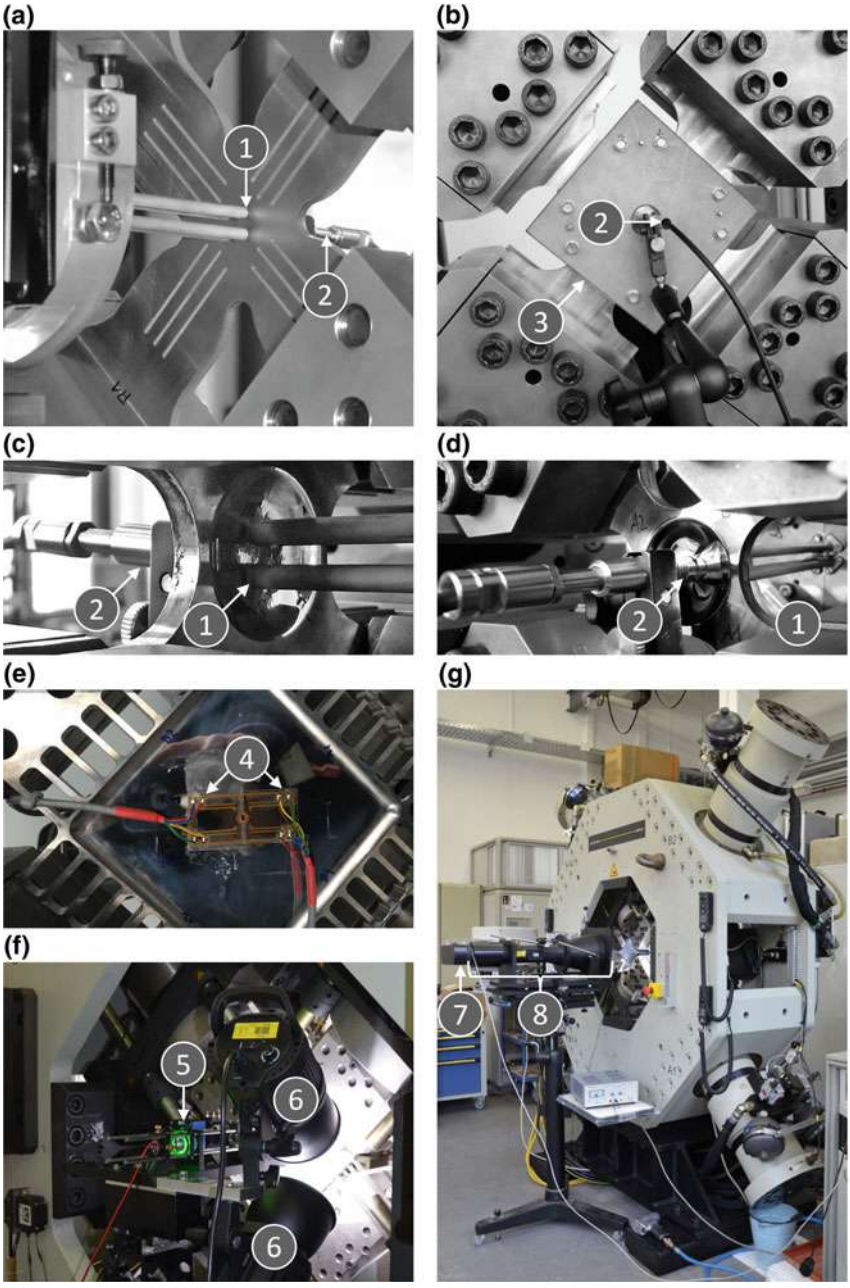

Fig. 14.6 Test setup for experiments with **a**, **b** quasi-static loading as well as **c**, **d** low cycle fatigue and **e**–**g** fatigue crack growth experiments and illustration of the measuring instruments used: #1 biaxial orthogonal extensometer, #2 ferrite sensor, #3 support plates, #4 crack gage, #5 high speed camera, #6 lighting, #7 high resolution scanner camera with #8 telecentric optics [23, 87]

crack edges using digital image correlation software (ARAMIS v6.3.1, GOM GmbH, Braunschweig, Germany). For this, it was important that the measuring spot is uniformly illuminated. This was achieved with two LED spotlights (Mettle EL-600, Mettle Photographic Equipment Corporation, Changzhou, China), cf. #6 in Fig. 14.6f.

The documentation of the crack tip coordinates and the measurement of the crack lengths for kinking crack paths was carried out with a line scanner camera (Pentacon SCAN 6000, Pentacon GmbH, Dresden, Germany) with telecentric optics, which was installed in front of the test rig, cf. #7 and #8 in Fig. 14.6g, cf. [71] for further details.

14.3 Quasi-static Loading

The evaluation of the uniaxial and the biaxial tests with constant load ratio λ are shown in Fig. 14.7a. The yield point used was the 0.2% yield point $R_{p0.2}$ applied for materials without a pronounced yield point. The yield strength of the uniaxial tests was 288 ± 21 MPa in tension and 288 ± 28 MPa in compression. Furthermore the symmetry points for the uniaxial loading are indicated. This material can be described with the von Mises equivalent stress hypothesis. A comparison of the results between the »Triple-slit« specimens and the »Double-slit« specimens shows a higher equivalent yield strength of the »Double-slit« specimens in comparison to the »Triple-slit« specimens. These differences are visible in quadrant I of the von Mises yield surface, cf. Fig. 14.7a. In quadrants II and IV, differences in yield strength between the two specimen geometries of up to 90 MPa are visible.

The comparison of the stress-strain curve of the uniaxial experiments with the stress-strain curve of the »Double-slit« specimens illustrates, that the »16-7-6 (Batch 1)« can be described with the von Mises equivalent stress hypothesis. For shear loading, i.e. $\lambda = -1$, strains of up to 20 % are possible. In the uniaxial experiments a significant scatter was found. The results of the biaxial tests are within this scatter band. From this it can be concluded that the partial unloading method is suitable for determining the stress-strain curve for those biaxial experiments.

By means of sequence tests on a »Triple-slit« specimen and a »Double-slit« specimen the subsequent yield surfaces were studied. Load sequence effects occurred. In this paper, only the results of the »Triple-slit« specimen are presented. The results of the »Double-slit« specimen are given elsewhere [85].

Figure 14.7b shows the load path and Fig. 14.7c shows the stress path in the principal stress plane $\sigma_1 - \sigma_2$ of the »Triple-slit« specimen. The corresponding stress-strain curve as well as the martensite evolution is given in Fig. 14.7d.

In the load sequence test of the »Triple-slit« specimen, the load was first increased at a load ratio of $\lambda = 0.3$ until (1) an equivalent plastic strain $\varepsilon_{\text{eq-pl}}$ of $\varepsilon_{\text{eq-pl}} = 2\%$ was reached, cf. Fig. 14.7c. At this equivalent plastic strain, the equivalent stress σ_{eq} was $\sigma_{\text{eq}} = 350$ MPa. Therefore, the yield surface for $\sigma_{\text{eq}} = 350$ MPa is shown in Fig. 14.7c (solid line) under the assumption of isotropic hardening. At this load, 0.3% of α'-martensite had already formed. Subsequently, the loading was gradually

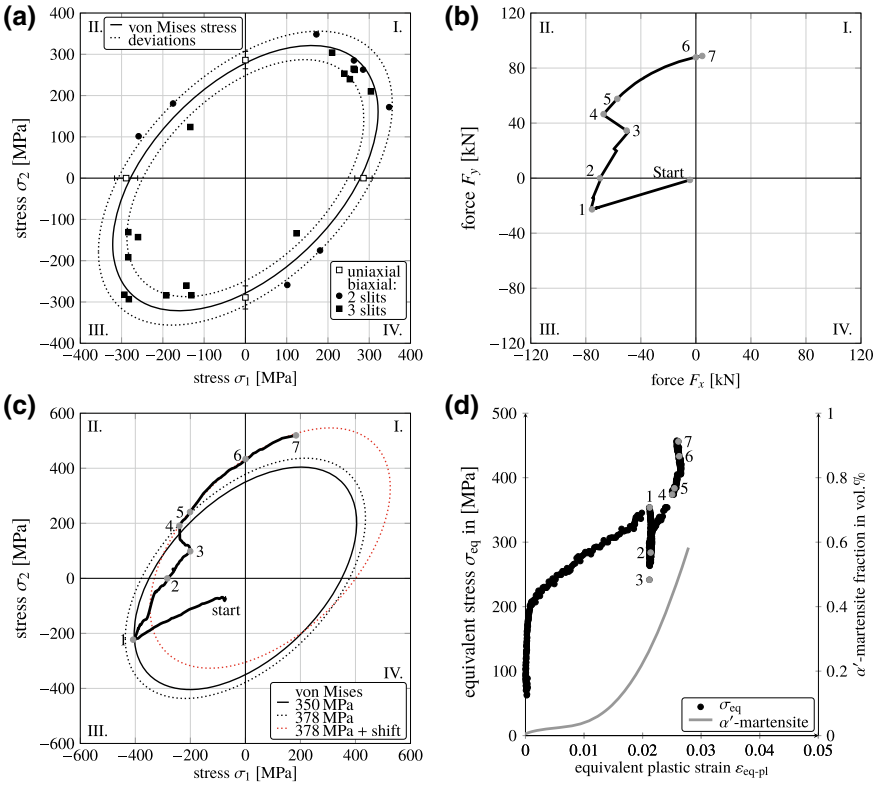

Fig. 14.7 Results of the quasi-static biaxial-planar experiments. **a** Experimentally determined von Mises yield surface of the »16-7-6 (Batch 1)« by uniaxial and planar-biaxial tests using the »Triple-slit« and the »Double-slit« specimens. **b** Load path and **c** stress paths of sequential tests within the principal stress plane with an initial load ratio of $\lambda = 0.3$ at the »Triple-slit« specimen with **d** the corresponding stress-strain curve and martensite evolution [85]

changed, starting (1) with the initial load ratio of $\lambda = 0.3$, through (2) a load ratio of $\lambda = 0$ and ending (3) with a load ratio of $\lambda = -0.7$. The load path passed through the elastic area. When the load ratio of $\lambda = -0.7$ was reached, the force was again increased up to (4) an equivalent plastic deformation of $\varepsilon_{\text{eq-pl}} = 2.5\%$. Further α'-martensite was formed. At the equivalent plastic strain of $\varepsilon_{\text{eq-pl}} = 2.5\%$, an equivalent stress of $\sigma_{\text{eq}} = 378\,\text{MPa}$ was reached. In the subsequent gradual loading change, starting (4) with the load ratio of $\lambda = -0.7$ and ending (5) with a load ratio of $\lambda = -1$, the equivalent stress followed the yield surface for $\sigma_{\text{eq}} = 378\,\text{MPa}$. The further stepwise change of the load ratio from (5) $\lambda = -1$ through (6) a load ratio of $\lambda = \infty$ to (7) $\lambda = 20$ was accompanied by further hardening and a further α'-martensite formation without further plastic deformation, i.e. elastic material behaviour was observed. This effect can be explained by kinematic hardening, so that a shifted yield surface for $\sigma_{\text{eq}} = 378\,\text{MPa}$ was drawn, cf. Fig. 14.7c, red dotted ellipse. The shift was

$\sigma_1 = 90\,\text{MPa}$ and $\sigma_2 = 110\,\text{MPa}$. This ellipse corresponds to the observed loading path. This confirms the hypothesis of kinematic hardening which is accompanied by the formation of further α'-martensite. The stresses were determined by means of partial unloading method. The results showed that the partial unloading method is also suitable for the measurement of kinematic hardening effects under multiaxial loading.

In the presented sequence test as well as in the sequence test of [85], no yield surface matching the load path could be determined. The reason for this is the formation of α'-martensite. This results in the assumption that the α'-martensite formation of the microstructure depends on the stress state. Changes in the stress state led to an activation of other glide systems. An intersection of these with the martensite led to strain hardening. Detailed explanation on this are made in the following paragraphs on microstructure. It is also assumed that anisotropic yield surface is present since strain hardening is correlated with a combination of isotropic and kinematic hardening. As long as no α'-martensite formation took place, isotropic material behaviour was present. A similar material behaviour with initial isotropic flow curve and kinematic hardening during subsequent deformation can also be found in the literature [87, 96–98].

The investigations of the microstructure were performed ex situ at »Triple-slit« specimen for shear loading with $\lambda = -1$ and equibiaxial tension with $\lambda = 1$ up to equivalent strains of $\varepsilon_{\text{eq-pl}} = 8.6\%$ and $\varepsilon_{\text{eq-pl}} = 8\%$, respectively. The scanning electron microscope (SEM) images in back scattered electron (BSE) contrast clearly showed the formation of deformation bands in the austenitic matrix [85]. α'-martensite nuclei were formed in these deformation bands in accordance with uniaxial reference tests, see e.g. [99, 100]. Uniaxial monotonic tests by the authors of [100] showed that the deformation bands were areas of strain localizations. These form large stacking faults due to the movement of partial dislocations. The stacking fault density, the local strain and the thickness of the deformation bands increased with increasing plastic strain. The α'-martensite nuclei were preferentially formed on the intersection points of deformation bands or at intersection points of individual stacking faults with deformation bands. This in turn corresponds to the increase in strain as a function of the crystallographic orientation of the α'-martensite nuclei in relation to the load axis. Shear loading resulted in austenitic grains being covered with deformation bands containing α'-martensite islands. In contrast, tensile loading resulted in a lower density of the deformation bands. The individual deformation bands of the austenitic matrix can be distinguished. Furthermore, the α'-martensite island density was significantly lower for uniaxial loading.

The electron backscatter diffraction (EBSD) investigations of the microstructure of the »Triple-slit« specimen for shear loading with $\lambda = -1$ and equibiaxial tension with $\lambda = 1$ show significant differences, cf. Fig. 14.8. The number of austenite grains containing deformation bands is significantly higher for shear loading, cf. Fig. 14.8a, than for equibiaxial loading, cf. Fig. 14.8b. Furthermore, much more α'-martensite nuclei were formed under shear loading, i.e. the density of α'-martensite nuclei is much higher for shear loading in comparison to the equibiaxial tension loading. In the EBSD images it becomes clear that the formation of deformation bands was inten-

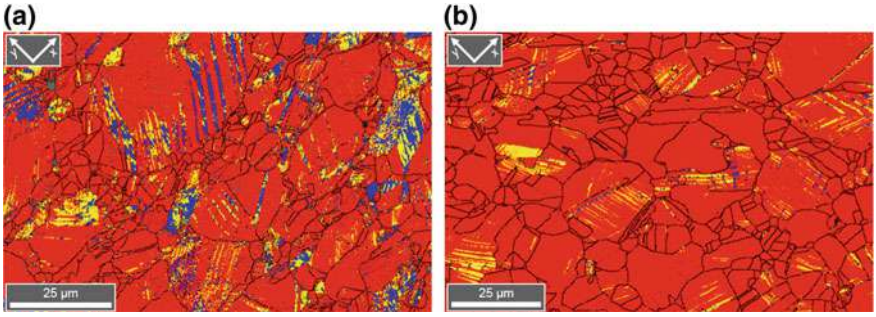

Fig. 14.8 EBSD phase maps of »Triple-slit« specimens after **a** shear loading up to $\varepsilon_{\text{eq-pl}} = 8.6\%$ and **b** equibiaxial tensile loading up to $\varepsilon_{\text{eq-pl}} = 8\%$ with austenite (red), ε-martensite (yellow) and α'-martensite (blue) [85]

sified due to the high stacking fault density, which had a hexagonal structure, when subjected to shear loading. This is particularly evident from the fact that in the specimen subjected to shear loading, individual austenite grains were completely covered with a hexagonal structure, cf. Fig. 14.8a, and their thickness or rather their density were much more pronounced than for equibiaxial loading. Furthermore, the volume fraction of the deformation-induced α'-martensite is considerably higher for shear loading than for equibiaxial tensile loading. This corresponds to the measurements of the ferromagnetic phase fraction by means of a ferrite sensor [85].

14.4 Low Cycle Fatigue

The cyclic deformation behaviour and the martensitic transformation were investigated for »16-7-6 (Batch 2)«. The characterization is based on the von Mises force amplitude $\Delta F_{\text{vM}}/2$. The LCF behaviour of the material can be divided into three stages, cf. Fig. 14.9 [94]. Due to the cyclic loading, primary hardening took place at the beginning. Subsequently softening took place, which was finally followed by secondary hardening. Such material behaviour is already well-known from uniaxial studies, see e.g. [7, 31, 32]. The course of the cyclic deformation curves for the investigated equibiaxial tensile loading, i.e. the strain ratios of $\Phi = 1$ and $\Phi = 0.5$, was almost identical, cf. [94]. However, with negative strain ratios Φ, the von Mises force amplitude $\Delta F_{\text{vM}}/2$ decreased with decreasing strain ratio Φ, cf. Fig. 14.9a.

With negative strain ratios, the onset of secondary hardening was earlier and the magnitude was increased, i.e. the more negative the strain ratio was, the stronger and earlier the secondary hardening was, cf. Fig. 14.9a. Furthermore, at negative strain ratios, it was found that the maximum fatigue life was measured for the strain ratio of $\Phi = -1$ and the shortest fatigue life for the strain ratio of $\Phi = -0.1$, i.e. the larger the strain ratio at negative strain ratio was, the longer the fatigue life was. This leads to the assumption that shear loading with $\Phi = -1$ supports yielding, secondary

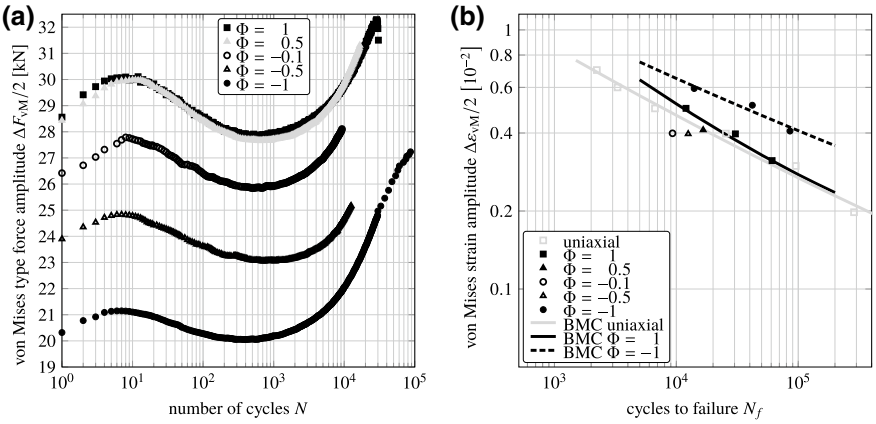

Fig. 14.9 **a** Cyclic deformation curves and **b** estimation of fatigue life of »16-7-6 (Batch 2)« [94] under uniaxial and biaxial cyclic loading with different strain ratios Φ showing the von Mises equivalent strain amplitude of $\Delta\varepsilon_{vM}/2$ versus N_f [94]

hardening and reduces axial forces. This was also reported in [18]. Due to the shear loading the secondary hardening was most pronounced due to an early start of cyclic hardening. Therefore the fatigue life for shear stress was also the highest.

In contrast to negative strain ratios, von Mises force amplitudes $\Delta F_{vM}/2$ were almost identical for positive strain ratios, cf. Fig. 14.9a. However, in these experiments the cross-sectional area was not identical, as was assumed for the von Mises force amplitude $\Delta F_{vM}/2$. Further experiments with an increase in von Mises strain amplitude $\Delta\varepsilon_{vM}/2$ in the range between $0.3 \cdot 10^{-2} \leq \varepsilon_{vM}/2 \leq 0.6 \cdot 10^{-2}$ showed an earlier onset of the secondary hardening due to a higher plastic deformation, as the martensitic phase transformation took place during the cyclic deformation.

For the investigated von Mises strain amplitude of $\Delta\varepsilon_{vM}/2 = 0.4 \cdot 10^{-2}$ for the strain ratios of $\Phi = -1$, $\Phi = -0.5$, $\Phi = -0.1$, $\Phi = 0.5$ and $\Phi = 1$ as well as for uniaxial experiments, a significant increase in the α'-martensite content was observed after an incubation period and correlated with the onset of secondary hardening, see [18]. The course of the martensite formation curves for the strain ratios of $\Phi = -1$, $\Phi = -0.5$, $\Phi = -0.1$ and the uniaxial investigations were almost identical up to the point of failure. However, for the strain ratios of $\Phi = 0.5$ and $\Phi = 1$, the martensitic transformation started later. The α'-martensite amount at fatigue failure ranged from an α'-martensite amount of 5 vol% at a strain ratio of $\Phi = 0.5$ up to an α'-martensite amount of 45 vol% at a strain ratio of $\Phi = -1$. In conclusion, it can be stated that the α'-martensite formation depends on the platic strain amplitude $\varepsilon_{vM}/2$, which is responsible for secondary hardening. This is in accordance to [7, 31, 32]. Furthermore, the formation of α'-martensite is promoted by uniaxial or shear loading, since the martensite content was significantly lower for all other types of loading, i.e. $\Phi = -0.5$, $\Phi = -0.1$, $\Phi = 0.5$ and $\Phi = 1$.

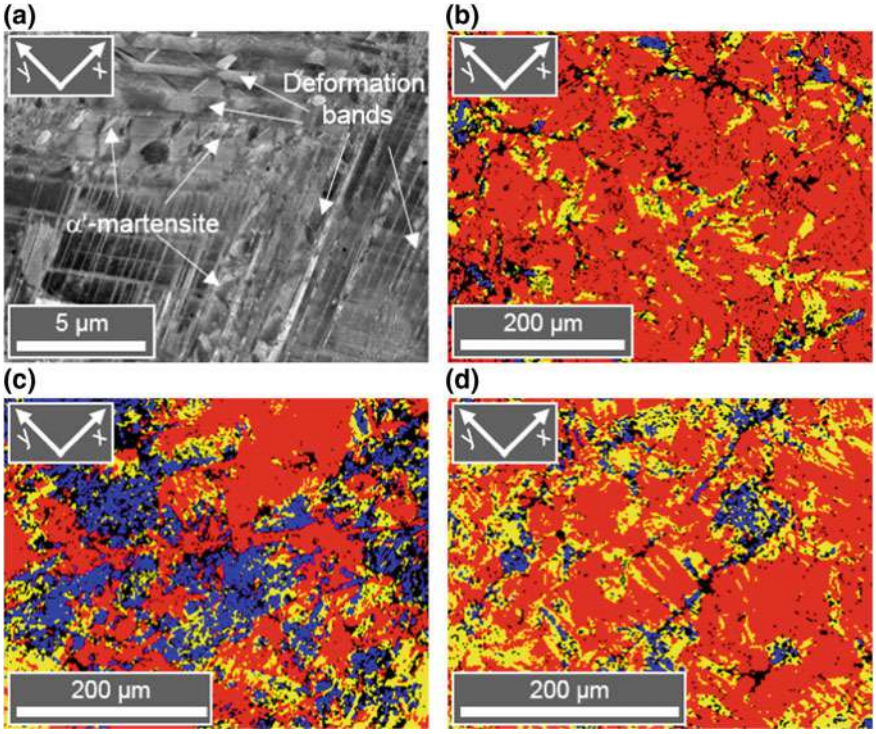

Fig. 14.10 SEM micrographs of the »16-7-6 (Batch 2)« after cyclic loading at $\Delta\varepsilon_{vM}/2 = 0.4 \cdot 10^{-2}$. **a** Deformation bands and α'-martensite shown in the BSE contrast after cylclic shear loading with $\Phi = -1$. **b–d** EBSD phase maps after cyclic **b** equibiaxial loading with $\Phi = 1$, **c** shear loading with $\Phi = -1$ and **d** loading with $\Phi = 0.5$ with austenite (red), ε-martensite (yellow) and α'-martensite (blue) [94]

The SEM images in BSE contrast, cf. Fig. 14.10a, show lens-shaped α'-martensite in the deformation bands. These are often located at the intersection points of deformation bands [101]. This is a typical microstructure for cyclic deformation and in accordance with the observations of e.g. [5]. The thin deformation bands do not contain α'-martensite nuclei. This is also consistent with findings by the authors of [5]. A high stacking fault density resulting in a hexagonal structure called ε-martensite was found by EBSD and electron channeling contrast imaging (ECCI) in the deformation bands, cf. [5].

EBSD measurements were made in the SEM on vibration-polished surfaces, Fig. 14.10b–d. The phase maps show fcc austenite (red), hexagonal ε-martensite (yellow) and bcc α'-martensite (blue) at different von Mises strain ratios Φ at a von Mises strain amplitude of $\Delta\varepsilon_{vM}/2 = 0.4 \cdot 10^{-2}$. Figure 14.10b–d show the phase maps after cyclic deformation with equibiaxial loading of $\Phi = 1$, shear loading of $\Phi = -1$, and deformation with $\Phi = -0.5$. It becomes clear that the α'-martensite always lies within the hexagonal phase (yellow). This in turn confirms the

assumption that the transformation from fcc austenite to α'-martensite took place via ε-martensite. The comparison of Fig. 14.10b–d shows that the largest fraction of α'-martensite and ε-martensite were formed under shear loading with a fraction of $\approx$15% each, cf. Fig. 14.10c. The lowest fraction of α'-martensite and ε-martensite was measured under equibiaxial loading, cf. Fig. 14.10b. The most intensive formation of ε-martensite was found after a loading with a strain ratio of $\Phi = 0.5$, although the regions with α'-martensite were very small, cf. Fig. 14.10d. A martensitic phase transformation was also measured in the plastic zone of the formed cracks. However, this is not shown here.

The fatigue life was compared by applying the von Mises strain amplitude $\Delta\varepsilon_{vM}/2$ versus the number of load cycles to failure, cf. Fig. 14.9b. The comparison of the fatigue life of the »16-7-6 (Batch 2)« at different strain ratios shows clearly, that fatigue lives were the shortest for $\Phi = 0.5$, $\Phi = -0.1$ and $\Phi = -0.5$ in comparison to the uniaxial as well as biaxial shear loading and the equibiaxial loading. To be more precise, these fatigue lives for uniaxial or equibiaxial loading are within the scatter band of 2. It can therefore be concluded that the Basquin-Manson-Coffin relationship (BMC) for uniaxial loading is conservative for equibiaxial loading for the investigated material. In contrast, the authors of [19] observed at AISI304 steel that the fatigue lives for $\Phi = -0.5$, $\Phi = 0$ and $\Phi = 0.5$ are between those of equibiaxial loading with $\Phi = 1$ and shear loading with $\Phi = -1$. Fatigue life of the »16-7-6 (Batch 2)« under shear loading $\Phi = -1$ is about 7–8 times higher than under equibiaxial $\Phi = 1$ or uniaxial loading, respectively. The differences in fatigue life decrease with increasing von Mises equivalent strain amplitude $\varepsilon_{vM}/2$ due to plastic deformation. This is in accordance with the findings of [18] for the cast material. Furthermore, the results show that the highest fatigue lives occurred at shear loading compared to uniaxial loading in agreement with the literature for planar biaxial investigations [16, 17, 19, 20, 23] and tension-torsion tests [21, 22, 102]. For austenitic steels with a low stacking fault energy, the differences in fatigue lives are larger than for austenitic steels with a high stacking fault energy [22].

The discussion of the resulting equivalent force amplitudes and fatigue lives is based on the assumption of von Mises. However, the deviations of equivalent force amplitudes and fatigue lives can also be interpreted that the von Mises hypothesis cannot be applied in the present case. The von Mises criterion was used, as the criterion is valid for plastically deformable materials. Under equibiaxial loading in the tension-compression regime there is a scatter of about 2–3, with a shorter fatigue life compared to uniaxial loading. Under shear loading the fatigue life is about 7–8.5 times higher than under uniaxial loading for the same von Mises strain amplitude, i.e. the damage caused by shear loading is overestimated. In order to be able to describe the service life reserve or the reduced damage caused by shear loading, alternative models should be used which take the effect of the hydrostatic part of the stress tensor on damage into account.

14.5 Fatigue Crack Growth

14.5.1 Crack Paths

The fatigue crack growth investigations on the »16-7-6 (Batch 3)« were carried out on five different specimens. One specimen was loaded unaixially (specimen »uni«), one specimen was loaded equibiaxially (specimen »equi«), two specimens were first equibiaxially and subsequently phase-shifted loaded (specimens »0°/22.5°« and »0°/180°«) and one specimen was first equibiaxially and then phase-shifted loaded with phase shift increases of 15° after given crack growth intervals (specimen »stepw. 0°–90°«). The courses of the two cracks of the respective specimens were identical or symmetrical, respectively. This is also valid for the crack paths of all four cracks of specimen »0°/180°«. As expected, the uniaxial loading of specimen »uni« led to a straight crack path, which runs perpendicular to the loading axis y, cf. Fig. 14.11a. Furthermore, the equibaixial loading during the entire test of specimen »equi« resulted in a crack path that runs at an angle of 45° to both loading axes in the direction of the starting notches, cf. Fig. 14.11b. This was due to the fact that the start notches were also aligned at an angle of 45° to both loading axes and that the equibiaxial loading led to a pure Mode I crack opening. SEM investigation of the crack path revealed that there was a micro crack branching at the end of the investigation, cf. Fig. 14.12a. The reason for this seems to be an edge influence as well as force coupling.

A change of the phase shift from in-phase loading to out-of-phase loading led to a change of the crack propagation direction in most investigations. The change from the initial equibiaxial loading to a subsequent phase-shifted loading of $\varphi = 22.5°$ for specimen »0°/22.5°« resulted in a gradual change of the crack propagation direction without branching, cf. Fig. 14.11c. Branching as a result of a phase-shifted loading occured after phase change to 180° in specimen »0°/180°«, cf. Fig. 14.11d. At the triple point of cracks 1, 1-1 and 1-2, i.e. at the point where the change from in-phase to out-of-phase loading and therefore branching occured, no further micro cracks were observed in SEM investigations, cf. Fig. 14.12b. The obtained crack paths are in accordance with those predicted in [103]. However, it was expected that both branched cracks would grow initially, but one crack would not grow further after some load cycles [75]. Due to the change to a $\varphi = 180°$ phase-shifted loading, there were two principal stress directions which occured in succession. They were shifted by exactly half of the load cycle, i.e. $N/2$. The cracks 1-1 and 1-2 or 2-1 and 2-2, respectively, grew on initially curved paths, but then finally perpendicular to the principal stress directions. This is in accordance with [104, p. 131]. The cracks strived for this crack path according to the maximum circumferential stress criterion according to [105]. This criterion is commonly used for crack growth direction predictions [106–108].

The change from an initial in-phase loading to a subsequent 15° phase-shifted loading of specimen »stepw. 0°–90°« resulted in a kinking at a very small angle, Figs. 14.11e, f and 14.13a. This relatively small angle of crack path kinking was

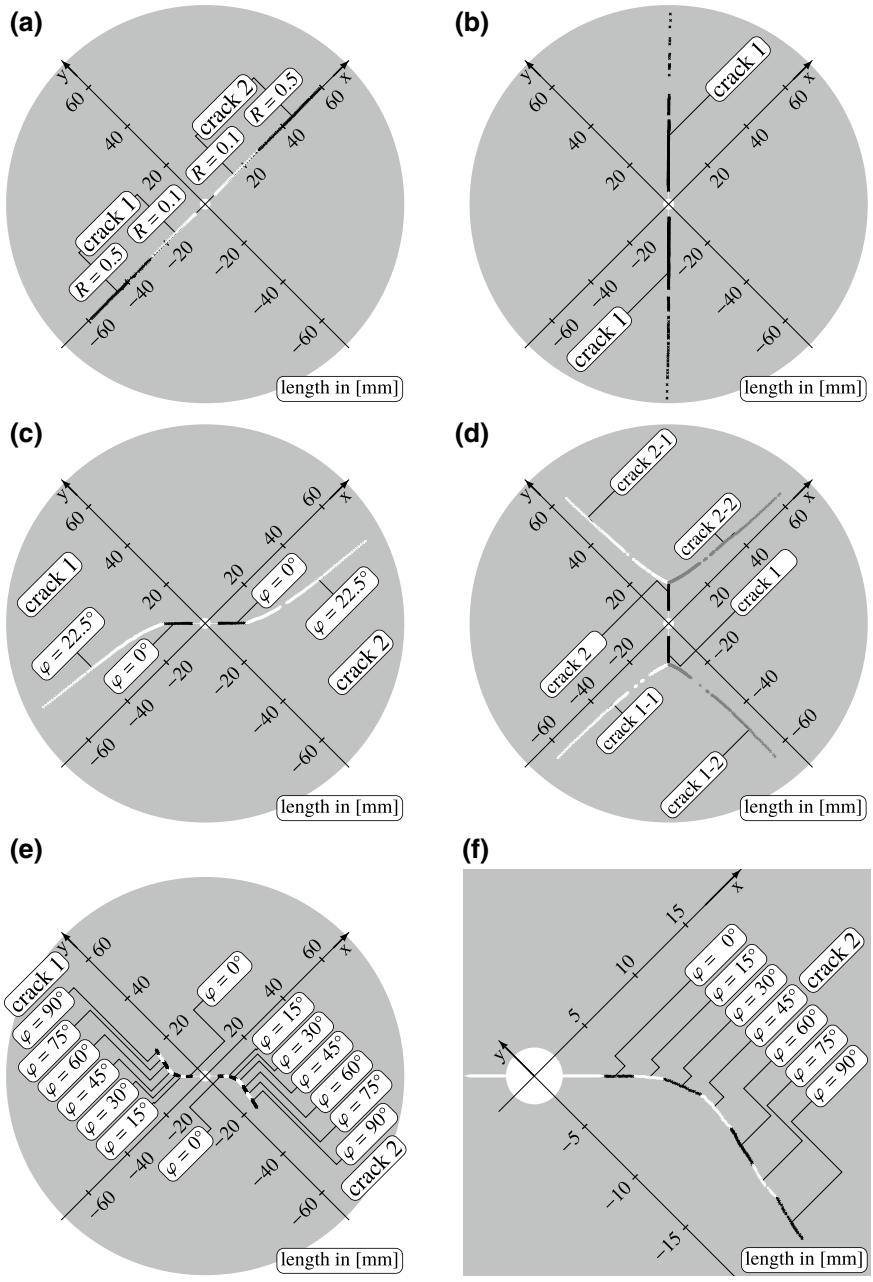

Fig. 14.11 Crack paths of the **a** uniaxially loaded specimen »uni«, **b** equibiaxially loaded specimen »equi«, **c** first equibiaxially and afterwards phase-shifted loaded specimen »0°/22.5°« with $\varphi = 22.5°$ and **d** »0°/180°« with $\varphi = 180°$. **e** First equibiaxially and afterwards phase-shifted loaded specimen »stepw. 0°–90°« with a stepwise increase of the phase shift in steps of 15° with $0° \leq \varphi \leq 90°$. **f** Enlarged view of (**e**), crack 2 [77]

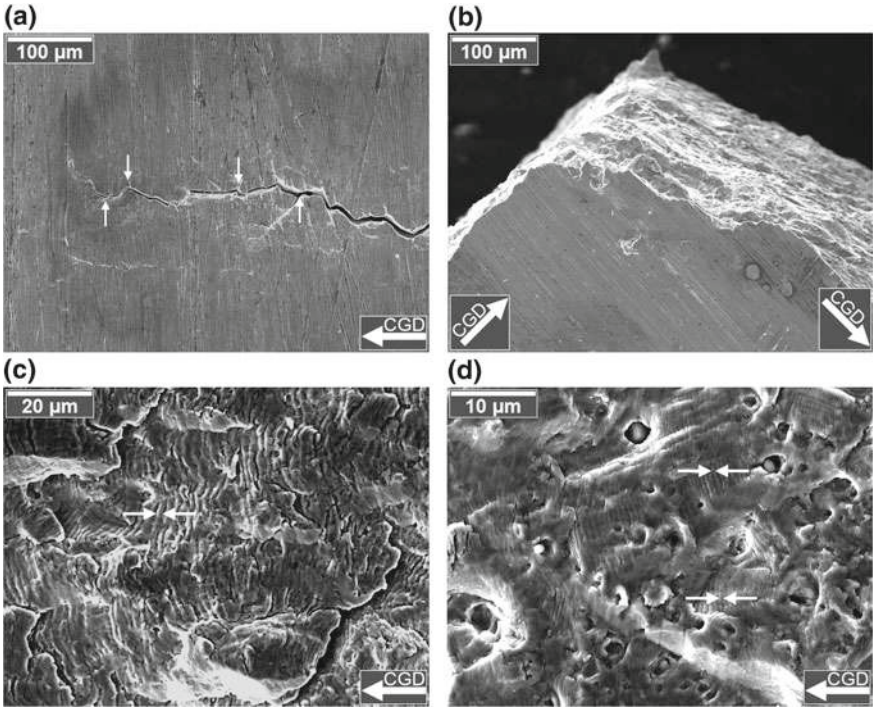

Fig. 14.12 SEM micrographs with crack growth direction (CGD) of the **a** crack paths and the **b–d** fractured surfaces of the specimens **a**, **c** »equi« as well as **b**, **d** »0°/180°«. **a** Crack path of crack 1 of the specimen »equi« at the end of the investigation. **b** Triple point of crack 1 branching into cracks 1-1 and 1-2 of the steel specimen »0°/180°«. **c** Fractured surface of crack 1 of specimen »equi« at a crack length of $a \approx 70\,\mathrm{mm}$ $\left(\Delta K_{\mathrm{eq}} \approx 70\,\mathrm{MPa}\sqrt{\mathrm{m}}\right)$. **d** Fractured surface of crack 1-2 of specimen »0°/180°« at a crack length of $a \approx 60\,\mathrm{mm}$ $\left(\Delta K_{\mathrm{eq}} \approx 80\,\mathrm{MPa}\sqrt{\mathrm{m}}\right)$ [77]

due to a small Mode II component, cf. [76], due to the slight phase shift φ. In the two changes of the phase shift φ, i.e. from $\varphi = 15°$ to $\varphi = 30°$ and from $\varphi = 30°$ to $\varphi = 45°$, a significant kinking of the crack path occured. In addition to kinking at a large angle, microbranching was observed at both changes of phase shift, Fig. 14.13b, c. The further increases of the phase shift by 15° had no further pronounced impact on the crack path.

14.5.2 Crack Growth Rates

The consideration of crack growth is carried out with both a–N plots, Fig. 14.14a, b, and $\mathrm{d}a/\mathrm{d}N$–ΔK plots, Fig. 14.14c, d. In addition to the symmetrical crack paths, the courses of the a–N curves of both cracks or even all four cracks were also identical.

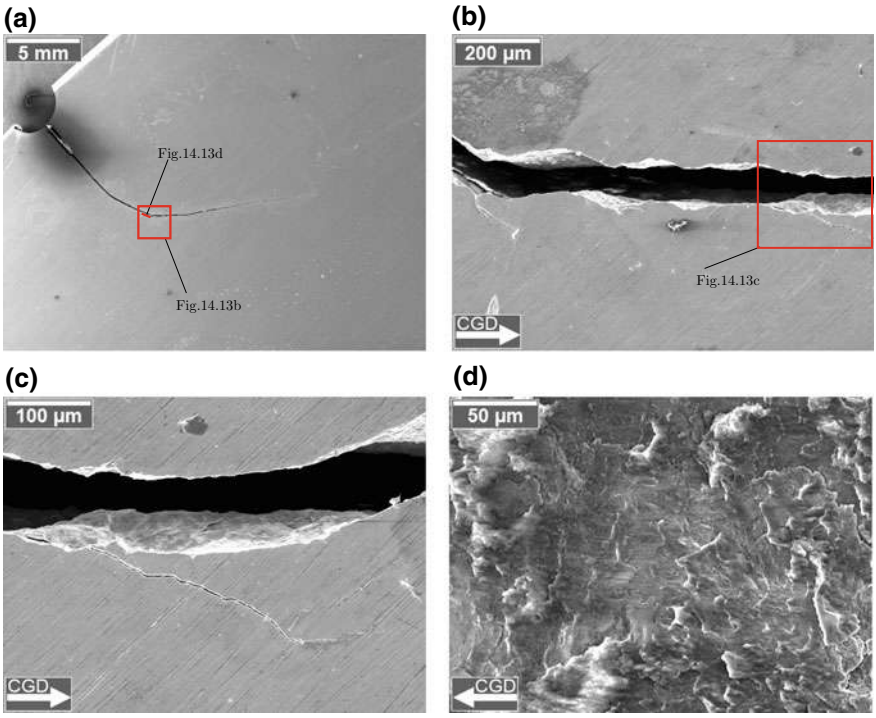

Fig. 14.13 SEM micrographs with crack growth direction (CGD) of the **a–c** crack paths and **d** the fractured surface of specimen »stepw. 0°–90°«. **a** Location of the enlarged view of image (**b**). **b** Location of the enlarged view of image (**c**). **c** Branching and subbranching as well as **d** face friction at the transition from straight to curved crack path, cf. Fig 14.13a [76]

Therefore only one complete crack with all of its branched cracks is plotted in the a–N and $\mathrm{d}a/\mathrm{d}N$–ΔK plots.

The a–N plot initially shows two main a–N curves, cf. Fig. 14.14a. The uniaxially loaded specimen »uni« appears to grow faster than the equibiaxially loaded specimen »equi«. However, the $\mathrm{d}a/\mathrm{d}N$–ΔK plot clearly shows that crack growth occured at almost the same rate $\mathrm{d}a/\mathrm{d}N$ at the same cyclic stress intensity ΔK_{eq}. The differences in the course of the a–N curve can be found in the specimen thickness and the various load situations, i.e. the equivalent stress intensity ranges were different for the same crack lengths, cf. [76]. The crack growth rate of the specimen »equi« was checked by measuring the fatigue striations in the captured SEM image, cf. Fig. 14.12c. The mean value of 10 load cycles was an increase of the crack length of $\Delta a \approx 1.5\,\mu\mathrm{m}$ per load cycle. This is consistent with the measurement and calculation of the crack growth rate $\mathrm{d}a/\mathrm{d}N$ using crack gage and the Fractomat, cf. Fig. 14.14c grey dots at $\Delta K_{\mathrm{eq}} \approx 70\,\mathrm{MPa}\sqrt{\mathrm{m}}$ with $\mathrm{d}a/\mathrm{d}N = 1.5 \times 10^{-3}$ mm per load cycle. By means of the $\mathrm{d}a/\mathrm{d}N$–ΔK course of the uniaxially and equibiaxially loaded specimens »uni« and »equi«, the Paris law was set up, cf. Fig. 14.14c, black dotted line. Thus a comparison

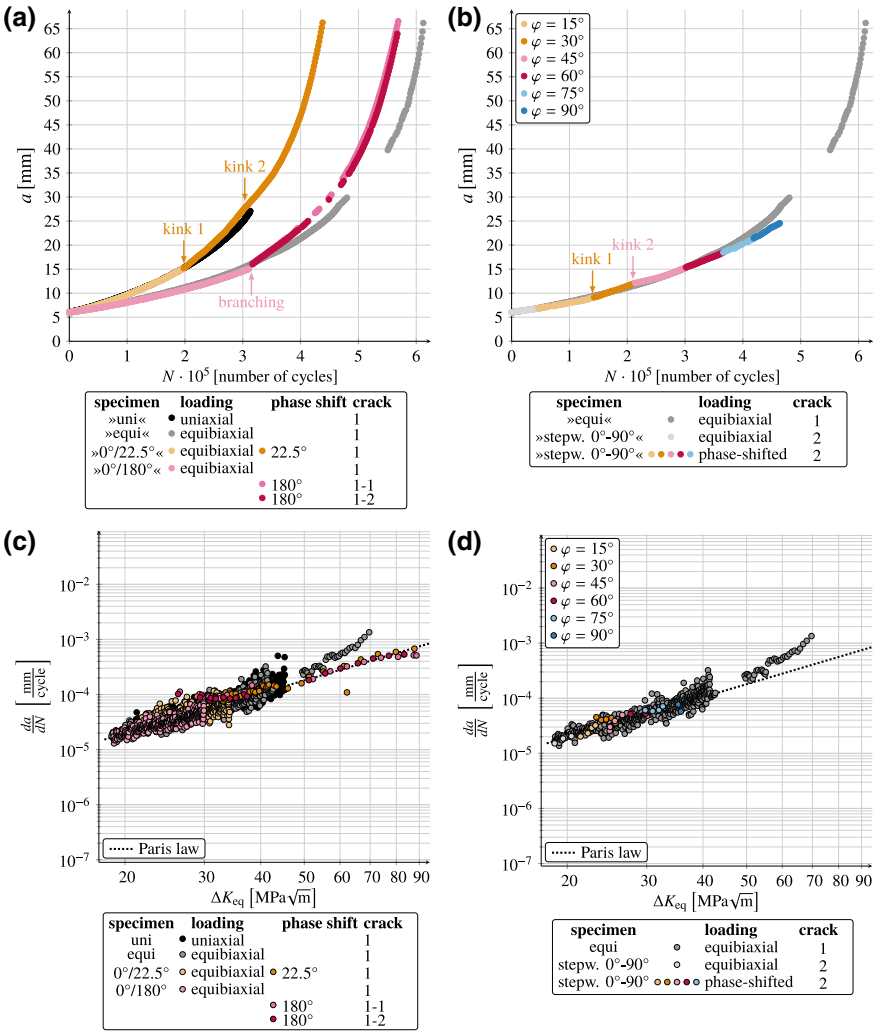

Fig. 14.14 Results of the fatigue crack growth experiments [76, 77]. a–N plots of specimens **a** »uni«, »equi«, »0°/22.5°« and »0°/180°« and **b** »stepw. 0°–90°« with representation of the phase shift φ compared to the equibiaxially loaded specimen »equi«. $\mathrm{d}a/\mathrm{d}N - \Delta K$ plots of specimens **c** »uni«, »equi«, »0°/22.5°« and »0°/180°« and **d** »stepw. 0°–90°« with representation of the phase shift φ compared to the equibiaxially loaded specimen »equi« [76, 77]

of the crack growth rates da/dN under phase-shifted loading is possible with uniaxial or rather equibiaxial loading.

Specimen »0°/22.5°« was first equibiaxially loaded and afterwards loaded with a phase shift of $\varphi = 22.5°$. The equibiaxially loaded crack of the specimen »0°/22.5°« followed the course of the uniaxially loaded specimen »uni« in the a–N plot, cf. Fig. 14.14a. The comparison of the crack growth rate da/dN versus the cyclic stress intensity factor ΔK reveals, that the crack growth rate was similar to the crack growth rate of the equibiaxially loaded specimen »equi«, cf. Fig. 14.14c. It has to be noted, that a thickness correction had to be carried out for calculation of ΔK, cf. [76]. Natural scattering in crack growth, as reported in [109], which is e.g. caused by inhomogeneities [110] can be excluded in the PM material.

The course of the a–N plot of the specimen »0°/22.5°« shows two kinks, cf. Fig. 14.14a, orange dots. The first kink occured after changing from in-phase to out-of-phase loading. This change led to a change in the crack opening Mode. As long as the crack was loaded equibiaxially, it was pure Mode I crack opening. As soon as the crack was loaded with phase shift, a Mixed Mode crack opening occurred. The kink in the a–N plot correlates with the start of the kinking of the crack path, cf. Fig. 14.11c. The second kink in the a–N plot occurred at the end of the kinking of the crack path, i.e. when no further curvature occured. The first kink in the a–N plot provided a faster fatigue crack growth rate and the second kink provided a slower fatigue crack growth rate. The reason for the faster crack growth was the Mode II portion of crack opening or rather the cyclic stress intensity factor ΔK_{eq}. This is in accordance to the findings of [48], that Mode II loaded cracks grow faster than Mode I loaded cracks.

Specimen »0°/180°« was first equibiaxially loaded and afterwards loaded with a phase shift of $\varphi = 180°$. As long as the crack was equibiaxially loaded, the course of the a–N plot of the specimen »0°/180°« is identical to the a–N course of the equibiaxially loaded specimen »equi«, cf. Fig. 14.14a, because both specimens had an almost identical thickness and were subjected to the same loading. Thus, the crack growth rates were almost equal for equibiaxial loading, cf. Fig. 14.14c. The subsequent change from in-phase loading to out-of-phase loading of specimen »0°/180°« with a phase shift of $\varphi = 180°$ led to a branching of the crack into two cracks. The two branched cracks seem to grew faster if one compares the a–N curves of both cracks with the a–N curves of the equibiaxially loaded specimen »equi«, cf. Fig. 14.14a. A comparison of the crack growth rates of the branched cracks with Paris' law line shows that first an accelerated fatigue crack growth took place in the two branched cracks, cf. Fig. 14.14c, red dots. After a certain crack growth, the crack growth rate followed Paris' law. The initially accelerated crack growth was due to the Mixed Mode loading. The decrease of the Mode II portion with increasing crack length at the two branched cracks led to the fact that the crack growth finally took place again under Mode I crack opening and the crack growth rate followed Paris' law. This is consistent with the findings by Wang et al. [48] who have found that Mode II loaded cracks grow faster than Mode I loaded cracks. The reduction of the Mode II fraction in the crack growth can be verified by FE calculations and SEM images. The crack growth rate measured with a scanner camera and then calculated could

also be validated with SEM images. At a crack length of about 60 mm, an average increase of the crack length of $\Delta a \approx 0.7\,\mu m$ per load cycle was measured as an average of 10 fatigue striations, cf. Fig. 14.12d. This is in accordance with the calculated crack growth rates, cf. Fig. 14.14c red dots at $\Delta K_{eq} \approx 80\,MPa\sqrt{m}$ with $da/dN = 0.7 \cdot 10^{-3}$ mm per load cycle.

Specimen »stepw. 0°–90°« was first equibiaxially loaded and afterwards phase-shifted loaded with a subsequent increase of the phase shift. As long as the crack was equibiaxially loaded, the course of the a–N plot of the specimen »stepw. 0°–90°« equals the a–N course of the equibiaxially loaded specimen »equi«, cf. Fig. 14.14b, because both specimens had an almost identical thickness and were subjected to the same loading. Furthermore, the crack growth rates were almost equal for equibiaxial loading, cf. Fig. 14.14d. In addition to the kinks in the crack path caused by the change in the phase shift φ, cf. Fig. 14.11e, f, kinks in the a–N curve can also be observed, cf. Fig. 14.14b. Analogous to the crack path, a kink in the a–N curve occured at the change from a phase-shifted loading of $\varphi = 15°$ to a phase-shifted loading of $\varphi = 30°$, cf. Fig. 14.14b. As with specimen »0°/22.5°«, the accelerated crack growth can be explained by Mode II contribution. The Mode II portion on the fatigue crack growth can also be seen on the fractured surface, where face friction is clearly visible, cf. Fig. 14.13d. In addition to the increased crack growth rate, the change of the phase shift φ reduced the cyclic equivalent crack intensity factor ΔK_{eq}, cf. Fig. 14.14d. The second kink occured when the phase shift was changed from $\varphi = 30°$ to $\varphi = 45°$. Initially, a slightly slower fatigue crack growth for the $\varphi = 45°$ loaded crack was observed, cf. Fig. 14.14d. Subsequently, the fatigue crack growth followed Paris' law.

14.6 Conclusions

The material behavior of a powder metallurgically produced high alloy X5CrMnNi16-7-6 austenitic stainless steel was investigated under both quasi-static and cyclic loading for low cycle fatigue and fatigue crack growth. The following results were achieved in quasi-static tests:

- The yield surface can be described by von Mises criterion.
- Sequence tests with permanently changing λ showed load sequence effects, i.e. a kinematic hardening with α'-martensite formation was observed.
- The highest martensite volume fraction was measured for shear loading.

The following results were achieved in low cycle fatigue tests:

- The fatigue life of low cycle fatigue tests can be divided into three stages: (i) primary hardening, (ii) softening and (iii) secondary hardening as observed for uniaxial tests by [7, 31, 32].

- The lowest fatigue lives were determined for loads with strain ratio of $\Phi = -0.5$, -0.1 and 0.5, the highest fatigue lives were determined for shear loading $\Phi = -1$.
- During secondary hardening, the von Mises force amplitude $F_{vM}/2$ increased.
- The larger the von Mises strain amplitude increased, the more α'-martensite was formed.
- The highest amount of α'-martensite was induced and the highest numbers of cycles to failure occurred for shear loading.
- Deviations of equivalent force amplitudes and fatigue lives can also be interpreted that the von Mises hypothesis cannot be applied in the case of multiaxial elastic-plastic cyclic loading.

The following results were achieved in fatigue crack growth investigations:

- The crack paths of the two single cracks of each specimen or in the further course the four branched cracks of specimen »0°/180°« revealed a symmetrical course.
- Differences in the a–N curves were due to differences in the specimens thickness and different load cases, respectively.
- The calculation of the cyclic stress intensity factor was based on the proposed geometry functions. This made a simple comparison with kinked or branched cracks under phase-shifted loading possible.
- It became clear that phase shift loaded cracks initially grew at an accelerated crack growth rate under Mode II crack opening. By kinking or branching, the Mode II proportion of the crack tip loading decreased in the further course and the crack growth rate followed the Paris' law.

Acknowledgements The authors thank and acknowledge gratefully funding of subproject B4 within Collaborative Research Center TRIP-Matrix-Composites (Project number 54473466—CRC 799) by the German Research Foundation or Deutsche Forschungsgemeinschaft (DFG). Further thanks go to Dipl.-Ing. Kai Nagel, Dr.-Ing. Dirk Kulawinski and Dipl.-Ing. Stephanie Ackermann, who were involved in the experiments. In particular, the authors want to thank the colleagues of the Collaborative Research Center for their support and cooperation.

References

1. S. Henkel, D. Kulawinski, S. Ackermann, H. Biermann, in *Moderne Methoden der Werkstoffprüfung* (Wiley-VCH, 2015), pp. 121–157. https://doi.org/10.1002/9783527670673.ch4
2. L. Krüger, S. Wolf, U. Martin, S. Martin, P.R. Scheller, A. Jahn, A. Weiß, J. Phys. Conf. Ser. **240**, 012098 (2010). https://doi.org/10.1088/1742-6596/240/1/012098
3. A. Jahn, A. Kovalev, A. Weiß, S. Wolf, L. Krüger, P.R. Scheller, Steel Res. Int. **82**(1), 39 (2010). https://doi.org/10.1002/srin.201000228
4. S. Martin, C. Ullrich, D. Šimek, U. Martin, D. Rafaja, J. Appl. Crystallogr. **44**(4), 779 (2011). https://doi.org/10.1107/s0021889811019558
5. A. Weidner, A. Glage, H. Biermann, Procedia Eng. **2**(1), 1961 (2010). https://doi.org/10.1016/j.proeng.2010.03.211
6. A. Weidner, S. Martin, V. Klemm, U. Martin, H. Biermann, Scr. Mater. **64**(6), 513 (2011). https://doi.org/10.1016/j.scriptamat.2010.11.028

7. M. Bayerlein, H.J. Christ, H. Mughrabi, Mater. Sci. Eng. A **114**, L11 (1989). https://doi.org/10.1016/0921-5093(89)90871-x
8. D. Hennessy, G. Steckel, C. Altstetter, Metall. Trans. A **7**(3), 415 (1976). https://doi.org/10.1007/bf02642838
9. A. Hannon, P. Tiernan, J. Mater. Process. Technol. **198**(1–3), 1 (2008). https://doi.org/10.1016/j.jmatprotec.2007.10.015
10. J.P. Boehler, S. Demmerle, S. Koss, Exp. Mech. **34**(1), 1 (1994). https://doi.org/10.1007/bf02328435
11. C.H. Busche, *Bestimmung und Beschreibung des Elastizitätsmoduls von Blechwerkstoffen nach dem Umformen* (Shaker Verlag, 2007)
12. S. Demmerle, J. Boehler, J. Mech. Phys. Solids **41**(1), 143 (1993). https://doi.org/10.1016/0022-5096(93)90067-p
13. V. Bonnand, J. Chaboche, P. Gomez, P. Kanouté, D. Pacou, Int. J. Fatigue **33**(8), 1006 (2011). https://doi.org/10.1016/j.ijfatigue.2010.12.018
14. M.W. Brown, K.J. Miller, Proc. Inst. Mech. Eng. **187**(1), 745 (1973). https://doi.org/10.1243/pime_proc_1973_187_161_02
15. M. Parsons, K. Pascoe, Mater. Sci. Eng. **22**, 31 (1976). https://doi.org/10.1016/0025-5416(76)90133-6
16. T. Ogata, Y. Takahashi, in *Multiaxial Fatigue and Fracture* (Elsevier, 1999), pp. 101–114. https://doi.org/10.1016/s1566-1369(99)80010-7
17. S. Henkel, J. Fischer, L. Balogh, T. Ungar, H. Biermann, J. Phys. Conf. Ser. **240**, 012042 (2010). https://doi.org/10.1088/1742-6596/240/1/012042
18. S. Ackermann, D. Kulawinski, S. Henkel, H. Biermann, Int. J. Fatigue **67**, 123 (2014). https://doi.org/10.1016/j.ijfatigue.2014.02.007
19. T. Itoh, M. Sakane, M. Ohnami, J. Eng. Mater. Technol. **116**(1), 90 (1994). https://doi.org/10.1115/1.2904261
20. K.J. Pascoe, J.W.R. de Villiers, J. Strain Anal. **2**(2), 117 (1967). https://doi.org/10.1243/03093247v022117
21. T. Yokobori, H. Yamanouchi, S. Yamamoto, Int. J. Fract. Mech. **1**(1), 3 (1965). https://doi.org/10.1007/bf00184149
22. V. Doquet, Fatigue Fract. Eng. Mater. Struct. **20**(2), 227 (1997). https://doi.org/10.1111/j.1460-2695.1997.tb00280.x
23. D. Kulawinski, S. Ackermann, A. Glage, S. Henkel, H. Biermann, Steel Res. Int. **82**(9), 1141 (2011). https://doi.org/10.1002/srin.201100111
24. B.R. You, S.B. Lee, Int. J. Fatigue **18**(4), 235 (1996). https://doi.org/10.1016/0142-1123(96)00002-3
25. E. Macha, C.M. Sonsino, Fatigue Fract. Eng. Mater. Struct. **22**(12), 1053 (1999). https://doi.org/10.1046/j.1460-2695.1999.00220.x
26. M.W. Brown, K.J. Miller, Fatigue Fract. Eng. Mater. Struct. **1**(2), 231 (1979). https://doi.org/10.1111/j.1460-2695.1979.tb00380.x
27. R. Lohr, E.G. Ellison, Fatigue Fract. Eng. Mater. Struct. **3**(1), 1 (1980). https://doi.org/10.1111/j.1460-2695.1980.tb01101.x
28. T. Itoh, M. Sakane, M. Ohnami, D.F. Socie, J. Eng. Mater. Technol. **117**(3), 285 (1995). https://doi.org/10.1115/1.2804541
29. A. Fatemi, D.F. Socie, Fatigue Fract. Eng. Mater. Struct. **11**(3), 149 (1988). https://doi.org/10.1111/j.1460-2695.1988.tb01169.x
30. A. Glage, A. Weidner, H. Biermann, Proc. Eng. **2**(1), 2085 (2010). https://doi.org/10.1016/j.proeng.2010.03.224
31. A. Glage, A. Weidner, H. Biermann, Steel Res. Int. **82**(9), 1040 (2011). https://doi.org/10.1002/srin.201100080
32. U. Krupp, C. West, H.J. Christ, Mater. Sci. Eng. A **481–482**, 713 (2008). https://doi.org/10.1016/j.msea.2006.12.211
33. M. Smaga, F. Walther, D. Eifler, Mater. Sci. Eng. A **483–484**, 394 (2008). https://doi.org/10.1016/j.msea.2006.09.140

34. A. Burgold, S. Henkel, S. Roth, M. Kuna, H. Biermann, Mater. Test. **60**(4), 341 (2018). https://doi.org/10.3139/120.111156
35. D.F. Martelo, A.M. Mateo, M.D. Chapetti, Int. J. Fatigue **80**, 406 (2015). https://doi.org/10.1016/j.ijfatigue.2015.06.029
36. H.J. Lim, Y.J. Lee, H. Sohn, Mech. Syst. Sig. Process. **120**, 356 (2019). https://doi.org/10.1016/j.ymssp.2018.10.018
37. O. Scott-Emuakpor, T. George, C. Cross, M.H.H. Shen, AIAA J. **48**(1), 63 (2010). https://doi.org/10.2514/1.39296
38. P.R.G. Anderson, G.G. Garrett, Int. J. Fract. **16**(3), R111 (1980). https://doi.org/10.1007/bf00013388
39. C.D. Hopper, K.J. Miller, J. Strain Anal. Eng. Des. **12**(1), 23 (1977). https://doi.org/10.1243/03093247v121023
40. S. Henkel, C.H. Wolf, A. Burgold, M. Kuna, H. Biermann, Fract. Struct. Int. **13**, 135 (2019). https://doi.org/10.3221/igf-esis.48.16
41. E. Breitbarth, M. Besel, S. Reh, Int. J. Fatigue **108**, 116 (2018). https://doi.org/10.1016/j.ijfatigue.2017.12.005
42. E. Breitbarth, M. Besel, Int. J. Fatigue **113**, 345 (2018). https://doi.org/10.1016/j.ijfatigue.2018.04.021
43. G. Dhondt, C. Kontermann, *Proceedings of 6th International Conference Crack Paths (CP 2018). Conference USB flash drive* (Verona (I), 2018)
44. V. Giannella, G. Dhondt, C. Kontermann, R. Citarella, Int. J. Fatigue **123**, 296 (2019). https://doi.org/10.1016/j.ijfatigue.2019.02.029
45. C.F. Qian, M.O. Wang, B.J. Wu, S.H. Dai, J.C.M. Li, J. Eng. Mater. Technol. **118**(3), 349 (1996). https://doi.org/10.1115/1.2806817
46. C.F. Qian, M.O. Wang, B.J. Wu, S.H. Dai, J.C.M. Li, J. Eng. Mater. Technol. **118**(3), 356 (1996). https://doi.org/10.1115/1.2806818
47. S. Mall, V. Perel, Int. J. Fatigue **74**, 166 (2015). https://doi.org/10.1016/j.ijfatigue.2015.01.005
48. M.O. Wang, R.H. Hu, C.F. Qian, J.C.M. Li, Fatigue Fract. Eng. Mater. Struct. **18**(12), 1443 (1995). https://doi.org/10.1111/j.1460-2695.1995.tb00867.x
49. R.K. Neerukatti, S. Datta, A. Chattopadhyay, N. Iyyer, N. Phan, Fatigue Fract. Eng. Mater. Struct. **41**(2), 387 (2017). https://doi.org/10.1111/ffe.12690
50. E.U. Lee, R.E. Taylor, Eng. Fract. Mech. **78**(8), 1555 (2011). https://doi.org/10.1016/j.engfracmech.2010.11.005
51. R. Yuuki, K. Akita, N. Kishi, Fatigue Fract. Eng. Mater. Struct. **12**(2), 93 (1989). https://doi.org/10.1111/j.1460-2695.1989.tb00516.x
52. H. Kitagawa, R. Yuuki, K. Tohgo, Fatigue Fract. Eng. Mater. Struct. **2**(2), 195 (1979). https://doi.org/10.1111/j.1460-2695.1979.tb01355.x
53. Z. Zhu, Z. Lu, P. Zhang, W. Fu, C. Zhou, X. He, Met. **9**(8), 823 (2019). https://doi.org/10.3390/met9080823
54. V. Shlyannikov, A. Zakharov, Eng. Fract. Mech. **123**, 86 (2014). https://doi.org/10.1016/j.engfracmech.2014.02.013
55. H.E. Misak, V.Y. Perel, V. Sabelkin, S. Mall, Int. J. Fatigue **55**, 158 (2013). https://doi.org/10.1016/j.ijfatigue.2013.06.003
56. V. Shlyannikov, A. Tumanov, A. Zakharov, Theor. Appl. Fract. Mech. **73**, 68 (2014). https://doi.org/10.1016/j.tafmec.2014.06.016
57. M. Lepore, F. Berto, D. Kujawski, Theor. Appl. Fract. Mech. **100**, 14 (2019). https://doi.org/10.1016/j.tafmec.2018.12.008
58. A. Shanyavskiy, Eng. Fract. Mech. **78**(8), 1516 (2011). https://doi.org/10.1016/j.engfracmech.2011.01.019
59. V. Shlyannikov, A. Zakharov, Theor. Appl. Fract. Mech. **91**, 52 (2017). https://doi.org/10.1016/j.tafmec.2017.03.014
60. C. Dalle Donne, K.H. Trautmann, H. Amstutz, in *Multiaxial Fatigue and Deformation: Testing and Prediction* (ASTM International, 2000), pp. 405–422. https://doi.org/10.1520/stp13517s

61. R. Sunder, B. Ilchenko, Int. J. Fatigue **33**(8), 1101 (2011). https://doi.org/10.1016/j.ijfatigue.2010.11.018
62. C.D. Donne, *Übertragbarkeit von Risswiderstandskurven von Standardproben auf biaxial belastete, bauteilähnliche Kreuzproben* (VDI Verlag, 1997)
63. A. Makinde, L. Thibodeau, K.W. Neale, Exp. Mech. **32**(2), 138 (1992). https://doi.org/10.1007/bf02324725
64. I.H. Wilson, D.J. White, J. Strain Anal. **6**(1), 27 (1971). https://doi.org/10.1243/03093247v061027
65. S. Taira, K. Tanaka, M. Kan, A. Yamada, Proc. 22nd Japan Cong. Mat. Res. pp. 130–137 (1979)
66. T. Hoshide, K. Tanaka, A. Yamada, Fatigue Fract. Eng. Mater. Struct. **4**(4), 355 (1981). https://doi.org/10.1111/j.1460-2695.1981.tb01132.x
67. K. Tanaka, T. Hoshide, A. Yamada, S. Taira, Fatigue Fract. Eng. Mater. Struct. **2**(2), 181 (1979). https://doi.org/10.1111/j.1460-2695.1979.tb01354.x
68. P. Bold, M. Brown, R. Allen, Wear **144**(1–2), 307 (1991). https://doi.org/10.1016/0043-1648(91)90022-m
69. M.W. Brown, K.J. Miller, in *Multiaxial Fatigue* (ASTM International, 1985), pp. 135–153. https://doi.org/10.1520/stp36221s
70. S. Datta, A. Chattopadhyay, N. Iyyer, N. Phan, Int. J. Fatigue **109**, 103 (2018). https://doi.org/10.1016/j.ijfatigue.2017.12.018
71. S. Henkel, D. Holländer, M. Wünsche, H. Theilig, P. Hübner, H. Biermann, S. Mehringer, Eng. Fract. Mech. **77**(11), 2077 (2010). https://doi.org/10.1016/j.engfracmech.2010.04.013
72. V.N. Shlyannikov, Eng. Fract. Mech. **108**, 3 (2013). https://doi.org/10.1016/j.engfracmech.2013.03.011
73. H. Theilig, D. Hartmann, M. Wünsche, S. Henkel, P. Hübner, Key Eng. Mater. **348–349**, 857 (2007). https://doi.org/10.4028/www.scientific.net/kem.348-349.857
74. A.C. Pickard, J. Strain Anal. Eng. Des. **50**(1), 25 (2014). https://doi.org/10.1177/0309324714551082
75. S. Henkel, E. Liebelt, H. Biermann, S. Ackermann, Fract. Struct. Int. **9**(34), 466 (2015). https://doi.org/10.3221/IGF-ESIS.34.52
76. C.H. Wolf, S. Henkel, A. Burgold, Y. Qiu, M. Kuna, H. Biermann, Adv. Eng. Mater. **21**(5), 1800861 (2018). https://doi.org/10.1002/adem.201800861
77. C.H. Wolf, S. Henkel, A. Burgold, Y. Qiu, M. Kuna, H. Biermann, Int. J. Fatigue **124**, 595 (2019). https://doi.org/10.1016/j.ijfatigue.2019.03.011
78. S. Xiao, M. Brown, in *Mechanical Behaviour of Materials V* (Elsevier, 1988), pp. 659–664. https://doi.org/10.1016/b978-0-08-034912-1.50089-8
79. M.. Wang, R.H. Hu, C.J. Zhang, S.H. Dai, in *Proceedings of the 7th International Conference on Pressure Vessel Technology*, vol. 2 (VdTÜV, 1992), pp. 1413–1427
80. J.J. Kibler, R. Roberts, J. Eng. Ind. **92**(4), 727 (1970). https://doi.org/10.1115/1.3427838
81. E. önch, D. Galster, Br. J. Appl. Phys. **14**(11), 810 (1963). https://doi.org/10.1088/0508-3443/14/11/319
82. J. Granlund, Structural steel plasticity: experimental study and theoretical modelling. Ph.D. thesis, Lulea University of Technology, 1997
83. J. Gozzi, Plastic behaviour of steel: Experimental investigation and modelling. Ph.D. thesis, Lulea University of Technology, 2004
84. J. Gozzi, A. Olsson, O. Lagerqvist, Exp. Mech. **45**(6), 533 (2005). https://doi.org/10.1007/bf02427907
85. D. Kulawinski, S. Ackermann, A. Seupel, T. Lippmann, S. Henkel, M. Kuna, A. Weidner, H. Biermann, Mater. Sci. Eng. A **642**, 317 (2015). https://doi.org/10.1016/j.msea.2015.06.083
86. M. Kuroda, V. Tvergaard, Acta Mater. **47**(14), 3879 (1999). https://doi.org/10.1016/s1359-6454(99)00213-x
87. D. Kulawinski, K. Nagel, S. Henkel, P. Hübner, H. Fischer, M. Kuna, H. Biermann, Eng. Fract. Mech. **78**(8), 1684 (2011). https://doi.org/10.1016/j.engfracmech.2011.02.021

88. A. Samir, A. Simon, A. Scholz, C. Berger, Int. J. Fatigue **28**(5–6), 643 (2006). https://doi.org/10.1016/j.ijfatigue.2005.08.010
89. C.M. Sonsino, V. Grubisic, Materialwiss. Werkstofftech. **15**(11), 378 (1984). https://doi.org/10.1002/mawe.19840151104
90. A.A. Griffith, *Proceedings of the 1st International Congress for Applied Mechanics* (Delft, 1924), pp. 55–63
91. C.H. Wolf, A. Burgold, S. Henkel, M. Kuna, H. Biermann, *Proceedings of 12th International Conference on Multiaxial Fatigue and Fracture* (2019) (In press)
92. A. Savitzky, M.J.E. Golay, Anal. Chem. **36**(8), 1627 (1964). https://doi.org/10.1021/ac60214a047
93. ASTM E647-15e1, Standard test method for measurement of fatigue crack growth rates. Technical Report (ASTM International, West Conshohocken, PA, 2015)
94. S. Ackermann, T. Lippmann, D. Kulawinski, S. Henkel, H. Biermann, Fract. Struct. Int. (34), 580 (2015). https://doi.org/10.3221/IGF-ESIS.34.64
95. J. Talonen, P. Aspegren, H. Hänninen, Mater. Sci. Technol. **20**(12), 1506 (2004). https://doi.org/10.1179/026708304x4367
96. D. Mohr, M. Oswald, Exp. Mech. **48**(1), 65 (2007). https://doi.org/10.1007/s11340-007-9053-9
97. D. Mohr, J. Jacquemi, J. Mech. Phys. Solids **56**(10), 2935 (2008). https://doi.org/10.1016/j.jmps.2008.07.003
98. A. Olsson, Stainless steel plasticity: material modelling and structural applications. Ph.D. thesis, Lulea University of Technology, 2001
99. S. Martin, S. Wolf, U. Martin, L. Krüger, Solid State Phenom. **172–174**, 172 (2011). https://doi.org/10.4028/www.scientific.net/ssp.172-174.172
100. A. Weidner, C. Segel, H. Biermann, Mater. Lett. **143**, 155 (2015). https://doi.org/10.1016/j.matlet.2014.12.098
101. G.B. Olson, M. Cohen, Metall. Trans. A **6**(4), 791 (1975). https://doi.org/10.1007/bf02672301
102. A. Nitta, T. Ogata, K. Kuwabara, Fatigue Fract. Eng. Mater. Struct. **12**(2), 77 (1989). https://doi.org/10.1111/j.1460-2695.1989.tb00515.x
103. D. Infante-Garcia, G. Qian, H. Miguélez, E. Giner, Int. J. Fatigue **123**, 87 (2019). https://doi.org/10.1016/j.ijfatigue.2019.01.019
104. M. Kuna, *Finite Elements in Fracture Mechanics* (Springer, Netherlands, 2013). https://doi.org/10.1007/978-94-007-6680-8
105. F. Erdogan, G.C. Sih, J. Basic Eng. **85**(4), 519 (1963). https://doi.org/10.1115/1.3656897
106. L. Pook, Eng. Fract. Mech. **167**, 2 (2016). https://doi.org/10.1016/j.engfracmech.2016.02.055
107. H. Richard, A. Eberlein, G. Kullmer, Eng. Fract. Mech. **174**, 10 (2017). https://doi.org/10.1016/j.engfracmech.2016.12.005
108. R. Brighenti, A. Carpinteri, A. Spagnoli, Acta Mech. **225**(11), 3123 (2014). https://doi.org/10.1007/s00707-014-1111-7
109. C. Lapetra, J. Mayo, J. Dominguez, Fatigue Fract. Eng. Mater. Struct. **19**(5), 589 (1996)
110. D.A. Virkler, B.M. Hillberry, P.K. Goel, J. Eng. Mater. Technol. **101**(2), 148 (1979). https://doi.org/10.1115/1.3443666

Chapter 15
Scanning Electron Microscopy and Complementary In Situ Characterization Techniques for Characterization of Deformation and Damage Processes

Anja Weidner, Robert Lehnert and Horst Biermann

Abstract This chapter presents results on in situ deformation experiments performed either inside the scanning electron microscope or in combination with other complementary in situ characterization techniques such as digital image correlation, acoustic emission or infrared thermography. The range of materials investigated extends from austenitic CrMnNi steels enabling TRIP (TRansformation Induced Plasticity) and/or TWIP (TWinning Induced Plasticity) effect and austenitic-martensitic-carbidic CrMnNi steels after quenching and partitioning to MgO-partially stabilized zirconia and TRIP matrix composites. The performed mechanical tests include both tensile and compressive loading as well as cyclic loading in a temperature range from room temperature up to 200 °C. The great potential of the applied in situ characterization techniques is their complementarity, which is shown, in particular, by the seven case studies presented. The combination of different techniques—such as the in situ deformation within the SEM combined with the digital image correlation—has a high potential to gain a deeper understanding on strain localizations by different microstructural features such as deformation bands, twin bundles or martensitic nuclei. In addition, these complementary in situ techniques can contribute to the modelling of the deformation behavior of TRIP/TWIP steels, in particular, or for any other kind of materials with complex deformation processes. Here, the acoustic emission measurements offer, in particular, a great potential, since this is the only real time in situ characterization technique delivering bulk information with a time-resolution in the range of microseconds.

A. Weidner (✉) · R. Lehnert · H. Biermann
Institute of Materials Engineering, Technische Universität Bergakademie Freiberg, Gustav-Zeuner-Str. 5, 09599 Freiberg, Germany
e-mail: weidner@ww.tu-freiberg.de

H. Biermann and C. G. Aneziris (eds.), *Austenitic TRIP/TWIP Steels and Steel-Zirconia Composites*, Springer Series in Materials Science 298,
https://doi.org/10.1007/978-3-030-42603-3_15

15.1 Introduction

Advanced High-Strength Steels (AHSS) have been the focus of automotive industry due to their improved formability and crash behavior. The TRIP (TRansformation Induced Plasticity)-assisted steels based on retained austenite belonging to the group of AHSS of the first generation exhibit high strength, but quite low ductility. In contrast, the group of high-alloy austenitic steels with displacive transformations—TRIP and TWIP (TWinning Induced Plasticity) steels—belonging to the AHSS of the second generation exhibits high tensile strengths between 500 to 900 MPa at concurrently excellent levels of ductility (between 40 and 70% of total elongation) [1].

High-alloy austenitic TRIP steels exhibit a phase transformation following the austenite (fcc)—ε-martensite (hcp)—α'-martensite (bcc) path. Olson and Cohen [2] described this two-step shear mechanism for the first time in 1972. The phase transformation occurs via the interaction of Shockley partial dislocations on two different slip systems. During the deformation of high-alloy austenitic TRIP steels, deformation bands are formed consisting of a high density of stacking faults arranged in average on each second {111} lattice plane of the austenite. Therefore, these deformation bands appear with a hexagonal lattice structure—referred in the literature as ε-martensite [3–5]. In contrast to TRIP steels, the high-alloy TWIP steels exhibit a pronounced twinning leading to even superior ductility. Twinning occurs via the accumulation of stacking faults on subsequent {111} lattice planes [5].

The chemical concept of the present high-alloy CrMnNi TRIP/TWIP steels is based on a low content of interstitial elements carbon and nitrogen, a high amount of chromium, manganese and nickel [6]. In particular, the variation of the nickel content allows to control both the austenite stability as well as the stacking fault energy. Therefore, the metastable austenitic steels can exhibit either a TRIP or TWIP effect or a combination of both, depending on the nickel content or the deformation temperature [7, 8].

During the last decade, numerous investigations have been performed on high-alloy CrMnNi cast steels regarding to both their mechanical behavior under different loading conditions as well as the corresponding microstructures and the related strain hardening mechanisms. Thus, CrMnNi steels were tested under (i) static [7], (ii) cyclic [9], (iii) biaxial [10], (iv) dynamic [11], and (v) hydrostatic high-pressure conditions [12]. Detailed microstructural investigations using different techniques such as (i) X-ray diffraction [13], (ii) scanning electron microscopy [14], and (iii) conventional as well as high-resolution transmission electron microscopy (HR-TEM) [5, 15] gained a deeper understanding and knowledge of the ongoing microstructural processes and their influence on the mechanical properties. In addition, these results were complemented by investigations on wrought steels [16] and powder-metallurgically produced steels [17] within the same alloying concept.

Since high-alloy CrMnNi cast TRIP steels are usually characterized by a low yield strength due to their coarse-grained microstructure, two approaches were considered to improve the yield strength: (i) manufacture of ultrafine grained (ufg) CrMnNi

TRIP steels [18], and (ii) application of quenching and partitioning (Q&P) process to slightly modified chemical design of the CrMnNi TRIP steels [19]. For the first approach, a thermo-mechanical-controlled process consisting of cold working and subsequent reversion annealing treatment was applied leading to grain sizes of less than 1 μm resulting in significant increase in yield strength at still reasonable ductility [18]. Furthermore, the fatigue life has been also improved for ufg TRIP steels at low strain amplitudes [20]. The aim of the Q&P treatment was a two-phase microstructure consisting of austenite and tempered martensite in order to achieve an increase in strength with only a slight reduction in ductility [19].

In addition, the studied CrMnNi steels were used for metal matrix composites (MMC) together with metastable zirconium dioxide as particle reinforcement. Partially MgO-stabilized zirconium dioxide exhibits a stress-assisted phase transformation from tetragonal into monoclinic phase. The combination of phase transformations in steel matrix and zirconia particles results in an increase in the capacity of absorption of mechanical energy [21].

The microstructure associated with TRIP and TWIP effects in the high-alloy CrMnNi cast steels is rather complex, and depends, in addition, on various parameters such as temperature, strain rate, grain size and grain orientation [22]. In order to understand the resulting strengthening behavior of TRIP/TWIP steels caused by this complex microstructure, it is necessary to gain a deeper knowledge of both: (i) local contribution of individual microstructural constituents to global deformation and strengthening behavior as well as (ii) evolution of underlying microstructural processes such as (i) dislocation glide, (ii) formation of stacking faults, (iii) twinning, and (iv) martensitic phase transformation operating often simultaneously during straining of material.

Therefore, in situ deformation experiments in combination with further characterization techniques are an excellent and powerful method for investigation of these aspects. The field of in situ experiments offers a broad spectrum of different methods such as (i) optical microscopy, (ii) SEM analysis, (iii) full-field measurements using digital image correlation (DIC) and infrared thermography (IR-TG), (iv) acoustic emission measurements (AE), and, finally, (v) fully-coupled, full-field measurements. Besides the fact that all these methods possess their respective advantages and disadvantages, their complementary application in combination with other post-mortem investigations provides great potential for the investigation of complex correlations.

This chapter cannot address all the above-mentioned techniques and results in detail. Therefore, it is focused on (i) in situ deformation in the scanning electron microscope in combination with digital image correlation, (ii) in situ acoustic emission measurements, (iii) thermographic measurements, and (iv) nanoindentation experiments inside SEM. In the first part of the chapter an overview on the used in situ characterization techniques is given combined with some selected state-of-the-art results. The second part describes in more detail the investigated materials: (i) high-alloy CrMnNi TRIP/TWIP steels, (ii) austenitic-martensitic-carbidic (AMC) steels after Q&P treatment, (iii) partially MgO-stabilized zirconia, and (iv) metal-matrix composite (MMC). Finally, the third part provides results on some case studies

on the above-mentioned materials using different types of in situ techniques such as (i) in situ SEM-DIC, (ii) acoustic emission, (iii) thermography, and (iv) nanoindentation.

15.2 In Situ Characterization Techniques

15.2.1 In Situ Deformation in Scanning Electron Microscope

In situ deformation in the scanning electron microscope (SEM) offers the possibility to observe deformation and damage mechanisms occurring under different loading conditions with high local resolution. In addition to direct imaging methods using secondary electrons (SE) or backscattered electrons (BSE), analytical methods such as energy dispersive X-ray spectroscopy (EDS), wavelength dispersive X-ray spectroscopy (WDS) or electron backscatter diffraction (EBSD) can be used to obtain a detailed knowledge on the deformation and damage behavior. Already in the 1970s, deformation experiments were transferred to the SEM to investigate deformation processes in more detail. Thus, the first in situ tensile tests in SEM were performed by Roberts et al. [23] in 1976 investigating the damage behavior around manganese-sulfide inclusions in steels. With the development of special loading stages suitable for operation in SEM, the possible load scenarios became more complex. Uniaxial tension and compression tests were joined by bending [24] and also fatigue tests [25]. In order to get a better understanding of the mechanisms involved, the experiments were combined with analytical methods such as electron backscattered diffraction [26]. Through the combination with other complementary methods such as DIC or AE, the in situ deformation in SEM has developed into a highly local, but at the same time volume-integral characterization method.

15.2.2 Full-Field Measurement Methods

Both the digital image correlation and the infrared-thermography are known as contactless and visual full-field measurement techniques. Both provide spatial distribution of physical quantities such as displacement, strain, or temperature on surface or even in bulk of specimens under external load. This is a great advantage compared to the application of strain gauges, extensometers or thermocouples, which provide integral information of regions only where they were applied (gauge length, contact point of thermocouple) [27].

Full-field measurements experienced a large improvement due to enormous development in camera as well as microcomputer technology enabling automated image processing within reasonable time [28] making these techniques very attractive for investigation of localized deformation processes and plastic instabilities occurring during plastic deformation of various kinds of materials. Even more information

can be gained by the combination of both methods known as fully-coupled full-field measurements using simultaneous recording of displacement/strain fields and thermal fields enabling investigations of phenomena of thermomechanical coupling during plastic deformation at microscopic scale [28].

15.2.2.1 Digital Image Correlation

With the possibility to perform in situ deformation tests in the SEM it was just a short step to combine these deformation experiments with digital image correlation. The advantage of deformation experiments within the SEM is the determination of deformation fields with a high lateral resolution and the combination with analytical characterization methods such as EBSD. In order to achieve the highest possible resolution of DIC, it is necessary to generate high-resolution micrographs. Therefore, it is essential to set optimal beam conditions to minimize image distortion, drift, charging and other artifacts [29]. Probably one of the most challenging tasks for the application of DIC on SEM micrographs is a good contrast pattern at the specimen surface without influencing the image conditions. Moreover, the size of the individual features of the pattern should have dimensions well below the features, which will be studied by DIC. In multiphase microstructures such as dual phase steels, the inherent microstructure can already provide a suitable contrast [30]. The only prerequisite in this case would be small size and a fine distribution of the phase components. Short-term etching and the different etching attack on the individual phases generate a topography on the surface which leads to a sufficient contrast for SEM micrographs using secondary electrons. The resolution of this method is determined by the grain size of the phase components. Single phase materials can also be contrasted by etching of the surface where the resulting etch pits are used for the correlation [31]. Another method to contrast surface structures are particle deposition methods using e.g. SiO_2 particles (colloidal silica). The advantage of this method lies in the large-area contrast of the surface, but particle agglomerations can be challenging. In order to achieve a high resolution of the DIC it is necessary to use as small particles as possible for the contrast. The smaller the particles are the higher the resolution of the DIC can be. Yan et al. [26] investigated the damage behavior of a dual phase (DP) steel under tensile load and used for describing the quality/resolution of DIC measurement the product of subset size in nm and subset size in px. In their work they achieved a subset size of 100 nm and 17 px, respectively, by deposition of colloidal silica. Gioacchino and Fonseca [32] investigated the deformation behavior of the steel AISI 304L under uniaxial load. The contrast patterns were achieved by the deposition of gold nanoparticles which result in a subset size of 216×216 nm^2 and 6×6 px, respectively. Due to the small subset size, occurring deformation bands with sub-μm resolution were recorded. Wang et al. [33] combined EBSD and DIC to investigate the deformation and damage behavior of a low-alloy Q&P steel showing initiation of micro-cracks in regions of tempered martensite where strain was accommodated. Similar observations were made by Ghadbeigi et al. [34] on a commercial

dual phase steel (DP 600) observing a heterogeneous strain distribution and localization within large ferritic grains. Na et al. [35] studied the behavior of a low carbon martensitic steel under tensile load. Using complementary EBSD measurements it was shown that the shear distribution in martensite correlates with the sub-cell formation and contributes, thus, to grain refinement. Weidner et al. [31] studied the deformation behavior of a high-alloy CrMnNi cast TRIP steel under tensile load. A short time etching was used for contrasting the surface which also resulted in a sub-μm resolution.

15.2.2.2 Thermography

Infrared thermography is an optical contactless temperature measurement method. Each body with a temperature above absolute zero emits electromagnetic radiation with a wavelength distribution in the range of 0.8 μm up to 14 μm depending on the temperature, which is described by Planck's radiation law [36]. The surface temperature of the body can be determined, therefore, by the detection of this infrared radiation. All plastic deformation processes are associated with the emission of energy and lead, thus, directly to an increase in temperature [37–39]. Therefore, IR thermography is suitable as a real-time in situ method to characterize temperature increase occurring during plastic deformation, strain localization and/or phase transformations [40].

Saeed-Akbari et al. [41] investigated the deformation behavior of high manganese TWIP steels showing a strong Portevin Le Chatelier (PLC) effect during deformation at varying strain rates using infrared thermography. It was shown that the increase in stacking fault energy due to the adiabatic heating caused by the formation of the PLC band is dependent on the chemical composition. Bodelot et al. [42] performed so-called fully-coupled full-field measurements by a combination of thermography and digital image correlation on an austenitic stainless steel under tensile loading. Due to the high resolution obtained, a correlation between dissipated energy in form of increased temperature and local plastic deformation on the grain scale was achieved. Chen et al. [43] also combined DIC and IR thermography during hole expansion test of an austenitic TWIP and an interstitial free (IF) steel.

15.2.3 Acoustic Emission

Acoustic emission is—according to ASTM—related to the sudden release of energy within a solid under certain stimulus (e.g. mechanical load, temperature, chemical attack etc.), which results in elastic waves in the ultrasonic frequency domain propagating through material [44]. These elastic waves can be detected by transducers (e.g. piezo, capacitive or optical sensors) attached to the surface. Among them, piezo transducers exhibit the highest sensitivity regarding surface displacements in the range of 10^{-14} m [44]. The AE method is a powerful tool for in situ application

during mechanical loading allowing studies on kinetics of both deformation and damage processes occurring in various kinds of materials. Due to the high sampling rate, acoustic emission has been established as a real in situ testing method, which supplies a fully integral volume information.

Basically, the acoustic signals can be divided into two types: (i) transient or so-called burst-type signals, and (ii) so-called continuous signals. Transient signals are caused by a spontaneous released energy due to fast processes like crack formation [44] or martensitic phase transformation [45]. They are characterized by a short rise time, a high amplitude and a certain dwell time. Continuous acoustic signals are, in particular, laboratory noise or noise generated by environmental influences like thermal, electric or mechanical noise [46]. These continuous signals are characterized by a high fluctuation with a lower amplitude and a longer duration, which can be described by a root mean square value of the voltage measured at the transducer. Well-known source of continuous signals is the movement of dislocations during plastic deformation [47]. In most cases, an overlap of both transient and continuous AE signals is observed, in particular, when different sources are activated during loading of the material. In contrast to the threshold-based AE data acquisition [48], continuous AE data acquisition provides the full volume integral information considering both the elastic waves generated by different AE sources (transient signals, continuous signals) as well as the wave propagation through the material and the transfer function of the transducer [47]. The recorded AE data can be evaluated in the time domain by various parameters such as (i) number of counts, (ii) rise time of the signal, and (iii) peak amplitude. Furthermore, recorded AE data can be analyzed in the frequency domain gaining additional information [49]. For this purpose, the complete AE data stream is treated by a Fast Fourier Transformation (FFT) of the AE signals measured by the transducer into the so-called source function (AE signals related to specific sources) and the transfer function (wave propagation, properties of the transducer etc.). Thus, the data stream is divided into windows with a size of 2^n readings with a defined overlap of these windows in order not to lose signals at the boundaries of these windows and a subtraction of the noise level of AE data is performed. The results of the FFT of the AE data stream are individual power spectral density (PSD) functions which can be characterized by numerous parameters [45]. The most important parameters are (i) the energy of the PSD function E, which corresponds to the area beneath the curve, and (ii) the median frequency f_m corresponding to the frequency at which the areas below a two-part PSD are equal in size [50]. Subsequently, AE signals of the same origin and, consequently, identical PSD have to be found, which is done by a cluster algorithm. Pomponi and Vinogradov [46] developed a special cluster algorithm (adaptive sequential k-means (ASK) clustering) which allows to differentiate AE signals of various origins. The advantage of this ASK-algorithm is the non-iterative way of working and the low required resources which allow a real time processing. Another advantage is that the number of clusters does not have to be set a priori, thus, it is a non-supervised, data driven process. Through continuous signal analysis, the AE has developed into a methodology that can be used to analyze and characterize microstructural deformation and damage processes. In particular, processes that are fast and involve large

volumes are suitable for detection by AE because the effected volume correlates directly with the energy of the acoustic signal.

Van Bohemen [51] investigated the martensitic transformation behavior of low alloy carbon steel and combined dilatometry with acoustic emission measurements. The investigations revealed a correlation between the energy of the acoustic signals, the formed martensite and the plastically deformed austenite. In addition, correlations between dislocation densities and acoustic signals were observed. Vinogradov et al. [45] investigated the deformation behavior of three different high-alloy austenitic TRIP/TWIP steels with different austenite stability under tensile load. Characteristic PSD functions could be assigned to different deformation mechanisms: (i) dislocation motion, (ii) martensitic phase transformation, (iii) formation of twins, and (iv) formation of stacking faults. Linderov et al. [52] showed the influence of temperature on the change of kinetics of deformation processes in high-alloy TRIP/TWIP steel under tensile load. Mandel et al. [53] investigated the corrosion behavior of a high-alloy TRIP steel. The acoustic signals showed a good correlation between hydrogen bubble formation and cathodic polarization and also a strong time dependency, since the material was polarized in the passive state.

15.2.4 Nanoindentation

Nanoindentation is a powerful method for the characterization of micromechanical properties of microstructural features of materials in the micrometer range. Thus, indentation hardness and/or indentation modulus can be measured for individual phases of a multiphase material or thin coatings. During nanoindentation, the complete indentation process of an indenter with a well-defined geometry is continuously recorded as a load-displacement curve. In contrast to conventional hardness tests such as Vickers or Knoop, the indentation hardness is evaluated from the load-displacement curve according to the well-known Oliver-Pharr method [54] and not from the size of the indent. However, due to the low penetration depth, additional effects have to be considered for the calculation of the indentation hardness such as (i) the true contact area between the indenter and the specimen surface, (ii) the stiffness of the testing device, and (iii) thermal drift during indentation [55].

In addition, the material behavior during the indentation process affects the true contact area between indenter and surface which is known as so-called pile-up or sink-in effect [56]. During pile-up, the material around the intender is bulged up, increasing the actual contact area in comparison to the calculated contact area leading to an overestimation of the hardness of the material. For the sink-in effect, the actual contact area is overestimated and the hardness of the material will be underestimated. A further effect, which can occur during nanoindentation experiments is the so-called pop-in effect reflecting a discontinuity in the load-displacement curve during the loading. This pop-in effect can be caused by an avalanche-like dislocation movement [57] or by phase transformations [58].

In the last years, nanoindentation has become a widely used method, in particular, in scanning electron microscopes which allows the combination of the determination of micromechanical properties with the high-lateral resolution of the SEM. Weidner et al. [59] investigated the hardness of individual structural components in a deformed high-alloy TRIP steel with reduced carbon content. Through the combination with EBSD, the indents could be assigned to the individual phases. The α'-martensite formed during prior deformation showed only a slight increase in hardness compared to the deformed austenite of only approx. 25% which was attributed to the low carbon content of the steel. Ahn et al. [58] observed the γ-austenite to α'-martensite transformation in a low-alloy TRIP steel as a cause for pop-in events. For high-alloy TRIP steels, the indentation-induced transformation of ε-martensite to α'-martensite can also be responsible for pop-in events [60].

15.3 Materials

A general overview is given on materials used for the in situ investigations: (i) high-alloy austenitic cast steels including CrMnNi TRIP/TWIP steels with different austenite stabilities and austenitic-martensitic-carbidic steel after Q&P treatment, (ii) a MgO partially stabilized zirconia (Mg-PSZ) ceramic, and (iii) a metal matrix composite material consisting of austenitic TRIP steel and Mg-PSZ produced by powder metallurgy.

15.3.1 High-Alloy Austenitic Steels

The chemical alloying concept of the studied high-alloy TRIP/TWIP steels is based on a low carbon and nitrogen content (< 0.05 wt%) with 16 wt% of Cr, 7 wt% Mn and Ni [61]. By a variation of the nickel content (3, 6 and 9 wt%), the austenite stability and, consequently, the tendency to form α'-martensite during mechanical loading can be adjusted. Thus, the steel with 9 wt% Ni exhibits the highest austenite stability and undergoes a mechanical twinning during loading (TWIP effect). In contrast, the steel with 3 wt% Ni has the lowest austenite stability resulting in most pronounced TRIP effect. The steel with 6 wt% Ni with a medium austenite stability exhibits depending on the deformation temperature and loading conditions either a TRIP and/or TWIP effect during deformation. The high-alloy CrMnNi TRIP steels undergo a two-step phase transformation from γ-austenite via the intermediate ε-martensite into α'-martensite. The formation of ε-martensite occurs via movement of Shockley partial dislocations $\vec{b} = \frac{a}{6}\langle 112\rangle$ forming extended stacking faults due to the low stacking fault energy [22]. If the stacking faults are arranged on in average each second closed packed lattice plane of the austenite, the austenitic ABCABC stacking sequence is transferred to the hexagonal stacking sequence ABAB and, thus, ε-martensite is identified with a hexagonal lattice structure by EBSD [3, 5]. If the stacking faults

Table 15.1 Chemical composition of the CrMnNi cast TRIP/TWIP steels in wt% (Fe bal.). Content of carbon was determined by combustion infrared detection technique and the content of nitrogen by inert gas fusion infrared and thermal conductivity detection. M_s—Martensite start temperature. SFE—Stacking fault energy determined according to Dai et al. [62]

Steel	C	Cr	Mn	Ni	Si	N	M_S (K)	SFE (mJ/m^2)
X5CrMnNi16-6-3	0.05	16.0	6.4	3.2	0.8	0.06	313	4–10
X5CrMnNi16-6-6	0.05	16.0	6.0	6.1	1.0	0.05	245	9–15
X5CrMnNi16-6-9	0.05	15.3	5.8	8.6	0.9	0.05	230	15–21

are arranged on each closed packed plane of the austenite the ABCAB stacking sequence is transferred into ABCBA resulting in twin orientation. Therefore, both the stacking fault energy and, related to it, the temperature have a significant influence on the deformation behavior. At high SFEs, the deformation behavior is dominated by movement of regular dislocations $\vec{b} = \frac{a}{2}\langle 110\rangle$, whereas with a decrease in SFE the movement of partial dislocations is more favorable resulting in formation of twins and ε-martensite. In parallel, the formation of α'-martensite is increasing with a decrease in SFE.

The chemical composition of investigated cast steels is provided in Table 15.1. The variation of the nickel content has a significant influence on the austenite stability characterized by the martensite start temperature M_s and the stacking fault energy SFE triggering the deformation mechanisms. Thus, the initial microstructure of the steel with 9 wt% nickel is fully austenitic, the steel with 6 wt% nickel contains about 1–2 vol% of δ-ferrite, whereas the steel with 3 wt% nickel consists of about 15 vol% of δ-ferrite and 15 vol% of cooling martensite. The as-cast steel variants were solution annealed at 1323 K for 0.5 h to dissolve precipitates. The grain sizes of the steel variants vary between 100 μm up to the range of several millimeters.

Austenitic-martensitic-carbidic TRIP steel. High-alloy austenitic TRIP steels have good formability and high strength, but due to the fully austenitic microstructure they are characterized by a low yield strength [63]. In order to increase the yield strength, a quenching and partitioning (Q&P) treatment was developed by Wendler et al. [19] to achieve a two-phase microstructure consisting of austenite and tempered α'-martensite. Compared to the previous low-carbon CrMnNi steels, Q&P steels are characterized by an increased carbon and nitrogen content. During Q&P treatment, the fully austenitic steels are quenched to the temperature range $M_s < T < M_f$ (M_f—martensite finish temperature) to achieve an austenitic-martensitic microstructure. If the M_s temperature is already below room temperature, a cryogenic cooling up to liquid nitrogen temperature may be necessary. Due to the increased amount of interstitial alloying elements carbon and nitrogen, α'-martensite is supersaturated and, thus, tetragonally distorted after quenching. In this state, the yield strength and the ultimate tensile strength are significantly increased, but the ductility is limited. The quenching is followed by a so-called partitioning process. During partitioning (723 K for 5 min) carbon and nitrogen partly precipitate as carbides and/or nitrides, and diffuse from the supersaturated martensite into the retained austenite resulting in a stabilization of the austenite [64, 65]. Due to the increased austenite stability and

the increased ductility of the tempered martensite due to partitioning, a considerable increase in ductility with small reduction of ultimate tensile strength can be achieved [17].

Based on the chemical design of the high-alloy CrMnNi cast TRIP/TWIP steels a class of austenitic-martensitic-carbidic steels was developed by Wendler et al. [19], where the manufacturing process is based on a Q&P treatment. The steel was produced in a vacuum induction furnace and cast into a copper mold, which led to rapid solidification of the melt. The chemical composition after casting is shown in Table 15.2. The SFE for the given chemical composition has been calculated according to Dai et al. [62] to 17–23 mJ/m^2. Subsequently, miniature flat tensile specimens were separated from the cast block. These were solution annealed at 1423 K for 0.5 h. Afterwards, the specimens were quenched in water to room temperature followed by subzero cooling down to 213 K in an ethanol bath using liquid nitrogen.

After subzero cooling, the specimens were annealed at 723 K for 5 min to induce diffusion of carbon and nitrogen from the supersaturated α'-martensite into the retained austenite as well as precipitation of carbides and/or nitrides. The microstructure after partitioning is shown in Fig. 15.1. It can be seen that the retained austenite is not homogeneously distributed in the microstructure. There are areas with austenitic grains several μm in size—the so-called interdendritic austenite and also austenitic areas between the tempered martensite laths which have a thickness of less than 1 μm—the so-called interlath austenite. Due to the ferritic solidification of the remaining melt, δ-ferrite can also be found in the interdendritic austenite.

Table 15.2 Chemical composition of the as-cast AMC steel in wt%, (Fe bal.). Content of carbon was evaluated by combustion infrared detection technique and content of nitrogen by inert gas fusion infrared and thermal conductivity detection

	C	N	Cr	Mn	Ni	Si
X16CrNiMnSiN 15-3-3	0.16	0.11	14.5	3.0	3.3	0.4

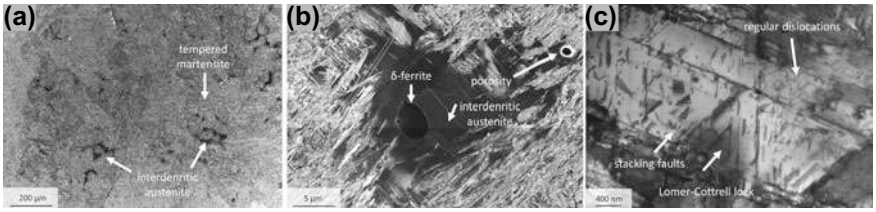

Fig. 15.1 Initial microstructure of austenitic-martensitic-carbidic steel. **a** SEM micrograph overview in backscattered electron contrast showing interdendritic austenite and tempered martensite. **b** Magnification of interlath austenite with marked δ-ferrite and porosity. **c** Interlath austenite with marked stacking faults, Lomer-Cottrell locks and regular dislocations observed in transmission SEM [66]

15.3.2 MgO Partially-Stabilized Zirconia

Zirconia can be present in three different modifications depending on temperature: (i) the cubic high-temperature phase (c)-ZrO_2 ($T > 2650$ K), (ii) the tetragonal phase (t)-ZrO_2 (1478 K $\leq T \leq$ 2650 K), and (iii) the monoclinic phase (m)-ZrO_2 which prevails at room temperature [67]. By addition of phase stabilizers like MgO, CaO, CeO or Y_2O_3 the cubic modification can be stabilized down to room temperature. During heat treatment, coherent tetragonal precipitates (lenses) are formed within the cubic lattice structure which can transform via a stress-assisted martensitic phase transformation into the monoclinic lattice structure. This martensitic phase transformation is accompanied by a shear of about 0.16 and a volume expansion of about 4.9% [68]. This volume expansion of ZrO_2 is related to the formation of compressive stresses, which can impede crack propagation. Thus, partially-stabilized ZrO_2 can yield good fracture toughness properties [69].

Porter et al. [70] modeled the transformation toughening in PSZ ceramics using Eshelby's analysis of transformed inclusions and observed a reasonable consistency with experimental results regarding the magnitude of the toughness. Porter and Heuer [71] investigated the evolution of microstructure during aging of MgO-partial stabilized ZrO_2 (Mg-PSZ) after solution annealing. The observations showed that the aging parameters have a strong influence on the microstructure and, thus, also on the mechanical properties. If the aging time is too short, too small (t)-ZrO_2 lenses are formed, which leads also to a reduction in fracture toughness. If the aging time is too long, the tetragonal precipitates continue to grow. If the size of the precipitates exceeds about 0.2 μm, the coherency is lost resulting in a transformation of the tetragonal lenses into monoclinic lattice structure during cooling to room temperature. Hannik [72] examined the growth of tetragonal precipitates in CaO, MgO and Y_2O_3 partially-stabilized ZrO_2 and observed similar behavior. The Mg-PSZ also showed a loss of tetragonal structure when the dimensions of the longest axis of the precipitates exceed 0.6 μm.

15.3.3 TRIP Matrix Composite

Metal matrix composites (MMC) combine properties of metals (high ductility and toughness) with those of ceramics (high strength and Young's modulus) to generate new material properties [73]. TRIP matrix composites merge the strain-induced martensitic phase transformation of a TRIP steel matrix and the stress-assisted martensitic phase transformation of Mg-PSZ resulting in a high capacity for absorption of mechanical energy [74]. TRIP matrix composites can be manufactured by a powder-metallurgical route followed either by conventional sintering process [75], hot pressing [76] or field-assisted sintering [77]. Hot pressing and field-assisted sintering result in shorter process times due to the superimposed mechanical load [77, 78] leading to lower porosity, smaller grain sizes and less pronounced diffusion

processes compared to conventional sintering regimes. Reduced diffusion processes are of high importance regarding the MgO stabilizer. Thus, the MgO stabilizer can diffuse out of the ZrO_2 particles during conventional sintering due to higher sintering times and temperatures leading to a destabilization of Mg-PSZ particles and a monoclinic phase transformation already during the manufacturing process.

Martin et al. [79] investigated the transformation behavior of a TRIP steel reinforced with Mg-PSZ under compressive stress. The MMC was manufactured using spark plasma sintering to keep the process time as short as possible. Compared to the unreinforced reference material, the MMC showed a higher stress level with the same compressive strain. Glage et al. [80] investigated a TRIP steel/Mg-PSZ composite in the regime of low-cycle fatigue and observed a strengthening effect under cyclic loading and a comparable fatigue life time for lower strain amplitudes.

For optimal mechanical properties the bonding of the ceramic particles to the metallic matrix is important. A weak bonding leads to rapid decohesion of the ceramic from the matrix and premature failure. Prüger et al. [81] investigated the correlation between interface strength and transformation behavior of the PSZ in a TRIP steel MMC under compressive load using micromechanical simulations. They could show that with increasing interface strength the phase transformation of the PSZ is favored and, thus, the work hardening behavior of the MMC increases.

15.4 Case Studies

15.4.1 Austenitic Cast Steels

15.4.1.1 Strain Localizations Studied by Digital Image Correlation

High-alloy CrMnNi cast TRIP/TWIP steels. Miniature flat tensile specimens were manufactured out of the solution annealed cast plates. The gauge length was 10 mm with a rectangular cross section of 2×4 mm^2. The specimens were carefully grinded and polished to obtain a deformation-free surface. Subsequently, the specimens were etched with a V2A agent (200 ml distilled water, 200 ml 32 pct hydrochloric acid, 20 ml 65 pct azotic acid, 0.6 ml Vogel's special reagent) for 1 min at 60 °C providing an excellent surface contrast pattern required for DIC calculations. Tensile tests were performed both at room temperature (RT) and elevated temperatures (373 K, 473 K) using a miniature push-pull loading stage (Kammrath & Weiss, Dortmund, Germany) placed in the chamber of a high-resolution scanning electron microscope. The higher temperatures were realized by a heating plate mounted on the back side of the specimens. Temperature was controlled by a thermocouple and kept constant over the entire deformation test using PID control. The quasi in situ tensile deformation was performed step wise and after each deformation step of $\Delta l = 50$ µm micrographs of predefined areas of interest (AOIs) were captured. The

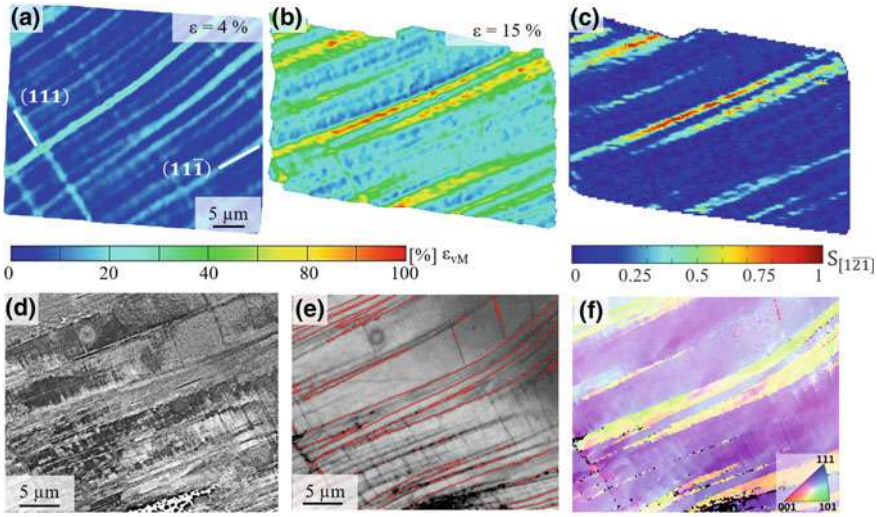

Fig. 15.2 Results of digital image correlation and EBSD measurements obtained on steel X5CrMnNi16-6-9 during tensile loading at RT and 4% (**a**) and 15% (**b**-**f**) of applied global strain. **a**, **b** Local strain field according to von Mises equivalent strain ε_{vM}. **c** Calculated magnitude of shear on the $(11\bar{1})$ plane in the direction of $\vec{b} = \frac{a}{6}[1\bar{2}\bar{1}]$. **d** SEM micrograph of formed deformation bands in backscattered electron contrast. **e** Band contrast map with highlighted Σ3 boundaries. **f** Crystallographic orientation in inverse pole figure coloring according to loading axis (horizontal)

deformation continued until a global strain of 15% was reached. After tensile deformation, specimens were vibration polished using colloidal silica for 24 h (or multiples of) to remove etching pits on the surface. Subsequently, AOIs were measured again using electron backscatter diffraction. Recorded high-resolution SEM micrographs were evaluated using software package ARAMIS [82] to calculate strain distribution. For more experimental details see [31].

*Steel with highest austenite stability (*9 wt*% nickel).* Figure 15.2 shows the deformation of the X5CrMnNi16-6-9 steel at room temperature where a pronounced twin formation is expected according to the higher SFE (compare Table 15.1). Figure 15.2a shows the strain distribution according to the von Mises equivalent strain (ε_{vM}) at the beginning of deformation (4% global strain). The formation of deformation bands related to the activation of two different slip systems oriented parallel to (111) and $(11\bar{1})$ plane, respectively, was observed. The strain is well localized and homogeneously distributed within these bands (about $\varepsilon_{vM} = 25\%$). With ongoing deformation, both the number of deformation bands as well as their thickness increase, in particular for the system belonging to $(11\bar{1})$ plane, which corresponds to the secondary slip system ($\mu = 0.36$). Moreover, the strain localization within these bands increases continuously (see Fig. 15.2b). Figure 15.2c shows the calculated magnitude of shear for the secondary slip system in the direction of the Burgers vector of the Shockley partial dislocations with the highest Schmid factor ($\vec{b} = \frac{a}{6}[1\bar{2}\bar{1}]$, $\mu = 0.34$). It turned out that not all deformation bands belonging to secondary slip

system exhibit similar magnitude of shear. Only few of these bands show a relatively high value of about 0.75. These bands with the highest magnitude of shear were identified by EBSD measurements as regions with a twin orientation to the matrix (see Fig. 15.2e, f) indicated by red lines according to the misorientation relationship of $60°\langle 111\rangle$ for $\Sigma 3$ (twin) boundaries. Figure 15.2d shows the deformation bands forming on the primary and secondary slip system in backscattered electron contrast. Slip bands or even twins were visible also for the primary slip system, but are quite narrow compared to the large and wide twins belonging to the secondary system. Furthermore, the pronounced distortion of the area of interest due to the favored deformation on the secondary system becomes apparent.

Figure 15.3 shows the deformation of X5CrMnNi16-6-9 steel at 473 K. The calculated von Mises equivalent strain at a global strain of 2% is shown in Fig. 15.3a. Here, the band-like distribution of the strain is recognizable as well. The deformation bands form on the primary slip system parallel to (111) and show von Mises equivalent strains of about $\varepsilon_{vM} = 10\%$. With increasing global strain, the deformation band structure is still visible, but the areas between the bands also show increased strain values, as can be seen in Fig. 15.3b. When considering the AOI using backscattered electrons (Fig. 15.3c), the formation of band-like structures can be seen as

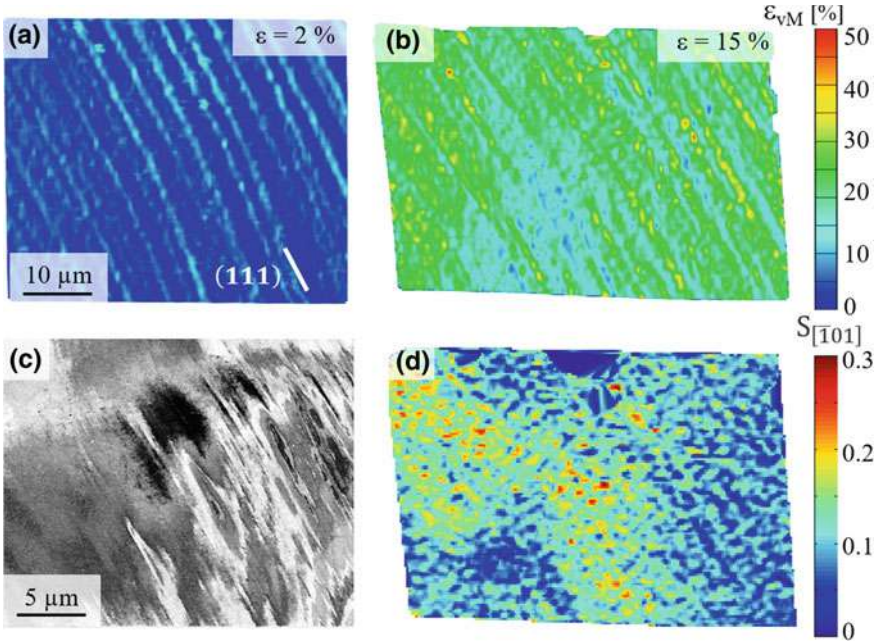

Fig. 15.3 Results of digital image correlation and EBSD measurements obtained on steel X5CrMnNi16-6-9 during tensile loading at 473 K. **a** Von Mises equivalent strain distribution (ε_{vM}) at 2% of applied global strain with marked primary slip system. **b** Von Mises equivalent strain distribution (ε_{vM}) at 15% of global strain. **c** SEM micrograph of area of interest in backscattered electron contrast. **d** Calculated magnitude of shear at 15% of global strain. Loading axis is horizontal

well. Twin formation was not observed using EBSD. In general, the strain is more homogeneously distributed over the AOI. This is due to the increased slip of regular dislocations due to the increased stacking fault energy compared to room temperature. This also becomes visible when considering the magnitude of shear, which is shown in Fig. 15.3d. In contrast to deformation at room temperature, where the magnitude of shear was highest in bands related to twins, a more or less homogeneous magnitude of shear between 0 and 0.2 is observed at 473 K.

Steel with medium austenite stability (6 wt% *nickel).* Figure 15.4 shows the evolution of strain during tensile deformation of X5CrMnNi16-6-6 cast steel at room temperature. Figure 15.4a shows localized strain within deformation bands at the beginning of the tensile deformation at 3.6% global strain. Noteworthy is the high lateral resolution of the SEM-DIC. The width of the deformation bands which are recognizable by digital image correlation is less than 1 μm.

The strain is very homogeneously distributed within the deformations bands, except the area marked with a white arrow which shows strain localization up to $\varepsilon_{vM} = 40\%$. With increase in macroscopic strain, the number of deformation bands increases, the deformation bands grow in their width and areas of local strain concentrations within these bands increase as well (see Fig. 15.4b). Figure 15.4d, e show the AOI in terms of backscattered electron (BSE) contrast and EBSD phase

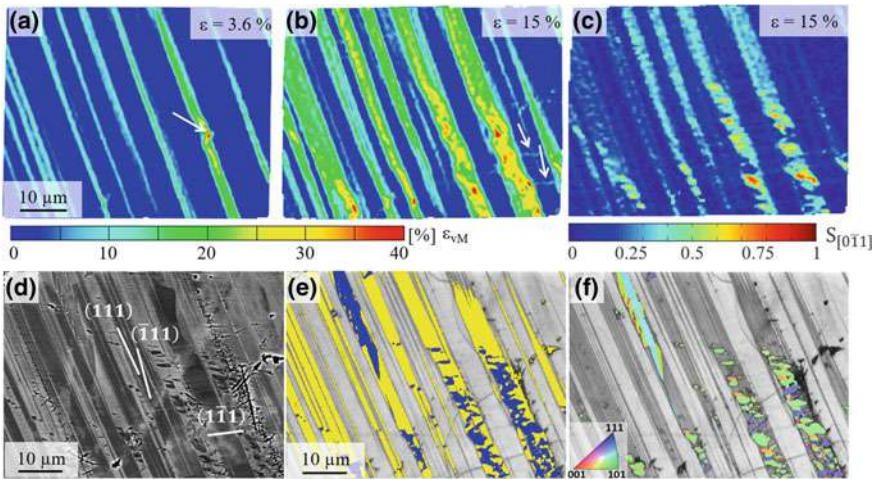

Fig. 15.4 Results of digital image correlation and EBSD measurements obtained on steel X5CrMnNi16-6-6 during tensile loading at RT. **a** Von Mises equivalent strain distribution (ε_{vM}) at 3.6% of applied global strain with marked area of enhanced strain. **b** Von Mises equivalent strain distribution (ε_{vM}) at 15% of applied global strain with indicated slip systems. **c** Calculated magnitude of shear on planes $(111)/(\bar{1}11)$ in the direction of $[0\bar{1}1]$. **d** SEM micrograph of area of interest in backscattered electron contrast. **e** Band contrast map with highlighted ε-martensite (yellow) and α'-martensite (blue). **f** Band contrast map with highlighted α'-martensite in inverse pole figure color code according to load axis (horizontal). Partly reproduced from [31]

map, respectively. Both figures reveal the formation of α'-martensite inside deformation bands. In Fig. 15.4e, grey areas correspond to austenite, yellow to ε-martensite and blue to α'-martensite. In comparison with Fig. 15.4b it can be seen that the formation of the deformation bands correlates with the formation of ε-martensite and the strain-increased regions within the bands correlate with the formation of α'-martensite. Figure 15.4f shows that only a certain number of different orientations of α'-martensite grains have been formed within the deformation bands, which is an indication for a variant selection. A comparison with Fig. 15.4c shows that the magnitude of shear calculated in the $[0\bar{1}1]$ direction correlates with the orientation of the α'-martensite grains. Only one martensite variant (green color) exhibits the highest magnitude of shear of about 0.7, while the other variants (orange and violet color) show significantly smaller values of shear [31]. In comparison, regions corresponding to ε-martensite show nearly homogeneously distributed shear of about 0.3, which is due to the fact that only one single ε-martensite variant has been formed [31].

Figure 15.5 shows the evolution of strain during tensile deformation of X5CrMnNi16-6-6 cast steel during tensile deformation at 373 K. Due to the increased temperature and, consequently, the increased SFE as well as reduced driving force

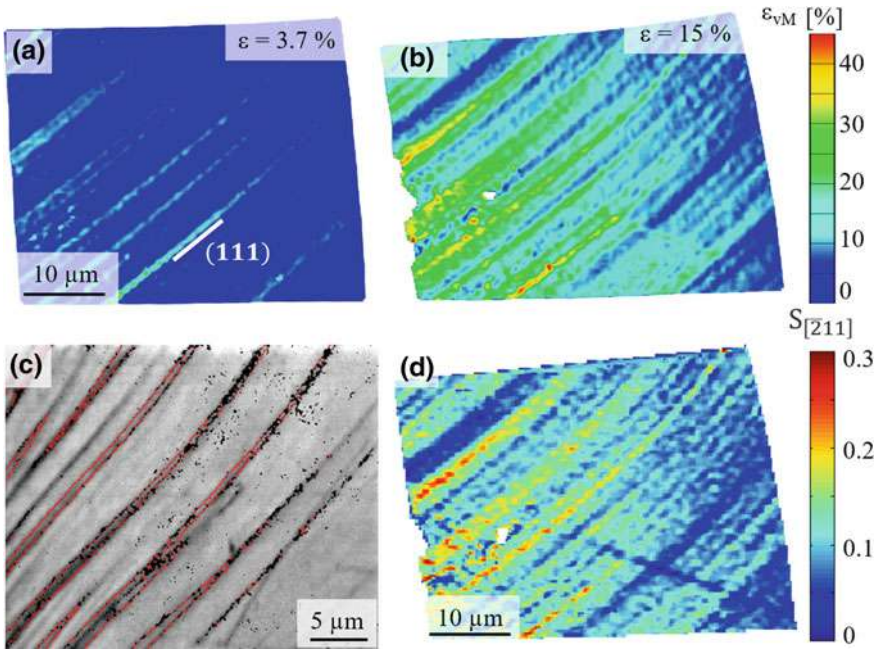

Fig. 15.5 Results of digital image correlation and EBSD measurements obtained on steel X5CrMnNi16-6-6 during tensile loading at 373 K. **a** Von Mises strain distribution (ε_{vM}) at ε = 3.7% with marked primary/secondary slip system. **b** Von Mises strain distribution (ε_{vM}) at ε = 15%. **c** Band contrast map with marked Σ3 boundaries. **d** Calculated magnitude of shear within the area of interest

of ΔG (Gibb's free energy), no formation of α'-martensite is observed. In Fig. 15.5a at 3.7% global strain, the localization of strain in bands was detected. The size of the bands which can be detected by DIC is below 1 μm and the strain distribution within these bands is quite homogeneous (Fig. 15.5b). With increase in macroscopic strain, the number of deformation bands further increases.

The von Mises strain localization within some bands is about 40% at $\varepsilon = 15\%$, but it is in other bands significantly lower. The comparison with results from EBSD measurements (Fig. 15.5c) reveals that regions with highest strain localizations correspond to areas where twins have been formed. The magnitude of shear (Fig. 15.5d) was calculated on (111) plane in $\left[\bar{2}11\right]$ direction. The regions with highest shear correspond well with the regions of twins. However, the magnitude of shear is about 0.25 and is, therefore, significantly lower than that Schumann predicted theoretically to be of about 0.7 for twinning [83]. One reason for lower magnitudes of shear could be that the thickness of twin bundles within the broader shear bands is below resolution of the DIC measurements [15]. On the other hand, it is more likely that twins formed in this steel variant are the results of movement and accumulation of partial dislocations. The theoretically calculated magnitude of shear for partial dislocations is of 0.3, which would be in good agreement with the experimentally determined values of about 0.25. Here obviously the areas with high von Mises strain correlate with areas with high shear, in comparison to the deformation at room temperature, where different α'-martensite variants led to a partially inhomogeneous shear distribution depending on which martensite orientation has formed. Such behavior was not observed at 373 K because twins with a uniform orientation have been formed during deformation. As a result, the twins also have a homogeneous shear distribution. Finally, the X5CrMnNi16-6-6 cast steel with medium austenite stability behaves at 373 K like the steel X5CrMnNi16-6-9 with higher austenite stability at room temperature.

Austenitic-martensitic-carbidic steel. Miniature flat tensile specimens were manufactured out of the Q&P treated steel X16CrNiMnSiN with same dimensions as described for the CrMnNi TRIP/TWIP steels. The surfaces of the specimens were grinded and vibration polished. Afterwards, AOIs were defined containing interdendritic austenitic grains, which were pre-characterized by EBSD. Subsequently the miniature specimens were etched for 2 min at 40 °C in V2A etching agent to achieve a structured surface. The quasi in situ deformation in the SEM was performed according to similar procedure as described above for CrMnNi TRIP/TWIP steels. After each deformation step several micrographs at two different magnifications were captured until uniform elongation of the specimen ($\varepsilon = 19\%$). The sequence of SEM images was stabilized using the VirtualDub software package [84] and local strain fields were evaluated using the VEDDAC software [85]. After tensile deformation, the gauge length of specimens were cut-off and vibration polished for four hours. Subsequently, EBSD measurements of the AOIs were carried out to evaluate the development of the microstructure after tensile deformation. In addition, XRD measurements were performed on both undeformed and deformed specimens. The phase analysis was carried out by a Rietveld–like refinement of the whole diffraction pattern using the MAUD software package [86]. According to the microstructure,

Table 15.3 Lattice parameters, volume fractions and related phases calculated according to Rietveld-like refinement using software package MAUD of steel X16CrNiMnSiN15-3-3 in Q&P condition, before and after deformation. According to [66]

	Lattice parameter (nm)	Volume fraction (%)	Phase
Non-deformed state	0.2875	69	Tempered martensite
	0.3597	25	Interdendritic austenite
	0.3609	6	Interlath austenite
Deformed state	0.2879	68	Tempered martensite
	0.2881	29	Fresh martensite
	0.3605	3	Interlath austenite

face-centered cubic and body-centered cubic iron were considered. The results are summarized in Table 15.3.

The XRD measurements on the initial state revealed 69 vol% of tempered martensite and 25 vol% of interdendritic austenite. In addition, 6 vol% of interlath austenite were identified based on a slightly increased lattice parameter of $a = 0.3609$ nm compared to the interdendritic austenite with $a = 0.3597$ nm. This difference of lattice constants for both austenitic phases is caused by different content of nitrogen and carbon due to various diffusion behavior. Diffusion occurs during partitioning from supersaturated, quenched martensite into austenite. The interdendritic austenite is characterized by grain sizes of >5 μm, whereas the grain size of interlath austenite is significantly smaller (<1 μm). Diffusion length of carbon was estimated by Ågren [87] to be less than 1 μm for partitioning at 723 K for 5 min. Due to the small size of the interlath austenite, it will have a higher carbon and nitrogen concentration than the interdendritic austenite. Thus, for interdendritic austenite the estimated diffusion length is too small to result in a significant increase in content of interstitial elements. The different lattice parameters are, therefore, explained by content of interstitial elements.

In the deformed state, no interdendritic austenite was identified by XRD and only 3 vol% of interlath austenite were remaining after tensile deformation up to $\varepsilon = 19\%$ with a lattice parameter of a = 0.3605 nm which is comparable to the undeformed state. This means, interlath austenite is much more stable during deformation. This is caused by the higher chemical stabilization due to the higher carbon and nitrogen content, but also due to the surrounding martensite which puts the austenite into a hydrostatic compression state, the so-called shielding effect [88]. In contrast, nearly all interdendritic austenite transformed during deformation. The amount of tempered martensite remains with 68 vol% nearly constant. After deformation, 29 vol% of fresh martensite were formed mostly from interdendritic austenite. The fresh martensite shows a small tetragonal distortion of about 0.6% in comparison to tempered martensite which is caused by higher carbon and nitrogen content, although interdendritic austenite does not gain significantly carbon and nitrogen during partitioning, as already mentioned above. However, the martensite existing before deformation has been tempered during partitioning, reducing the tetragonal distortion.

The influence of the grain orientation on the local deformation behavior of the interdendritic austenite was investigated by DIC in combination with EBSD measurements. Here, two different grain orientations were selected: (i) ⟨101⟩ and (ii) ⟨001⟩ lattice directions, respectively, parallel to the loading axis. The first one was oriented for slip of partial dislocations and the latter one was oriented for preferential slip of regular dislocations. The microstructural evolution during tensile deformation of ⟨101⟩ oriented interdendritic austenite grain is shown in Fig. 15.6a, b. At the beginning of deformation, a two-phase microstructure consisting of austenite and tempered martensite is present. With beginning of deformation, bands are evolving parallel to the primary slip system. Close to uniform elongation ($\varepsilon = 19\%$) a massive martensitic phase transformation occurs starting from the interface of interdendritic austenite/tempered martensite. Figure 15.6b shows that both ε-martensite (hcp) and fresh α'-martensite (bcc) can be found within deformation bands. In contrast,

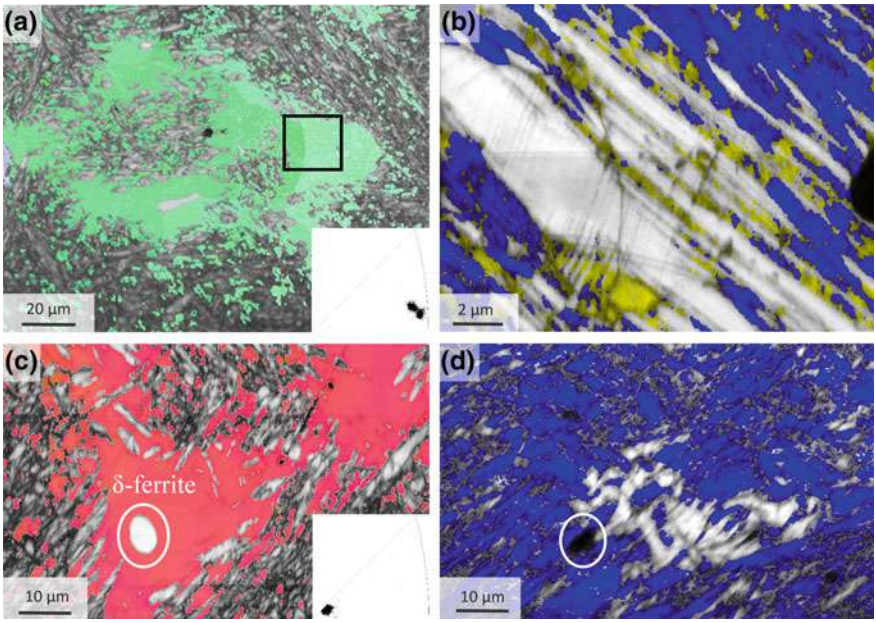

Fig. 15.6 Results of EBSD measurements of AOIs before and after tensile deformation of Q&P treated steel X16CrNiMnSiN15-3-3 at RT. **a** ⟨101⟩ grain orientation. Band contrast map of tempered martensite with austenite colored according to inverse pole figure color code of loading axis. **b** Band contrast map of marked area of (**a**) after deformation up to $\varepsilon = 19\%$ with γ-austenite (grey), ε-martensite (yellow) and fresh α'-martensite (blue). This AOI is studied in more detail in Fig. 15.7. **c** ⟨001⟩ grain orientation. Band contrast map of tempered martensite and marked δ-ferrite with austenite colored in inverse pole figure color code of loading axis. **d** Band contrast map after deformation up to $\varepsilon = 19\%$ with γ-austenite (grey) and tempered and fresh α'-martensite (blue) of the AOI with a marked place of the δ-ferrite shown in **c**. Loading axis is horizontal. Partly reproduced from [66]

Fig. 15.6c, d show the results for the deformation of the ⟨001⟩ oriented interdendritic austenitic grain. Here, no formation of deformation bands was observed. The EBSD measurements reveal only fresh-formed α'-martensite and no ε-martensite was detected. This is what was expected for these two different grain orientations and can be understood by the different behavior of dislocations. Whereas dislocations in grain ⟨101⟩ dissociate into Shockley partials leading to stacking faults, grain ⟨001⟩ is oriented for preferred movement of regular dislocations. Figure 15.6d shows the ⟨001⟩ oriented grain after 19% global strain. Within the austenite pronounced formation of fresh α'-martensite has occurred via the $\gamma \rightarrow \alpha'$ transformation. Thus, both grain orientations exhibit as expected different behavior in terms of the formation of fresh martensite during tensile deformation at RT.

Figure 15.7 shows the marked area of Fig. 15.6a (black rectangle) in more detail. Figure 15.7a shows the interdendritic austenitic grain with tempered martensite before deformation in secondary electron contrast after etching. Etching was optimized for a good contrast of the austenite. Therefore, both tempered martensite and

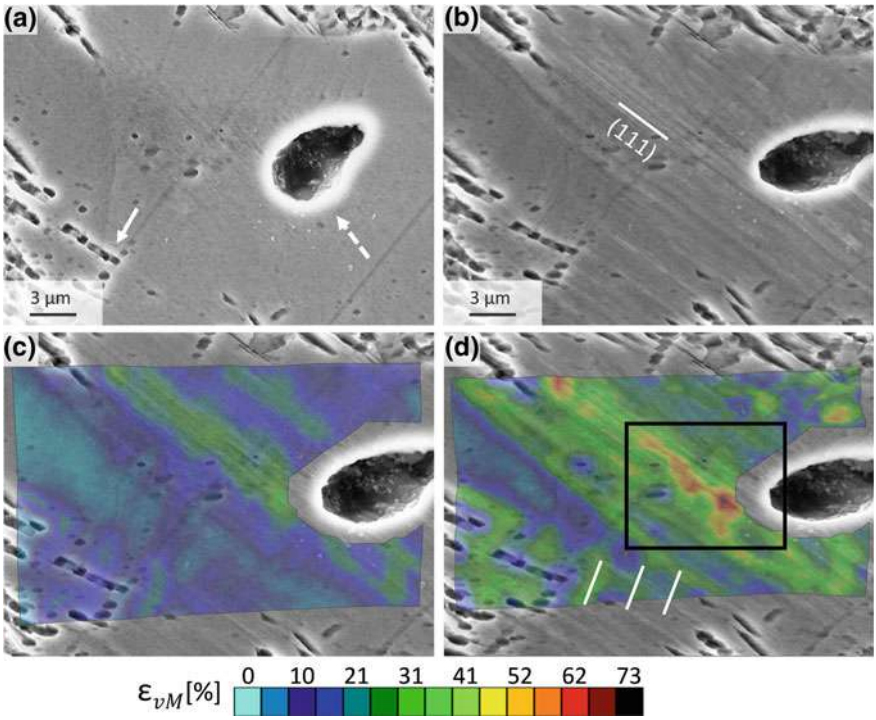

Fig. 15.7 ⟨101⟩ oriented austenitic grain during tensile deformation. **a** Area of interest at zero strain, etched, in secondary electron contrast with over etched δ-ferrite and α'-martensite marked by dashed and bold arrows. **b** Area of interest at 19% of global strain with marked trace of primary slip system. **c**, **d** Calculated von Mises equivalent strain (ε_{vM}) at 11% (**c**) and 19% (**d**) of global strain, respectively. Areas with increased strain levels are marked by black rectangle in (**d**). Partly reproduced from [66]

δ-ferrite were slightly over etched (marked by bold and dashed arrows in Fig. 15.7a, respectively). Figure 15.7b shows the same AOI at $\varepsilon = 19\%$. The formation of deformation bands within the interdendritic austenite is well observed. Furthermore, additional contrast changes within the deformation bands are recognizable. Figure 15.7c, d show the calculated von Mises equivalent strain at 11% and 19% of global strain, respectively. At $\varepsilon = 11\%$, the local accumulation of strain within deformation bands is clearly visible. Furthermore, the strain is homogeneously distributed within these bands. During tensile deformation, ε-martensite is formed which is associated with a homogenous shear operation leading to homogenous von Mises equivalent strain values of about $\varepsilon_{\mathrm{vM}} = 0.3$. With further tensile deformation, these bands grow in width and the activation of a secondary slip system is observed (see white lines in Fig. 15.7d). Furthermore, within the primary deformation bands, areas with enhanced strain localization are formed with values of $\varepsilon_{\mathrm{vM}}$ up to 0.7. Looking to the microstructure of the AOI at $\varepsilon = 19\%$ in Fig. 15.7b it can be seen that the areas of increased strain correlate well with the formation fresh α'-martensite.

Figure 15.6b showed also that α'-martensite formed during tensile deformation, in particular, at the previous interface of tempered martensite and interdendritic austenite. The formation of fresh martensite in this region could not be resolved by DIC. The very pronounced formation of α'-martensite resulted in a high local strain from one deformation step to the other resulting in a loss of the correlation between individual subsets in these areas. The preferred formation of fresh martensite at the austenite/tempered martensite interface can be assigned to the constraining effect [89]. Due to the high defect density at the interfaces caused by the formation of tempered martensite, the formation of fresh martensite is preferred.

Figure 15.8 shows the area of high strain values marked in Fig. 15.7d in more detail. It is visible that the areas of high strain values (see Fig. 15.8a) correlate well with the fresh-formed α'-martensite grains shown in Fig. 15.8b. Thus, two different α'-martensite variants have been formed exhibiting a twin orientation relationship ($\Sigma 3$ boundaries marked by green line).

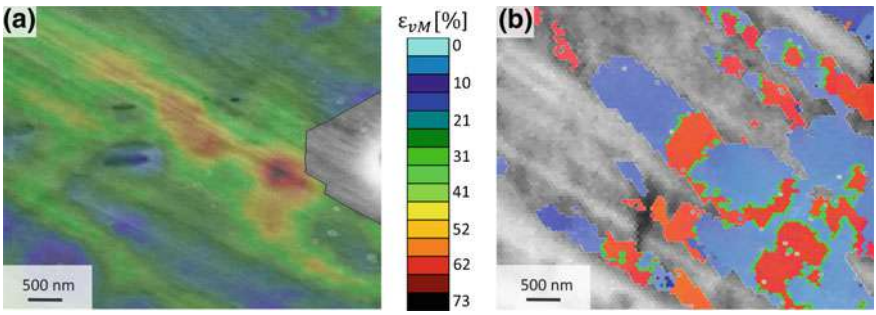

Fig. 15.8 AOI marked by black rectangle in Fig. 15.7d. **a** Calculated von Mises equivalent strain ($\varepsilon_{\mathrm{vM}}$) within deformation band after tensile deformation up to $\varepsilon = 19\%$. **b** Band contrast map with freshly formed α'-martensite shown in inverse pole figure color code according to loading axis. $\Sigma 3$ twin boundaries are indicated by green lines. Partly reproduced from [66]

15.4.1.2 Temporal Evolution of Deformation Mechanisms Studied by Acoustic Emission

Measurements of acoustic emission were performed in situ during tensile deformation of high-alloy X5CrMnNi16-6-x ($x = 3$, 6 or 9 wt%) cast steels in order to study the temporal evolution of ongoing deformation processes. Therefore, threshold-less, continuous AE signal acquisition method using a single AE sensor was applied. Different individual deformation mechanisms were identified as sources of acoustic emission and their evolution over the entire deformation process was evaluated. In addition, the influence of temperature on operating deformation mechanisms was evaluated. Details on experimental setup were published elsewhere [45, 90]. As demonstrated in [45], the detailed analysis of AE data obtained during tensile tests both in the time as well as frequency domain allowed for the separation of the following deformation mechanisms: (i) dislocation glide (movement of regular dislocations), (ii) formation of stacking faults (partial dislocation movement), (iii) twin nucleation, (iv) formation of α'-martensite, and (v) formation of Portevin Le Chatelier bands. Each of these mechanisms can be characterized by a specific set of AE parameters such as median frequency f_m and energy E of AE signals forming individual clusters of signals. The evolution of these individual clusters was followed over the entire deformation process. Thus, it was possible to evaluate which deformation mechanism becomes dominant at what stress or strain level during the tensile deformation. An example out of the variety of results is shown for the steel with the highest austenite stability (9 wt% nickel) in Fig. 15.9. For this steel it is known from microstructural investigations that mechanical twinning is the dominant deformation mechanism (Fig. 15.2), whereas at temperature $T > 80$ °C the movement of regular dislocations becomes dominant. Figure 15.9a, c show the results obtained at RT and Fig. 15.9b, d the results from tests at 373 K. The results are plotted either in terms of the cumulated AE energy E_Σ (Fig. 15.9a, b) or the cumulated number of AE cluster elements (Fig. 15.9c, d) always combined with the stress versus time response. These results illustrate well both the differences between the two AE sources (i) dislocation glide (low energy signals) and (ii) twin nucleation (high energy signals) as well as the influence of temperature on these mechanisms. Thus, both mechanisms are active at RT and 373 K. However, the mechanical twinning is dominant at RT whereas its activity is reduced at 373 K. In contrast, the dislocation glide becomes more important at 373 K compared to RT.

Furthermore, it was shown that the evolution of the identified clusters related to individual AE sources correlates well with other microstructural parameters or properties. Thus, it was shown in [45] that the evolution of the identified cluster for the α'-martensite formation correlates well with the evolution of the ferromagnetic phase fraction in case of steels X5CrMnNi16-6-6 and X5CrMnNi16-6-3 with medium and low austenite stability, respectively. Figure 15.10 summarizes the results from AE data analysis (magenta lines), the volume fraction of α'-martensite obtained from ferromagnetic phase fraction measurements using a feritescope (symbols) and the calculation of the volume fraction of α'-martensite according to the Olson-Cohen model [91] (dashed lines).

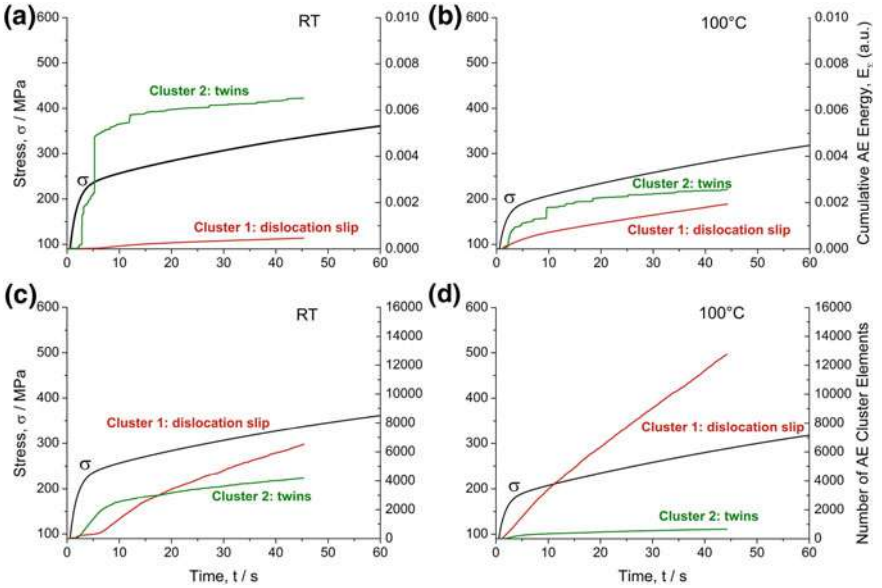

Fig. 15.9 Results of the AE measurements for steel X5CrMnNi16-6-9 tested in tension at RT (**a**, **c**) and 373 K (**b**, **d**). Temporal evolution of the identified mechanisms (i) dislocation glide and (ii) twin nucleation over the entire deformation process in terms of cumulative AE energy (**a**, **b**) and of number of AE cluster elements (**c**, **d**). Reproduced from [90]

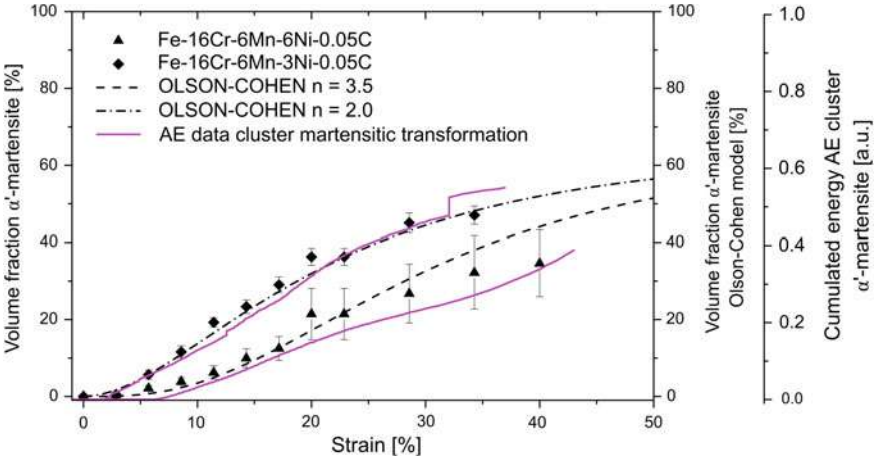

Fig. 15.10 Comparison of cumulated AE energy and volume fraction of strain-induced α'-martensite determined from feritescope measurements obtained during tensile tests at RT at a strain rate of 10^{-3} s^{-1} with model description of Olson and Cohen [91] for steel variants X5CrMnNi16-6-6 and X5CrMnNi16-6-3. Reproduced from [92]

Figure 15.10 demonstrates an excellent qualitative agreement between experimentally determined volume fraction of strain-induced α'-martensite with the evolution of the cumulated AE energy of the cluster related to α'-martensite formation. Both the onset of martensite formation as well as the different kinetics of α'-martensite formation are very well described by the evolution of the cumulated AE energy of signals related to the cluster corresponding to α'-martensite formation. In addition, both experimental data—AE and feritscope measurements—fit well with the Olson-Cohen model description of the kinetics of α'-martensite formation.

15.4.1.3 Portevin Le Chatelier Behavior Studied by Full-Field Measurements

The high-alloy X5CrMnNi17-7-4 cast steel exhibits an excellent strengthening behavior and high ductility yielding, as a consequence, a delay of the macroscopic strain localizations resulting in retarded necking and, finally, failure of the material at higher strain values. However, TRIP steel with the lowest nickel content (3 wt%) exhibits, in addition, serrated plastic flow known as the Portevin Le Chatelier (PLC) effect [93].

The PLC effect was studied on the high-alloy CrMnNi steel X5CrMnNi17-7-4 with 0.05% C, 17% Cr, 7% Mn, 3.7% Ni in the as cast condition after solution heat treatment (0.5 h at 1323 K followed by N_2 gas quenching). Due to the low austenite stability ($M_s = 333$ K), the initial microstructure consists beside the metastable austenite of about 15 vol% of martensite formed during cooling and 10 vol% of δ-ferrite due to ferritic solidification. The tensile tests were performed at room temperature using an electro-mechanical testing system (Zwick, Germany) using flat tensile specimens having a rectangular cross section of 8×4 mm^2 and a gauge length of 35 mm at a total length of 205 mm. The tests were carried out under crosshead displacement control with different nominal initial strain rates (10^{-4} s^{-1}, 10^{-3} s^{-1}, 10^{-2} s^{-1} and 10^{-1} s^{-1}, respectively). The mechanical tests were complemented by full-field measurements using in situ thermography measurements with the infrared thermography system VarioCamhr (InfraTec, Dresden, Germany) and digital image correlation using digital camera (Canon EOS 420D). One side of the gauge parts of the specimens was prepared for thermographic measurements by mechanical grinding and, subsequently, covered with a black thermo lacquer enabling a constant thermal emission of 0.96. The back side was prepared for digital image correlation using etching procedure as described above for SEM-DIC. Ferromagnetic measurements using feritescope were performed before and after the tensile tests in order to evaluate the volume fraction of strain-induced α'-martensite. Finally, the tensile tests were corroborated, in addition, by in situ acoustic emission measurements. For more experimental details see [93].

The mechanical tests revealed that for strain rates in the range of $10^{-4} \leq \dot{\varepsilon} \leq 10^{-2}$ s^{-1} pronounced inhomogeneous macroscopic flow was observed characterized by numerous serrations occurring in stress-strain curves. Moreover, a shift of the onset of serrated plastic flow within the stress-strain curve was recorded with an increase

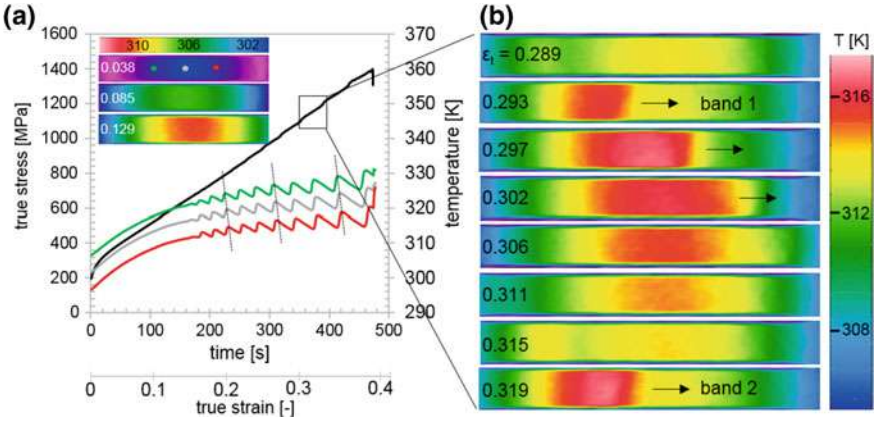

Fig. 15.11 Results of in situ infrared thermographic measurements during tensile tests of steel X5CrMnNi17-7-4 at room temperature and a nominal strain rate of 10^{-3} s^{-1}. **a** True stress versus true strain curve in combination with temperature-time curves measured at three points along the gauge length (green, grey, red points in the insert) and a sequence of infrared thermograms of the whole gauge length at three different strain levels for lower strain levels $\varepsilon < 0.15$. **b** Sequence of infrared thermograms of the whole gauge length for higher strain levels ($\varepsilon > 0.15$) showing the formation and propagation of two individual macroscopic bands of localized plastic strain. Reproduced from [92]

in strain rate. The tensile deformation was accompanied by both an increase in global temperature as well as volume fraction of strain-induced martensite. No serrated plastic flow was observed at the highest strain rate ($\dot{\varepsilon} = 10^{-1}$ s^{-1}), c.f. [93]. The serrations can be related, according to the common understanding in the literature [94], to the localization of plastic strain in macroscopic bands of several micrometer thickness propagating along the gauge length—known as PLC bands. The formation of these macroscopic bands of strain localizations is accompanied by temperature increase which can be recorded using infrared thermography [93]. Figure 15.11 shows exemplarily the results of in situ thermographic measurements during tensile test at room temperature and a nominal strain rate of 10^{-3} s^{-1}. Figure 15.11a shows the true stress versus true strain curve (black) in combination with temperature evolution profiles evaluated at three different points along the gauge length (green, grey, red). For better visibility, the temperature-time curves are shifted by $\Delta T = 5$ K. A continuous temperature increase was recorded in the first part of the stress-strain curve ($\varepsilon < 0.15$) which can be correlated directly with both the onset of plastic deformation as well as the martensitic phase transformation. It is well known from previous investigations [95] that the martensitic phase transformation in this CrMnNi steel variant with 3 wt% Ni starts immediately after passing the yield point. The course of temperature-time curves at higher strain levels ($\varepsilon > 0.15$) reveals clearly an oscillating behavior related to the formation and movement of PLC bands along the gauge length. The PLC bands form on the left side of the gauge length (green curve) and move along the gauge length (grey and red curve). The temperature maxima for the three different points

can be followed indicating that one band is followed by another one. In addition, Fig. 15.11b shows a sequence of thermograms taken at different subsequent strain levels (given as ε_t) illustrating the development and propagation of two individual bands along the gauge length. The macroscopic localization of strain inside these bands is related to an increase of temperature of few Kelvin. Moreover, the frequency of emerging PLC bands is quite high. Thus, the specimen gauge length cannot cool down completely before the next band appears resulting in a continuous increase of temperature over the whole test. The analysis of the recorded thermograms allowed for the evaluation of the number of PLC bands, the maximum temperature increase within individual bands as well as their velocity propagating along the gauge length in dependence on the nominal strain rate. It was revealed that with increasing strain rate the number of emerging bands is decreasing whereas the temperature itself is increasing [96].

Furthermore, the evolution of local strain fields related to PLC bands was evaluated by digital image correlation. For this purpose, optical micrographs were taken using a digital camera during the tensile tests at RT and different nominal strain rates. The strain fields were recorded on the opposite side of specimens used for IR-TG measurements. The initiation and propagation of bands along the gauge length is accompanied not only by an increase in temperature, as described already above, but also by an increase in strain. This is exemplarily shown in Fig. 15.12a–c. Figure 15.12a shows not the entire deformation process. Instead, only a short sequence between 0.22 and 0.32 of true strain is plotted. The thermograms and the calculated strain fields are related to numbers 1 to 6 indicated in the stress-strain curve showing the sequence of two consecutive PLC bands. In the present case, the PLC bands initiated always at the lower part of the gauge length and propagated in bottom-up direction on both sides of the specimen as seen from the thermograms and DIC images in Fig. 15.12b–c. The local strain fields are provided in terms of von Mises equivalent strain ε_{vM}. It turned out from the fully-coupled measurements that the PLC bands are characterized by both temperature and strain localization. Thus, the localized strain within an individual band is about 3%. In addition, the nominal strain rate has a significant influence on the formation of PLC bands. In general, it can be summarized

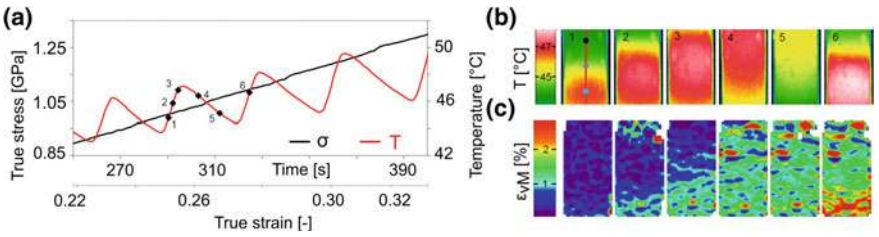

Fig. 15.12 Results of the full-field measurements on two opposite sides of the gauge length of the specimen of X5CrMnNi17-7-4 steel tested in tension at room temperature and a nominal strain rate of 10^{-3} s^{-1}. **a** Section of the true stress-true strain curve and the temperature-time curve. **b** Infrared thermograms taken at points 1 to 6 indicated in (**a**). **c** Corresponding local strain fields calculated for the opposite side of the gauge length. Partly reproduced from [93]

that as lower the strain rate is as more frequently PLC bands occurs. In contrast, both the increase in temperature as well as the velocity of PLC bands are smaller than at higher strain rates. Moreover, different band propagation directions were observed. Thus, at lower strain rates, bands nucleate at different places and run either top-down or bottom-up. At higher strain rates, bands nucleate either at the upper or lower part of the gauge length and propagate then in one direction only [96].

15.4.1.4 Local Hardness of Individual Microstructure Constituents Studied by Nanoindentation

In addition to microstructure evolution and kinetics of deformation processes, the local mechanical behavior of CrMnNi TRIP steel with medium austenite stability X5CrMnNi16-6-6 was investigated by nanoindentation. The focus was set on the local hardness of individual microstructural components (γ-austenite, ε-martensite and α'-martensite). To investigate the strain-hardening behavior, initial hardness of the austenite was determined on an undeformed reference specimen and compared to the local hardness of tensile pre-deformed specimen ($\varepsilon = 15\%$). For this purpose, different grain orientations were chosen both with respect to the loading axis during tensile pre-deformation as well as with respect to the indentation axis. Details on the experimental setup can be found in [60].

In the initial state, the measured indentation hardness is between 4.1 and 4.9 GPa and only slightly dependent on grain orientation. In accordance with literature [97], grain orientations with indentation axis near ⟨111⟩ show the highest indentation hardness. In some of the indentation experiments, pronounced pop-in events occurred during the indentation of undeformed austenite as shown exemplarily by a load-displacement curve in Fig. 15.13a. At about 550 μN a pronounced deviation from

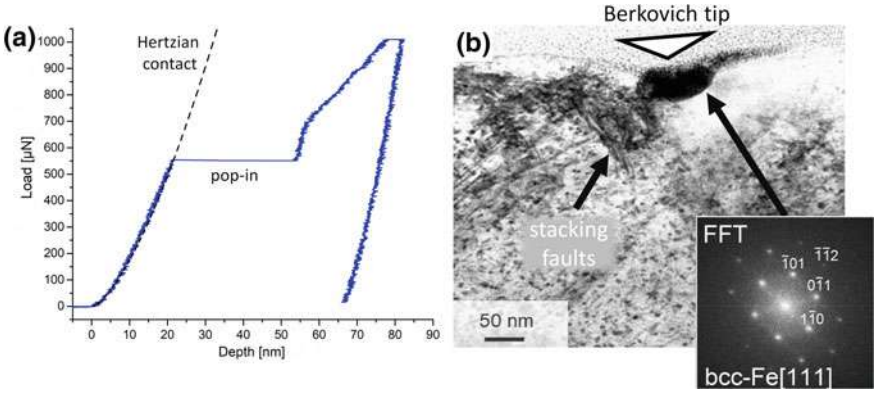

Fig. 15.13 Nanoindentation on undeformed austenite. **a** Load-displacement curve with occurring pop-in event and Hertzian elastic contact solution fitted to the elastic part of the curve. **b** α'-martensite nucleus formed during nanoindentation experiment with stacking faults located close to the indent

the Hertzian elastic contact solution (dashed line) is observed—the so-called pop-in event. The displacement of this single pop-in event is quite large of about 30 nm. In order to clarify whether the pop-in is the result of an avalanche-like movement of dislocations or of an indentation-induced martensitic phase transformation, a lamella was extracted across the indentation area using focused ion beam (FIB) technique. The lamella was investigated in TEM and the results are shown in Fig. 15.13b.

Figure 15.13b shows that directly below the indent an α'-martensite grain has been formed which was proofed by the diffraction pattern obtained from the Fast-Fourier Transformation of high-resolution TEM image (see insert). In the direct vicinity to the α'-martensite nucleus, stacking faults were found which are assumed to be caused by the indentation of the austenite. In order to examine whether α'-martensite formation can be regarded as the reason for the pop-in event, the theoretical displacement caused by α'-martensite transformation was calculated. The maximum shape strain of the martensitic transformation is assumed to be of 0.24 [98] for the case that the indentation axis is parallel to the direction of maximum shape change. The thickness of the α'-martensite nucleus was measured to be 50 nm which corresponds to a pop-in displacement of about 12 nm. Consequently, α'-martensite formation cannot be the only reason for the pop-in event which corresponds to a displacement of more than 30 nm. More likely, the combination of the formation of stacking faults and α'-martensite together caused this huge displacement. Ahn et al. [99] observed similar pop-in behavior in a high nitrogen steel and excluded also the α'-martensite formation as the only reason for the pop-in event.

In order to determine the indentation hardness of the microstructural constituents in the tensile pre-deformed state, indentation maps were placed within austenitic grains of different orientations covering all three microstructural constituents in a pre-deformed state of $\varepsilon = 15\%$: (i) austenite, (ii) deformation bands with ε-martensite, and (iii) α'-martensite grains. The indentation was performed with a load of 1 mN and the indents were placed with a minimum distance of 1.5 µm. An example for a grain with ⟨125⟩ as indentation axis is shown in Fig. 15.14 (see [60]).

Here, Fig. 15.14a, b show results of EBSD measurements for the area with indentation map and Fig. 15.14c of a single indent placed within the area of a deformation band yielding a pop-in event in the load-displacement curve. The area of FIB lamella for TEM investigations is indicated by white rectangle. Figure 15.14d–f show the corresponding t-SEM and TEM results. In the EBSD maps the austenitic phase is shown in grey, the ε-martensite bands in yellow and the α'-martensite in blue color. Details on all load-displacement curves and indentation hardness and modulus are summarized in [60]. In general, it can be summarized that the overall indentation hardness values of the tensile pre-deformed state are increased in average of about 19% compared to the non-deformed state as it was expected. In addition, an orientation dependency was found for indentation hardness values in the pre-deformed specimen. Thus, austenitic grains with ⟨101⟩ or ⟨111⟩ orientation of the loading axis during the tensile pre-deformation showed higher indentation hardness values compared to other grain orientations such as ⟨001⟩. These grain orientations are favored for the formation of largely extended stacking faults resulting in a significant reduction of mean free path of dislocations yielding pronounced strain hardening. In contrast,

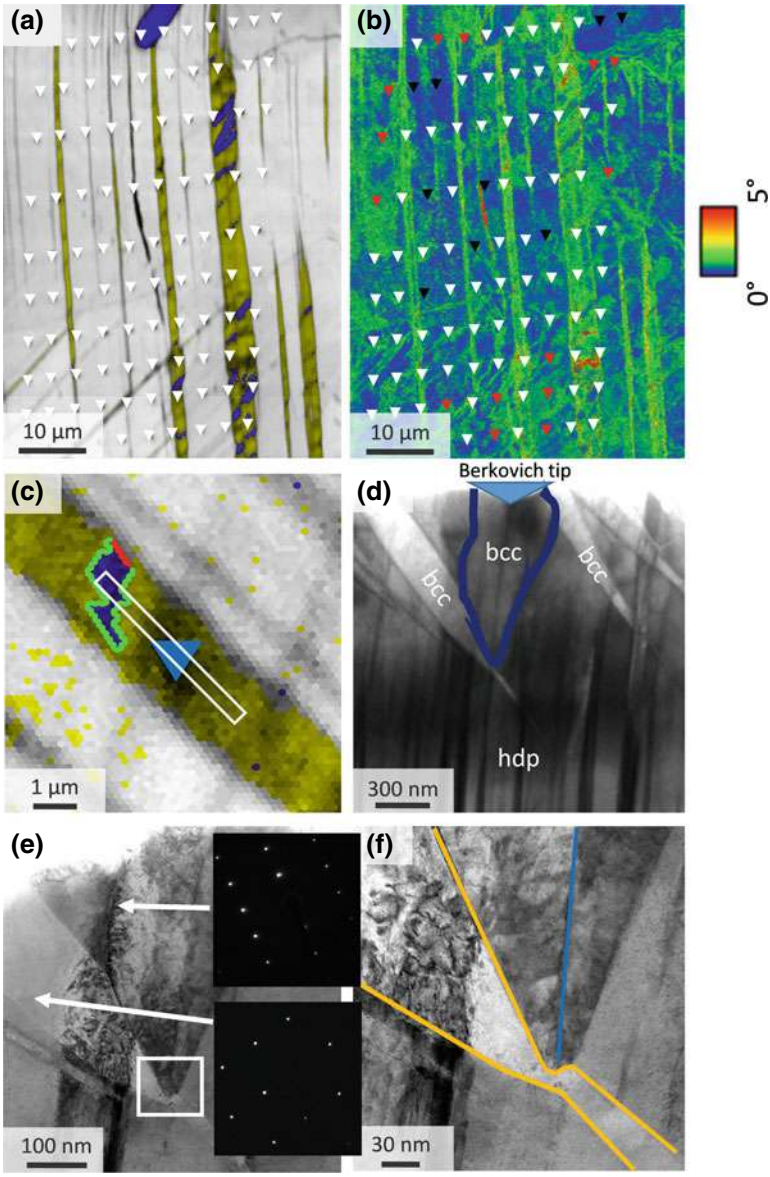

Fig. 15.14 Results of microstructural investigation complementing nanoindentation measurements on steel X5CrMnNi16-6-6. **a** EBSD phase map of austenitic grain with ⟨125⟩ orientation of the indentation axis. Grey—austenite, yellow—ε-martensite, blue—α'-martensite, indents marked by white triangles. **b** Overlay of Kernal average misorientation map (max. misorientation angle of 5°) with 10 × 10 indentation map. Indents corresponding to maximum or minimum indentation hardness are indicated by red and black triangles, respectively. **c** Detail of deformation band with ε-martensite and α'-martensite and an indent yielding pronounced pop-in event. Area for taking FIB lamella is indicated by white rectangle. **d** Transmission-SEM (t-SEM) micrograph of the FIB lamella. **e**, **f** Results of TEM investigations. Partly reproduced from [60]

grain orientations close to ⟨001⟩ are favored for slip of regular dislocations resulting in a lower density of deformation bands and α'-martensite nuclei causing lower strain hardening effect. Such an example is shown in Fig. 15.14a for orientation ⟨125⟩ of loading axis.

In addition, austenite orientations which showed increased slip of regular dislocations can experience clear differences in the strain hardening. Figure 15.14b shows a kernal average misorientation (KAM) map with marked indents within austenite. Red triangles correspond to indents within an austenite with high KAM and black triangles correspond to indents within austenite with low KAM. Thus, areas with increased KAM show an average indentation hardness increase of about 12% compared to indents within lower KAM. This is due to the higher defect density; the higher KAM is a result of a higher number of geometrically necessary dislocations and thus correlates with a higher dislocation density [100].

The indentation hardness of ε-martensite was always higher than the hardness of the deformed austenite and was between 5.7 and 8.5 GPa. A dependency of the hardness on the orientation of the ε-martensite was recognizable. (0001) perpendicular to the direction of indentation showed the highest indentation hardness. In addition, some ε-martensite orientations showed also a distinct pop-in behavior. Figure 15.14c shows a band contrast map with a deformation band consisting of ε-martensite and an α'-martensite nucleus which has formed by the pre-deformation. The green and red lines mark the Kurdjumov-Sachs orientation relationship [101] between α'/ε and α'/γ. The blue triangle marks the position of an indent with occurring pop-in event within ε-martensite. In order to investigate the reason for the pop-in event a FIB lamella was extracted (marked by white box). Figure 15.14d, e show the cross section of the extracted FIB lamella observed in SEM in transmission mode (t-SEM) and in TEM, respectively.

The lamella shows numerous bcc nuclei with a plate-like structure which are inclined at an angle of approximately 45°. By selected area diffraction (SAED) it was shown that all of that plate-like α'-martensite nuclei had the same orientation. Due to the similar orientation and morphology, it can be concluded that these α'-martensite nuclei are the result of the pre-deformation. Directly beneath the indent an additional bcc grain has formed. In contrast to all other martensite nuclei, this one has a different morphology and also a different orientation, which implies that this α'-martensite is the result of indentation. In addition, the 45° tilted α'-martensite grain shows a small misalignment which is marked by the white box in Fig. 15.14e and is shown in detail in Fig. 15.14f. This misalignment (marked by orange lines) is caused by the indentation-induced martensite. The expanding α'-martensite grain ran up to or even into the already existing deformation-induced α' martensite and caused a small shearing effect. Furthermore, the indentation-induced martensite contains a grain boundary (marked by blue line). SAED observations and the fact that just one pop-in event was noticeable in the load displacement curve indicate that the formed indentation-induced α'-martensite grains are twins [60].

The hardness of the α'-martensite introduced by the pre-deformation was determined to 6.3 GPa up to 10.5 GPa. However, the hardness of α'-martensite depends on several aspects. On the one hand, hardness is determined by the orientation of the

crystal. For example, α'-martensite grains with an orientation close to $\langle 111 \rangle$ showed the highest indentation hardness. Furthermore, the grain size does affect the determined indentation hardness since additional interfacial effects between dislocations and grain boundaries have to be considered. In addition, also the defect density of the studied α'-martensite additionally influences the determined indentation hardness [60].

15.4.2 Phase Transformation Behavior of Mg-PSZ Studied by Acoustic Emission

The phase transformation and damage behavior of MgO partially-stabilized zirconia (Mg-PSZ) provided by FRIATEC (Germany) was studied by acoustic emission corroborated by SEM investigations. The microstructure of the initial state before deformation in Fig. 15.15a shows polycrystalline grain structure with cubic-tetragonal crystal lattice, pores and spinels [102]. In particular, tetragonal lenses are embedded into a cubic matrix. Spinels are formed typically at the grain boundaries, but also inside grains. Moreover, in the vicinity of spinels a further microstructural feature becomes apparent—monoclinic lenses. This transformation of the cubic/tetragonal phase into the monoclinic phase in these regions is the consequence of a separation of the MgO as the stabilizer of the tetragonal phase occurring during the sinter process.

Figure 15.15b, c show the microstructure of Mg-PSZ after compression test up to 2 GPa. Both the martensitic phase transformation as well as the damage of Mg-PSZ can be revealed. Thus, band-like structures exhibiting monoclinic crystal lattice evolve under various angles with respect to the loading axis (horizontal) within some grains. This tetragonal/monoclinic phase transformation is associated with a volume expansion of about 4.9% [103] enabling enhanced damage tolerance of the ceramic due to crack-closure effects. However, pronounced damage is observed in addition to the phase transformation. Thus, numerous short cracks where observed within

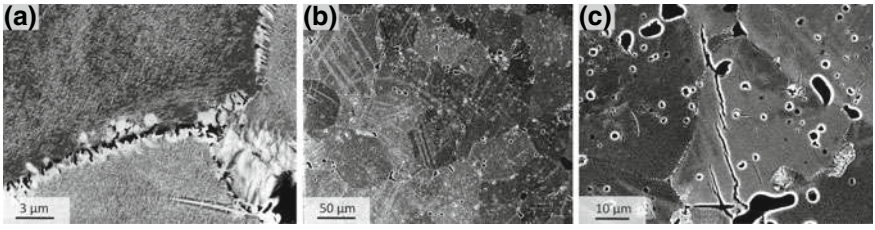

Fig. 15.15 Microstructure of Mg-PSZ. **a** Initial state showing tetragonal lenses in individual grains of Mg-PSZ. Secondary phases like spinel and silicates are formed at the grain boundaries leading to local transformation into monoclinic zirconia phase. **b** Microstructure of a Mg-PSZ after compression test up to 2 GPa showing both phase transformation and damage behavior. **c** Cracks running along monoclinic deformation bands

grains initiating either on pores or spinel precipitates. Cracks were also observed running along deformation bands with monoclinic structure (see Fig. 15.15c). The formation of cracks as well as the martensitic phase transformation release elastic waves within the Mg-PSZ which can be recorded as acoustic signals by a transducer placed at the specimen surface. For the in situ acoustic emission measurements a rectangular specimen of $2 \times 2 \times 4$ mm^3 was stepwise deformed under compression with stress intervals of 200 MPa in the stress range of 1.2–2 GPa applying partial unloading at each stress interval.

For the mechanical test, the push-pull loading stage described above for in situ tensile tests was modified using two compression platens made from tungsten-carbide. One side of the compression parts was manufactured as a ball-shaped scraper for self-centering of the whole setup including ceramic specimen. For each loading step the AE data stream was continuously recorded. Figure 15.16 shows the results of the compression tests and the acoustic emission measurements. Thus, Fig. 15.16a shows the stress versus compressive strain curves for five loading steps. In Fig. 15.16b, the complete AE data stream (grey) is shown together with the stress versus time curve for the last loading sequence between 1 and 2 GPa (grey curve in Fig. 15.16a). The results of the analysis of the AE data are summarized in Fig. 15.16c, d showing two

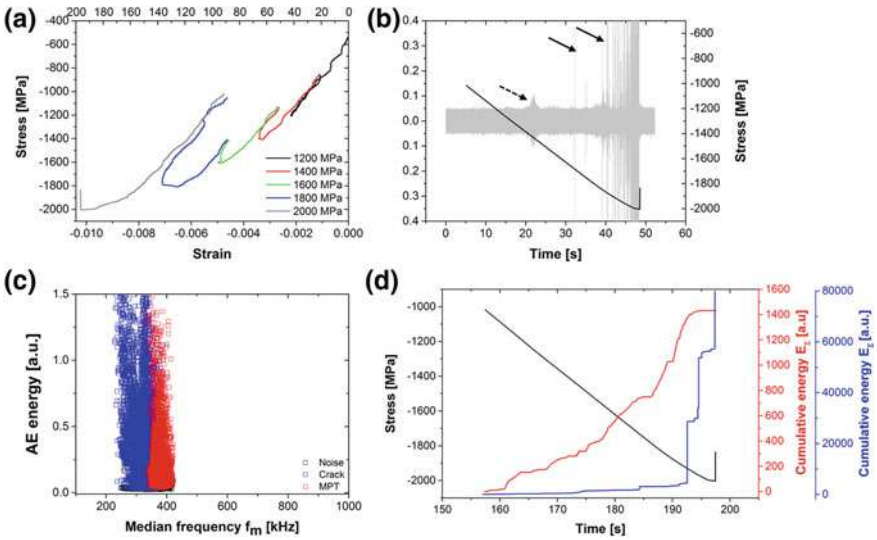

Fig. 15.16 Results of acoustic emission measurements during compression tests up to 2 GPa including partial unloading. **a** Stress-compressive strain curves. **b** Overlay of stress versus time curve and recorded acoustic emission stream measurement for the last loading cycle from 1 GPa up to 2 GPa. **c** Results of the AE cluster analysis showing two identified clusters with different properties (AE energy E and median frequency f_m) in frequency domain revealing two different source mechanisms: (i) phase transformation—red, (ii) crack formation—blue. **d** Temporal evolution of the two clusters during compression. Note the two different scales for the cumulative AE for both clusters

identified sources of acoustic emission (Fig. 15.16c) and their temporal evolution (Fig. 15.16d).

It becomes obvious that during the first loading sequence between 400 MPa and 1.2 GPa no pronounced changes occur in the specimen. Thus, the loading and unloading curves follow the same path without any change in the slope showing a fully elastic behavior. The same is observed from the acoustic emission. No special features beside the laboratory noise were detected. However, the situation is changing with increase in stress level applied to the specimen already starting with the second loading cycle between 800 MPa and 1.4 GPa. Here, a deviation of the stress-strain response for the loading and unloading path is observed above 1.2 GPa, which may be explained by damage occurring within the specimen or by the begin of phase transformation from tetragonal to monoclinic phase. This deviation between loading and unloading path becomes more pronounced with increase in applied stress levels. Thus, most pronounced difference is observed for the last loading sequence between 1.0 and 2.0 GPa, which finally led to the brittle failure of the specimen at 2.0 GPa. Moreover, a pronounced and increasing deviation from the elastic behavior is observed during the loading paths up to 1.6, 1.8 and 2.0 GPa giving rise to the assumption that a martensitic phase transformation occurred at these load levels. This assumption is well supported by the results of the AE data analysis. For these three stress levels, two different types of transient AE signals can be revealed from the complete data stream.

Whereas the first type is of high amplitude transient signals characterized by a very short rise time (close to the end of the data stream, bold arrows Fig. 15.16b), the second type is of low amplitude, but still transient signals with increased rise time (dashed arrow Fig. 15.16b). The results of the AE cluster analysis revealed two different clusters of signals (beside the laboratory noise), which can be related due to their different parameters in the frequency domain clearly to two different sources. Thus, cluster 1 contains all signals characterized by high AE energy and narrow band of median frequency around 300 kHz (blue symbols). Signals of this cluster are caused by initiation and propagation of brittle cracks. This is supported by the signals with the highest AE energies corresponding to the cracks leading to final failure (marked by bold arrows in Fig. 15.16b). Cluster 2 is composed by signals with lower AE energy compared to members of Cluster 1 and also a narrow band of median frequency at around 400 kHz (red symbols). Signals of this cluster are caused by the martensitic phase transformation from tetragonal to monoclinic phase (marked by dashed arrow in Fig. 15.16b). These findings are supported by the temporal evolution of these clusters over the entire compression path shown in Fig. 15.16d. Here, the evolution of the cumulated AE energy is shown for both clusters in combination with the stress versus time curve. Beside the different scale of cumulative AE energy, both clusters reveal also different temporal evolution. Whereas for Cluster 1 a moderate increase of E_{Σ} is observed until a significant rise right before the final failure, Cluster 2 shows a continuous increase until the end of the test. The results of the AE data analysis can be supported by additional XRD measurements for interrupted tests at different stress levels (1.2, 1.6, 1.8 GPa). At 2.0 GPa no XRD measurements were performed since the specimens failed and only

small pieces were retained. The phase analysis done by XRD revealed clearly an increase in the volume fraction of monoclinic phase from 18% in the undeformed state up to 36% obtained after compression test up to 1.8 GPa. Both the AE results and the results of XRD measurements are supported by literature data claiming on a transformation stress in compression of above 800 MPa for the tetragonal/monoclinic phase transformation [104].

15.4.3 Damage Behavior of TRIP Matrix Composite Studied by Digital Image Correlation

TRIP matrix composites made of TRIP steel X5CrMnNi16-6-6 and 10 vol% of Mg-PSZ were studied using in situ deformation in SEM both under uniaxial tensile or cyclic loading at room temperature. The TRIP matrix composites were manufactured by a powder metallurgical route and consolidated by uniaxial pressing at 1523 K. Typical microstructure is shown in Fig. 15.17. Here, different types of Mg-PSZ particles are visible. First of all, along grain boundaries or at the steel/ceramic interface additional phases enriched with silicon and aluminum were detected corresponding to spinel or silicate. In addition, different microstructures of Mg-PSZ

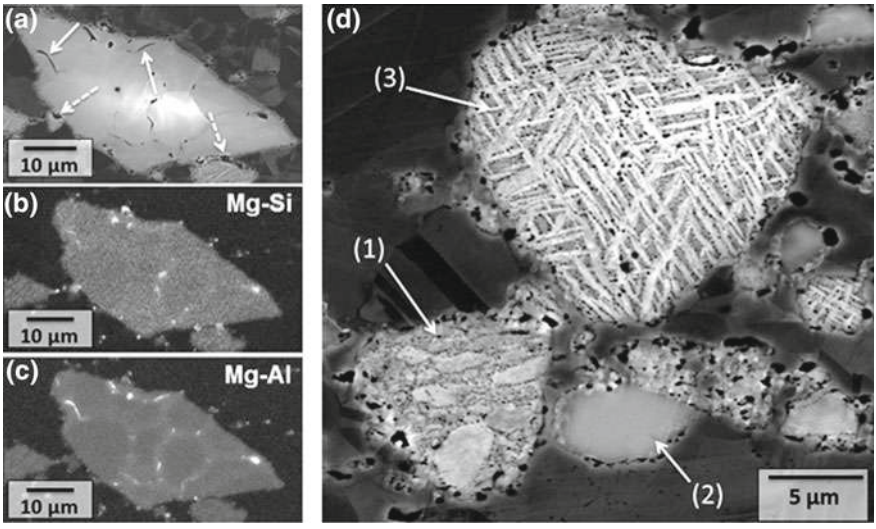

Fig. 15.17 Microstructure of Mg-PSZ particles embedded in steel matrix of X5CrMnNi16-6-6 after uniaxial pressing. **a**, **d** SEM micrographs in backscattered electron contrast. Spinel marked by bold white arrows. Silicate marked by dashed white arrows. **b**, **c** EDX element maps of Mg–Si (**b**) and Mg–Al (**c**). (**d**) Three different types of microstructures of Mg-PSZ particles. (1) Agglomerate of small monoclinic Mg-PSZ particles. (2) Cubic/tetragonal Mg-PSZ particle with monoclinic rime. (3) Mg-PSZ particle with monoclinic needles embedded in cubic/tetragonal matrix [105]

were observed such as (1) agglomerates of small monoclinic Mg-PSZ particles, (2) cubic/tetragonal Mg-PSZ particles with a rime of monoclinic structure in the vicinity of the steel/ceramic interface, and (3) large Mg-PSZ particles with monoclinic needles embedded in a cubic/tetragonal matrix. In the cubic/tetragonal areas of Mg-PSZ grains no tetragonal lenses as described above for the pure Mg-PSZ ceramic were observed. The formation of spinel or silicate particles at grain boundaries or interfaces of the ceramic is the consequence of diffusion processes of MgO as the stabilizer for the cubic/tetragonal phase. As a further consequence, the Mg-PSZ particles are destabilized and transform into the monoclinic phase already during the manufacturing process.

Figure 15.18 shows exemplarily the development of damage of a ceramic particle during cyclic loading with a total strain amplitude of $\varepsilon_{a,t} = 4 \times 10^{-3}$ as a function of number of cycles. Figure 15.18a shows the initial microstructure around individual Mg-PSZ particle demonstrating good bonding between steel matrix and ceramic particle. Nevertheless, spinel and silicate precipitates were found. Already after few cycles, the crack formation can be seen on a silicate at the interface between particle and steel matrix (see arrow Fig. 15.18b). The crack grows in the further course of cyclic loading (Fig. 15.18c) along the interface and leads, thus, to the decohesion of the particle from the steel matrix. At $N = 1750$, additional decohesion is clearly visible on the opposite side (see arrow Fig. 15.18c). Preferably the debonding of the particles occurs at boundaries perpendicular to the load direction starting at silicate precipitates. The second damage mechanism observed is the fracture of the ZrO_2 particles. Similar to the decohesion, the fracture occurs perpendicular to the load direction (horizontal). Furthermore, both the formation of deformation bands as well as the formation of α'-martensite within these bands was observed in austenitic grains of the steel matrix. However, within the ceramic particles no martensitic phase transformation was detected neither in the middle of the particle nor in the vicinity of cracks.

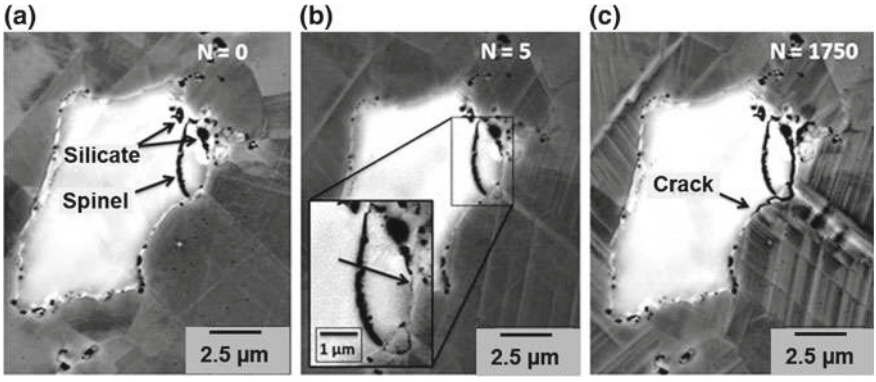

Fig. 15.18 Damage evolution on a Mg-PSZ particle in X5CrMnNi16-6-6 TRIP steel during cyclic deformation with a total strain amplitude of $\varepsilon_{a,t} = 4 \times 10^{-3}$. **a** Initial microstructure. **b** After 5 cycles. **c** After 1750 cycles. Load direction is horizontal [105]

Investigations on the damage behavior of TRIP-matrix composites were performed also under tensile loading at room temperature and were complemented by DIC calculations. Both the damage behavior as well as the strain localization within the austenitic matrix were studied. In comparison to DIC measurements on pure steel specimens, the application of DIC on composite materials is somehow more challenging. Thus, the etching procedure used for the steel specimens was not applicable since, in particular, the interface boundaries were attacked by the etching agent. To obtain a small-sized point pattern at the specimen surface a plasma process was used for the deposition of fine precipitates. Using this contrast, it was possible to perform DIC calculations for composite material under tensile load using SEM micrographs in secondary electron contrast. Figure 15.19 shows two SEM micrographs (Fig. 15.19a, b) taken at different macroscopic strain levels ($\varepsilon = 1.09\%$ and $\varepsilon = 3.47\%$) and the corresponding results of the DIC calculations in terms of von Mises equivalent strain (Fig. 15.19c, d). Both the SEM images as well as the local strain fields reveal that damage at the steel/ceramic interface occurs quite early in the deformation process already at 1% of elongation (marked by black arrows). In addition, the formation of deformation bands as well as α'-martensite were detected by DIC at strain levels of about $\varepsilon = 3.47\%$ (marked by white arrows). At $\varepsilon = 3.47\%$,

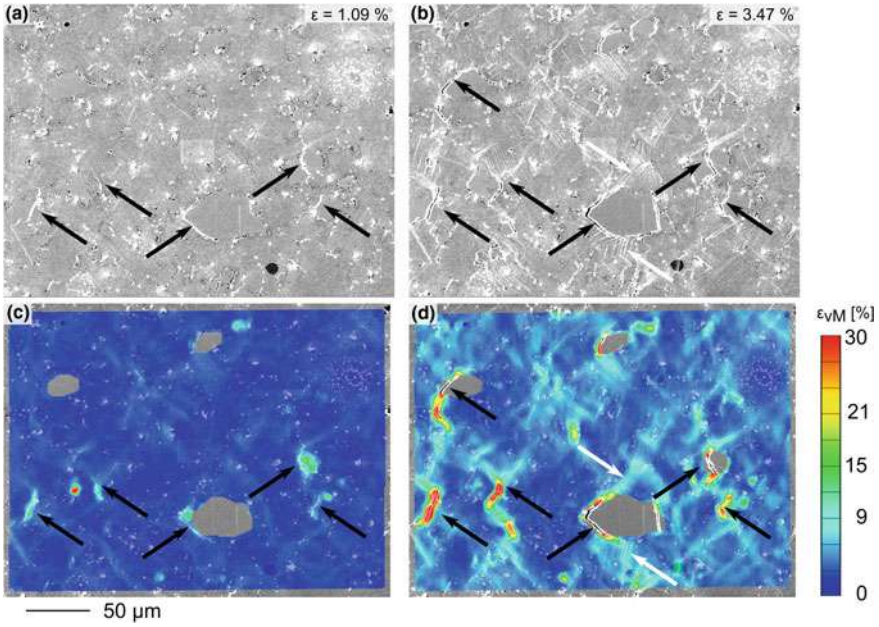

Fig. 15.19 Results of digital image correlation applied on SEM micrographs obtained during in situ tensile deformation at RT up to 4% global strain on TRIP matrix composite made of X5CrMnNi-16-6-6 with 10 vol% Mg-PSZ. (**a**, **b**) SEM micrographs in secondary electron contrast at $\varepsilon = 1.09\%$ (**a**) and $\varepsilon = 3.47\%$ (**b**), respectively. (**c**, **d**) Local strain fields obtained from DIC calculations at $\varepsilon = 1.09\%$ (**a**) and $\varepsilon = 3.47\%$ (**b**), respectively. Loading axis horizontal [92]

certain amount of steel/ceramic interface boundaries has been damaged and individual short cracks are grown together leading to final failure of the specimen (outside AOI). Furthermore, fracture of individual Mg-PSZ particles was also observed.

15.5 Conclusions

The local deformation behavior of high-alloy CrMnNi TRIP/TWIP steels, Q&P steels, MgO-partially stabilized zirconia and TRIP matrix composite have been studied using various in situ techniques such as (i) in situ deformation in scanning electron microscope in combination with digital image correlation, (ii) nanoindentation, (iii) acoustic emission measurements, and (iv) full-field measurements using infrared thermography and digital image correlation. The following general conclusions regarding the application of complementary in situ techniques can be drawn:

- The applied SEM-DIC technique for studies on strain localizations both in TRIP/TWIP as well as Q&P steels allowed a sub-micrometer resolution both at room temperature as well as at elevated temperatures enabling the calculation of the magnitude of shear for stacking fault mediated deformation bands, twin bundles and α'-martensite grains. Even in small regions (<5 μm) of interdendritic austenite in Q&P steel, the strain localization was measured for the fresh-formed martensite.
- The AE measurements during tensile deformation of CrMnNi TRIP/TWIP steels both at room temperature and at 373 K allowed the separation of the individual deformation mechanisms such as (i) dislocation glide, (ii) movement of partial-dislocations, (iii) twinning, and (iv) the martensitic phase transformation. The application of the ASK-cluster algorithm allowed to study the kinetics of these different deformation mechanisms. Furthermore, an excellent agreement of the temporal evolution of AE data related to martensitic phase transformation with the evolution of the martensitic volume fraction both experimentally obtained by ferromagnetic measurements as well as from the Olson-Cohen model was obtained.
- The application of infrared thermography and digital image correlation based on optical microscopy allowed the investigation of propagating macroscopic strain localizations in terms of Portevin Le Chatelier effect in the steel with the lowest austenite stability. Macroscopic strain is localized in PLC bands causing also a temperature increase. The propagating bands were well characterized and analyzed by both full-field measurement techniques. A good correlation of temperature fields and local strain fields was obtained, which allowed the determination of characteristic parameters for the evolution and propagation of these bands.
- Nanoindentation experiments performed on non-deformed and pre-deformed CrMnNi TRIP steel specimens revealed both pop-in effects caused by either martensitic phase transformation and/or formation of stacking faults as well as an

orientation dependence of the indentation hardness. Furthermore, different indentation hardness values were obtained with increasing values in the following order: (i) pre-deformed austenite, (ii) deformation bands consisting of stacking faults, and (iii) α'-martensite.

- For MgO-partially stabilized zirconia, the application of AE measurements during compressive loading up to 2 GPa revealed that the onset of phase transformation from tetragonal to monoclinic phase occurs above 1200 MPa. As a second AE source the formation of cracks leading to final failure of the specimens was identified.
- The deformation and damage behavior of TRIP matrix composite studied by in situ tensile and cyclic loading experiments in SEM revealed that the steel/ceramic interface undergoes a decohesion quite early during the deformation process, mainly caused by the presence of silicate precipitates at the interface. Beside this fact, the application of the DIC techniques bears also some difficulties. Thus, the contrast patterning at the surface for getting high-resolution DIC results is challenging. Nevertheless, first results showed that both strain localization inside deformation bands in the steel matrix as well as crack initiation and propagation at the steel/ceramic interface can be detected by DIC.

Acknowledgements This work was funded by the German Research Foundation (Deutsche Forschungsgemeinschaft, DFG) in subproject B5, and was created as part of the Collaborative Research Center TRIP-Matrix-Composites (Project number 54473466—CRC 799). The experimental work and research of Dipl.-Ing. Christian Segel is gratefully acknowledged providing substantial contribution on in situ testing in SEM and DIC. In addition, the authors thank Dipl.-Ing. Alexandra Illgen for performing the investigations on Portevin Le Chatelier effect using thermography and digital image correlation. Dr. Mikhail Motylenko is gratefully acknowledged for TEM investigations and Dr. Christian Schimpf for XRD analysis on the Q&P steel. Special thanks go to Prof. Alexei Vinogradov and Ph.D. Mikhail Linderov for their support regarding the AE data acquisition and analysis. In addition, many thanks go to K. Zuber, A. Leuteritz and R. Prang for preparation of specimens for SEM and TEM investigations and to G. Schade for support during mechanical tests.

References

1. D. Raabe, D. Ponge, O. Dmitrieva, B. Sander, Scr. Mater. **60**, 1141 (2009). https://doi.org/10.1016/j.scriptamat.2009.02.062
2. G.B. Olson, M. Cohen, J. Less-Common Metals **28**, 107 (1972)
3. A. Weidner, S. Martin, V. Klemm, U. Martin, H. Biermann, Scripta Mater. **64**, 513 (2011). https://doi.org/10.1016/j.scriptamat.2010.11.028
4. S. Martin, C. Ullrich, D. Šimek, U. Martin, D. Rafaja, J. Appl. Crystallogr. **44**, 779 (2011). https://doi.org/10.1107/S0021889811019558
5. S. Martin, C. Ullrich, D. Rafaja, Mater. Today: Proc. **2**, S643 (2015). https://doi.org/10.1016/j.matpr.2015.07.366
6. A. Jahn, A. Kovalev, A. Weiß, S. Wolf, L. Krüger, P.R. Scheller, Steel Res. Int. **82**, 39 (2011). https://doi.org/10.1002/srin.201000228

7. A. Jahn, A. Kovalev, A. Weiβ, P.R. Scheller, S. Wolf, L. Krüger, S. Martin, U. Martin, in *Composite Structures* (2009)
8. S. Martin, S. Wolf, U. Martin, L. Krüger, D. Rafaja, Metall. Mater. Trans. A **47**, 49 (2016). https://doi.org/10.1007/s11661-014-2684-4
9. H. Biermann, A. Glage, M. Droste, Metall. Mater. Trans. A **47**, 84 (2016). https://doi.org/10.1007/s11661-014-2723-1
10. D. Kulawinski, S. Ackermann, A. Seupel, T. Lippmann, S. Henkel, M. Kuna, A. Weidner, H. Biermann, Mater. Sci. Eng., A **642**, 317 (2015). https://doi.org/10.1016/j.msea.2015.06.083
11. R. Eckner, L. Krüger, M. Motylenko, A.S. Savinykh, S.V. Razorenov, G.V. Garkushin, EPJ Web Conf. **183**, 03007 (2018). https://doi.org/10.1051/epjconf/201818303007
12. S. Ackermann, S. Martin, M.R. Schwarz, C. Schimpf, D. Kulawinski, C. Lathe, S. Henkel, D. Rafaja, H. Biermann, A. Weidner, Metall. Mater. Trans. A **47**, 95 (2016). https://doi.org/10.1007/s11661-015-3082-2
13. D. Rafaja, C. Krbetschek, D. Borisova, G. Schreiber, V. Klemm, Thin Solid Films **530**, 105 (2013). https://doi.org/10.1016/j.tsf.2012.07.067
14. A. Weidner, A. Glage, H. Biermann, Proced. Eng. **2**, 1961 (2010). https://doi.org/10.1016/j.proeng.2010.03.211
15. D. Borisova, V. Klemm, S. Martin, S. Wolf, D. Rafaja, Adv. Eng. Mater. **15**, 571 (2013). https://doi.org/10.1002/adem.201200327
16. A. Jahn, A. Kovalev, A. Weiß, P.R. Scheller, Steel Res. Int. **82**, 1108 (2011). https://doi.org/10.1002/srin.201100063
17. C. Weigelt, G. Schmidt, C.G. Aneziris, R. Eckner, D. Ehinger, L. Krüger, C. Ullrich, D. Rafaja, J. Alloys Compd. **695**, 9 (2017). https://doi.org/10.1016/j.jallcom.2016.10.176
18. A. Weidner, A. Müller, A. Weiss, H. Biermann, Mater. Sci. Eng., A **571**, 68 (2013). https://doi.org/10.1016/j.msea.2013.02.008
19. M. Wendler, C. Ullrich, M. Hauser, L. Krüger, O. Volkova, A. Weiß, J. Mola, Acta Mater. **133**, 346 (2017). https://doi.org/10.1016/j.actamat.2017.05.049
20. M. Droste, C. Ullrich, M. Motylenko, M. Fleischer, A. Weidner, J. Freudenberger, D. Rafaja, H. Biermann, Int. J. Fatigue **106**, 143 (2018). https://doi.org/10.1016/j.ijfatigue.2017.10.001
21. D. Ehinger, L. Krüger, U. Martin, C. Weigelt, C.G. Aneziris, Steel Res. Int. **83**, 565 (2012). https://doi.org/10.1002/srin.201100302
22. S. Martin, S. Wolf, U. Martin, L. Krüger, SSP **172–174**, 172 (2011). https://doi.org/10.4028/www.scientific.net/SSP.172-174.172
23. W. Roberts, B. Lehtinen, K.E. Easterling, Acta Metall. **24**, 745 (1976). https://doi.org/10.1016/0001-6160(76)90109-7
24. H. Zhou, L. Mishnaevsky, P. Brøndsted, J. Tan, L. Gui, Chin. Sci. Bull. **55**, 1199 (2010). https://doi.org/10.1007/s11434-009-0560-1
25. J. Geathers, C.J. Torbet, J.W. Jones, S. Daly, Int. J. Fatigue **70**, 154 (2015). https://doi.org/10.1016/j.ijfatigue.2014.09.007
26. D. Yan, C.C. Tasan, D. Raabe, Acta Mater. **96**, 399 (2015). https://doi.org/10.1016/j.actamat.2015.05.038
27. M. Grediac, F. Hild, *Full-Field Measurements and Identification in Solid Mechanics* (Wiley, New York, NY, 2012)
28. M. Grédiac, Compos. A **35**, 751 (2004). https://doi.org/10.1016/j.compositesa.2004.01.019
29. H. Schreier, J.-J. Orteu, M.A. Sutton, *Image Correlation for Shape, Motion and Deformation Measurements* (Springer, US, Boston, MA, 2009)
30. C.C. Tasan, J.P.M. Hoefnagels, M.G.D. Geers, Scr. Mater. **62**, 835 (2010). https://doi.org/10.1016/j.scriptamat.2010.02.014
31. A. Weidner, C. Segel, H. Biermann, Mater. Lett. **143**, 155 (2015). https://doi.org/10.1016/j.matlet.2014.12.098
32. F. Di Gioacchino, J. Quinta da Fonseca, Exp. Mech. **53**, 743 (2013). https://doi.org/10.1007/s11340-012-9685-2
33. M.-M. Wang, J.-C. Hell, C.C. Tasan, Scr. Mater. **138**, 1 (2017). https://doi.org/10.1016/j.scriptamat.2017.05.021

34. H. Ghadbeigi, C. Pinna, S. Celotto, Mater. Sci. Eng., A **588**, 420 (2013). https://doi.org/10.1016/j.msea.2013.09.048
35. H. Na, S. Nambu, M. Ojima, J. Inoue, T. Koseki, Scr. Mater. **69**, 793 (2013). https://doi.org/10.1016/j.scriptamat.2013.08.030
36. N.A. Fouad, T. Richter, *Leitfaden Thermografie im Bauwesen: Theorie, Anwendungsgebiete, praktische Umsetzung*, 4., überarb. und erw. Aufl (Fraunhofer IRB-Verl, Stuttgart, 2012)
37. S. Bagavathiappan, B.B. Lahiri, T. Saravanan, J. Philip, T. Jayakumar, Infrared Phys. Technol. **60**, 35 (2013). https://doi.org/10.1016/j.infrared.2013.03.006
38. W. Boas, M.E. Hargreaves, Proc. R. Soc. A **193**, 89 (1948)
39. W.S. Farren, G.I. Taylor, Proc. Royal Soc. A: Math. Phys. Eng. Sci. **107**, 422 (1925). https://doi.org/10.1098/rspa.1925.0034
40. E.A. Pieczyska, S.P. Gadaj, W.K. Nowacki, H. Tobushi, Exp. Mech. **46**, 531 (2006). https://doi.org/10.1007/s11340-006-8351-y
41. A. Saeed-Akbari, A.K. Mishra, J. Mayer, W. Bleck, Metall. Mater. Trans. A **43**, 1705 (2012). https://doi.org/10.1007/s11661-011-1070-8
42. L. Bodelot, E. Charkaluk, L. Sabatier, P. Dufrénoy, Mech. Mater. **43**, 654 (2011). https://doi.org/10.1016/j.mechmat.2011.08.006
43. L. Chen, J.-K. Kim, S.-K. Kim, G.-S. Kim, K.-G. Chin, B.C. De Cooman, Steel Res. Int. **81**, 552 (2010). https://doi.org/10.1002/srin.201000044
44. C.U. Große, M. Ohtsu (eds.), *Acoustic Emission Testing: Basics for Research—Applications in Civil Engineering* (Springer, Berlin, 2008)
45. A. Vinogradov, A. Lazarev, M. Linderov, A. Weidner, H. Biermann, Acta Mater. **61**, 2434 (2013). https://doi.org/10.1016/j.actamat.2013.01.016
46. E. Pomponi, A. Vinogradov, MSSP **40**, 791 (2013). https://doi.org/10.1016/j.ymssp.2013.03.017
47. C.B. Scruby, J. Phys. E: Sci. Instrum. 946 (1987)
48. A. Weidner, H. Biermann, JOM **67**, 1729 (2015). https://doi.org/10.1007/s11837-015-1456-y
49. A. Vinogradov, M. Nadtochiy, S. Hashimoto, S. Miura, Mater. Trans., JIM **36**, 496 (1995) https://doi.org/10.2320/matertrans1989.36.496
50. A. Vinogradov, A. Lazarev, Scr. Mater. **66**, 745 (2012). https://doi.org/10.1016/j.scriptamat.2012.01.053
51. S.M.C. van Bohemen, Phil. Mag. **95**, 210 (2015). https://doi.org/10.1080/14786435.2014.994574
52. M.L. Linderov, C. Segel, A. Weidner, H. Biermann, A.Y. Vinogradov, Phys. Met. Metall. **119**, 388 (2018). https://doi.org/10.1134/S0031918X18040130
53. M. Mandel, W. Kietov, L. Krueger, Defect Diffus. Forum **367**, 42 (2016). https://doi.org/10.4028/www.scientific.net/DDF.367.42
54. W.C. Oliver, G.M. Pharr, J. Mater. Res. **7**, 1564 (1992). https://doi.org/10.1557/JMR.1992.1564
55. K.L. Johnson, *Contact Mechanics* (Cambridge University Press, Cambridge, 1985)
56. Y. Wang, D. Raabe, C. Klüber, F. Roters, Acta Mater. **52**, 2229 (2004). https://doi.org/10.1016/j.actamat.2004.01.016
57. C. Begau, A. Hartmaier, E.P. George, G.M. Pharr, Acta Mater. **59**, 934 (2011). https://doi.org/10.1016/j.actamat.2010.10.016
58. T.-H. Ahn, C.-S. Oh, D.H. Kim, K.H. Oh, H. Bei, E.P. George, H.N. Han, Scr. Mater. **63**, 540 (2010). https://doi.org/10.1016/j.scriptamat.2010.05.024
59. A. Weidner, U.D. Hangen, H. Biermann, Philos. Mag. Lett. **94**, 522 (2014). https://doi.org/10.1080/09500839.2014.941027
60. R. Lehnert, A. Weidner, M. Motylenko, H. Biermann, Adv. Eng. Mater. (2019). https://doi.org/10.1002/adem.201800801
61. A. Weiss, H. Gutte, M. Radtke, P.R. Scheller, WO 2008/009722 A1 (24 Jan 2008)
62. D. Qi-Xun, W. A.-D. Xiao-Nong Cheng, L. Xin-Min, Chin. Phys. **11**, 596 (2002) https://doi.org/10.1088/1009-1963/11/6/315

63. A. Glage, A. Weidner, H. Biermann, Steel Res. Int. **82**, 1040 (2011). https://doi.org/10.1002/srin.201100080
64. J. Mola, B.C. De Cooman, Metall. Mat. Trans. A **44**, 946 (2013). https://doi.org/10.1007/s11661-012-1420-1
65. M. Wendler, M. Hauser, O. Fabrichnaya, L. Krüger, A. Weiß, J. Mola, Mater. Sci. Eng., A **645**, 28 (2015). https://doi.org/10.1016/j.msea.2015.07.084
66. R. Lehnert, A. Weidner, C. Schimpf, M. Wendler, H. Biermann, Materialia 100498 (2019) https://doi.org/10.1016/j.mtla.2019.100498
67. S. Martin, H. Berek, C.G. Aneziris, U. Martin, D. Rafaja, J. Appl. Crystall. **45**, 1136 (2012). https://doi.org/10.1107/S0021889812038733
68. R.H.J. Hannink, P.M. Kelly, B.C. Muddle, J. Am. Ceram. Soc. **83**, 461 (2004). https://doi.org/10.1111/j.1151-2916.2000.tb01221.x
69. A.G. Evans, A.H. Heuer, J. Am. Ceram. Soc. **63**, 241 (1980). https://doi.org/10.1111/j.1151-2916.1980.tb10712.x
70. D.L. Porter, A.G. Evans, A.H. Heuer, Acta Metall. **27**, 1649 (1979). https://doi.org/10.1016/0001-6160(79)90046-4
71. D.L. Porter, A.H. Heuer, J. Am. Ceram. Soc. **62**, 298 (1979). https://doi.org/10.1111/j.1151-2916.1979.tb09484.x
72. R.H.J. Hannink, J. Mater. Sci. **13**, 2487 (1978). https://doi.org/10.1007/BF00808066
73. C.G. Aneziris, W. Schärfl, H. Biermann, U. Martin, Int. J. Appl. Ceram. Technol. **6**, 727 (2009). https://doi.org/10.1111/j.1744-7402.2008.02321.x
74. S. Martin, S. Richter, A. Poklad, H. Berek, S. Decker, U. Martin, L. Krüger, D. Rafaja, J. Alloys Compd. **577**, S578 (2013). https://doi.org/10.1016/j.jallcom.2012.02.014
75. H. Berek, A. Yanina, C. Weigelt, C.G. Aneziris, Steel Res. Int. **82**, 1094 (2011). https://doi.org/10.1002/srin.201100064
76. A. Glage, C. Weigelt, J. Räthel, H. Biermann, Adv. Eng. Mater. **15**, 550 (2013). https://doi.org/10.1002/adem.201200334
77. S. Martin, S. Richter, S. Decker, U. Martin, L. Krüger, D. Rafaja, Steel Res. Int. **82**, 1133 (2011). https://doi.org/10.1002/srin.201100099
78. R. Eckner, M. Krampf, C. Segel, L. Krüger, Mech. Compos. Mater. **51**, 707 (2016). https://doi.org/10.1007/s11029-016-9541-z
79. S. Martin, S. Decker, L. Krüger, U. Martin, D. Rafaja, Adv. Eng. Mater. **15**, 600 (2013). https://doi.org/10.1002/adem.201200330
80. A. Glage, S. Martin, S. Decker, C. Weigelt, M. Junghanns, C.G. Aneziris, U. Martin, L. Krüger, H. Biermann, Steel Res. Int. **83**, 554 (2012). https://doi.org/10.1002/srin.201100288
81. S. Prüger, L. Mehlhorn, U. Mühlich, M. Kuna, Adv. Eng. Mater. **15**, 542 (2013). https://doi.org/10.1002/adem.201200323
82. GOM GmbH, *ARAMIS GOM Optical Measuring Techniques* (2008)
83. H. Schumann, Krist. Tech. **9**, 1141 (1974)
84. *VirtualDub* (n.d.)
85. Chemnitzer Werkstoffmechanik GmbH, *VEDDAC* (Chemnitz, 2017)
86. L. Lutterotti, S. Matthies, H. Wenk, CPD Newslett. **21**, 14 (1999)
87. J. Ågren, Scr. Metall. 1507 (1986)
88. P.J. Jacques, F. Delannay, J. Ladrière, Metall. Mater. Trans. A **32**, 2759 (2001). https://doi.org/10.1007/s11661-001-1027-4
89. D. De Knijf, R. Petrov, C. Föjer, L.A.I. Kestens, Mater. Sci. Eng., A **615**, 107 (2014). https://doi.org/10.1016/j.msea.2014.07.054
90. M. Linderov, C. Segel, A. Weidner, H. Biermann, A. Vinogradov, Mater. Sci. Eng., A **597**, 183 (2014). https://doi.org/10.1016/j.msea.2013.12.094
91. G.B. Olson, M. Cohen, Metall. Mater. Trans. A **6**, 791 (1975)
92. A. Weidner, *Deformation mechanisms of TRIP/TWIP steels—in situ characterization techniques* (Springer Nature, Berlin, 2020)
93. A. Müller, C. Segel, M. Linderov, A. Vinogradov, A. Weidner, H. Biermann, Metall. Mater. Trans. A **47**, 59 (2016). https://doi.org/10.1007/s11661-015-2953-x

94. A. Portevin, F. Le Chatelier, Acad. Sci. **176**, 507 (1923)
95. H. Biermann, J. Solarek, A. Weidner, Steel Res. Int. **83**, 512 (2012). https://doi.org/10.1002/srin.201100293
96. A. Weidner, A. Müller, H. Biermann, Mater. Today: Proc. **2**, S623 (2015). https://doi.org/10.1016/j.matpr.2015.07.361
97. J.J. Roa, G. Fargas, A. Mateo, E. Jiménez-Piqué, Mater. Sci. Eng., A **645**, 188 (2015). https://doi.org/10.1016/j.msea.2015.07.096
98. S. Morito, H. Tanaka, R. Konishi, T. Furuhara, T. Maki, Acta Mater. **51**, 1789 (2003). https://doi.org/10.1016/S1359-6454(02)00577-3
99. T.-H. Ahn, S.B. Lee, K.-T. Park, K.H. Oh, H.N. Han, Mater. Sci. Eng., A **598**, 56 (2014). https://doi.org/10.1016/j.msea.2014.01.030
100. M. Calcagnotto, D. Ponge, E. Demir, D. Raabe, Mater. Sci. Eng., A **527**, 2738 (2010). https://doi.org/10.1016/j.msea.2010.01.004
101. G. Kurdjumow, G. Sachs, Zeitschrift Für Physik **64**, 325 (1930). https://doi.org/10.1007/BF01397346
102. D. Pavlyuchkov, S. Martin, B. Reichel, C. Weigelt, O. Fabrichnaya, Adv. Eng. Mater. **17**, 1323 (2015). https://doi.org/10.1002/adem.201400521
103. Y. Ma, E.H. Kisi, J.K. Shane, A.J. Studer, J. Am. Ceram. Soc. **87**, 465 (2004)
104. L.S. Pan, S. Horibe, J. Mater. Sci. **31**, 6523 (1996). https://doi.org/10.1007/BF00356258
105. C. Segel, A. Weidner, H. Biermann, in (Verbundwerkstoffe Tagungsband Chemnitz, 2013)

Chapter 16
X-Ray Computer Tomography for Three-Dimensional Characterization of Deformation and Damage Processes

Harry Berek, Marie Oppelt and Christos G. Aneziris

Abstract The investigation of phase transformations in metastable ceramic systems such as zirconia often requires local phase analysis within the areas of interest. Electron backscatter diffraction is a suitable method. The effect of the combination with focused ion beam sample preparation was determined in this work. In addition metal matrix compositemetal matrix composite honeycombs and foams as well as beads were investigated. The foams and honeycombs were composed of austenitic steel exhibiting TRansformation Induced Plasticity (TRIP) and magnesia partially stabilized zirconia. Both components exhibit martensitic phase transformation during deformation, thus generating the potential for improved mechanical properties such as strength, ductility, and energy absorption capability. The aim of these investigations was to show that stress-assisted phase transformations within the ceramic reinforcement correspond to strong local deformation, and to determine whether they can trigger martensitic phase transformations in the steel matrix. To this end, in situ interrupted compression experiments were performed in an X-ray Computed Tomography Device (XCT). By using a recently developed reconstruction algorithm, local deformation was calculated and regions of interest were defined. Corresponding cross sections were prepared and used to analyze the local phase composition by electron backscatter diffraction. The results show a strong correlation between local deformation and phase transformation.

16.1 Introduction

Metal matrix composites (MMCs) have been in the focus of research and development for many years. The growing demand on light-weight materials with acceptable mechanical properties is one reason. In general, the metal matrix consists of low-density materials like aluminum or magnesium. A new generation of MMCs, the

H. Berek · M. Oppelt (✉) · C. G. Aneziris
Institute of Ceramic, Glass and Construction Materials, Technische Universität Bergakademie Freiberg, Agricolastr. 17, 09599 Freiberg, Germany
e-mail: marie.oppelt@ikgb.tu-freiberg.de

H. Biermann and C. G. Aneziris (eds.), *Austenitic TRIP/TWIP Steels and Steel-Zirconia Composites*, Springer Series in Materials Science 298,
https://doi.org/10.1007/978-3-030-42603-3_16

so-called TRIP-matrix composites, has been developed within the last decade [1, 2]. Its constituents are TRIP steel and Mg-PSZ ceramic particles. The steel matrix of these MMCs exhibits a TRIP effect (TRansformation Induced Plasticity), thus possessing excellent mechanical properties with concurrent high strength and high ductility [3]. The TRIP effect is caused by a deformation induced martensitic phase transformation from austenite (fcc) to α'-martensite (bcc) via an intermediate state of highly faulted austenite or ε-martensite (hcp).

There are three different Zirconia modifications; namely cubic ($2650\ \mathrm{K} < T < T_\mathrm{m}$), tetragonal ($1478\ \mathrm{K} < T < 2650\ \mathrm{K}$), and monoclinic ($T < 1478\ \mathrm{K}$) [4]. The phase transformation from the tetragonal phase to the monoclinic phase is accompanied by a volume expansion of 3–5%, which leads to deformations in the areas surrounding the zirconia particles and high shear. The tetragonal high-temperature phase can be stabilized down to room temperature by the addition of certain stabilizers as Y_2O_3, CaO, or MgO. Partially stabilized zirconia exhibits a stress-assisted martensitic phase transformation [5]. In the TRIP matrix composites, MgO partially stabilized zirconia (Mg-PSZ) is used. The combination of the deformation-induced phase transformation of the steel matrix with the stress-assisted martensitic phase transformation of the Mg-PSZ produces composite materials with high damage tolerance [6]. This opens up a wide field of application for high-strength materials that possess the capability of absorbing mechanical energy during, for example, crash loading.

Suitable designs for this purpose are in particular honeycomb structures, foams and hollow spheres. They offer a combination of low density and high energy absorption capability. Therefore, in situ deformation experiments of such specimens were performed by X-ray computed tomography XCT. The aim was, in addition to the three-dimensional mapping of deformation and damage, to investigate the relationship between local deformation and local phase composition. This should also allow statements on the trigger stress. Wide space occupied the development of the required investigation methods. For the in situ compression deformation in the XCT a special apparatus was developed and built. This allows forces up to 100 kN. Furthermore, it was necessary to carry out local phase analysis with a resolution of less than 1 µm. A suitable method for this is electron backscatter diffraction (EBSD) [7]. This is a surface-sensitive method. The information depth is a maximum of 100 nm. In this near-surface area, no disturbances of the original deformation-related microstructure due to sample processing must be present. Therefore, methods of target preparation had to be developed. It was ascertained that the local chemical composition of the examined MMC has a decisive influence on the local phase composition. In particular, the ZrO_2 particles can be destabilized in the sintering process. This reduces the fraction of metastable (transformable) phases. The result is the formation of silicates and spinels from reactions of impurities in the powder constituents used and an associated diffusion of the stabilizers to the steel/ceramic interfaces. The consequence is a wide dispersion of the local phase composition. The corresponding distribution functions must be determined in order to be able to describe the influence of a deformation on the phase composition [8, 9].

Within this work the target preparation for a optimal EBSD and XCT analysis of composites was investigated [10]. One method for determining the mechanical

properties of small samples at relatively small forces is the small punch test. First researches has been conducted. Furthermore MMC foams [11] and honeycombs [12] were examined. The aim of these investigations was to show that stress-assisted phase transformations within the ceramic reinforcement correspond to strong local deformation, and to determine whether they can trigger martensitic phase transformations in the steel matrix. Besides, in situ interrupted compression experiments were performed in an X-ray computed tomography device. Furthermore composite beads with graded layer structures (prepared with the alginate gelation technology) were examined and valued with X-ray computed tomography [13].

16.2 Experimental Details

Figure 16.1 shows the used XCT CT-Alpha from ProCon X-Ray Garbsen. It displays the punctiform X-ray source, the rotation table and the flat detector. Alternatively, two different X-ray sources can be used. Three different detectors were used. The technical data are:

- Directional ray tube 225 kV, Feinfocus Garbsen, Germany, 2008
- Transmission tube 160 kV, Feinfocus Garbsen, Germany, 2008
- Detector Hamamatsu C7942SK-05, Hamamatsu Photonics K.K. Hamamatsu City, Japan, 2008, 2400 × 2400 pixel, 50 µm × 50 µm pixel size
- Detector Dexela 1512, 1944 × 1536 pixel, 75 µm × 75 µm pixel size
- Detector PerkinElmer XRD 1620 AN CS, Perkin Elmer Optoelectronics, Fremont, Kanada, 2008, 2448 × 2448 pixel, 200 µm × 200 µm pixel size.

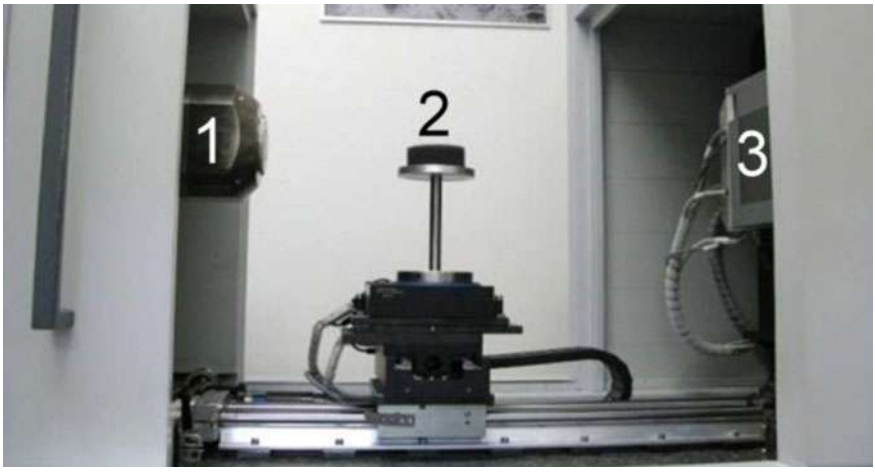

Fig. 16.1 Laboratory XCT with the main components 1 X-ray tube (left). 2 Turning device with sample plate (center). 3 Flat detector (right)

The device for in situ compressive deformation was manufactured by the company Hegewald & Peschke (Nossen, Germany) after co-development. Figure 16.2 illustrates the basic structure. It displays a transmission system that transmits the torque of an electric motor to a spindle. This spindle moves a pressure plate. The sample is located between this lower and an upper pressure plate. The load cell is firmly connected to the gearbox housing via flanges and a CFC tube. During movement of the spindle the sample and the CFC tube are simultaneously under compression and tension respectively. A CT scan is possible, because the entire system can be mounted on the turntable of XCT. The absorption of X-radiation by the CFC tube is negligible. The CFC tube used for the experiments was supplied by the Institute for Construction and Composite Construction e.V. (TU Chemnitz, Germany).

One method for determining the mechanical properties of small samples at relatively small forces is the small punch test [15]. Cylindrical discs are deformed with the aid of spherical pressure stamp in the middle. The entire load within the specimen is rotationally symmetric with defined areas of compressive and tensile loading. Figure 16.3 shows the basic arrangement. Because of the rotational symmetry, the method is very well suited for in situ investigations in XCT at low forces. In order to

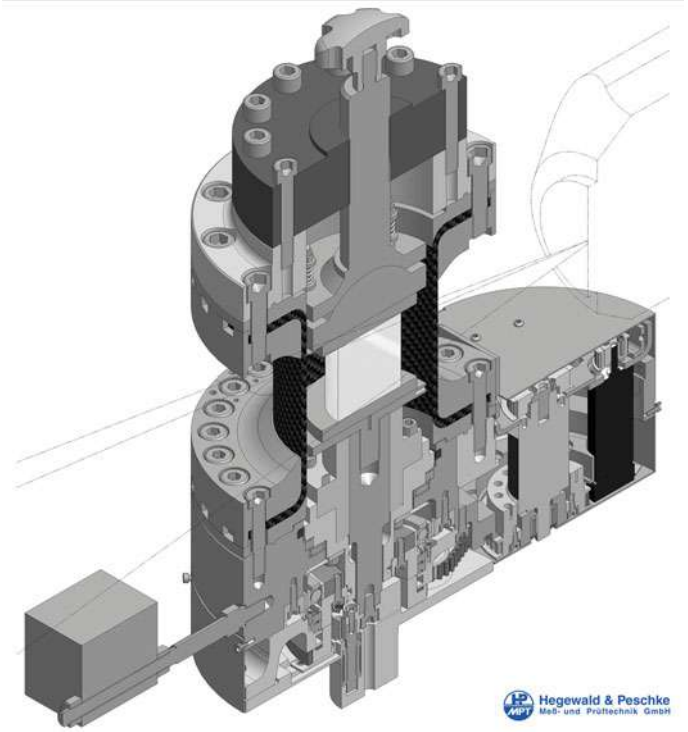

Fig. 16.2 Schematic representation of the structure of the in situ device for pressure deformation [14]

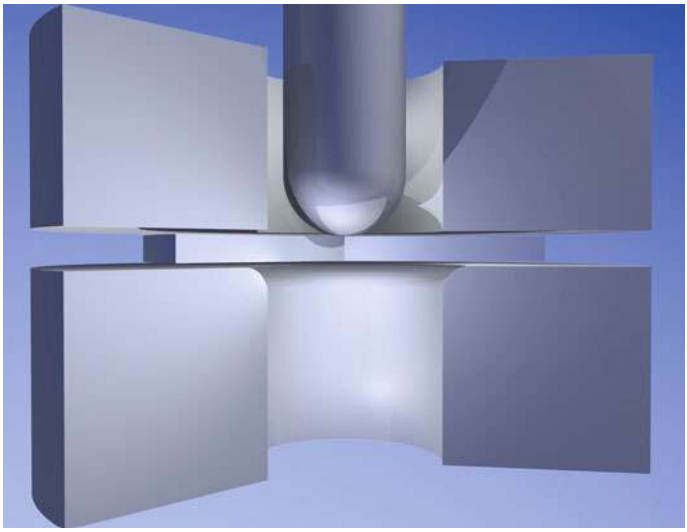

Fig. 16.3 Basic arrangement of the small punch test [15]

avoid a superposition of the absorbance contrasts of sample holder and sample, the entire sample holder shown in Fig. 16.3 consists of Si_3N_4. This material is characterized by extremely low X-ray absorption and high fracture toughness at the same time. In the present study, an in situ deformation device Deben CT5000 was used (Deben UK Ltd, Bury St. Edmunds Suffolk, UK). This is designed for forces up to 5000 N and a higher resolution in the XCT is possible, due to the small dimensions. It was installed for this purpose in a XCT ZEISS Xradia510 type. In this combination a volume resolution (voxel size) of 0.7 µm was possible at a sample diameter of 4 mm. Figure 16.4 illustrates the arrangement with installed deformation device. Part of the microstructure analysis was investigated in a SEM XL30 from Philips equipped with a EDX/EBSD-System from Edax. FIB preparation and characterization of the microstructure were performed in a FEI Versa3D dual beam system. This microscope is equipped with a 30 kV Ga+ ion source. An EDX- and EBSD analytical system Team from EDAX was used. Phase analysis was carried out for single points or for defined scans. The topographic information was obtained using the forward scatter detector (FSD), which was positioned below the EBSD screen. The preparation in the Versa3D microscope was performed by milling of cross sections at sharp edges of the samples. Thus, areas in the range of 50 μm^2 could be investigated. In addition, embedded and polished samples were used in order to get defined initial surface conditions for the FIB preparation. The final preparation step for the embedded samples was vibration polishing in a Buehler VibroMet2. The polished samples were coated with PtPd20 layers in the range between 0.1 and 0.5 nm using a Cressington 208 HR Sputter Coater. Lattice parameters for the phase identification by EBSD were taken from an ICDD database [16]. These data were also the starting point for the XRD-whole-pattern fitting process.

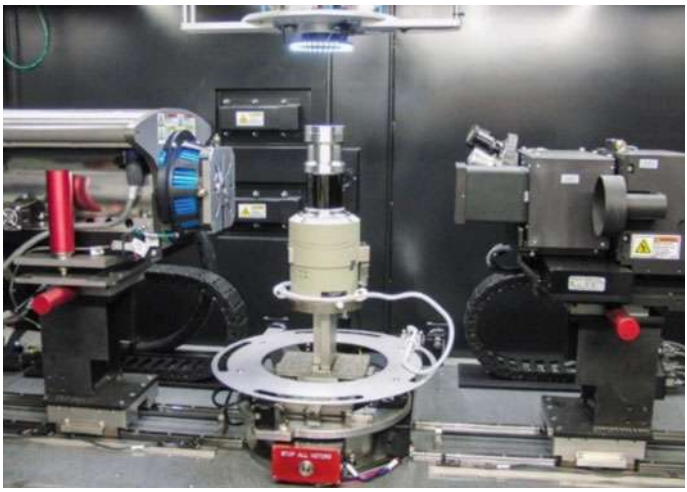

Fig. 16.4 Deformation instrument Deben CT5000 in XCT Zeiss XRadia510, left: X-ray tube, middle: deformation device on the turntable, right: X-ray microscope

To characterize the graded beads, the X-ray computed tomography (X-ray CT) was conducted using a Zeiss Xradia 510 Versa X-ray microscope (XRM). This XRM is equipped with a 160 kV tungsten target X-ray source and scintillator detectors filmed from the back by a CCD camera (2048 × 2048 pixel) through a microscopy system. Therefore the total magnification results from the geometric magnification of the cone beam multiplied by the optical magnification of the microscope. The volume reconstruction was done using the Zeiss XRM reconstructor software. This software works with a filtered back projection algorithm and an additional beam hardening correction method. Detailed parameters used for tomography studies as well as for volume reconstruction are given by Oppelt et al. [13].

16.3 Results and Discussion

16.3.1 Target Preparation and Effect of Focused Ion Beam Sample Preparation

If specimen areas of interest can be optically detected with an accuracy of approximately 0.5 mm, a metallographic ground preparation is possible. For this purpose, the samples are cut with a diamond saw, embedded in epoxy resin, ground and polished to a particle size of 1 μm. The last step is followed by vibration polishing with a SiO_2 suspension MasterMet2 from Buehler. This was done by a polishing machine VibroMet2 from Buehler. To ensure sufficient electrical conductivity of the samples,

all polished surfaces were coated with about 0.2 nm Pt/Pd (Cressington 208 HR Sputter Coater). All corresponding parameters are the result of an optimization prozess [9].

Another method of target preparation is Focused Ion Beam (FIB). Here, the areas of interest can be selected directly in the SEM. After determining a suitable cut surface, this is exposed by means of FIB and polished. It has been found that ceramic materials not only show the radiation damage known from metals and semiconductors, but also phase transformations are possible [10].

In case of metastable Y-PSZ and Mg-PSZ, phase transformations or damage were observed independence of the parameters ion energy, ion current and incidence angle. Damage was the dominating effect for angles of 72° while phase transformations occurred during FIB-preparation with 30 kV, 30 nA and 5° incidence angle. The expected local temperature increase due to the ion bombardment (30 kV, 30 nA) is about 700 K for ZrO_2. Thus, the observed phase transformations could be explained on the basis of the increased temperature (700 °C) in the corresponding Y-PSZ phase diagram. In case of Mg-PSZ, the transition temperature is 1083 °C. The local temperature rise was obviously lower. The excitation energy for the observed phase transformation was smaller than expected from the phase diagrams of the thermodynamic equilibrium. Using 5 kV, 4.8 nA and 5° incidence angle no phase transformations and no damage were observed. Thus, these conditions are suited for the FIB preparation of metastable zirconia. The investigation of phase transformations in zirconia requires a separation between zirconia and the other phases of the structure. Otherwise cubic structures of the steel matrix, zirconia and precipitations cannot be distinguished. This discrimination was realized using the combination of EDX- and EBSD-mapping. One has to keep in mind, that the interaction volumes of EDX and EBSD are different. However the given zirconia particle sizes enable the definition of phase boundaries by EDX with a sufficient resolution. A complete analysis of a scanned sample contains the following steps [8, 9]:

(1) Scanning of at minimum 10 typical areas for each sample:
For each point of a scanned sample area the EDX spectrum and the EBSP are analyzed simultaneously. The typical map size was 20 μm × 20 μm with a step size of 0.2 μm.
(2) Analysis of the EDX maps and determination of the threshold values at phase boundaries.
(3) Filtering of the EBSD maps:
This is carried out on the base of the EDX threshold values and separation into different phase areas.
(4) Calculation of the phase distributions within the different phase areas:
The decision for one of the possible phases for each EBSP is based on the number of detected diffraction bands on the one hand and the difference between the measured angles between the diffraction bands and the corresponding angles between expected lattice planes on the other hand (fit). The phase with the highest number of corresponding diffraction bands and the lowest fit is taken.

The aim of the analysis of the target preparation was to study the influence of a FIB preparation on the phase composition of Mg-PSZ and Y-PSZ. Figure 16.5 illustrates a typical FIB cross section preparation.

As a first step, a platinum layer is deposited on the sample surface in order to get a defined cross section with little curtaining and without further damage of the sample. A metal-organic compound is used as a precursor for Pt. Typically this is dissociated with the aid of the ion beam and the metal is deposited. During the first seconds of this process, interactions between the ion beam and the sample surface have to be considered. Modifications may be necessary in case of fine sensitive surface structures. The stopping range of ions is in the same order of magnitude as the depth of possible damage. Therefore electrons may be used for the formation of a first layer of Pt. After deposition of the first layer of Pt atoms the damage stops. The second step is milling at an angle perpendicular to the sample surface followed by low energy polishing as a third step. As a result the sample surface is characterized by a damage depth Y smaller than the EBSD information depth [10].

Figure 16.6 shows a typical fractured surface of Y-PSZ. As it can be clearly observed, the structure was bimodal with grains in the range of 10 μm and below

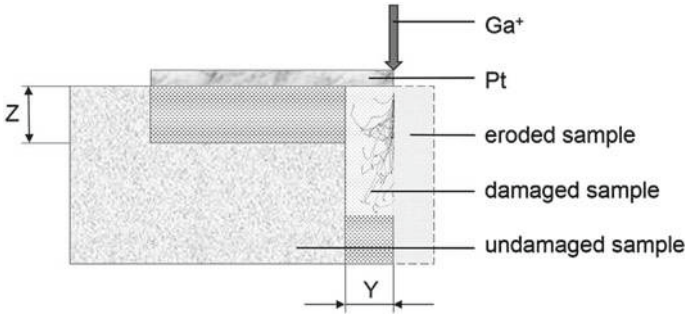

Fig. 16.5 Scheme of the sample damage during FIB cross sectioning [10]

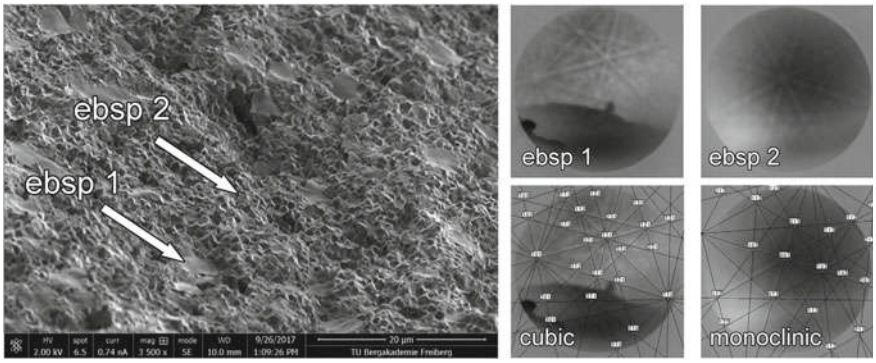

Fig. 16.6 EBSD phase analysis on a fractured surface of Y-PSZ [10]

1 μm. Electron backscatter diffraction patterns (EBSP) could be obtained without further preparation. The only problem was to find a matching geometry. As expected, the peaks were indexed as monoclinic or cubic/tetragonal. Examples are given in Fig. 16.6. Note that the cubic and tetragonal crystal structures of stabilized zirconia cannot be distinguished by EBSD. The crystal parameters may change continuously with the concentration of the stabilizer as mentioned above. Each state between cubic and tetragonal is possible. Thus, the resolution of EBSD is not sufficient as opposed to XRD [10].

Typical results of the EBSD phase analysis on polished cross sections are given in Fig. 16.7. The bimodal microstructure can be clearly recognized in the SEI image. It also appears in the phase map. The bigger particles were indexed as cubic/tetragonal zirconia (green), while the smaller particles consisted of monoclinic zirconia (red). The inverse pole figure (IPF) exhibits a random distribution of crystallographic orientation. The band contrast map also shows the bimodal structure. It represents the contrast at the observed diffraction bands in a greyscale. Thus, it illustrates the distribution of the local crystal perfection. The monoclinic grains exhibit a higher number of lattice defects than cubic/tetragonal grains. As stated in the introduction, the concentration of the stabilizer Y is not homogeneous. In particular, it is higher in the cubic/tetragonal grains than in the monoclinic ones. Hence the system is partially destabilized. As a result, the monoclinic fraction within the sample shows a variability in the local Y concentration [10].

After a FIB preparation of cross sections, a complete different phase composition was found. Corresponding results are presented in Fig. 16.8. As it can be seen in the SEI image, a tip was coated with platinum and then cut with 30 kV Ga+ ions at an angle of 90° relative to the Pt-coated surface. The beam current during the final polishing with an incident angle of 1° to the cut surface was 3 nA. Curtaining occurred due to inhomogeneity of the initial sample surface as well as of the Pt coating. This effect let to the dark lines in the band contrast map and also in the phase map. Surprisingly, the EBSD phase analysis showed a dense structure and clear diffraction patterns without much damage. The microstructure was completely cubic/tetragonal, in contradiction to the XRD and initial EBSD phase analysis on polished samples. The Yttrium distribution was comparable to the initial state, indicating that no further destabilization occurred. In order to explain this behavior, FIB milling and polishing were conducted on mechanically polished surfaces with different incident angle and energy of the ion beam [10] Detailed phase maps and results are given by Berek et al. [10]. Identical areas of mechanically polished samples were scanned before and after additional FIB preparation with different ion energy and angle. A summary of the results is given in Table 16.1. The fraction of indexed points represents the ratio between the number of indexed points and the total number of points within the scan. The band contrast is a measure of the sharpness of the diffraction bands and also for the crystal perfection. The values of the band contrast can be compared if all diffraction patterns are taken under equal experimental conditions.

Differences in the initial states (from vibration polish) are attributed to local inhomogeneities. Note that after FIB with 30 kV, 30 nA and 5° incidence angle the fraction of indexed points rose while the fit and the band contrast were stable. The fit

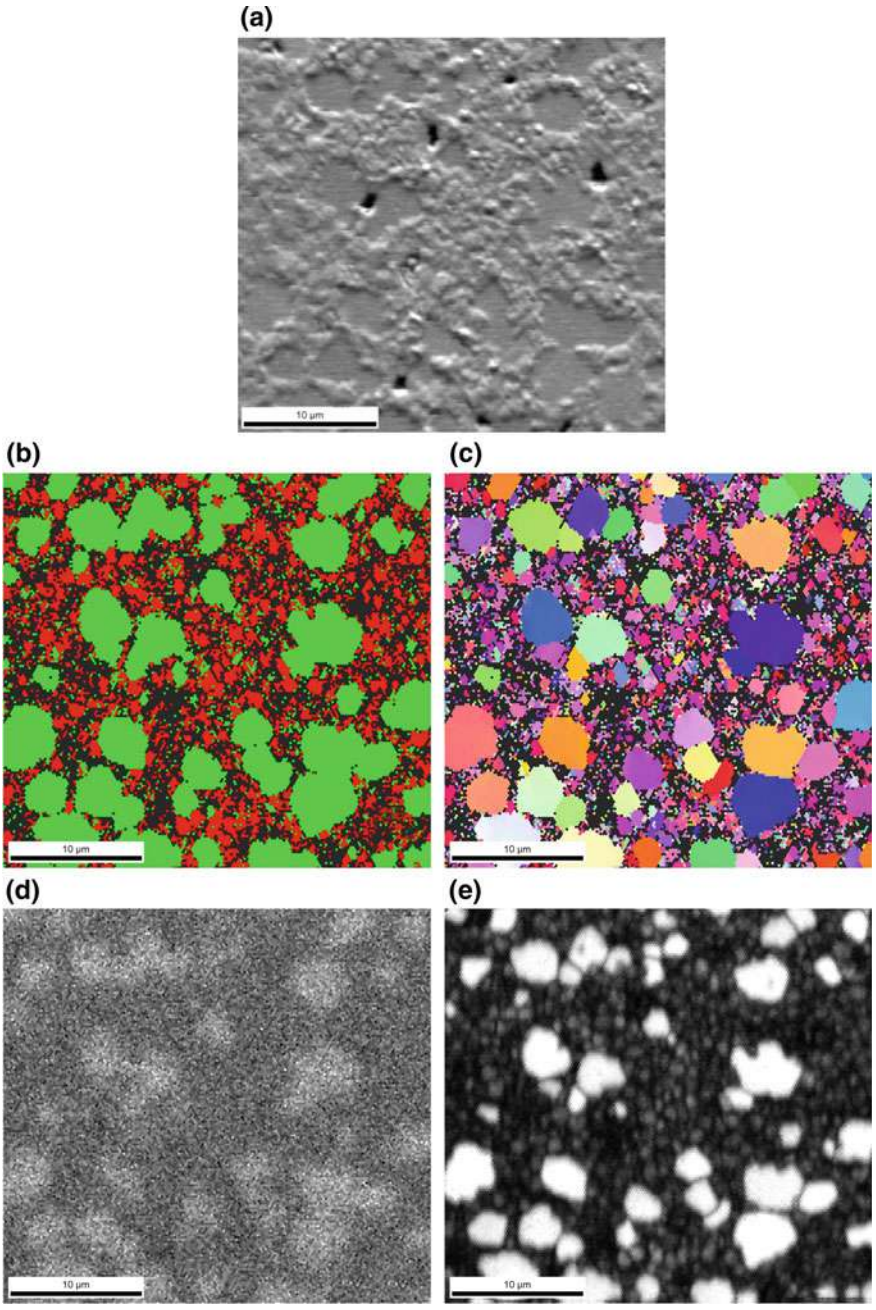

Fig. 16.7 EBSD phase analysis on a polished surface of Y-PSZ. **a** SEI image of the analyzed area. **b** Phase map (green: cubic/tetragonal, red: monoclinic). **c** Inverse pole figure image. **d** EDX elemental distribution for Y. **e** Band contrast [10]

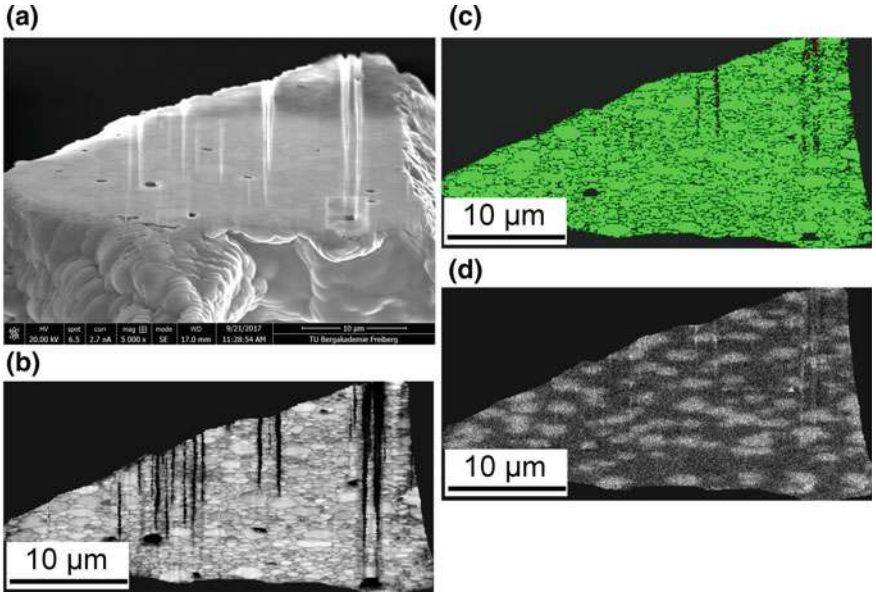

Fig. 16.8 EBSD phase analysis on a FIB cross section of Y-PSZ with the FIB parameters 30 kV and 3 nA. **a** SEI image. **b** Band contrast. **c** Phase map (green: cubic/tetragonal). **d** EDX elemental distribution for Y [10]

Table 16.1 Influence of FIB preparation on EBSD phase analysis of Y-PSZ [10]

	Monoclinic fraction	Fit	Fraction of indexed points	Band contrast (defined above in text)
	(Mol-%)	(°)	(%)	(–)
Vibration polished	21.1	1.05	38.4	3977
FIB (30 kV, 30 nA, 72°)	5.2	1.35	26.8	1772
Vibration polished	23.4	1.06	40.1	3962
FIB (5 kV, 4.8 nA, 72°)	2.0	1.21	34.0	3834
Vibration polished	35.8	1.03	43.1	4747
FIB (30 kV, 30 nA, 5°)	1.1	1.06	64.1	4501
Vibration polished	37.4	1.07	48.9	4380
FIB (5 kV, 4.8 nA, 5°)	34.0	1.06	49.7	3954

is defined as the medium difference of angles between all identified diffraction bands and the corresponding lattice planes of the crystal structure of interest. Obviously the structural transformation was followed by a crystal growth. FIB with 5 kV, 4.8 nA and 5° incidence angle led to nearly unchanged values. Thus, one can conclude that the influence of crystal damage at 5 kV is negligible. No amorphous layer could be

identified. Phase transformations in zirconia are connected with volume changes. However, no cracks were observed in the transformed regions.

16.3.2 MMC Foams

Open cell foam structures were produced with the aid of 30 pore per inch (ppi) polyurethane foam (pore size distribution in the range of 0.5 up to 3 mm) of size $50 \times 50 \times 20$ mm^3 as templates [16–18].

One typical MMC foam is shown in Fig. 16.9. Three mixtures based on 100 vol% steel powder (0Z), 95 vol% steel/5 vol% Mg-PSZ-powder (5Z) and 90 vol% steel/vol% Mg-PSZ-powder (10Z) were mixed with organic additives. The manufacturing technology and the composition of the organic additives is described in [16–18]. The used process is one of the most promising manufacturing routes to produce open cell composite foams and is based on the patent of Schwartzwalder et al. [19]. It is a replication method using polyurethane sponge as a template.

In the given case the steel powder (Bitterfeld, Germany) had a mean particle size of 45 μm and the ceramic powder (Saint Gobain, USA) had a mean particle size of 3.1 μm respectively. Tables 16.2 and 16.3 give the corresponding chemical compositions.

The sintering conditions of the samples were 2 h at 1350 °C in Ar atmosphere. The in situ experiments were performed in a CT-ALPHA (ProCon X-Ray Garbsen, Germany), using a 160 kV transmission X-ray tube (Feinfocus Garbsen, Germany). High resolution X-ray absorption images were taken with a flat detector C7942SK-05

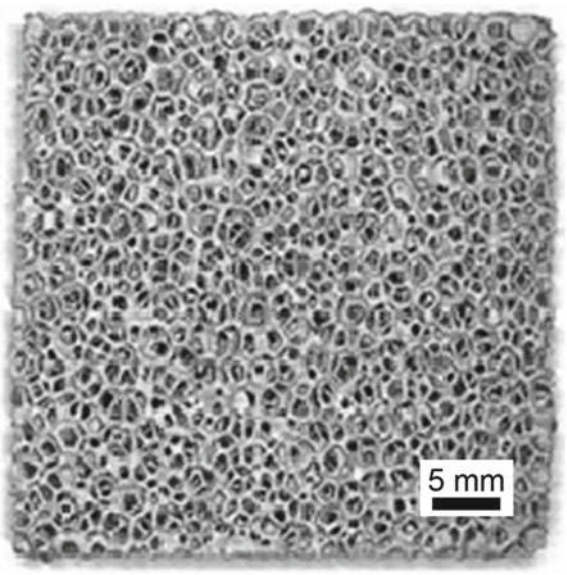

Fig. 16.9 Typical MMC foam [21]

Table 16.2 Chemical composition of the steel matrix in wt% [11]

C	Cr	Mn	Ni	Si	P	S	N	Fe
0.027	18.1	1.3	7.8	0.4	0.04	0.02	0.06	Bal.

Table 16.3 Oxide content of Mg-PSZ in wt% [11]

ZrO_2	MgO	TiO_2	Al_2O_3	HfO_2	SiO_2	CaO
Bal.	2.84	0.19	0.5	1.85	0.07	0.2

(Hamamatsu, Japan). This detector has 2400 × 2400 pixels with a size of 50 µm × 50 µm each on an area of 120 mm × 120 mm. The typical resulting spatial resolution (voxel size) within the sample was 15 µm. The maximum possible sample size was always determined by the X-ray attenuation coefficients.

Loading plates of different geometries were used in order to enable full transmission of the samples without shadowing. The displacement was measured below the sample in the actuator. The deformation of the mechanical setup was found to be negligible. In the given case foam samples with a size of 10 mm × 10 mm × 20 mm were investigated. The deformation speed was about 10^{-3} s^{-1}. The CT data were analysed with the software package VGSTUDIO MAX 2.1 (Volume Graphics GmbH Heidelberg, Germany). This program provides the possibility to calculate the exact position of the sample surface with a sub voxel resolution thus correcting the so called partial volume effect. The partial volume effect normally leads to undefined three dimensional surfaces because voxels on the sample surface belong partly to the sample and partly to the surrounding.

A typical result of this kind of sample surface calculation is given in Fig. 16.10. Note that there are pores inside the foam material. This is a result of the manufacturing technology. We assume that these pores are acting as week areas during deformation. Therefore they are included in the calculation of the total sample surface. Based on the defined surface of the foam including the surfaces of pores, cell wall thicknesses can be calculated. This is realized by the determination of shortest distances between nearest surface areas within a search angle of 30°. Triple points of the foam cells always have a higher thickness than single cell walls due to surface tension effects of the slurry used. As a result of the manufacturing process pores are located mainly in the triple points. This is connected with weak points. Therefore the cell wall thickness at pores is included in the analysis.

Figure 16.11 shows typical stress-strain curves for a steel—5 vol% zirconia composite. Three areas are clearly visible. Following DIN 50134 [22] there are different ranges for the compressive stress (elastic deformation, cracking, densification) they can be separated using different ranges for the compressive stress R where R_{100} is the stress in the plateau:

(R_x: $x = x\%$ of plateau stress $R_{\text{pland the foam respectively. Ourt}}$; R_{plt} = average value of stresses between $e_d = 20\%$ and $e_d = 40\%$; e_d = strain [22]).

1. Elastic deformation between R_{20} and R_{70}

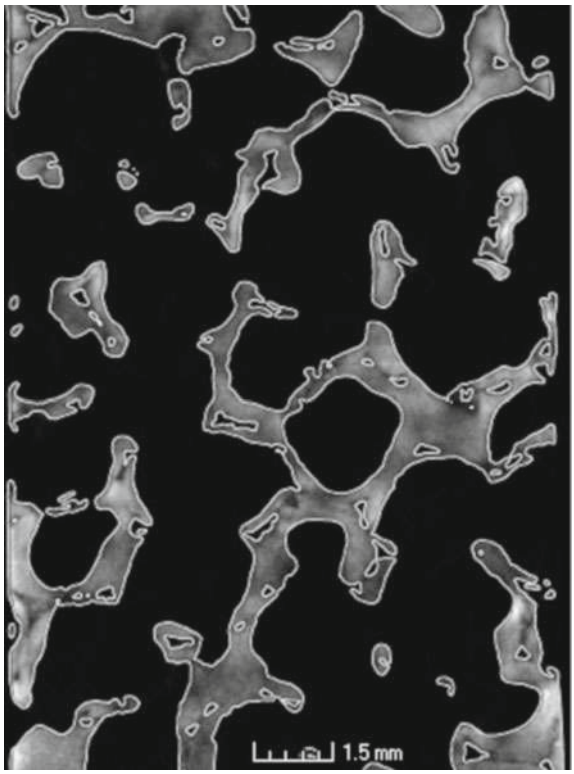

Fig. 16.10 Reconstructed cross section [11]

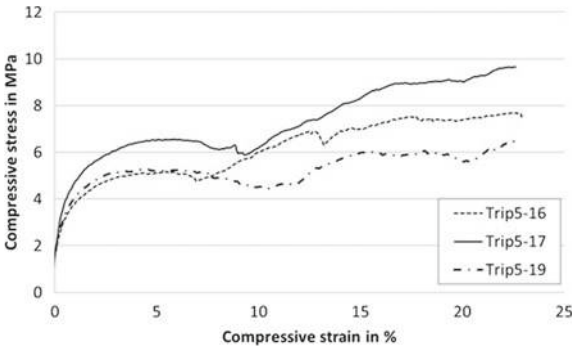

Fig. 16.11 Stress strain curves of three foams [11]

2. Cracking leading to a plateau between R_{70} and R_{130}
3. Densification leading to a significant increase above R_{130}.

Note, that there is a large scatter in the data. The cell wall thickness is inhomogeneous within the sample depending on the inhomogeneity of the starting materials and the manufacturing technology.

Results of a stopped in situ experiment are shown in Fig. 16.12.

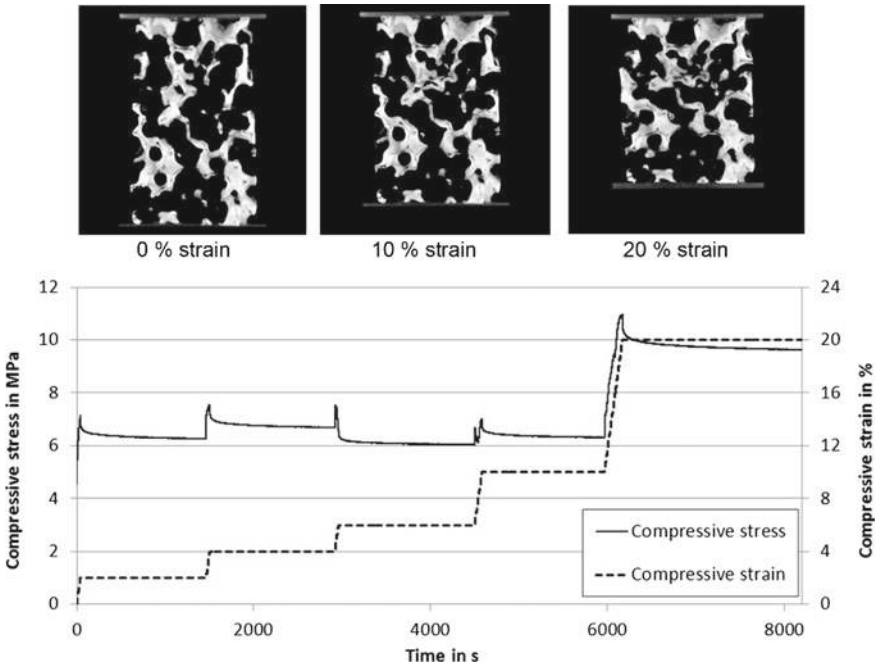

Fig. 16.12 Scheme of a stopped in situ deformation experiment and calculated sections for 0, 10 and 20% strain [11]

The compression was stopped after 2, 4, 6, 10 and 20% compressive strain respectively. After stopping the deformation process stress relaxation occured. This is connected with a significant dropdown of the compressive stress within a few minutes while the compressive strain was held constant. After this period an equilibrium state is reached. The maxima in the curves of the compressive stress correspond to the curves in Fig. 16.11. XCT scans were taken in the equilibrium state under constant stress. In order to show deformation processes with a sufficient spatial resolution, defined regions of interest were considered. In the case of Fig. 16.12 calculated 3D pictures of thin layers taken at the same position of the sample after 0, 10 and 20% compressive strain are shown. First cracks appear at the weakest cells. These are cells of a rather big size, a small cell wall thickness and an extension perpendicular to the deformation axis. A localized damage is clearly visible. Starting point in deed are smaller cell walls. As can be seen in Fig. 16.13, there is a typical deformation band starting from the area of first cracks.

For the deformation of MMC foams under compressive stress in agreement with the literature three regimes were found: elastic deformation, plastic collapse and densification. The normalized deformation maps given by Ashby [23] show the principal behaviour of the stress strain curves in dependence on the densities of the bulk material of the foam and the foam respectively. Our results confirm this view. The data are shifted slightly to smaller compressive stress values. As Elliott [24] found

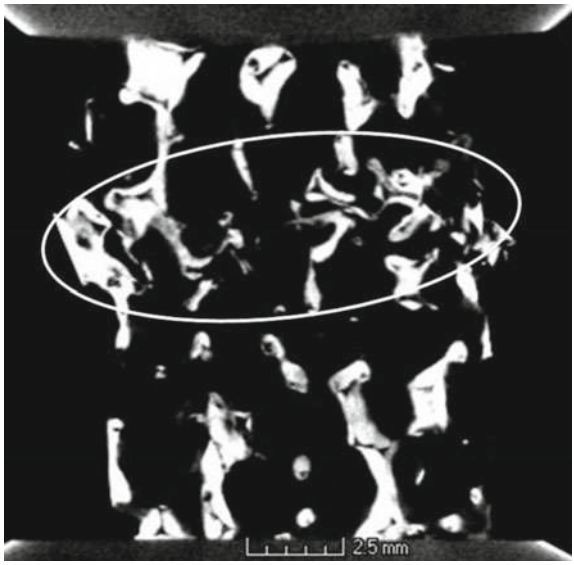

Fig. 16.13 Reconstructed cross section after 20% compression [11]

for polyurethane foams the compression of MMC foams also lead to the cooperative collapse of connected cells. Note that the foams of the given study were manufactured by the replica technique on the base of polyurethane foam (as shown in Chap. 1 of this volume). We observed deformation bands arising in regions of smaller cell wall thicknesses. Singh [25] found this kind of anisotropy in open celled Ti foams. The deformation was dependent on size, shape and orientation of the cells under consideration. Obviously deformation bands start at bigger cells with a small cell wall thickness and some extension perpendicular to the deformation direction. The rising of this kind of deformation bands can be explained by the dramatic change of the stress distribution in the neighbouring cells after the first brake of a cell wall. The correlation between local deformation and local phase composition was investigated by Berek et al. [21].

Figure 16.14 shows the result of a digital volume correlation calculation. The gradient magnitude is a measure of the local deformation. Thus, region 3 shows maximum deformation. Figure 16.15 exhibits a typical cross section of this region as the result of a local preparation process with its correspondence to the reconstructed XCT image. Local phase analyses of a number of particles like the one in Fig. 16.16 lead to the results in Fig. 16.17.

Note, that the transformation from the cubic structure to the tetragonal one is a continuous deformation process in dependence on the local concentration of stabilizers as was shown in [26]. Thus, the distinction between cubic and tetragonal zirconia is not possible by EBSD. However, it becomes clear, that the regions of high deformation (c.f. Fig. 16.14) correspond to regions of pronounced phase transformation (Fig. 16.17).

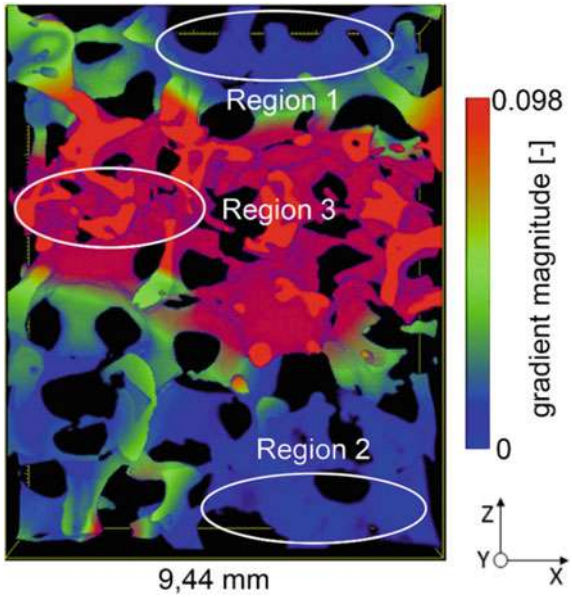

Fig. 16.14 Overlay of the slice of a reconstructed 3D image (background) and the gradient magnitude of the deformation field (highlighting) with defined regions of interest after 20% compressive deformation in the Z direction [21]

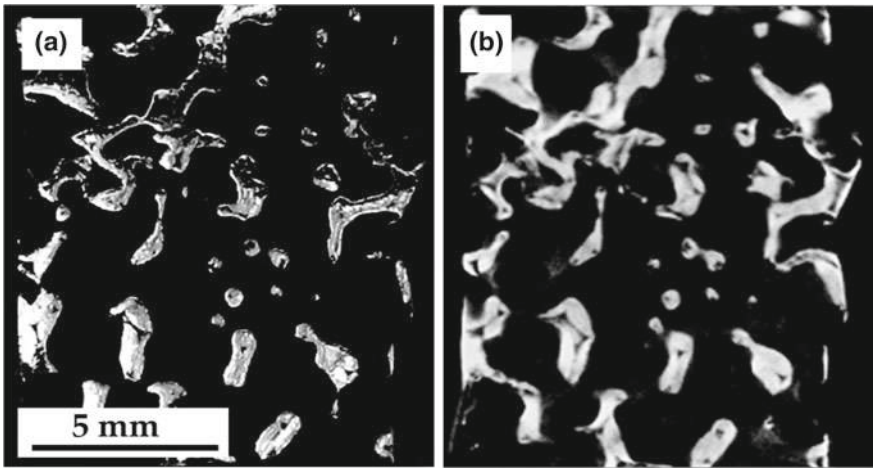

Fig. 16.15 Correlation between a reconstructed 2D image and the corresponding cross section after 20% compression in the Z direction. **a** Photograph of the cross section. **b** 2D slice from the reconstructed 3D image [21]

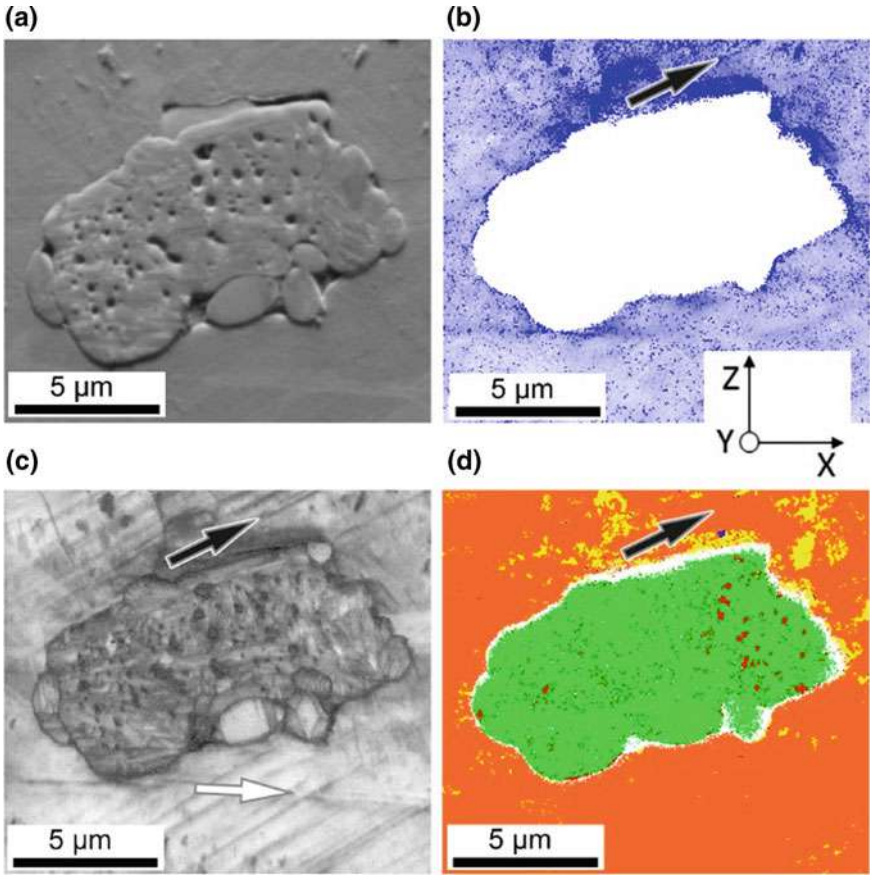

Fig. 16.16 EBSD analysis of a zirconia agglomerate after 20% compression in the Z direction. **a** EDS image. **b** Kernel average misorientation map for the steel matrix. **c** Band contrast map. **d** Phase map (green: monoclinic zirconia; red: cubic/tetragonal zirconia; orange: austenite; blue: α'-martensite; yellow: ε-martensite; white: points not indexed) [21]

16.3.3 MMC-Honeycomb Structures

The manufacturing technology of honeycomb square cell composites is based on the well-established extrusion technique [27, 28] and is described in Chap. 5 of this volume. Before extrusion the inorganic powder materials were mixed within 30 min in a tumble drum with yttria stabilized zirconia balls. In a second step the plasticizers and binders were added and the material was further mixed in a conventional mixer (Toni Technik, Germany) for 5 min. Finally, water was added and the recipes were kneaded until a homogeneous and plastic paste was achieved. Due to a combined de-airing single screw extruder with vacuum chamber and sigma kneader type LK III 2A (LINDEN, Germany) honeycomb structures were extruded with a square

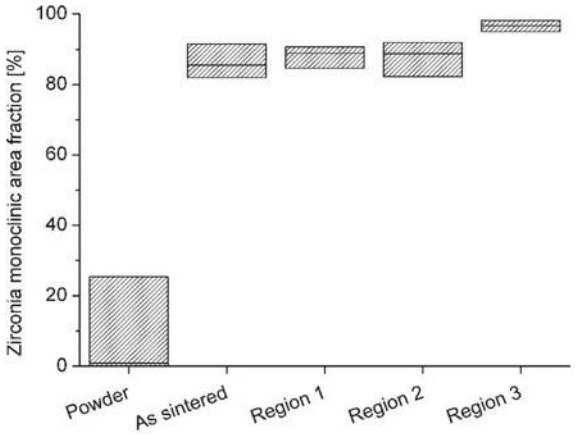

Fig. 16.17 Box plots of the distributions of monoclinic zirconia fractions at different states and in different regions showing the 25th percentiles at the lower edges and the 75th percentiles at the upper edges of the boxes [21]

Table 16.4 Chemical composition of the steel matrix in wt%

C	Cr	Mn	Ni	Si	Mo	N	Fe
0.031	16.2	7.1	5.9	1.12	0.06	0.011	Bal.

Table 16.5 Chemical composition of Mg-PSZ zirconia powder in wt%

ZrO_2	MgO	SiO_2	HfO_2	Al_2O_3	TiO_2
Bal.	3.4	2.4	1.7	0.6	0.1

shape of 25 × 25 mm^2 and a honeycomb structure of 14 × 14 channels (200 cpsi—channels per square inch). After extrusion the specimens were dried stepwise at 40–80–110 °C in an air-circulated dryer within 12 h at each temperature and decreasing humidity from 80 to 20%. Afterward cubic samples of 25 mm length were cut and placed on alumina tiling. The debinding step took place at 350 °C for 90 min in air atmosphere with a heating rate of 1 K/min. To prevent oxidation effects during further heat treatment the honeycombs were placed with stock in graphite crucibles after debinding. Finally the samples were sintered pressure less in a 99.999% argon atmosphere using an electrical furnace type HT 1600 GT Vac (LINN, Germany) with oxidic furnace lining and $MoSi_2$ heating elements. After heating with 5 K/min the temperature of 1350 °C was kept constant for 120 min followed by cooling with 10 K/min to room temperature. Open porosity and bulk density were determined based on Archimedes principle and DIN EN 1389 with toluol as immersion fluid [27]. In the given case 10 vol% of Mg-PSZ powder was mixed with TRIP-steel powder. The chemical compositions are given in Tables 16.4 and 16.5.

In order to perform in situ compression experiments in an XCT, samples with 2 × 2 channels were used. Figure 16.18a, b show corresponding photographs.

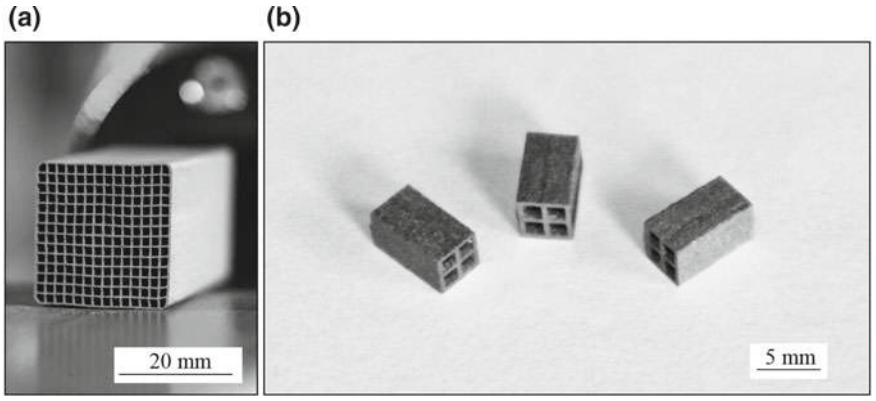

Fig. 16.18 Extruded MMC honeycomb structure (**a**) and samples for in situ experiments under compressive load in an XCT (**b**)

The experiments were performed in a CT-ALPHA in the same procedure as shown for the foams. The typical resulting spatial resolution (voxel size) within the honeycomb sample was 10 μm. A specially constructed load frame from Hegewald & Peschke Measuring Technology Nossen, Germany, was used. Two loading plates are positioned in a carbon fibre reinforced polymer tube between the top load cell and the bottom mechanical actuator. The deformation speed was about 10^{-3} s^{-1}.

The CT data were analysed in the same way as mentioned before with the software package VGSTUDIO MAX 2.1 from Volume Graphics GmbH Heidelberg, Germany. Within previous work ex situ compressive out of plane deformation experiments on honeycomb structures based on Austenitic stainless steel AISI 304L were performed [1, 2, 27, 29]. As a result of EBSD phase analysis it was concluded that stress induced martensitic phase transformations of metastable tetragonal zirconia to the stable monoclinic structure occured below 10% of compressive strain [27, 29]. A rather high amount of the monoclinic phase (>80%) was observed in the as sintered state. The reason for this behaviour was found to be destabilisation due to diffusion of magnesium and the formation of grain boundary precipitations at sintering temperature and during subsequent cooling.

The most important differences to the present work are the composition of the steel alloy used and the performance of quasi in situ deformation in the XCT. The steel alloy 16-7-6 has a significantly higher amount of manganese while the nickel content was slightly reduced. Figure 16.19 shows typical deformation curves of MMC samples (see Fig. 16.18b). Force and deformation were measured directly. The real sample cross section area was determined using wall thicknesses, which were calculated on the base of the XCT-scans.

The geometrical dimensions of the samples were 3.5 × 3.5 × 6 mm^3 with cell wall thicknesses of about 0.37 mm. After linear elastic deformation there was a broad range of plastic deformation with typical strain hardening. This strain hardening is a superposition of both martensitic transformation processes of steel and zirconia. The

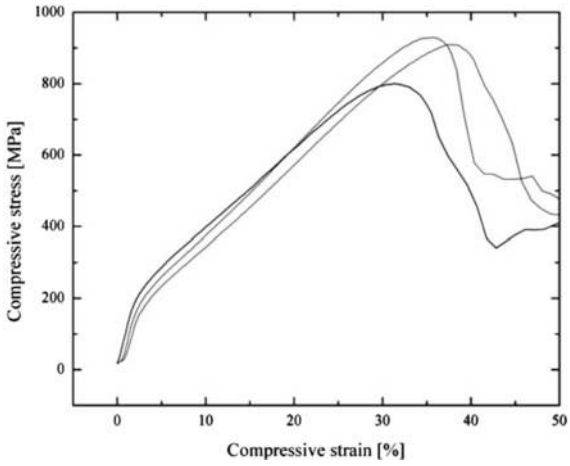

Fig. 16.19 Deformation curves of MMC honeycombs under compressive load in out of plane direction [12]

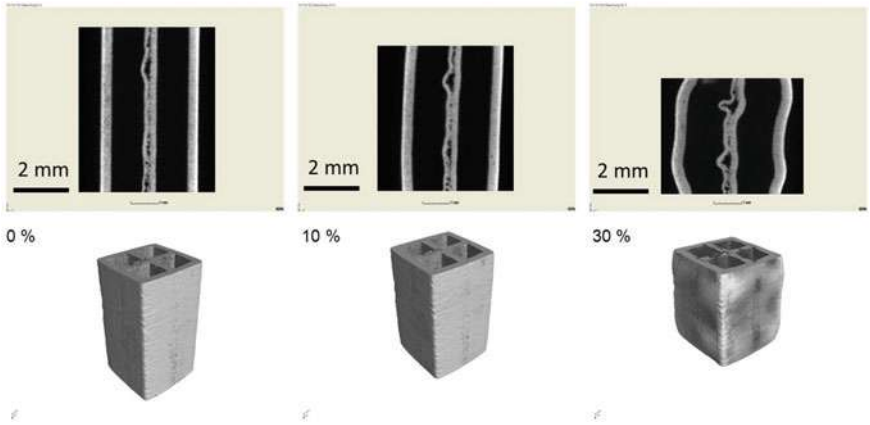

Fig. 16.20 XCT images of MMC honeycombs at different levels of compressive strain [12]

expected deformation behaviour of such kind of square celled honeycombs is torsion-flexural buckling of the cell walls [30] followed by a progressive folding process [6, 31, 32]. For stresses higher than the so called bifurcation stress the structure becomes instable and a softening is observed [30, 33]. In the given case this bifurcation stress is close to the maximum compressive stress. During the deformation process the X-ray absorption picture can be observed directly. In every case the first cracks occurred immediately after passing the maximum. Figure 16.20 gives typical XCT results. Sections were calculated at the same sample position but different levels of deformation thus allowing the study of the deformation behaviour directly.

The deformation is still in the plastic range without breaking of the walls. The sections show a porous region in the middle. Buckling is observed after 30% compression. These results are in correspondence with [14]. The investigation of the deformation behaviour of cruciform honeycomb MMC-samples (as seen in Fig. 16.20 but without the outside wall) within the XCT showed that cruciform MMC-specimens underwent a plastic deformation with irreversible torsion and warping actions. Even small imperfections, particularly piercing defects in the cell walls, had an effect on their critical bifurcation. After finishing the XCT scans, samples we prepared for the EBSD phase analysis. After embedding in epoxy, they were carefully polished. As a result, one can directly compare the calculated XCT sections with the polished sample areas. A minimum of 10 sample areas was scanned by EBSD thus enabling the study of the distribution of the phase composition. The agglomerates of zirconia typically contain a cubic/tetragonal core in a monoclinic body. Note that the lattice parameters of cubic and tetragonal zirconia differ only about 2%. Thus the resolution of EBSD is not sufficient to distinguish these structures. Furthermore there are intermediate metastable states. The lattice parameters can be directly related to the magnesia concentration [26]. Nevertheless the monoclinic structure can be clearly distinguished from the cubic/tetragonal structure by EBSD and the martensitic tetragonal-monoclinic transformation is responsible for transformation toughening. Hence, the determination of the monoclinic phase content is essential. Figure 16.21 gives the corresponding results.

These box plots exhibit minima, maxima and the 25, 50 and 75% percentiles of the corresponding distributions of the measured monoclinic phase fractions. Obviously similar to earlier investigations there is a considerable phase transformation during sintering and subsequent cooling. However the change is much smaller in this study in comparison to earlier studies with low manganese alloyed steels [8, 29]. In the as sintered state the value for the 25 percentile is about 60% of monoclinic zirconia. That

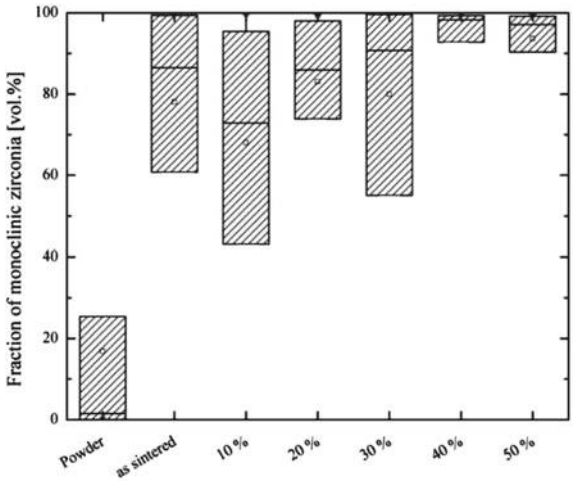

Fig. 16.21 Box plots of the distributions of monoclinic zirconia fractions at different states and in different regions showing the 25th percentiles at the lower edges and the 75th percentiles at the upper edges of the boxes [12]

means a remarkable amount of metastable zirconia for phase transformation is left. The range between 0 and 10% of compressive strain was investigated in more detail because earlier investigations show, that most of the phase transformation occurred in this region. However, in the present case the phase distribution stays stable up to 30% of deformation. This effect can be related to the higher manganese content of the steel alloy used. Mn^{2+} stabilizes metastable zirconia in a similar way as Mg^{2+} [34, 35]. On the other hand manganese forms precipitates with silicon and aluminum like magnesium thus acting as a competitor. In the end there is less diffusion of magnesium out of the zirconia and some diffusion of manganese into the zirconia thus stabilizing the metastable phases. Most of the stress-assisted phase transformation takes place between 30 and 40% of compressive deformation. Obviously, the stress limit for the phase transformation in Mn stabilised zirconia is much higher than in Mg stabilised zirconia. It is in the range of the stress maximum of the stress-strain-curve.

16.3.4 Composite Beads with Graded Layer Structures

The manufacturing technology of the composite beads is based on an alginate gelation and described detailed in Chap. 1 of this volume. Beads with graded layer compositions were prepared using a gel-casting process by alginate gelation. The used method is based on the gelation of sodium alginate in direct contact with calcium ions in an aqueous solution as solidifying agent. The used sodium alginate serves as gelation agent. During the forming process, alginate and bivalent ions react by attracting each other's molecular chains and the transition of water-soluble Na- to water-insoluble Ca-alginate takes place. Suspensions for the fabrication of composite beads with graded layer structures were prepared from austenitic stainless steel powder (TLS Technik, Germany) and magnesia (3.25 wt%) partially stabilized zirconia (Saint Gobain) [13].

The core of the beads consists of a mixture of 90% steel-powder and 10% zirconia powder and are coated with a slurry of 95% steel-powder and 5% zirconia powder. The outmost layer consisted of 100% steel. To get an overview about the complete bead, an investigation in XRM (Versa X-ray microscope) with a voxel size of 1.1 µm was conducted. The bead was fixed on a block of Si_3N_4. No additional preparation of the bead was necessary. Figure 16.22a shows a section through the reconstructed volume. Three essential components which are the steel matrix, ZrO_2-particles/agglomerates with precipitations and pores can be distinguished in the particle section. The study with the XRM proves the result of SEM that there are no gradation zone and no cracks between the different layers. The histogram during measurement shows an asymmetric peak of absorption. It comprises a wide impulse edge to higher absorption coefficients. This impulse edge can be traced back to ZrO_2. Therefore, the different areas were coloured based on the histogram. As a result, the position of ZrO_2 within the (less absorbing) steel matrix can be distinguished. It is particularly clear that the surface layer does not contain ZrO_2. Further tests were performed to show if a higher image resolution can be reached using the

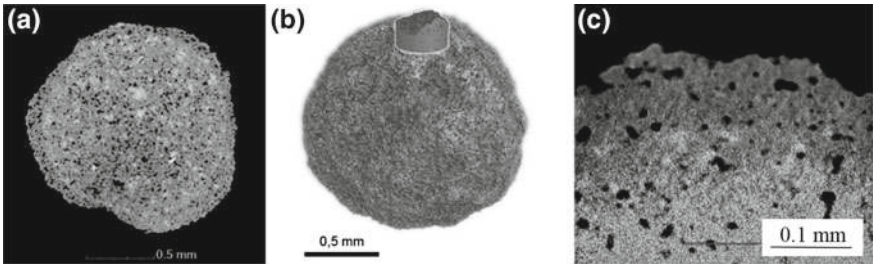

Fig. 16.22 Reconstructed cross section based on a XRM-scan of MMC bead sample; grey: austenite; light grey: ZrO_2 and precipitations; black: pores resp. ambient; **a** XRM-scan of a volume part of MMC sphere using a Zeiss Xradia 510 Versa, **b** position of part c in the volume, **c** reconstructed cross section (grey: austenite, light grey: ZrO_2 and precipitations, black: pores resp. not indicated) [13]

Zeiss Xradia 510 Versa. Therefore a high resolution scan with a 20 ×-objective for large optical magnification was performed. A pixel size of 0.41 µm using a camera binning of 2 (2 × 2 pixels are averaged and combined to one) was reached. Figure 16.22a–c illustrates the reconstructed cross section of a part of the volume. The Zeiss Xradia 510 Versa enables different types of drift corrections. Besides the default thermal drift correction of the X-ray spot on the tungsten target, a mechanical sample drift correction can be applied which takes into account the unwanted movement of the sample. With respect to the appearance of different drift phenomena, the reconstruction required the use of an additional binning 2. Thus, the voxel size of the reconstructed volume results in about 0.8 µm. Nevertheless, a surface zone free of ZrO_2 can be observed [13].

Additional to the XRM-scans of the beads after sintering, XRM-scans of deformed beads were performed. The goal was to show potential differences in crack initiation and crack morphology after deformation by uniaxial compressive loading. Layered beads (Bead a), particle reinforced beads with 90 vol% steel and 10 vol% zirconia (Bead b) as well as pure steel beads (Bead c) were tested. Figure 16.23a–c shows reconstructed cross sections of these three different beads after deformation up to 20%. The voxel size of the reconstructed volumes is 2.2 µm. As it was found for the XRM-scan of the MMC bead sample, the histogram comprises an asymmetrical peak of absorption. There is a wide impulse edge to higher absorption coefficients which is related to ZrO_2. Therefore, the different areas were coloured in the histogram, plotted in yellow. As a result, the position of ZrO_2 within the (less absorbing) steel matrix can be illustrated. Figure 16.23a shows a boundary zone free of zirconia, whereby Fig. 16.23b illustrates a regular distribution of zirconia particles. The crack initiation into the specimens was of major interest. Therefore, cross sections in the area of maximal crack width were chosen. The sample surface is marked in white. It can be seen in the cross sections that the crack in sample a (graded layer bead) does not reach the bead's centre. Bead b (90 vol% steel + 10 vol% zirconia) shows a greater crack propagation. The crack in sample c (pure steel bead) nearly reaches through the complete sample. As expected, the crack initiation starts at the surface

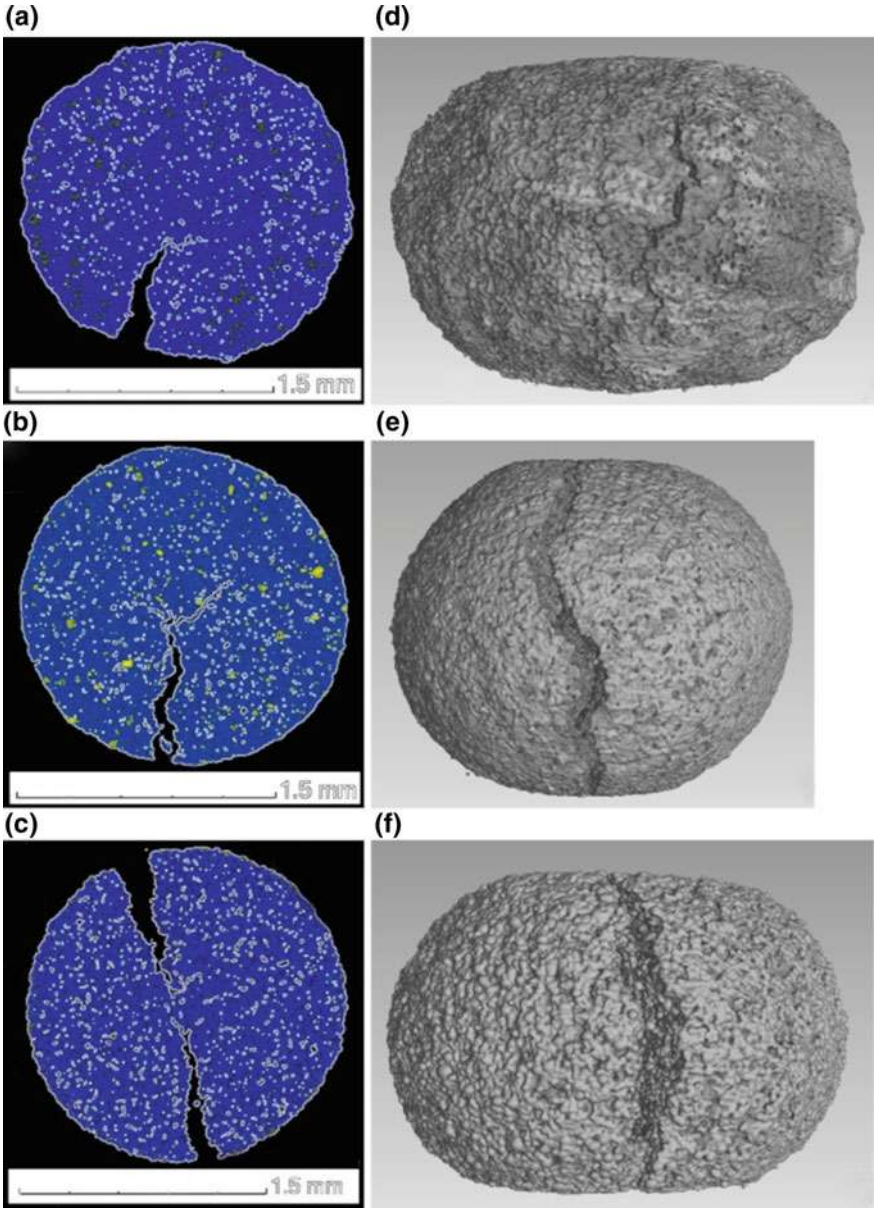

Fig. 16.23 **a–c**: Reconstructed cross sections in x-y-plane with maximal crack length. **a** graded layer bead; **b** 90 vol% steel and 10 vol% zirconia; **c** pure steel bead; blue: steel matrix; yellow: zirconia particles; white: surface marks; **d–f**: Reconstructed volumes with crack in y-plane; **d** graded layer bead; **e** 90 vol% steel and 10 vol% zirconia; **f** pure steel bead [13]

in the range of maximal tension. Figure 16.23d–f illustrates these areas in side view. Sample a (graded layer bead) shows an incipient crack while the other beads present continuous cracks. All pictures of XRM illustrate a very good gradation between the different layers and no detachment of the coating. Further studies with in situ-CT load cells are planned to verify the findings and show the mechanism of failure [13].

16.4 Conclusions

Within this work the target preparation for an optimal EBSD and XCT analysis of composites was investigated and furthermore MMC foams and honeycombs were examined. Focused ion beam preparation is a very helpful tool for producing polished cross sections of defined regions in inhomogeneous samples with complicated shape. The different aspects of the interaction between the ion beam and the sample should be considered. In case of metastable Y-PSZ and Mg-PSZ, phase transformations were observed after FIB preparation with 30 kV, 30 nA and 5° incidence angle. Damage was the dominating effect for angles of 72°. The expected local temperature increase due to the ion bombardment (30 kV, 30 nA) is about 700 K for ZrO_2. Thus, the observed phase transformations could be explained on the basis of the increased temperature (700 K) in the corresponding Y-PSZ phase diagram. In case of Mg-PSZ, the transition temperature is 1083 °C. The local temperature rise was obviously lower. The excitation energy for the observed phase transformation was smaller than expected from the phase diagrams of the thermodynamic equilibrium. Using 5 kV, 4.8 nA and 5° incidence angle no phase transformations and no damage were observed. Thus, these conditions are suited for the FIB preparation of metastable zirconia [10].

An experimental setup for in situ investigations under compressive stress in a laboratory XCT was developed and successfully tested. Complete deformation curves can be taken. The size of the samples is limited due to the transferability. Nevertheless the results for MMC foams based on TRIP-steel and Mg-PSZ correspond to results on rather bulk samples investigated by a conventional testing machine. XCT scans can be taken in the frame of stopped in situ experiments. In this way the deformation behavior of defined sample regions can be investigated. Thus interrupted in situ experiments as described by Berek et al. [11] are well suited to investigate the deformation behavior of foams and other samples which are transferable for the X-rays used. For the deformation of MMC foams under compressive stress three regimes were found in agreement with the literature: elastic deformation, plastic collapse, and densification. The deformation was dependent on size, shape and orientation of the cells under consideration. Obviously deformation bands start at bigger cells with a small cell wall thickness and some extension perpendicular to the deformation direction. The occurence of this kind of deformation bands can be explained by the dramatic change of the stress distribution in the neighbor cells after the first brake of a cell wall [11].

Furthermore the experimental setup for interrupted in situ investigations under compressive load in a laboratory XCT up to 100 kN load was developed and successfully tested to demonstrate that the crush resistance and equally the energy absorption capability of cruciform TRIP-steel structures (honeycombs) are improved by the addition of 10 vol% of Mg-PSZ. The strain hardening of the composite material can be explained by the combined effects of particle reinforcement and martensitic phase transformations in the TRIP-steel and the Mg-PSZ reinforcement at the same time. The XCT investigations showed that the cruciform specimens underwent a plastic deformation with irreversible torsion and warping effects. The composite specimens exhibit a higher initial compressive peak stress followed by structure softening and the formation of an expanded plateau region. Even small imperfections, particularly piercing defects, in the honeycomb's cell walls had an appreciable effect on their critical bifurcation load. An accelerated inhomogeneous buckling in the flange edge regions was observed in case of cruciform samples. On the basis of these experimental studies, the characterization of the deformation and failure behavior of the honeycomb structures or comparable cellular materials by analytical modeling can be promoted [14].

With the aid of XRM and X-ray CT it was possible to examine and evaluate layered composite beads. To show potential differences in crack initiation and crack morphology after deformation by uniaxial compressive loading XRM scans of deformed beads were performed. All pictures show the perfect layer formation and the crack initiation starts at the surface in the range of maximal tension.

Acknowledgements The authors gratefully acknowledge the financial support of the Deutsche Forschungsgemeinschaft (DFG, German Research Foundation) for funding this research project B5 within the frame of the Collaborative Research Center (CRC) 799—TRIP-Matrix-Composites—project number 54473466. The authors would like to thank all colleagues and student assistants for their help in measurements and for their work in sample preparation within the runtime of CRC 799.

References

1. C. Aneziris, W. Schärfl, H. Biermann, U. Martin, Int. J. Appl. Ceram. **6**, 727–737 (2009)
2. H. Biermann, U. Martin, C. Aneziris, A. Kolbe, A. Müller, W. Schärfl, Adv. Eng. Mater **11**, 1000–1006 (2009)
3. S. Martin, S. Wolf, U. Martin, L. Krüger, D. Rafaja, Metall. Mater. Trans. A **47A**, 49–58 (2016)
4. E. Kisi, C. Howard, Key Eng. Mater. 153–154, 1–36 (1998)
5. D. Green, R. Hannink, M. Swain, *Transformation Toughening Of Ceramics* (CRC Press, Boca Raton, Florida) (1998)
6. D. Ehinger, L. Krüger, U. Martin, C. Weigelt, C. Aneziris, Steel Res. Int. **82**, 1048–1056 (2011)
7. Schwartz, M. Kumar, B. Adams, *Electron Backscatter Diffraction in Materials Science* (Kluwer Academic, Plenum New York (2000)
8. H. Berek, A. Yanina, C. Weigelt and C. Aneziris, Steel Res. Int. **82**(9) (2011)
9. H. Berek, *In-situ-Druckverformung zellularer Werkstoffe in einem Röntgen-Tomographen* (TU Bergakademie Freiberg, Habilitation) (2013)
10. H. Berek, C. Aneziris, Ceram. Int. **44**, 17643–17654 (2018)

11. H. Berek, U. Ballaschk,C. Aneziris, Adv. Eng. Mater. **13**, 1101–1107 (2011)
12. H. Berek, U. Ballaschk, C. Aneziris, S. Hahn, in *Proceedings: International Conference on Cellular Materials CELLMAT2012*, Dresden (2012)
13. M. Oppelt, T. Leißner, H. Berek, C. Baumgart, L. Krüger, Adv. Eng. Mater. 1800615, (2018)
14. U. Ballaschk, H. Berek, D. Ehinger, C. Aneziris, L. Krüger, Adv. Eng. Mater. **15**, 590–599 (2013)
15. M. Abendroth, Private communication, TU Bergakademie Freiberg (2018)
16. ICDD, ICDD PDF-2 database release 2008 [online]. https://www.icdd.com
17. C. Aneziris, H. Berek, M. Hasterok, H. Biermann, S. Wolf, L. Krüger, Adv. Eng. Mater. **12**(3) (2010)
18. H. Berek, C. Aneziris, M. Hasterok, H. Biermann, S. Wolf, L. Krüger, in *PTM2010 Solid-Solid Phase Transformations in Inorganic Materials*, Avignon, France (2010)
19. H. Berek, C. Aneziris, M. Hasterok, H. Biermann, S. Wolf, L. Krüger, Solid State Phenom. 172–174, 709–714 (2011)
20. K. Schwartzwalder, A. V. Somers, U.S. Patent 3,090,094, 1963
21. H. Berek, U. Ballaschk, C. Aneziris, K. Losch, K. Schladitz, Mater. Charact. **107**, 139–148 (2015)
22. Testing of metallic materials-Compression test of metallic cellular materials, in *DIN 50134*, ed. (2008)
23. M. Ashby, Met. Trans. A **14** A, 1755–1769 (1983)
24. J. Elliott, A. Windle, J. Hobdell, G. Eeckhaut, R. Oldman, W. Ludwig, Am. J. Mater. Sci. **37**, 1547–1555 (2002)
25. R. Singh, P. Lee, T. Lindley, C. Kohlhauser, C. Hellmich, M. Bram, Acta Biomater. **6**, 2342–2351 (2010)
26. S. Martin, H. Berek, C. Aneziris, U. Martin, D. Rafaja, J. Appl. Cryst. **45**, 1136–1144 (2012)
27. C. Weigelt, C. Aneziris, H. Berek, D. Ehinger, U. Martin, Adv. Eng. Mater. 1–2 (2012)
28. C. Weigelt, C. G. Aneziris, A. Yanina, S. Guk, Steel Res. Int. **82**(9), 1080–1086 (2011)
29. H. Berek, C. Aneziris, M. Hasterok, C. Weigelt, in Werkstoffe und werkstofftechnische Anwendungen, 13. Werkstofftechnisches Kolloquium; TU Chemnitz, Chemnitz (2010)
30. F. Coté, V. Deshpande, N. Fleck, A. Evans, Mat. Sci. Eng. A. **83**, 272–280 (2004)
31. R. K. Mc Farland, AIAA J. **1**(6), 1380–1385 (1963)
32. T. Wierzbicki, Int. J. Impact Eng. **1**(2), 157–174 (1983)
33. M. Yang, P. Quiao, J. Sandw. Struct. Mater **10**, 133–160 (2008)
34. V. Dravid, V. Ravikumar, J. Am. Ceram. Soc. **77**, 2758–2762 (1994)
35. M. Lajavardi, D. Kenney, S. Lin, J. Chin. Chem. Soc. **47**, 1055–1063 (2000)

Chapter 17
The Corrosion Behavior of High-Alloy CrMnNi Steels—A Research Work on Electrochemical Degradation in Salt- and Acid-Containing Environments

Marcel Mandel, Volodymyr Kietov and Lutz Krüger

Abstract The electrochemical corrosion behavior of high-alloy cast steels as well as of steel/ceramic composites was analyzed by conventional polarization, electrochemical impedance and long term-outdoor exposure tests in sulfuric acid and chloride containing solutions. Additionally, for the determination of corrosion initiation processes and its subsequent implications, potentiodynamic polarization and electrochemical noise were combined with the acoustic emission technique. The results of these studies show that several corrosion mechanisms occur simultaneously when the surface is potentiodynamically stressed, and that pitting corrosion starts with a specific time-shift to its initiation at the surface.

17.1 Introduction

A wide range of techniques and analysis tools have been developed for studying the electrochemical corrosion behavior of high-alloy steels, with such techniques providing detailed information about the specific characteristics of steels in defined environments. The subsequent chapter explains how the electrochemical corrosion of high-alloy TRIP/TWIP steels with zirconium dioxide particle reinforcement was analyzed by a number of methods, such as conventional cyclic polarization, electrochemical impedance, indoor and outdoor exposure tests and special analytical tools, such as the combination of linear polarization and electrochemical noise measurement, as well as the acoustic emission method. For the presented results, the corrosion behavior of the analyzed steel and composite materials in salt- and/or acid-containing media was dictated primarily by the main alloying elements chromium, manganese and nickel as well as by the zirconia particle reinforcement. Due to the pronounced

M. Mandel (✉) · V. Kietov · L. Krüger
Institute of Materials Engineering, Technische Universität Bergakademie Freiberg, Gustav-Zeuner Str. 5, 09599 Freiberg, Germany
e-mail: mandel@iwt.tu-freiberg.de

H. Biermann and C. G. Aneziris (eds.), *Austenitic TRIP/TWIP Steels and Steel-Zirconia Composites*, Springer Series in Materials Science 298,
https://doi.org/10.1007/978-3-030-42603-3_17

passivity, pitting and uniform corrosion were observed, which are the predominant corrosion mechanisms and the focus for the subsequent interpretation of data in the relevant media.

17.2 The Effect of Transformation-Induced Plasticity (the TRIP Effect) on the Electrochemical Degradation of a High-Alloy CrMnNi Steel

Due to the large number of their excellent mechanical properties, their high corrosion resistance and acceptable cost-benefit ratios, high-alloy stainless steels are commonly used in a wide range of applications. As a certain type of this material class, high-alloy TRIP steels offer further enhancement of the mechanical characteristics due to the transformation induced plasticity effect, which arises from a microstructural phase transformation of the metastable austenite phase into a martensite phase during an energy-absorbing process [1–3]. This characteristic combined with good corrosion durability facilitates their integration in the technical configuration for safety-relevant components by reducing costs for subsequent corrosion-protection measures.

With the focus on the material's corrosion behavior, a particular advantage of high-alloy steels is their good corrosion resistance and durability in most aggressive environments. This corrosion resistance is predominantly due to the formation of a chromium-enriched passive oxide layer that restrains the metal-dissolution process during corrosion attack to a technically acceptable level. A further improvement is achieved by the addition of nickel and manganese. Nickel tends to agglomerate as an interlayer at the metal/oxide interface in its metallic state and can also affect the dissolution rate of the entire steel component, whereas manganese increases the solubility of nitrogen and molybdenum, elements that significantly enhance the pitting-corrosion durability of steels [4].

The effect of plastic deformation on the pitting corrosion sensitivity of high-alloy CastX6CrMnNi16-7-3—with the composition given in Table 17.1—was analyzed in a sodium chloride solution [5].

For the evaluation, two degrees of deformation—with $\varepsilon = 9\%$ and $\varepsilon = 18\%$—were defined and the influence of plastic deformation was investigated by cyclic voltammetry before comparison with the initial state. Figure 17.1 presents the scanning electron microscopy (SEM) micrographs for the initial state and after plastic deformation of the TRIP steel, with those components identified that acted in an anodic/cathodic manner during the corrosion attack.

Table 17.1 Chemical composition of high-alloy CastX6CrMnNi16-7-3 TRIP steel in wt%

C	N	Cr	Mn	Ni	Mo	Al	Ti	Si	Fe
0.06	0.13	16.3	6.71	3.06	0.037	0.061	0.0023	0.91	Bal.

In addition to the δ-ferrite, which was the dominant anodic component in the initial state (Fig. 17.1a), a number of deformation bands formed inside the austenitic phase during the deformation process (Fig. 17.1b) and also served as anodic components, whereas beside the δ-ferrite for $\varepsilon = 18\%$, elongated α'-martensite needles dictated the anodic dissolution process of the cast steel (Fig. 17.1c). The results of the polarization tests and the electron micrographs after the corrosion process are shown in Figs. 17.2 and 17.3.

The anodic polarization behavior clearly exhibited a strong dependency on the state of deformation. The initial state revealed the expected passivation and the initiation of metastable pitting corrosion when the anodic potential increased. For $\varepsilon = 9\%$, the corrosion potential $E_{\mathrm{Corr},1}$ increased significantly, but the range of passivity was reduced. It was assumed that this effect could be attributed to the homogeneously formed and distributed micro-anodes inside the large austenite grains (Fig. 17.1b). For the highest analyzed degree of deformation of $\varepsilon = 18\%$, the corrosion potential dropped again to the level of the initial state, and no significant passivation or pitting behavior was detected. In comparison to the initial state and $\varepsilon = 9\%$, the

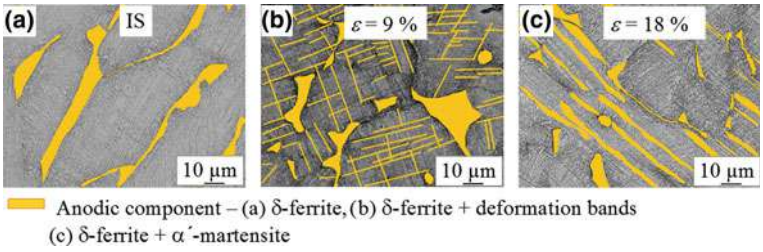

Fig. 17.1 SEM micrographs of **a** the initial state, **b** $\varepsilon = 9\%$ and **c** $\varepsilon = 18\%$, and the anodically active components during a corrosion attack [5]

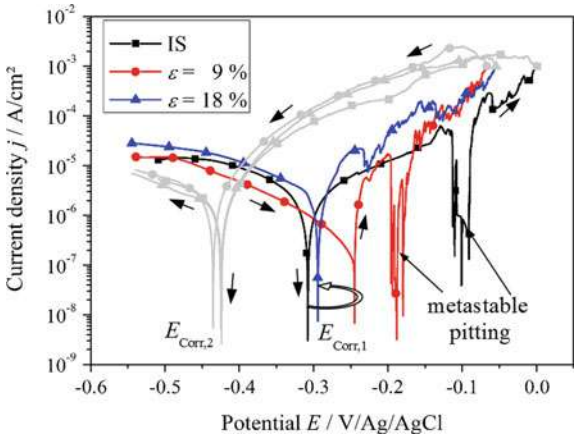

Fig. 17.2 Cyclic polarization curves of the high-alloy CrMnNi steel at different degrees of deformation in 5 wt% sodium chloride solution. $E_{\mathrm{Corr},1}$—corrosion potential before polarization, $E_{\mathrm{Corr},2}$—corrosion potential after polarization. IS—initial state [5]

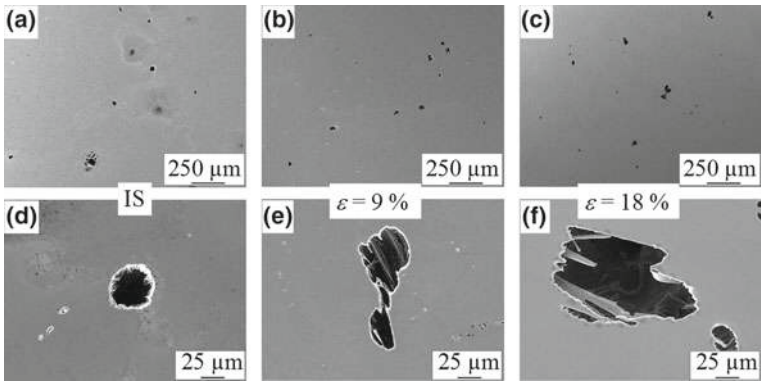

Fig. 17.3 SEM micrographs after polarization in 5 wt% sodium chloride solution. **a** Initial state. **b** $\varepsilon = 9\%$. **c** $\varepsilon = 18\%$. **d**, **e** and **f** detailed views [5]

highest degree of deformation also resulted in the highest degree of corrosion sensitivity during anodic polarization. In comparison, the reverse scan did not indicate any clear difference in polarization behavior, with all deformation states exhibiting similar curve trends and secondary corrosion potentials $E_{\mathrm{Corr},2}$. This characteristic clearly shows that after its initiation, the pitting corrosion attack—which was found for each state after the cyclic polarization (Fig. 17.3)—dictates the ongoing corrosion behavior of the whole steel sample and is independent of the degree of deformation.

17.3 Influence of Particle Reinforcement on the Corrosion Behavior of a High-Alloy Steel in Sodium Chloride Solution

The corrosion behavior of the spark plasma sintered zirconia particle-reinforced high-alloy X5CrMnNi14-6-6 steel was investigated by potentiodynamic polarization in a sodium chloride solution [6]. The chemical compositions of the steel and zirconia powder used are given in Tables 17.2 and 17.3.

Table 17.2 Chemical composition of the high-alloy X5CrMnNi14-6-6 steel in wt%

C	Cr	Mn	Ni	Al	S	Si	Fe
0.04	14.02	6.14	6.11	0.11	0.02	0.91	Bal.

Table 17.3 Chemical composition of the Mg-PSZ powder in wt%

ZrO_2	MgO	HfO_2	SiO_2	Al_2O_3	TiO_2
Bal.	3.37	1.73	2.43	0.63	0.14

Figure 17.4 presents the micrographs of the sintered materials without Mg-PSZ (i.e., 0 vol%) and with contents of 5 and 10 vol%. In comparison to the reinforced composites, the material without particle reinforcement exhibited an increased degree of porosity (Fig. 17.4a). For the composite materials (Fig. 17.4b, c), it was obvious that when the particle content increased, the matrix/particle interfaces also increased significantly, which drastically affected the corrosion behavior of the materials.

In Fig. 17.5 the potentiodynamic polarization curves in a 5 wt% sodium chloride solution are shown, while Fig. 17.6 presents the corresponding electron micrographs after corrosion of the sintered materials.

The polarization curves of the material without (0 vol%) and with 5 vol% particle content showed slight passivation, which was more pronounced for the unreinforced material than for the composite. In comparison, the composite material with 10 vol% Mg-PSZ exhibited the lowest corrosion potential and no significant passivation behavior, which indicated a higher degree of corrosion sensitivity.

The micrographs observed after corrosion attack clearly showed the formation of corrosion pits for the materials with 0 and 5 vol% Mg-PSZ (Fig. 17.6a, b), which was

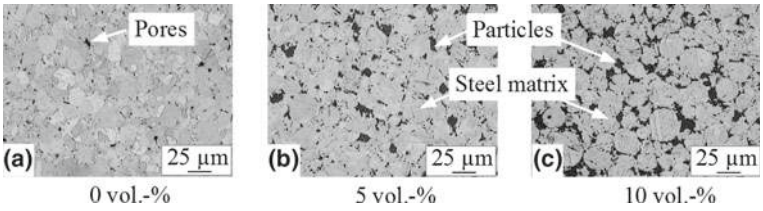

Fig. 17.4 Optical micrographs of the spark plasma sintered and Mg-PSZ particle-reinforced high-alloy steel. **a** without (0 vol%), **b** with 5 vol% and **c** with 10 vol% particle contents [6]

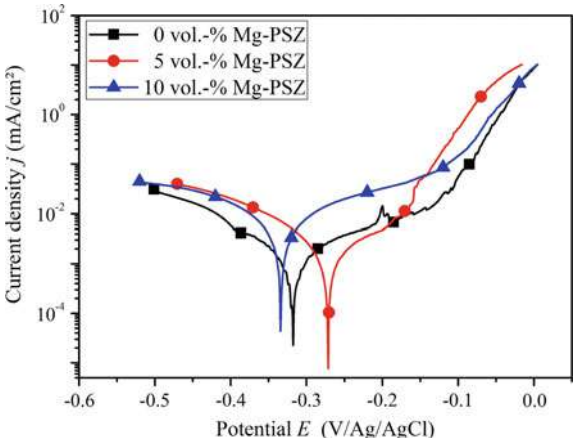

Fig. 17.5 Potentiodynamic polarization curves of the spark plasma sintered high-alloy steel with different Mg-PSZ particle contents in 5 wt% sodium chloride solution [6]

in full agreement with the anodic polarization behavior identified. It was assumed that pitting was initiated at the pores for the unreinforced material, because such pores represented critical weak points in and on the surface that interrupted the formation of a dense and continuous passive oxide layer. For the composite with 5 vol% Mg-PSZ, the micrograph clearly indicated that pitting had its origin at the matrix/particle interface. For the composite with 10 vol% Mg-PSZ, the corrosion attack was more homogeneous and no pitting was observed, with the entire surface indicating a uniform corrosion attack (Fig. 17.6c). As a primary result, the polarization curves and the micrographs clearly indicated that by increasing the Mg-PSZ particle content, the corrosion mechanism changed from pitting to general corrosion. Due to the increase in the particle content up to 10 vol%, the formation of a dense and compact passive oxide layer was suppressed and the composite became more susceptible to corrosion. To evaluate the passive oxide destabilization, the contents of iron and the main alloying elements found in the electrolyte was analyzed by ICP-MS (Inductively Coupled Plasma Mass Spectrometry) after the polarization. The results are presented in Fig. 17.7.

The comparison clearly shows that significant increases in the contents of iron, chromium, nickel and manganese are detectable in the solution when the Mg-PSZ

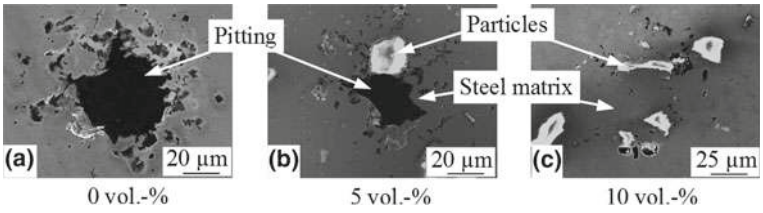

Fig. 17.6 SEM micrographs of the spark plasma sintered Mg-PSZ particle-reinforced steel after polarization in 5 wt% sodium chloride solution [6]

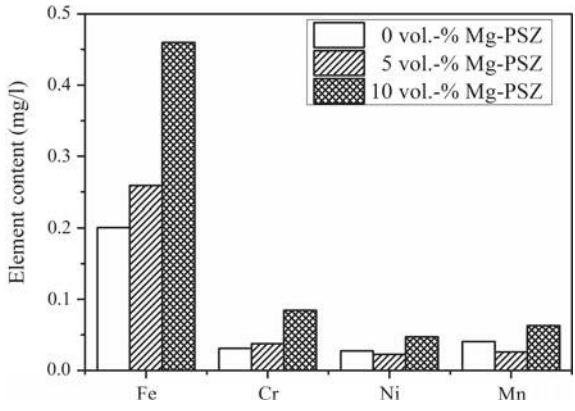

Fig. 17.7 Content of iron and main alloying elements in the electrolyte after potentiodynamic polarization in 5 wt% sodium chloride solution [6]

content is increased up to 10 vol%. The electrolyte analysis confirms that the passivation behavior of the steel matrix is drastically reduced when the particle content increases and the entire composite is more susceptible to an aggressive medium.

In a further study, the corrosion behavior of the unreinforced material (0 vol%) and the composite with 10 vol% Mg-PSZ particle content was investigated by a one-year outdoor exposure test and compared to the results obtained after potentiodynamic polarization in a 5 wt% sodium chloride solution [7]. For the outdoor exposure test, the specimens were stored in an outdoor exposure test rig in Dresden, Germany and sprayed weekly with a 3 wt% sodium chloride solution.

Figure 17.8 presents the micrographs after the polarization test in the 5 wt% sodium chloride solution and after the one-year outdoor exposure test.

After polarization, the material without particle reinforcement was attacked by pitting corrosion (I in Fig. 17.8a), whereas the particle-reinforced composite exhibited a uniform corrosion attack and an attack at the particle/matrix interface (II in Fig. 17.8b), which was accompanied by intensified particle detachment (III in Fig. 17.8b). Similar behavior was observed after one year of outdoor exposure testing. Pits were identified on the surface of the unreinforced material (Fig. 17.8c), while a large number of small cavities were found on the composite material that had resulted from the detachment of Mg-PSZ particles (Fig. 17.8d). In addition to these localized corrosion attacks, the intensified formation of red rust was observed. This behavior was more pronounced for the composite material and also confirmed the higher corrosion sensitivity and lower passivation ability that was identified

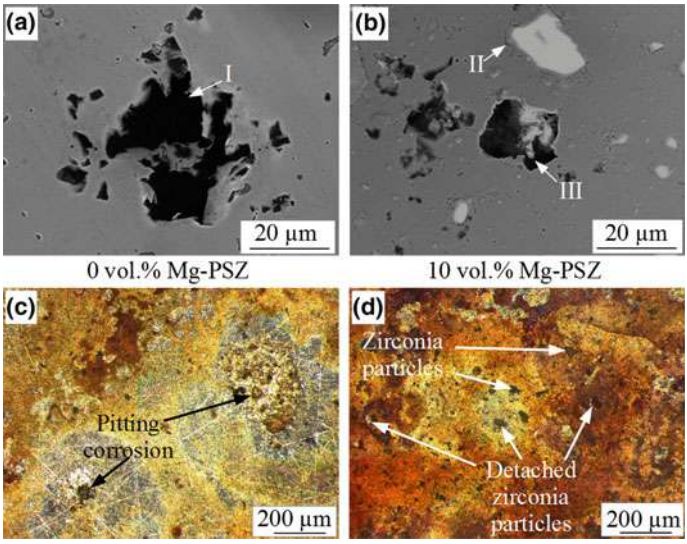

Fig. 17.8 Micrographs of the spark plasma sintered high-alloy steel after potentiodynamic polarization in 5 wt% sodium chloride solution and after one year of outdoor exposure. **a** and **c** without particle reinforcement. **b** and **c** with 10 vol% Mg-PSZ. For I, II and III, see text [7]

during the polarization test. The results of the study show that under similar conditions, the results of the short-time polarization test can be used to approximate the corrosion behavior associated with long-term outdoor exposure tests.

17.4 Electrochemical Corrosion of the Particle-Reinforced High-Alloy Steel at Different Temperatures

The electrochemical corrosion behavior of the composite material with 10 vol% Mg-PSZ was investigated in a 5 wt% sodium chloride solution by cyclic polarization and electrochemical impedance at temperatures of 25, 35, 45 and 55 °C. In a separate test, the critical temperature for intensified particle detachment was determined [8]. Figure 17.9 presents the optical micrographs of the composite material in its initial state.

Figure 17.10 shows the impedance spectra at different temperatures before the cyclic polarization, which clearly indicate a strong temperature dependency. In the Nyquist plot (Fig. 17.10a) for each temperature, a simple semi-circle is described by the data points, which indicate the reduction of the charge-transfer resistance when the temperature increases. From the Bode illustrations (Fig. 17.10b, c), one time constant was extracted for each temperature. Figure 17.11 shows the electrode configuration and the equivalent circuit that was used for modeling and curve fitting. The results are summarized in Table 17.4. The parameters Q and α did not depend on the temperature to a significant degree, whereas $R_{t,bp}$ declined when the temperature increased, indicating an increase in the charge transfer processes when the temperature increased. Similar behavior was noted for the electrolyte resistance R_e, signifying an increase in the conductivity of the test solution. Figure 17.12 presents the cyclic polarization curves for the selected temperatures, which clearly illustrate the significant enhancement of the corrosion kinetics when the temperature rises. The corrosion potentials before (1 in Fig. 17.12) and after (2 in Fig. 17.12) the polarization process did not exhibit any significant dependency on the temperature, whereas the anodic parts of the curves revealed that there was no passivation and that the slopes

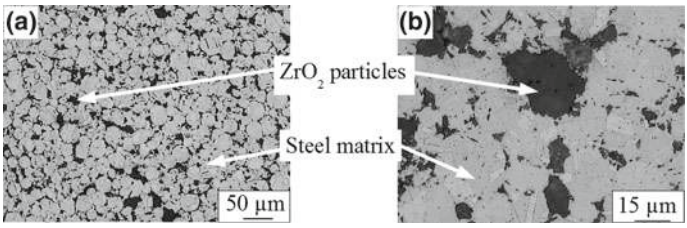

Fig. 17.9 Micrographs of the spark plasma sintered particle-reinforced high-alloy steel with 10 vol% Mg-PSZ. **a** Overview of particle distribution in the steel matrix. **b** Detailed view of particle agglomeration [8]

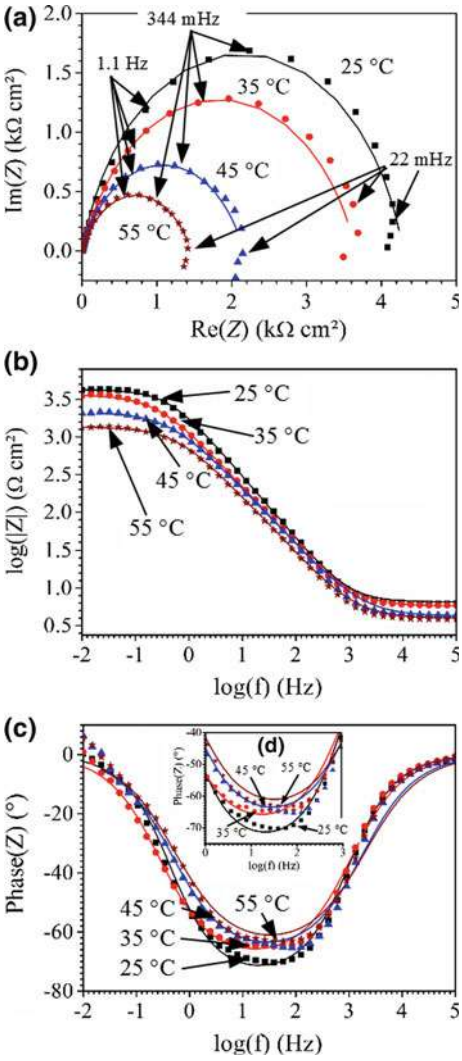

Fig. 17.10 Electrochemical impedance spectra of the spark plasma sintered high-alloy steel before cyclic polarization at different temperatures [8]

increased in line with the temperature. The more negative values for the corrosion potential 2 in Fig. 17.12 clearly indicated a more corrosion-sensitive electrode state at each temperature after the polarization. From the progression of the curve, it was deduced that the temperature influenced the corrosion potentials minimally, though it affected the polarization behavior significantly. Figure 17.13 shows the electron micrographs of the composite material after cyclic polarization. For 25 and 35 °C, the surfaces showed evidence of a predominantly homogenous corrosion attack with weak localized corrosion attacks (arrows in Fig. 17.13a, b), which were related to the increased porosity due to Mg-PSZ particle detachment.

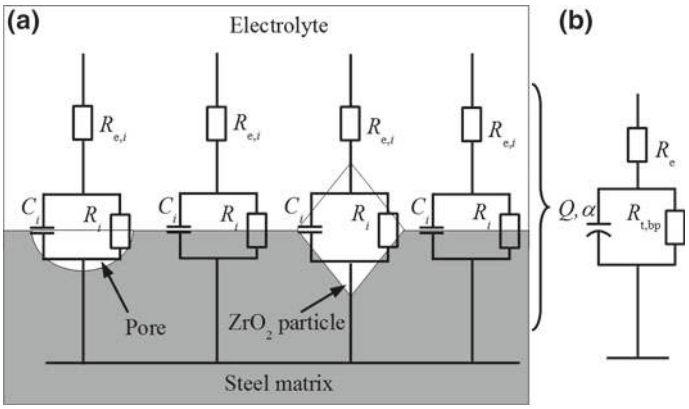

Fig. 17.11 **a** Schematic illustration of the electrode configuration before cyclic polarization, and **b** equivalent circuit used for curve fitting. R_i, C_i and $R_{e,i}$ stand for the local and R_e, Q, α, and $R_{t,bp}$ the global impedance parameters before polarization

Table 17.4 Impedance curve fitting results before polarisation in 5 wt% NaCl solution on 10 vol% Mg-PSZ particle-reinforced steel

T (°C)	R_e (Ω cm^2)	Q ($\mu\Omega^{-1}$ cm^{-2} s$^{\alpha}$)	α	$R_{t,bp}$ (kΩ cm^2)
25	6.2	176	0.82	4.0
35	5.3	302	0.74	2.1
45	5.0	180	0.80	1.6
55	4.5	322	0.74	1.5

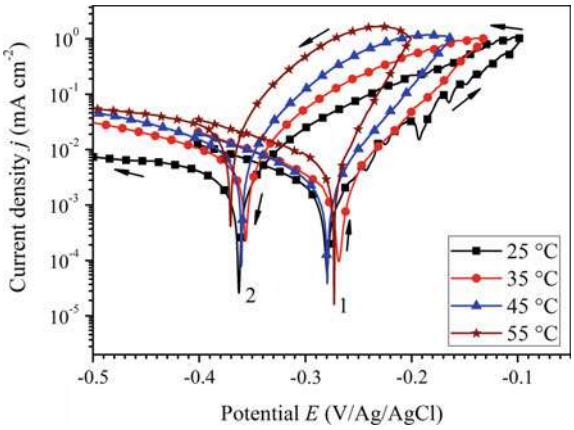

Fig. 17.12 Cyclic polarization curves of the spark plasma sintered particle-reinforced high-alloy steel at different temperatures. 1—E_{Cor} before polarization. 2—E_{Cor} after polarization [8]

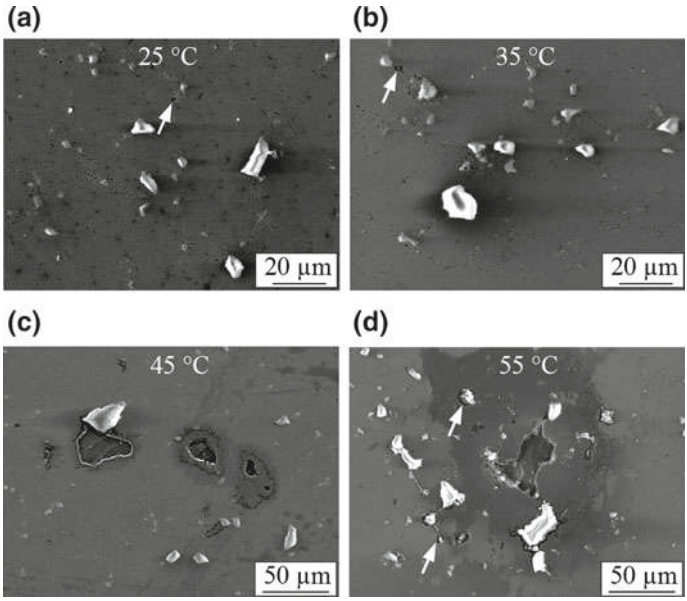

Fig. 17.13 SEM micrographs of the particle-reinforced composite after cyclic polarization in 5 wt% NaCl solution at different temperatures [8]

The micrographs observed for 45 and 55 °C clearly show an attack by localized corrosion that had its origin at the particle/matrix interface (arrows in Fig. 17.13d). It was obvious that when the temperature increased above 35 °C, particle detachment occurred in a more intensified fashion as a result of the enhanced corrosion kinetics at the interface. From the results of the electron microscope observations, it was certain that a critical temperature for intensified particle detachment had to exist in the range of 35 to 45 °C. Figure 17.14 presents the electrochemical impedance spectra measured after the polarization test. Similarly to the initial state shown in Fig. 17.10, the Nyquist illustration revealed a semi-circle for each temperature with a significant decrease of the charge transfer resistance for $T = 45$ °C and $T = 55$ °C (Fig. 17.14a). From the Bode plots (Fig. 17.14b, c), two time constants were identified for all temperatures, which were related to charge transfer processes at the interface between the composite and the layer generated by film formation and redox reactions inside the film formed. The surface structure and the equivalent circuit used for curve fitting are presented in Fig. 17.15.

After polarization, the global impedance parameters of the composite/film interface were expressed by Q_1, α_1 and $R_{t,ap}$ and for the film by Q_2, α_2 and R_f. The results obtained by curve fitting are summarized in Table 17.5.

For 25 and 35 °C, the parameters Q_1, α_1 and $R_{t,ap}$ were dictated by the pores and Mg-PSZ particles. At temperatures of $T = 45$ °C and $T = 55$ °C, the impedance values included the increased porosity, the attacked interface at the particles and the pits that were formed. For the determination of the critical pitting temperature, the

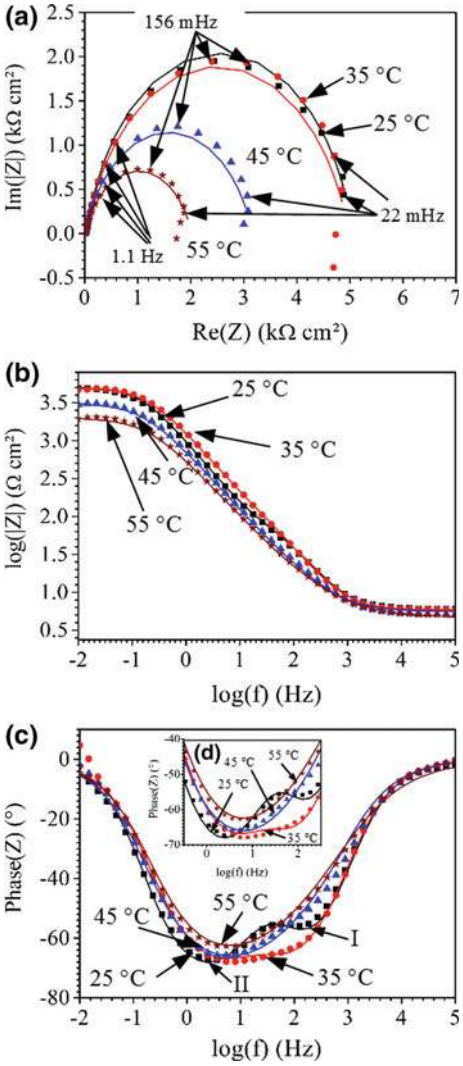

Fig. 17.14 Electrochemical impedance spectra of the particle-reinforced composite determined after cyclic polarization in 5 wt% sodium chloride solution for different temperatures [8]

current-time relationship for continuously increasing temperature was recorded, and is shown in Fig. 17.16.

The correlation revealed a slight increase in current density up to a temperature of 34 °C, including a peak between 32 and 33 °C. This characteristic was related to particle detachment. When the temperature increased further, the current density increased significantly and exhibited fluctuations up to a temperature of 38 °C—which was related to the intensified particle detachment that was evident. For higher temperatures, the current density increased drastically and indicated pitting corrosion

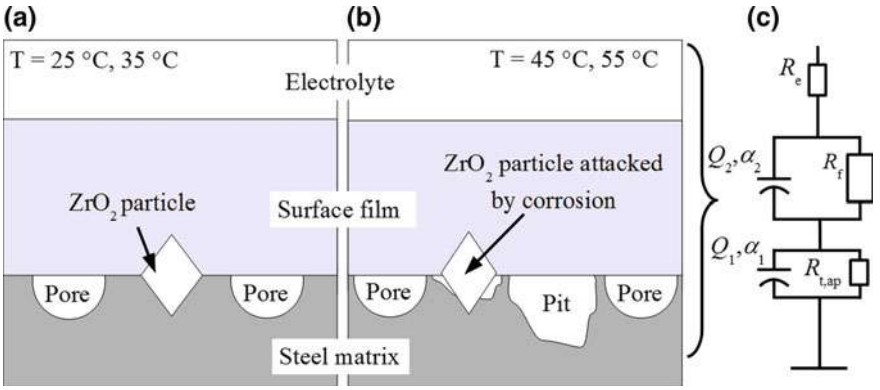

Fig. 17.15 **a**, **b** Schematic illustration of the composite interface after polarization in 5 wt% sodium chloride solution at different temperatures. **c** Equivalent circuit used for curve fitting of the impedance spectra [8]

Table 17.5 Impedance curve fitting results after polarisation in 5 wt% NaCl solution on 10 vol% Mg-PSZ particle-reinforced steel. T in °C, R_e, $R_{t,ap}$ in Ω cm^2 and R_f in kΩ cm^2, Q_1, Q_2 in μΩ^{-1} cm^{-2} s$^{\alpha}$

T	R_e	Q_1	α_1	$R_{t,ap}$	Q_2	α_2	R_f
25	6.3	390	0.92	17	215	0.83	5.4
35	5.5	496	0.91	29	64.3	0.79	4.3
45	5.2	229	0.77	13	54.5	0.83	3.2
55	4.8	1260	0.58	11	104	0.78	1.8

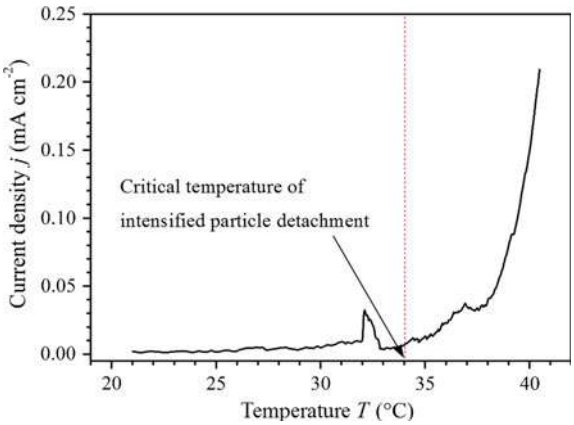

Fig. 17.16 Current density—temperature relationship for determination of the critical temperature of the composite [8]

attack. Consequently, the critical temperature for intensified particle detachment and subsequent pitting corrosion attack on the composite was approximately 34 °C.

17.5 Potentiodynamic Polarization of CastX5CrMnNi16-7-9 in Sulfuric Acid Solution Combined with Acoustic Emission Analysis

The acoustic emission (AE) technique for the investigation of corrosion phenomena is an excellent method for analyzing the different processes taking place in parallel at the electrode surface [9, 10]. As shown by Boinet et al. [9], acoustic emission analysis facilitates the separation of surface degradation processes and gas bubble evolution by determination of the frequency of AE signals. To evaluate the corrosion activity of the high-alloy cast steel CastX5CrMnNi16-7-9 in sulfuric acid solution, the AE method was applied during potentiodynamic polarization. The chemical composition and characteristic microstructure of the initial state are given in Table 17.6 and Fig. 17.17.

In contrast to the widely used two-cell configuration, which is discussed in detail elsewhere [11], the modified test set-up shown in Fig. 17.18 was used, which also facilitated the observation of the gas bubble stream leaving the electrode surface [12].

The polarization characteristic and corresponding AE activity is presented in Fig. 17.19. To illustrate the correlation between polarization and acoustic emission as well as the involvement of the 30-minute OCP measurement (OCP—open circuit

Table 17.6 Chemical composition of the high-alloy cast steel CastX5CrMnNi16-7-9 in wt%

C	N	Cr	Mn	Ni	Mo	Al	Cu	W	Si	Fe
0.048	0.076	15.7	6.29	9.23	0.082	0.047	0.011	0.02	0.853	Bal.

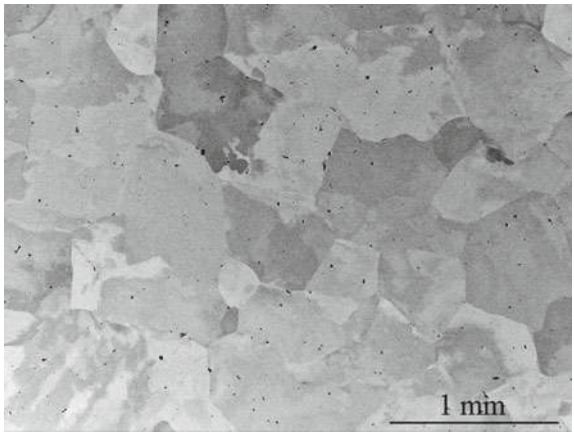

Fig. 17.17 Electron micrograph of CastX5CrMnNi16-7-9 [12]

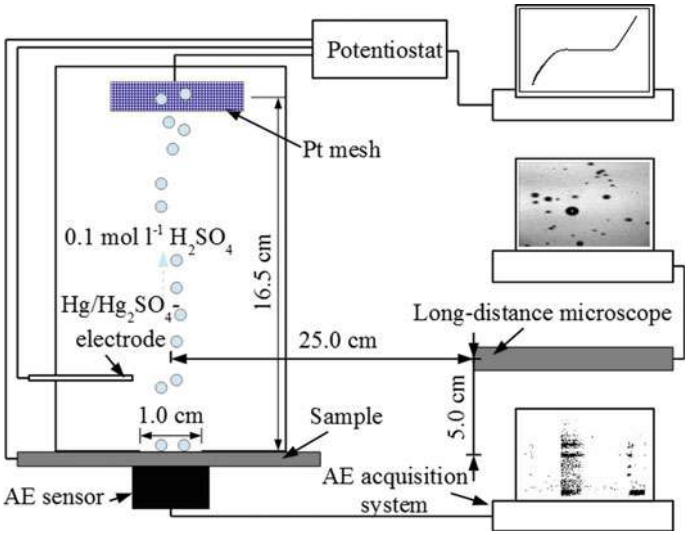

Fig. 17.18 Schematic illustration of the test set-up used for investigation of the acoustic activity and gas bubble evolution process for a steel electrode during potentiodynamic polarization in a 0.1 M H_2SO_4 solution [12]

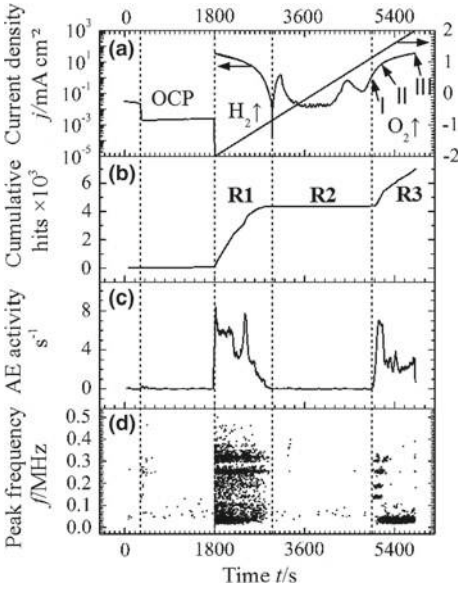

Fig. 17.19 Correlation between the potentiodynamic polarization and measured acoustic emissions. **a** Open circuit measurement (OCP) and polarization behavior. **b** Cumulative AE hit number. **c** AE activity. **d** Peak frequency of AE signals. I, II and III indicate current densities upon oxygen evolution analysis [12]

potential), the time t was chosen as the common x-axis. In general, 3 regions of acoustic activity (R1, R2 and R3) where recognized during the polarization. Region R1 was indicated by a high level of acoustic activity (Fig. 17.19b, c) and corresponded fully to the cathodic branch of the polarization curve when intensified H_2 gas bubble evolution was initiated. Region 2 (R2) was characterized by low AE activity, whereas region 3 (R3) indicated a further increase in acoustic emissions, which was attributed to the evolution of oxygen at the electrode.

Before polarization, the OCP measurement revealed a conspicuous AE event number in the frequency range of $f = 150$–460 kHz after approximately $t \sim 400$ s (Fig. 17.19d) that corresponded to a significant decline in potential of $\Delta E = 570$ mV (Fig. 17.19a). The literature indicates that this frequency range is typical for the evolution of a hydrogen bubble at the electrode surface. Consequently, it was concluded that the decline in potential observed indicated the transition of the electrode into the steady state, which was accompanied by the release of hydrogen gas bubbles from the steel surface. The analysis of region 1 (R1) showed the existence of two characteristic processes which occurred almost simultaneously at the steel electrode. One of these was the intensified hydrogen bubble evolution observed during cathodic polarization (see Fig. 17.20a), and generated AE signals in the frequency range of $f =$ 100–430 kHz. The hydrogen gas bubbles had a diameter in the range of 200–640 μm. The second type of AE was observed in the lower frequency range of $f = 20$–100 kHz and was attributed to the hydrogen-assisted exfoliation process (Fig. 17.20b). The AE data analysis of region R1 revealed two classes of AE signals by determination of its spectral AE energy and signal duration. The results are presented in Fig. 17.20c and clearly show two specific clusters (C1 and C2).

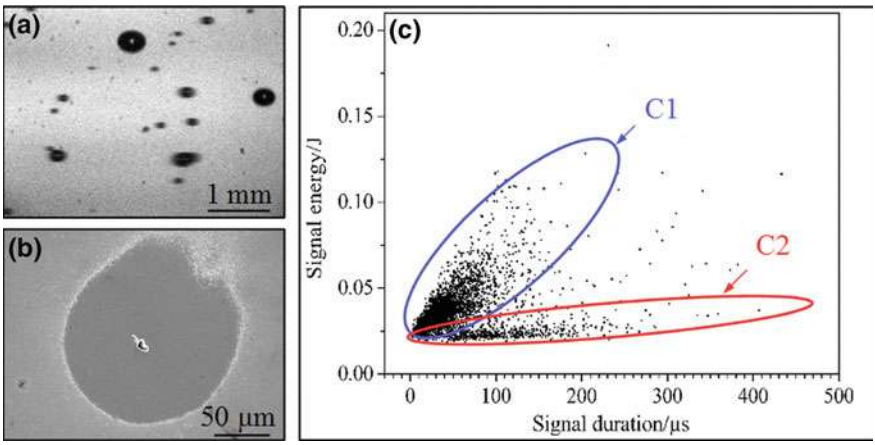

Fig. 17.20 Hydrogen evolution **a** and hydrogen-assisted exfoliation of the passive oxide **b** are the characteristic AE sources during cathodic polarization. The AE data analysis **c** indicated a high energy and low duration for the hydrogen bubble evolution process (cluster C1), and low energy with high signal duration for the exfoliation process (cluster C2) [12]

Cluster C1 was characterized by a high spectral energy and low signal duration and corresponded to hydrogen bubble evolution. In cluster C2, the signals were typified by lower spectral energies and higher durations, and correlated to the hydrogen-assisted exfoliation process.

At the transition into anodic polarization, the AE hit number and activity (Fig. 17.19 b, c) decreased drastically. Just a low number of AE signals were identified in region R2, with most of them in the frequency range below 100 kHz, which was attributed to electrochemical degradation processes on the steel surface. The surface analysis by SEM identified a corrosion attack at the pore edges (Fig. 17.21) that remained constant when the potential increased within region R2.

Figure 17.22 presents a detailed view of the AE peak frequency characteristics of region R3 (Fig. 17.22a) and the corresponding cluster analysis (Fig. 17.22b). Similar to region R1, the subsequent AE data analysis exhibited a high signal energy and low duration for the AE hits with $f > 100$ kHz and low energy and high duration for the AE signals with $f < 100$ kHz.

After passing the potential of $E_1 = 1.15$ V versus Hg/Hg_2SO_4, a second increase in AE activity occurred that correlated with the onset of oxygen gas bubble formation.

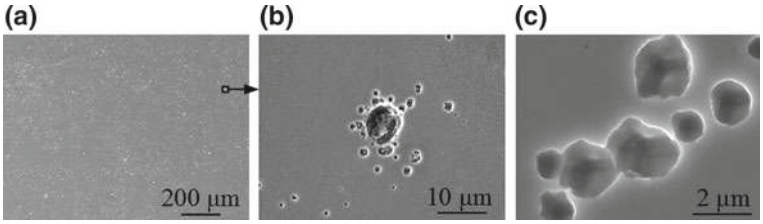

Fig. 17.21 Characteristic damage evolution on the steel surface during anodic polarization in region R2. **a** Overview. **b** Detailed view showing corrosion attack at the pore edges. **c** Detailed view showing corrosion attack at the passive oxide [12]

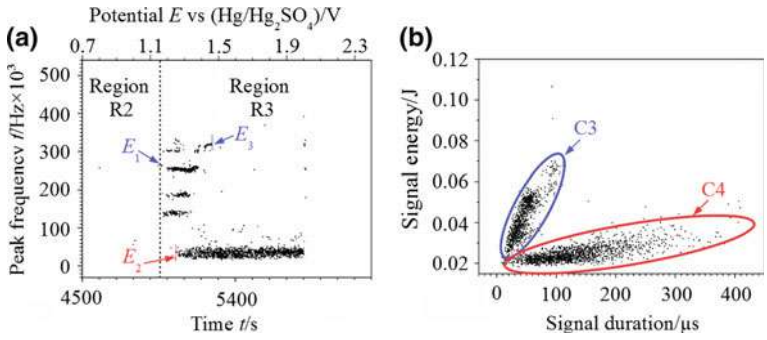

Fig. 17.22 **a** Observed peak frequency-time relations as a function of the applied potential. **b** The corresponding AE cluster analysis. E_1, E_2 and E_3 denote the specific potentials of the clusters C3 and C4 [12]

The analysis of the gas stream revealed a bubble diameter in the range of 240–430 μm and the AE data exhibited a corresponding peak frequency of $f > 100$ kHz, which was similar to the hydrogen bubble diameter and peak frequency range observed in region R1. Additionally, when the potential was increased further up to $E_2 = 1.25$ V versus Hg/Hg_2SO_4, gas bubbles of significantly lower diameters of approximately 50 μm were identified in the gas stream (Fig. 17.23b). Simultaneously, an increase in the number of AE events within the peak frequency of $f = 20$–60 kHz was observed (Fig. 17.22a), which was in a similar frequency range to the signals attributed to the hydrogen-assisted exfoliation in region R1 (Fig. 17.19 d). The oxygen gas bubbles with diameters of 240–430 μm were designated as oxygen bubbles of Type 1, while the bubbles with a diameter of approx. 50 μm were designated as oxygen bubbles of Type 2.

Moreover, when the potential was increased further up to $E \sim 1.45$ V versus Hg/Hg_2SO_4, the AE signals with a peak frequency of $f > 100$ kHz ended abruptly, which corresponded well with the disappearance of Type 1 oxygen bubbles in the gas stream. Up to the end of the polarization process, only Type 2 oxygen gas bubbles were identified in the gas stream (Fig. 17.23c).

The damage evolution of the steel surface observed by scanning electron microscopy showed a clearly inhomogeneous corrosion attack (Fig. 17.24a) when the steel was polarized up to point II (II in Fig. 17.19a). In accordance with the observations made after cathodic polarization, pores were the preferred locations for the genesis of Type 1 oxygen gas bubbles (Fig. 17.24b). In addition, the rest of the surface was marked by regions of localized corrosion attacks (F-I in Fig. 17.24c) and areas of full depassivation (F-II in Fig. 17.24c). The drastic increase in damage evolution was attributed to an oxygen-assisted exfoliation process, which identified the steel surface as the location for the formation of Type 2 oxygen gas bubbles. Up to the end of the polarization process (III in Fig. 17.19a), the scanning electron micrographs showed a fully depassivated steel surface and corrosion attack at the grain boundaries due to intergranular corrosion (Fig. 17.24d). As a side effect of the exfoliation process (Fig. 17.24f), a dissolution of the pores was observed that eliminated the basis of Type 1 oxygen bubble evolution (Fig. 17.24e).

Consequently, the rate at which oxygen bubbles was released at the pores had to decrease when the passive oxide dissolution increased. This behavior was in full

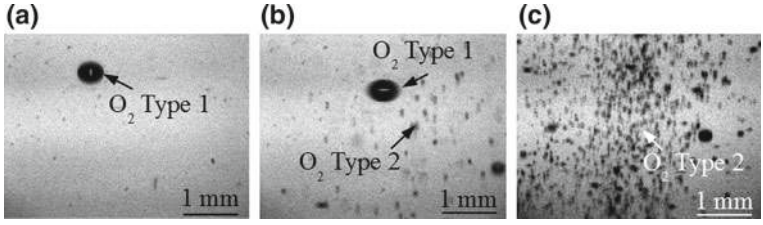

Fig. 17.23 Photographs of the oxygen gas bubble stream at anodic applied potential **a** at I in Fig. 17.19a, **b** at II in Fig. 17.18a, **c** at the end of the polarization test (III in Fig. 17.19a) [12]

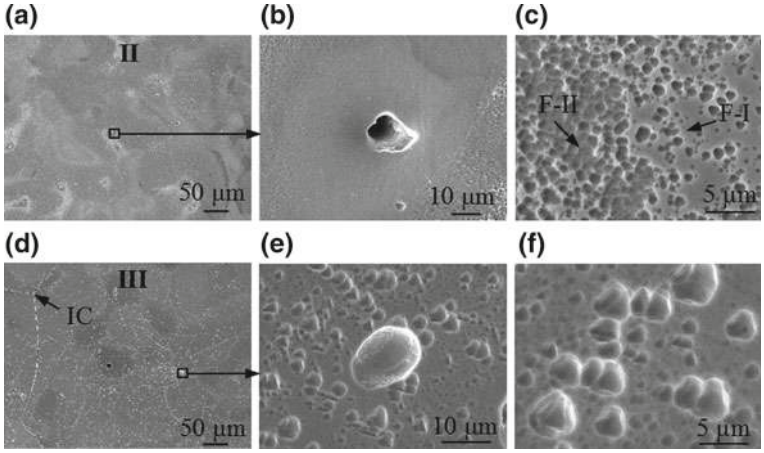

Fig. 17.24 SEM micrographs of the steel surface after polarization up to point II (**a–c**) and up to the end of the polarization test (**d–f**). IC—Intergranular corrosion. For F-I and F-II, see text [12]

accordance with the observed decline in the release of Type 1 oxygen bubbles and the identified potential limitation of AE events with frequencies of $f > 100$ kHz (Fig. 17.19d).

17.6 Analysis of Pit Initiation on CastX3CrMnNi16-7-9 by the Combination of Electrochemical Noise and Acoustic Emission Measurement

The electrochemical noise (EN) and acoustic emission (AE) methods are highly suitable monitoring and analysis tools for the investigation of corrosion initiation processes under steady state conditions [9–17]. The EN technique is based on the measurement of potential and/or current fluctuations, which facilitates the determination of the activity of a corrosion system. The AE technique—based on the measurement of elastic waves—is useful in identifying different corrosion mechanisms occurring at the same time on a surface [12]. One outstanding characteristic is that both methods are non-destructive and highly sensitive, which facilitates the identification of corrosion initiation processes.

Due to these advantageous properties, the EN and AE techniques were combined in the identification of pit initiation at the surface of the high-alloy cast steel CastX5CrMnNi16-7-9—with the chemical composition and microstructure given in Table 17.6 and Fig. 17.17—in a 5 wt% sodium chloride solution [18]. The investigation was carried out with the test set-up shown in Fig. 17.25. Details of the experimental specifications of the electrochemical noise and acoustic emission measurements are given in [18].

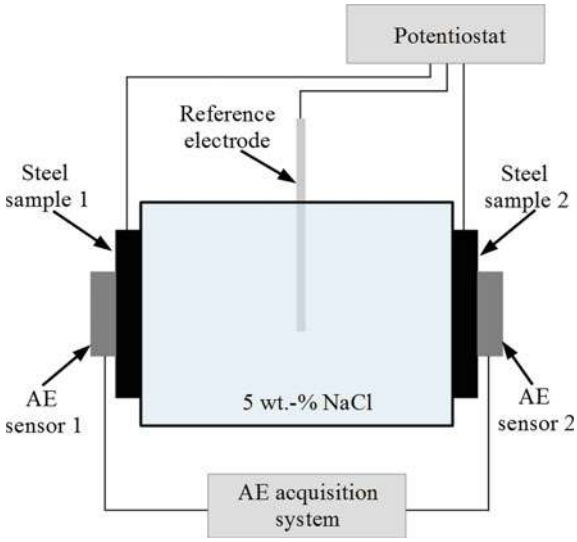

Fig. 17.25 Test set-up used for characterization of the pit initiation behavior of Cast X5CrMnNi16-7-9 by means of combined electrochemical noise and acoustic emission measurement [18]

Figure 17.26 presents the results of the 70-hour test, which exhibited two characteristic types of AE events and four specific regions of noise behavior. For a more sensitive analysis of the EN behavior, the standard deviations of the potential and current noise—σ_E and σ_i—were determined and evaluated. The results are shown in Fig. 17.27.

From the point of view of the EN behavior (Fig. 17.27), region EN-I was characterized by strong fluctuations, indicating the high electrochemical activity of the steel surface before transitioning into a nearly steady state after approximately 3 h, which is given by region EN-II. In region EN-II, the signal fluctuations were significantly lower, indicating that the steel surface had transitioned into a passive state. In addition to this predominantly inactive electrochemical state, a spontaneous short-time event was observed after approximately 16 h of exposure. This event was attributed to localized passive oxide deterioration caused by the chloride ions in the solution, indicating metastable pitting corrosion. Region EN-II ended abruptly after approximately 20 h of exposure, which was indicated by a drastic increase in potential and current fluctuations that characterized region EN-III. The high degree of fluctuations in region EN-III indicated a highly active surface state. This behavior was related to the onset of an active pitting corrosion attack. Region EN-III had a duration of 15 h and ended after approximately 35 h of exposure. The transition into region EN-IV was characterized by a continuous decline in the fluctuations to the point of low electrochemical activity, indicating the repassivation of active pits. Nevertheless, EN-IV also exhibited time intervals of increased activity, which were attributed to a spontaneous and irregular reactivation of previously formed pits and active pit growth. When considering the results of the acoustic emission test, no acoustic activity could

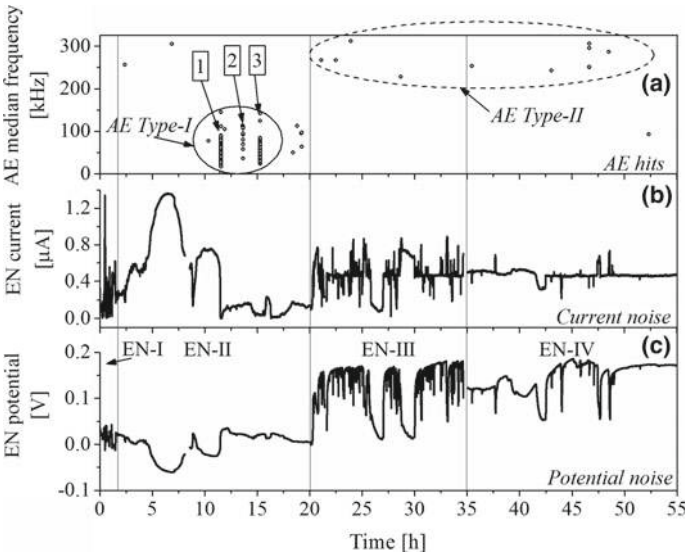

Fig. 17.26 Electrochemical noise behavior and corresponding AE characteristics of CastX5CrMnNi16-7-9 during a 70 h exposure test in 5 wt% NaCl solution. **a** Median frequency of the AE signals. **b** and **c** Current and potential noise signals [18]

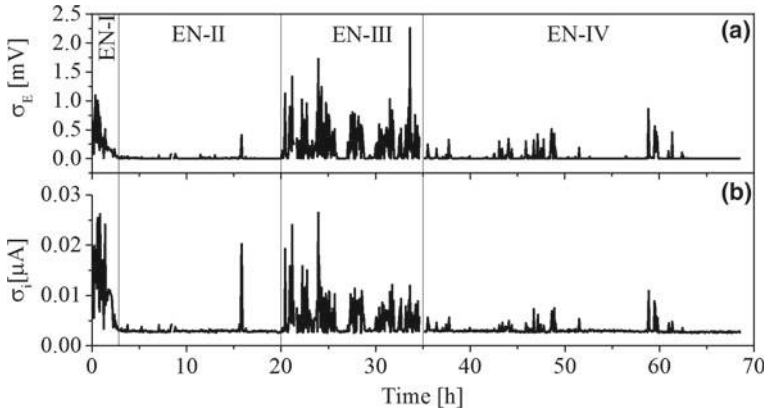

Fig. 17.27 Standard deviation of the potential **a** and current **b** noise extracted from the signals given in Fig. 17.26b, c [18]

be observed after 10 h of exposure (see Fig. 17.26a). Indications of AE activity were identified after $t = 11.6$ h, $t = 13.7$ h and $t = 15.3$ h, which were marked by the numbers 1, 2 and 3 in Fig. 17.26a and which lay entirely within region EN-II. The events arose in three clusters with a median peak frequency of $f < 100$ kHz, indicating three corrosion attacks at the steel surface. For higher exposure times—especially in the regions EN-III and EN-IV—a second class of events with a median peak frequency

of $f > 100$ kHz were observed. The AE signal analysis and the characteristic shape of the waveform (Fig. 17.28) clearly described two different types of AE signals.

The signals with a peak frequency of $f < 100$ kHz were designated as AE Type I signals and the events with $f > 100$ kHz were characterized as AE Type II signals (see Fig. 17.26a). With respect to the findings described in the literature [9, 12], it can be stated that AE Type I signals are characteristic for spontaneous and localized passive oxide breakdown, whereas the irregularly distributed events that give rise to AE Type II signals may be attributed to subsequent hydrogen bubble evolution inside previously formed pits [19, 20]. SEM observations after test completion confirmed localized deterioration in the form of three pits that developed on the steel surface under corrosive attack (Fig. 17.29). Consequently, the electrochemical noise and corresponding acoustic emission development made it possible to identify and follow the point of pit initiation ($t = 11.6$ h) and the subsequent pit evolution process.

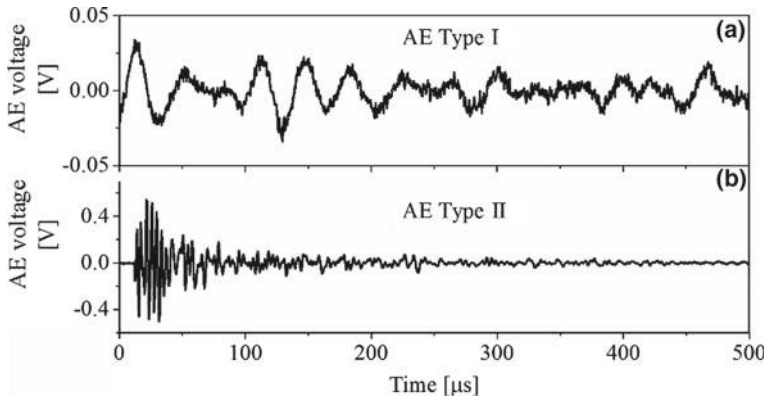

Fig. 17.28 Wave forms of the **a** AE Type I and **b** AE Type II signals [18]

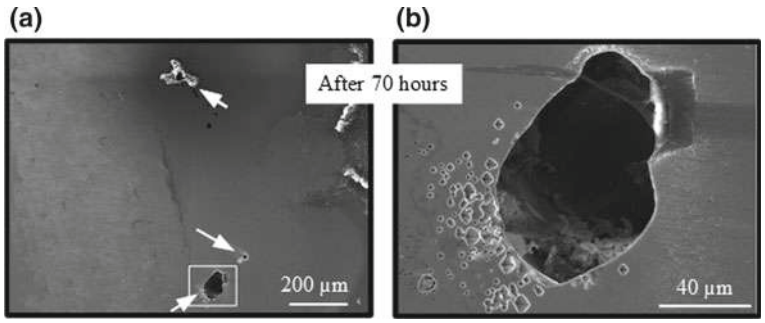

Fig. 17.29 SEM micrograph of the CastX5CrMnNi16-7-9 steel after the 70 h electrochemical noise and acoustic emission measurement test. **a** Overview. Arrows indicate the locations of pitting corrosion. **b** Detailed view of the pit marked with a rectangle in **(a)** [18]

17.7 Analysis of Electrochemical Noise by Continuous Wavelet Transform

As shown in [18], the electrochemical noise technique is a highly sensitive and, therefore, highly appropriate analysis method for online corrosion monitoring and the identification of different stages in pit evolution. Several techniques in noise data analysis were developed to ensure the precise acquisition of information about the corrosion process. Widely used techniques such as certain statistical methods, the Fourier transformation and wavelet analysis are practiced [14, 21, 22], though highly specified analytical procedures have also been developed to identify and isolate localized and uniform corrosion attacks [23, 24]. In principle, the above-mentioned mathematical techniques analyze the changes in the fluctuations of the noise signal and provide information about the onset, duration and kinetics of a corrosion system [25–27]. A corrosion system that is highly active electrochemically is identified by transients of high frequencies and high amplitudes, whereas a noise signal of lower intensity indicates a more passive corrosion state [14, 28]. Aballe et al. use the discrete wavelet transform (DWT) for subsequent noise data analysis [29, 30], which provides specific information about short-time and long-term corrosion processes. The DWT method was applied for the noise transient analysis of CastX5CrMnNi16-7-9 (with the chemical composition and microstructure presented in Table 17.6 and Fig. 17.17) in sulfuric acid and sodium chloride solutions. In the acid medium, the hydrogen bubble evolution was identified as the process that generated characteristic short-time corrosion events, whereas long-term transients in the salt-containing solution are characteristic for pit initiation and subsequent evolution processes [17]. As a further method for noise analysis, the continuous wavelet transform (CWT) is used for identification of the dynamic behavior of a system [31]. In consideration of the findings in the literature [21, 29–31], the CWT was applied for the investigation of the noise behavior of the high-alloy cast steel CastX15CrNiMnN19-3-4 (with the chemical composition given in Table 17.7) in sulfuric acid and in sodium chloride solutions, as well as in a combination of both media.

The noise behavior was measured for 2 h and the corresponding CWT analysis was carried out for a time interval of 20 min for each system. Figure 17.30 presents the results in a 0.1 M H_2SO_4 solution.

The normalized and detrended noise signal exhibited many short-time current transients of high amplitude, indicating a high proportion of corrosion events of short duration. The subsequent CWT analysis exhibited maxima of the CWT coefficients in the upper and middle frequency region between $f = 0.063$–16 Hz, but with the highest value for the transient after approximately 40 min (Fig. 17.30a) with $f = 4$–10 Hz (marked by the ellipse in Fig. 17.30b). In contrast, the current noise signal for the

Table 17.7 Chemical composition of the CastX15CrMnNiN19-3-4 in wt%

C	N	Cr	Ni	Mn	Si	Fe
0.148	0.165	19.1	4.12	2.85	0.5	Bal.

cast steel in sodium chloride solution exhibited significantly less transients of lower amplitude, indicating a system that was less active electrochemically (Fig. 17.31a). The signal analysis exhibited a clear maximum in the lower frequency region with $f =$ 0.063–0.25 Hz (Fig. 17.31b), which corresponded to the highest transient identified after approximately 6 min of exposure. Figure 17.32a) presents the results of the noise measurement in the mixed electrolyte, which contained identical volume fractions of sulfuric acid and sodium chloride solutions.

The comparison to the results using the unmixed solutions (Figs. 17.31 and 17.32) clearly indicates a drastic increase in the number of transients. The subsequent signal analysis identified maxima in the lower frequency region (with $f = 0.016$–1 Hz) of significantly higher duration, indicating long-lasting corrosion processes in the range of 1 s to 1 min. The scanning electron micrographs observed after the noise measurements revealed an enhanced intergranular corrosion attack in the unmixed acid solution (Fig. 17.33a) and in the combined electrolyte (Fig. 17.33c). In the sodium chloride solution, the corrosion attack was significantly less. Localized corrosion and the formation of corrosion products arranged in a circle around the pit were observed (Fig. 17.33b), which was a quite different mode of behavior in comparison to that observed in the acid solution.

From the micrographs, it was obvious that the corrosion attack in the unmixed acid and the combined electrolyte was nearly identical. This behavior clearly indicated that the acid dominated the corrosion attack in the combined solution, and that the sodium chloride seemed to have little or no effect on the corrosion attack. When considering the CWT noise analysis, however, the influence of the salt became clear. The

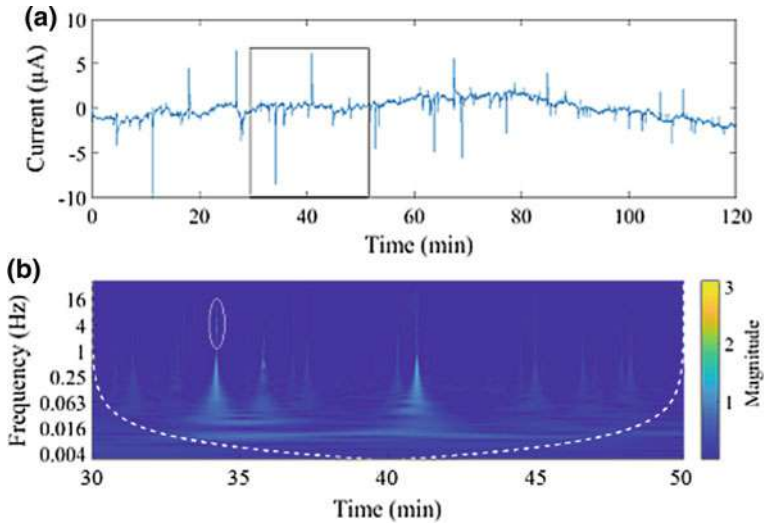

Fig. 17.30 **a** Current noise-time relation of CastX15CrMnNiN19-3-4 in 0.1 M sulfuric acid solution and **b** corresponding CWT analysis of the noise signal for the time interval marked by the rectangle in (**a**). The ellipse marks the magnitude maximum. Dashed line—the cone of influence

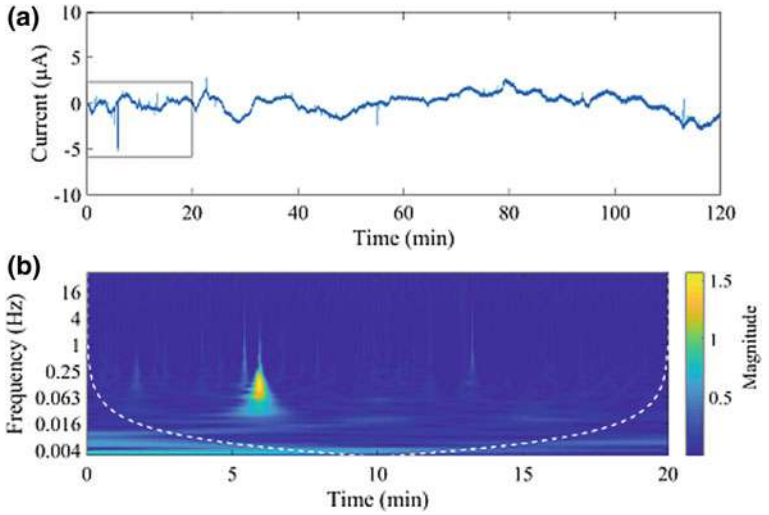

Fig. 17.31 **a** Current noise-time signal of CastX15CrMnNiN19-3-4 in 5 wt% sodium chloride solution. **b** CWT analysis for the time interval marked by the rectangle in (**a**). Dashed line—the cone of influence

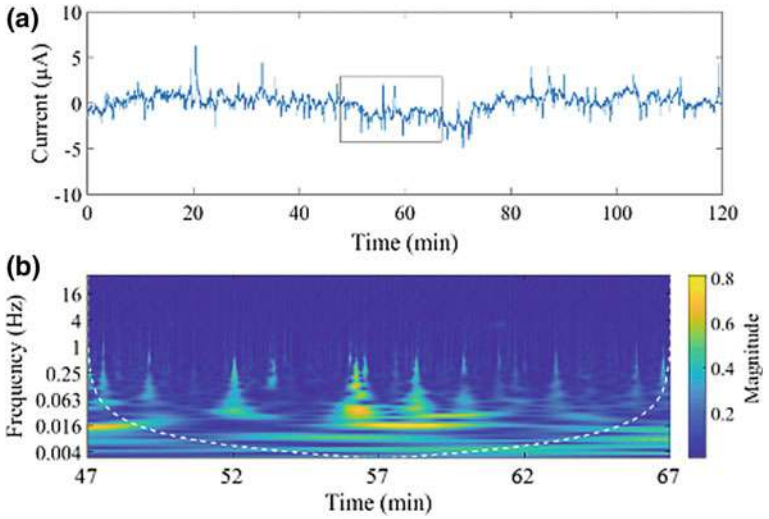

Fig. 17.32 **a** Noise-time signal of CastX15CrMnNiN19-4-3 in a combined 0.1 M H_2SO_4 + 5 wt% sodium chloride solution. **b** Continuous wavelet transform for the time interval marked by the rectangle in (**a**). Dashed line—the cone of influence

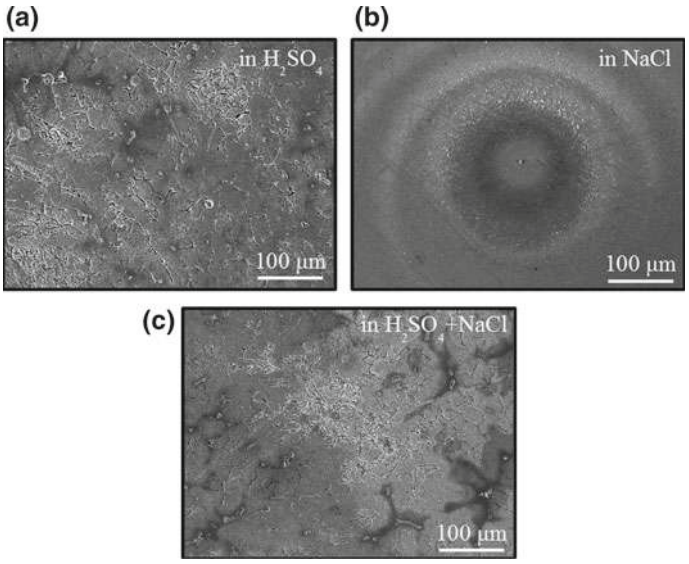

Fig. 17.33 SEM micrographs of the CastX15CrMnNiN19-3-4 after noise measurement in **a** 0.1 M H_2SO_4, **b** in 5 wt% NaCl, and **c** in 0.1 M H_2SO_4 + 5 wt% NaCl at a ratio of 1:1 vol%

maxima in the low-frequency range (Fig. 17.32b)—indicating long-term corrosion processes—indicated a longer-lasting intergranular corrosion attack. Consequently, it was assumed that in the unmixed acid solution, the corrosion attack was characterized by spontaneous active dissolution of the grain boundaries, accompanied by spontaneous repassivation. In the combined electrolyte, the attack also occurred spontaneously, but the repassivation process was drastically hindered, which was predominantly attributed to the Cl^- ions.

The study shows the advantage of utilizing electrochemical noise analysis, which facilitated the identification and isolation of short-time and long-term corrosion events simultaneously. In comparison, the effect was not identifiable by SEM observation after a two-hour exposure test.

17.8 Conclusion

In this chapter, several studies of the electrochemical corrosion behavior of high-alloy cast steels and steel/ceramic composite materials in sulfuric acid and chloride containing aqueous solutions are presented and discussed. For the analysis numerous polarization techniques, outdoor exposure tests and combined methods were carried out. The analyzed characteristics in dependence of applied potential, frequency and temperature give specific information about the influence of the TRIP effect to the corrosion characteristics, were used to design and describe the composite/electrolyte interphase and let extract specific parameters for the evaluation of the pitting

corrosion sensitivity. Finally, the combination of polarization, electrochemical noise and acoustic emission was used to estimate and separate simultaneous occurring corrosion mechanisms, and more precisely, to identify the time-dependence of specific initiation phenomena and corresponding corrosions damage evolution processes.

Acknowledgements The authors greatly acknowledge the financial support of this works by the Deutsche Forschungsgemeinschaft (DFG, German Research Foundation) as part of the Collaboration Research Centre 799 "TRIP-Matrix Composites" project—Projektnummer 54473466—SFB 799, subproject B6.

References

1. S. Wolf, S. Martin, L. Krüger, U. Martin, U. Lorenz, Steel Res. Int. **83**, 529 (2012)
2. L. Krüger, S. Wolf, S. Martin, U. Martin, A. Jahn, A. Weiß, P.R. Scheller, Steel Res. Int. **82**, 1087 (2011)
3. S. Martin, S. Wolf, U. Martin, L. Krüger, D. Rafaja, Metall. Mater. Trans. A **47**, 49 (2016)
4. C.-O.A. Olsson, D. Landolt, Electrochim. Acta **48**, 1093 (2003)
5. M. Mandel, F. Böhme, M. Hauser, M. Wendler, F. Tuchscheerer, L. Krüger, Steel Res. Int. **87**, 1105 (2016)
6. M. Mandel, L. Krüger, S. Decker, Mater. Corros. **66**, 1456 (2015)
7. M. Mandel, L. Krüger, S. Decker, Materialwiss. Werktofftech. **46**, 1039 (2015)
8. M. Mandel, L. Krüger, S. Decker, Corros. Sci. **90**, 323 (2015)
9. M. Boinet, J. Bernard, M. Chatenet, F. Dalard, S. Maximovitch, Electrochim. Acta **55**, 3454 (2010)
10. H. Inoue, R. Tsuzuki, S. Nohara, C. Iwakura, Electrochem. Solid-State Lett. **9**, A504 (2006)
11. J. Xu, X. Wu, E.-H. Han, Corros. Sci. **53**, 448 (2011)
12. M. Mandel, V. Kietov, T. Dubberstein, L. Krüger, Electrochim. Acta **240**, 350 (2017)
13. W. Liu, D. Wang, X. Chen, C. Wang, H. Liu, Corros. Sci. **124**, 93 (2017)
14. Y. Hou, C. Aldrich, K. Leokova, L.L. Machuca, B. Kinsella, Corros. Sci. **112**, 63 (2016)
15. L. Calabrese, L. Bonaccorsi, M. Galeano, E. Proverbio, D. Di Pietro, F. Cappuccini, Corros. Sci. **98**, 573 (2015)
16. M. Mandel, W. Kietov, L. Krüger, Defect and Diffusion Forum **367**, 42 (2016)
17. M. Mandel, V. Kietov, L. Krüger, Diffusion Foundations **22**, 48 (2019)
18. V. Kietov, M. Mandel, L. Krüger, Combination of electrochemical noise and acoustic emission for analysis of the pitting corrosion behavior of an austenitic stainless cast steel. Adv. Eng. Mater. (2018). https://doi.org/10.1002/adem.201800682
19. K. Wu, W.-S. Jung, J.-W. Byeon, Corros. Sci. **105**, 8 (2016)
20. C. Jirarungsatian, A. Prateepasen, Corros. Sci. **52**, 187 (2010)
21. A. Aballe, M. Bethencourt, F.J. Botana, M. Marcos, J.M. Sánchez-Amaya, Electrochim. Acta **46**, 2353 (2001)
22. F.H. Cao, Z. Zhang, J.X. Su, Y.Y. Shi, J.Q. Zhang, Electrochim. Acta. **51**, 1359 (2006)
23. A.M. Homborg, E.P.M. van Westing, T. Tinga, X. Zhang, P.J. Oonincx, G.M. Ferrari, J.H.W. de Wit, J.M.C. Mol, Corros. Sci. **66**, 97 (2013)
24. A.M. Homborg, R.A. Cottis, J.M.C. Mol, Electrochim. Acta **222**, 627 (2016)
25. M.G. Pujar, U. Kamachi Mudali, S. Sekhar Singh, Corros. Sci. **53**, 4178 (2011)
26. Y.-J. Tan, N.N. Aung, T. Liu, Corros. Sci. **48**, 23 (2006)
27. K. Hladky, J.L. Dawson, Corros. Sci. **21**, 317 (1981)
28. B.P. Markhali, R. Naderi, M. Mahdavian, M. Sayebani, S.Y. Arman, Corros. Sci. **75**, 269 (2013)
29. A. Aballe, M. Bethencourt, F.J. Botana, M. Marcos, Electrochim. Acta **44**, 4805 (1999)
30. A. Aballe, M. Bethencourt, F.J. Botana, M. Marcos, Electrochem. Commun. **1**, 266 (1999)
31. P. Montes-García, F. Castellanos, J.A. Vásquez-Feijoo, Corros. Sci. **52**, 555 (2010)

Chapter 18
CFD Analysis of the Particle and Melt Flow Behavior During Fabrication and Processing of TRIP-Matrix-Composites

Sebastian Borrmann, Sebastian Neumann and Rüdiger Schwarze

Abstract Computational fluid dynamics simulations are conducted to supplement experimental investigations in order to gain a deeper understanding of physical effects during fluid flow and heat transfer in steel making and processing. This offers the possibility to examine physical effects of the liquid steel in greater detail and isolated of entire processes. Liquid steel is present in the fabrication processes of TRIP-Matrix-Composites, namely gas atomization of the steel melt to produce powder, and liquid steel infiltration into ceramic structures. It also occurs during further processing, e.g. in welding or coating. Numerical simulations of these processes are performed with the finite volume method using the free open-source software package OpenFOAM. The libraries are extended where needed. This includes formulations for phase change, heat sources, latent heat, additional forces, calculations for material properties in multiphase flows, and particle tracking. The models are used to simulate electron beam welding, infiltration, gas atomization, and flame spraying and to reveal significant effects for each particular process.

18.1 Introduction

Producing TRIP-steels and TRIP-Matrix-Composites through casting and powder metallurgy involves many physical effects both in the solid and molten state. This also applies for further processing like welding or flame spraying. A detailed understanding of these physical effects is crucial to achieve desired properties of the final product. Besides various experimental investigations, which are thoroughly described in this book, numerical simulations can be carried out to enhance this understanding.

The infiltration of ceramic structures like foams or bulk material is one route of producing TRIP-Matrix-Composites. In a second route, powder metallurgical processes, like e.g. atomization (Chap. 3), sintering (Chaps. 6 and 9) and powder

S. Borrmann (✉) · S. Neumann · R. Schwarze
Institute of Mechanics and Fluid Dynamics, Technische Universität Bergakademie Freiberg, Lampadiusstr. 4, 09599 Freiberg, Germany
e-mail: sebastian.borrmann@imfd.tu-freiberg.de

H. Biermann and C. G. Aneziris (eds.), *Austenitic TRIP/TWIP Steels and Steel-Zirconia Composites*, Springer Series in Materials Science 298,
https://doi.org/10.1007/978-3-030-42603-3_18

forging (Chap. 8), are used. In order to produce the steel powder, gas atomization of the steel melt is performed. In both routes, the behavior of the molten steel is one main cause for the final material character. During further processing of the material, steel melts particularly occur during coating and joining processes. For the former, flame spraying can be used for metal matrix composites (MMC). For the latter, electron beam (EB) welding was found to show excellent weldability for TRIP-steels [1] and was therefore used.

For the numerical simulation of infiltration, atomization, flame spraying, and EB welding, computational fluid dynamics (CFD) simulations are used. The aim of these simulations is to create numerical models of the actual processes in order to reduce the amounts of costly experiments and to gain additional insights into the melt flow behavior and further related physical effects. In order to represent processes as effectively as possible, the right choice of fundamental equations to be solved and correct numerical model setups are crucial.

All CFD simulations of the described processes are based on the numerical solution of the conservation equations of mass, momentum and energy. The mass conservation equation for incompressible fluids with constant density has the form:

$$\nabla \cdot \boldsymbol{u} = 0, \tag{18.1}$$

with the velocity vector $\boldsymbol{u}$. The momentum conservation equation for incompressible fluids has the form

$$\frac{\partial \boldsymbol{u}}{\partial t} + \nabla \cdot (\boldsymbol{u}\boldsymbol{u}) = -\frac{1}{\varrho}\nabla p + \nabla \cdot (\nu \nabla \boldsymbol{u}), \tag{18.2}$$

where t is the time, ϱ is the density, p is the pressure and ν is the kinematic viscosity. Since melt flow problems are accompanied by large temperatures and temperature gradients, the energy conservation equation is also solved to take the influence of temperature into account:

$$c_p \frac{\partial T}{\partial t} + c_p \nabla \cdot (\boldsymbol{u}T) = \frac{1}{\varrho}\nabla \cdot (k \nabla T), \tag{18.3}$$

with the temperature T, the heat capacity c_p, and the thermal conductivity k.

Equations (18.1)–(18.3) form a system of partial differential equations, which is solved by means of the finite volume method (FVM) [2, 3] within the free, open source CFD software OpenFOAM [4].

If in addition to the steel melt, other fluid phases like gases are involved, the phases need to be distinguished. This is accomplished by using the volume of fluid (VOF) method and solving the transport equation for the phase fraction α:

$$\frac{\partial \alpha}{\partial t} + \mathbf{u} \cdot \nabla \alpha = 0. \tag{18.4}$$

A very detailed description of the VOF method employed in OpenFOAM is given by Klostermann et al. [5].

For the particular processes, (18.1)–(18.3) were extended by source terms and other refinements. These extensions and their applications will be shown in the following sections for infiltration, gas atomization and EB welding.

18.2 Infiltration

Besides powder metallurgical processes, combination of steel and ceramic structures on the macro-scale is another possibility for the creation of TRIP-Matrix-Composites. In this production route, two different main approaches are investigated. One is the casting of liquid steel into molds that are filled with ceramic structures or particles. The other is the infiltration of ceramic foam structures with liquid steel (Chap. 4) [6]. The latter was investigated by means of CFD intensively by Klostermann et al. [7, 8] and Schwarze et al. [9, 10]. In order to perform beneficial CFD simulations, different steps need to be considered. These are efficient meshing strategies [8], steel flow and heat transfer inside the foam structure [7], and melt surface dynamics for the 2-phase-flow system [9, 10].

18.2.1 Meshing Strategies

Sophisticated meshing strategies are the first step to efficient CFD simulations. The mesh is used to generate grid points in order to discretize the fundamental equations (18.1)–(18.3). The mesh offers a significant impact on the quality and time-consumption of the simulation. In order to evaluate a meaningful meshing strategy for the discussed infiltration simulations, two different approaches were examined. A mesh, produced by a semi-automatic generation algorithm for hexahedral meshes, developed by Klostermann et al. [8], is compared with a mesh generated by a full-automatic tetrahedral meshing technique. The comparison is performed for the flow in a Kelvin structure.

The main advantage of full-automatic techniques with tetrahedral or mixed tetrahedral/hexahedral grid cells is its independence of the geometry. Any forms can be meshed and automatically refined at critical areas. As an example, Fig. 18.1 shows a CT scan of realistic ceramic foam (Fig. 18.1a) and the respective mesh (Fig. 18.1b). The automatic meshing also leads to quickly accessible meshing results. However, when the investigation of specific physical phenomena is desired, abstracted and well defined geometries are often examined. In these cases, structured meshes might lead to faster simulations and possibly more accurate results. To keep the meshing effort small, it is useful to employ automation for the geometry and mesh generation as much as possible. Since the Kelvin structure is a popular approach to approximate foam structures, Klostermann et al. [8] developed a strategy that does both geometry

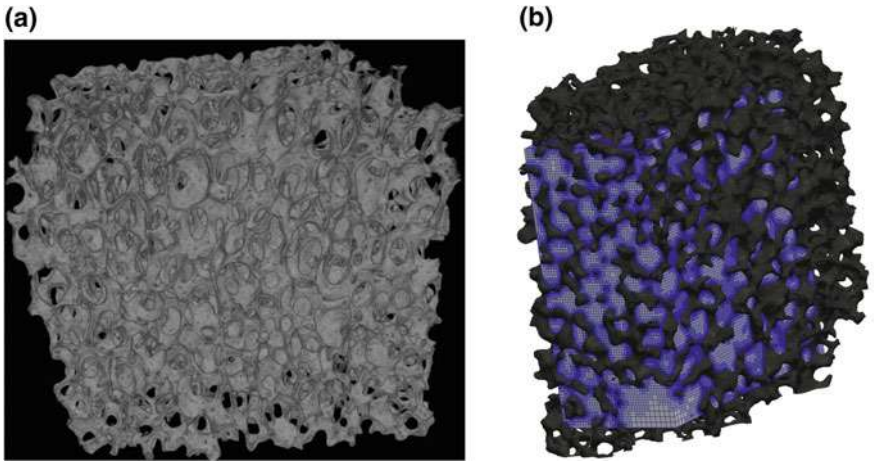

Fig. 18.1 **a** CT scan of a real ceramic foam [8] and **b** the automatically generated unstructured mesh with mesh refinement near foam boundaries [9]

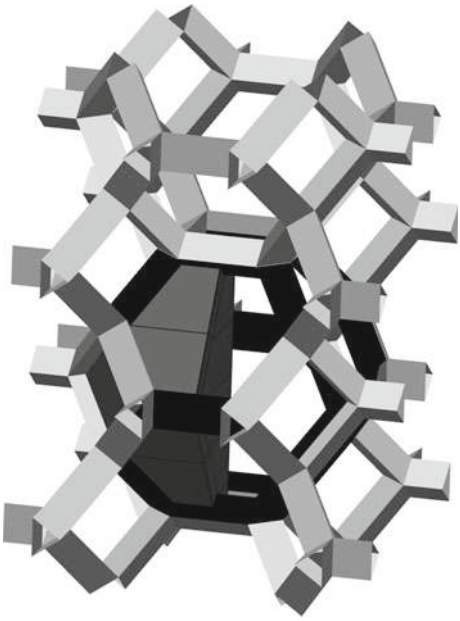

Fig. 18.2 A section of the generated Kelvin cell structure with triangular struts of one Kelvin cell (black) and one quarter of a Kelvin cell volume (dark grey) [8]

and block-structured mesh generation for composed macroscopic forms that consist of single Kelvin structures. Figure 18.2 shows an excerpt of the geometry. For a detailed explanation of the meshing strategy, the reader is referred to Klostermann et al. [8].

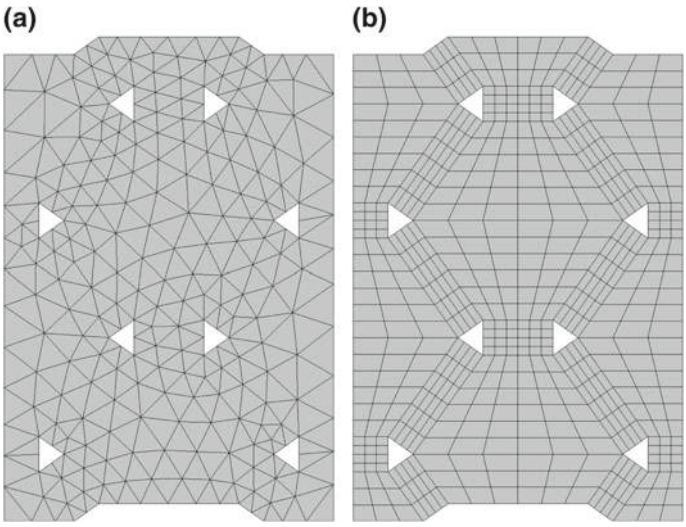

Fig. 18.3 Comparison of two different meshing approaches: **a** automatic unstructured mesh and **b** semi-automatic block-structured mesh [8]

In order to directly compare the two meshing approaches, the same geometry was meshed. Figure 18.3 shows sections of the two approaches. Both meshes were created with a similar number of grid cells. Steady, incompressible flow simulations through the Kelvin structure were performed to compare the mesh qualities, simulation errors and calculation time. Firstly, the block-structured hexahedral mesh mostly showed lower errors for different error estimates and two different Reynolds-number flows. Only in some cases, the errors of the unstructured tetrahedral mesh were slightly smaller. Secondly, the necessary number of iterations that was needed for convergence, was a lot smaller for the structured hexahedral mesh in all cases. Thirdly, the calculation time per iteration was lower with the hexahedral mesh. All in all, the performance of the hexahedral mesh was up to 94% better than of the tetrahedral mesh. In order to minimize computational costs the block-structured technique was consequently used for further studies of flow infiltration into Kelvin structures.

18.2.2 Mesoscale Flow in Kelvin Structure

Meshing the pores of the ceramic foam, as shown in Sect. 18.2.1 is very useful if only the melt flow is simulated. In order to represent the process of infiltration more physically, heat transfer between the liquid steel melt and the solid ceramic foam struts needs to be accounted for as well. To track the heating of the foam itself, the solid structure is meshed.

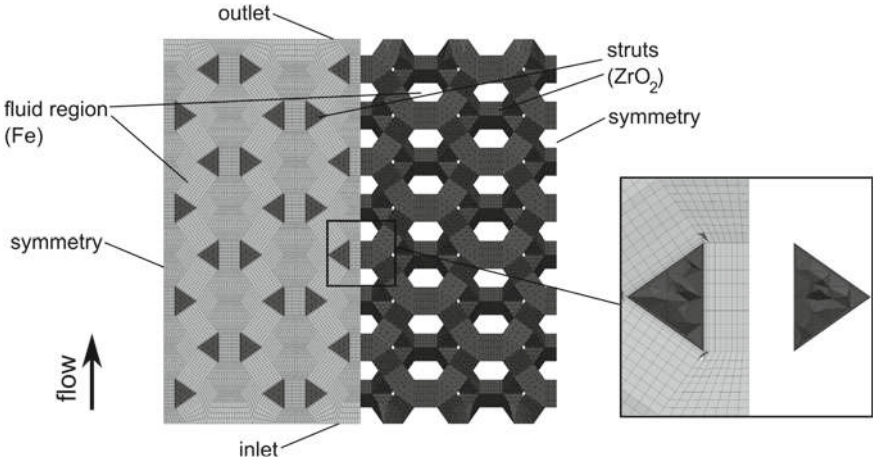

Fig. 18.4 Simulation domain with boundaries, regions and mesh for the fluid zone (light grey), primary meshed with hexahedric cells, and the solid structure (dark grey), primary meshed with tetrahedric cells [7]

Therefore, the mesh was extended to the ZrO_2 struts in order to simulate complete heat transfer between the infiltrating liquid steel melt and the solid ceramic foam [7]. Figure 18.4 shows both parts of the composed mesh in the calculation domain. The left part of Fig. 18.4 shows the grid for the fluid region, while the right part demonstrates the mesh in the solid region in more detail.

The aim of the performed CFD simulations was to investigate the flow and the heat transfer on the pore-scale (mesoscale). The single-phase flow focused on thermal effects with constant material properties and neglected the free surface flow and solidification. The equations for mass (18.1), momentum (18.2) and energy (18.3) were solved. The energy equation (18.3) is reassembled with the thermal diffusivity $a = \frac{\lambda}{\varrho c_p}$ to:

$$\frac{\partial T_{\mathrm{Fe}}}{\partial t} + \mathbf{u} \cdot \nabla T_{\mathrm{Fe}} = a_{\mathrm{Fe}} \nabla \cdot \nabla T_{\mathrm{Fe}}. \tag{18.5}$$

Additionally, a heat transfer equation for the solid region was solved:

$$\frac{\partial T_{\mathrm{ZrO_2}}}{\partial t} = a_{\mathrm{ZrO_2}} \nabla \cdot \nabla T_{\mathrm{ZrO_2}}. \tag{18.6}$$

The following explicit boundary conditions were used at the interface between the melt and the struts:

$$T_{\mathrm{Fe}} = T_{\mathrm{ZrO_2}} \tag{18.7}$$

$$k_{\mathrm{Fe}} \nabla T_{\mathrm{Fe}} = k_{\mathrm{ZrO_2}} \nabla T_{\mathrm{ZrO_2}}. \tag{18.8}$$

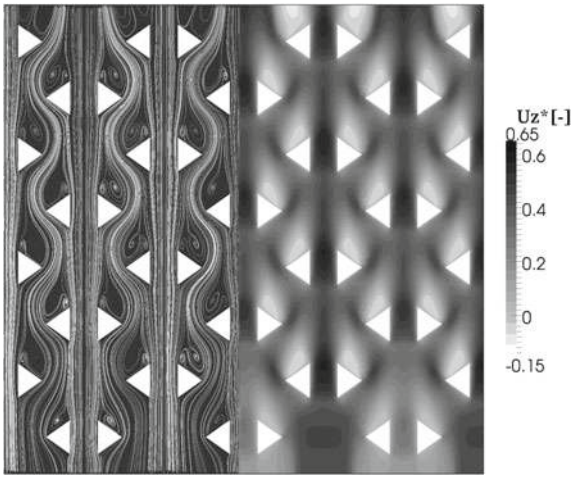

Fig. 18.5 Flow visualization via stream lines (left) and normalized flow velocity in mean flow (z-)direction (right) [7]

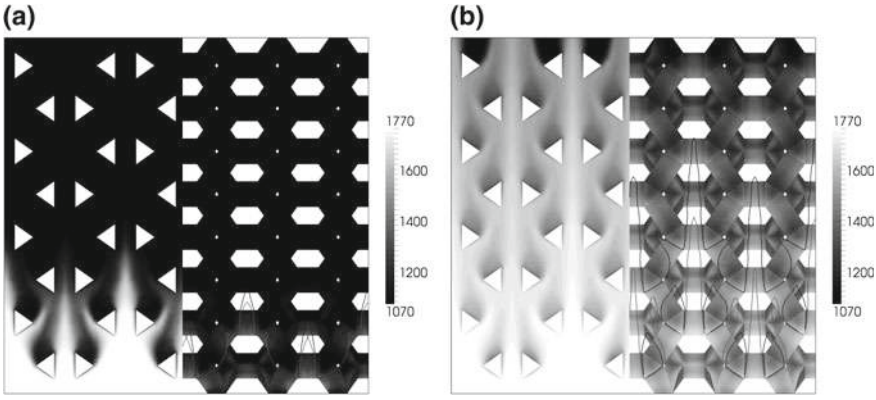

Fig. 18.6 Temperature fields in the liquid zone (left) and the solid struts (right) after **a** $t^* = 0.49$ and **b** $t^* = 6.14$ melt through time [7]

For details about the numerical model setup and the thermophysical properties, the reader is referred to Klostermann et al. [7].

The flow field is represented in Fig. 18.5. On the left hand side, the flow is visualized by streamlines, which illustrates the channeling of the flow in two alternating patterns, straight and meandering. Recirculation is visible through swirls behind the struts. On the right hand side, these recirculation areas are quantified, where the normalized velocity U_z^* in z-direction is negative, and therefore white. In realistic infiltration processes with a free melt surface, these recirculation areas could result in cavities as gas entrapment would possibly occur.

Figure 18.6 shows the temperature field of (a) the flow field and (b) the struts for the melt through times $t^* = 0.49$ (Fig. 18.6a) and $t^* = 6.14$ (Fig. 18.6b). The

ceramic was preheated to 1080 K. While the temperature field followed the fluid flow, the heating of the solid struts was delayed. Both behaviors were as expected. The temperature field of the liquid steel also revealed areas of lower temperatures in the recirculation areas behind the struts. We expect the melt to solidify in this area first, where gas entrapment is very likely as well.

18.2.3 Melt Surface Dynamics

In the previous considerations, the free melt surface and the gas phase have been neglected. An additional investigation of the multiphase system is, however, essential to cover further effects like cavity development. In order to investigate the behavior of the free surface of the steel melt in the porous ceramic foam during infiltration and to distinguish between the fluid phases, the model was extended by the VOF method [see (18.4)]. The material properties density ϱ and dynamic viscosity η were averaged between the steel melt phase (index m) and the gas phase (index g) depending on α in each grid cell [9]:

$$\varrho = \alpha\varrho_{\mathrm{m}} + (1-\alpha)\varrho_{\mathrm{g}} \tag{18.9}$$

$$\eta = \alpha\eta_{\mathrm{m}} + (1-\alpha)\eta_{\mathrm{g}}. \tag{18.10}$$

Figure 18.7 shows a simulation of the infiltration of liquid steel into the ceramic matrix with a highly resolved surface tracking [9]. The gas is noticeable as dark entrapped bubbles in between the lighter steel melt. The bubbles form as a consequence of the rapid infiltration behind the struts.

The detailed simulations came with tremendous computational effort because very small time steps Δt were necessary. The required time step for free surface flow is calculated by the following condition [11]:

$$\Delta t = C_\eta \frac{\eta \Delta x}{\sigma}, \tag{18.11}$$

where C_η is a constant and Δx is the cell length. As described by Schwarze and Klostermann [10], this time step condition is much more dominant than the usual Courant-Friedrichs-Lewy-condition, which reads:

$$\Delta t = \mathrm{Co}\frac{u\Delta t}{\Delta x}. \tag{18.12}$$

Here Co is the Courant number, which is in most cases $\mathrm{Co} \leq 1$ to ensure stability, and u is the velocity magnitude. In (18.11) C_η most widely depends on numerical treatment of the model equations and therefore the time step is very sensitive to adequate implementations. Schwarze and Klostermann [10] have found that the material parameter averaging between the phases have a particular impact. Thus, an

improved strategy was found for the viscosity interpolation and the harmonic mean was adopted:

$$\eta = \frac{\eta_g \eta_m}{(1-\alpha)\eta_m + \eta_g \alpha} \tag{18.13}$$

Testing different time steps with the different viscosity averaging equations reveals their impact on the stability of the simulation. In Fig. 18.8, the standard (18.10) and the improved (18.13) viscosity averaging algorithms are compared. For the low time-step Δt_1 both implementations worked stable. By increasing the time step to Δt_2, the standard implementation destabilized. However, with the improved viscosity

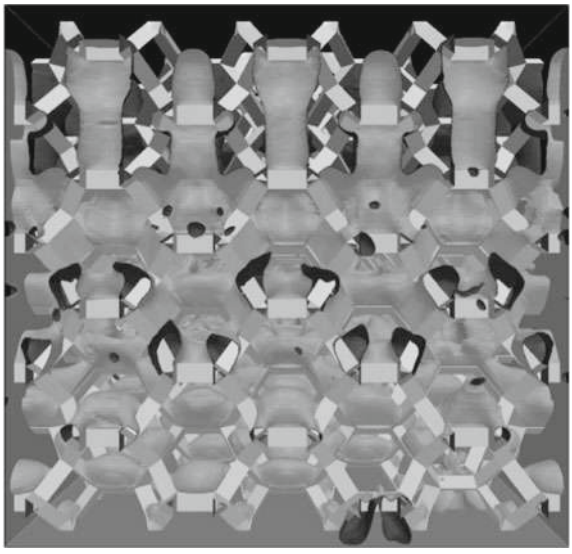

Fig. 18.7 Contour of the infiltrating steel melt (bright) with gas and entrapped bubbles (dark) [9]

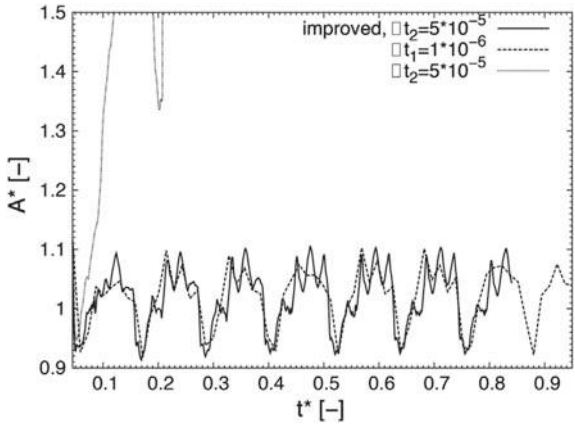

Fig. 18.8 Melt surface area as a function of time. Comparison of the low time step $t_1 = 1 \cdot 10^{-6}$ (dashed line) with a higher time step $t_2 = 5 \cdot 10^{-5}$ for non-improved (dotted line) and improved (solid line) viscosity algorithms [10]

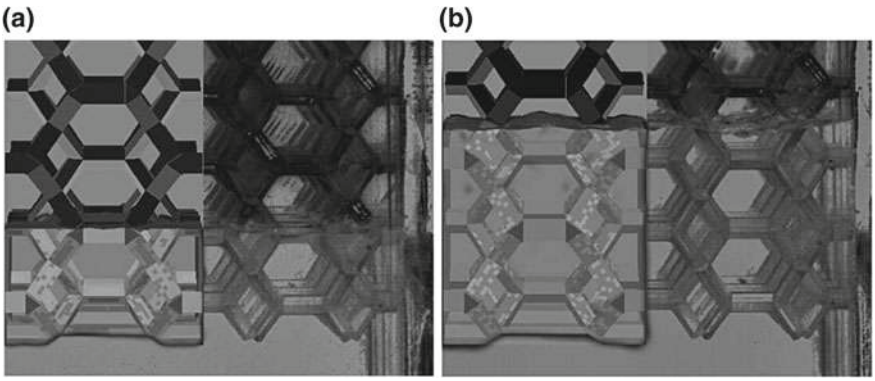

Fig. 18.9 Comparison of the free surface between simulation (left) and model experiment (right) for two different through times **a** $t^* = 0.199$ and **b** $t^* = 0.364$ [10]

averaging, the results were comparable to the smaller time step and the simulations remained stable. Figure 18.9 shows a qualitative comparison of the infiltration process between simulation and experiment, It reveals a very good agreement.

18.3 Atomization

Alongside infiltration of macroscopic structures, powder metallurgy is the main route for the fabrication of TRIP-Matrix-Composites. The controlled production of steel powder with desired properties and particle size distributions is one of the major challenges. In the light of this, CFD models were developed and simulations were performed to gain an understanding of parameters that influence the development of steel droplets during the primary breakup of molten steel [12]. In order to apply additional models like secondary breakup or applications like flame spraying, particle size distributions need to be tracked. By converting the continuous Euler phase of the VOF simulations to disperse Lagrangian particles, this can be accomplished. For that purpose, a particle tracking and conversion model has been developed and implemented [13]. The application of tracked particle size distributions for powder flame spraying is shown accordingly.

18.3.1 Influence of Process Parameters on Primary Breackup

The production of MMC using a sintering process needs analog particle sizes for the ceramic and steel powders to obtain a high green strength [14]. Atomization, the predominant production process for steel powder, subdivides into two main tech-

niques, the free fall design and the close coupled (confined) design [15]. The main difference of the designs is the positioning of the nozzles, which deliver the inert gas for the atomization of the steel melt jet. Therefore, different atomization states are feasible. In case of the closed coupled design, a prefilming process of the metal melt jet develops due to the flow structure of the inert gas, which finally atomizes the melt into droplets. On contrary, a compact metal melt jet develops for the free fall design, which is atomized by an inert gas stream at a defined distance. Due to the inert gas atomization, steel powder particles with diameters in range of 0.04–2000 µm are generated [16]. A method to enforce the atomization process is the direct manipulation of the free falling melt jet. Therefore, a primary breakup process is forced by defined disturbances for the inflow of the melt in the nozzle. This leads to a pre-disintegration of the metal melt jet into ligaments and larger droplets [12]. In general, an experimental investigation of the steel melt atomization is very complex. Mainly, the high melt temperature limits the measurements [17]. The management and control of the process of metal melt gas atomization is a kind of 'black art' due to the demanding process conditions and requirements [18]. Furthermore, experimental setups require a certain durability and stability as well as optical accessibility for a detailed analysis of the process. Consequently, numerical simulations are a meaningful alternative to research metal melt atomization processes to shed light on specific influencing attributes.

Critical factors for primary breakup of the metal melt jet using a free fall design are constructive parameters (e.g. the nozzle design, nozzle obstruction via the stopper rod) and operation conditions (e.g. rotation of the melt flow, nozzle inlet flow disturbances). Basically, a numerical investigation determines their influence to the metal melt jet behavior downstream of the nozzle. Figure 18.10 shows sketches of a tube nozzle (Fig. 18.10a) and a divergent-convergent industrial nozzle (Fig. 18.10b). The presented numerical simulation depends on different assumptions such as:

- three-dimensional and transient flow behavior,
- fully developed laminar melt inflow,
- the flow regime is in transition range between laminar and turbulent flow,
- isothermal and incompressible conditions with constant material properties.

Therefore, the governing equations for continuity (18.1) and momentum (18.2) are solved. The turbulence is not modeled with an explicit subgrid model. Instead, implicit large eddy simulations (ILES) were performed, which generate the dissipation of the small structures by a specific spatial numerical discretization scheme of the convection terms in the momentum equation. By the means of the VOF, introduced in Sect. 18.2.3 [see (18.4), (18.9), (18.10)] the dynamics of the phase interface between the melt and gas is tracked during the simulation.

Figure 18.11 shows the a simulation result of a temporal metal melt jet behavior downstream the industrial nozzle. The nozzle outlet diameter is consistent $D = 4\,\mathrm{mm}$ for both geometries (see Fig. 18.10). The axial nozzle inlet velocity is constant $U_{\mathrm{ax}} = 1.55\,\mathrm{ms}^{-1}$ based on the fluid column of the melt inside the tundish. Additionally, a circumferential velocity of $u_{\mathrm{rot}} = 1.83\,\mathrm{ms}^{-1}$ is defined, which mimics the rotation of the melt inside the tundish caused by the magnetic heating process. For

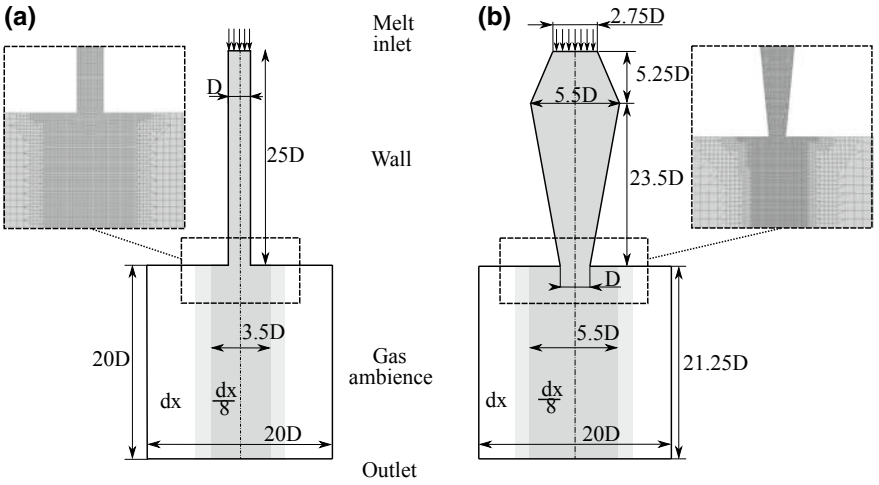

Fig. 18.10 Sketch of the simulation domains for **a** constant tube nozzle and **b** divergent-convergent industrial nozzle with boundary conditions, dimensions ($D = 4$ mm) and mesh refinement area (gray background and details in frame) [12]

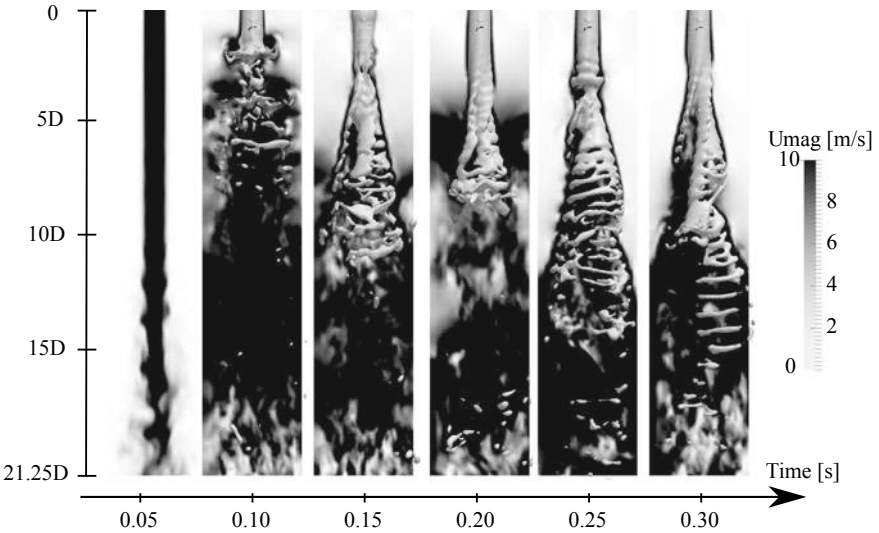

Fig. 18.11 Temporal jet behavior regarding the industrial nozzle for a circumferential velocity of $u_{\mathrm{rot}} = 1.83\,\mathrm{ms}^{-1}$ at the nozzle inlet. The contour plot of the jet ($\alpha = 0.5$) and the gas velocity field (background) are shown

detailed information of the specifications, the reader is kindly referred to the work of Neumann et al. [12]. In Fig. 18.11, the contour plot of the jet is depicted by the phase fraction $\alpha = 0.5$ for the industrial nozzle. It should be noted that the interface between the melt and gas phase smears over 4–5 cells [8]. However, respecting this criterion a high computational grid resolution is defined. Additionally, the gas velocity field is shown in the background. In general, the temporal behavior of the melt jet shows the primary breakup of ligaments and larger droplets. A helical structure superposed by a hollow-cone jet shape develops, whereas close to the nozzle a compact almost cylindrical jet occurs with less surface waves. Here, the disintegration is directly driven by the circumferential velocity of the steel melt, which shows a high potential to improve the secondary atomization process due to the high excitation of the melt jet. Therefore, Fig. 18.12 displays a detailed analysis of the different nozzle designs considering different circumferential velocities. Depending on the nozzle design different stages of the jet behavior can be observed. The tube nozzle (Fig. 18.12a) shows for:

- $u_{\mathrm{rot}} = 0$ less disturbances of the melt jet, which lead to surface waves and diameter changes,
- $u_{\mathrm{rot}} < u_{\mathrm{ax}}$ a stabilization of the jet leading to a smoothing of the secondary structures,
- $u_{\mathrm{rot}} \approx u_{\mathrm{ax}}$ a helix shaped metal melt jet with less excitations onto the jet surface,
- $u_{\mathrm{rot}} > u_{\mathrm{ax}}$ an irregular jet behavior, which splits into two parts.

On contrary, the results for the industrial nozzle design (Fig. 18.12b) show a higher excitation level of the melt surface. However, there are also different jet behavior stages considering the circumferential velocity contribution. In case of $u_{\mathrm{rot}} < 0.5u_{\mathrm{ax}}$, the general jet behavior is preserved compared to the undisturbed variant. Surface waves, diameter changes and partial disintegration occurs. A helical jet shape develops by increasing the circumferential velocity to $u_{\mathrm{rot}} > 0.5u_{\mathrm{ax}}$. Furthermore, the jet tip moves with time and ligaments and larger droplets disintegrate. However, the surfaces waves are persistent. For $u_{\mathrm{rot}} > u_{\mathrm{ax}}$, the helical jet is superposed by a hollow-cone shape and the jet oscillates frequently. Higher velocity increases the spreading and separation of the jet. The ligaments and particles are in magnitude of the secondary structures. In summary, the nozzle design mainly influences the jet excitation due to surface waves. However, the decay of the melt jet is primarily forced by specific operation conditions. Deeper insights in this research can be found in the work of Neumann et al. [12].

18.3.2 Particle Tracking and Conversion

Originally, the VOF method is capable of resolving arbitrarily formed interfaces (e.g. water surface). However, a direct tracking of specific parameter (e.g. particle size) is not immediately available for VOF simulations. This is comparable to experimental research, where a specific evaluation process is required to identify the desired

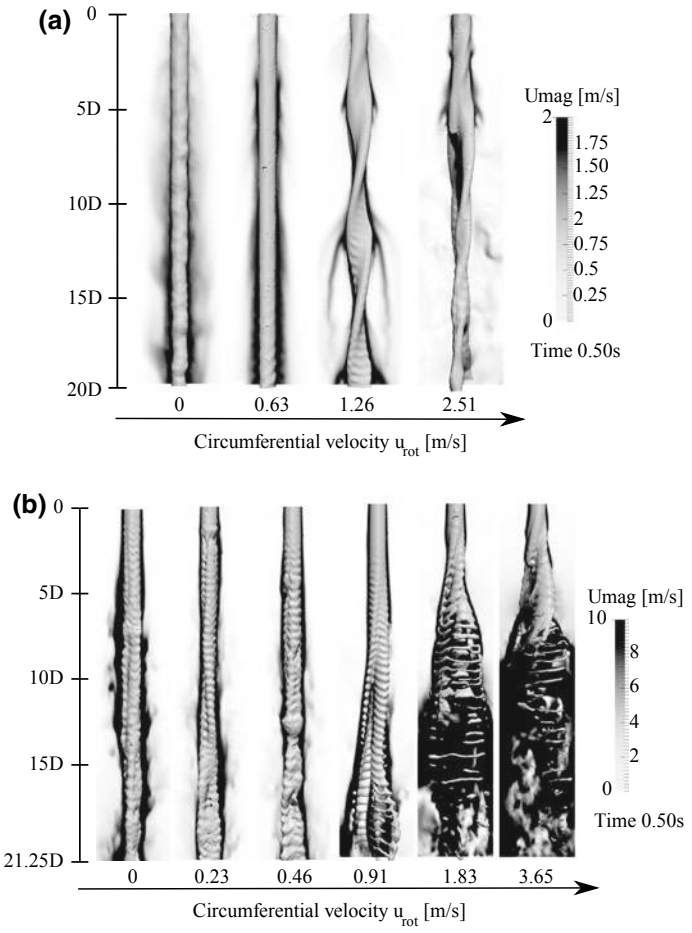

Fig. 18.12 The jet behavior for different nozzle designs **a** tube nozzle and **b** industrial diverging-converging nozzle and different circumferential velocities of the melt at the nozzle inlet for the time of 0.5 s. The contour plot of the jet ($\alpha = 0.5$) and the gas velocity field (background) are shown

variable [19]. The same applies for VOF simulations, where a specific tracking routine manages this task. In case of steel melt atomization, droplet or particle related characteristics are of particular interest (e.g. particle size distribution). However, a VOF simulation of a steel melt atomization needs a sufficient mesh resolution to resolve the droplets, which are in the magnitude of 0.1–1000 μm [16]. This in combination with a multiplicity of droplets in the dense spray region would cause excessive computational costs [20, 21]. Here, VOF simulations are limited to the complete primary breakup process, where the droplet sizes are reasonable for VOF. Secondary breakup processes are mostly described by an Eulerian-Lagrangian approach, where the com-

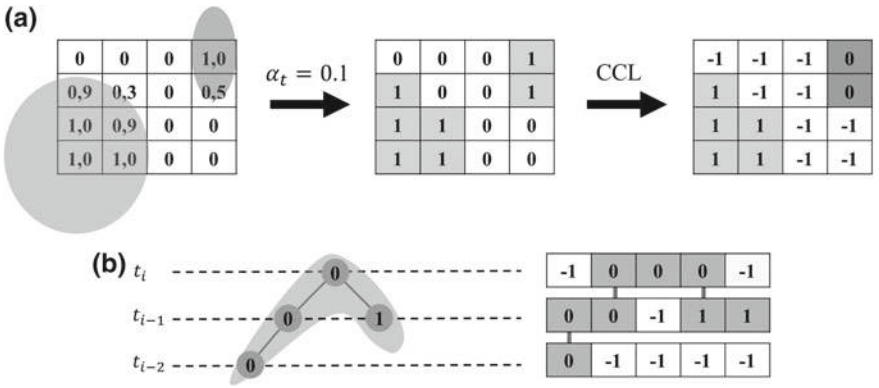

Fig. 18.13 **a** Spatial CCL: Particles (grey) represented by the phase fraction field (left), particle face identification via phase fraction threshold (middle), grouping of cells by CCL to particle slices (right) and **b** temporal CCL: Particle movement through layer evaluation over time

putational costs are much lower [22, 23]. Therefore, the VOF droplet information (e.g. particle size, position and velocity) have to be transferred from the Eulerian to the Lagrangian simulation. Here, a capable tracking algorithm is indispensable.

In general, there are two fundamental methods, namely three- or two-dimensional tracking [24–30]. 3D-tracking detects particles in the entire domain, while 2D-tracking defines a fixed positioned evaluation layer for the detection of the Eulerian particles. Both methods employ the connected component labeling (CCL) approach, which is based on the graph theory. However, whereas the 3D-tracking demands exclusively spatial CCL, 2D-tracking needs spatial and additionally temporal CCL for the Eulerian particle detection. In Fig. 18.13, the variants are outlined exemplarily. The basis for the tracking algorithm is the phase fraction α field given by the VOF simulation. Regarding the spatial detection (Fig. 18.13a), particles have to be identified first. Therefore, an interrogation sequence of the phase fraction threshold has to be satisfied in order to be considered for the actual CCL step for the condition $\alpha > \alpha_t$. Afterwards, neighborhood relationships between the detected cells have to be analyzed. Finally, individual particles are classified. The 3D spatial CCL directly detects an entire particle, whereas the 2D spatial CCL identifies slices of the particles due to the 2D evaluation layer (arbitrarily placeable). Therefore, an additional temporal CCL is important to connect multiple slices to one particle.

The simulations considering VOF metal melt atomization are performed in OpenFOAM v1812 [31]. Therefore, the officially implemented tracking algorithm, called the extract Eulerian Particles function object, is advanced to incorporate sophisticated source code for the temporal tracking. Figure 18.13b shows the correct temporal connection of the individual slices over ensuring correct neighborhood relationships within different particles.

To study the performance of the enhanced tracking algorithm, an extensive numerical validation of a well-known test case is intended where almost all circumstances

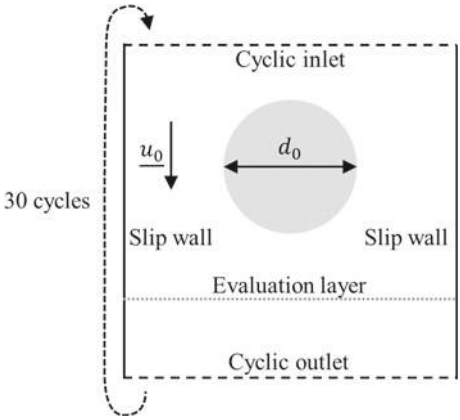

Fig. 18.14 Numerical case setup for a recirculating water droplet in air with the related boundary conditions [13]

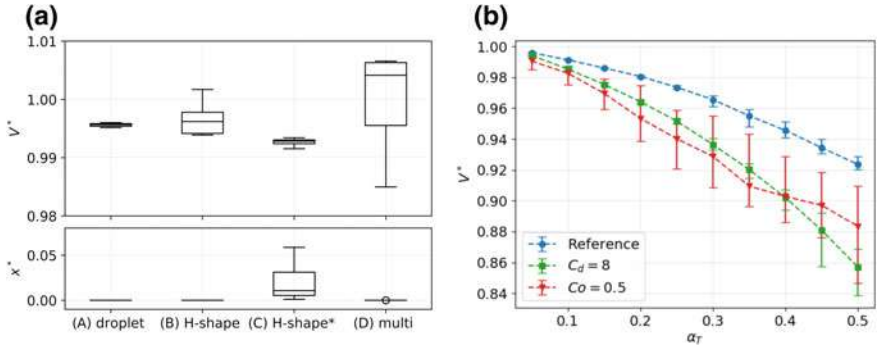

Fig. 18.15 **a** Particle tracking results with enhanced algorithm for (A) spherical particle, (B) and (C) H-shaped particle and (D) 12 particles of various shapes and sizes [13]. **b** Sensitivity analysis of the phase fraction threshold α_t (Reference $\alpha_t = 0.05$, $C_d = 16$ and $Co = 0.1$)

of the simulation are controllable. Therefore, the test case of a moving water droplet in air is chosen using different setups, see Fig. 18.14. Different particle shapes (spherical, H-shaped) and number of particles (single, multiple particles) are analyzed defining different diameters d_0 and velocities $\underline{u}_0$. Furthermore, the influence of the mass and momentum equations are analyzed. Using the frozenFlow option of OpenFOAM enables simulations with constant domain velocity and negligence of the surface tension of the droplet. The simulation domain is defined by cyclic boundary conditions at the inlet and outlet, such that the particle can directly reenter the domain after leaving. This allows an iterative analysis of the tracking algorithm for constant particle conditions. In total, 30 cycles for each setup are performed. The mesh resolution is 32 cells per diameter.

Figure 18.15a shows the simulation results of the VOF simulation with the enhanced 2D-tracking algorithm, with the normalized droplet volume V^* and normalized displacement x^*, which are described by:

$$V^* = V_p / V_0, \tag{18.14}$$

$$x^* = \sqrt{(x_{x,p} - x_{x,0})^2 + (x_{y,p} - x_{y,0})^2} \frac{1}{d_0}, \tag{18.15}$$

within the box plot diagram. The diagram reveals a very good accuracy of the considered particle attributes. The discrepancy of all regarded setups is less than 3% for the normalized volume. Noticeable aberrations are existent for H-shaped droplet B) and the setup with multiple droplets of different shapes and sizes D). The normalized position of the particle is generally almost zero. However, if surface tension is considered (marked with *), the shape of the particle cannot be preserved and partially the droplet breaks up and shift in position. This leads to the higher discrepancies in case C) of Fig. 18.15a. Altogether, the enhanced tracking algorithm shows satisfying results for all tested parameters.

Since the reliability of the enhanced tacking algorithm is proven, a sensitivity analysis of the most influencing parameter should declare its limitations. Therefore, the influence of the phase fraction threshold α_t, the droplet resolution $C_d = \frac{d_0}{\Delta x}$ and the Courant number [Co, see (18.12)] to the normalized volume V^* are investigated and illustrated in Fig. 18.15b. The reference configuration (blue) is defined by $\alpha_t = 0.05$, $C_d = 16$ and $\mathrm{Co} = 0.1$. Alternative 1 (green) has a reduced droplet resolution of $C_d = 8$ and alternative 2 (red) has a increased Courant number of $\mathrm{Co} = 0.5$ compared to the reference. The remaining variables are equal to the reference. Figure 18.15b shows comparable trends for the different configurations. With rising phase fraction threshold increases the deviation of the tracked particle volume to the initialized. Regarding the reference configuration, the normalized volume differs ≈8% for the maximal tested phase fraction threshold. However, compared to the alternatives it shows less aberration and a low standard deviation. Less stringent adjustments for the droplet resolution and Co (green and red line) highly impair the particle volume detection. With rising phase fraction threshold, the difference to the reference results increases. Furthermore, the standard deviation is significantly influenced. In summary, the phase fraction threshold is the most critical parameter, which can highly influence the tracking results in VOF simulations. For further details, the reader is referred to the work of Spitzenberger et al. [13].

18.3.3 Flame Spraying

Flame Spraying is a coating technique, where steel and ceramic powders or sintered rods are molten to droplets and sprayed on a substrate. During flame spraying, the hot gas mixture is combusted in order to melt the coating material, which is either feeded

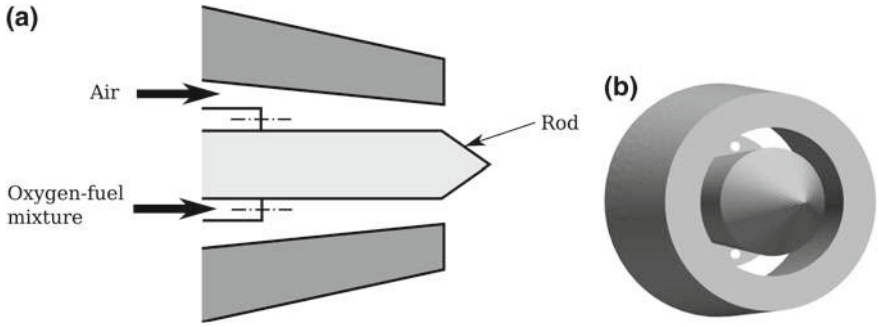

Fig. 18.16 **a** Sketch of the nozzle with an annular air inlet and orifices for the oxygen-fuel mixture inlet and **b** front view of the 3D nozzle geometry

as powder or a sintered rod. The air stream then atomizes the molten material and carries the droplets towards the substrate. For the basic principle of thermal spraying techniques, the reader is referred to the literature [32]. This technique is shown as an example for the need of Lagrangian particle tracking.

In the CFD model, the process is subdivided into two decoupled calculations for gas and droplet injection. At first, an oxygen-fuel mixture and air are injected through different inlets in the nozzle. An annular orifice is used for the air while the oxygen-fuel mixture enters through twelve circular orifices. Figure 18.16a shows a sketch of the nozzle geometry, and Fig. 18.16b a 3D view of the nozzle used in the simulation. In the CFD model, combustion and melting are not taken into account. The hot oxygen-fuel mixture and cold air are injected in the nozzle and subsequently form a free jet. The hot mixture streams towards the substrate, whereas the temperature and velocity fields are calculated in a steady state simulation. An example of the resulting velocity field is shown in Fig. 18.17.

Since combustion, melting and atomization are not calculated in this model, Lagrangian particles are injected into the domain at the rod tip in the second part of the simulation. Therefore, the particle size distribution of the introduced melt droplets needs to be predefined. It can be estimated through upstream calculations of the gas atomization (Sect. 18.3.1) and tracking of the particle sizes (Sect. 18.3.2). This approach is most accurate for powder flame spraying processes, where the powder is used directly instead of the intermediate sintering into rigid rods. Therefore, in the case of rod flame spraying, Gaussian distribution with an estimated mean diameter can be used alternatively.

After introducing the droplets into the domain, they are carried by the pre-calculated gas jet toward the substrate and impact and stick to its surface. Figure 18.18 visualizes this process. The impact of the Lagrangian particles is only sufficient to estimate the location of the coating. In order to calculate the actual coating buildup, the Lagrangian point particles need to be transformed into particles with finite sizes that are able to deform and solidify after the surface impact. This procedure is part

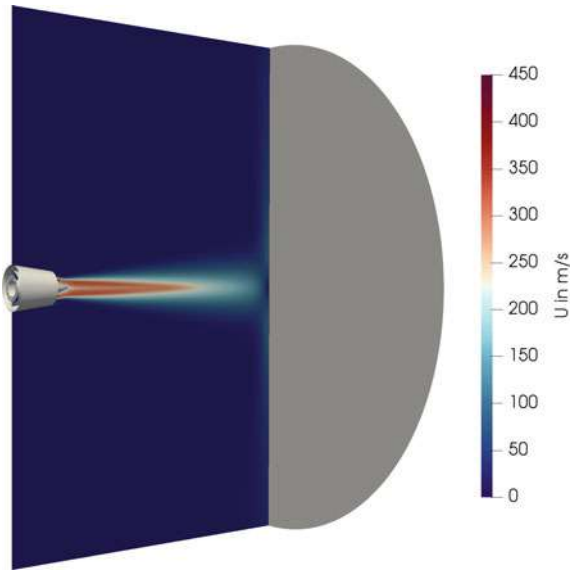

Fig. 18.17 Velocity field of the free gas jet behind the flame spraying nozzle

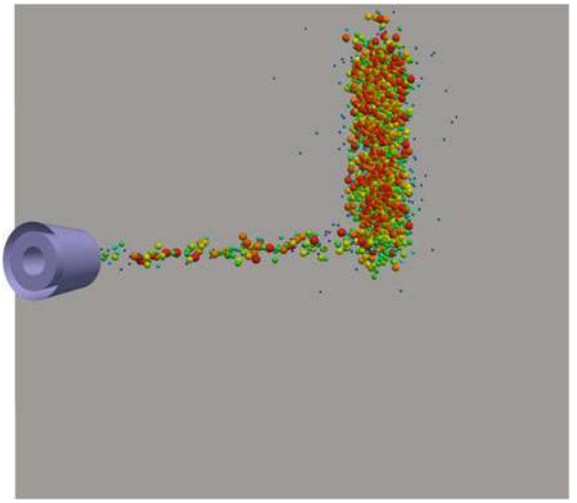

Fig. 18.18 Flight of the Lagrangian droplets behind the flame spraying nozzle and impact on the substrate. Droplets are colored by their size and are oversized for visualization

of ongoing studies. Furthermore, more accurate particle size distributions could be achieved by directly measuring the particles after flame spraying.

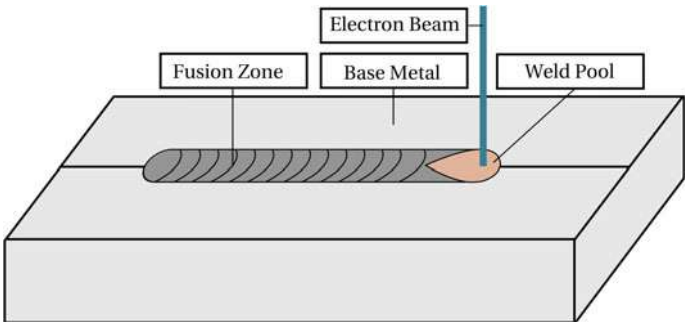

Fig. 18.19 Sketch of the physical domain during EB welding with essential regions for consideration within the numerical model

18.4 Electron Beam Welding

Experimental investigations of EB welding of TRIP-steels and TRIP-Matrix-Composites are thoroughly described by Halbauer and Buchwalder (Chap. 10). While Buchwalder et al. has already proven the excellent weldability of CrMnNi cast-steels [1], Halbauer et al. intensified the investigations for cold-rolled steels [33] and dissimilar joints [34, 35]. The numerical models described here are based on their experimental work.

The basis for numerical investigations of EB welding are, on the one hand, underlying physical effects, and on the other hand, the experimental conditions. The former are described by fundamental mathematical equations and their translation into numerical equations via discretization on finite grids that reproduce the experimental domain. The latter are described by the structure and components of the domain and boundary and initial conditions. Recently, a comprehensive CFD study of the melt flow and keyhole dynamics was carried out by Huang et al. [36] with constant thermophysical properties. Furthermore, Borrmann et al. investigated the temperature sensitivity of the thermophysical properties of X3CrMnNi 16-7-6 TRIP-steel during EB welding [37] and the coupling between steel melt and ceramic particles in EB welding of TRIP-Matrix-Composites [38] in their CFD simulations.

The basic domain for EB welding simulations can be seen in Fig. 18.19. It sketches the essential parts of the welding process that need to be taken into account.

The welding seam is produced by heating the base material up to the melting point. As a result, a tear-drop-shaped weld pool forms. When the melt cools down at the trailing edge of the weld pool, it solidifies and forms the fusion zone. The in-depth weld pool and fusion zone shapes are illustrated in Fig. 18.20. It is evident that the geometry is highly anisotropic and therefore its three-dimensional character needs to be considered.

In the experiments, the weld pool is formed in consequence of the EB energy input, which has a highly transient behavior. In order to reduce computational costs to an acceptable level, the EB is not resolved as such. Instead, a heat source is

Fig. 18.20 3D-view of fusion zone (dark grey) and molten weld pool (red)

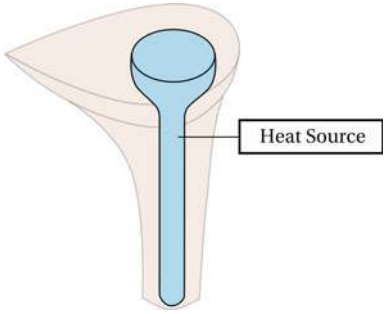

Fig. 18.21 Sketch of the heat source (light blue) inside the weld pool (red). It is used for modeling the heat input, rather than calculating the electron beam itself

operated, which mimics the EB heat input into the material. Figure 18.21 sketches its basic idea. The value and form of the heat source is constant throughout the whole simulation. However, the form of the weld pool is varying over time.

Detailed explanations of the physical effects and their numerical implementations are described in the following sections.

18.4.1 Phase Change and Heat Source Model

The increased complexity of the physical problem that arises as a consequence of heating and phase change requires additional source terms. For this reason, the fundamental equations (18.2) and (18.3) were extended, based on the elaborations of Voller and Prakash [39], Rösler and Brüggemann [40], and Miehe [41]. The momentum equation (18.2) is extended by the source term S_m, which accounts for the solid fraction and damps flow in solid and partially solid regions:

$$S_\mathrm{m} = -\frac{\nu}{d^2}\frac{f_\mathrm{s}^2}{(1-f_\mathrm{s})^3 + c_2}, \tag{18.16}$$

and the source term S_b, which accounts for the Boussinesq approximation, with which the density dependents linearly on the temperature in the gravity term:

$$S_\mathrm{b} = \boldsymbol{g}[1 - \beta(T - T_\mathrm{liq})]. \tag{18.17}$$

In the preceding source terms, d is a characteristic length scale of the solid material like e.g. a grain size, f_s represents the solid fraction, which lies in between 0 and 1,

c_2 is a numerical constant to prevent division by zero for $f_s = 1$, $\boldsymbol{g}$ is the gravitational acceleration, β is the thermal expansion coefficient and T and T_{liq} are the temperature of the fluid element and the liquidus temperature, respectively. Extending (18.2) with (18.16) and (18.17) leads to the final momentum equation that is solved in the EB welding model:

$$\frac{\partial \boldsymbol{u}}{\partial t} + \nabla \cdot (\boldsymbol{u}\boldsymbol{u}) = -\frac{1}{\varrho_0}\nabla p + \nabla \cdot (\nu \nabla \boldsymbol{u}) + S_m + S_b. \tag{18.18}$$

To account for the latent heat of fusion H_ℓ during melting and solidification, (18.3) is extended by the source term S_ℓ, which is denoted as:

$$S_\ell = H_\ell \left(\frac{\partial f_s}{\partial t} + \nabla \cdot (\boldsymbol{u} f_s) \right), \tag{18.19}$$

Additionally, the heat source term S_q, which is sketched in Fig. 18.21 is added to the energy conservation equation:

$$S_q = \frac{1}{\varrho} q(x, y, z). \tag{18.20}$$

Combining (18.3), (18.19) and (18.20) leads to the form:

$$c_p \frac{\partial T}{\partial t} + c_p \nabla \cdot (\boldsymbol{u} T) = \frac{1}{\varrho} \nabla \cdot (k \nabla T) + S_\ell + S_q, \tag{18.21}$$

which is solved in the numerical model for EB welding.

The heat source model is responsible for forming the weld pool during melting and subsequently the fusion zone after solidification. Because of the complex shape of the welding seam, which the heat source needs to mimic, it consists of a double ellipsoidal part for the weld nail head and a conical part for the middle and lower region, as proposed by Lundbäck and Runnemalm [42]. The double ellipsoidal part q_e, recommended by Goldak et al. [43], was used:

$$q_e(x, y, z) = \frac{6\sqrt{3} Q_{in}}{a_e b_e c_e \pi^{3/2}} \exp\left(\frac{-3x^2}{a_e^2}\right) \exp\left(\frac{-3y^2}{b_e^2}\right) \exp\left(\frac{-3z^2}{c_e^2}\right). \tag{18.22}$$

The conical part q_c is:

$$q_c(x, y, z) = \frac{6 Q_{in}}{a_c b_c c_c \pi (1 + d_c)} \exp\left(\frac{-3x^2}{a_c^2}\right) \left[1 - \frac{(1 - d_c)|y|}{b_c}\right] \exp\left(\frac{-3z^2}{c_c^2}\right). \tag{18.23}$$

Here, Q_{in} is the heat, which is produced by the electron beam, $a_{c/e}$, $b_{c/e}$, and $c_{c/e}$ are the width, height and length of the heat source parts conical c and double ellipsoidal e, respectively. x, y and z are the Cartesian coordinates and d_c is the narrowing of

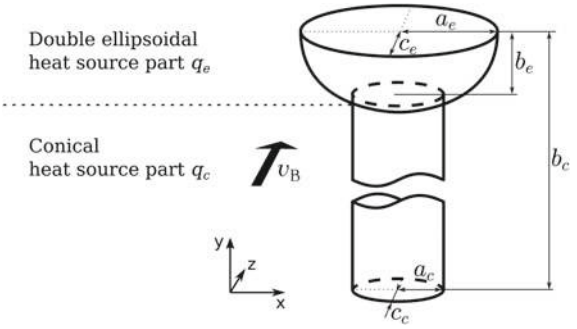

Fig. 18.22 Heat source geometry with the geometrical heat source parameters that define the size of the individual heat source parts [37]

Table 18.1 Material composition of the X3CrMnNi 16-7-6 TRIP-steel

	C	Cr	Mn	Ni	Si	Fe
Mass fraction w_t (%)	0.044	16.2	7.07	6.52	0.88	Bal.

the conical part, if its diameter is decreasing with depth. Figure 18.22 illustrates the heat source geometry and the related parameters.

Combining (18.22) and (18.23) leads to

$$q(x, y, z) = \gamma q_e(x, y, z) + (1 - \gamma) q_c(x, y, z), \tag{18.24}$$

with the weighting factor γ. Then, (18.24) is inserted into (18.20).

The fundamental equations (18.18) and (18.21) were discretized with FVM with second order accuracy schemes. For thorough details about the numerical model, and the values of all thermophysical properties, the reader is referred to Borrmann et al. [37].

The introduced model was used to calculate the formation of the weld pool and subsequently the fusion zone of a welding seam that has been produced experimentally beforehand. The chemical composition of the welded base metal is shown in Table 18.1. Based on this composition, temperature dependent thermophysical properties were derived and transferred to the numerical model. Details about these properties and their importance are described by Borrmann et al. [37].

In order to determine target values for the outcome of the numerical model, welding seams have been produced within a vacuum chamber. The related parameters, which are deduced from the evaluation of the welds, are listed in Table 18.2. A cross section of the welding seam that is used here is shown in Fig. 18.23. The typical fusion zone geometry with upper nail head and long and narrow middle and bottom part is clearly recognizable. The weld reinforcement and root are also apparent in the experimental cross section. However, in the numerical simulation those are not considered.

Due to melt convection and heat conduction, the weld pool enlarges over time and therefore, the related heat source needs to be significantly smaller than the weld pool.

Table 18.2 Welding conditions and geometrical dimensions of the weld cross section

Weld geometry	Unit	Value
Beam voltage U_B	kV	80
Beam current I_B	mA	40
Efficiency η	–	0.9
Heat input Q_{in}	W	2880
Nail head width w_{NH}	mm	2.35
Nail head height h_{NH}	mm	1.40
Weld width w_{WS}	mm	0.70
Weld height h_{WS}	mm	10.0

Table 18.3 Heat source geometry parameters

γ (%)	a_e (mm)	b_e (mm)	c_e (mm)	a_c (mm)	b_c (mm)	c_c (mm)	d_c (%)
0.38	1.18	1.40	1.18	0.12	10	0.12	1

Appropriate parameters are shown in Table 18.3. Figure 18.24 illustrates the coherence between heat source and weld pool. Due to the choice of heat source parameters, the upper double-ellipsoidal part of the heat source appears as a hemisphere, which is significantly smaller than the nail head of the weld pool. This applies for length, width and depth, likewise. The conical part of the heat source is noticeably smaller as well.

During the transient simulation, the weld pool and fusion zone are created gradually. Figure 18.25 shows process snapshots for four consecutive points in time. At the beginning of the simulation, the base material is heated exactly at the location of the heat source. The melting follows this behavior and therefore, the weld pool is shaped according to the heat source geometry in Fig. 18.25a. In the process of time, the weld pool widens and prolongs due to heat transfer through convection in the weld pool, heat conduction and further melting of the base material. This can be seen in Fig. 18.25b, c. Furthermore, the weld pool clearly solidifies and builds the fusion zone, which is indicated as a new area in blue. At later time steps, the geometry of the weld pool and fusion zone sustains, as seen in Fig. 18.25d. The cross section of the welding seam can be obtained once the weld pool is solidified and the fusion zone is formed. Comparing it to the experimental weld geometry, see Fig. 18.26, reveals the accordance between experiment and numerical model. Further examples for weld geometries can be found in Borrmann et al. [37].

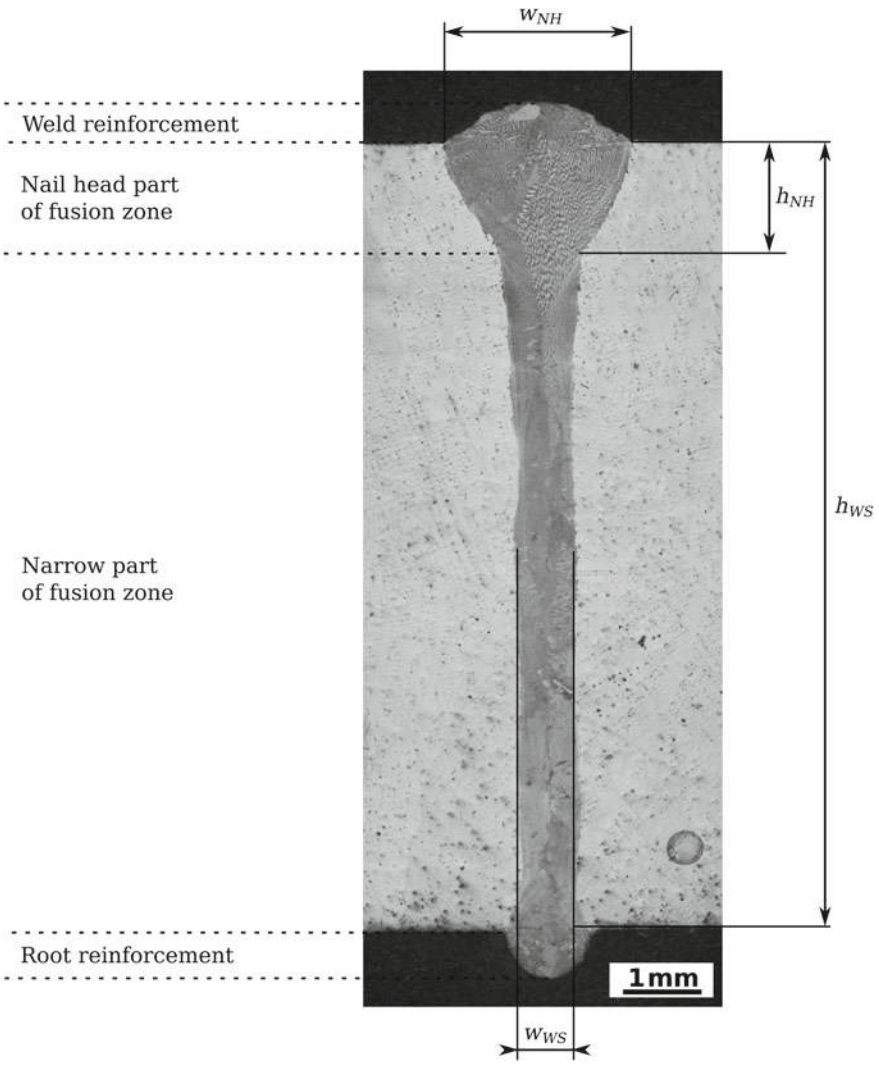

Fig. 18.23 Cross section of the experimentally obtained EB welding seam with definitions of fusion zone areas and dimensions [37]

18.4.2 Influence of Keyhole on Fluid Flow

In EB welding, the formation of a vapor column, the so called keyhole, plays an important roll for the formation of deep welds. The necessity to perform EB welding under very low ambient pressure, like in our experiments $p_A = 2\,\text{Pa}$, leads to a physical particularity during vaporization. The saturated vapor pressure $p_{s,0}$, which is the balanced pressure that determines the related vaporization temperature $T_{s,0}$, is

Fig. 18.24 Heat source (dark blue) and weld pool (red) that forms due to heat conduction and convection during the simulation

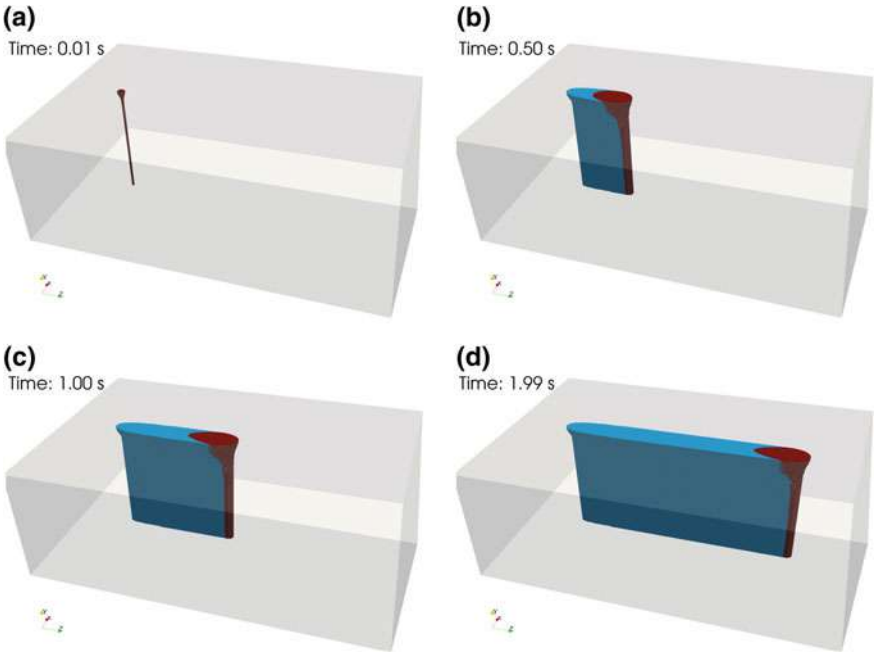

Fig. 18.25 States of the material at four different time steps (**a** $t = 0.01$ s, **b** $t = 0.50$ s, **c** $t = 1.00$ s, **d** $t = 1.99$ s) during the simulation: weld pool (red), welding seam (blue) and base material (light grey)

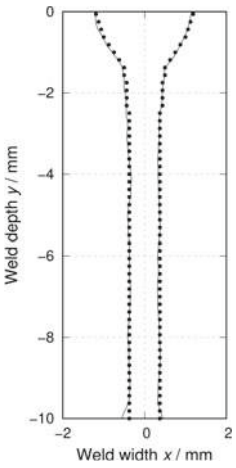

Fig. 18.26 Comparison of the welding seam cross sections of experiment (solid line) and simulation (dotted line) [37]

significantly lower than the pressure p_0 with vaporization temperature T_0 under standard conditions. $p_{s,0}$ is composed of the ambient pressure, the hydrostatic pressure of the steel column, and the dynamic pressure, which is affected by the melt flow velocity. Depending on the locally balanced $p_{s,0}$, $T_{s,0}$ can be calculated by using the simplified Clausius-Clapeyron equation [44]:

$$\ln \frac{p_{s,0}}{p_0} = \frac{\Delta H_{m,v}}{R} \left(\frac{1}{T_{vap}} - \frac{1}{T_{s,0}} \right). \tag{18.25}$$

Solving (18.25) for $T_{s,0}$ leads to:

$$T_{s,0} = \frac{1}{\frac{1}{T_0} - \frac{R}{\Delta H_{m,v}} \ln \left(\frac{p_{s,0}}{p_0} \right)}. \tag{18.26}$$

Since $T_{s,0}$ is considerably lower than T_0, vaporization occurs a lot earlier and closer to the melting temperature.

Due to the low ambient pressure, the hydrostatic pressure of the steel melt column gains in importance. Therefore, the vaporization temperature increases noticeably with increasing depth, due to a rising steel melt column. Additionally, the melting occurs very rapidly during EB welding with very high beam intensities. This leads to an overheating of the steel regarding its vaporization temperature $T_{s,0}$ to an increased vaporization temperature T_s. As a consequence of the overheating, the vapor pressure after vaporization increases noticeably. The now occurring pressure difference results in the so-called recoil pressure p_r. It might as well be solved with the Clausius-Clapeyron equation:

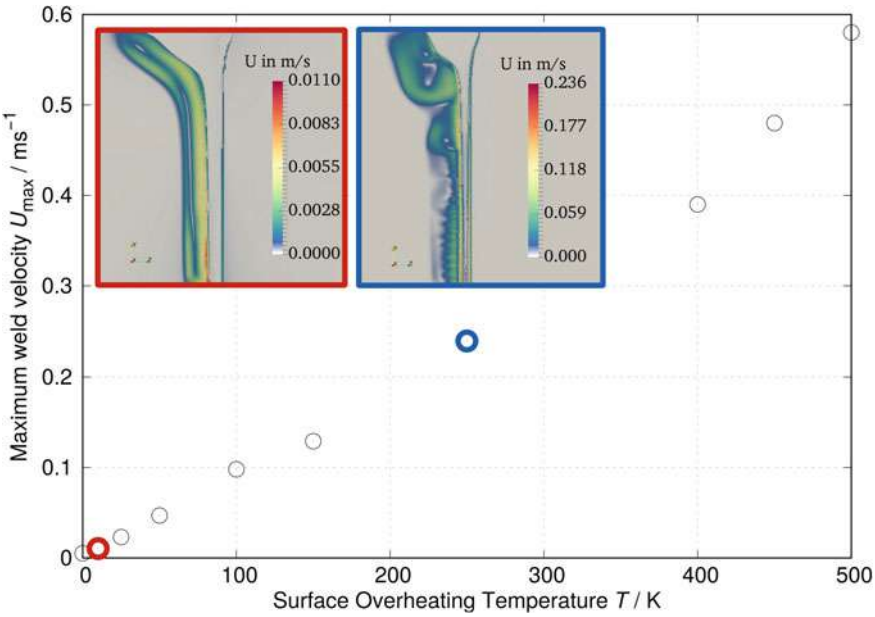

Fig. 18.27 Maximum weld velocity u_{max} as a function of surface overheating temperature ΔT. Examples are given for $\Delta T = 10\,\mathrm{K}$ (red) and $\Delta T = 250\,\mathrm{K}$ (blue)

$$p_r = p_{s,0}\left\{\exp\left[\frac{\Delta H_{m,v}}{R}\left(\frac{1}{T_{s,0}} - \frac{1}{T_s}\right)\right] - 1\right\} \tag{18.27}$$

In dependence of the overheating temperature, the recoil pressure has a significant impact on the surface velocity of the melt around the keyhole. Figure 18.27 clarifies this dependence by showing the maximum keyhole surface velocity, depending on the overheating temperature ΔT. A nearly linear correlation arises. Two example velocity profiles are given for $\Delta T = 10\,\mathrm{K}$ (red circle) and $\Delta T = 250\,\mathrm{K}$ (blue circle). The keyhole is indicated as the grey area within the weld pool. While the maximum weld velocity occurs at the keyhole surface in both cases, it is more than 20 times greater for the higher overheating temperature. Two additional effects are noticeable. Firstly, with increasing surface overheating, the keyhole tends to be tighter, because vaporization occurs at higher temperatures, whereby the keyhole has less time to develop. Secondly, the melt flow shows increased vorticity due to higher velocities and, as a consequence thereof, a higher Reynolds number. Since the simulations were performed without turbulence modeling, only vortexes that are resolvable through the mesh resolution are calculated.

The consideration of vaporization and the keyhole emergence, lead to an altered geometry of the weld cross-section in the simulation due to a widening of the weld pool. To correct this deviation, the heat source model parameters can be adjusted. In order to further refine the model, the front and rear length of the heat source,

Table 18.4 Heat source parameters for the adjusted geometry

γ (%)	a_e (mm)	b_e (mm)	$c_{e,r}$ (mm)	$c_{e,f}$ (mm)	a_c (mm)	b_c (mm)	$c_{c,r}$ (mm)	$c_{c,f}$ (mm)	d_c (%)
0.52	1.18	1.40	4.6	1.18	0.085	10	0.34	0.085	1

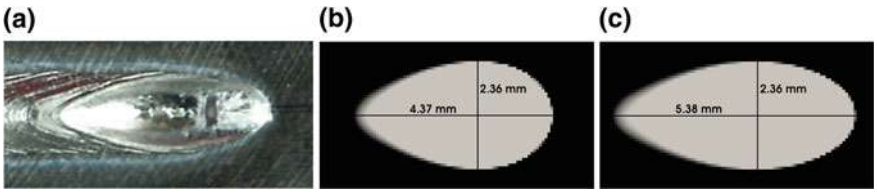

Fig. 18.28 Comparison of the solidified weld pool length in **a** the experiment with the top view of the simulated weld pool, **b** without keyhole and **c** with keyhole [37]

indicated by f and r, respectively, were adjusted according to recommendations by Goldak et al. [43]. While the front part stays half the size of the weld width, the rear part parameter is increased to the double weld width. Nevertheless, the melt pool doesn't follow the heat source specifications precisely, because of further heat conduction, convection in the melt pool, and the recoil pressure. The refined heat source parameters are shown in Table 18.4. In order to restrict the infinite expansion of the Gaussian distribution, values with less than 5% of the integral size were truncated. The clipped amount was added to the integral distribution size accordingly.

The weld pool length is indicated in Fig. 18.28. Figure 18.28a shows the experimental size, after solidification. The visible length of the solidified weld pool is 6.5 mm. Figure 18.28b, c present the weld pool sizes without and with the keyhole, respectively. While the welding seam cross section matches in both cases, the weld pool length agrees better to the experiment with using the keyhole and further heat source refinements. The relative error in case (b) is $\delta = 32.8\%$ and in case (c) $\delta = 17.2\%$. The remaining error indicates that further improvements like free surface representation together with surface tension and corresponding effects need to be considered for more precise studies.

18.4.3 Dissimilar Welding of MMC-Steel

The weldabilty of TRIP-steel has been shown to work very well [1]. The situation is different, however, for the TRIP-Matrix-Composite. Steel and ZrO_2 powder is combined to form the MMC. The presence of ZrO_2 particles in the melt leads to effects that impair the weld result, like melt ejection and cavities. We assume that direct interaction between the particles and the electron beam and the interaction with the overheated melt pool and keyhole can lead to large energy input and potentially

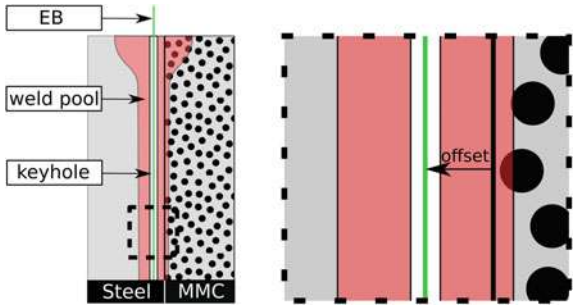

Fig. 18.29 Sketch of the dissimilar welding strategy with beam offset [38]

even rapid vaporization of the ceramic particles. In order to find solutions to ensure the weldabilty of the MMC, experimental studies were performed [34, 35]. Very good weldability was achieved, when the MMC plate was welded together with a particle-free TRIP-steel plate. By using a beam offset towards the latter, the electron beam as well as the melt pool are shifted. In that way, the disturbance of the ceramic particles is avoided. The main principle of this beam offset welding strategy is shown in Fig. 18.29. The weld pool cross-section is illustrated by the typical geometry in red. By shifting the beam as far as indicated, neither the beam, nor the emerging keyhole are interacting with the ceramic particles, illustrated as black spheres. However, they might still be present in the weld pool. In that way, they are separated from the steel matrix in the MMC and might float up or through the weld pool toward the particle-free steel. In order to investigate this behavior, the numerical model was further extended with the coupling between melt flow and ceramic particles. The necessary extensions are presented, together with parameter studies and results. For the complete numerical model and investigations, the interested reader is referred to Borrmann et al. [38].

The particle movement was driven by forces that are exerted to the particles by the melt flow. This was considered by solving their equation of motion, which reads

$$m_\mathrm{p}\frac{\mathrm{d}\mathbf{u}_\mathrm{p}}{\mathrm{d}t} = \mathbf{F}_\mathrm{B} + \mathbf{F}_\mathrm{G} + \mathbf{F}_\mathrm{D}. \tag{18.28}$$

Here, m_p is the particle mass and u_p is the particle velocity. The gravity force $\mathbf{F}_\mathrm{G}$ and buoyancy force $\mathbf{F}_\mathrm{B}$ are calculated with

$$\mathbf{F}_\mathrm{G} + \mathbf{F}_\mathrm{B} = m_\mathrm{p}\mathbf{g}\left(1 - \frac{\varrho_0}{\varrho_\mathrm{p}}\right) \tag{18.29}$$

with the particle density ϱ_p. The drag force $\mathbf{F}_\mathrm{D}$ is calculated by

$$\mathbf{F}_\mathrm{D} = \frac{1}{2}\rho_0 C_\mathrm{D} A|\mathbf{u} - \mathbf{u}_\mathrm{p}|\left(\mathbf{u} - \mathbf{u}_\mathrm{p}\right), \tag{18.30}$$

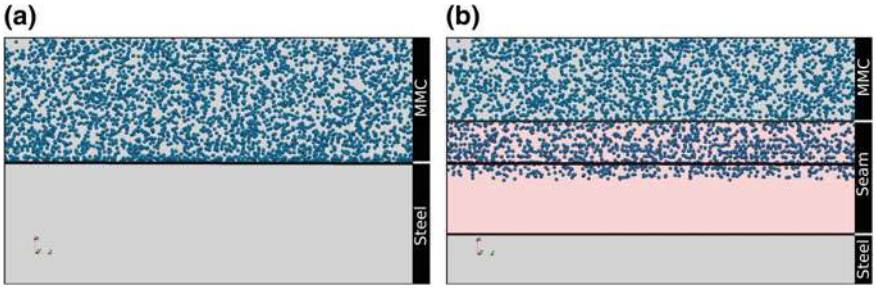

Fig. 18.30 Top view of the calculation domain **a** before and **b** after welding simulation with base material (grey) and welding seam (red). One welding partner is filled with particles (blue), the other is particle-free [37]

where C_D is the drag coefficient, and A is the representative particle area. The particles were moved in each time step subsequently to the melt flow calculation. C_D is defined with:

$$C_D = \begin{cases} 24\left(1 + \frac{1}{6}\mathrm{Re}^{\frac{2}{3}}\right) & \mathrm{Re} \leq 1000 \\ 0.424\,\mathrm{Re} & \mathrm{Re} > 1000. \end{cases} \tag{18.31}$$

Re is the particle Reynolds number, which is:

$$\mathrm{Re} = \frac{\varrho|\mathbf{u} - \mathbf{u}_p|d_p}{\eta}. \tag{18.32}$$

After the field calculations for the melt are finished, particle forces are calculated. The particles are displaced at the beginning of each time step. Figure 18.30 shows the particle displacement.

Figure 18.30a shows the top view of an initial particle distribution. The particles are generated at one half of the continuous domain on an equidistant mesh before the simulation starts. During the formation of the welding seam, particles were moved and displaced. Figure 18.30b shows the particle distribution after the end of the simulation. The welding seam, which connects the particle-free steel and the MMC, is now present. An offset of the seam reveals the offset of the heat source toward the particle-free steel. It is evident that ceramic particles were moved to a region inside the seam, where no particles were present previously.

Depending on the offset-ratio, it can be estimated if the particles would move toward the keyhole and interact with the steel vapor and the electron beam, which would still cause bad weldabilty. Therefore, different offset ratios were investigated. In Fig. 18.31, the total number of particles $n_{p,d}$ that were displaced and enriched in the previously particle-free steel is shown. Depending on the beam offset, the particle count differs significantly. The beam offset values are referring to the half of the nail head width such that for 100% offset, the welding seam is located completely on the particle-free welding partner. Between no beam offset (0%) and a small beam offset

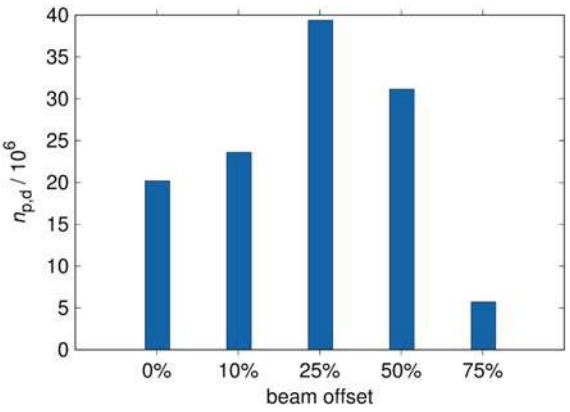

Fig. 18.31 Total number of particles that are enriched in the particle-free steel after welding in dependence of the relative beam offset [38]

(25%), the total number of enriched particles doubles. Even though less particles are extracted from the MMC in the second case, the separation is higher than in the first case, because the particles were transported towards a greater region in the particle-free steel. For higher offsets, the trend reverses and the particle enrichment decreases as the count of separated particles is much smaller than for low beam offsets. One reason for this is the fact that for high beam offsets, the total weld pool area decreases disproportionately, because the offset has a higher impact on the displacement of the narrow area of the weld pool. For the highest beam offset (75%), the narrow welding seam part is completely located at the particle-free steel welding partner, which leads to a kind of braze welding. Therefore, the total number of displaced particles decreases largely.

The number of particles in the core area of the weld pool is of special interest. The core area is defined as a cylinder with half the diameter of the narrow part of the welding seam. A comparison between the state before and after welding is shown in Fig. 18.32. It is evident that the particle-count in the core area nearly remains the same for 0 and 10% beam offset. Increasing the offset leads to a shift toward a region, where no particles were present in the initial state. However, for 25 and 50% beam offset, particles were enriched in this area, after welding. While this is possible in the simulation, for real EB welding applications, particle would interact with the electron beam and disturb the process. Because of the particle enrichment, this would even be the case for the higher beam offsets. Only for the highest investigated beam offset of 75% no particles occurred in the core of the weld pool. This means that optimal welding conditions occur for high beam offsets, where the majority of the weld pool lies on the particle-free steel side. Because of the braze welding effect, the bond of the welding partners is still given [34].

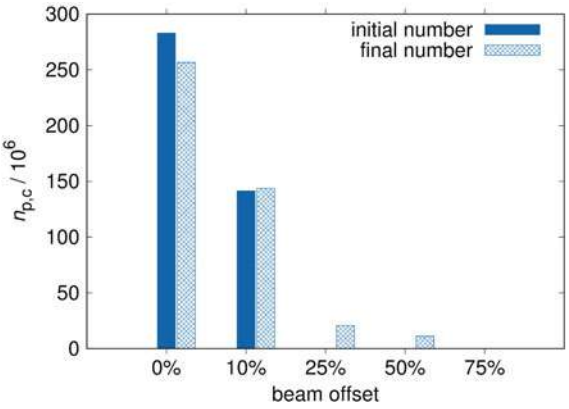

Fig. 18.32 Number of particles in the weld pool core before (solid) and after (meshed) welding [38]

18.5 Conclusion

The relevant processes for the production and further processing of TRIP-steel and TRIP-Matrix-Composites were investigated using CFD simulations. Various numerical models were implemented and existing solvers were extended.

Implementations into OpenFOAM have been made to improve stability, reduce computational costs in VOF calculations, to transform between different approaches, namely Eulerian and Lagrangian, and to calculate and couple particular physical effects. All implementations have been applied for chosen examples. The ability to calculate the infiltration of steel melt into macroscopic foam structures and free surface tracking to predict the possibility of infiltration and cavities has been achieved. The atomization model is able to predict primary breakup and reinforcing process parameters and track droplet sizes, position and velocity after primary breakup. Lagrangian particle distributions can be used to investigate sizes of coatings in flame spraying and the impacting positions and speed of droplets. The EB welding model is able to calculate weld pool shapes and melt velocities. Furthermore, the movement, depletion and accumulation of ceramic particles in the welded components can be evaluated. Through the calculation of the keyhole and therefore the penetration depth, the welding model is also able to estimate the weldability for varying EB parameters like beam intensity and feed rate.

Further extensions of the numerical models are possible. This includes the secondary breakup of the Lagrangian phase particles during gas atomization to get final particle size distributions. Furthermore, the coating buildup during flame spraying can be achieved with a reverse particle tracking algorithm which creates VOF droplets from Lagrangian particles. Models for solidification and surface tracking can be combined to include further effects like surface tension and Marangoni convection into the welding model and to evaluate their influence on particle-melt-interaction.

Acknowledgements Gefördert durch die Deutsche Forschungsgemeinschaft (DFG)—Projektnummer 54473466—SFB 799 (Funded by the Deutsche Forschungsgemeinschaft (DFG,

German Research Foundation)—Projektnummer 54473466—SFB 799). The authors thank Jens Klostermann under co-supervision of Prof. Christoph Brücker for his fundamental work in SFB 799, subproject C1 and for setting the course for the further developments in the present research. The following subprojects that particularly supported our work are highly acknowledged: A1, A2, A7, C2, C5, and T4. The authors want to explicitly thank all the contributors to the models and results that have been presented in this chapter: Richard Acker, Amjad Asad, Horst Biermann, Kinnor Chattopadhyay, Tobias Dubberstein, Patrick Gehre, Lars Halbauer, Martin Heinrich, Christoph Kratzsch, Markus Radajewski, Paul Rähmer, Ivan Saenko, Andy Spitzenberger, Marco Weider, Anja Weidner, and Christian Weigelt. The computations were performed on a Bull Cluster at the Center for Information Services and High Performance Computing (ZIH) at TU Dresden and the High Performance Compute Cluster at University Computer Centre (URZ) at TU Bergakademie Freiberg.

References

1. A. Buchwalder, K. Rüthrich, R. Zenker, H. Biermann, Adv. Eng. Mater. **15**, 566 (2013)
2. J.H. Ferziger, M. Perić, *Computational Methods for Fluid Dynamics* (Springer, Berlin, 1996)
3. H.K. Versteeg, W. Malalasekera, *An introduction to Computational Fluid Dynamics: The Finite*, vol. method, 2nd edn. (Pearson, Harlow, 2007)
4. H.G. Weller, G. Tabor, H. Jasak, C. Fureby, Comput. Phys. **12**, 620 (1998)
5. J. Klostermann, K. Schaake, R. Schwarze, Int. J. Numer. Meth. Fluids **71**, 960 (2013)
6. M. Weider, K. Eigenfeld, Steel Res. Int. **82**, 1064 (2011)
7. J. Klostermann, R. Schwarze, M. Weider, C. Brücker, Steel Res. Int. **82**, 1113 (2011)
8. J. Klostermann, R. Schwarze, C. Brücker, Eng. Comput. **29**, 95 (2013)
9. R. Schwarze, J. Klostermann, C. Brücker, Steel Res. Int. **82**, 56 (2011)
10. R. Schwarze, J. Klostermann, Steel Res. Int. **87**, 465 (2016)
11. J. Brackbill, D. Kothe, C. Zemach, J. Comput. Phys. **100**, 335 (1992)
12. S. Neumann, T. Dubberstein, H. Chaves, C. Kirmse, R. Schwarze, Steel Res. Int. **87**, 1002 (2016)
13. A. Spitzenberger, S. Neumann, M. Heinrich, R. Schwarze, SoftwareX **11**, 100382 (2020)
14. A. Glage, S. Martin, S. Decker, C. Weigelt, M. Junghanns, C.G. Aneziris, U. Martin, L. Krüger, H. Biermann, Steel Res. Int. **83**, 554 (2012)
15. N. Ashgriz (ed.), *Handbook of Atomization and Sprays: Theory and Applications* (Springer, Boston, 2011)
16. T. Dubberstein, H.P. Heller, Steel Res. Int. **84**, 845 (2013)
17. S. Markus, U. Fritsching, K. Bauckhage, Mater. Sci. Eng. A Struct. **326**, 122 (2002)
18. J. Thompson, O. Hassan, S. Rolland, J. Sienz, Powder Technol. **291**, 75 (2016)
19. C. Kirmse, H. Chaves, Steel Res. Int. **87**, 1295 (2016)
20. M. Gorokhovski, M. Herrmann, Annu. Rev. Fluid Mech. **40**, 343 (2008)
21. K. Warncke, S. Gepperth, B. Sauer, A. Sadiki, J. Janicka, R. Koch, H.J. Bauer, Int. J. Multiphase Flow **91**, 208 (2017)
22. P.J. O'Rourke, A.A. Amsden, SAE Technical Paper, 872089 (1987)
23. F.X. Tanner, SAE Technical Paper, 970050 (1997)
24. W. Edelbauer, F. Birkhold, T. Rankel, Z. Pavlovi, P. Kolar, Comput. Fluids **157**, 294 (2017)
25. H. Grosshans, R.Z. Szász, L. Fuchs, Int. J. Numer. Methods Fluids **74**, 898 (2014)
26. M. Herrmann, J. Comput. Phys. **229**, 745 (2010)
27. Y. Ling, S. Zaleski, R. Scardovelli, Int. J. Multiphase Flow **76**, 122 (2015)
28. H. Ström, S. Sasic, O. Holm-Christensen, L.J. Shah, Int. J. Heat Fluid Flow **62**, 104 (2016)
29. A. Vallier, Ph.D. thesis, Lund University, 2013
30. D. Zuzio, J.L. Estivalézes, B. DiPierro, Comput. Fluids **176**, 285 (2018)

31. OpenFOAM® v1812, https://www.openfoam.com/releases/openfoam-v1812/. Accessed 20 Dec 2018
32. P.L. Fauchais, J.V.R. Heberlein, M.I. Boulos, *Thermal Spray Fundamentals: From Powder to Part* (Springer, Boston, 2014)
33. L. Halbauer, R. Zenker, A. Weidner, A. Buchwalder, H. Biermann, Steel Res. Int. **86**, 436 (2015)
34. L. Halbauer, A. Buchwalder, R. Zenker, H. Biermann, Weld World **60**, 645 (2016)
35. L. Halbauer, R. Laubstein, M. Radajewski, A. Buchwalder, L. Krüger, H. Biermann, Adv. Eng. Mater. **21** (2018)
36. B. Huang, X. Chen, S. Pang, R. Hu, Int. J. Heat Mass Transf. **115**, 159 (2017)
37. S. Borrmann, C. Kratzsch, L. Halbauer, A. Buchwalder, H. Biermann, I. Saenko, K. Chattopadhyay, R. Schwarze, Int. J. Heat Mass Transf. **139**, 442 (2019)
38. S. Borrmann, A. Asad, L. Halbauer, A. Buchwalder, H. Biermann, R. Schwarze, Adv. Eng. Mater. **21**, 1800741 (2019)
39. V.R. Voller, C. Prakash, Int. J. Heat Mass Transf. **30**, 1709 (1987)
40. F. Rösler, D. Brüggemann, Heat Mass Transf. **47**, 1027 (2011)
41. A. Miehe, Ph.D. thesis, TU Bergakademie Freiberg, 2014
42. A. Lundbäck, H. Runnemalm, Sci. Technol. Weld. Join. **10**, 717 (2005)
43. J. Goldak, A. Chakravarti, M. Bibby, Metall. Trans. B **15**, 299 (1984)
44. A.N. Volkov, L. Zhigilei, Int. J. Heat Mass Transf. **112**, 300 (2017)